Università di Camerino

Università degli Studi di Napoli
Federico II

Consiglio Nazionale
delle Ricerche

Ph.D. program in **Quantum Technologies**
XXXVI cycle

Coordinator: Prof. Francesco Tafuri

Reprogrammable flat optics
from maskless photo-morphing of azopolymers

Ph.D. dissertation by

Francesco Reda

Settore scientifico disciplinare:
FIS-01 - Fisica sperimentale

Tutors

Dr. Stefano Luigi Oscurato

Prof. Pasqualino Maddalena

a.y. 2022/2023

Abstract

The inherent limitations of refractive optics, such as bulkiness, limited field of view, and significant size and weight, have prompted a shift toward the development of ultra-thin, cost-effective optical solutions. The adoption of flat optics is crucial for a wide range of applications, from consumer electronics such as smartphones, wearables, and virtual reality, to specialized fields such as quantum technologies, space exploration, and communication systems. As the technology landscape is expected to shift from electronic to photonic technologies that use light for information processing and data exchange, there is an urgent need for the next generation of flat optical components. These components promise to modulate the light wavefront in dimensions comparable to the wavelength of light. However, conventional manufacturing methods present several challenges, including complex lithographic processes, inefficient use of resources, generation of hazardous waste, and high energy consumption. Maskless lithography on amorphous polymers containing azobenzene molecules is emerging as a groundbreaking alternative.

This Thesis presents the development of an azomaterial-based lithography technique for the fabrication of flat diffractive optical elements with reprogrammable light response. The fabrication process is driven by a large-scale surface mass transport that occurs in azopolymers under structured light absorption, allowing the direct and all-optical inscription of reconfigurable optical devices in a single lithographic step. This process enables the fabrication of fully reconfigurable diffraction gratings with varying periodicity and chromatic dispersion, flat lenses with tunable focal lengths at low cost and high quality, and pixel-free holographic projectors, with efficient and advanced image formation capabilities. This sets the stage for future innovations in optical device fabrication, and provides a sustainable, versatile, and cost-effective pathway of prototyping and manufacturing flat optics.

Preface

This dissertation represents a review of three years of Ph.D. research conducted at the Optics of Materials Laboratory within the Department of Physics of the University of Naples Federico II. As usual in science, the research outcomes presented here have been made possible by the collaboration of many scientists who, day after day, have provided the foundations on which this work is based.

Foremost, my deepest gratitude goes to Prof. Pasqualino Maddalena, who has guided me from my first exams in experimental Physics through my bachelor's and master's degrees, despite our strong incompatibility in terms of football allegiance. I would also like to thank to Dr. Marcella Salvatore, with whom I have shared many scientific goals. Thank you for the hours we spent in the lab aligning our optical setups -usually followed by a quick disassembly - and for the efforts dedicated to the optimization of the interference experiments. Thanks for everything you have taught to me. I extend my thanks to Prof. Fabio Borbone for his enlightening work on the chemistry of azopolymers, without which no scientific results would have been possible. Thanks also to my fellow doctoral colleagues, with a special mention to Komang Januariyasa, with whom I shared many hours in the lab.

During my Ph.D. program, in the summer of 2022, I had the opportunity to be hosted at the University of Tampere in Finland. This experience was invaluable in broadening my horizons and strengthening international collaborations. I am grateful to Prof. Arri Priimägi, Dr. Alex Berdin and all the researchers in the SPM group for their hospitality and for this constructive time.

I express my deep appreciation to the reviewers of this work, Prof. David J. McGee of The College of New Jersey, and Prof. Svetlana Santer of the University of Potsdam, for their meticulous evaluation and constructive feedback.

I would like to take these final words to dedicate this work to Dr. Stefano Luigi Oscurato as a small token for all he has done for me. I am deeply grateful for the countless hours he invested in our discussions, and the insightful feedback he provided me. His high standards, commitment to excellence, and the way he challenged me to think critically were instrumental in my growth from student to researcher. The work presented in these pages reflects the knowledge, skills, and dedication he instilled in me, with the hope that his influence will continue to guide me as a scientist. Thank you for being an extraordinary mentor and source of inspiration.

Francesco Reda

Napoli – March 2024

Table of contents

List of abbreviations and symbols

AFM	Atomic Force Microscope
CGH	Computer Generated Holography (or Hologram)
c-PZP	cosinusoidal Phase Zone Plate
DE	Diffraction Efficiency (alternatively η)
DHM	Digital Holographic Microscopy (or Microscope)
DLW	Direct Laser Writing
DOE	Diffractive Optical Element
$\vec{E}$	Electric field
EBL	Electron Beam Lithography
EUV	Extreme Ultraviolet (lithography)
FIB	Focused Ion Beam (lithography)
$\mathcal{FT}$	Fourier transform
GS	Gerchberg–Saxton (algorithm)
∇	Gradient
Δh	Modulation depth
i	Imaginary unit
I	Intensity, precisely irradiance (power per area)
IFTA	Iterative Fourier Transform Algorithm
λ	Wavelength
n	Refractive index
NIL	Nanoimprint Lithography
SLM	Spatial Light Modulator
SPL	Scanning Probe Lithography
SRG	Surface Relief Grating
OFS	Optical Fourier Surface
OL	Optical lithography
PDMS	Polydimethylsiloxane
PMMA	Polymethylmethacrylate

List of publications

Publication I: M. Salvatore, F. Borbone, **F. Reda**, P. Maddalena, and S. L. Oscurato, *Programmable surface anisotropy from polarization-driven azopolymer reconfiguration*, Journal of Physics: Photonics 3(3), 034013 (2021).

Publication II: F. Borbone, S. Luigi Oscurato, S. D. Sorbo, F. Pota, M. Salvatore, **F. Reda**, P. Maddalena, R. Centore, and A. Ambrosio, *Enhanced photoinduced mass migration in supramolecular azopolymers by H-bond driven positional constraint*, Journal of Materials Chemistry C 9(34), 11368–11375 (2021).

Publication III: S. L. Oscurato, **F. Reda**, M. Salvatore, F. Borbone, P. Maddalena, and A. Ambrosio, *Large-scale multiplexed azopolymer gratings with engineered diffraction behavior*, Advanced Materials Interfaces 2101375, 1–9 (2021).

Publication IV: **F. Reda**, M. Salvatore, F. Borbone, P. Maddalena, and S. L. Oscurato, *Accurate morphology-related diffraction behavior of light-induced surface relief gratings on azopolymers*, ACS Materials Letters 4(5), 953–959 (2022).

Publication V: S. L. Oscurato, **F. Reda**, M. Salvatore, F. Borbone, P. Maddalena, and A. Ambrosio, *Shapeshifting diffractive optical devices*, Laser & Photonics Reviews 16(4), 2100514 (2022).

Publication VI: **F. Reda**, M. Salvatore, F. Borbone, P. Maddalena, A. Ambrosio, and S. L. Oscurato, *Varifocal diffractive lenses for multi-depth microscope imaging*, Optics Express, 30(8), 12695–12711 (2022).

Publication VII: S. Fusco, S. L. Oscurato, M. Salvatore, **F. Reda**, S. Moujdi, M. De Oliveira, A. Ambrosio, R. Centore, and F. Borbone, *Efficient high-refractive-index azobenzene dendrimers based on a hierarchical supramolecular approach*, Chemistry of Materials 35(9), 3722–3730 (2023).

Publication VIII: M. Salvatore, **F. Reda**, F. Borbone, I. K. Januariyasa, P. Maddalena, and S. L. Oscurato, *Diffractive refractometer based on scalar theory*, Polymers 15(7), 1605 (2023).

Publication IX: **F. Reda**, M. Salvatore, M. Astarita, F. Borbone, and S. L. Oscurato, *Reprogrammable holograms from maskless surface photomorphing*, Advanced Optical Materials 11(21), 2300823 (2023).

Conference proceedings:

- **F. Reda**, M. Salvatore, F. Borbone, and S. L. Oscurato, *Reprogrammable diffractive micro-optical elements*, in Advanced Fabrication Technologies for Micro/Nano Optics and Photonics XVI, G. Von Freymann, E. Blasco, and D. Chanda, eds. (SPIE, 2023), p. 15.

- M. Salvatore, **F. Reda**, F. Borbone, P. Maddalena, and S. L. Oscurato, *Multiplexed surface reliefs on azopolymer thin films*, in Photosensitive Materials and Their Applications II (SPIE, 2022), 12151, pp. 77–83.

- S. L. Oscurato, **F. Reda**, M. Salvatore, F. Borbone, P. Maddalena, and A. Ambrosio, *Light-induced structuration of azopolymer films for reconfigurable diffractive optical elements*, in Conference on Lasers and Electro-Optics (2022), Paper SM3P.3 (Optica Publishing Group, 2022).

- M. Salvatore, **F. Reda**, F. Borbone, P. Maddalena, and S. L. Oscurato, *Photoinduced surface reshaping from azopolymer micropillars with programmable anisotropy*, in Conference on Lasers and Electro-Optics (2022), Paper SM3P.2 (Optica Publishing Group, 2022).

1

Introduction

From the earliest cave paintings to the most advanced semiconductor manufacturing processes, the art and science of surface engineering has played a central role in the evolution of human civilization.

Over the course of evolution, both animals and plants have developed a wide variety of structures to ensure their interaction with the environment, including the ability to modulate light. This can be achieved through micro- and nanostructures that bend, reflect, and scatter light to produce color without pigments.[1] For example, light waves interfering with surface microstructures on the wings of a *Morpho butterfly* produce its signature iridescent blue.[2] This natural ability to manipulate light serves as a profound inspiration for human research advances.[3] It outlines a pathway that aims first to replicate and subsequently extend the solutions observed in nature and then to extend them to new emerging frontiers. This ambition is driven by the expected transition from electronics to photonics, which will represent a significant leap in technological evolution. In the field of IoT, photonics can facilitate the development of more efficient and faster communication between devices, enhancing connectivity and functionality in smart homes, industries, and cities.[4] Similarly, in quantum computing, photonics plays a crucial role in the development of systems that use the principles of quantum mechanics to perform computations at speeds unattainable by conventional computers.[5] Optical elements have traditionally been represented by refractive components such as glass-made prisms and lenses. They have been represented the core of optical systems, allowing us to access the cosmos or the micro-world with the advent of telescopes and microscopes, respectively.[6,7] Despite their effectiveness, refractive optics impose several limitations in terms of size, weight, and optical performance. The advent of flat optical elements has been a transformative shift,[8–10] and it is linked to the revolution that quietly began more than 200 years ago with the fabrication of the first diffraction grating.[11] A diffraction grating is an optical component with a regular pattern of closely spaced lines, apertures, or microstructures, with a scale size comparable to the wavelength of light.[12,13] When light interacts with the microstructures, it is shifted or dispersed in a manner complementary to refractive prisms, but in this case the mechanism responsible for these effects is diffraction. Despite their longstanding development, diffraction gratings remain a key technology,[14] because they enable the miniaturization of optical systems, such as spectrometers,[15]

where light needs to be dispersed. This ability to miniaturize and integrate into devices such as smartphones[16] or tissue-detection systems[17] marks a significant advance that was once considered unimaginable, and demonstrates the innovation that diffraction gratings can bring to modern optical applications.

Diffraction gratings pioneered a new era in photonics by introducing the principle of manipulating light through diffraction, paving the way for the advent of Diffractive Optical Elements (DOEs) for light shaping.[18,19] Diffractive lenses took this revolution a step further by using the phenomenon of diffraction to precisely focus and shape light beams by changing the amplitude or phase of incoming light waves.[20] They can even outperform standard refractive lenses in terms of functionality. In hybrid refractive-diffractive systems, diffractive lenses with complementary dispersion properties to that of glass can be used to correct chromatic aberrations.[21] Alternatively, they can be combined with polarization optics to implement vector diffractive optical elements such as full-Stokes parameter sensors.[22] Their design can be further extended and empowered by deep learning models,[23] to achieve the light focusing beyond the diffraction limit from light superoscillations,[24] or to develop diffractive lenses capable of broadband achromatic imaging.[25] For these reasons, flat lenses are listed among the world's top ten most promising technologies.[26] The main advantage of flat diffractive optics over their standard counterparts is the possibility to design planar components capable of arbitrarily shaping of an incident light wavefront, enabling the next generation of displays and holographic projectors.[27–29] In addition, DOEs are inherently thin and flat, with typical sizes on the scale of light wavelength, making them significantly more compact and lightweight than refractive components. By integrating multiple functions into a single diffractive element, optical systems can be simplified, reducing the number of optical components, alignment challenges, and size.[8] This advantage is particularly critical for applications where size and weight constraints are paramount. Photonic devices designed for space exploration are a notable example. Here, additional weight and size are severe limitations. In this field, diffractive optical elements have proven to be the core component of space telescopes,[30,31] and even at the basis of solar sails.[32,33] Several other technological fields can benefit from DOEs, such as virtual and augmented reality,[34–36] green energy harvesting,[37] healthcare[38,39] and, most notably, quantum photonics.[40,41]

Despite the enormous applicability of DOEs, the landscape of flat optical components has been dominated by metasurfaces in recent years. Metasurfaces are artificially structured thin films with subwavelength features. The geometry and the orientation of these subwavelength resonators induce a phase shift in the incident wavefront of light, allowing a full control of light propagation, including phase, amplitude, and polarization.[42–44] Metasurfaces have been used to implement various optical components, including blazed gratings,[45,46] lenses,[47–49] and holograms,[50–52] with unprecedented functionalities and applications.[53] Compared to DOEs, metasurfaces face more demanding design and fabrication processes that are complex and resource-intensive.[54] This complexity arises from the intricate structures of metasurfaces, which require precise engineering and fabrication at the nanoscale to achieve their novel light manipulation capabilities. As a result, the development of metasurfaces entails significant challenges, including higher costs and longer production times. Consequently,

despite the theoretical advantages of metasurfaces in terms of their superior control of light, the practical advantages of these surfaces over traditional DOEs for conventional applications, such as imaging, remain a subject of ongoing debate within the scientific community.[55–57]

The enhanced performance of planar optical elements is achieved at the cost of precise surface geometries, which must be manufactured at the (sub-)wavelength scale, using fabrication processes similar to those employed in the chip industry. Optical lithography and e-beam lithography stand out as the dominant fabrication techniques for planar optics.[13,58,59] The conventional fabrication workflow of optical lithography begins with the exposure of a photoresist to UV light, which is patterned by a photomask.[60] Electron beam lithography replaces this process with an electron beam raster scanning, resulting in a higher lateral resolution,[59,61] typically required for metasurfaces fabrication.[54] Optical lithography methods are generally more resource efficient than e-beam lithography, offering higher throughput and lower cost, at the expense of limited resolution. After exposure, a series of chemical, physical, and thermal treatments are typically required to transfer the pattern to a suitable substrate capable of modulating light.[58] This is a significant challenge, as this methodology is associated with the generation of waste products, including residual materials and chemicals that pose a significant health risk to those involved in the manufacturing process.[62] In addition, the need for high-resolution equipment for the photomasks fabrication,[63] as well as the requirement for cleanroom conditions,[13] further compounds the complexity and cost of those standard process. Advances to improve sustainability include the adoption of nanoimprint lithography,[64,65] or scanning probe approaches[66,67] which remain severely limited by mask dependency and extremely low throughput, respectively. Another key limitation of conventional lithographic techniques is that they inherently produce static surface geometries. This means that the functionality of a planar optical device is frozen at the fabrication stage, limiting its adaptability to future requirements or applications. Currently, liquid crystal technology stands as the only method to implement fully reconfigurable DOEs, although it faces significant challenges in terms of electronics and miniaturization.[28] Conversely, experimental efforts have been directed at enabling the post-fabrication tuning of metasurfaces to provide them with adjustable functionalities, however the tunability range that can be achieved remain limited.[68–71]

As a result, the development of *fully reprogrammable planar optical components*, manufactured using a scalable and environmentally sustainable methodology remains a challenge.

1.1 Research motivations

The Ph.D. program in "Quantum Technologies" aims to foster a new scientific awareness based on interdisciplinary skills useful for the development of quantum devices and technologies. This approach is crucial, especially considering the current landscape where quantum computing resources are only accessible to large corporations and research institutions. From a purely photonic perspective, the gap between the

theoretical foundations of quantum sciences and their practical applications is significantly influenced by the challenges associated with the physical implementation of quantum computers. To illustrate the scale of these challenges, consider that a functional linear optics quantum computer would require an experimental setup consisting of approximately 10^4 optical components,[72] such as beam splitters and phase shifters. Building such an extensive optical table is beyond our current capabilities and imagination, making the task seemingly insurmountable using conventional approaches. The path forward a working device therefore lies in the miniaturization and integration of all the necessary optical components, including photon sources and detectors, onto a single chip.[73] Micro- and nanostructure fabrication facilities are dominated by a few key players scattered around the world.[74] From a pure research perspective, this monopolization significantly limits the research focused on the development of novel planar optical components. This complexity arises because the design process, material synthesis, fabrication, and subsequent testing of the device may need to be carried out in different facilities, often outside the researcher's own institution and dispersed around the globe.

During my three-year Ph.D. program, my research focused on the development of a direct, all-optical, maskless lithography technique for the fabrication of fully reconfigurable diffractive optical elements. The core of my research was the use of azobenzene-containing polymers as an alternative to conventional photoresists. Amorphous azopolymer thin films incorporate azo dye molecules within their polymer chains. Absorption of UV-visible light by these molecules initiates a photoisomerization process, that causes a macroscopic mass migration within the polymer matrix. This migration results in the creation of surface relief structures, whose geometries are precisely defined by the pattern of the illuminating light and its constituent parameters such as intensity, polarization, and wavefront shape.[75] Unlike conventional photoresists, these surface relief patterns are developed directly under illumination and remain stable after the light source is turned off. This process unfolds in a single photopatterning step, eliminating the need for the post-exposure treatments required in standard lithography. By employing a simple optical setup where two beams interfere at the material surface, periodic structures acting as diffraction gratings can be produced in one all-optical step. The use of a digital light modulator, capable of generating and projecting a grayscale spatially structured intensity distribution of light onto the film surface, allows for the creation of even arbitrarily complex structures.

The essence of my research revolved around the arbitrary spatio-temporal modulation of the writing beam, laying the foundation for a maskless lithographic tool designed for the complex fabrication of DOEs. This approach brings several advantages to the field. First, the ability to generate arbitrary surface patterns by tailoring the light distribution at the azomaterial surface facilitates the fabrication of highly customized optical elements. In addition, by circumventing the conventional lithographic post-exposure steps, and eliminating the need for a physical mask, this technique significantly reduces the materials consumption and operating costs for DOEs fabrication. This direct patterning method also introduces the promising capability to test DOEs during their actual fabrication process. This integration facilitates real-time analysis and optimization of the surface geometry throughout the entire fabrication process, ensuring

that adjustments can be made instantaneously to achieve the desired results. An additional turning point in this methodology is the reconfigurability of the generated structures. It is possible to optically erase and rewrite the intended surface geometry, allowing for a dynamic modification and tuning of the optical properties of the DOEs. This feature not only increases the flexibility and utility of the fabricated devices, but also opens up new avenues for adaptive optics, where devices can be tailored in situ without the need for a physical replacement.

The proposed technique has been demonstrated and validated by experiments carried out over the last three years. This approach has enabled the fabrication of **Shapeshifting Diffractive Optical Devices** such as diffraction gratings with fully controllable and reprogrammable periodicity and geometries, diffractive lenses with variable focal lengths, and holographic projectors that can be reprogrammed on demand to generate images or encode and store encrypted information. The guiding principle of my research has been *shaping microstructures with light and shaping light with microstructures.* This dual-focus approach encapsulates the essence of not only using light as a tool to shape microstructures, but also using those microstructures to manipulate light itself.

A fundamental aspect of this research project was that it was carried out entirely within the University of Naples, without any dependence on external facilities. The research was fully conducted at the Department of Physics in the *Optics of Materials Laboratory*, headed by Dr. Stefano Luigi Oscurato and Prof. Pasqualino Maddalena. Here the azomaterial photopatterning framework for the fabrication of DOEs was developed and refined. This was also made possible through a collaborative effort with the Department of Chemistry, particularly with the research group of Prof. Fabio Borbone, responsible for the material synthesis and engineering.

1.2 Structure of the Thesis and Author's contribution

This Thesis adopts the format of an article dissertation, consisting of a four-chapter summary and a collection of nine original articles, which constitute the central body of the work. These articles, which have been published in peer-reviewed journals spanning the disciplines of optics, materials science, and chemistry, reflect the interdisciplinary nature of my research. It's important to note that while the articles are listed according to their publication dates, they are discussed in a different order within the Thesis. This deviation from chronological order is intentional, as it better represents the collaborative and parallel nature of the research efforts. This approach ensures a coherent narrative that follows the thematic and conceptual development of the research, rather than its temporal progression. This idea also drove the decision to structure this Thesis as an article dissertation, in order to give equal weight to all the works involved. A monographic dissertation would not have adequately captured the breadth and depth of the contributions made across the various studies.

The structure of this Thesis meticulously delineates the comprehensive exploration of diffractive optical elements, from theoretical foundations to innovative fabrication techniques. Each chapter is designed to contribute significantly to the overarching narrative of the study. **Chapter 2** sets the stage by introducing the concept of DOEs and their mathematical description through the Fourier optics formalism and scalar diffraction theory. This chapter provides an essential theoretical framework for the design and analysis of DOEs, equipping the reader with the necessary tools to understand their operation and the challenges in their development. **Chapter 3** then provides an in-depth examination of the conventional lithography techniques employed in the fabrication of flat optics. It addresses the complexities, limitations, and practical challenges encountered within standard lithography workflows, and highlights the need for advancements to overcome these hurdles. This discussion is critical for contextualizing the novel approaches presented later. **Chapter 4** represents the core of the Thesis, where the innovative use of azopolymer photopatterning for the fabrication of DOEs is detailed. Through a comprehensive review of the relevant literature, this chapter frames the research within the broader scientific dialogue and showcases the unique contributions of the study. It discusses the key findings, their significance in advancing the field, and potential directions for future research, underscoring the impact of this work. The final section of the Thesis comprises a collection of appended articles, which constitute the intellectual cornerstone of the research. Focusing on different aspects of the study, these articles present the methods and results of the experiments, enriching the thesis with detailed insights into each area of investigation.

As usual in scientific research, all the work presented in this Thesis is the result of collaborative efforts involving several scientists. The Author's contribution to each publication is summarized in Table 1. Three key areas encompass the contribution to the published scientific work:

- **Conception:** this involves the conception of the research question and theoretical framework. It also includes the critical thinking and idea generation that guides the project from its inception to its final dissemination, ensuring its meaningful contribution to the scientific field.

- **Research execution:** this stage involves the design of the experimental setup, data collection, and analysis, ensuring that the research concept is put into practice through rigorous experimental techniques.

- **Reporting:** includes writing, editing, and revising the manuscript, to ensure that the results of the experimental research are disseminated clearly and coherently to the scientific community and readers. It also involves feedback from co-authors and peers.

PUB.	CONCEPTION	RESEARCH EXECUTION	REPORTING
I	Low	Medium	Low
II	Low	Medium	Low
III	Medium	High	Medium
IV	High	High	High
V	Medium	High	Medium
VI	High	High	High
VII	Low	Medium	Low
VIII	Medium	High	Medium
IX	High	High	High

Table 1: Author contribution for each of the reprinted publications.

2

Design of diffractive optical elements

For centuries, refractive optical components have been the backbone of optical systems, such as microscopes and telescopes.[6] These components operate on the principles of Snell's law, bending light as it passes through the material interface that makes up the optical element.[76] The result is that the manipulation of light depends on the macroscopic shape of the component and to its optical properties, represented by the refractive index n of the component material (typically glass) at the wavelength of light being considered. In refractive optics, light accumulates a gradual phase retardation as it propagates through the bulk of the optical element, which is proportional to both the thickness and the refractive index. In most transparent materials, the phase retardation depends on the light wavelength as n decreases in the visible region of the light spectrum with increasing wavelength λ. This property is typically referred to as normal dispersion.[7] For this reason, refractive optics exhibit a chromatic behavior when used with broadband light. Common examples of refractive optical components include prisms and lenses, which allow light to be deflected and focused, respectively. When light enters a prism, it is refracted at each of its tilted faces. The refraction angle $\vartheta(\lambda)$ depends on the wavelength, resulting in the different colors of the spectrum being spread out. A refractive lens, on the other hand, uses the principles of refraction to converge or diverge light. The shape of the lens, the curvature of its surfaces, and the refractive index determine its focal length $f(\lambda)$ for each chromatic component of light. The chromatic behavior of refractive optics is fully summarized in Figure 1. Refractive optical elements, and their reliance on the principles of refraction gives rise to several inherent problems. In addition to chromatic aberrations, the bulk and weight associated with refractive optical elements pose a challenge for their integration into miniaturized or complex optical systems.[28,46]

The bulk refractive prism can be converted into a thin optical element using the Fresnel's technique,[13] illustrated in Figure 1. Suppose the prism is sliced into one-wavelength-high (λ) pieces, removing all the rectangular sections that do not contribute to the path length.[13] The resulting optical element is called a blazed grating. A blazed diffraction grating encodes similar optical functionality to a prism, except that the light bending, and chromatic dispersion is produced by diffraction rather than refraction and is determined by the periodicity Λ and the thickness $\Delta h = \lambda$.[77] This concept can be applied to the design of any diffractive optical element starting from its refractive

counterpart. The Fresnel lens, designed over a century ago, is a well-known example of a thin diffractive equivalent of a refractive lens.[78] The blaze grating and the Fresnel lens are the first examples of *Diffractive Optical Elements*, DOEs.

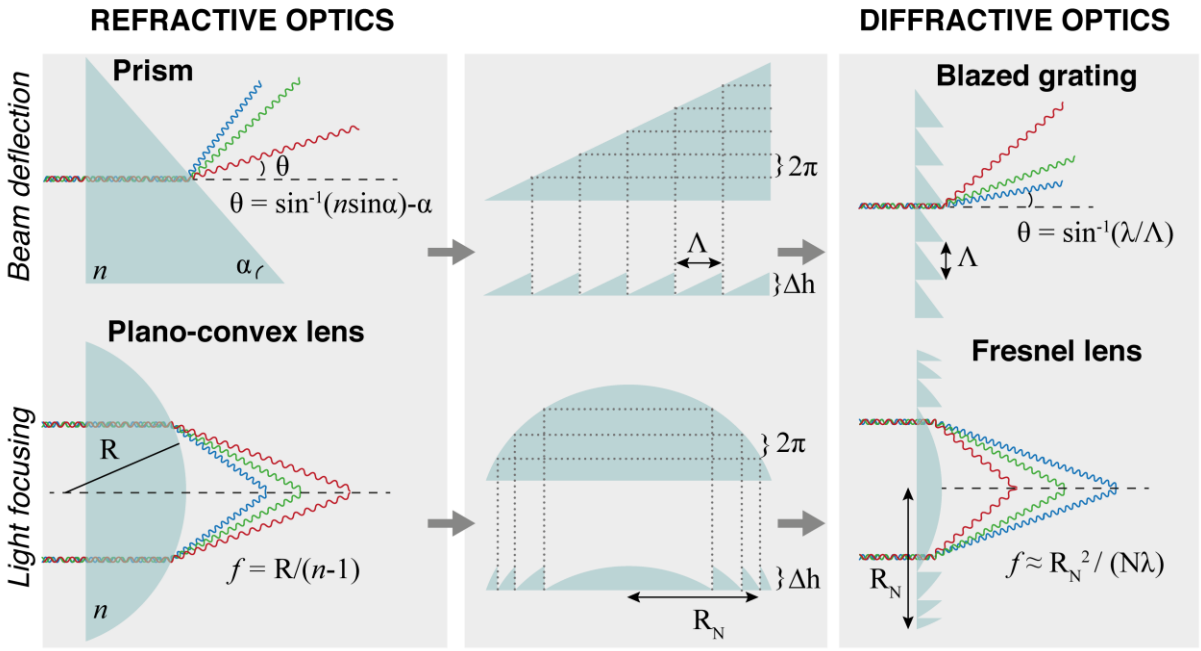

Figure 1: From refractive to diffractive optical components using the Fresnel's technique. Refractive prisms and lenses can be converted to their equivalent DOE by removing all the bulk sections that do not contribute to the path length. The chromatic behavior of both refractive and diffractive optics can be found in ref.[6]

Diffractive optical elements modulate light waves, by imposing either a phase shift or an amplitude change when light is transmitted or reflected through the device. For amplitude modulating DOEs, the mechanism of modulation primarily involves changing the transmission or reflection properties at different points of the DOE. This is typically accomplished by a series of apertures or opaque zones.[76,78] However, this directly affects the energy distribution of the light wave, resulting in a lossy form of light modulation. In contrast, phase-modulating DOEs manipulate light without changing its amplitude. This is accomplished by introducing variations in the optical path length that the light travels over the DOE, resulting in a pure phase modulation.[13] Engineering phase-only DOEs can be achieved by two primary methods. One is to generate a patterned refractive index within the bulk of the material while maintaining a constant surface shape. This technique is often employed using liquid crystals.[19] The alternative approach utilizes modulated surfaces, where the physical geometry of the surface is altered to achieve the desired modulation in the light path. Regardless of the implementation strategy, phase-modulating DOEs are characterized by their ability to offer a flat and lightweight form factor, enabling light modulation in an inherently lossless manner. The optical properties of a DOE completely determine how the light diffracts and interferes with itself. Consequently, the design of a DOE requires careful consideration of several parameters, including the shape, size, and spacing of the microstructures, as well as the

wavelength of the light and its corresponding refractive index. To optimize the performance of DOEs for specific applications, mathematical tools such as Fourier optics are often used in the design process.[13]

2.1 Introduction to Fourier optics

Fourier optics is a branch of optics that applies the principles of Fourier analysis to the study of optical systems and phenomena by decomposing a complex waveform into a set of Fourier components. The Fourier transform is used to describe the propagation of light waves, which is particularly powerful for understanding the diffraction and interference patterns produced by diffractive optical elements. These optical devices typically manipulate the phase and amplitude of light, creating complex wavefronts that are easier to understand and design by using a frequency domain representation. Under this formalism, optical fields can be decomposed as a superposition of plane and evanescent waves, both of which are intuitive solutions of Maxwell's equations.

Assume that the electric field $\vec{E}(x,y,z)$ is well defined at each point in the space. In the angular spectrum picture, considering $\vec{E}$ in a plane at $z = constant$, the two-dimensional Fourier transform $\hat{\vec{E}}$ of the field can be defined as:[79]

$$\hat{\vec{E}}(k_x,k_y,z) = \frac{1}{2\pi}\iint_{-\infty}^{+\infty} \vec{E}(x,y,z)e^{-i(k_x x+k_y y)}\,dxdy \tag{2.1}$$

where (x,y) are the transverse Cartesian coordinates and (k_x,k_y) are the corresponding *spatial frequencies* or reciprocal coordinates. The Fourier transform allows the field to be decomposed into a superposition of plane waves. This becomes evident when defining the inverse transform as:

$$\vec{E}(x,y,z) = \frac{1}{2\pi}\iint_{-\infty}^{+\infty} \hat{\vec{E}}(k_x,k_y,z)e^{i(k_x x+k_y y)}\,dk_x dk_y \tag{2.2}$$

The exponential term appearing in the integrand represents a plane wave propagating with wave vector $\vec{k}$, whose complex amplitude $\hat{\vec{E}}(k_x,k_y,z)$ is defined by the Fourier relation (2.1). Since the magnitude of the vector $|\vec{k}| = k$ is fixed, the third reciprocal coordinate can be derived from the relation:

$$k_z = \sqrt{k^2 - k_x^2 - k_y^2} \tag{2.3}$$

Note that in the notation of equations (2.1) and (2.2), the field $\vec{E}$ represents a vector, thus the Fourier integrals hold separately for each vector component (E_x, E_y, E_z).[79]

2.1.1 Light propagation in homogeneous media

The introduced formalism can be applied to describe the propagation of monochromatic radiation in a medium that is homogeneous, isotropic, linear, and source-free. Then, a time-harmonic optical field with angular frequency ω must satisfy the vector Helmholtz equation:

$$\nabla^2 \vec{E}(x,y,z) + k^2 \vec{E}(x,y,z) = 0 \tag{2.4}$$

where $k = \omega n/c$ is the magnitude of the wave vector $\vec{k}$ and n is the refractive index of the medium. Substituting the Fourier representation of $\vec{E}(x,y,z)$, represented by equation (2.2), into the Helmholtz equation, allows the evolution of the Fourier spectrum along the z-axis to be evaluated as:

$$\frac{\partial^2}{\partial^2 z}\hat{\vec{E}}(k_x,k_y,z) + k_z^2 \hat{\vec{E}}(k_x,k_y,z) = 0 \tag{2.5}$$

This differential equation can be solved component-wise and has the following solution:[79]

$$\hat{\vec{E}}(k_x,k_y,z) = \hat{\vec{E}}(k_x,k_y,0)e^{\pm ik_z z} \tag{2.6}$$

The $\pm$ sign specifies that two distinct solutions are possible: the solution with the positive sign refers to a wave propagating in the positive direction of the z-axis, while the solution with the negative sign refers to a wave propagating in the negative direction of the z-axis. This solution thus shows that the Fourier spectrum of the field in an arbitrary *image plane* at a fixed z can be calculated by multiplying the spectrum in the *object plane* $(z = 0)$ by the factor $\hat{H}(k_x,k_y,z) \equiv e^{\pm ik_z z}$, which is called the *propagator in reciprocal space* or the *optical transfer function*.

As shown in equation (2.3), given the pair (k_x, k_y), two different solutions for k_z are possible: if $k_x^2 + k_y^2 \leq k^2$, then k_z is a real quantity, making the propagator an oscillating exponential; conversely, if $k_x^2 + k_y^2 \geq k^2$, the k_z component becomes purely imaginary, making the propagator take the form of an exponential decaying along z. In general, both solutions are possible, meaning the field can always be described by the superposition of both plane waves and evanescent waves. From a physical point of view,

the propagation of the field over distances much larger than the wavelength (*far-field*) always involves a loss of information, specifically related to the presence of non-propagating evanescent terms; they can contribute significantly only when the propagation occurs over distances comparable to the light wavelength (*near-field*). For this reason, in practical applications where long-range propagation is considered the field will be supposed to have a finite bandwidth.[79] In other words, the field at z is a low-pass filtered representation of the field at the object plane and from near- to far-field propagation only features with lateral dimensions greater than $1/k$ can be accurately reproduced.[79]

To determine how the fields themselves evolve, equation (2.2) must be extended for any arbitrary z, using equation (2.6), considering the action of the optical transfer function:

$$\vec{E}(x,y,z) = \frac{1}{2\pi} \iint_{-\infty}^{+\infty} \hat{\vec{E}}(k_x,k_y,0) e^{i[k_x x + k_y y \pm k_z z]}\, dk_x dk_y \tag{2.7}$$

Alternatively, the Fourier spectrum can be expressed in terms of the direct-space field, using equation (2.1) to determine how the field evolves in direct space:

$$\vec{E}(x,y,z) = \frac{1}{2\pi} \iint_{-\infty}^{+\infty} \vec{E}(x,y,0) e^{i[k_x(x-x\prime)+k_y(y-y\prime)\pm k_z z]}\, dk_x dk_y dx' dy' \tag{2.8}$$

This relation connects the field in an arbitrary image plane with the optical field in the object plane. From equation (2.8) it is possible to define the *propagator in direct space* $H(x,y,z)$, which turns out to be the Fourier Transform ($\mathcal{FT}$) of the propagator in reciprocal space:

$$H(x,y,z) = \frac{1}{2\pi} \iint_{-\infty}^{+\infty} e^{i(k_x x + k_y y \pm k_z z)}\, dk_x dk_y = \mathcal{FT}\left[e^{\pm i k_z z}\right] \tag{2.9}$$

As predicted by fundamental properties of the Fourier transform, the evolution of the optical field in direct space is equal to the convolution product:[79]

$$\vec{E}(x,y,z) = \vec{E}(x,y,0) \otimes H(x,y,z) \tag{2.10}$$

This equation poses the basis of Fourier optics. The optical field in any plane of the space is determined from the Fourier spectrum of the field in the source plane. Indeed, by using the convolution theorem,[80] equation (2.10) is equivalently rewritten as:[79]

$$\vec{E}(x,y,z) = \mathcal{FT}^{-1}\left\{\mathcal{FT}\left\{\vec{E}(x,y,0)\right\} \times \mathcal{FT}\{H(x,y,z)\}\right\} \tag{2.11}$$

where $\mathcal{FT}$ and $\mathcal{FT}^{-1}$ denote the Fourier transform and its inverse operation, respectively. From this relationship, once the spectrum of the source field is known, the spatial distribution of the propagated field depends only on the transfer function, which is determined by the geometry of the source and observation planes, but it is independent of the source field. The different levels of approximation of the transfer function for far-field propagation lead to the Rayleigh-Sommerfeld, Fresnel and Fraunhofer theories, which are widely used to solve diffraction problems.[81]

A first approximation can be made by assuming that the wavevectors constituting the spectrum of the source field are parallel to the propagation axis, and therefore the transverse components are small compared to k. This approximation is valid in many physical cases, as with laser beams, where light propagates along a specific direction. In this scenario, relation (2.3) can be expanded to obtain:

$$k_z \approx k - \frac{k_x^2 + k_y^2}{2k} \tag{2.12}$$

This approximation, known as the *paraxial approximation*, simplifies the Fourier integrals.[79] As an example, considering the propagator in direct space described by equation (2.9) and introducing the paraxial approximation, the following result is obtained:[80]

$$H(x,y,z) = \frac{2\pi}{\lambda z} e^{ikz} e^{-i\frac{\pi}{2}} e^{i\frac{k}{2z}(x^2+y^2)} \tag{2.13}$$

where the well-known result of the Gaussian integral has been used. The form of the propagator in the paraxial approximation allows for the analytical derivation of significant relationships between the focal planes of a thin lens, which are fundamental relations to describe light propagation in various optical systems.

The above formalism predicts how the filed propagates and how it is mapped at any arbitrary position z. An interesting result is found when considering the propagation to a very remote plane, resulting from the asymptotic far-field evaluation of the filed for $z \to \infty$. Introducing the following dimensionless vector $\vec{s} = (x/r, y/r, z/r)$ where $r = (x^2 + y^2 + z^2)^{1/2}$ is the distance from the origin, the asymptotic angular spectrum representation $\vec{E}_\infty$ can be written as:[79]

$$\vec{E}_\infty(s_x, s_y) = \lim_{kr\to\infty}\left[\frac{1}{2\pi}\iint_{\Sigma} \hat{\vec{E}}(k_x, k_y, 0) e^{ir[k_x s_x + k_y s_y \pm k_z s_z]}\right] dk_x dk_y \tag{2.14}$$

The integration domain $\Sigma = \left(k_x^2 + k_y^2\right) \leq k^2$ has been restricted to the plane waves domain since evanescent waves do not contribute to the field at infinite distance because of their exponential decay. This allows the integral to be solved by the stationary phase method.[79] The result of equation (2.14) can be expressed as:

$$\vec{E}_\infty(s_x, s_y) = -ik_z \frac{e^{ikr}}{r} \hat{\vec{E}}(k_x, k_y, 0) \tag{2.15}$$

This equation shows that the far-field is completely determined by the Fourier spectrum of the field in the object plane. In other words, the far-field $\vec{E}_\infty$ forms a Fourier transform pair with the field at $z = 0$. The only deviation is given by the k_z term, but in the paraxial approximation, where $k_z \approx k$, the two fields form a perfect Fourier-transform pair.[79] As it will be demonstrated in the next section, a similar result can also be derived for finite distances by exploiting the optical relations between the conjugate planes of a thin lens.

2.1.2 Fourier transforming properties of a thin lens

A lens is an optical component made of an optically dense material, typically glass, and is the best-known example of a refractive optical component.[7] The case of a thin lens is considered, which, by definition, is a valid approximation when the translation of optical rays within the lens itself is negligible. Therefore, a thin lens introduces only a phase delay to the incident wavefront that is proportional to the thickness of the lens at each point. Under this approximation, it is possible to define a complex transmission coefficient $t(x, y)$ that allows to determine the field at the rear surface of the lens ($\vec{E}_{out}$), given the expression of the field at the front surface of the lens ($\vec{E}_{in}$), as illustrated in Figure 2. This formalism will be extended in the next section to describe any thin optical component, acting as a pure phase-modulating device. The complex transmission coefficient for a thin lens under paraxial approximation is:[80]

$$t(x, y) = e^{ikn\Delta_0} e^{-ik\frac{x^2+y^2}{2f}} \tag{2.16}$$

where Δ_0 is the maximum thickness of the lens, n is the refractive index of the medium from which the lens is made, and f is the focal length of the lens. Considering $\vec{E}_{in}$ the field on the front surface of the lens, equation (2.16) represents the phase delay accumulated by the field because of the propagation through the lens, resulting in an output field $\vec{E}_{out}(x, y, \Delta_0) = \vec{E}_{in}(x, y, 0) \cdot t(x, y)$. Let us now consider that the field propagates in the second focal plane of the lens. Recalling the action of the propagator

in direct space in paraxial approximation, as shown in equation (2.13), the optical field in the focal plane of the lens is:

$$\vec{E}(x,y,f) = E_0 e^{ik\frac{x^2+y^2}{2f}} \iint_{-\infty}^{+\infty} \vec{E}(x',y',0) e^{-i\frac{k}{f}[xx'+yy']} dx'dy' \tag{2.17}$$

where E_0 includes all constant terms; the integral in (2.17) is the Fourier transform of the field in the source plane, once that the spatial frequencies are defined as $k_x \equiv kx/f$ and $k_y \equiv ky/f$.

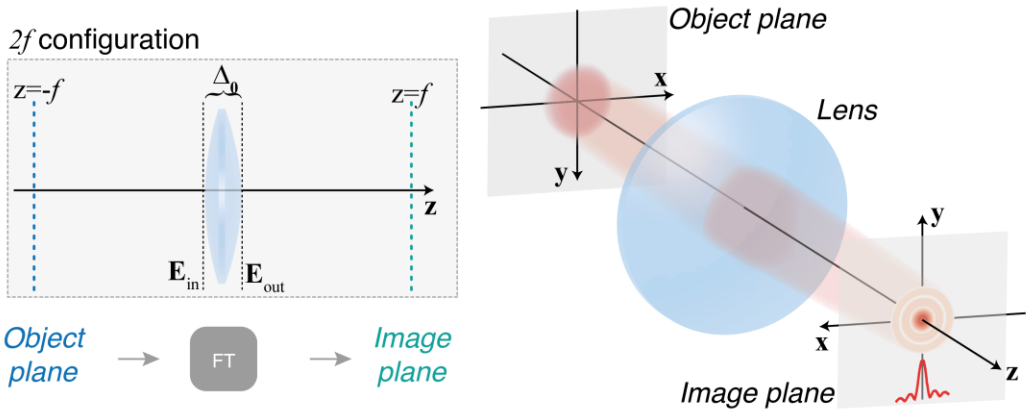

Figure 2: Fourier transforming property of a thin lens. The optical field in the image plane at distance $z = f$ is proportional to the two-dimensional Fourier transform of the field in the object plane, at $z = -f$.

Therefore, the field in the second focal plane of the lens is given, except for a phase factor, by the Fourier transform of the field incident on the lens itself. Moreover, this phase factor can be rewritten in paraxial approximation, introducing the spatial frequencies just defined:

$$\vec{E}(x,y,f) = E_0 e^{ikf} e^{-ik_z f} \cdot \mathcal{FT}\left[\vec{E}(x,y,0)\right] \tag{2.18}$$

Recalling the action of the propagator in reciprocal space, the exponential term $e^{-ik_z f}$ represents a propagation factor for a distance equal to $-f$. In conclusion, the following fundamental result is obtained:

$$\vec{E}(x,y,f) = E_0 e^{ikf} \cdot \mathcal{FT}\left[\vec{E}(x,y,-f)\right] \tag{2.19}$$

The field in the second focal plane of a thin lens (*image plane*) is proportional to the Fourier transform of the field in the first focal plane (*object plane*). A visual example is

provided in Figure 2 where a circular aperture in the object plane, produces the well-known Airy pattern[80] of light in the image plane. This configuration, called the *2f* configuration,[80] suggests an operational way to generate fields in a given plane of the optical axis based on the ability to appropriately modulate the field in one of the two focal planes of a thin lens.

2.2 Scalar theory of diffractive optical elements

Equation (2.11) also represents the core to design the diffraction of light by engineering the spectral content of the field in the source plane. A diffractive optical element can be modeled as an amplitude and/or a phase mask, described by the functions $A(x,y)$ and $\varphi(x,y)$, which modulates an incident beam through a complex space-dependent transmission function $t(x,y)$, resulting in a field modulation that can be written as:[80]

$$\vec{E}_{out}(x,y,\Delta h) = \vec{E}_{in}(x,y,0)\cdot t(x,y) = \vec{E}_{in}(x,y,0)\cdot A(x,y)\cdot e^{i\varphi(x,y)} \tag{2.20}$$

where Δh is the *modulation depth,* representing the effective modulating thickness of the device excluding any layer or substrate that does not contribute to the wavefront shaping. If the incident field is a plane wave propagating along the z-axis, then equations (2.20) and (2.11) fully determine the diffracted field, which is only dependent on the transfer function of the system and the Fourier transform of the complex transmission function $t(x,y)$. In the following sections, phase-only modulating DOEs will be considered, neglecting any effects related to amplitude modulation. The wavefront modulation occurring in a DOE encoded as a modulated surface is illustrated in Figure 3. The microscale surface geometry produces complex diffraction patterns. The phase modulation is the result of the optical path difference accumulated by the incident plane with respect to the surrounding medium with refractive index n_s. The phase term appearing in equation (2.20) can be written as:[80]

$$\varphi(x,y) = [n(x,y) - n_s]\cdot k_0 \cdot h(x,y) \tag{2.21}$$

where $k_0 = 2\pi/\lambda$ is the magnitude of the wavevector in vacuum, with λ being the wavelength of light. Equation (2.21) fully determines the functionality of a phase-modulating DOE. This class of DOEs can be implemented by varying the refractive index of the material $n(x,y)$ at a microscopic scale, while keeping the device thickness flat $h(x,y) = \Delta h$. Different regions of the DOE will have different refractive indices, causing the light to speed up or slow down and thus changing its phase as it passes through. This type of modulation is typically used for refractive elements by using birefringent materials such as liquid crystals.

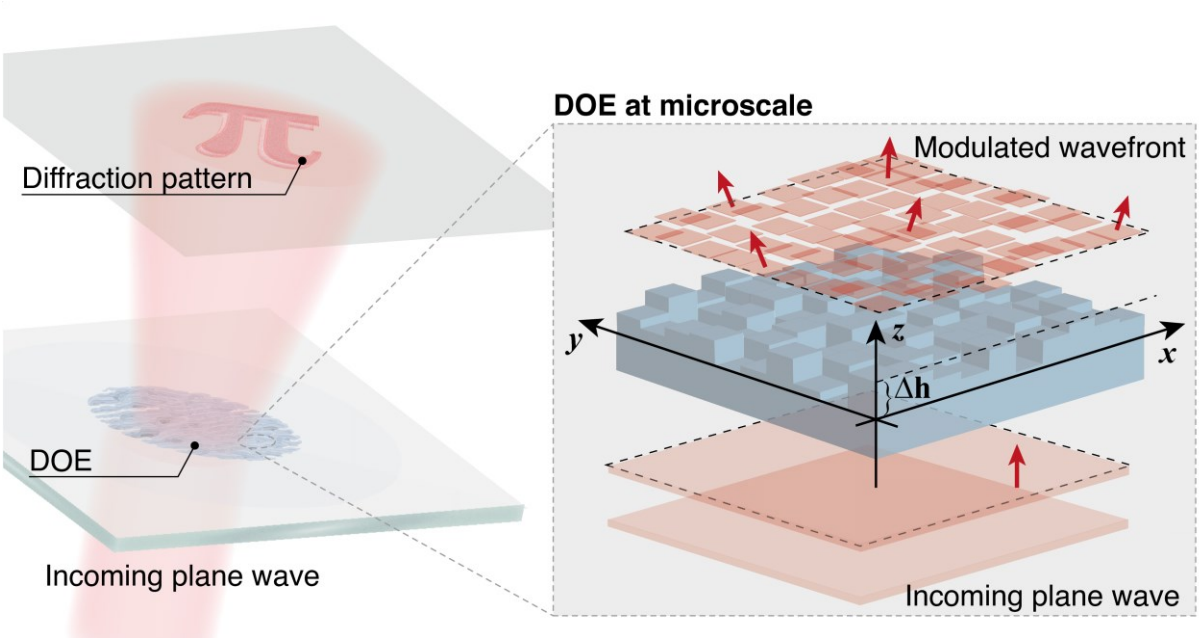

Figure 3: Light wavefront modulation occurring in a diffractive optical element implemented as a structured surface. The output modulated wavefront depends only on the input optical field and the complex transmission function of the DOE.

On the other hand, height modulation $h(x, y)$ involves physically shaping the surface of the DOE into a specific relief pattern. The height variations change the optical path length of different parts of the wavefront, resulting in phase shifts that manipulate the light as it passes through the device with uniform refractive index $n(x, y) = n$. Equation (2.21) also allows to estimate the effective modulation depth required for an efficient modulation. The maximum phase excursion for the filed is 2π, a condition achieved for surface modulated DOEs when $\Delta h = \lambda/(n - n_s)$. This condition sets the maximum required height modulation. Its value is typically of the same order of magnitude with the light wavelength. Excluding the contribution of substrates or the unmodulated layer of the material, this demonstrates that DOEs can shape light within a significant thickness (and consequently weight) reduction if compared to refractive optics.

2.2.1 From sinusoidal gratings to Optical Fourier Surfaces

Diffractive optical elements fabricated as microstructured surfaces can have both smooth and stepped profiles. Smooth profiles provide continuous phase modulation, making them suitable for applications such as holography. On the other hand, step profiles offer simplified fabrication and can exhibit better performance over a wider range of wavelengths.[13] Smooth and step profiles are interchangeable with proper design considerations. The choice between smooth and step profiles depends on the specific design requirements and desired results of the optical system in question.

As first example of smooth DOE, let us consider a periodic sinusoidal phase modulating surface constituted of a surface relief $h(x,y)$ in a medium of index n immersed in air ($n_s = 1$). For such diffracting surface, acting as a diffraction grating, equation (2.11) can be solved analytically, allowing to highlight the connection between the Fourier spectrum of the surface geometry and the diffracted field in far-field. The phase transmission function of the sinusoidal surface can be written as:

$$t(x,y) = e^{ik_0(n-1)\frac{1}{2}\left[1+sin\frac{2\pi x}{\Lambda}\right]\Delta h} \tag{2.22}$$

where Λ is the spatial period of the sinusoidal relief, as illustrated in Figure 4a. Due to the symmetry of the surface geometry, the analysis can be simplified by solving the simple unidimensional problem. Let us consider a plane wave $\vec{E}_{in}(x,y,0) = \vec{E}_0 e^{ik_0(x\,sin\alpha)}$, incident on the surface in the source plane at $z = 0$ with an angle α. The field in source plane is then $\vec{E}_{in}(x,y) \cdot t(x)$. To retrieve an analytic expression of the diffracted field, the complex transmittance is expanded in terms of the Jacobi–Anger identity:82

$$t(x) = t_0 \sum_{m=-\infty}^{m=+\infty} J_m\left(\frac{k_0(n-1)\Delta h}{2}\right) e^{i\left(m\frac{2\pi x}{\Lambda}\right)} \tag{2.23}$$

By substituting the field and the complex transmittance in equation (2.11), the following diffracted field is obtained:

$$\vec{E}(x,z) = \vec{E}_0\, t_o \sum_{m=-\infty}^{m=+\infty} J_m\left(\frac{k_0(n-1)\Delta h}{2}\right) e^{i\left(k_0 sin\alpha + m\frac{2\pi}{\Lambda}\right)x}\; e^{iz\sqrt{k_0^2 - \left(k_0 sin\alpha + m\frac{2\pi}{\Lambda}\right)^2}} \tag{2.24}$$

where J_m is a first kind Bessel function of the m^{th} order. The diffracted field is a superposition of waves characterized by the wavevector components:

$$\begin{cases} k_x = k_0 sin\theta_m = k_0 sin\alpha + m\dfrac{2\pi}{\Lambda} \\ \\ k_z = \sqrt{k_0^2 - \left(k_0 sin\alpha + m\dfrac{2\pi}{\Lambda}\right)^2} \end{cases} \tag{2.25}$$

which include a finite number of propagating orders and evanescent non-propagating terms.

Equation defining the transversal k_x component is the familiar Bragg's relation,[12] which defines the diffraction angle θ_m of the propagating orders produced by the sinusoidal

diffracting surface in terms of diffraction order m and surface periodicity Λ. Figure 4b shows the simulation of the far-field diffraction pattern produced by a sinusoidal diffraction grating for an incident plane wave with unitary amplitude for three different wavelengths. The diffracted field is evaluated considering the Rayleigh–Sommerfeld diffraction integral in Fresnel approximation.[81]

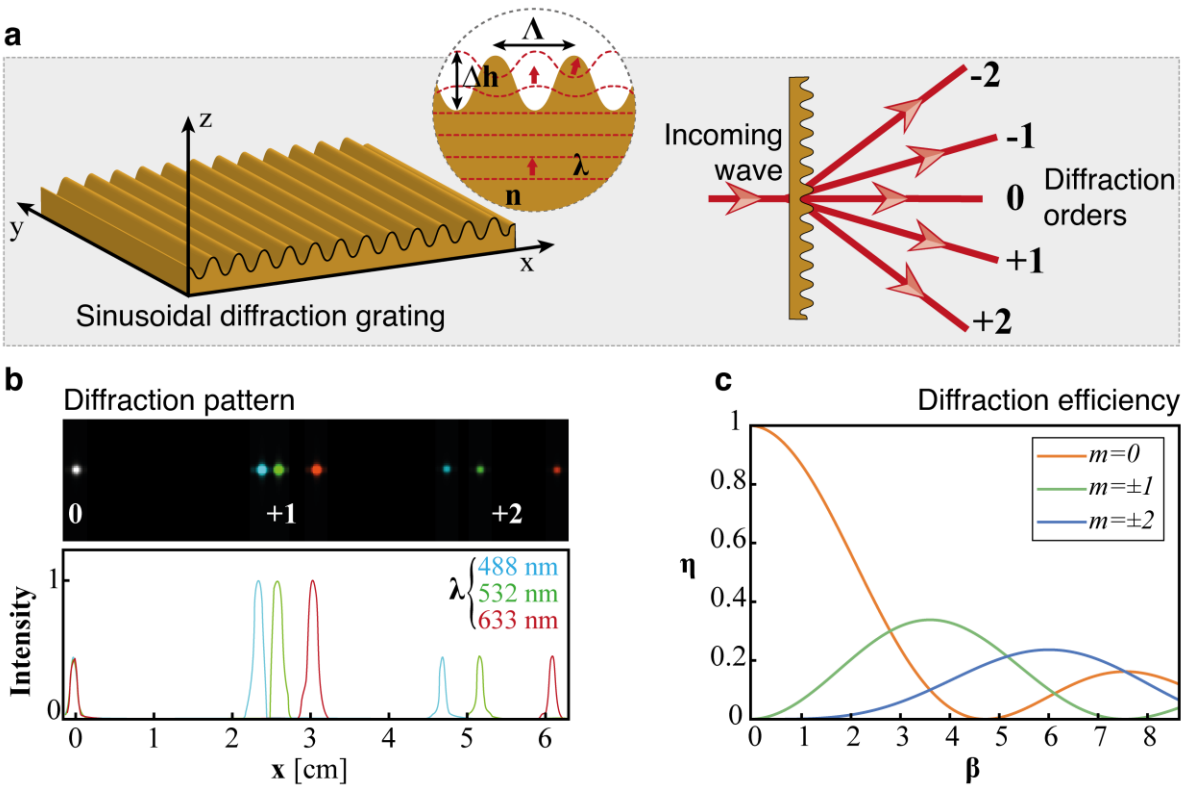

Figure 4: Diffraction behavior of sinusoidal diffraction gratings. a) Schematic illustration of the wavefront modulation and the Bragg's diffraction for a sinusoidal diffraction grating. b) Simulation of the diffraction pattern produced by a superposition of three wavelengths ($488\,nm$, $532\,nm$ and $633\,nm$). A periodicity equal to $\Lambda = 2.0\,\mu m$ was considered for the simulation. The diffraction pattern is evaluated at a distance of $z = 10\,cm$ from the modulated surface, and it has been normalized to the maximum diffraction efficiency. c) Diffraction efficiency as a function of the dimensionless parameter β for the first five diffraction orders of a sinusoidal grating.

The power fraction η_m carried by each of the terms of the field expansion, with respect the total intensity $\left|\vec{E}_0\right|^2$, is:

$$\eta_m = \left| J_m\left(\frac{k_0(n-1)\Delta h}{2}\right)\right|^2 \tag{2.26}$$

which is also typically referred to as *diffraction efficiency* of the grating. The power distribution across the diffraction orders is directly related to the phase modulation depth of the surface through the values of refractive index and surface modulation depth Δh. Figure 4c shows the diffraction efficiency for the first five diffracted orders with $m =$

$0; \pm 1; \pm 2$ as function of the parameter $\beta = k_0(n-1)\Delta h$. The plot shows that the maximum efficiency for each order happens for different values of Δh and hence that, once the material is fixed, the amplitude of the relief is the structural parameter to be tuned to control the relative distribution of light intensity in the diffracted pattern. Maximum efficiency for the first order is $\eta_{\pm 1} = 0.34$, obtained for the value $\beta = 3.68$. As an example, for a dielectric surface with $n = 1.70$ this condition is achieved, for monochromatic light at $\lambda = 633\ nm$, at $\Delta h \sim 0.530\ \mu m$.

Equation (2.23) can be generalized to any periodic one-dimensional function $h(x)$ with the same formalism developed explicitly for the sinusoidal surface profile, by expanding the periodic phase modulation in terms of a Fourier series. In this case the Bessel functions must be substituted with the actual Fourier coefficient:[83]

$$t(x) = \sum_{m=-\infty}^{m=+\infty} V_m \, e^{i\left(m\frac{2\pi x}{\Lambda}\right)} \tag{2.27}$$

The diffracted field from these surfaces assumes the same form of the equation (2.24), with an equivalent Bragg's relation. The diffraction efficiency from a generic periodic surface is equal to $\eta_m = |V_m|^2$. On one hand, this model can be used to reconstruct the diffraction efficiency considering the experimental surface profile, including deviation from the desired analytic function due to fabrication defects. On the other hand, it also suggests a practical design tool to engineer the diffracted field by tailoring the weight of each of the surface geometry components appearing in the equation (2.27).

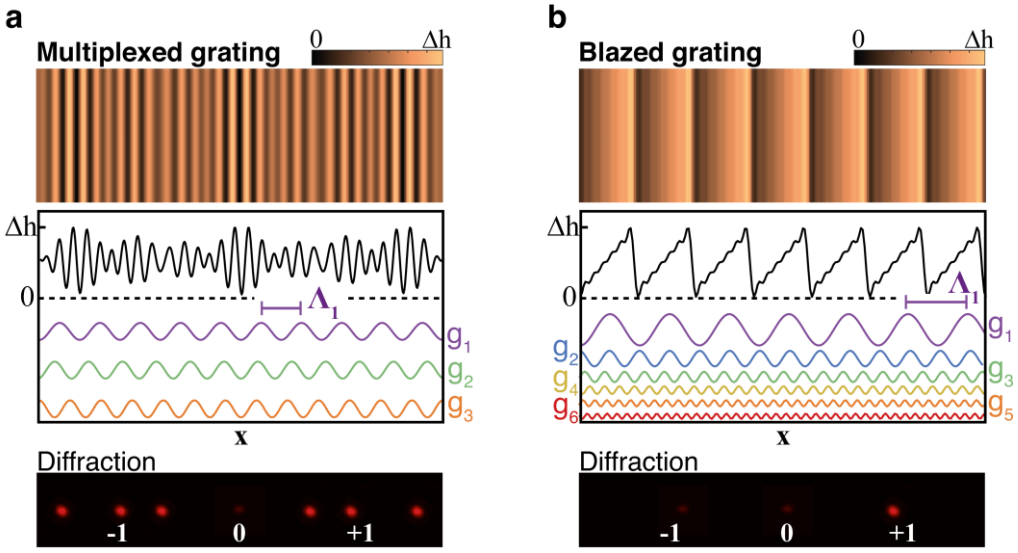

Figure 5: Design of unidimensional multiplexed gratings ($\gamma_i = 0$). a) Multiplexed sinusoidal diffraction grating obtained with three equally weighted sinusoidal functions with periodicity $\Lambda_i = (\Lambda_1,\ 0.91 \cdot \Lambda_1,\ 0{,}77 \cdot \Lambda_1)$ and $\phi_i = 0$. b) Design of a Fourier-synthesized blazed grating from six sinusoidal functions with $w_i = 1/i$, $\Lambda_i = \Lambda_1/1$ and $\phi_i = (-1)^i \pi/2$. Each panel shows, from top to bottom, the designed surface geometry, the lateral profile, and the simulated diffraction pattern.

Those results can be indeed generalized to diffractive surfaces built as sum of multiple bidimensional sinusoidal functions $g_i(x,y)$ each of periodicity Λ_i and relative height modulation w_i:

$$h(x,y) = \sum_{i=1}^{N} \mathrm{w}_i g_i(x,y) = \sum_{i=1}^{N} \mathrm{w}_i \left[1 + sin\left(\frac{2\pi}{\Lambda_i \cos(\gamma_i)} x + \frac{2\pi}{\Lambda_i \sin(\gamma_i)} y + \phi_i\right)\right] \quad (2.28)$$

where the angle γ_i represents the in-plane orientation angle with respect to the x direction of the i^{th} sinusoidal function, and ϕ_i is a relative phase between sinusoids. In the simple case where $\gamma_i = 0$, the symmetry of the surface geometry allows to simplify the analysis by solving a simple unidimensional problem. In this case, the transmission function is the product of N terms, each representing the Jacobi–Anger expansion of the $g_i(x,y)$ function. According to equation (2.24), the optical field diffracted by this surface is:

$$\vec{E}(x,z) = \vec{E}_0 \left[\prod_{i=1}^{N} t_{0i} \left(\sum_{a_i=-\infty}^{a_i=+\infty} J_{a_i}\left(\frac{\beta}{2} w_i\right)\right)\right] e^{i\left(k_0 \sin\alpha + \sum_i a_i \frac{2\pi}{\Lambda_i}\right)x} e^{iz\sqrt{k_0^2 - \left(k_0 \sin\alpha + \sum_i a_i \frac{2\pi}{\Lambda_i}\right)^2}} \quad (2.29)$$

The diffracted field is again a superposition of a finite number of propagating and evanescent waves, determined from a generalized Bragg's relation. Each diffracted order carries an optical power determined by each of the Bessel functions composing the complex surface geometry expansion.

The synthesis of DOEs according to equation (2.28) allows the design of multiplexed gratings, where two or more sinusoidal diffraction gratings are combined into a single structure. This integration allows multiple optical functions to be performed simultaneously or to operate efficiently over a wider angular range. In principle, a similar surface can be not globally periodic, but it is still characterized by a discrete Fourier spectrum, such as the multiplexed grating in Figure 5a. On the other hand, if the one-dimensional multiplexed grating is obtained as a superposition of a finite number of harmonic Fourier functions, a periodic diffraction grating is achieved, such as the Fourier-synthesized blazed grating shown in Figure 5b. This DOE, resulting from the combination of six harmonic gratings with the same orientation but different amplitudes and phases, can diffract light into a target diffraction order. This approach can be easily extended to two-dimensional geometries, including periodic, quasi-periodic and non-periodic surfaces obtained as a finite superposition of sinusoidal functions, as shown in Figure 6a. Again, the diffracted optical field in the far-field regime is characterized by a discrete set of intensity spots, occurring at the angular positions predicted by the Bragg's relation, extended in two dimensions. Each diffraction order carries a fraction of the incident power, which is related to the geometrical shape of the surface and the phase modulation imposed on the incident field by the diffractive phase mask in the source plane. This category of ideally infinitely extended surfaces, typically referred to as *Optical Fourier Surfaces*,[84] includes many diffractive surfaces that can be

used to angularly and spectrally split a light beam, as illustrated in Figure 6b. Examples are quasicrystal and spiral-quasicrystal gratings.

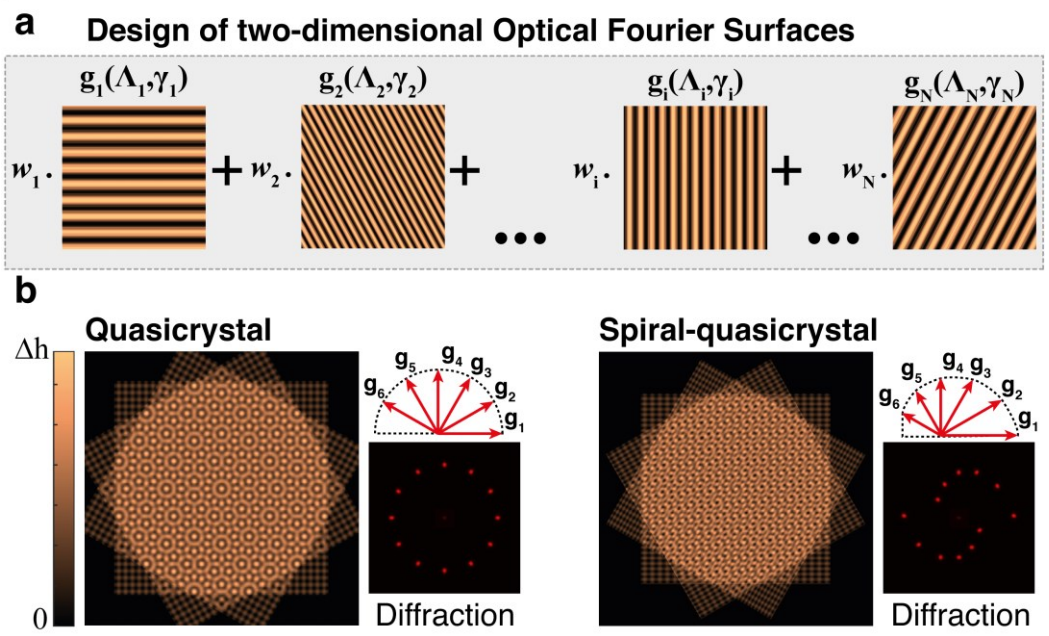

Figure 6: Design of Optical Fourier Surfaces. a) Schematic representation of the sequential multiplexing of sinusoidal gratings with different periodicity Λ_i, orientation γ_i and amplitude w_i. b) Two-dimensional diffraction gratings with a quasicrystalline design and engineered Fourier spectra. The inset shows the decomposition of the surface in terms of the multiplexed Fourier components and the corresponding diffraction pattern. Both DOEs are designed by imposing $w_i = 1$, $\phi_i = 0$, and $\gamma_i = \gamma_{i-1} + 30°$. For the quasicrystal $\Lambda_i = \Lambda_0$, while for the spiral-quasicrystal $\Lambda_i = \Lambda_0 - id$, where d is a fixed quantity.

2.2.2 Cosinusoidal phase zone plates

Diffractive optical elements can also be designed to focus light, in a similar way to standard glass-made lenses. A relevant example is the Fresnel zone plate discussed in the previous section. Here it is discussed the diffraction behavior of the cosinusoidal Phase Zone Plate (c-PZP), representing the smooth counterpart of the Fresnel zone plate,[85,86] whose profile is represented in Figure 7a. The smooth cosinusoidal focusing diffractive surface is a surface relief in a medium of refractive index n, whose 2D radial distribution $h(r)$ is given by:[78]

$$h(r) = \left(\frac{1 + \cos(\alpha r^2)}{2}\right)\Delta h \tag{2.30}$$

where $r = (x^2 + y^2)^{1/2}$. Here the parameter α sets the lateral size of the relief and defines the distance on the optical axis where constructive interference occurs. This parameter is then directly related to the focal lenght f of the diffractive lens.

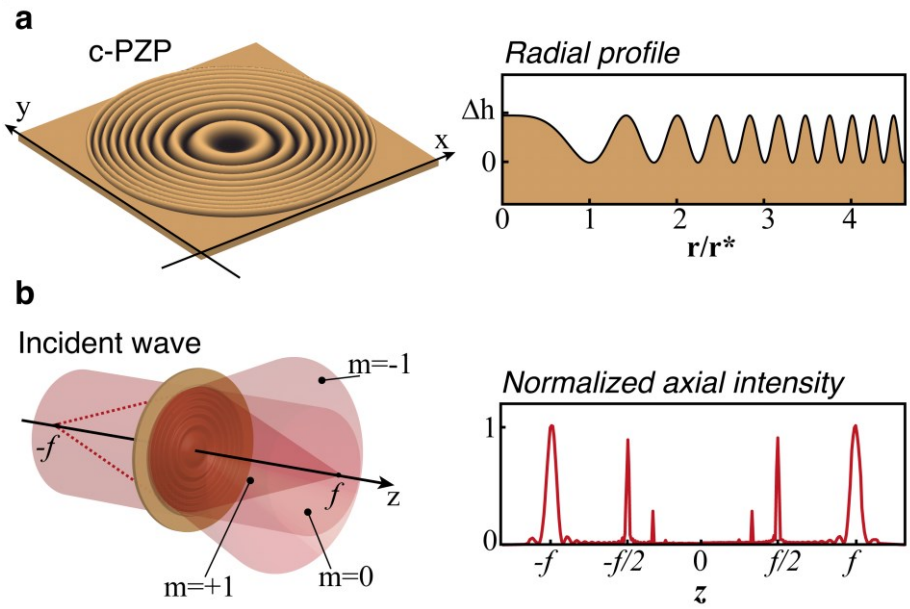

Figure 7: Design and functionality of a phase-only cosinusoidal zone plate (c-PZP) lens. a) Schematic of a Gabor zone plate with the corresponding radial profile. The radial coordinate has been renormalized with respect to the distance of the first minima in the phase mask: $r^* = (\pi/\alpha)^{1/2}$. b) Illustration of the multiple diffraction foci produced by a c-PZP lens. Normalized axial intensity profile of the simulated point spread function. The Fresnel transfer function was used for the simulation.[81]

Due to the axial symmetry of the system with respect to the optical axis, the problem can be simplified in one dimension. The total phase delay accumulated by a plane wave of wavelength λ modulated by the surface relief (acting as a pure phase mask) as it travels to the axial position $z = f$ takes into account two space-dependent contributions: the phase delay accumulated due to the propagation for a distance $h(r)$ in the material and the optical path accumulated due to propagation in air from the lens to the focal plane. To have an intensity maximum in the focal plane, different points of the surface must give rise to wavelets differing in phase at that point by multiples of 2π. This condition of constructive interference is guaranteed for:[78]

$$\alpha = \frac{2\pi}{\lambda^2 - 2\lambda f} \tag{2.31}$$

Equation (2.31) is the operative relation between the focal length of the focusing diffractive surface and the relief lateral structure. An incident monochromatic plane wave of wavelength λ, travelling in the positive z direction, accumulates a phase delay described by the complex transmittance:

$$t(r) = e^{ik_0(n-1)\frac{1}{2}[1+cos(\alpha r^2)]\Delta h} \tag{2.32}$$

This expression can be again expanded in the base of radial harmonics using the Jacobi expansion:

$$t(r) = t_0 \sum_{m=-\infty}^{+\infty} i^m J_m\left(\frac{\beta}{2}\right) e^{(im\alpha r^2)} \tag{2.33}$$

Assuming that the light wavelength is negligible compared to the focal length ($\lambda \ll f$), the term λ^2 appearing in equation (2.31) can be neglected. The expansion in equation (2.33) demonstrates that a c-PZP has a transmission function of a multifocal lens as each of the terms appearing in the series has the same form as that appearing in equation (2.16). A plane wave incident on the device emerges as a sum of spherical waves with focal lengths that are fractions of the first order focal length $f_m = f/m$. In the same way that a diffraction grating separates an incident plane wave into a sum of emerging plane waves with different wavevectors, a c-PZP acts as a phase grating with circular symmetry and radially variable groove spacing, splitting an incident wave into a sum of spherical emerging waves, each converging at distances f_m from the lens, where the integer number m again defines the focal diffraction order. Figure 7b shows this diffractive behavior resulting from an axial simulation of the light power distribution from a c-PZP. The emerging waves representing a specific diffraction order can be spherically divergent if $m < 0$, spherically convergent if $m > 0$ and a plane wave ($m = 0$), that corresponds to the unmodulated component.[78] For an ideal c-PZP, the fraction of light power diffracted in each order follows exactly the same dependence on the modulation depth Δh derived for a sinusoidal grating, equation (2.26).

Cosinusoidal phase zone plates can also be used for imaging. In geometrical optics, the imaging process of a lens is a form of information transfer between the object plane and an imaging plane. The axial position where the image is formed (the imaging plane) is determined by both the axial object position (object plane) and by the focal length of the lens, according to the conjugate planes law. These relations remain valid also for the description of the image formation from a multifocal c-PZP, which simply requires a generalization of the Newton's equation[6,7] for thin lenses to account for the simultaneous presence of multiple focal lengths:

$$\left(p - \frac{f}{m}\right)\left(q - \frac{f}{m}\right) = \left(\frac{f}{m}\right)^2 \tag{2.34}$$

As usual, in equation (2.34), p is the distance between the object and the plane of the lens, q is the position of the image plane relative to the plane of the lens, and f is the designed focal length for the first diffraction order. This relation can be useful to design versatile optical imaging systems working as multifocal diverging or converging lenses, including telescope imaging systems or multi-depth hybrid microscopes, able to focus on objects placed at different positions.

2.2.3 Holographic projectors

Conventional projection displays exploit amplitude-modulating pixels to locally and selectively block a portion of the incident light to form images. A DOE can be engineered to project images by implementing a phase-only planar device for coherent monochromatic light modulation. The result is the possibility to reconstruct a desired light pattern without the use of absorption phenomena. Phase-only holographic plates, producing arbitrary intensity distribution, are typically named *kinoforms*.[87] According to the diffraction theory, the emerging modulated field $\vec{E}_{out}(x,y)$ produces a far field $\vec{E}_{\infty}(x,y)$ corresponding to the two-dimensional spatial Fourier transform of the beam modulated at the kinoform plane, resulting in a reconstructed image $I_{\infty}(x,y)$ determined by the relation:[80]

$$I_{\infty}(x,y) = \left|FT\left[\vec{E}_{in}(x,y)\cdot e^{i\varphi(x,y)}\right]\right|^2 \tag{2.35}$$

where $\varphi(x,y)$ is the phase modulation imposed by the kinoform to the incoming field $\vec{E}_{in}(x,y)$. An analogous result can be also found between the two focal planes of a thin lens, reducing the image reconstruction to finite distances. By inverting equation (2.35), the kinoform phase profile $\varphi(x,y)$ and the relative surface relief pattern $h(x,y)$ for any given holographic target image $I_{\infty}(x,y)$ could be potentially computed, allowing the design of DOEs with almost arbitrary optical functionality. However, for a phase-only modulator, the kinoform can only be retrieved through numerical algorithms.[88]

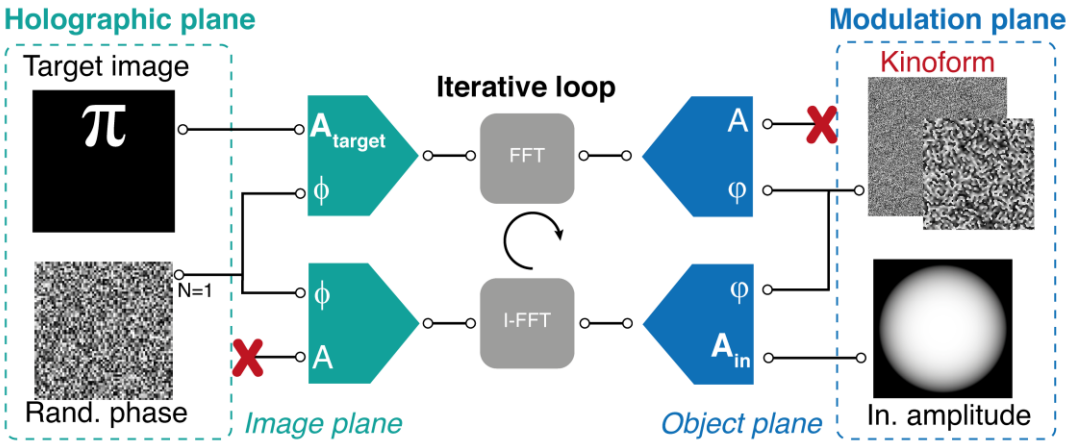

Figure 8: Block diagram of the Gerchberg–Saxton algorithm.

Figure 8 schematically shows this process for the case of the desired output image $I_{\infty}(x,y)$ representing the Greek letter "π", where the conventional Gerchberg–Saxton (GS) algorithm[89] is used as the Iterative Fourier Transform Algorithm (IFTA).[90,91] The GS algorithm is an iterative method typically used to solve for phase retrieval problems. The algorithm works with two main planes, the *modulation plane* where the amplitude

of the field is known, and the phase is to be retrieved, and the *holographic plane*, where the desired intensity pattern is known. An initial guess of the phase distribution in the input plane is typically performed. This guess may be random or based on some a priori conditions.[88,92] The algorithm then enters a loop in which each iteration consists of a few steps. Forward propagation combines the known amplitude with the estimated phase in the input plane to form a complex field. A discrete Fast Fourier Transform (FFT) is then performed to propagate this field to the target plane. In the target plane, a new complex field is obtained whose intensity is generally not the same as the desired one. The phase of this field is maintained but its intensity is replaced by the square root of the desired intensity distribution. At this point, back propagation is performed by applying the inverse FFT to this modified complex field. Once back in the input plane, the intensity of the field is replaced by the known original amplitude while maintaining the newly calculated phase. If the algorithm has not converged, the newly calculated phase from the input plane is used in the next iteration step. When the algorithm converges or reaches a preset number of iterations, the phase in the input plane is taken as the retrieved phase solution. There are several modifications and extensions to the basic GS algorithm that aim to improve convergence speed, robustness, and accuracy.[88]

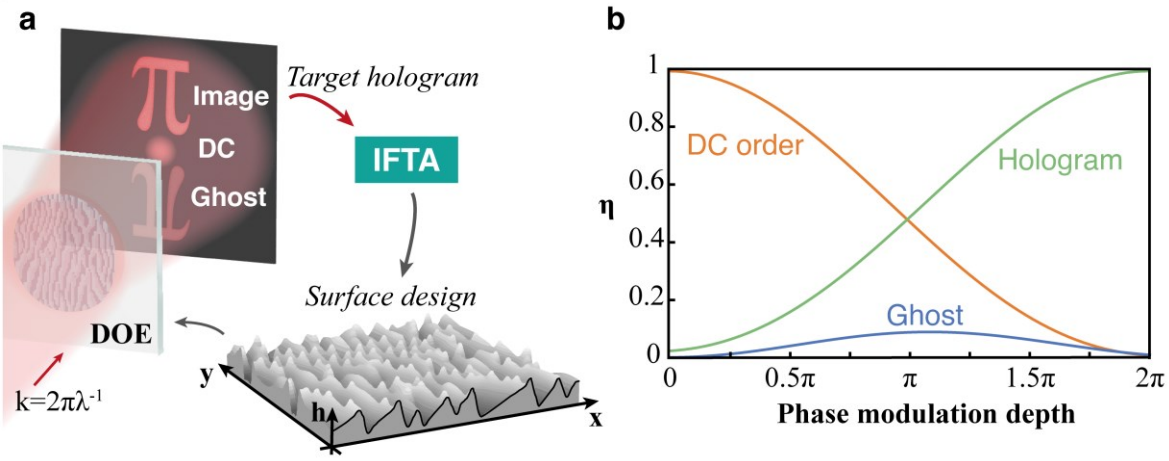

Figure 9: Optical functionality of holographic projectors. a) A kinoform DOE can generate an arbitrary far-field diffraction pattern with unmodulated and ghost orders. b) Diffraction efficiency the holographic image, the DC term, and the ghost hologram as function of the imposed phase modulation depth.

Once the kinoform is calculated, the design of the holographic projector is fixed, and all the all the challenges are at the manufacturing level. Optimal image reconstruction requires an accurate transfer of the designed phase mask. Any defect arising in this process will degrade the hologram quality, causing the reduction in the diffraction efficiency and the appearance of spurious contributions in the target holographic image, as shown in Figure 9a. Suppose that the holographic projector is represented by a complex transverse transmittance function in the form of $t(x,y) = e^{i\varphi(x,y)}$. The phase encoding process, starting with the proper phase design, and ending with the fabrication process, generally leads to a device whose experimental transmittance $t^{exp}(x,y)$, and in

particular its phase modulation provided on the transmitted field, is a function g of the design phase:[93]

$$t^{exp}(x,y) = e^{ig[\varphi(x,y)]} \tag{2.36}$$

In the best case, this functional relationship is linear, allowing the total surface relief amplitude Δh to be tuned to reach a 2π modulation depth. According to equation (2.21), this condition is achieved for $\Delta h = \lambda/(n - n_s)$. This condition guarantees the maximum diffraction efficiency and ensures that all the incident optical power is effectively shaped into the reconstructed holographic pattern. During the encoding process, more complex distortion effects may impose a non-linear shape on g. These certainly include quantization and pixelation effects, as well as non-linear responses of the material to the patterning process, leading to a DOE in which phase mismatches are included. Assuming that the deformation is space invariant, the spatial coordinates in equation (2.36) can be omitted and the function t^{exp} can be expanded in terms of its argument, according to the generalized harmonic analysis:[94]

$$t^{exp}(x,y) = \sum_{\alpha=-\infty}^{+\infty} G_\alpha e^{i\alpha\varphi} \tag{2.37}$$

where the coefficients G_α can be determined as:

$$G_\alpha = \int_0^{2\pi} t^{exp} e^{i\alpha\varphi}\, d\varphi \tag{2.38}$$

where α is an integer number. The term of the series obtained for $\alpha = 1$ is the only one whose Fourier transform gives an optical field whose intensity profile in the reconstruction plane corresponds to $I_\infty(x,y)$. The amount of optical power shaped in the reconstructed intensity profile with respect to the total transmitted power, is equal to $|G_1|^2$ and is equal to unity only when the ideal case is reached ($g(\varphi) = \varphi$), as demonstrated by the plot in Figure 9b. The other terms of the series, apart from the term $\alpha = 0$ which determines an unmodulated optical component named DC term, contribute with shifted and scaled replicas of the desired intensity pattern, known as ghosts or false images.[93,95] The total reconstructed pattern is a weighted sum of the desired image, the DC term, and the false images with a relative efficiency related to $|G_\alpha|^2$. These contributions may overlap in the reconstruction plane, eventually requiring an off-axis design for the hologram, reducing the available target image domain by half of the field of view.[95] However, even in the case of a defect-free lateral pattern transfer, a deviation from a full 2π modulation depth, associated with eventual total relief heigh errors induced in the dielectric structured surface, will still cause the emergence of the spurious holographic terms.[93]

3

Standard manufacturing processes

The surface relief geometry of a DOE can be designed in a wide range of shapes, each defining a specific functionality of the final device. The required phase modulation can be a binary two-phase step, a multilevel discrete distribution, or even a continuous phase profile. Once that the target phase modulation has been determined from the design process, it is necessary to reproduce this phase geometry in a physical device. As specified by the DOE design equation (2.21), the target phase profile $\varphi(x,y)$ should be proportionally encoded as a specific height distribution $h(x,y)$ at the material surface. In some cases, $h(x,y)$ can be represented by a relatively simple equation, while in other cases it can be designed numerically and iteratively on a computer. As in the case of a holographic projector design, the resulting phase solution of equation (2.35) may assume a continuous geometry with an almost random distribution of phase discontinuities and sharp variations. This results in an elaborate and complex structure, which makes the DOE fabrication a non-trivial process.

In addition to the lateral patterns, which can be one or two dimensional with varying degrees of symmetry or asymmetry, the modulation depth plays a fundamental role in determining the final diffraction efficiency of the fabricated DOE. While the typical lateral resolution required for the fabrication of diffractive optical elements is on the order of the light wavelength λ, the modulation depth tolerance is typically smaller on the order of fractions of λ. Over the years, many different methods have been developed to fabricate diffractive microstructures, including optical lithographic techniques, direct micropattern inscription, or replication from a mold. Optical lithography uses photosensitive polymers, and the patterning process is the result of controlled exposure and subsequent chemical and physical processes. In direct writing processes, the surface relief structure is created by controlled removal of material without any intermediate processes. Finally, replication techniques allow the creation of copies of surface relief structures in polymers or other optical materials from a master element. The choice of fabrication method is generally driven by the target function and cost, as each of them has different advantages and disadvantages.

3.1 Fabrication of DOEs by photolithography

Optical Lithography (OL), also known as *photolithography*, is the backbone process for the semiconductor manufacturing, also representing a standard for the fabrication of optical microstructures.[13,96] Despite the development of even more advanced lithographic techniques, photolithography remains at the forefront of scientific research.[58] The core of the process is the use of photoresists, which are photosensitive materials that can polymerize or depolymerize under the influence of light, thereby changing their physical or chemical properties. Figure 10 illustrates the complete sequence of steps that characterize optical lithography, for surfaces micropatterning. First, the photoresist is spin-coated onto the substrate, with the film thickness being controlled by changing the resist viscosity and the spinning speed. The most commonly used substrate material to form the photolithographic wafer, is silicon, due to its semiconducting properties, and the mature chip industry that surrounds it. For optical applications, other materials may be used, depending on the desired properties.[13,97] After the coating process, the wafer is prebaked to drive off excess photoresist solvent. The coated substrate is then exposed to a light pattern produced by a lithographic mask, that defines the exposure areas.[60]

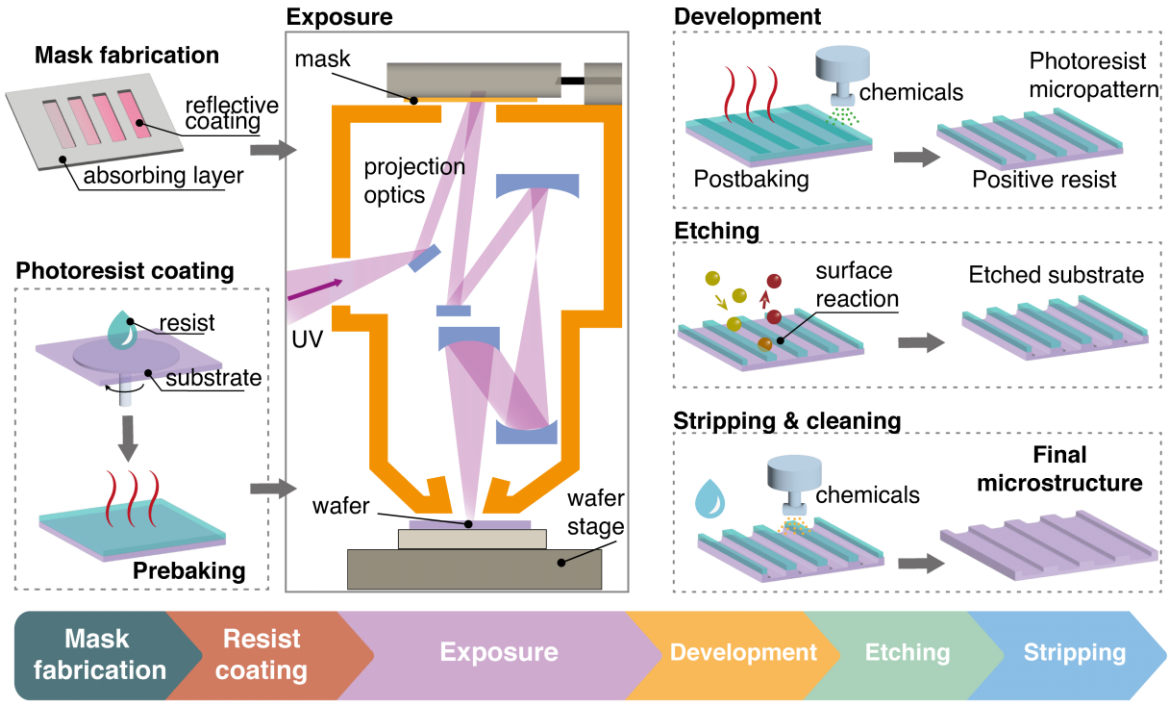

Figure 10: Typical workflow for standard EUV optical lithography.

In optical lithography, the mask, also known as the *photomask*, is a critical component used to transfer patterns onto the photoresist. The base material of a photomask is usually a transparent, flat, and pure substrate. Quartz and fused silica are commonly used due to their high transparency to ultraviolet light, which is often used in the lithography process. A layer of material that can absorb or block the writing light is

applied to the substrate. This layer is usually a metal such as chromium.[60] An antireflective coating may be applied between the chromium layer and the substrate to reduce reflections that could lead to exposure errors. The chrome layer is either present or absent, defining the binary pattern of the mask. Phase shift masks are also used to improve image resolution by manipulating the phase of the light passing through different areas of the mask.[98] The early process used for photolithography was contact printing. In this process, the mask is in direct contact with the resist during exposure to light. The major challenge with this approach is that the proximity effects arising from the contact between the mask and the wafer produce a high level of defects.[13] A different approach is represented by the projection exposure. The mask, which encodes the desired pattern, is positioned between the light source and the resist. The mask pattern, generated by the transmitted light, is reduced, and projected onto the wafer surface through a series of optical lenses or mirrors. Typical pattern demagnification values range from 0.1 to 1.[13,60] Precision alignment and focusing systems ensure that the pattern is accurately aligned with any existing patterns on the wafer and is sharply focused to achieve the required pattern size.[60,99]

The achievable lateral resolution Δx of the lithographic system can be evaluated by the Rayleigh equation:[7]

$$\Delta x = \frac{k_1 \lambda}{NA} \tag{3.1}$$

where λ is the exposing radiation wavelength and NA is the numerical aperture of the projection system. The constant k_1 is an empirical coefficient depending on the on the photoresist, the illumination system, and the mask pattern. The actual lower limit is $k_1 = 0.25$.[99] To achieve high resolution, a high numerical aperture or shorter wavelength is required. Since achieving high numerical aperture is typically challenging, the trend over the years has been to reduce the wavelength, with challenges related to finding compatible optical elements, light sources, and resists. The current standards for photolithography involve the use of UV radiation at wavelengths of $436\,nm$, $405\,nm$ or $365\,nm$, defining the G-, H-, and I-line standards, respectively. These standards also refer to mercury spectral lines, as the common light source of the optical lithography systems were vaporized mercury arc gas lamps.[60] The continuous downscaling roadmap, required by the chip and semiconductor industry, led to the replacement of mercury lamps with excimer lasers. Typical wavelengths in the deep ultraviolet range are reached with these sources (e.g. $193\,nm$ for ArF laser).[100,101] The use of shorter wavelength sources has allowed higher lateral resolution at the expense of the setup complexity. The ultimate limit today is represented by the extreme ultraviolet (EUV) lithography.[60] The basic concept of EUV lithography is to produce a bright source of $13.5\,nm$ radiation using a laser-pulsed tin (Sn) plasma.[102,103] Since common optical materials, including air, absorb in the EUV range, the projection system is typically designed with reflective optics, typically requiring high manufacturing standards. The entire optical system must be kept under vacuum, as air absorption and scattering can compromise the entire process.[60] An alternative to the transmissive mask is required for EUV sources. In this

standard, a reflective mask is typically used. Unlike the transparent substrates used in traditional masks, reflective masks are based on a multi-layer structure that reflects light. On top of the reflective coating, an absorber layer is added where the patterns are defined. To further improve the lateral resolution, immersion fluids can be introduced into the gap between the projection system and the resist to increase the numerical aperture. However, immersion lithography suffers of severe limitations related to the presence of the fluid, which causes imperfections and defects on the wafer.[104] In UV optical lithography, the actual resolution limit is set at around $0.1\,\mu m$,[97] which is still acceptable for the fabrication of diffractive optical elements, but out of the demand of the integrated circuit industry. EUV lithography, can easily achieve higher resolution with a resolution limit below $0.01\,\mu m$.[101,105]

After exposure, the wafer is moved one step forward by a stepper, implementing the so-called *step-and-repeat* method. A small grid area of the wafer is exposed at a time, and then it is moved to the next step until the entire wafer is exposed.[97] At this stage, the wafer is treated with a chemical development to remove the unwanted resist. For positive photoresists, the exposed areas become more soluble in the developer solution, so during development, these regions are washed away, leaving the unexposed areas intact. Conversely, negative photoresists become less soluble where they are exposed to light, leaving only the exposed regions remain after the development step. The most widely and commercially used resists in the G-line and I-line are positive photoresists, which often contain Novolak resin that provides the structural framework of the film. The resin contains photoactive compounds that generate acid upon exposure, which then catalyzes a solubility change in the resin. Developers are usually alkaline solutions (such as sodium or potassium hydroxide) that selectively dissolve the more soluble areas of the photoresist after exposure. The result is a copy of the photomask micropattern, formed by the resist resin on the wafer substrate.[59,97] The final pattern transfer from the resist to the substrate is performed by etching, which is a subtractive pattern transfer technique. At this stage, any portion of the wafer that is not protected by the photoresist is removed. Wet etching uses liquid chemicals or etchants (such as hydrofluoric acid for silicon dioxide) to remove material. It typically results in isotropic and rough surfaces, and it is not recommended for high-accurate micropatterns. Dry etching, instead, involves using gases, plasmas, or particles (such as sulfur hexafluoride for silicon) to etch materials. This process can be highly material selective and can result in an anisotropic process, allowing for relatively high aspect ratio geometries. After the etching process, a stripping process removes the remaining photoresist by using organic solvents or oxidizing acids. Finally, a cleaning solution is used to remove contaminants and particles from the wafer surface.[13,59,60]

3.2 Direct fabrication and replication techniques

While optical lithography is a cornerstone in the fabrication of diffractive microstructures, it has significant limitations. One of the primary constraints is its dependence on masks. The process requires prefabricated photomasks, which in turn are

produced using other lithographic techniques, like Electron Beam Lithography (EBL).[60] This dependency creates several challenges. First, the reliance on masks means that the geometries of the DOEs are predetermined by the mask design. This restricts the flexibility of the DOE design, as any change in the DOE pattern necessitates the creation of a new mask, making the process less adaptable and more time consuming. In addition, the fabrication of these masks is not only expensive but also impacts to the overall cost and duration of the DOE manufacturing process. Optical lithography predominantly produces binary surface profiles.[96] However, many advanced applications of DOEs require smooth, continuous surface profiles.[13] To achieve these continuous profiles using binary lithography, several strategies must be employed, each with its own drawbacks.

Multilevel lithography, involving multiple lithography and etching steps to approximate a continuous profile, is a first example of continuous DOEs manufacturing.[13,106] This process is not only complex, but also introduces more opportunities for error and misalignment, and requires a different mask at each iteration. Other approaches, typically used for blazed grating fabrication, involve precise control over an anisotropic etching process to create slanted profiles,[107,108] or the use of grayscale masks.[109,110] Masks are the major limitation associated with optical lithography, pushing the transition to direct writing techniques. This shift has been driven by the need for greater precision, flexibility, and efficiency in the fabrication of small-scale features, especially for the semiconductor industry. The simplest approach for the fabrication of DOEs without masks is the holographic interference lithography.[111,112] This technique is particularly effective for creating periodic structures such as photonic crystals and diffraction gratings.[13] It involves splitting a laser beam into two or more coherent beams that interfere on the photoresist coated substrate. The interference of these beams produces a periodic intensity pattern. This is a primary method for producing diffractive gratings with extremely controlled periods:[112]

$$\Lambda = \frac{\lambda}{2\sin(\vartheta/2)} \tag{3.2}$$

where λ is the illumination wavelength and ϑ is the angle between the two interfering beams. Interference lithography has been used to produce diffraction gratings with periods of less than $0.3\,\mu m$[113–115], however complex gratings typically require multiple beams or exposure steps.[116–118] Moreover, this method lacks the flexibility to create arbitrary patterns. In direct writing techniques, the exposure pattern is generated directly and sequentially on the photoresist layer using an electron beam or laser beam. Instead of using a mask exposure, the intensity of the beam is locally controlled so that the local exposure is proportional to the required depth of the resist. When the resist is developed, the depth of the local surface relief structure is proportional to the dose delivered to that area by the e-beam or laser source.[13]

Electron beam lithography involves directing a focused beam of electrons to draw custom shapes on a surface covered with an electron-sensitive film acting as a resist.[59,61] The pattern is written on the resist by a raster scanning, in which the beam moves back

and forth across the resist. The resolution of EBL is determined by factors such as the diameter of the electron beam, the e-resist, and the proximity effect, which is an effect related to electron scattering. EBL can achieve resolutions of less than $10\,nm$ nanometers, making it an invaluable tool in nanotechnology.[61] This technique is often deemed an inefficient and costly for the fabrication of DOEs. The high resolution achieved by EBL is not essential for the fabrication of diffractive devices and does not offer significant advantages when considering the high facility costs[119] and the slow manufacturing speed.[120] However, blazed gratings[121] and microlenses[122,123] with a continuous profile can be fabricated using this technique. Conversely, the scenario is different in the field of metasurface fabrication. Metasurfaces, which manipulate light on scales smaller than the wavelength, require the kind of high-resolution patterning that EBL provides.[54]

A similar approach can be developed by replacing electrons with photons, considering a Direct Laser Writing (DLW) lithography. DLW allows for reduced costs than EBL at the expense of lower resolution. Laser direct write systems typically use tightly focused beams from helium-cadmium or argon-ion lasers to produce spots on the order of a micrometer in size. This approach has been demonstrated to be particularly suitable for the fabrication of DOEs.[124] Complex surface patterns, also resulting from complex computer design, can be directly transferred to an appropriate optical material, enabling the realization of diffractive optical elements with advanced optical functionality such as broadband lenses.[25,125,126] The exploitation of nonlinearities in the photoresist optical response, can also allow the implantation of two-photon techniques,[127] with a further increase in axial and lateral resolution beyond the diffraction limit, resulting in near-perfect DOEs profiles.[127,128]

The use of direct writing approaches allows the creation of continuous surface relief structures. These processes eliminate the need for lithographic masks, reducing the time and cost of producing prototype elements. A disadvantage of direct writing is that it is a serial process. Each element must be written one at a time by the scanning beam, before performing the postexposure processes, making it unsuitable for volume production of DOEs.[13] Differently from these techniques, direct machining methods for DOEs do not require any intermediate processing step such, as developing or etching as the microstructures are formed by direct removal of the material. Early examples are represented by mechanical ruling and diamond turning methods, where a sharp diamond tip is used to scrape the substrate.[13,129] Despite their past use for the fabrication of gratings[130] and diffractive lenses,[131] their widespread application has been limited by fabrication errors due to the tip shape and the limitation to fabricating structures composed of either straight line or circularly symmetric gratings.

Mechanical ruling and diamond turning can be considered the prototypes of modern Scanning Probe Lithography (SPL) techniques. Unlike traditional lithography techniques that use light or electrons to pattern surfaces, SPL employs a physical probe to create patterns at the nanoscale. This allows for very precise control of pattern size, often down to the atomic or molecular scale, and represents a widely accessible form of lithography by eliminating the need for high power sources and large facilities. At the core of SPL is a sharp probe similar to those used in Atomic Force Microscopy (AFM).

The probe interacts with the surface of the material that is to be patterned, with direct mechanical interaction causing material removal,[132] local deposition of materials,[133] or inducing a thermal evaporation of the substrate if the tip is properly heated up.[66] In particular, the thermal scanning probe has proven to be a powerful and accessible tool for fabricating DOEs, ranging from complex gratings and lenses geometries,[84] up to plasmonic nanostructures.[67] Scanning probe lithography offers a significant advantage as the pattern is created directly in the optical material substrate, eliminating the need for photoresists. A similar approach is represented by Focused Ion Beam (FIB) lithography. In this process, a focused beam of ions, typically gallium ions, is directed at the material surface. The high-energy ions collide at the surface, sputtering away material on a nanometer scale.[58] This direct etching of the surface allows the fabrication of DOEs with continuous profiles and high accuracy.[134–136] However, FIB lithography has significant drawbacks. The ion beam can damage the substrate material, and ion implantation effects and material redeposition can cause severe fabrication errors. In addition, FIB systems are expensive, and the process can be slower than other lithography methods, making it less suitable for high-volume production. Similarly, laser ablation can be employed to fabricate DOEs.[137–139] Here, a high-energy laser beam heats, melts, and vaporizes the material at the surface. Laser ablation can be performed on a wide range of materials, but it shares the same limitations as FIB lithography.[140]

Because of the time and cost required to fabricate diffractive optics by direct machining and lithography techniques, it is attractive to produce replicas of these surface relief structures in other materials at low cost starting from a master or a mold. In these processes, the master element is brought into contact with a formable material, usually a curable polymer or a thermoplastic material. Several methods, such as molding, embossing, or casting can be employed.[13,141,142] Nanoimprint Lithography (NIL) is an example of a replication technique. The master template is pressed into the resist-coated substrate. This can be done at room temperature (cold embossing) or with the application of heat (thermal nanoimprint lithography). The resist is deformed and takes on the inverse pattern of the master template. After the resist is deformed it is cured, and the master template is removed, leaving a negative replica of its pattern on the substrate.[64,65] NIL allows for the rapid production of large areas and high volumes of patterned surfaces at relatively low cost,[143] but its dependence on the master element makes it unsuitable for versatile DOE prototyping.

3.3 Need of alternative form of lithography

Standard lithographic techniques, described in the previous sections, face several limitations that make them less suitable for the fabrication of DOEs. Figure 11 summarizes the major strengths and weaknesses of the discussed techniques. The main problem with optical lithography is its strong dependence on photomasks, which define once and for all the patterns to be replicated on the substrate. This dependency not only limits design flexibility, but also increases the cost and time required to fabricate custom or complex diffractive devices. EBL, DLW, and FIB partially solve this problem

with a maskless approach, but the equipment cost and the usage of resources are critical factors to be considered.[144,145] OL, EBL, and FIB, especially in their more advanced forms, demand high energy consumption and specialized equipment, making it a resource-intensive process. This aspect can be particularly challenging when scaling up production or pursuing green solutions.[146] Another primary constraint is the limited choice of materials available for optics. Standard lithography often requires materials that are compatible with its process parameters, which are typically optimized for the chip industry and do not always match with the ideal optical properties required for diffractive elements. When specific materials are required, additional processes are typically used, such as lift-off processes, which involve an additional resist coating after the exposure.[147,148]

	Strenghts	Weaknesses	Throughput	Geometry
Photolithography & etching	Surface precision	Mask dependent	Medium	Binary modulation
Electron Beam lithography	High resolution	Slow process	Low	Analog modulation
Direct Laser Writing	Optical maskless system	Serial process	Medium	Analog modulation
Interference lithography	Large area maskless pattering	Limited flexibility	High	Periodic modulation
Scanning probe lithography	Direct surface inscription	Serial process	Low	Analog modulation
Focused Ion Beam lithography	Direct high-resolution inscription	Equipment cost	Low	Analog modulation
Laser ablation	Wide material range	High fabrication error rate	Low	Analog modulation
Replication	Volume and cheap production	Master dependent	High	Mask determined

Figure 11: Comparison of standard lithographic techniques.

The use of hazardous chemicals is another significant concern. These processes typically involve various chemicals for etching and pattern development, many of which pose environmental and health risks.[62,149] This, in addition to expensive lithography equipment that requires substantial energy consumption and cleanrooms, limits lithographic facilities, with a limited number of key players in the word.[74] This prevents the accessibility of lithography to smaller research institutions or companies and increases the overall cost of DOEs. On the other hand, SPL and NIL together represent a more accessible form of lithography, allowing DOEs to be produced in high volumes and on a large scale, once that the master template is defined by one of the SPL techniques. However, at the research level they still have severe limitations, related to the slow serial processes required to fabricate the molds and the limited flexibility.

To overcome these bottlenecks, maskless lithography has emerged in recent years as a promising alternative to traditional mask-based lithography for the fabrication of microstructures. At its core is the use of Spatial Light Modulators (SLM) to replace photomasks. Both liquid crystal devices[63,150,151] and Digital Micromirror Devices (DMDs)[152–155] have been validated as good candidates for mask replacement. In the first case, the SLM consists of an array of pixels, each of which can be individually controlled to modulate the light passing through or reflected by the device. DMDs, on the other hand, consist of an array of micromirrors, each corresponding to a pixel in the projected image. These mirrors can be individually tilted to control the reflection of light, directing it either into the projecting lens to expose the photoresist, or out of the lens to leave it unexposed. SLMs allow the amplitude, phase, or polarization of light beams to modulate in space and time, enabling rapid prototyping and customization of optical patterns. Because the design is controlled by software, it can be modified easily and quickly, allowing for a high degree of optimization in diffractive optics design and prototyping.

The introduction of maskless approaches does not completely solve the problem, because whatever it is, any lithographic approach leads to a static nature of the surfaces after fabrication, which is a notable limitation. Once the pattern is created by lithography, it cannot be modified or adjusted, which limits the functionality of the diffractive elements in dynamic or adaptive optical systems. The combination of a maskless approach with innovative photosensitive materials can be a complete game changer. Such materials should have the property to be directly patterned with low power light sources, allowing the use of low intensity lasers, and avoiding any post exposure process. One class of photosensitive materials with these properties already exists and is represented by azopolymers, where **direct and reversible** structuring of the surface can occur under low power light absorption.

4

DOEs from photopatterning of azopolymers

Azomaterials are chemical systems that incorporate azobenzene molecules into their matrix. They are a unique class of materials that has garnered significant interest in the field of materials science in recent years.[156] The chemical structure of the azobenzene consists of two phenyl rings linked through the azo bond (−N=N−).[157] Azobenzene can exist in two isomeric forms, the thermodynamically stable *trans* state and the metastable *cis* state.[158,159] While the trans molecule has a rod-like and planar geometry, the cis azobenzene has a folded chemical structure with the two phenyl rings forming an angle of about 90° and the emergence of a molecular dipole moment. The isomerization process from trans to cis can be triggered by photon absorption in the UV-visible region, as this process has a broad absorption band around $320\,nm$ (pi-pi* transitions) and a weak absorption band centered at $450\,nm$ (n-pi* transitions).[75] The reverse isomerization can occur due to thermal relaxation or when the molecule absorbs a new photon with an energy matching the absorption band of the cis isomer.[160] For this reason, bare azobenzene represent a two-state photo-switchable system.[161,162]

The chemical structure of azobenzene can be modified by adding functional groups to the phenyl rings while retaining the nitrogen double bond. This process allows the creation of a wide range of materials known as azomolecules. These molecules can be designed to have an overlap in the trans and cis absorption curve, resulting in a cyclic photoisomerization process under the absorption of monochromatic light.[75,163] This cyclic process can give rise to some interesting phenomena as a photo-orientation effect of an ensemble of azomolecules illuminated with linearly polarized light. Considering the light absorption process as a dipole interaction, its probability varies with $\cos^2\delta$, where δ is the angle between the electric field of the polarized light and the molecular dipole direction.[75] A trans azomolecule can absorb a photon, initiating a photo-isomerization cycle. After each isomerization, a new photon absorption can return the molecule from the cis to the trans state. However, the orientation of the molecular axis changes randomly, and after a certain number of isomerization cycles, it could be oriented orthogonal to the light polarization direction. A new isomerization cycle has an almost zero probability to take place even if the light irradiation continues. The result of this orientational alignment is that after many isomerization cycles, the population of molecules oriented in the direction perpendicular to the electric field increases. The photo-orientation effect of the azomolecules under linearly polarized light irradiation

leads to strong birefringence and dichroism, but it is a completely reversible and reconfigurable state. A new alignment can be induced by rotating the irradiating linear polarization direction, or circularly polarized or unpolarized light can eventually be used to restore the isotropic molecular distribution.[157]

When azomolecules are embedded in a host material, the cyclic isomerization process can generate a photoinduced stress at the nanoscale,[164–166] which can be translated into macroscopic effects.[75,167] In particular, a light-induced reversible and directional mass migration is observed in amorphous azomaterial films. This phenomenon leads to the formation of stable surface reliefs on the free surface of the film, whose geometries depend on the intensity distribution, polarization state, and wavefront shape of the irradiating light beam.[75] Because of this effect, amorphous azomaterial films are different from any other photosensitive material, such as standard photoresists used in optical lithography. Photoinduced mass migration has been studied for a long time and a large literature has been produced, which is the foundation of my research.

4.1 Interference lithography using azopolymers

Light induced mass migration is the most captivating phenomenon occurring in azobenzene-containing materials as a result of the cyclic photoisomerization processes. This effect is widely observed in azopolymers, prepared in the form of amorphous thin films.[75] In these materials, the azobenzene unit is bonded to a polymeric matrix by supramolecular or covalent interaction.[156] Upon irradiation with patterned light, the isomerization of the azo chromophores leads to local photoinduced forces that result in a mass transport of the polymer from the illuminated areas to the dark regions. This mass migration manifests as surface relief patterns on the polymer film. The morphology of these patterns can be intricately controlled by the intensity, polarization, and duration of light exposure. The surface geometry is not just the result of surface-level changes, but involves the movement of material, essentially reshaping the surface of the polymer.[75] The first observation of this phenomenon was made independently in 1995 by Natansohn and Rochon[168] and Kim et al[169]. They observed that the free surface of an azopolymer thin film develops a large-scale periodic modulation when irradiated with a two-beam interference pattern, as shown in Figure 12a-b. The polymer surface geometry exactly matches the sinusoidal spatially modulated light pattern as stable sinusoidal surface reliefs, now called *Surface Relief Gratings* (SRGs). While the periodicity Λ of the SRGs matches the periodicity of the interferogram, the modulation depth Δh varies with the exposure time. For sufficiently low intensity, the relief depth increases approximately linearly with the exposure time Δt:[170,171]

$$\Delta h = c \cdot \Delta t \tag{4.1}$$

where $c > 0$ is a phenomenological parameter depending on the material and the illumination conditions.

The surface modulation occurs at very low light intensities, ruling out any ablative or destructive processes. The phenomenon is indeed a light-triggered mass migration process, occurring at temperatures considerably below the glass transition temperature (T_g) of the amorphous azomaterial.[75] These early experiments represented the moment when a Pandora's box was opened. Things became immediately even more fascinating when subsequent experiments demonstrated that the polarization state of the two beams plays a crucial role.[172,173] It was observed that under polarized light irradiation, the material motion is highly directional, with the polarization direction fixing a preferential direction for the mass transport.[174,175] In other words, an intensity modulation across the azopolymer surface alone is not enough to induce the SRG formation. The presence of both a spatially varying intensity pattern and a non-zero component of the optical electric field in the direction of the intensity gradient is required for efficient material motion.[75]

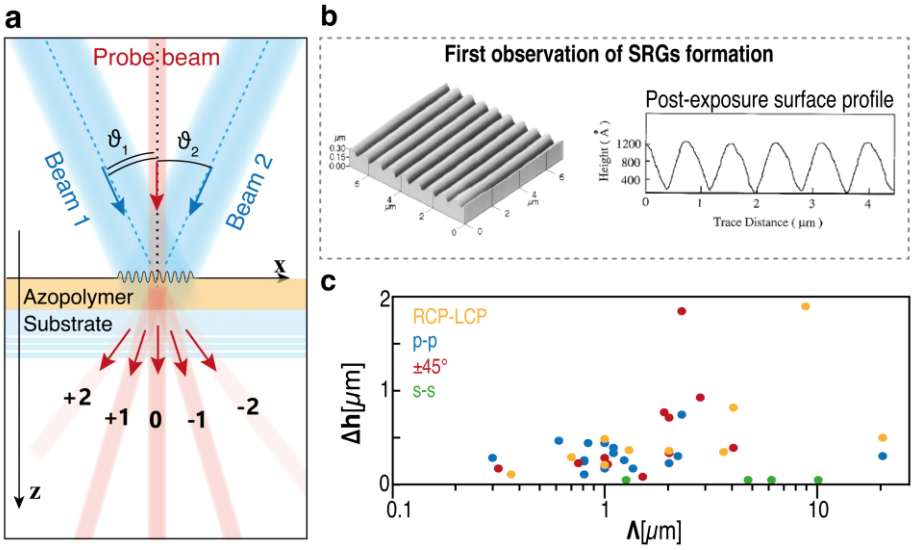

Figure 12: Interference lithography on azopolymer films. a) Schematic of the typical experimental setup for interference-based inscription of azopolymer SRGs and diffraction efficiency measurement in real-time. b) Surface profile obtained from AFM scan of the surface right after the exposure, as first observed by Kim et al. in 1995. The panel is reproduced from ref.[169]. c) Plot showing the typically reported SRG modulation depth Δh as a function of the periodicity Λ. Different colors refers to different polarization configurations. The periodicities are plotted on a logarithmic scale to improve data visualization.

In the case of interference illumination, depending on the polarization state of the two interfering beams, both periodically varying intensity and polarization patterns can occur, which also affect the SRG inscription efficiency. A schematic representation of a two-beam interference setup for the SRGs formation is given in Figure 12a. Two coherent light beams, with arbitrary polarization state and wavevectors $\vec{k}_1$ and $\vec{k}_2$ interfere at the azopolymer surface. The effect of the polarization state on the interferogram generation can be taken into account by considering a generalized interference picture, obtained as the vectorial addition of the two beams.[176] Interference can result in a spatial variation of light intensity or polarization, depending on the polarization ellipse of each beam. The two beams, with amplitudes $\vec{E}_1$ and $\vec{E}_2$, intersect

at the azopolymer surface at angles ϑ_i so that wavevector component along the x-direction for each beam can be written as:

$$k_{1x} = ksin(\vartheta_1)\hat{x}$$
$$k_{2x} = -ksin(\vartheta_2)\hat{x} \tag{4.2}$$

where $\hat{x}$ is the unitary vector in x-direction and $k = 2\pi/\lambda$. The two interfering beams generate a total electric field amplitude distribution at the azopolymer surface equal to:

$$\vec{\mathrm{E}}_{tot} = \vec{E}_1 \cdot e^{ik_{1x}x} + \vec{E}_2 \cdot e^{ik_{2x}x} \tag{4.3}$$

The intensity distribution in the interference region of the material (with refractive index n) can be calculated as:[176]

$$\mathrm{I}_{tot} = I_1 + I_2 + 2\Delta I \cdot cos(qx) \tag{4.4}$$

Here, q represents the grating vector magnitude, related to the optical path difference between the two beams. It can be evaluated as follows:

$$q = k_{1x} - k_{2x} = \frac{2\pi}{\lambda}\left(2sin\left(\frac{\vartheta}{2}\right)cos\left(\frac{\Delta\vartheta}{2}\right)\right) \tag{4.5}$$

where $\vartheta = \vartheta_1 + \vartheta_2$ and $\Delta\vartheta = \vartheta_1 - \vartheta_2$. Equation (4.4) predicts that the total intensity varies sinusoidally in the x-direction with a spatial periodicity equal to $\Lambda = 2\pi/q$, expressed in terms of the wavelength λ and the angle ϑ between the two interfering beams. For symmetric interference, $\Delta\vartheta = 0$ and the spatial period corresponds to the expression in equation (3.2).

To consider the SRG inscription process under different polarization combinations for the writing beams, the intensity variation range ΔI can be expressed as the trace of a three-by-three generalized interference matrix:[176]

$$\Delta I = tr\{M_{ij}\} \tag{4.6}$$

where $M_{ij} = E_{1i}E_{2j}^*$ and the indices i,j stand for the spatial coordinates. Here, the off-diagonal elements correspond to the polarization variations in the interference region. Using the above formalism, the periodic spatial variations of the polarization ellipse can be calculated for any polarization configuration. The first polarization configuration

used since early experiments[168,169,177] is the p-p configuration. In this case, the interfering beams are linearly polarized perpendicular to the y-direction in the x-z plane, such that $E_{1,2y} = 0$. By imposing this condition in equation (4.6), is found that this configuration results in both intensity and polarization variations in the interference plane. For small angles ϑ, the electric field component along the z-direction can be neglected and the resulting electric field can be considered parallel to the x-direction, favoring the mass migration process. However, as the interfering angle ϑ increases, the intensity modulation ΔI decreases and vanishes for $\vartheta = 90°$, due to the z-component.[176] This, among other effects, contributes to the lower efficiency in writing small periodicity gratings, which typically requires to be compensated by reducing the inscription wavelengh.[178] This configuration has been widely used to fabricate SRGs acting as diffraction gratings[178–181], templates with different periodicity for soft molding[182] or to implement tunable lasers from inscribed SRGs.[183]

Contrary to the previous configuration, the SRG formation is unfavored when the two interfering beams are linearly polarized in the y-direction. This configuration, called s-s, produces a pure intensity modulation in the interference plane and a high contrast $\Delta I = I_0$ for beams of equal intensity I_0. However, even if the surface is exposed for a long time, the resulting SRGs show a low modulation depth[184–187] because the total electric field is orthogonal to the intensity gradient. This represents the fingerprint of azopolymers. In fact, this configuration ensures a favorable condition for any photosensitive material that responds solely to the light intensity pattern. For azopolymers, where polarization plays a fundamental role, the fabrication of periodic structures in this configuration is instead completely disfavored. To further demonstrate the role of the polarization in SRGs inscription, the s-p configuration can be considered. In this case, both beams are linearly polarized in the x-z plane, one along and the other orthogonal to the y-direction. In this situation, a pure polarization pattern is generated since there is no spatial variation of the intensity ($\Delta I = 0$). The polarization state of the total electric field varies with half of the periodicity predicted by equation (4.5) resulting in the surprising inscription of half-period SRGs.[188,189] Mixed polarization and intensity modulation can be achieved in many other configurations by orienting the beams polarization at $\pm 45°$ with respect to the y-direction or by using right and left circularly polarized beams (RCP-LCP configuration).[176] In both cases the fabrication of SRGs with high modulation depth has been demonstrated.[190–193]

In addition to the illumination configuration, several other factors influence the SRGs inscription, including the chemical structure of the material,[185,194] azo concentration,[195–197] film preparation,[184] and film thickness.[198] Recently, azo-nanocomposites with incorporated nanorods have been found to exhibit a higher patterning efficiency.[199] The large number of parameters involved in the mass migration process, has complicated the development of a theoretical framework to fully explain the relationship between the molecular azo dye interaction with light and the macroscopic material transport. Various models have been proposed based on photoinduced mechanical stress,[166] pressure forces,[200] force gradient,[171] and even diffusive transport driven by the Marangoni effect.[201] The different combinations of material properties and illumination configurations have led to the realization of SRGs with different characteristics such as periodicity, modulation depth, efficiency, and fabrication times. A detailed review is

presented in Appendix, while the plot in Figure 12c shows the relationship between Δh and Λ extracted from several works in the literature reporting SRGs under different polarization configurations. Typical values for Λ range from a few hundred of nanometers up to $20\,\mu m$, depending on the angle between the two interfering beams.

Although not fully explained, the SRGs formation process from interference illumination suggests an alternative way to fabricate periodic surfaces, allowing for the implementation of a direct interference lithography. The photoinduced surface geometry is stable immediately after the exposure process, eliminating the need for complex intermediate lithographic processes such as development and etching steps. This behavior allows the surface of azopolymers to be inspected in real-time for the topographic acquisition of the developing surface, which can be accomplished by integrating a microscope system into the illumination setup. Both atomic force microscopy[202] and digital holographic microscopy[203] have been successfully used for this purpose. Real-time inspection also means that the optical properties of the grating can be characterized in-situ, without the need for separate test phases. By integrating a probe beam (Figure 12a), at a wavelength outside of the absorption band of the azopolymer, the diffraction behavior of the SRG can be measured without interfering with the inscription process. A typical parameter to be measured is the real-time diffraction efficiency, which, according to equation (2.26), provides the information about the grating modulation depth.[190,191,204–206] Another fundamental aspect lies in the non-destructive and reversible process at the core of the SRGs inscription. The first implication is that two consecutive interference exposures produce the inscription of a complex two-dimensional periodic surface, where the two structures that would be produced by two independent exposures are linearly multiplexed.[182,186] The second fundamental aspect is that the pristine flat surface can be easily restored by locally heating the polymer,[207] or by illuminating the target area with a uniform light beam[208]. In addition, the complete erasure of an inscribed SRG has also been demonstrated by a half-period shift of the interference pattern,[209] again confirming the full reversibility of the phenomenon. Figure 13 summarizes the state of the art in the fabrication of complex DOEs by azopolymer-based interference lithography.

The deterministic realization of quasicrystals over large scales certainly belongs on this list. Quasicrystal-like DOEs are realized by sequential rotations of the azopolymer film upon multiexposure steps to a fixed interference pattern of light.[210] The diffraction pattern fully reproduces the theoretical prediction of the Bragg's diffraction law, with a discrete distribution of spots composing the far field diffraction pattern (Figure 13a). This approach represented a fundamental milestone, demonstrating that engineered discrete Fourier spectra of the surface geometry allows to fully shape the angular distribution of monochromatic light. Similarly, surface multiplexing via sequential exposures was also shown to be a valid tool for fabricating DOEs with control over the chromatic dispersion properties. This requires high accuracy over the periodicity of the light pattern, which can be achieved by using a piezo-controlled interference setup and integrating a digital holographic microscope for surface inspection.[203] The result is a large-scale patterning where multiple exposures are combined to fabricate DOEs able to manifest structural color patterns (Figure 13b). One of the limitations in using azopolymers as a DOE platform is related to their high absorbance in the UV-visible

range, which typically limits their use as diffractive optical elements in the visible-NIR region of the spectra. However, the DOEs inscribed on an azopolymer film can be used as a mold to be replicated on other materials with more suitable optical properties. This has allowed the fabrication of SRGs for virtual and augmented reality applications,[211,212] by using a polydimethylsiloxane (PDMS) stamp, fabricated from prestructured optical Fourier surfaces (Figure 13c). Such DOEs allow light of different wavelengths to be efficiently coupled, guided, and outcoupled through the PDMS layer.

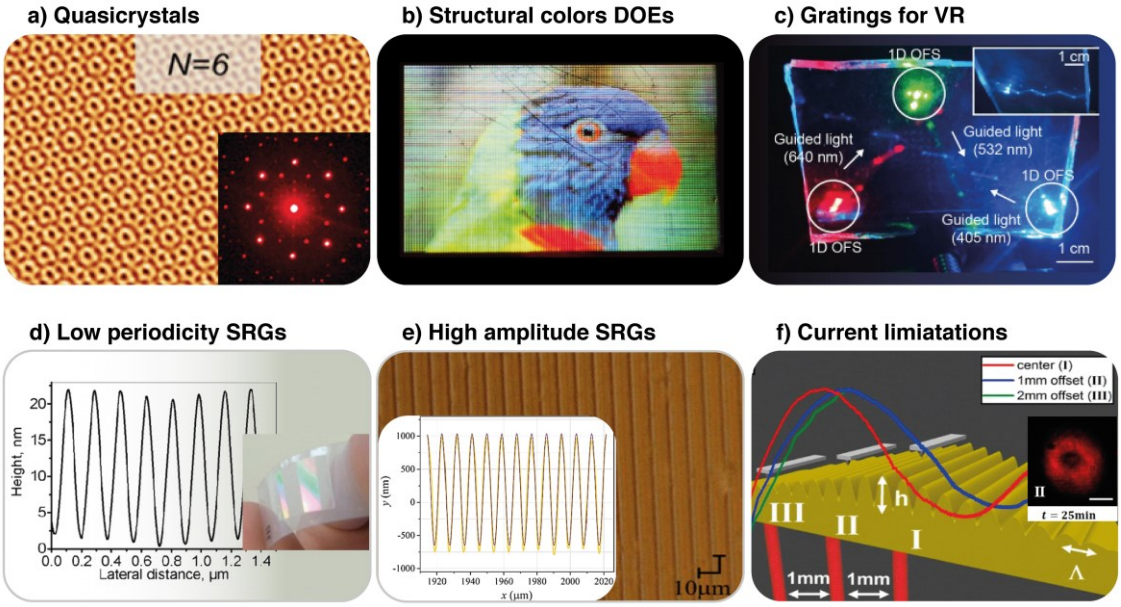

Figure 13: State of the art of DOEs fabrication by azopolymer interference patterning. a) Quasicrystal-like structure achieved with six serial exposures, and relative diffraction pattern. Image reproduced from ref.[210] b) Photograph of a Rainbow Lorikeet written on an azopolymer film. Each pixel of the image contains three gratings that reflect red, green, and blue light toward the camera to create the image. Reproduced from ref.[203] c) Spatially multiplexed waveguides for VR display, developed by multiple interference inscriptions and replicated on PDMS stamps. Reproduced from ref.[211] d) AFM profile of SRG fabricated with a Lloyd's interferometer setup using UV exposure, producing sub-micron periodicity. After the fabrication, a PDMS replica is deposited on a flexible polycarbonate sheet for lasing applications. Images reproduced from ref.[178] e) AFM profile micrograph and corresponding profile of a SRG with high modulation depth. Reproduced from ref.[191] f) Plot of DE as a function of the SRG modulation depth measured at three different positions. The mismatch occurs due to the SRG amplitude modulation, which also causes a spatial intensity modulation of the first-order diffraction spot during the irradiation time. Images reproduced from ref.[213]

The first demonstrations of SRG structures with nanometer-scale periodicity were performed with a Lloyd's mirror interferometer operating at $355\,nm$.[178] The use of UV wavelength enabled the fabrication of SRG in the form of one- and two-dimensional gratings with different periodicities in the range below $1\,\mu m$ (Figure 13d). On the other hand, different strategies have been proposed to achieve a high modulation depth to maximize the diffraction efficiency towards larger wavelengths. The actual reported maximum depth is $\Delta h = 1.7\mu m$, using the RCP-LCP configuration.[191] Due to the Gaussian shape of the inscribing beams, the SRGs exhibit an amplitude modulated

geometry, resulting in a modulated shape for the diffraction spots (Figure 13f). While interference-based inscription facilitates the fabrication of SRGs over large areas with a specific periodicity, any beam misalignment can introduce deviations from the ideal sinusoidal target profile. Since the cross-sectional profile of the writing beams is typically Gaussian, the corresponding modulation depth of the SRG changes over the inscribed area.[213] When a wide probe beam is used to test the diffraction behavior, this results in a fine structure in the spatial profile of the diffraction spot, that changes even during the exposure process (Figure 13f). Additional effects, such as the appearance of SRG superstructures, can even further impact the SRG diffraction behavior, when long exposures are performed.[214,215]

4.2 Comment to author's published papers, part I

The preceding literature review serves as the backbone of my research, providing a foundational context from which my work can be framed. The findings in these studies (and several others that are not reported here) have directly guided my research. The following section describes the first part of my own contributions, where interference photopatterning of azopolymers has been used to test new material designs and to precisely engineer and study the diffraction behavior of SRGs. **Publication I-IV** and **Publication VIII** belong to this section.*

In **Publication II**, a novel molecular design for the azopolymer was proposed. It is characterized by a double supramolecular interaction acting on two positions of the aromatic ring of the azobenzene unit. This results in a highly directional azo-chromophore and polymer chain interaction, preventing additional rotational degree of freedom around the long molecular axis of the azobenzene. In this work, this novel design has been directly compared to single-bonded supramolecular structures. The hypothesis is that a greater directional constraint on the bond results in a more efficient mass migration. A p-p interference configuration was used as a test platform. Optimization of the material resulted directly from the quantitative characterization of the SRGs inscription process, suggesting effective feedback between the chemical design

---

* **Publication I:** M. Salvatore et al. *Programmable surface anisotropy from polarization-driven azopolymer reconfiguration*, Journal of Physics: Photonics 3(3), 034013 (2021).
Publication II: F. Borbone et al. *Enhanced photoinduced mass migration in supramolecular azopolymers by H-bond driven positional constraint*, Journal of Materials Chemistry C 9(34), 11368–11375 (2021).
Publication III: S. L. Oscurato et al. *Large-scale multiplexed azopolymer gratings with engineered diffraction behavior*, Advanced Materials Interfaces 2101375, 1–9 (2021).
Publication IV: F. Reda et al. *Accurate morphology-related diffraction behavior of light-induced surface relief gratings on azopolymers*, ACS Materials Letters 4(5), 953–959 (2022).
Publication VIII: M. Salvatore et al. *Diffractive refractometer based on scalar theory*, Polymers 15(7), 1605 (2023).

of the azopolymers and their use as photoresponsive materials. The comparative study led to the optimization of a new molecular design, characterized by a significant improvement in mass migration and surface relief grating inscription efficiency. SRGs fabricated from a double-bonded system showed a final first-order diffraction efficiency of 0.31. Under the same illumination conditions, SRGs inscribed in single-bonded azopolymer films prepared with the same thickness produced a diffraction efficiency of 0.019. In addition, in this work, the extraction of the azobenzene units from a photopatterned film by solvent rinsing was demonstrated. This process leaves the periodicity and the profile of the inscribed SRGs unchanged, but with a visible reduction of the SRG modulation depth (from about $110\,nm$ to $60\,nm$). This promising process may in the future expand the possibility of using inscribed DOEs over a wide range of wavelengths, typically limited by the absorption range of azo chromophores.

Publication III represents a first fundamental milestone of my research activity. In this work, a sequential p-p interference-based inscription of sinusoidal SRGs was used to realize diffraction gratings with multiplexed geometry and engineered chromatic behavior. A multiplexed grating that diffracts polychromatic light in the same direction was designed according to the prescriptions of the scalar diffraction theory. This grating was designed by multiplexing three sinusoidal gratings with periodicity Λ_i, defined by requiring that the three gratings diffract light of wavelengths $\lambda_1 = 633\,nm$ (red), $\lambda_2 = 532\,nm$ (green), and $\lambda_3 = 488\,nm$ (blue) under the same target angle. Despite the simplicity of the design, the subsequent fabrication step poses many challenges. First, the correct superposition of sinusoidal reliefs with accurate periodicity must be achieved. In addition, each of the components of the multiplexed structures must have the same relative weight. To optimize the superposition of the individual sinusoidal components, real-time diffraction efficiency measurements were used, with a probe laser beam integrated in the optical path. This allowed an empirical tuning of the exposure time for each sinusoidal component, by imposing the same diffraction efficiency in the first order on the superimposed sinusoidal reliefs. The result was an approximately equal amplitude weights in the multiplexed structure. The same exposure process, performed with a priori calibration of the exposure times, gave the worst results, demonstrating the improvement in terms of patterning accuracy derived from the indirect real-time monitoring of the process. The final DOE was tested under the simultaneous irradiation of three collinear laser beams at design wavelengths. The spatial distribution of diffraction orders was quantitatively consistent with the simulated pattern from the design. The presence of a white diffraction spot in which the three colors were angularly superimposed confirmed the excellent transfer of the target functionality into an operational device.

Publication IV is directly related to Publication III and provides a comprehensive characterization of the SRG inscription process. It is based on the simplistic idea that the diffraction efficiency in a single diffraction order is a typical parameter to be controlled during the inscription process to retrieve complete information about the evolving surface geometry. However, scalar diffraction theory correctly predicts the diffraction behavior for an ideal sinusoidally modulated surface. The diffraction pattern produced by the experimental surface may differ from the theoretical predictions. A direct measure of diffraction efficiency can give incorrect predictions if the deviations

from the sinusoidal profile are not included in the theoretical framework. In fact, although often described as having ideal sinusoidal profiles, the evolving surface morphology in large-amplitude SRGs can affect the light distribution of the writing interferogram, causing a feedback effect between the developing surface and the illumination pattern. The result is the appearance of profile deformations and deviations from the expected diffraction behavior, which lead to false results if the diffraction efficiency alone is used to monitor the writing process. In this paper, the precise description of the surface grating morphology from an AFM characterization allowed to build a phenomenological model of the evolution of the grating morphology, taking into account its deviations from the ideal sinusoidal profiles. The AFM characterization of the SRGs was performed with increasing exposure doses to writing interferograms characterized by different asymmetries in the writing beams to deliberately introduce manufacturing errors. The model is based on the decomposition of the AFM profile into a Fourier series as a more general method to describe SRGs. The results were used to phenomenologically model the time evolution of the grating morphology and its deviations from the ideal sinusoidal profiles. Scalar diffraction theory was used to fully describe the diffraction behavior of SRGs, including surface deformations. This allowed to perform an accurate analysis of the efficiency measured in the diffraction pattern. The proposed model could have a significant impact, as it may allow a more careful rationalization of all the results reported over the years, contributing to a more precise definition of the phenomenology and mechanism of SRG inscription.

Publication VIII proposed a theoretical and experimental framework for an operational diffraction-based method capable of measuring the refractive index of structured material layers. This technique is directly based on the results of Publication IV. In a first step, the surface of the material to be measured is structured with a one-dimensional sinusoidal diffraction grating. A photopatterned azopolymer film is used as a master. The sinusoidal SRG is transferred to a polymethylmethacrylate (PMMA) film by soft lithographic replication through a PDMS mold fabricated directly from the azopolymer master. The measurement of the transmitted diffraction efficiency in one of the propagating orders and the topographic analysis of the surface profile enter a fitting process where the refractive index is retrieved from the scalar diffraction model. The refractive index of PMMA has been measured at several discrete wavelengths ranging from the visible to the near infrared. The proposed technique represents a simple and accessible tool for a wide audience working in optics, chemistry, and materials science, with reduced cost and high versatility. It is applicable to measure the refractive index of structured materials where other techniques such as ellipsometry are ineffective.

Publication I is the last work in this list, and it has been left at the end because it needs a brief introduction to be framed in this scenario. Interference lithography is not the only technique capable of producing a periodic surface modulation on an azopolymer surface, even if it is used extensively. Surprisingly, surface relief gratings can appear even when the azomaterial is illuminated by a single coherent laser beam with a wavelength in the absorption band of the azomolecule at normal incidence. These structures are typically referred to as spontaneous SRGs.[216–218] Many studies have focused on exploiting this effect to fabricate gratings,[219–222] but because this mechanism is not fully rationalized, fabrication by single-beam illumination is not highly controlled.

Instead, a completely different approach to induce complex surface patterns on azomaterial surfaces is based on the controlled light reconfiguration of pre-structured surfaces, again using a single beam.[223,224]

In **Publication I** the light-induced reconfiguration of prestructured azopolymer surfaces in a large deformation regime is demonstrated. In the experiment, a silicon wafer, lithographically patterned with an array of micro-pillars (arranged in a square lattice with pitch $p = 10.0\,\mu m$, diameter $d = 4.5\,\mu m$ and height $h = 10.0\,\mu m$), was used as master template. This geometry was transferred to an azopolymer film firs creating a negative PDMS mold from the silicon wafer. An azopolymer solution was then poured onto a glass slide and covered with the fabricated PDMS stamp. After complete evaporation of the solvent, a replica of the silicon master texture was realized on the azopolymer film. The pre-structured film was irradiated with a uniform beam, linearly polarized along one of the grating vectors of the pillar array, with different time doses. During irradiation, the material flows in the direction of polarization according to the photo response of the azopolymer. This causes a structural reconfiguration of the pre-patterned pillar geometry, which eventually becomes elongated in the direction of light polarization, creating a grating-like structure. While the periodicity is fixed by the pitch of the pillar array, the modulation depth can be tuned by the exposure dose. Gratings with different orientation and periodicity can also be inscribed by a simple polarization rotation of the reconfiguring light beam, connecting the pillars along different principal directions of the micro-pillar square lattice. Six different geometries were fabricated from the same prestructured array, demonstrating a versatile and cost-effective surface patterning technique. It allowed the discrete array to be reconfigured into a continuous and periodic diffraction grating characterized by a few micrometers in height and a high degree of structural anisotropy.

4.3 Maskless holographic azopolymers photomorphing

For the past thirty years, azopolymer films photopatterning has been based predominantly on interference techniques. This method is widely recognized for the possibility to produce highly regular and periodic microstructures, with resolutions that are easily determined by the wavelength of the light source and the interference angle. It generally offers high throughput because large areas can be patterned in a single exposure, making it highly suitable for mass production. However, this technique is limited in terms of pattern versatility. The employment of serial exposures has enabled the fabrication of even complex geometries.[203,210] In cases where the target topography is not periodic or lacks of specific symmetries, the number of exposures required to approximate it would be so immense that such geometries would be difficult to design and nearly impossible to fabricate. This significant limitation underscored the need for a different approach. Differently from interference, holography is an alternative way of shaping light. The two interfering beams are replaced by a single beam that, when locally modulated in phase, amplitude, or polarization, interferes with itself to create complex illumination patterns. Holography is at the core of a direct maskless surface

patterning, where a spatial light modulator is used to shape light. Figure 14a summarizes the complete sequence of steps required for this promising approach. The very first step involves the azopolymer film preparation. The film is prepared by dissolving the polymer in tetrachloroethane to form a solution.[223] The desired film thickness, typically in the range of $0.5\,\mu m - 3.0\,\mu m$, can be properly obtained by a controlled spin-coating of the solution onto a glass substrate. In the final stage, the samples are kept under vacuum at room temperature to remove any residual solvent. This process partially matches the first step of standard photolithography. The main difference is that the azopolymer serves directly as the structure material for the final optical device, while the resist typically serves as an intermediate layer in the patterning process and is typically completely dissolved by the development and stripping process.

The second and final step involves the azopolymer exposure step. The experimental configuration is based on a phase-only Computer-Generated Holograms (CGHs) scheme.[27] A coherent and collimated laser beam is phase-modulated by a computer-controlled reflective phase-only SLM. The light wavelength λ is chosen to match the absorption band of the azopolymer. A reflective SLM consists of a liquid crystal array deposited on a reflective surface. Applying a voltage across each pixel of the liquid crystal layer creates an electric field that affects the orientation of the liquid crystal molecules. This reorientation changes the effective refractive index for the reflected light. By controlling the voltage pixel by pixel, the phase of the reflected light can be precisely controlled. Assuming that each pixel has a constant size Δ, this phase modulation can be written as:[6]

$$\psi(p\Delta, q\Delta) = \frac{2\pi}{\lambda} n(p\Delta, q\Delta) d \tag{4.7}$$

where d is to the total distance traveled by the light in the device, approximately corresponding to twice the thickness of the cell. Discrete indices p, q are used to account for the discrete nature of the modulator. These coordinates range from N discrete integers, corresponding to the number of pixels composing the SLM. Note that equation (4.7) exactly corresponds to a discretized version of equation (2.21), where the phase modulation is fully encoded in the refractive index variations instead of in the topographic shape of the device surface. For this reason, a spatial light modulator is a DOE.[80] Assuming that the incident field is homogeneous, such that all the $N \times N$ pixels are uniformly illuminated, the reflected field from the modulator can be written as:[95]

$$\vec{E}_{SLM}(p\Delta, q\Delta) = \vec{E}_0 \cdot rect\left(\frac{p\Delta}{\mathrm{L}}, \frac{\mathrm{q}\Delta}{\mathrm{L}}\right) \cdot e^{i\psi(p\Delta, q\Delta)} \tag{4.8}$$

where the optical field is assumed to be p-polarized with respect to the SLM plane, so that the vectorial amplitude can be written as $\vec{E}_0 = (E_0, 0)$. This ensures the maximum modulation efficiency for the field.[80] Equation (4.7) represents the expression for the field after the SLM modulation. For this reason, this plane is also referred to as the

modulation plane. Here, the finite dimensions of the illuminated area of the modulator, specifically $L = N\Delta$, are considered by the rectangle function.

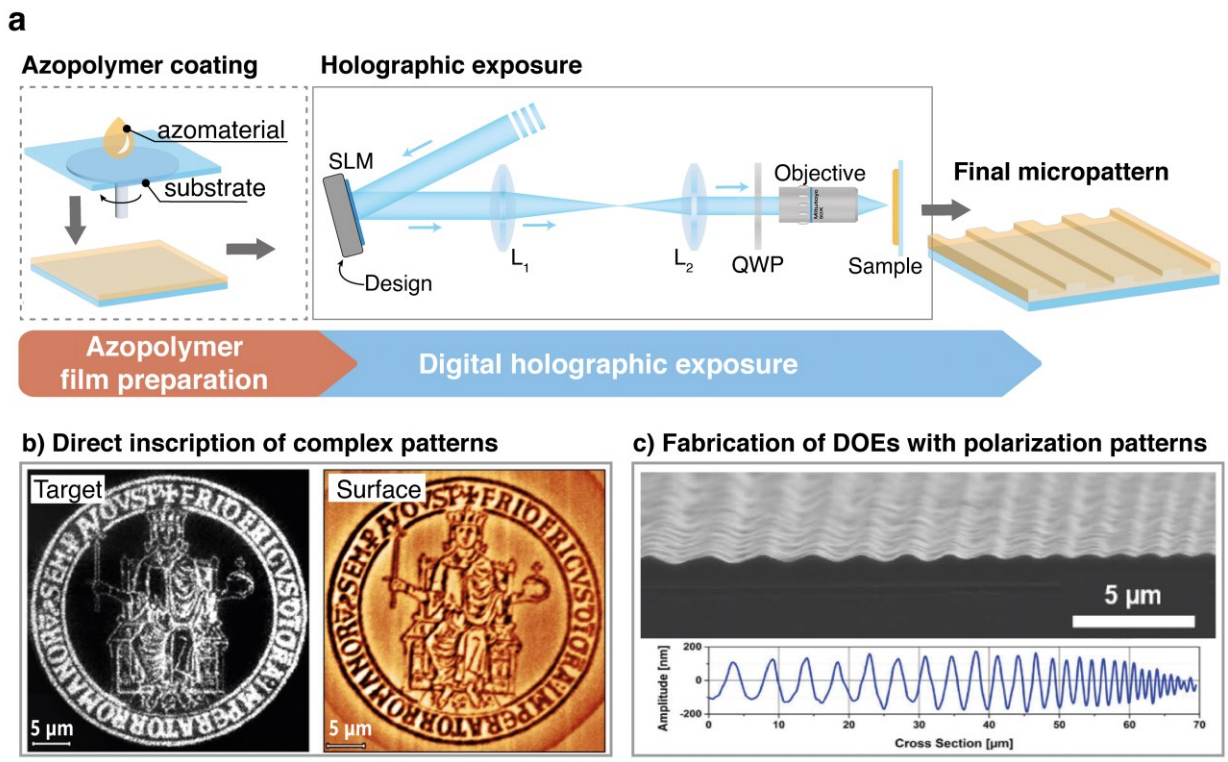

Figure 14: Maskless holographic photomorphing azopolymers. a) Schematic of the inscription process, starting with the film preparation and leading to the final micropattern. b) Experimental holographic pattern and corresponding AFM image of the surface relief inscribed in a single illumination step under circular polarization. Reproduced from ref.[225] c) Scanning electron microscope image and relative AFM profile of a chirped grating fabricated in single exposure under a digitally generated polarization pattern. Reproduced from ref.[226]

The modulated beam is propagated through a *4f* lenses system with the input plane located in the SLM plane. These projection optics allow to generate a scaled version of $\vec{E}_{SLM}$ in the back focal plane of a long-working distance objective, placed in the output plane of the *4f* system. In this plane, the optical field can be written as:

$$\vec{E}_{obj}(-p\Delta', -q\Delta') = \vec{E}_0 \cdot rect\left(-\frac{p\Delta'}{\mathrm{L}'}, -\frac{\mathrm{q}\Delta'}{\mathrm{L}'}\right) \cdot e^{i\psi(p\Delta', q\Delta')} \tag{4.9}$$

where both the pixel size Δ' and the SLM aperture L' have been scaled by a factor f_2/f_1 corresponding to the focal lengths of the lenses composing the projection system. This step makes it possible to perfectly match the SLM aperture to the rear aperture of the objective and to introduce intermediate planes to be used to spatially filter the field.[27]

The objective, which is the last optical component of the system, projects this optical field distribution onto the azopolymer film surface, placed at the working distance of the objective. The field distribution in this plane is equal to:[225]

$$\vec{E}_{azo}(p\Lambda, q\Lambda) = \vec{E}_0 \cdot \sum_{m,n=1}^{N} e^{i\psi(p\Delta,q\Delta)} \cdot e^{-ik\frac{p\Lambda m\Delta + q\Lambda n\Delta}{f}} \tag{4.10}$$

This expression can be derived from equation (2.19) by approximating the objective transformation with a discrete Fourier transform. Here, f represents the equivalent focal length of the system and it defines the pixel size on the azopolymer surface $\Lambda = \lambda f/L$ and the size of the hologram $D = N\Lambda$ in this plane. Once that the setup parameters are defined, this equation fully summarizes the ability of the described optical system in generating complex intensity patterns $I_{azo}(p\Lambda, q\Lambda)$ over the azopolymer surface. The SLM acts here as a holographic projector, encoding all the hologram information in a pure phase profile, the kinoform $\psi(p\Delta, q\Delta)$. It allows to generate an arbitrary grayscale distribution of light on the azopolymer surface, corresponding to the *holographic plane*. Furthermore, by properly defining the optical setup parameters, such as the focal length of the lenses and the SLM pixel density, it is possible to set a pixel size in the image plane smaller than the diffraction limit of the optical system, resulting in a continuous distribution of diffraction-limited light $I_{azo}(x, y)$ for the generated hologram. Despite the simple Fourier relationship between the intensity distribution and the kinoform, the correct modulation must be retrieved with an IFTA,[88] as showed in Figure 8. In a sense, this process is similar to the mask creation process typically used in OL standards. However, no physical mask is required, and the correct light modulation can be retrieved and updated in a few minutes, depending on computing resources. This is a huge difference to the time scale of several days and the cost required to implement a photomask. Prior to the objective transformation, light is converted into circular polarization by means of a quarter waveplate. This eliminates the anisotropy of light-induced relief associated with linearly polarized light. By irradiating a circularly polarized light pattern $I_{azo}(x, y)$ in a low-focusing regime, the evolution of the azopolymer surface morphology $h(x, y, t)$ can be described phenomenologically as:[170,171]

$$h(x, y, t) = \nabla^2 [I_{azo}(x, y)] \cdot \Delta h(t) \tag{4.11}$$

where $\Delta h(t)$ evolves according to equation (4.1). Equations (4.10) and (4.11) encapsulate the true essence of this technique, which can be interpreted as a 2.5-dimensional lithographic technique. In standard optical lithography, patterns are created on a two-dimensional plane with a binary modulation whose value must be tuned during the etching step. The digital maskless lithography implemented with azomaterials allows a semi-three-dimensional lithography, where the grayscale intensity distribution defines the lateral geometry of the patterned surface, while the local intensity and the exposure time define the depth of the structures point by point. The patterns can thus have a more complex morphology than a simple binary modulation, even if they do not fully

extend into three-dimensional structures. Exposure with the digital holographic pattern is the final fabrication step required to produce patterned surfaces using this technique. In one of its early implementations, this technique was proposed to induce spiral relief patterns under the illumination of vortex beams with varying topological charge and wavefront handedness.[170] The resulting surface reliefs showed a strong dependence on the shape of the wavefront of the illuminating beam, demonstrating the complex light-matter occurring in this class of materials and opening up for the formalization of a phenomenological model.[171]

This technique was extended a few years later by Oscurato et al.[225] Although still in a primitive form and not yet suitable for the fabrication of DOEs, the study demonstrated high-quality complex surface reliefs from structured holographic light patterns, with the limitation of a low modulation depth due to the low contrast in the holographic pattern and a mismatch between the wavelength used with respect to the azopolymer absorption band. However, this work stands as a critical foundation for future research, presenting the first significant results that could be applied to the fabrication of DOEs (Figure 14b). The core of this study emphasizes that the key to improving the quality of the surface patterns lies in the optimization of the illumination hologram. This suggested route represented a turning point and inspired the subsequent research. In parallel with the work supporting this Thesis, other groups have proposed different strategies. An alternative approach relies on the use of a holographic setup to generate polarization patterns instead of intensity distributions on the azopolymer surface.[226,227] The key is an optical setup in which the SLM is sandwiched between two quarter waveplates. This configuration allows the polarization plane of a linearly polarized beam to be locally rotated through an angle determined by the grayscale value sent to the SLM from a computer. Unique advantages of this system are realized when combined with the use of an azopolymer as the polarization-sensitive photoresponsive material, allowing for the single-step fabrication of variable periodicity or chirped gratings that are unattainable with interference-based patterning (Figure 14c).

4.4 Comment to author's published papers, part II

The digital maskless photomorphing scheme, schematically illustrated in Figure 14a, was the core of my research activities, which are summarized in this paragraph and detailed in **Publication V-VII** and **Publication IX**.* In these works, the digital

---

* **Publication V:** S. L. Oscurato et al. *Shapeshifting diffractive optical devices*, Laser & Photonics Reviews, 16(4), 2100514 (2022).
Publication VI: F. Reda et al. *Varifocal diffractive lenses for multi-depth microscope imaging*, Optics Express, 30(8), 12695–12711 (2022).
Publication VII: S. Fusco et al. *Efficient high-refractive-index azobenzene dendrimers based on a hierarchical supramolecular approach*, Chemistry of Materials, 35(9), 3722–3730 (2023).
Publication IX: F. Reda et al. *Reprogrammable holograms from maskless surface photomorphing*, Advanced Optical Materials, 11(21), 2300823 (2023).

maskless optical scheme was used to generate and project a grayscale spatially structured intensity distribution of light onto an azobenzene-containing polymer film whose surface is locally deformed according to the irradiated light. This process allowed the direct fabrication of several reprogrammable DOEs.

The innovative and promising approach resulting from this research activity was the use of a customized holographic setup, which was updated during the experiments to achieve the highest possible quality and control of the developed patterned surfaces. The general experimental scheme was integrated with a camera that allowed visual access to the holographic pattern at the sample plane in real-time. Additional beams were combined to implement real-time characterization of the evolving structures. These included a bright field source to directly image the surface during the writing process and a probe beam to collect the real-time far-field or Fourier transform pattern diffracted from the developing surface. This enabled the fabrication of DOEs whose functionality could be directly controlled, characterized, and optimized during the fabrication process. An additional beam was used to assist the patterning process or to optically erase the structured surfaces, enabling the fabrication of *fully reprogrammable diffractive optical elements.*

Publication V has represented a fundamental milestone in my research. It demonstrated, for the first time, the fabrication of shapeshifting diffractive optical elements using the digital holographic inscription of the azopolymer surface. One of the major results of this work, was the use of an additional light source acting as assisting or erasing beam. This additional laser beam, with a wavelength highly absorbed by our azopolymer, improved the grating inscription rate by depleting the population of oriented azomolecules in the orthogonal direction of the writing beam polarization when used at low power regimes. The experimental results allowed to estimate an enhancement in the patterning speed of seven times. The same beam, when used at higher power, favored the complete erasing of the structured surfaces. In combination with the digital holographic setup, it was first used to fabricate transformable sinusoidal diffraction gratings, implementing multiple write-erase cycles of sinusoidal SRGs with different periodicity. No significant surface degradation was observed after at least 15 write-erase cycles. The same approach has been used to realize shapeshifting DOEs with arbitrary grating vector distributions, such as an RGB grating and optical Fourier surfaces. These results showed a complete shift in terms of interference inscription. Since the grating multiplexing process was directly encoded in the analytical design of the digital hologram, no further demanding and sequential light exposures were needed to achieve these results. A relevant example was the fabrication of a blazed grating resulting from the combination of six gratings with the same direction but different periodicities and weighted amplitudes. Another fundamental aspect of this work was the possibility of directly integrating shapeshifting DOEs into operational optical systems. To this end, the proof-of-concept of a reconfigurable monochromator was realized by reshaping the grating periodicity under simultaneous illumination with a probe white beam. To further demonstrate the power of this approach, reconfigurable diffractive lenses were also realized and integrated into a working imaging system. Focal length reconfiguration resulting from surface reshaping was demonstrated, achieving a shift in focal position of about 70%. This tunable shape-shifting lens, with theoretical efficiency,

was used to realize an imaging system capable of dynamically providing different magnifications of an extended object. This work represented the state of the art in azopolymer photopatterning for arbitrary reshapable DOEs resulting from digitally structured illumination patterns. It has also been recognized as an outstanding scientific paper published in a peer-reviewed journal by the *2023 Annual WITec Paper Award (Bronze).* In the same year, a popular science article about these results was published on *Advanced Science News.*[*]

Publication VI follows the results presented in Publication V. Here, the realization of reshapable cosinusoidal phase zone plates with precise focal length design and controlled diffraction efficiencies was demonstrated. After fabrication, the diffractive lenses were tested by experimentally reconstructing the axial point spread function under illumination with a monochromatic beam. Direct comparison with the results predicted by the Rayleigh-Sommerfeld diffraction integral in the Fresnel approximation showed an almost perfect agreement between the fabricated device and the theoretical design. The characterization of the lens quality was also extended to evaluate the geometrical aberrations in the focal spot. The Strehl ratio was used as an estimator and values close to 0.8 were obtained. This is typically set as a diffraction limited performance for a real lens. This value is also comparable to those reported for high quality metalenses. In addition, the noise contribution from the spurious defocused diffraction orders in the focal plane was measured. A signal-to-noise ratio of $22\,dB$ and a spot visibility of 0.99 were achieved. The same quality was also reported for a wide range of focal lengths, from $0.3\,mm$ to $1.2\,mm$, limited only by the resolution of the holographic system and the field of view of the objective. Diffractive lenses have also been used to implement a motionless multi-depth imaging system based on a Barlow configuration. In this work, varifocal diffractive lenses are used to further extend the functionality of a hybrid refractive-diffractive microscope system. By tuning the focal length and position of the diffractive lens, simultaneous and independent control of the magnification, field of view, and working distance of the hybrid imaging system was achieved. It was used to reconstruct in-focus images of small objects placed at different positions on the optical axis with high contrast and reduced vignetting effects.

Publication VII In this work, supramolecular chemistry has been used as a powerful tool to design efficient azomaterials, following the results of Publication II, where a highly directional double hydrogen bond produces stable amorphous azopolymers with enhanced mass transport properties. Here, a dendrimeric supramolecular assembly approach is proposed to maximize the photoresponse of the material. In addition, metal coordination (based on a Zn(II)-carboxylate coordination interaction) has been demonstrated as a simple and efficient strategy to produce high refractive index azomaterials. An increase in refractive index of 0.1 was reported over conventional acrylate azopolymer and supramolecular polymers with similar azobenzene concentration. The combination of high refractive index and high inscription efficiency

---

[*] Robert Lea, *How shape-shifting gratings and lenses are changing optical devices*, Advanced Science News, 2023.

allowed the fabrication of a thinner diffractive lens with the same optical functionality as those proposed in Publication VI, demonstrating that flexible supramolecular chemistry for the design of new azomaterials is a key factor in the development of real-time reconfigurable planar photonic devices.

Publication IX was the last fundamental result of my research. In this work, the accurate all-optical transfer of complex 2D geometries with a binary or grayscale relief depth on the surface of azobenzene-containing polymer films was demonstrated. In a preliminary experiment, a two-level QR code was proposed as the target binary surface geometry. Although not a DOE, this structure was used to test the possibility of direct photopatterning of complex lateral geometries on the azopolymer surface. After inscription, an AFM characterization confirmed the correct pattern transfer on the surface, faithfully reproducing the target geometry. Even in the presence of fabrication mismatches in the order of 10% of the total modulation depth, the QR code still stores the original information, which can be read directly from the AFM image. The holo-lithographic technique was then extended to the realization of diffractive kinoforms acting as holographic projectors, where both complex lateral distribution and grayscale modulation depth are required. The setup was used to directly inscribe the grayscale profile of a kinoform resulting from an IFTA onto the azopolymer surface. The evolving diffraction pattern was continuously recorded in real-time, providing the relative diffraction efficiency in the target holographic image as a function of exposure time. This real-time characterization led to a holographic projector with a surprising efficiency of more than 60%, fabricated in less than two minutes. Multiplexed holographic projectors with axially separated spurious orders were also demonstrated, with comparable optical functionalities. Finally, the surface was completely erased and reshaped to produce time-averaged holographic images with reduced speckle noise or to update the holographic image. This allowed the fabrication of fully reprogrammable pixel-free morphological holographic projectors with turnaround times of a few minutes. Although still far from the refresh time of electrically tunable DOEs, azopolymer holographic projectors result in higher efficiency and ultra-compact size, with performance levels comparable to the state of the art in planar optics.

Conclusions and outlook

Two centuries after the development of the first diffraction grating, diffractive optical elements remain at the forefront of scientific research into advanced photonic devices. DOEs allow standard optical components to be redesigned into planar, lightweight, and multifunctional devices, with the potential to significantly reduce the footprint and complexity of optical systems. However, this is just the tip of the iceberg. For example, DOEs have been used to compensate for normal chromatic dispersion or to circumvent the diffraction limit of imaging systems. This ability to overcome classical limitations while maintaining a relatively simple analytical design makes diffractive optical elements invaluable for photonics applications. This is also confirmed by the longevity of the history of diffractive optics, which underscores the iterative refinement and innovation that has brought and will bring new paradigms for shaping light. Predicting future designs and strategies is always challenging, especially considering that they will be dictated by the needs of future technologies and the desire to integrate planar optics into customer products. As we move into the future, the connection between diffractive optics design and artificial intelligence emerges as an intriguing possibility. The integration of AI can create unprecedented designs with unimaginable optical functionalities. This will require an appropriate technology to translate theoretical results easily and seamlessly into functional devices, from a rapid prototyping step to mass production. However, current lithography techniques have significant limitations.

This inspired and drove my research during the three years of my Ph.D., which focused on demonstrating that maskless fabrication of fully reprogrammable diffractive optical elements could be achieved by replacing standard photoresists with azobenzene-containing polymers. The development of this promising form of lithography for DOEs fabrication was an enormous interdisciplinary effort. It started conceptually by contributing to the chemical optimization of new materials through comparative studies between different molecular designs, looking for more efficient photopatterning responses and improved optical performance. A major task was to refine of light modulation techniques in different configurations to induce more complex patterns. On the other hand, this also required new design strategies and an accurate modeling and description of the micropatterns and their relationship to their diffractive behavior, typically to be acquired and controlled during the development of the DOE. As usual in science, all these tasks were carried out in parallel with the contribution of several scientists, and each improvement on one side of the research had a ripple effect, influencing all other aspects of the study. Although much work remains to be done to address the true limitations of this technique, this approach holds the potential for immense benefits. It could improve the resource and energy efficiency typically required to produce structured surfaces. By eliminating the need for chemicals in the processes, it could significantly reduce environmental impact and material waste, promoting more sustainable lithography. In addition to the potential technological and industrial implications, all of this can also benefit research by making micropatterning a technology more accessible to research groups and fostering interdisciplinary

collaboration. Potential applications extend far beyond the fabrication of optical elements, including the fabrication of substrates for cell growth, the creation of memory supports with multilevel architectures, and the fabrication of microdevices for green energy harvesting, to name just a few.

What's next

The results detailed in this Thesis are not intended to be conclusive, but rather a foundational steppingstone for future research. Figure 15 presents some preliminary results for the next iteration of this research.

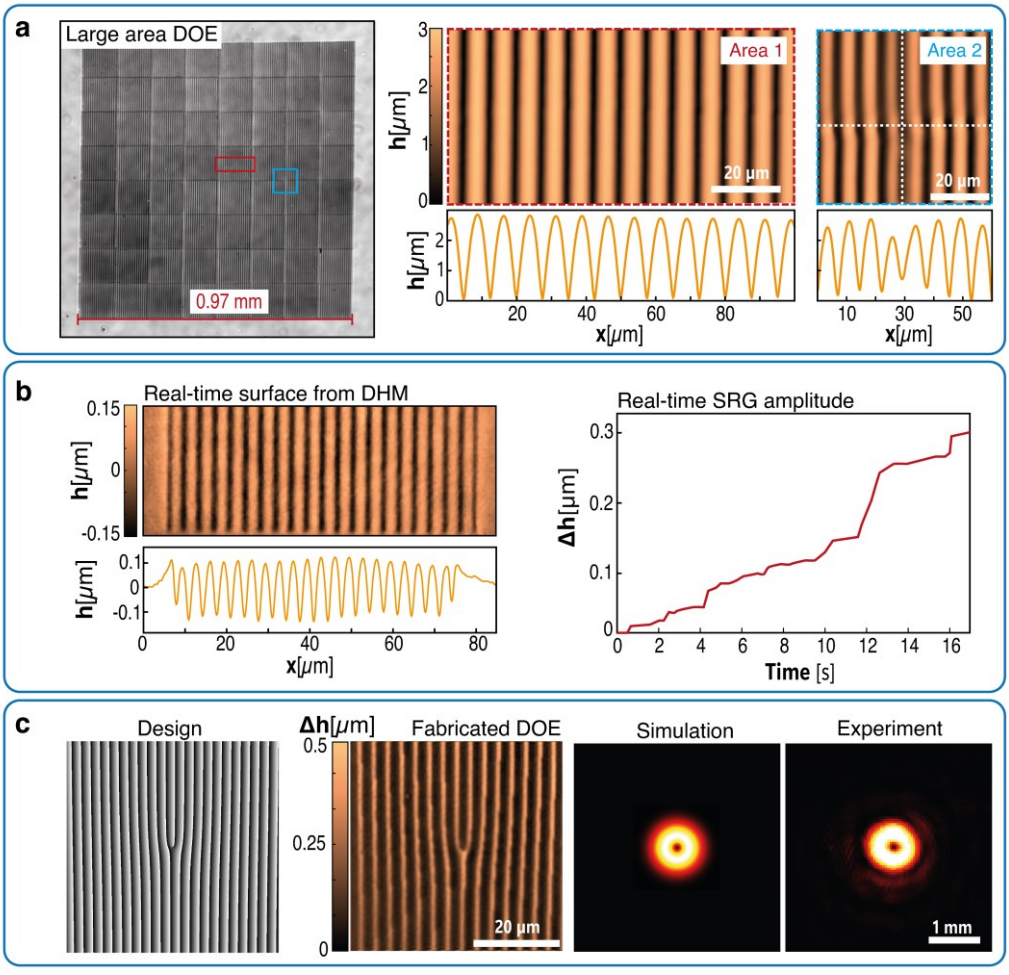

Figure 15: Preliminary data for future research. a) Optical image and AFM characterization of a large area sinusoidal diffraction grating fabricated by a step and repeat technique implemented with the digital azopolymer photopatterning scheme. The grating has an area of about $1\,mm^2$, a spatial periodicity of $\Lambda = 7.5\,\mu m$, and a uniform modulation depth of $\Delta h = 3.1\,\mu m$. AFM scan in the stitching regions shows minimal fabrication errors. b) Real-time surface profile of a sinusoidal SRG acquired during the digital inscription process by means of a DHM and the corresponding modulation depth as a function of the inscription time. Preliminary data acquired at the University of Tampere, under the supervision of Prof. Arri Priimägi. c) Design and fabrication of a pitchfork hologram to generate vortices with helical wavefronts. The simulation and the experimental pattern correspond to the diffraction order carrying orbital angular momentum equal to $+1$.

The first area of focus will be on the development of sinusoidal diffraction gratings with unprecedented modulation depths. In a preliminary experiment, the remarkable stability of the digital holographic setup facilitated the fabrication of a sinusoidal diffraction grating with a record modulation depth of $\Delta h = 3.1\,\mu m$. In addition, the precise visual control of the holographic writing beam enabled extensive area patterning using a multi-exposure technique, inspired by the step-and-repeat framework of standard photolithography. This approach resulted in minimal surface profile errors in the stitching regions and maintained a consistent modulation depth across the entire patterned area, as shown in Figure 15a. These achievements pave the way for the fabrication of large-area diffractive optical devices with arbitrary surface profiles for infrared applications.

During my Ph.D. program, I had the opportunity to spend part of my time in the Smart Photonic Materials (SPM) group at the University of Tampere, Finland, under the supervision of Prof. Arri Priimägi. My internship focused on the real-time controlled fabrication method of structured surfaces using digital holographic lithography in azobenzene-containing materials. This resulted from the real-time characterization of the developing structures using digital holographic microscopy (DHM). Figure 15b shows preliminary data demonstrating how the integration of a DHM into the digital lithography system can provide a direct, real-time measurement of the amplitude of an inscribed diffraction grating, a significant improvement over relying on indirect measures derived from diffraction efficiency. This methodology has the potential to significantly improve the fabrication capabilities and warrants further investigation in future studies.

Fully reprogrammable flat optics hold the promise to extend light manipulation capabilities to include non-classical states of light, ushering in a new era of quantum technologies. Central to this advancement is the ability to shape and control quantum states of light for use in quantum communication protocols, quantum holography, and quantum imaging. An illustrative example of this potential is the generation of optical vortex beams via a pitchfork hologram, as shown in Figure 15c. This class of devices shapes the phase of an incoming light beam to create light vortices with helical wavefronts, converting a standard laser beam into one endowed with orbital angular momentum. This is characterized by an on-axis phase singularity, resulting in a zero-intensity center surrounded by a doughnut-shaped intensity profile.

References

[1] V. Greanya, *Bioinspired Photonics: Optical Structures and Systems Inspired by Nature*, 1st ed. (CRC Press, 2015).

[2] J. Sun, B. Bhushan, and J. Tong, "Structural coloration in nature," RSC Adv. 3(35), 14862 (2013).

[3] F. Müller, C. Kunz, and S. Gräf, "Bio-Inspired Functional Surfaces Based on Laser-Induced Periodic Surface Structures," Materials 9(6), 476 (2016).

[4] M. Shafiq, Z. Gu, O. Cheikhrouhou, W. Alhakami, and H. Hamam, "The Rise of 'Internet of Things': Review and Open Research Issues Related to Detection and Prevention of IoT-Based Security Attacks," Wireless Communications and Mobile Computing 2022, e8669348 (2022).

[5] J.L. O'Brien, "Optical Quantum Computing," Science 318(5856), 1567–1570 (2007).

[6] B. Saleh, and M. Teich, *Fundamentals of Photonics*, 3rd ed. (Wiley, New York, 2019).

[7] M. Born, and E. Wolf, *Principles of Optics: Electromagnetic Theory of Propagation, Interference and Diffraction of Light*, 7th ed. (Cambridge University Press, Cambridge, 2019).

[8] Q. Zhang, Z. He, Z. Xie, Q. Tan, Y. Sheng, G. Jin, L. Cao, and X. Yuan, "Diffractive optical elements 75 years on: from micro-optics to metasurfaces," Photonics Insights 2(4), R09 (2023).

[9] W.T. Chen, and F. Capasso, "Will flat optics appear in everyday life anytime soon?," Applied Physics Letters 118(10), 100503 (2021).

[10] F. Capasso, "The future and promise of flat optics: a personal perspective," Nanophotonics 7(6), 953–957 (2018).

[11] F. Hopkinson, and D. Rittenhouse, "An Optical Problem, Proposed by Mr. Hopkinson, and Solved by Mr. Rittenhouse," Transactions of the American Philosophical Society 2, 201–206 (1786).

[12] E.K. Popov, L.V. Tsonev, and E.G. Loewen, "Scalar theory of transmission relief gratings," Optics Communications 80(5), 307–311 (1991).

[13] D.C. O'Shea, T.J. Suleski, A.D. Kathman, and D.W. Prather, *Diffractive Optics: Design, Fabrication, and Test* (SPIE Press, 2004).

[14] Y. Ebata, "A well designed diffraction grating is key for innovation," Nature Advertorial, https://www.nature.com/articles/d42473-020-00054-7 (2020).

[15] Z. Yang, T. Albrow-Owen, W. Cai, and T. Hasan, "Miniaturization of optical spectrometers," Science 371(6528), eabe0722 (2021).

[16] A. McGonigle, T. Wilkes, T. Pering, J. Willmott, J. Cook, F. Mims, and A. Parisi, "Smartphone Spectrometers," Sensors 18(2), 223 (2018).

[17] G.Y. Belay, W. Hoving, A. van der Put, M. Vervaeke, J. Van Erps, H. Thienpont, and H. Ottevaere, "Miniaturized broadband spectrometer based on a three-segment diffraction grating for spectral tissue sensing," Optics and Lasers in Engineering 134, 106157 (2020).

[18] S. Katz, N. Kaplan, and I. Grossinger, "Using Diffractive Optical Elements: DOEs for beam shaping – fundamentals and applications," Laser Technik Journal 15(4), 29–32 (2018).

[19] L. De Sio, D.E. Roberts, Z. Liao, J. Hwang, N. Tabiryan, D.M. Steeves, and B.R. Kimball, "Beam shaping diffractive wave plates [Invited]," Appl. Opt. 57(1), A118 (2018).

[20] K. Huang, F. Qin, H. Liu, H. Ye, C.-W. Qiu, M. Hong, B. Luk'yanchuk, and J. Teng, "Planar Diffractive Lenses: Fundamentals, Functionalities, and Applications," Advanced Materials 30(26), 1704556 (2018).

[21] A. Flores, M.R. Wang, and J.J. Yang, "Achromatic hybrid refractive-diffractive lens with extended depth of focus," Appl. Opt., AO 43(30), 5618–5630 (2004).

[22] A. Soria-Garcia, J. del Hoyo, L.M. Sanchez-Brea, V. Pastor-Villarrubia, V. Gonzalez-Fernandez, M.H. Elshorbagy, and J. Alda, "Vector diffractive optical element as a full-Stokes analyzer," Optics & Laser Technology 163, 109400 (2023).

[23] W. Jia, D. Lin, R. Menon, and B. Sensale-Rodriguez, "Multifocal multilevel diffractive lens by wavelength multiplexing," Appl. Opt., AO 62(26), 6931–6938 (2023).

[24] E.T.F. Rogers, J. Lindberg, T. Roy, S. Savo, J.E. Chad, M.R. Dennis, and N.I. Zheludev, "A super-oscillatory lens optical microscope for subwavelength imaging," Nature Mater 11(5), 432–435 (2012).

[25] N. Mohammad, M. Meem, B. Shen, P. Wang, and R. Menon, "Broadband imaging with one planar diffractive lens," Sci Rep 8(1), 2799 (2018).

[26]"The Top 10 Emerging Technologies of 2019," US News & World Report, (2019).

[27] K. Matsushima, *Introduction to Computer Holography: Creating Computer-Generated Holograms as the Ultimate 3D Image*, 1st ed. 2020 edition (Springer, Cham, Switzerland, 2020).

[28] B.C. Kress, and P. Meyrueis, *Applied Digital Optics: From Micro-Optics to Nanophotonics* (Wiley, Chichester, U.K., 2009).

[29] H. Wang, Y. Liu, Q. Ruan, H. Liu, R.J.H. Ng, Y.S. Tan, H. Wang, Y. Li, C. Qiu, and J.K.W. Yang, "Off-Axis Holography with Uniform Illumination via 3D Printed Diffractive Optical Elements," Advanced Optical Materials 7(12), 1900068 (2019).

[30] H. Zhang, H. Liu, W. Xu, and Z. Lu, "Large aperture diffractive optical telescope: A review," Optics & Laser Technology 130, 106356 (2020).

[31] W. Zhao, X. Wang, H. Liu, Z. Lu, and Z. Lu, "Development of space-based diffractive telescopes," Front Inform Technol Electron Eng 21(6), 884–902 (2020).

[32] P.R. Srivastava, Y.-J.L. Chu, and G.A. Swartzlander, "Stable diffractive beam rider," Opt. Lett., OL 44(12), 3082–3085 (2019).

[33] A.L. Dubill, and G.A. Swartzlander, "Circumnavigating the sun with diffractive solar sails," Acta Astronautica 187, 190–195 (2021).

[34] Y. Wu, C. Pan, Y. Gao, C. Lu, Y. Zhang, and Z. Huang, "Design of ultra-compact augmented reality display based on grating waveguide with curved variable-period grating," Optics Communications 529, 128980 (2023).

[35] T. Zhan, K. Yin, J. Xiong, Z. He, and S.-T. Wu, "Augmented Reality and Virtual Reality Displays: Perspectives and Challenges," iScience 23(8), 101397 (2020).

[36] B.C. Kress, and I. Chatterjee, "Waveguide combiners for mixed reality headsets: a nanophotonics design perspective," Nanophotonics 10(1), 41–74 (2020).

[37] A. Peter Amalathas, and M. Alkaisi, "Nanostructures for Light Trapping in Thin Film Solar Cells," Micromachines 10(9), 619 (2019).

[38] F. Doroodgar, F. Niazi, A. Sanginabadi, F. Karimian, S. Niazi, C. Alinia, and M.A. Javadi, "Visual performance of four types of diffractive multifocal intraocular lenses and a review of articles," Int J Ophthalmol 14(3), 356–365 (2021).

[39] R. Rampat, and D. Gatinel, "Multifocal and Extended Depth-of-Focus Intraocular Lenses in 2020," Ophthalmology 128(11), e164–e185 (2021).

[40] E. Pelucchi, G. Fagas, I. Aharonovich, D. Englund, E. Figueroa, Q. Gong, H. Hannes, J. Liu, C.-Y. Lu, N. Matsuda, J.-W. Pan, F. Schreck, F. Sciarrino, C. Silberhorn, J. Wang, and K.D. Jöns, "The potential and global outlook of integrated photonics for quantum technologies," Nat Rev Phys 4(3), 194–208 (2021).

[41] A. Crespi, R. Ramponi, R. Osellame, L. Sansoni, I. Bongioanni, F. Sciarrino, G. Vallone, and P. Mataloni, "Integrated photonic quantum gates for polarization qubits," Nat Commun 2(1), 566 (2011).

[42] F. Aieta, P. Genevet, N. Yu, M.A. Kats, Z. Gaburro, and F. Capasso, "Out-of-Plane Reflection and Refraction of Light by Anisotropic Optical Antenna Metasurfaces with Phase Discontinuities," Nano Lett. 12(3), 1702–1706 (2012).

[43] X. Ni, N.K. Emani, A.V. Kildishev, A. Boltasseva, and V.M. Shalaev, "Broadband Light Bending with Plasmonic Nanoantennas," Science 335(6067), 427–427 (2012).

[44] D. Lin, P. Fan, E. Hasman, and M.L. Brongersma, "Dielectric gradient metasurface optical elements," Science 345(6194), 298–302 (2014).

[45] P. Genevet, F. Capasso, F. Aieta, M. Khorasaninejad, and R. Devlin, "Recent advances in planar optics: from plasmonic to dielectric metasurfaces," Optica 4(1), 139 (2017).

[46] F. Aieta, M.A. Kats, P. Genevet, and F. Capasso, "Multiwavelength achromatic metasurfaces by dispersive phase compensation," Science 347(6228), 1342–1345 (2015).

[47] M. Khorasaninejad, W.T. Chen, R.C. Devlin, J. Oh, A.Y. Zhu, and F. Capasso, "Metalenses at visible wavelengths: Diffraction-limited focusing and subwavelength resolution imaging," Science 352(6290), 1190–1194 (2016).

[48] H. Liang, Q. Lin, X. Xie, Q. Sun, Y. Wang, L. Zhou, L. Liu, X. Yu, J. Zhou, T.F. Krauss, and J. Li, "Ultrahigh Numerical Aperture Metalens at Visible Wavelengths," Nano Lett. 18(7), 4460–4466 (2018).

[49] W.T. Chen, A.Y. Zhu, J. Sisler, Z. Bharwani, and F. Capasso, "A broadband achromatic polarization-insensitive metalens consisting of anisotropic nanostructures," Nat Commun 10(1), 355 (2019).

[50] Q. Jiang, G. Jin, and L. Cao, "When metasurface meets hologram: principle and advances," Adv. Opt. Photon. 11(3), 518 (2019).

[51] G. Lee, J. Sung, and B. Lee, "Recent advances in metasurface hologram technologies (Invited paper)," ETRI Journal 41(1), 10–22 (2019).

[52] Y. Hu, X. Luo, Y. Chen, Q. Liu, X. Li, Y. Wang, N. Liu, and H. Duan, "3D-Integrated metasurfaces for full-colour holography," Light Sci Appl 8(1), 86 (2019).

[53] N.A. Rubin, G. D'Aversa, P. Chevalier, Z. Shi, W.T. Chen, and F. Capasso, "Matrix Fourier optics enables a compact full-Stokes polarization camera," Science 365(6448), eaax1839 (2019).

[54] A. Patoux, G. Agez, C. Girard, V. Paillard, P.R. Wiecha, A. Lecestre, F. Carcenac, G. Larrieu, and A. Arbouet, "Challenges in nanofabrication for efficient optical metasurfaces," Sci Rep 11(1), 5620 (2021).

[55] J. Engelberg, and U. Levy, "The advantages of metalenses over diffractive lenses," Nat Commun 11(1), 1991 (2020).

[56] S. Banerji, M. Meem, A. Majumder, F.G. Vasquez, B. Sensale-Rodriguez, and R. Menon, "Imaging with flat optics: metalenses or diffractive lenses?," Optica, OPTICA 6(6), 805–810 (2019).

[57] R. Menon, and B. Sensale-Rodriguez, "Inconsistencies of metalens performance and comparison with conventional diffractive optics," Nat. Photon. 17(11), 923–924 (2023).

[58] E. Sharma, R. Rathi, J. Misharwal, B. Sinhmar, S. Kumari, J. Dalal, and A. Kumar, "Evolution in Lithography Techniques: Microlithography to Nanolithography," Nanomaterials 12(16), 2754 (2022).

[59] P. van Assenbergh, E. Meinders, J. Geraedts, and D. Dodou, "Nanostructure and Microstructure Fabrication: From Desired Properties to Suitable Processes," Small 14(20), 1703401 (2018).

[60] Y.-M. Lee, in *Efficient Extreme Ultraviolet Mirror Design: An FDTD Approach* (IOP Publishing, 2021).

[61] M. Altissimo, "E-beam lithography for micro-/nanofabrication," Biomicrofluidics 4(2), 026503 (2010).

[62] S.-Z. Huang, and K.-Y. Wu, "Health Risk Assessment of Photoresists Used in an Optoelectronic Semiconductor Factory," Risk Analysis 39(12), 2625–2639 (2019).

[63] M.S. Khan, R. lachmayer, and B. Roth, "Maskless lithography for versatile and low cost fabrication of polymer based micro optical structures," OSA Continuum 3(10), 2808 (2020).

[64] D.K. Oh, T. Lee, B. Ko, T. Badloe, J.G. Ok, and J. Rho, "Nanoimprint lithography for high-throughput fabrication of metasurfaces," Front. Optoelectron. 14(2), 229–251 (2021).

[65] M.C. Traub, W. Longsine, and V.N. Truskett, "Advances in Nanoimprint Lithography," Annual Review of Chemical and Biomolecular Engineering 7(1), 583–604 (2016).

[66] S.T. Howell, A. Grushina, F. Holzner, and J. Brugger, "Thermal scanning probe lithography—a review," Microsyst Nanoeng 6(1), 21 (2020).

[67] L. Ramò, M.C. Giordano, G. Ferrando, P. Canepa, F. Telesio, L. Repetto, F. Buatier de Mongeot, M. Canepa, and F. Bisio, "Thermal Scanning-Probe Lithography for Broad-Band On-Demand Plasmonic Nanostructures on Transparent Substrates," ACS Appl. Nano Mater. 6(19), 18623–18631 (2023).

[68] J. Yang, S. Gurung, S. Bej, P. Ni, and H.W. Howard Lee, "Active optical metasurfaces: comprehensive review on physics, mechanisms, and prospective applications," Rep. Prog. Phys. 85(3), 036101 (2022).

[69] K. Du, H. Barkaoui, X. Zhang, L. Jin, Q. Song, and S. Xiao, "Optical metasurfaces towards multifunctionality and tunability," Nanophotonics 11(9), 1761–1781 (2022).

[70] J. Li, P. Yu, S. Zhang, and N. Liu, "A Reusable Metasurface Template," Nano Lett. 20(9), 6845–6851 (2020).

[71] S.C. Malek, H.-S. Ee, and R. Agarwal, "Strain Multiplexed Metasurface Holograms on a Stretchable Substrate," Nano Lett. 17(6), 3641–3645 (2017).

[72] A.J.F. Hayes, A. Gilchrist, C.R. Myers, and T.C. Ralph, "Utilizing encoding in scalable linear optics quantum computing," J. Opt. B: Quantum Semiclass. Opt. 6(12), 533 (2004).

[73] Y. Li, P.C. Humphreys, G.J. Mendoza, and S.C. Benjamin, "Resource costs for fault-tolerant linear optical quantum computing," Phys. Rev. X 5(4), 041007 (2015).

[74] MMR, "Photolithography Market: Global Industry Analysis and Outlook," (2023).

[75] S.L. Oscurato, M. Salvatore, P. Maddalena, and A. Ambrosio, "From nanoscopic to macroscopic photo-driven motion in azobenzene-containing materials," Nanophotonics 7(8), 1387–1422 (2018).

[76] E. Hecht, *Optics*, 4° edition (Addison-Wesley, Reading, Mass, 2001).

[77] R. Magnusson, and T.K. Gaylord, "Diffraction efficiencies of thin phase gratings with arbitrary grating shape," J. Opt. Soc. Am. 68(6), 806 (1978).

[78] V. Moreno, J.F. Román, and J.R. Salgueiro, "High efficiency diffractive lenses: Deduction of kinoform profile," American Journal of Physics 65(6), 556 (1998).

[79] L. Novotny, and B. Hecht, *Principles of Nano-Optics*, 2nd ed. (Cambridge University Press, Cambridge, 2012).

[80] J.W. Goodman, *Introduction to Fourier Optics* (Roberts and Company Publishers, 2005).

[81] D. Voelz, *Computational Fourier Optics: A MATLAB Tutorial* (Society of Photo Optical, Bellingham, Wash, 2011).

[82] N.M. Temme, *Special Functions: An Introduction to the Classical Functions of Mathematical Physics* (John Wiley & Sons, 1996).

[83] I. Andries, T. Galstian, and A. Chirita, "Approximate analysis of the diffraction efficiency of transmission phase holographic gratings with smooth non-sinusoidal relief," Journal of Optoelectronics and Advanced Materials 18(January-February 2016), 56–64 (2016).

[84] N. Lassaline, R. Brechbühler, S.J.W. Vonk, K. Ridderbeek, M. Spieser, S. Bisig, B. Le Feber, F.T. Rabouw, and D.J. Norris, "Optical Fourier surfaces," Nature 582(7813), 506–510 (2020).

[85] G.L. Rogers, "Gabor Diffraction Microscopy: the Hologram as a Generalized Zone-Plate," Nature 166(4214), 237–237 (1950).

[86] D. Gabor, "A New Microscopic Principle," Nature 161(4098), 777–778 (1948).

[87] L.B. Lesem, P.M. Hirsch, and J.A. Jordan, "The Kinoform: A New Wavefront Reconstruction Device," IBM J. Res. & Dev. 13(2), 150–155 (1969).

[88] T. Latychevskaia, "Iterative phase retrieval for digital holography: tutorial," J. Opt. Soc. Am. A 36(12), D31 (2019).

[89] R.W. Gerchberg, "A practical algorithm for the determination of the phase from image and diffraction plane pictures," Optik 35, 237–246 (1972).

[90] F. Wyrowski, and O. Bryngdahl, "Iterative Fourier-transform algorithm applied to computer holography," J. Opt. Soc. Am. A 5(7), 1058 (1988).

[91] A.E.G. Madsen, R.L. Eriksen, and J. Glückstad, "Comparison of state-of-the-art Computer Generated Holography algorithms and a machine learning approach," Optics Communications 505, 127590 (2022).

[92] M. Pasienski, and B. DeMarco, "A high-accuracy algorithm for designing arbitrary holographic atom traps," Opt. Express, OE 16(3), 2176–2190 (2008).

[93] I. Moreno, J. Campos, C. Gorecki, and M.J.Y.M.J. Yzuel, "Effects of Amplitude and Phase Mismatching Errors in the Generation of a Kinoform for Pattern Recognition," Jpn. J. Appl. Phys. 34(12R), 6423 (1995).

[94] T.-C. Poon, *Digital Holography and Three-Dimensional Display: Principles and Applications*, 1st edition (Springer, New York, 2006).

[95] M. Agour, E. Kolenovic, C. Falldorf, and C. von Kopylow, "Suppression of higher diffraction orders and intensity improvement of optically reconstructed holograms from a spatial light modulator," J. Opt. A: Pure Appl. Opt. 11(10), 105405 (2009).

[96] H.P. Herzig, editor , in *Micro-Optics* (CRC Press, 1997).

[97] Y. Wang, G. Zheng, N. Jiang, G. Ying, Y. Li, X. Cai, J. Meng, L. Mai, M. Guo, Y.S. Zhang, and X. Zhang, "Nature-inspired micropatterns," Nat Rev Methods Primers 3(1), 68 (2023).

[98] G.A. Cirino, R.D. Mansano, P. Verdonck, L. Cescato, and L.G. Neto, "Diffractive phase-shift lithography photomask operating in proximity printing mode," Opt. Express, OE 18(16), 16387–16405 (2010).

[99] B. Lin, *Optical Lithography: Here Is Why*, 2nd ed. (SPIE Press, 2021).

[100] S. Owa, K. Nakano, H. Nagasaka, T. Fujiwara, T. Matsuyama, Y. Ohmura, and H. Magoon, "Immersion Lithography Ready for 45 nm Manufacturing and Beyond," 2007 IEEE/SEMI Advanced Semiconductor Manufacturing Conference, 238–244 (2007).

[101] D.Z. Pan, L. Liebmann, B. Yu, X. Xu, and Y. Lin, in *2015 52nd ACM/EDAC/IEEE Design Automation Conference (DAC)* (2015), pp. 1–6.

[102] H. Levinson, "Extreme Ultraviolet Lithography," PM 198, 425–459 (2011).

[103] M. Masnavi, and H. Parchamy, "Calculation of the extreme-ultraviolet radiation conversion efficiency for a laser-produced tin plasma source," Physics Open 1, 100003 (2019).

[104] C.A. Mack, in *IEEE/SEMI Conference and Workshop on Advanced Semiconductor Manufacturing 2005.* (2005), pp. 58–63.

[105] B. Päivänranta, A. Langner, E. Kirk, C. David, and Y. Ekinci, "Sub-10 nm patterning using EUV interference lithography," Nanotechnology 22(37), 375302 (2011).

[106] P.W.R. Connolly, X. Ren, A. McCarthy, H. Mai, F. Villa, A.J. Waddie, M.R. Taghizadeh, A. Tosi, F. Zappa, R.K. Henderson, and G.S. Buller, "High concentration factor diffractive microlenses integrated with CMOS single-photon avalanche diode detector arrays for fill-factor improvement," Appl. Opt. 59(14), 4488 (2020).

[107] S. Zha, D. Li, Q. Wen, Y. Zhou, and H. Zhang, "Design and Fabrication of Silicon-Blazed Gratings for Near-Infrared Scanning Grating Micromirror," Micromachines 13(7), 1000 (2022).

[108] H. Ju, P. Zhang, J. Liang, S. Wang, and Y. Wu, "Blazed silicon gratings fabricated by deflecting crystal orientation (111) silicon wafer," JM3.1 4(1), 019701 (2005).

[109] T.J. Suleski, and D.C. O'Shea, "Gray-scale masks for diffractive-optics fabrication: I Commercial slide imagers," Appl. Opt. 34(32), 7507 (1995).

[110] J.-S. Sohn, M.-B. Lee, W.-C. Kim, E.-H. Cho, T.-W. Kim, C.-Y. Yoon, N.-C. Park, and Y.-P. Park, "Design and fabrication of diffractive optical elements by use of gray-scale photolithography," Appl. Opt. 44(4), 506 (2005).

[111] A.G. Poleshchuk, A.A. Kutanov, V.P. Bessmeltsev, V.P. Korolkov, R.V. Shimanskii, A.I. Malyshev, A.E. Matochkin, N.V. Goloshevskii, K.V. Makarov, V.P. Makarov, I.A. Snimshchikov, and N. Sydyk Uulu, "Microstructuring of optical surfaces: Technology and device for direct laser writing of diffractive structures," Optoelectron.Instrument.Proc. 46(2), 171–180 (2010).

[112] Y. Shimizu, "Laser Interference Lithography for Fabrication of Planar Scale Gratings for Optical Metrology," Nanomanuf Metrol 4(1), 3–27 (2021).

[113] M.L. Dakss, L. Kuhn, P.F. Heidrich, and B.A. Scott, "Grating coupler for efficient excitation of optical guided waves in thin films," Applied Physics Letters 16(12), 523–525 (1970).

[114] R.C. Enger, and S.K. Case, "Optical elements with ultrahigh spatial-frequency surface corrugations," Appl. Opt. 22(20), 3220 (1983).

[115] C.G. Chen, P.T. Konkola, R.K. Heilmann, C. Joo, and M.L. Schattenburg, in edited by D.K. Sood, A.P. Malshe, and R. Maeda (Melbourne, Australia, 2002), p. 126.

[116] C. Lu, and R.H. Lipson, "Interference lithography: a powerful tool for fabricating periodic structures," Laser & Photonics Reviews 4(4), 568–580 (2010).

[117] A. Hassanzadeh, M. Mohammadnezhad, and S. Mittler, "Multiexposure laser interference lithography," J. Nanophoton 9(1), 093067 (2015).

[118] J.H. Moon, J. Ford, and S. Yang, "Fabricating three-dimensional polymeric photonic structures by multi-beam interference lithography," Polym. Adv. Technol. 17(2), 83–93 (2006).

[119] L. Pain, Y. Blancquaert, J. Pradelles, S. Landis, G. Rademaker, I. Servin, G. De Boer, P. Brandt, M. Dansberg, R. Jager, J.J. Peijster, E. Slot, S. Steenbrink, and M. Wieland, in *34th European Mask and Lithography Conference*, edited by U.F. Behringer and J. Finders (SPIE, Grenoble, France, 2018), p. 14.

[120] J.A. Liddle, and G.M. Gallatin, "Lithography, metrology and nanomanufacturing," Nanoscale 3(7), 2679–2688 (2011).

[121] T. Shiono, T. Hamamoto, and K. Takahara, "High-efficiency blazed diffractive optical elements for the violet wavelength fabricated by electron-beam lithography," Appl. Opt. 41(13), 2390 (2002).

[122] T. Fujita, H. Nishihara, and J. Koyama, "Fabrication of micro lenses using electron-beam lithography," Opt. Lett. 6(12), 613 (1981).

[123] A. Kowalik, K. Góra, Z. Jaroszewicz, and A. Kołodziejczyk, "Multi-step electron beam technology for the fabrication of high performance diffractive optical elements," Microelectronic Engineering 77(3–4), 347–357 (2005).

[124] M.J. Low, H. Lee, C.H.J. Lim, C.S. Suchand Sandeep, V.M. Murukeshan, S.-W. Kim, and Y.-J. Kim, "Laser-induced reduced-graphene-oxide micro-optics patterned by femtosecond laser direct writing," Applied Surface Science 526, 146647 (2020).

[125] M. Meem, A. Majumder, S. Banerji, J.C. Garcia, O.B. Kigner, P.W.C. Hon, B. Sensale-Rodriguez, R. Menon, and R. Menon, "Imaging from the visible to the longwave infrared wavelengths via an inverse-designed flat lens," Opt. Express, OE 29(13), 20715–20723 (2021).

[126] M. Meem, S. Banerji, C. Pies, T. Oberbiermann, A. Majumder, B. Sensale-Rodriguez, and R. Menon, "Large-area, high-numerical-aperture multi-level diffractive lens via inverse design," Optica, OPTICA 7(3), 252–253 (2020).

[127] H. Wang, H. Wang, W. Zhang, and J.K.W. Yang, "Toward Near-Perfect Diffractive Optical Elements *via* Nanoscale 3D Printing," ACS Nano 14(8), 10452–10461 (2020).

[128] Z. Sekkat, and S. Kawata, "Laser nanofabrication in photoresists and azopolymers.," Laser & Photonics Reviews 8(1), 1–26 (2014).

[129] S. Hatefi, and K. Abou-El-Hossein, "Review of single-point diamond turning process in terms of ultra-precision optical surface roughness," Int J Adv Manuf Technol 106(5–6), 2167–2187 (2020).

[130] C. Palmer, *Diffraction Grating Handbook*, 8th ed. (Newport Corporation, 2005).

[131] C.G. Blough, M. Rossi, S.K. Mack, and R.L. Michaels, "Single-point diamond turning and replication of visible and near-infrared diffractive optical elements," Appl. Opt., AO 36(20), 4648–4654 (1997).

[132] R. Garcia, A.W. Knoll, and E. Riedo, "Advanced scanning probe lithography," Nature Nanotech 9(8), 577–587 (2014).

[133] R.D. Piner, J. Zhu, F. Xu, S. Hong, and C.A. Mirkin, "'Dip-Pen' Nanolithography," Science 283(5402), 661–663 (1999).

[134] Y. Fu, N.K.A. Bryan, and O.N. Shing, "Microfabrication of diffractive optical element with continuous relief by focused ion beam," Microelectronic Engineering 54(3), 287–293 (2000).

[135] R. Janeiro, R. Flores, P. Dahal, and J. Viegas, "Fabrication of a phase photon sieve on an optical fiber tip by focused ion beam nanomachining for improved fiber to silicon photonics waveguide light coupling," Opt. Express, OE 24(11), 11611–11625 (2016).

[136] R.S. Rodrigues Ribeiro, P. Dahal, A. Guerreiro, P.A.S. Jorge, and J. Viegas, "Fabrication of Fresnel plates on optical fibres by FIB milling for optical trapping, manipulation and detection of single cells," Sci Rep 7(1), 4485 (2017).

[137] X. Wang, J.R. Leger, and R.H. Rediker, "Rapid fabrication of diffractive optical elements by use of image-based excimer laser ablation," Appl. Opt., AO 36(20), 4660–4665 (1997).

[138] A.A. Aesa, and C.D. Walton, "Realisation of a biocompatible diffraction grating using an ArF excimer laser," IOP Conf. Ser.: Mater. Sci. Eng. 871(1), 012058 (2020).

[139] J.-H. Klein-Wiele, T. Fricke-Begemann, P. Simon, and J. Ihlemann, "Complex diffractive surface patterns on metals by UV-ps laser ablation," Opt. Express, OE 27(20), 28902–28914 (2019).

[140] S. Ravi-Kumar, B. Lies, X. Zhang, H. Lyu, and H. Qin, "Laser ablation of polymers: a review," Polymer International 68(8), 1391–1401 (2019).

[141] M.T. Gale, "Replication techniques for diffractive optical elements," Microelectronic Engineering 34(3–4), 321–339 (1997).

[142] M.T. Gale, "Replication Technology for Holograms and Diffractive Optical Elements," Jist 41(3), 211–220 (1997).

[143] Z. Peng, Y. Zhang, C.L.R. Choi, P. Zhang, T. Wu, and Y.K. Chan, "Continuous roller nanoimprinting: next generation lithography," Nanoscale 15(27), 11403–11421 (2023).

[144] B.J. Kampherbeek, and M. Wieland, "How to save over $ 100 mln per year on lithography cost," Mikroniek 8, (2009).

[145] E. Mullen, and M.A. Morris, "Green Nanofabrication Opportunities in the Semiconductor Industry: A Life Cycle Perspective," Nanomaterials 11(5), 1085 (2021).

[146] Advanced Semiconductor Materials Lithography, "Annual Report ASML," (2022).

[147] K. Akamatsu, S. Samitsu, T. Tsuruoka, J. Hasegawa, and H. Nawafune, "Site-Selective Integration of Monolayer-Protected Inorganic Nanoparticles onto Surface Monolayer Templates by a Solvent-Induced Lift-Off Process," Small 2(10), 1130–1133 (2006).

[148] W.-S. Liao, S. Cheunkar, H.H. Cao, H.R. Bednar, P.S. Weiss, and A.M. Andrews, "Subtractive Patterning via Chemical Lift-Off Lithography," Science 337(6101), 1517–1521 (2012).

[149] M. Jang, C. Yoon, J. Park, and O. Kwon, "Evaluation of Hazardous Chemicals with Material Safety Data Sheet and By-products of a Photoresist Used in the Semiconductor-Manufacturing Industry," Safety and Health at Work 10(1), 114–121 (2019).

[150] C. Zhang, Y. Hu, W. Du, P. Wu, S. Rao, Z. Cai, Z. Lao, B. Xu, J. Ni, J. Li, G. Zhao, D. Wu, J. Chu, and K. Sugioka, "Optimized holographic femtosecond laser patterning method towards rapid integration of high-quality functional devices in microchannels," Sci Rep 6(1), 33281 (2016).

[151] L. Huang, K. Xu, D. Yuan, J. Hu, X. Wang, and S. Xu, "Sub-wavelength patterned pulse laser lithography for efficient fabrication of large-area metasurfaces," Nat Commun 13(1), 5823 (2022).

[152] Y. Jung, H. Lee, T.-J. Park, S. Kim, and S. Kwon, "Programmable gradational micropatterning of functional materials using maskless lithography controlling absorption," Sci Rep 5(1), 15629 (2015).

[153] R. He, S. Wang, G. Andrews, W. Shi, and Y. Liu, "Generation of Customizable Micro-wavy Pattern through Grayscale Direct Image Lithography," Sci Rep 6(1), 21621 (2016).

[154] S. Huang, M. Li, L. Wang, Y. Su, and Y. Liang, "Precise fabrication of large-area microstructures by digital oblique scanning lithography strategy and stage self-calibration technique," Appl. Phys. Express 12(9), 096501 (2019).

[155] Z. Xiong, P. Kunwar, and P. Soman, "Hydrogel-Based Diffractive Optical Elements (hDOEs) Using Rapid Digital Photopatterning," Advanced Optical Materials 9(2), 2001217 (2021).

[156] A. Priimagi, and A. Shevchenko, "Azopolymer-based micro- and nanopatterning for photonic applications," Journal of Polymer Science Part B: Polymer Physics 52(3), 163–182 (2014).

[157] A. Natansohn, and P. Rochon, "Photoinduced Motions in Azo-Containing Polymers," Chem. Rev. 102(11), 4139–4176 (2002).

[158] K.G. Yager, and C.J. Barrett, "Novel photo-switching using azobenzene functional materials," Journal of Photochemistry and Photobiology A: Chemistry 182(3), 250–261 (2006).

[159] T.G. Pedersen, P.S. Ramanujam, P.M. Johansen, and S. Hvilsted, "Quantum theory and experimental studies of absorption spectra and photoisomerization of azobenzene polymers," J. Opt. Soc. Am. B 15(11), 2721 (1998).

[160] Ľ. Vetráková, V. Ladányi, J.A. Anshori, P. Dvořák, J. Wirz, and D. Heger, "The absorption spectrum of cis-azobenzene," Photochem. Photobiol. Sci. 16(12), 1749–1756 (2017).

[161] C. Zhang, M.-H. Du, H.-P. Cheng, X.-G. Zhang, A.E. Roitberg, and J.L. Krause, "Coherent Electron Transport through an Azobenzene Molecule: A Light-Driven Molecular Switch," Phys. Rev. Lett. 92(15), 158301 (2004).

[162] B.-Y. Choi, S.-J. Kahng, S. Kim, H. Kim, H.W. Kim, Y.J. Song, J. Ihm, and Y. Kuk, "Conformational Molecular Switch of the Azobenzene Molecule: A Scanning Tunneling Microscopy Study," Phys. Rev. Lett. 96(15), 156106 (2006).

[163] H.M.D. Bandara, and S.C. Burdette, "Photoisomerization in different classes of azobenzene," Chem. Soc. Rev. 41(5), 1809–1825 (2012).

[164] B. Yadav, J. Domurath, K. Kim, S. Lee, and M. Saphiannikova, "Orientation Approach to Directional Photodeformations in Glassy Side-Chain Azopolymers," J. Phys. Chem. B 123(15), 3337–3347 (2019).

[165] B. Yadav, J. Domurath, and M. Saphiannikova, "Modeling of Stripe Patterns in Photosensitive Azopolymers," Polymers 12(4), 735 (2020).

[166] N. Tverdokhleb, S. Loebner, B. Yadav, S. Santer, and M. Saphiannikova, "Viscoplastic Modeling of Surface Relief Grating Growth on Isotropic and Preoriented Azopolymer Films," Polymers 15(2), 463 (2023).

[167] Z. Mahimwalla, K.G. Yager, J. Mamiya, A. Shishido, A. Priimagi, and C.J. Barrett, "Azobenzene photomechanics: prospects and potential applications," Polym. Bull. 69(8), 967–1006 (2012).

[168] P. Rochon, E. Batalla, and A. Natansohn, "Optically induced surface gratings on azoaromatic polymer films," Applied Physics Letters 66(2), 136–138 (1995).

[169] D.Y. Kim, S.K. Tripathy, L. Li, and J. Kumar, "Laser-induced holographic surface relief gratings on nonlinear optical polymer films," Applied Physics Letters 66(10), 1166–1168 (1995).

[170] A. Ambrosio, L. Marrucci, F. Borbone, A. Roviello, and P. Maddalena, "Light-induced spiral mass transport in azo-polymer films under vortex-beam illumination," Nat Commun 3(1), 1–9 (2012).

[171] A. Ambrosio, P. Maddalena, and L. Marrucci, "Molecular Model for Light-Driven Spiral Mass Transport in Azopolymer Films," Phys. Rev. Lett. 110(14), 146102 (2013).

[172] F. Lagugné Labarthet, T. Buffeteau, and C. Sourisseau, "Azopolymer Holographic Diffraction Gratings: Time Dependent Analyses of the Diffraction Efficiency, Birefringence, and Surface Modulation Induced by Two Linearly Polarized Interfering Beams," J. Phys. Chem. B 103(32), 6690–6699 (1999).

[173] A. Sobolewska, S. Bartkiewicz, A. Miniewicz, and E. Schab-Balcerzak, "Polarization Dependence of Holographic Grating Recording in Azobenzene-Functionalized Polymers Monitored by Visible and Infrared Light," J. Phys. Chem. B 114(30), 9751–9760 (2010).

[174] S. Bian, L. Li, J. Kumar, D.Y. Kim, J. Williams, and S.K. Tripathy, "Single laser beam-induced surface deformation on azobenzene polymer films," Applied Physics Letters 73(13), 1817–1819 (1998).

[175] N.S. Yadavalli, S. Loebner, T. Papke, E. Sava, N. Hurduc, and S. Santer, "A comparative study of photoinduced deformation in azobenzene containing polymer films," Soft Matter 12(9), 2593–2603 (2016).

[176] N.K. Viswanathan, S. Balasubramanian, L. Li, S.K. Tripathy, and J. Kumar, "A Detailed Investigation of the Polarization-Dependent Surface-Relief-Grating Formation Process on Azo Polymer Films," Jpn. J. Appl. Phys. 38(10R), 5928 (1999).

[177] N.K. Viswanathan, D.Y. Kim, S. Bian, J. Williams, W. Liu, L. Li, L. Samuelson, J. Kumar, and S.K. Tripathy, "Surface relief structures on azo polymer films," J. Mater. Chem. 9(9), 1941–1955 (1999).

[178] O. Sakhno, L.M. Goldenberg, M. Wegener, C. Dreyer, A. Berdin, and J. Stumpe, "Generation of sub-micrometer surface relief gratings in an azobenzene-containing material using a 355 nm laser," Optical Materials 128, 112457 (2022).

[179] B. Audia, P. Pagliusi, C. Provenzano, A. Roche, L. Oriol, and G. Cipparrone, "Influence of Photoanisotropies on Light-Controllable Structuration of Azopolymer Surface," ACS Appl. Polym. Mater. 2(4), 1597–1604 (2020).

[180] J. Yang, J. Zhang, J. Liu, P. Wang, H. Ma, H. Ming, Z. Li, and Q. Zhang, "Holographic grating recording in azobenzene polymer films," Optical Materials 27(3), 527–532 (2004).

[181] L.M. Goldenberg, O. Kulikovska, and J. Stumpe, "Thermally Stable Holographic Surface Relief Gratings and Switchable Optical Anisotropy in Films of an Azobenzene-Containing Polyelectrolyte," Langmuir 21(11), 4794–4796 (2005).

[182] B. Liu, M. Wang, Y. He, and X. Wang, "Duplication of Photoinduced Azo Polymer Surface-Relief Gratings through a Soft Lithographic Approach," Langmuir 22(17), 7405–7410 (2006).

[183] L. Rocha, V. Dumarcher, C. Denis, P. Raimond, C. Fiorini, and J.-M. Nunzi, "Laser emission in periodically modulated polymer films," Journal of Applied Physics 89(5), 3067–3069 (2001).

[184] A. Sobolewska, and S. Bartkiewicz, "Surface relief grating in azo-polymer obtained for *s*-*s* polarization configuration of the writing beams," Applied Physics Letters 101(19), 193301 (2012).

[185] E. Schab-Balcerzak, A. Sobolewska, and A. Miniewicz, "Comparative studies of newly synthesized azo-dyes bearing poly(esterimide)s with their poly(etherimide) analogues. Light-induced optical anisotropy," Optical Materials 31(2), 405–411 (2008).

[186] K.-H. Kim, and Y.-C. Jeong, "One-step fabrication of hierarchical multiscale surface relief gratings by holographic lithography of azobenzene polymer," Opt. Express 26(5), 5711 (2018).

[187] A. Sobolewska, S. Bartkiewicz, and A. Priimagi, "High-Modulation-Depth Surface Relief Gratings Using $s - s$ Polarization Configuration in Supramolecular Polymer–Azobenzene Complexes," J. Phys. Chem. C 118(40), 23279–23284 (2014).

[188] F.L. Labarthet, T. Buffeteau, and C. Sourisseau, "Time dependent analysis of the formation of a half-period surface relief grating on amorphous azopolymer films," Journal of Applied Physics 90(7), 3149–3158 (2001).

[189] J. Jelken, C. Henkel, and S. Santer, "Formation of half-period surface relief gratings in azobenzene containing polymer films," Appl. Phys. B 126(9), 149 (2020).

[190] O. Sakhno, L.M. Goldenberg, M. Wegener, and J. Stumpe, "Deep surface relief grating in azobenzene-containing materials using a low-intensity 532 nm laser," Optical Materials: X 1, 100006 (2019).

[191] A. Kozanecka-Szmigiel, A. Hernik, K. Rutkowska, J. Konieczkowska, E. Schab-Balcerzak, and D. Szmigiel, "Surface Relief Modulated Grating in Azo Polymer—From the Tailoring of Diffraction Order to Reshaping of a Laser Beam," Materials 15(22), 8088 (2022).

[192] A. Meshalkin, S. Robu, E. Achimova, A. Prisacar, D. Shepel, V. Abaskin, and G. Triduh, "Direct photoinduced surface relief formation in carbazole-based azopolymer using polarization holographic recording," (n.d.).

[193] A. Kravchenko, A. Shevchenko, V. Ovchinnikov, A. Priimagi, and M. Kaivola, "Optical Interference Lithography Using Azobenzene-Functionalized Polymers for Micro- and Nanopatterning of Silicon," Advanced Materials 23(36), 4174–4177 (2011).

[194] L.M. Goldenberg, L. Kulikovsky, O. Kulikovska, and J. Stumpe, "Extremely high patterning efficiency in easily made azobenzene-containing polymer films," J. Mater. Chem. 19(34), 6103 (2009).

[195] A. Priimagi, K. Lindfors, M. Kaivola, and P. Rochon, "Efficient Surface-Relief Gratings in Hydrogen-Bonded Polymer−Azobenzene Complexes," ACS Appl. Mater. Interfaces 1(6), 1183–1189 (2009).

[196] J. Stumpel, M. Saccone, V. Dichiarante, O. Lehtonen, M. Virkki, P. Metrangolo, and A. Priimagi, "Surface-Relief Gratings in Halogen-Bonded Polymer–Azobenzene Complexes: A Concentration-Dependence Study," Molecules 22(11), 1844 (2017).

[197] J. Konieczkowska, A. Kozanecka-Szmigiel, K. Bujak, D. Szmigiel, J. Grzegorz Małecki, and E. Schab-Balcerzak, "Photoresponsive behaviour of 'T-type' azopolyimides. The unexpected high efficiency of diffraction gratings, modulations and stability of the SRG in azopoly(ether imide)," Materials Science and Engineering: B 273, 115387 (2021).

[198] L. Nedelchev, D. Ivanov, N. Berberova, V. Strijkova, and D. Nazarova, "Polarization holographic gratings with high diffraction efficiency recorded in azopolymer PAZO," Opt Quant Electron 50(5), 212 (2018).

[199] L. Nedelchev, G. Mateev, V. Strijkova, V. Salgueiriño, D.S. Schmool, N. Berberova-Buhova, E. Stoykova, and D. Nazarova, "Tunable Polarization and Surface Relief Holographic Gratings in Azopolymer Nanocomposites with Incorporated Goethite (α-FeOOH) Nanorods," Photonics 8(8), 306 (2021).

[200] D. Bublitz, B. Fleck, and L. Wenke, "A model for surface-relief formation in azobenzene polymers," Appl Phys B 72(8), 931–936 (2001).

[201] A. Miniewicz, A. Sobolewska, W. Piotrowski, P. Karpinski, S. Bartkiewicz, and E. Schab-Balcerzak, "Thermocapillary Marangoni Flows in Azopolymers," Materials 13(11), 2464 (2020).

[202] N.S. Yadavalli, M. Saphiannikova, N. Lomadze, L.M. Goldenberg, and S. Santer, "Structuring of photosensitive material below diffraction limit using far field irradiation," Appl. Phys. A 113(2), 263–272 (2013).

[203] H. Rekola, A. Berdin, C. Fedele, M. Virkki, and A. Priimagi, "Digital holographic microscopy for real-time observation of surface-relief grating formation on azobenzene-containing films," Sci Rep 10(1), 19642 (2020).

[204] J. Jelken, and S. Santer, "Light induced reversible structuring of photosensitive polymer films," RSC Adv. 9(35), 20295–20305 (2019).

[205] S. Moujdi, A. Rahmouni, T. Mahfoud, D.V. Nesterenko, M. Halim, and Z. Sekkat, "Surface relief gratings in azo-polymers revisited," Journal of Applied Physics 124(21), 213103 (2018).

[206] O. Kulikovska, L.M. Goldenberg, and J. Stumpe, "Supramolecular Azobenzene-Based Materials for Optical Generation of Microstructures," Chem. Mater. 19(13), 3343–3348 (2007).

[207] A. Tofini, L. Levesque, O. Lebel, and R.G. Sabat, "Erasure of surface relief gratings in azobenzene molecular glasses by localized heating using a CO2 laser," J. Mater. Chem. C 6(5), 1083–1091 (2018).

[208] J. Vapaavuori, R.H.A. Ras, M. Kaivola, C.G. Bazuin, and A. Priimagi, "From partial to complete optical erasure of azobenzene–polymer gratings: effect of molecular weight," J. Mater. Chem. C 3(42), 11011–11016 (2015).

[209] J. Krüger, N. Bolle, T. Calvelo, S. Bergmann, H. Abourahma, and D.J. McGee, "Optical reconfiguration of surface relief gratings on supramolecular polymer films using grating translation and superposition," Journal of Applied Physics 125(24), 243108 (2019).

[210] M. Salvatore, F. Borbone, and S.L. Oscurato, "Deterministic Realization of Quasicrystal Surface Relief Gratings on Thin Azopolymer Films," Advanced Materials Interfaces 7(11), 1902118 (2020).

[211] Y. Lim, B. Kang, S.J. Hong, H. Son, E. Im, J. Bang, and S. Lee, "A Field Guide to Azopolymeric Optical Fourier Surfaces and Augmented Reality," Advanced Functional Materials 31(39), 2104105 (2021).

[212] Y. Lim, B. Kang, and S. Lee, "Photo-Transformable Gratings for Augmented Reality," Advanced Functional Materials 31(28), 2100839 (2021).

[213] J. Jelken, C. Henkel, and S. Santer, "Solving an old puzzle: fine structure of diffraction spots from an azo-polymer surface relief grating," Appl. Phys. B 125(11), 218 (2019).

[214] F. Rodriguez, J. Jelken, N. Delpouve, A. Laurent, B. Garnier, J.-L. Duvail, F. Lagugné-Labarthet, and E. Ishow, "Exploiting Light Interferences to Generate Micrometer-High Superstructures from Monomeric Azo Materials with Extensive Orientational Mobility," Advanced Optical Materials 9(19), 2100525 (2021).

[215] E. Ishow, R. Camacho-Aguilera, J. Guérin, A. Brosseau, and K. Nakatani, "Spontaneous Formation of Complex Periodic Superstructures under High Interferential Illumination of Small-Molecule-Based Photochromic Materials," Adv Funct Materials 19(5), 796–804 (2009).

[216] C. Hubert, C. Fiorini-Debuisschert, I. Maurin, J.-M. Nunzi, and P. Raimond, "Spontaneous Patterning of Hexagonal Structures in an Azo-Polymer Using Light-Controlled Mass Transport," Advanced Materials 14(10), 729–732 (2002).

[217] A. Ambrosio, S. Girardo, A. Camposeo, D. Pisignano, and P. Maddalena, "Controlling spontaneous surface structuring of azobenzene-containing polymers for large-scale nano-lithography of functional substrates," Applied Physics Letters 102(9), 093102 (2013).

[218] L. Mazaheri, S.R. Bobbara, O. Lebel, and J.-M. Nunzi, "Photoinduction of spontaneous surface relief gratings on Azo DR1 glass," Opt. Lett., OL 41(13), 2958–2961 (2016).

[219] J. Noga, A. Sobolewska, S. Bartkiewicz, M. Virkki, and A. Priimagi, "Periodic Surface Structures Induced by a Single Laser Beam Irradiation," Macromol. Mater. Eng. 302(2), 1600329 (2017).

[220] J. Wang, Y. Zheng, L. Li, E. Liu, C. Zong, J. Zhao, J. Xie, F. Xu, T.A.F. König, M.G. Saphiannikova, Y. Cao, A. Fery, and C. Lu, "All-Optical Reversible Azo-Based Wrinkling Patterns with High Aspect Ratio and Polarization-Independent Orientation for Light-Responsive Soft Photonics," ACS Applied Materials & Interfaces, (2019).

[221] E. Liu, L. Li, J. Wang, X. Han, X. Li, F. Xu, Y. Cao, and C. Lu, "Light-Induced In Situ Dynamic Ordered Wrinkling with Arbitrarily Tailorable Wrinkling Orientation for Photoresponsive Soft Photonics," Adv Funct Materials 33(24), 2300182 (2023).

[222] B. Yang, Y. Ji, F. Cai, and H. Yu, "Surface Morphing of Azopolymers toward Advanced Anticounterfeiting Enabled by a Two-Step Method: Light Writing and Then Reading in Liquid," ACS Appl. Mater. Interfaces 15(19), 23804–23812 (2023).

[223] S.L. Oscurato, F. Borbone, P. Maddalena, and A. Ambrosio, "Light-Driven Wettability Tailoring of Azopolymer Surfaces with Reconfigured Three-Dimensional Posts," ACS Appl. Mater. Interfaces 9(35), 30133–30142 (2017).

[224] I.K. Januariyasa, F. Borbone, M. Salvatore, and S.L. Oscurato, "Wavelength-Dependent Shaping of Azopolymer Micropillars for Three-Dimensional Structure Control," ACS Appl. Mater. Interfaces 15(36), 43183–43192 (2023).

[225] S.L. Oscurato, M. Salvatore, F. Borbone, P. Maddalena, and A. Ambrosio, "Computer-generated holograms for complex surface reliefs on azopolymer films," Scientific Reports 9(1), 6775 (2019).

[226] J. Strobelt, D. Stolz, M. Leven, M.V. Soelen, L. Kurlandski, H. Abourahma, and D.J. McGee, "Optical microstructure fabrication using structured polarized illumination," Opt. Express 30(5), 7308 (2022).

[227] J. Strobelt, M. Van Soelen, H. Abourahma, and D.J. McGee, "Supramolecular Azopolymers for Dynamic Surface Microstructures Using Digital Polarization Optics," Advanced Optical Materials 11(8), 2202245 (2023).

Appendix: SRGs parameters from literature

This appendix summarizes in a table the main results obtained over the years by interferometric lithography on azopolymer films. Columns 2-4 of this table have been used for the plot in Figure 12c. Column 1 indicates the publication from which the data were taken. The list follows a chronological order based on the year of publication. Column 2 lists the polarization configuration used, with only one being considered in the case of comparative studies. Columns 3-5 contain the typical structural parameters of the SRGs observed in the corresponding work, such as modulation depth, periodicity, and diffraction efficiency, if reported, in the first order of diffraction. Theoretical diffraction efficiency means that the entire curve has been reconstructed for more than one diffraction order. Column 6 reports the typical exposure time to produce SRGs.

Article	**Pol.**	Δh [μm]	Λ [μm]	η_1 [%]	Δt [s]
Kim, *Appl. Phys. Lett.* 66, 1166–1168 (1995)	p-p	0.12	1.00	4.00	10
Rochon, *Appl. Phys. Lett.* 66, 136–138 (1995)	p-p	0.25	1.10	25.00	-
Labarthet, *J. Phys. Chem. B.* 103, 6690–6699 (1999)	p-p	0.35	1.00	20.00	25
Viswanathan, *J. Mater. Chem.* 9, 1941–1955 (1999)	p-p	0.10	1.00	15.00	40
Labarthet, *J. Appl. Phys.* 90, 3149–3158 (2001)	s-p	0.01	0.67	0.10	10
Rocha, *J. Appl. Phys.* 89, 3067–3069 (2001)	p-p	0.37	0.61	-	-
Perschke, *Adv. Mater.* 14, 841 (2002)	RCP-LCP	0.04	0.36	-	120
Kang, *Appl. Phys. Lett.* 82, 3823–3825 (2003)	-	0.05	0.50	-	120
Yang *et al.*, *Opt. Mater.* 27, 527–532 (2004)	p-p	0.04	0.80	2.00	23
Goldenberg, *Langmuir*. 21, 4794–4796 (2005)	p-p	0.63	2.30	37.00 (?)	120
Zhou, *Opt. Lett.* 31, 1370 (2006)	±45°	0.02	1.50	1.60	3
Liu, *Langmuir*. 22, 7405–7410 (2006)	p-p	0.17	0.80	-	-
Kulikovska, *Chem. Mater.* 19, 3343–3348 (2007)	±45°	1.65	2.30	Theor.	60
Schab-Balcerzak, *Opt. Mater.* 31, 405–411 (2008)	s-s	0.07	4.70	1.60	20
Goldenberg, *J. Mater. Chem.* 19, 6103 (2009)	±45°	0.60	2.00	30.00	5
Ishow, *Adv. Funct. Mater.* 19, 796–804 (2009)	p-p	0.35	0.84	25.00	3
Priimagi, *Appl. Mater. Interfaces*. 1, 1183–1189 (2009)	p-p	0.30	1.10	25.00	30
Sobolewska, *J. Phys. Chem. B.* 114, 9751–9760 (2010)	p-p	0.18	1.24	17.00	50
Kravchenko, *Adv. Mater.* 23, 4174–4177 (2011)	±45°	0.10	0.32	-	30

Goldenberg, *J. Opt.* 13, 075601 (2011)	±45°	0.65	1.90	40.00 (?)	15
Sobolewska, *Appl. Phys. Lett.* 101, 193301 (2012)	s-s	0.10	10.00	22.00	60
Wang, *Appl. Phys. Lett.* 102, 031103 (2013)	WM (*)	0.01	0.17	-	20
Yadavalli, *Appl. Phys. A.* 113, 263–272 (2013)	±45°	0.20	1.00	-	15
Sobolewska, *J. Phys. Chem. C.* 118, 279–284 (2014)	s-s	0.59	6.00	30.00	70
Vapaavuori, *J. Mater. Chem. C.* 3, 011–016 (2015)	p-p	0.18	0.80	7.00	15
Kim, *Opt. Express*. 24, 25242 (2016)	p-p	0.10	1.35	10.40	20
Meshalkin, *J. Opt. Adv. Mater.* 18, 763–768 (2016)	RCP-LCP	0.13	1.00	3.00	7
Stumpel, *Molecules* 22, 1844 (2017)	RCP-LCP	0.39	1.00	30.00	60
Moujdi, *J. Appl. Phys.* 124, 213103 (2018)	±45°	0.14	1.03	5.00	6
Kim, *Macromol. Res.* 26, 1042–1047 (2018)	p-p	0.15	2.00	1.30	10
Kim, *Opt. Express*. 26, 5711 (2018)	s-s	0.10	1.26	-	360
Nedelchev, *Opt. Quantum Electron.* 50, 212 (2018)	RCP-LCP	0.27	2.00	40.00 (?)	5
Jelken, *RSC Adv.* 9, 20295–20305 (2019)	±45°	0.25	2.00	1.30	10
Jelken, *Appl. Phys. B.* 125, 218 (2019)	±45°	0.25	2.00	2.00	15
Sakhno, *Opt. Mater. X.* 1, 100006 (2019)	±45°	0.80	2.80	Theor.	40
Krüger, *J. Appl. Phys.* 125, 243108 (2019)	RCP-LCP	0.70	4.00	24.00	8
Pagliusi, *Appl. Mater. Interf.* 11, 34471–34477 (2019)	RCP-LCP	0.40	20.00	-	12
Jelken, *Appl. Phys. B.* 126, 149 (2020)	s-p	0.05	1.00	0.30	10
Audia, *ACS Appl. Polym. Mater.* 2, 1597–1604 (2020)	p-p	0.22	20.00	-	12
Rekola, *Sci. Rep.* 10, 19642 (2020)	±45°	0.30	4.00	8.00	0.1
Salvatore, *Adv. Mater. Interfaces*. 7, 1902118 (2020)	p-p	0.22	2.20	-	40
Konieczkowska, *Mater. Sci. Eng. B*. 273, 115387 (2021)	RCP-LCP	0.26	3.60	20.00	90
Lim, *Adv. Funct. Mater.* 31, 2100839 (2021)	RCP-LCP	0.21	0.70	11.00	10
Rodriguez, *Adv. Opt. Mater.* 9, 2100525 (2021)	±45°	0.15	0.75	8.00	7
Nedelchev, *Photonics*. 8, 306 (2021)	RCP-LCP	0.28	1.30	26.00	41
Sakhno, *Opt. Mater.* 128, 112457 (2022)	p-p	0.20	0.30	14.00	120
Kozanecka-Szmigiel, *Materials*. 15, 8088 (2022)	RCP-LCP	1.70	8.70	Theor.	200

(*) waveguide mode interference lithography

Publications

In the concluding section of this dissertation, I am proud to present a compendium of my published research papers, each reprinted in its original form. The papers have been reprinted under the Creative Commons license. This license permits copying and distribution of the material in any medium or format, in its original form, for non-commercial purposes only. In addition, where available, supplementary text and images are provided to complement the articles. Additional media content, such as movies, can be found on the individual journal websites. This comprehensive collection of original works fully summarizes my research journey and provides an invaluable resource for readers of this Thesis.

Publication I

M. Salvatore, F. Borbone, F. Reda, P. Maddalena, and S. L. Oscurato

Programmable surface anisotropy from polarization-driven azopolymer reconfiguration

Reprinted from

Journal of Physics: Photonics 3(3), 034013 (2021)

Journal of Physics: Photonics

OPEN ACCESS

RECEIVED
30 December 2020

REVISED
6 April 2021

ACCEPTED FOR PUBLICATION
19 April 2021

PUBLISHED
15 June 2021

PAPER

Programmable surface anisotropy from polarization-driven azopolymer reconfiguration

Marcella Salvatore[1,3], **Fabio Borbone**[2], **Francesco Reda**[1], **Pasqualino Maddalena**[1,3,*] and **Stefano Luigi Oscurato**[1,3]

[1] Dipartimento di Fisica "E. Pancini", Università degli Studi di Napoli "Federico II", Complesso Universitario di Monte Sant'Angelo, Via Cintia, Naples 80126, Italy
[2] Dipartimento di Scienze Chimiche, Università degli Studi di Napoli "Federico II", Complesso Universitario di Monte Sant'Angelo, Via Cintia, Naples 80126, Italy
[3] Centro Servizi Metrologici e Tecnologici Avanzati (CESMA), Università degli Studi di Napoli "Federico II", Complesso Universitario di Monte Sant'Angelo, Via Cintia, Naples 80126, Italy
[*] Author to whom any correspondence should be addressed.

E-mail: pasqualino.maddalena@unina.it

Keywords: azopolymer, mass migration, anisotropic surface texturing, periodic structures photopatterning

Abstract

The ability to accurately realize complex textures is of great relevance for tailoring surface-driven functionalities as wettability, adhesion and light diffraction. The fabrication of superficial micro-textures, in a simple and cost-effective way, is high desiderable in this framework. A versatile technique for surface micropatterning is based on reconfiguration of photosensitive azobenzene-containing polymers, in which a macroscopic light-induced motion of polymer chains, fueled by the photo-isomerizing azobenzene molecules, allows the controlled optical reshaping of prestructured superficial micro-textures. Here, azopolymer surfaces, prepatterned with an array of discrete cylindrical micropillars, are reconfigured through a polarization-driven large-scale surface deformation until achieving superficial gratings with programmable amplitude, orientation and periodicity. The high degree of structural surface anisotropy, the possibility to program the directionality of such anisotropy from the reconfiguration of basic pristine surfaces, and the simplicity of the optical setup, make the proposed structuration method attractive for versatile and cost-effective surface patterning.

1. Introduction

The engineering of surface geometry of polymeric materials is of great interest for several application fields. Examples include light diffraction, adhesion properties, bio-interfaces for substrate-influenced cell cultures, tuning of the wetting effects [1–8]. A high degree of control over surface properties and their tuning, can be achieved through the fabrication of surface geometries with a significant degree of complexity and anisotropy [9]. Standard lithographic techniques, including photolithography, electron beam and focused ion beam lithography, self-assembly, and soft lithography [10–13], are extensively used in this framework but require high costs and complex equipment [11]. Furthermore, the need of designing the desired final surface before the manufacturing process even starts, without the possibility of modifications of the realized geometries post-fabrication, represents an additional limit for these techniques.

Overcoming some of these limits has led to research efforts toward the development of new microfabrication methods. A promising photolithographic approach is based on the light-induced mass transport occurring in azobenzene-containing polymers (briefly named azopolymers) under irradiation of their surface with spatially-structured UV/visible light [1, 14]. In these materials, the absorption of a photon with suitable energy ($\lambda = 300$–550 nm) induces cyclic structural transitions of the photo-active azobenzene molecules between their *trans* and *cis* isomerization states. The isomers have different chemical, physical and geometrical properties, which can affect the properties and the functionalities of materials in which are embedded, acting as molecular photo-switches.

The *trans-cis* structural photo-switch is of great interest in several scientific fields. Some examples of technological applications in which the suitability of azomaterials photo-switch has recently been investigated, are the photo-responsive biosensors for antiproliferative activity against cancer cells [15, 16], or as alternatives data storage devices in electronics, where traditional phase-change materials are widely used [17, 18]. Additionally, the propagation of the molecular azobenzene dynamics at macroscopic level induces the photo-actuation effect observed in azo-LCEs (azobenzene-containing liquid–crystalline elastomers) [1]. Such phenomenon is very attractive for direct optical-to-mechanical energy conversion devices, aimed at the realization of light-driven soft-robots and energy-harvesting devices [19]. An example is the chaotic self-oscillation induced by the sunlight in azo-LCEs films, permitting the conversion of the solar energy in controlled isomerization-initiated mechanical motion [20, 21].

When the azomolecules are embedded in amorphous materials, the cyclic azobenzene photoisomerization, through intricate interactions with the material matrix, gives rise to a macroscopic light-driven material movement (known as mass migration phenomenon), which results in the appearance of topographic reliefs at the free surface of thin films [22–24]. The photoinduced surface structuration is very attractive for surface patterning technologies because, unlike traditional lithographic techniques, is a cost-effective method that can require simple illumination schemes and even allows to reconfigure previously structured surfaces. Taking advantage of the strong dependence of the phenomenon on the irradiated intensity pattern and the peculiar anisotropic response to the polarization distribution of the optical field over the surface, a wide range of large-scale topographical textures can be produced by tuning few illumination parameters. The largely investigated anisotropic structuration of a flat azopolymer surface is achieved with a sinusoidal intensity pattern produced by two interfering beams, that generates large-scale sinusoidal surface reliefs (the surface relief gratings, SRGs) [25]. Different degrees of surface complexity and anisotropy can be achieved acting on the illumination scheme. For example, quasicrystal surface reliefs are obtained by means of sequential inscriptions of SRGs with different orientation across the surface [6, 26, 27], and 3D topographic reliefs can be made using complex holographic structured intensity patterns [28, 29]. Furthermore, periodic and complex superficial topographies can also be obtained by using the light-induced material motion to reconfigure a properly structured azopolymer surface. The photo-driven reconfiguration of controlled prestructured surfaces is typically investigated for the tuning of anisotropic wetting effects (such as controlled directionality or unidirectional spreading) [30–32] or cell culture influencing [4, 33].

To date, however, the reported experimental situations have been focused on small deformations of the pre-patterned surfaces (typically with microvolumes arranged in square arrays) reaching asymmetric geometries, while maintaining, even if deformed, the discrete nature of the pristine texture [34–39].

In this work, we show the ability to reconfigure prepatterned azopolymer film surfaces in a large deformation regime. In this reconfiguration scheme, the single microvolumes of the initial 2D discrete texture are deformed until they are joined together to form continuous structures with 1D symmetry. We demonstrate that different grating-like structures, with a very high degree of anisotropy and programmable amplitude, periodicity and orientation, can be produced with this approach by simply acting on light polarization direction and light exposure dose.

The evolution of the light diffraction patterns, produced by the obtained surface textures, is used as a prototype of possible programmable functionalities achievable through our light-driven surface reconfiguration method.

The proposed approach allows remarkable flexibility in fabrication and a high degree of control over achievable surface geometries and their anisotropy.

2. Methods

2.1. Sample fabrication

Azopolymer films with prestructured surfaces were fabricated by means of a soft-lithography technique (replica molding process) as schematized in figure 1(a). The process involves two steps of fabrication: first the preparation of a polydimethylsiloxane (PDMS) mold that reproduces the negative of the desired surface pattern, and then the use of the mold to transfer the texture on azopolymer films.

2.1.1. PDMS mold

A silicon wafer, lithographically patterned with an array of micro-pillars (arranged in a square lattice of pitch $p = 10.0\ \mu$m, diameter $d = 4.5\ \mu$m and height $h = 10.0\ \mu$m), was used as the master template for making the PDMS molds. First, a surface antistacking treatment was performed on the master using a silanization process. The silicon wafer was exposed to the silanizing vapors (trichloro(1 H,1 H,2 H,2 H-perfluorooctyl) silane in our case) in a hermetically sealed glass box, kept at 125 °C for 90 min. Afterwards, the box was opened, and the temperature was increased to 150 °C for 90 min to remove the vapor excess. PDMS (Sylgard

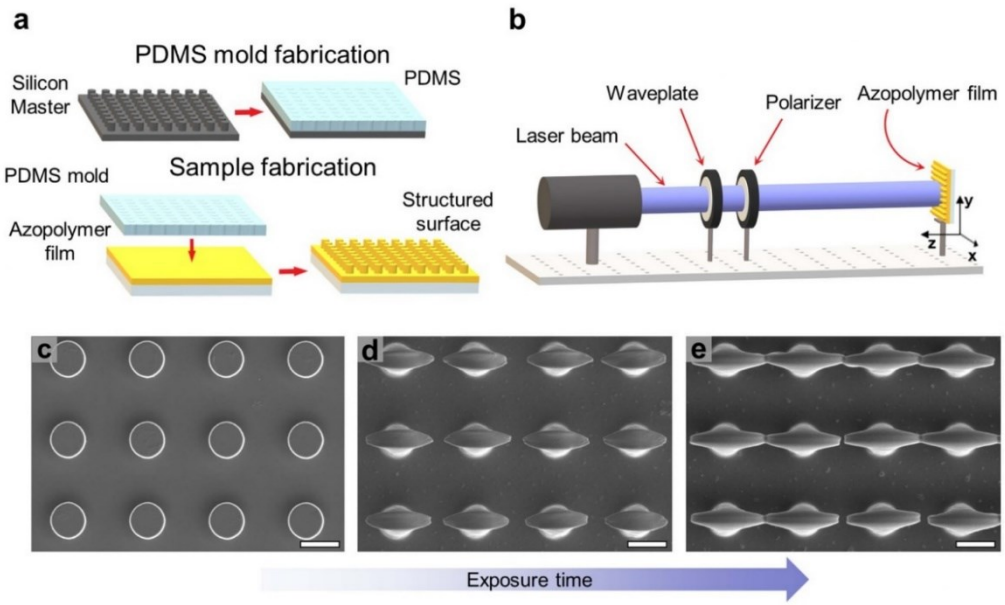

Figure 1. Samples fabrication and light-induced reconfiguration of azopolymer surfaces. (a) Replica molding manufacturing steps used to produce prestructured azopolymer surfaces. The fabrication of PDMS mold starts from a silicon master lithographically fabricated (top panel). In the bottom panel, the azopolymer patterning process to reproduce the same superficial structure as the silicon master; (b) schematic of the optical setup used to reconfigure the micro-posts. The laser beam, incident on the sample surface (placed in the x–y plane) at normal incidence, is first circularly polarized using a waveplate and then reconverted to arbitrary linear polarization by a linear polarizer mounted on a rotational stage; (c) SEM image of the as-prepared array on a 1×1 cm^2 area of cylindrical micro-pillars fabricated by soft imprinting from the PDMS stamp; (d)–(e) SEM images of the azopolymer microposts reconfigured by the linearly polarized laser beam in x axis direction for 1 and 3 min of exposure, respectively. The material displacement follows the polarization direction of the incident light. The SEM images were collected with 5000× of magnification and scale bars reported in each panel are 5 μm.

184, Dow Corning) mixture was prepared by mixing the precursor and the curing agent in a 10:1 ratio by weight. After degassing in a vacuum chamber, the mixture was gently poured over the silicon master and cured at 80 °C for 120 min. At the end of the process, the PDMS mold was accurately detached from the master (see the top of the figure 1(a)) and directly used for azopolymer patterning.

2.1.2. Azopolymer thin film patterning

To obtain polymer films with prestructured surfaces, few drops of 10 wt% solution of the azo-polymer in N-methyl-2-pyrrolidone were casted onto a glass slide and then covered by the fabricated PDMS stamp. The whole system was maintained at 45° for 12 h in order to allow the complete evaporation of the solvent, taking advantage of the porous nature of the PDMS mold. Once the process was completed, the PDMS stamp was carefully removed and a replica of the silicon master texture was realized onto the polymer film (bottom of the figure 1(a)). Details about azopolymer synthesis and its thermal and chemical characterizations are reported in previous works [34, 40].

2.2. Optical setup for azopolymer surface reshaping

In figure 1(b), the experimental configuration used to reshape the azopolymer prepatterned surfaces is schematically reported. The illumination source was a solid-state diode laser emitting at the wavelength of 405 nm. The linear polarization direction of the laser beam in the azopolymer film plane (x–y plane) is properly controlled by a quarter waveplate and a linear polarizer mounted on a rotational stage. The micropillar reconfiguration was obtained at normal incidence with intensity of approximately 200 mW cm^{-2}.

2.3. Morphological characterization

The 3D shape of the reconfigured grating structures was analyzed by means of scanning electron microscope (SEM) and atomic force microscope (AFM) and corroborated by the observation of the light diffraction patterns produced by the reconfigured surfaces.

2.3.1. Structural analysis

The pillar structural characterization was performed by SEM using a FEI Nova NanoSEM 450 system. The samples were previously sputtered with a nanometric layer of an Au/Pd alloy using a Benton Vacuum Desk V deposition system. The 3D topographies of the reconfigured surfaces were characterized by means of an AFM (WITEC Alpha RAS300) [41] operating in tapping mode using a cantilever with 75 kHz resonance frequency. The AFM scans were performed over a sample area of $60 \times 15\ \mu m^2$ with resolution of 512×128 pixels. The image analysis was accomplished by means of the open source software 'Gwyddion'.

2.3.2. Diffraction light patterns

To confirm different orientations and grating pitches of the anisotropic structures produced, photographs of diffraction patterns related to reconfigured surfaces were collected. As schematized in figure 2(q), the azopolymer films were illuminated with a p-polarized He–Ne laser at $\lambda = 633$ nm at normal incidence, and the patterns were projected onto a screen placed at distance $d \approx 11.5$ cm from the surface.

3. Results

The prepatterned azopolymer surfaces were prepared using the standard replica molding technique through a PDMS stamp, as schematically shown in figure 1(a) (see 'Methods' section). This structuration method produced $1 \times 1\ cm^2$ azopolymer area, homogenously patterned with a square array of cylindrical micropillars. Figure 1(c) presents the SEM image of the typical as-prepared textured polymer surface.

The first analysis involved the evaluation of the deformation regime for the micro-posts illuminated by the laser with different exposure doses. Whereby, in the initial experiment, the light intensity and the linear polarization direction, oriented along the *x*-axis direction of the sample plane (here defined as horizontal polarization), were kept fixed and the deformation of the pillars was analyzed as the exposure time increased. Figures 1(c)–(e) show SEM images of the sample surface collected before the illumination starts and after 1 and 3 min of film exposure, respectively. It is immediately evident that, after just 1 min of exposure, the material displacement at the top surface of the pillars produced a transition from the initial circular section to a pseudo-elliptic section [34], with the major axis oriented in the polarization direction. The increase in the exposure time resulted in an elongation of the pillars top layers, which came in contact after 3 min of irradiation. Starting from this point, the deformation at longer exposure times was so large that the pillars were definitely connected.

In this deformation regime, that we refer as large deformation regime as opposed to the deformation regimes reported so far [34–37], it is reasonable to assume that the pristine 2D array of discrete pillars is gradually transformed in a continuous and periodic 1D grating structures, with properties similar to the SRG observed when an azopolymer thin film with flat surface is structured via an interference light pattern [25, 42]. This hypothesis has been experimentally demonstrated by 3D characterization of the morphology of the azopolymer micropillars in the large deformation regime performed by means of SEM and AFM. To this aim, a study of the deformation dynamics of the pillars has been accomplished as function of the exposure time. The results are presented in figure 2. In this experiment, the light-induced pillar reconfiguration was repeated at 5, 10, 20, 30 and 60 min of exposure, while maintaining fixed the light intensity and polarization direction (vertical). The resulting superficial morphologies are shown by the SEM images in figures 2(a)–(e). After 5 min of illumination (figure 2(a)), the reconfigured pillars were already stretched along the direction of polarization with their ends in close contact, but the original positions of each pillar were still recognizable. Increasing the illumination time to 10 min (figure 2(b)), the microposts began to merge together in a single linear structure oriented along the light polarization direction, until their geometry as single discrete pillar was no longer recognizable after 20 min of illumination (as shown in figure 2(c)). SEM characterization confirms that as the exposure time increases (figures 2(c)–(e)), the reconfigured pattern becomes more and more similar to 1D superficial gratings. Additionally, to analyze the 3D properties of the reconfigured structures, we performed an AFM analysis with the aim of studying the illumination time-dependence of the structure heights. The collected AFM images for the different illumination times are reported in figures 2(f)–(j), while the figures 2(k)–(o) show the cross-section surface profiles traced along gray dashed lines. The relief heights were measured as indicated by the black arrows drawn on each topographic profile and reported as function of the exposure time in the plot shown in figure 2(p). As expected from azopolymer volume conservation during the reconfiguration process, the height of the structures decreased as the exposure time, and the resulting structural deformation, increased. Height data of figure 2(p), together with SEM images of lateral views of the micropillars at different stages of the reshaping process (figures 2(r)–(t), for pristine, and reconfigured structures at 10 and 60 min, respectively) allow a deeper insight in the dynamic of 3D structural reconfiguration of the pillars. The height

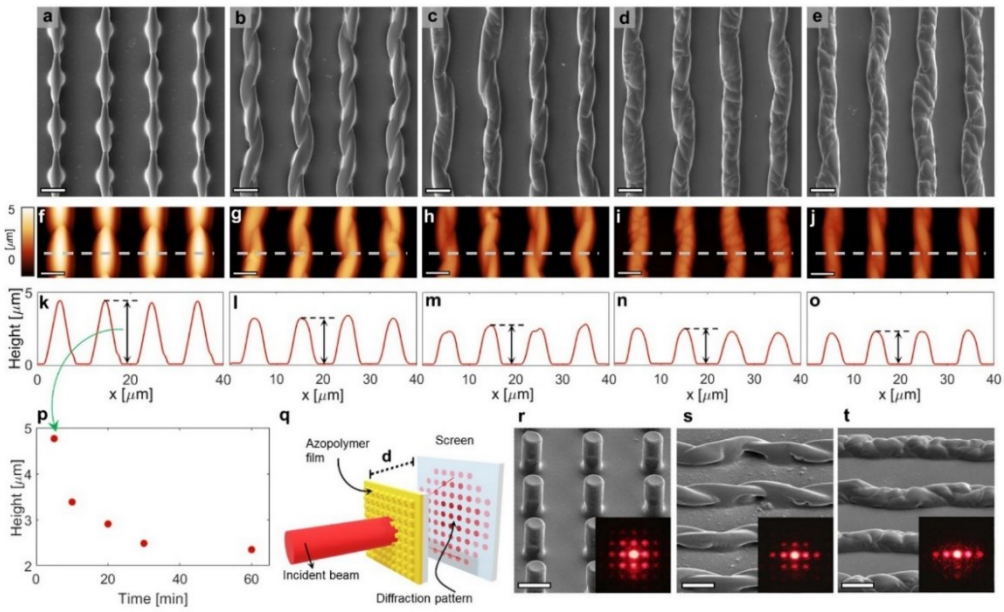

Figure 2. Azopolymer pillar reconfiguration dynamics and morphological characterization. (a)–(e) SEM images of pillars reconfigured for exposure times of 5, 10, 20, 30 and 60 min respectively, collected with 5000× of magnification; (f)–(j) AFM scans collected on an area of 60 × 15 μm^2 with resolution of 512 × 128 pixels, on the surfaces of samples reported in (a)–(e); (k)–(o) Topographic profiles traced for each sample, along the gray dashed line shown in AFM images. The black arrows, drawn in each panel, indicate how the gratings height measurements were performed; (p) Amplitudes of the experimental reconfigured structures measured from the AFM images of the samples reported in (f)–(j) as function of the exposure time; (q) Schematic for the diffraction pattern produced by illumination of the azopolymer film at normal incidence with an He–Ne laser at $\lambda = 633$ nm, on a screen placed at distance $d \approx 11.5$ cm; (r) Side view of SEM image collected on pristine micropillar array (magnification 5000×). The photograph of the diffraction pattern obtained as schematized in (q) is shown as inset; (s)–(t) Side view of SEM images shown in (b) and (e), collected with 6500× of magnification, as a demonstration of the entire microvolume involved in the reconfiguration process, and their diffraction patterns as insets. All white scale bars shown in SEM and AFM images are 5 μm.

of the pristine micropillars showed a substantial reduction in the first few minutes of the light-induced reconfiguration process, changing from the pristine 10.0 to 5.0 μm after 5 min of illumination. In this condition, however, while the upper layers of the pillars were largely deformed to have adjacent structures merging together, the pillars bases remained less deformed (figure 2(s)). At longer illumination times, the volume reconfiguration produced a further reduction in the amplitude of superficial architectures following a non-linear trend, until a saturation condition was reached after 30 min of exposure. SEM image in figure 2(t) shows that at this reconfiguration stage the transition from the discrete pristine 2D array to a continuous 1D grating was completed. The analysis of the 3D reconfiguration dynamics was further supported by the evolution of light diffraction patterns that the azopolymer surfaces produced at each reconfiguration step. To this aim, as schematized in figure 2(q), a camera was used to acquire the photographs of the light patten projected, in the illumination of the azopolymer surfaces with a He–Ne laser, on an opaque screen placed at distance $d \approx 11.5$ cm from the sample. According to the discrete 2D geometry of the initial square array of pillars, pristine surfaces were characterized by a square 2D arrangement of diffraction spots (inset, figure 2(r)), emerging at angles predicted by Bragg's diffraction law. For the first diffraction orders in both horizontal and vertical directions, the diffraction angles θ in respect to the surface normal were directly related to the periodicity p of the pristine pillar array ($\sin\theta = \lambda/p$). However, as the pillar reconfiguration proceeded in one direction, the vertical diffraction spots of the initial 2D square pattern gradually faded (inset, figure 2(s)), until the diffraction pattern turned, in the final reconfiguration stage, into the typical one produced by a 1D diffraction grating of periodicity p, oriented vertically (inset, figure 2(t)). Due to the peculiar polarization-driven directionality of the mass migration in azopolymers, the anisotropic reconfiguration of the pristine pillar pattern was repeated also for directions other than the principal ones (horizontal and vertical for the square array). In this case, the large light-induced deformation demonstrated above have produced grating structures with different orientation and periodicity, by a simple polarization rotation of the reconfiguring light beam. As an example, six gratings structures, with different periodicities and/or grating orientation, were fabricated starting from the square lattice of azopolymer micropillars. In order to select the directions for pillar reconfiguration, we considered the periodic pristine square array of pillars and we identified the positions of first, second and fourth nearest neighbors, each lying

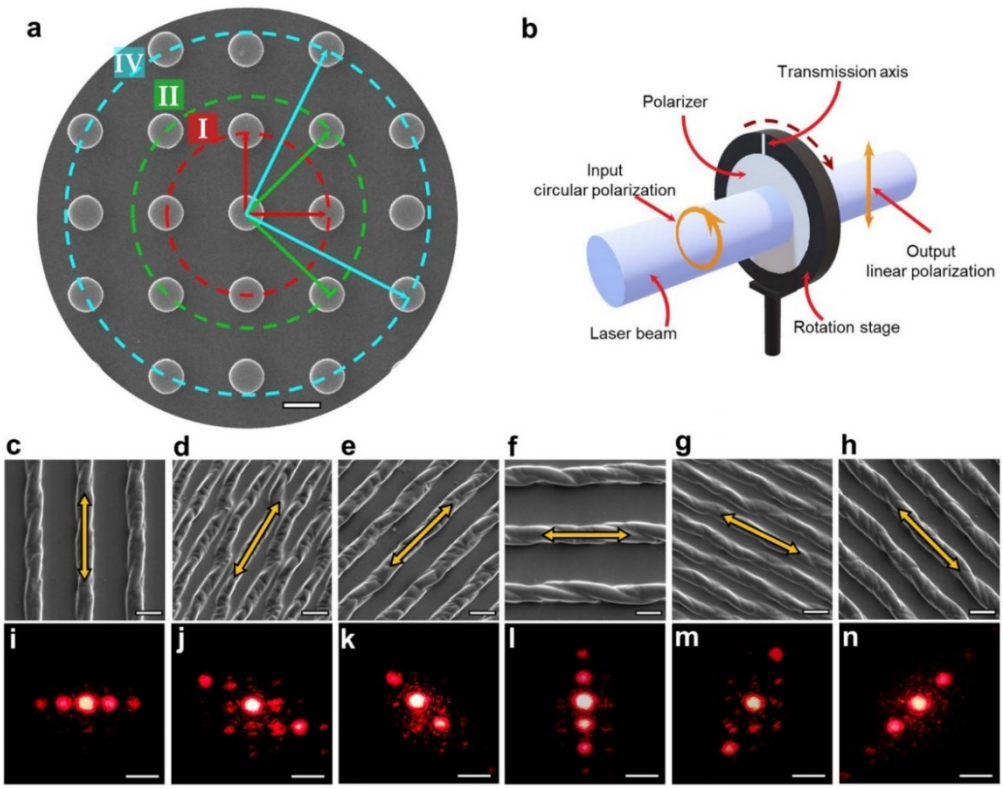

Figure 3. Realization of programmed polarization-driven gratings. (a) SEM image of the pristine pillar lattice with a schematic representation to identify relative rotation angles to connect pillars in different directions. Dashed colored rings indicate the position of the first (in red), second (in green) and fourth (in light blue) nearest neighbors of the central micropost. Their related colored arrows indicate the directions along which microvolumes can be connected by the light-driven material motion simply by rotating the linear polarization. In particular, knowing the pitch of the array $p = 10\ \mu$m and choosing the vertical direction as the reference as $\vartheta = 0°$, angles calculated from simple geometric considerations are $\vartheta_{I,1} = 0°, \vartheta_{I,2} = 90°$; $\vartheta_{II,1} = 45°, \vartheta_{II,2} = 135°$; $\vartheta_{IV,1} = 26°, \vartheta_{IV,2} = 116°$; (b) detail of the optical setup scheme reported in figure 1(b). Circularly polarized incident light passes through a linear polarizer mounted on a rotational stage. The direction of output linear polarization is determined by the orientation of the transmission axis. Polarization states are indicated by the yellow arrows; (c)–(h) SEM images collected with magnification of 5000× on reconfigured surfaces obtained by rotate the light polarization by angles calculated and using a laser intensity approximately of 200 mW cm^{-2} for 16 min of exposure time. The polarization directions are indicated by the yellow arrow shown in each panel. For all SEM images the scale bars are 5 μm. (i)–(n) Photographs of diffraction patterns produced by illumination of the azopolymer films reconfigured shown in (c)–(h) at normal incidence with an He–Ne laser at $\lambda = 633$ nm. The scale bars are 1 cm.

on the respective colored ring drawn on the SEM image shown in figure 3(a) (the third nearest neighbors are not mentioned since they lay in the same directions identified for the first neighbors). For each nearest neighbor, the relative arrows indicate the directions of the shortest distances between adjacent structures. The micropillars can be elongated and connected together along the identified directions using the light-induced reshaping, resulting in 1D architectures with three different periods.

In each reconfiguration experiment, the linear polarizer was rotated to match the desired polarization direction for the reconfiguring laser beam, as schematically represented in figure 3(b). The laser intensity (200 mW cm^{-2}) and the illumination time (16 min) were kept fixed for all the reconfiguration experiments. The SEM images of the surface at the end of the different directional reconfiguration processes are reported in figures 3(c)–(h), together with their He–Ne diffraction patterns (figures 3(i)–(n)). In each panel, the reconfiguring polarization direction is represented by the yellow arrow. This direction is orthogonal to the grating vector of the 1D periodic pattern obtained as result of the reconfiguration of the micro-posts. As expected, according to the geometry of the pristine array, the obtained gratings presented the three different periodicities $p_1 = 10\,\mu$m, $p_2 = p_1/\sqrt{2}$ and $p_3 = p_1/\sqrt{5}$, and two sets of grating orientations as confirmed by SEM analysis and light diffraction patterns in figures 3(i)–(n), which quantitatively reproduced the diffraction angles predicted for the first diffraction orders by Bragg's relation with the relative grating periodicity ($\sin\theta_i = \lambda/p_i$).

4. Conclusions

We have demonstrated that the light-induced reconfiguration of prestructured surfaces of materials containing azobenzene molecules is a suitable approach to produce a high degree of superficial structural anisotropy. This technique is relevant for several application fields in which the topography controls surface functionalities.

Here we reported the experimental analysis of the process of the light-induced reconfiguration of an array of azopolymer cylindrical micropillars, which produce structured surfaces with controlled degree and orientation of structural anisotropy, exploiting the polarization sensitivity of azopolymer structuration. In particular, morphological analysis conducted on the reshaped surfaces has shown that, after a reasonable exposure time of a few minutes, the transition from small to large deformations regime allows to reconfigure a discrete texture in a continuous and periodic grating, characterized by few microns in height and high degree of structural anisotropy.

Additionally, by simply varying the direction of the reconfiguring light polarization, even different grating periodicities are easily achievable starting from the same prestructured array, bringing to a versatile and cost-effective surface structuration technique.

This approach could even be generalized to achieve higher degrees of anisotropy and complexity of textured surfaces, for example by multistep sequential irradiations of the same prepatterned surface, changing the polarization directions, or even using more complex polarization states (such as radial or azimuthal polarization), besides different pre-structuration configurations.

Data availability statement

The data that support the findings of this study are available upon reasonable request from the authors.

Acknowledgments

We thank Professor Carlo Altucci of the University of Naples Federico II for the useful discussion about azobenzene bio-applications.

ORCID iDs

Marcella Salvatore https://orcid.org/0000-0002-1497-5306
Fabio Borbone https://orcid.org/0000-0001-7433-9267
Pasqualino Maddalena https://orcid.org/0000-0001-5823-3331
Stefano Luigi Oscurato https://orcid.org/0000-0002-1814-8033

References

[1] Oscurato S L, Salvatore M, Maddalena P and Ambrosio A 2018 From nanoscopic to macroscopic photo-driven motion in azobenzene-containing materials *Nanophotonics* **7** 1387–422
[2] Zhao Y, Lu Q, Li M and Li X 2007 Anisotropic wetting characteristics on submicrometer-scale periodic grooved surface *Langmuir* **23** 6212–7
[3] Rianna C, Calabuig A, Ventre M, Cavalli S, Pagliarulo V, Grilli S, Ferraro P and Netti P A 2015 Reversible holographic patterns on azopolymers for guiding cell adhesion and orientation *ACS Appl. Mater. Interfaces* **7** 16984–91
[4] Oscurato S L, Formisano F, De Lisio C, D'Ischia M, Gesuele F, Maddalena P, Manini P, Migliaccio L and Pezzella A 2019 Spontaneous wrinkle emergence in nascent eumelanin thin films *Soft Matter* **15** 9261–70
[5] Salvatore M, Oscurato S L, D'Albore M, Guarino V, Zeppetelli S, Maddalena P, Ambrosio A and Ambrosio L 2020 Quantitative study of morphological features of stem cells onto photopatterned azopolymer films *J. Funct. Biomater.* **11** 8
[6] Salvatore M, Borbone F and Oscurato S L 2020 Deterministic realization of quasicrystal surface relief gratings on thin azopolymer films *Adv. Mater. Interfaces* **7** 1902118
[7] Patankar N A 2003 On the modeling of hydrophobic contact angles on rough surfaces *Langmuir* **19** 12949–1253
[8] Blossey R 2003 Self-cleaning surfaces—virtual realities *Nat. Mater.* **2** 301–6
[9] Chen Y, He B, Lee J and Patankar N A 2005 Anisotropy in the wetting of rough surfaces *J. Colloid Interface Sci.* **281** 458–64
[10] Barbieri L, Wagner E and Hoffmann P 2007 Water wetting transition parameters of perfluorinated substrates with periodically distributed flat-top microscale obstacles *Langmuir* **23** 1723–34
[11] Chu K-H, Xiao R and Wang E N 2010 Uni-directional liquid spreading on asymmetric nanostructured surfaces *Nat. Mater.* **9** 413–7
[12] Chaudhury M K and Whitesides G M 1992 How to make water run uphill *Science* **256** 1539–41
[13] Wu S-Z, Wu D, Yao J, Chen Q-D, Wang J-N, Niu L-G, Fang H-H and Sun H-B 2010 One-step preparation of regular micropearl arrays for two-direction controllable anisotropic wetting *Langmuir* **26** 12012–6
[14] Priimagi A and Shevchenko A 2014 Azopolymer-based micro- and nanopatterning for photonic applications *J. Polym. Sci.* B **52** 163–82
[15] Imperatore C *et al* 2019 Photo-control of cancer cell growth by benzodiazo N-substituted pyrrole derivatives *J. Photochem. Photobiol.* A **377** 109–18

[16] Imperatore C et al 2020 Exploring the photodynamic properties of two antiproliferative benzodiazopyrrole derivatives *Int. J. Mol. Sci.* **21** 1246
[17] Gerislioglu B, Bakan G, Ahuja R, Adam J, Mishra Y K and Ahmadivand A 2020 The role of $Ge_2Sb_2Te_5$ in enhancing the performance of functional plasmonic devices *Mater. Today Phys.* **12** 100178
[18] Bakan G, Gerislioglu B, Dirisaglik F, Jurado Z, Sullivan L, Dana A, Lam C, Gokirmak A and Silva H 2016 Extracting the temperature distribution on a phase-change memory cell during crystallization *J. Appl. Phys.* **120** 164504
[19] Zeng H, Wasylczyk P, Wiersma D S and Priimagi A 2018 Light robots: bridging the gap between microrobotics and photomechanics in soft materials *Adv. Mater.* **30** 1703554
[20] Yin R, Xu W, Kondo M, Yen -C-C, Mamiya J, Ikeda T and Yu Y 2009 Can sunlight drive the photoinduced bending of polymer films? *J. Mater. Chem.* **19** 3141–3
[21] Kumar K, Knie C, Bléger D, Peletier M A, Friedrich H, Hecht S, Broer D J, Debije M G and Schenning A P H J 2016 A chaotic self-oscillating sunlight-driven polymer actuator *Nat. Commun.* **7** 11975
[22] Natansohn A and Rochon P 2002 Photoinduced motions in azo-containing polymers *Chem. Rev.* **102** 4139–76
[23] Viswanathan N K, Kim D Y, Bian S, Williams J, Liu W, Li L, Samuelson L, Kumar J and Tripathy S K 1999 Surface relief structures on azo polymer films *J. Mater. Chem.* **9** 1941–55
[24] Cojocariu C and Rochon P 2009 Light-induced motions in azobenzene-containing polymers *Pure Appl. Chem.* **76** 1479–97
[25] Rochon P, Batalla E and Natansohn A 1995 Optically induced surface gratings on azoaromatic polymer films *Appl. Phys. Lett.* **66** 136–8
[26] Kim D Y, Tripathy S K, Li L and Kumar J 1995 Laser-induced holographic surface relief gratings on nonlinear optical polymer films *Appl. Phys. Lett.* **66** 1166–8
[27] Lee S, Jeong Y-C and Park J-K 2007 Facile fabrication of close-packed microlens arrays using photoinduced surface relief structures as templates *Opt. Express* **15** 14550–9
[28] Oscurato S L, Salvatore M, Borbone F, Maddalena P and Ambrosio A 2019 Computer-generated holograms for complex surface reliefs on azopolymer films *Sci. Rep.* **9** 6775
[29] Goodman J W 2005 *Introduction to Fourier Optics* (New York: W. H. Freeman)
[30] Gritsai Y, Goldenberg L M and Stumpe J 2011 Efficient single-beam light manipulation of 3D microstructures in azobenzene-containing materials *Opt. Express* **19** 18687–95
[31] Lee S, Shin J, Lee Y-H, Fan S and Park J-K 2010 Directional photofluidization lithography for nanoarchitectures with controlled shapes and sizes *Nano Lett.* **10** 296–304
[32] Salvatore M, Oscurato S L, Maddalena P and Ambrosio A 2020 Chapter 10—light-induced complex surface structuring of azobenzene-containing materials *Advances in Nanostructured Materials and Nanopatterning Technologies Advanced Nanomaterials* ed V Guarino, M L Focarete and D Pisignano (Amsterdam: Elsevier) pp 273–96
[33] Bae W-G, Eui Jeong H and Kim J 2015 Multiscale engineered hierarchical structures with precisely controlled sizes for bio-inspired cell culture *Mater. Lett.* **159** 213–7
[34] Oscurato S L, Borbone F, Maddalena P and Ambrosio A 2017 Light-driven wettability tailoring of azopolymer surfaces with reconfigured three-dimensional posts *ACS Appl. Mater. Interfaces* **9** 30133–42
[35] Pirani F, Angelini A, Frascella F, Rizzo R, Ricciardi S and Descrovi E 2016 Light-driven reversible shaping of individual azopolymeric micro-pillars *Sci. Rep.* **6** 31702
[36] Pirani F, Angelini A, Ricciardi S, Frascella F and Descrovi E 2017 Laser-induced anisotropic wettability on azopolymeric micro-structures *Appl. Phys. Lett.* **110** 101603
[37] Lee S, Kang H S, Ambrosio A, Park J-K and Marrucci L 2015 Directional superficial photofluidization for deterministic shaping of complex 3D architectures *ACS Appl. Mater. Interfaces* **7** 8209–17
[38] Kang H S, Lee S, Lee S-A and Park J-K 2013 Multi-level micro/nanotexturing by three-dimensionally controlled photofluidization and its use in plasmonic applications *Adv. Mater.* **25** 5490–7
[39] Lee S-A, Kang H S, Park J-K and Lee S 2014 Vertically oriented, three-dimensionally tapered deep-subwavelength metallic nanohole arrays developed by photofluidization lithography *Adv. Mater.* **26** 7521–8
[40] Ambrosio A, Marrucci L, Borbone F, Roviello A and Maddalena P 2012 Light-induced spiral mass transport in azo-polymer films under vortex-beam illumination *Nat. Commun.* **3** 989
[41] Alfieri M L, Panzella L, Oscurato S L, Salvatore M, Avolio R, Errico M E, Maddalena P, Napolitano A, Ball V and D'Ischia M 2019 Hexamethylenediamine-mediated polydopamine film deposition: inhibition by resorcinol as a strategy for mapping quinone targeting mechanisms *Front. Chem.* **7** 407
[42] Kim D Y, Li L, Jiang X L, Shivshankar V, Kumar J and Tripathy S K 1995 Polarized laser induced holographic surface relief gratings on polymer films *Macromolecules* **28** 8835–9

Publication II

F. Borbone, S. Luigi Oscurato, S. D. Sorbo, F. Pota,
M. Salvatore, F. Reda, P. Maddalena, R. Centore, and A. Ambrosio

Enhanced photoinduced mass migration
in supramolecular azopolymers by H-bond driven positional constraint

Reprinted from

Journal of Materials Chemistry C 9(34), 11368–11375 (2021)

with the permission of Royal Society of Chemistry

Journal of Materials Chemistry C

ROYAL SOCIETY OF CHEMISTRY

PAPER

View Article Online
View Journal | View Issue

Cite this: J. Mater. Chem. C, 2021, 9, 11368

Enhanced photoinduced mass migration in supramolecular azopolymers by H-bond driven positional constraint†

Fabio Borbone, *[ab] Stefano Luigi Oscurato, [bc] Salvatore Del Sorbo, [b] Filippo Pota, [a] Marcella Salvatore, [c] Francesco Reda, [c] Pasqualino Maddalena, [bc] Roberto Centore [a] and Antonio Ambrosio *[b]

Here we investigated the role of hydrogen bonding in the design of supramolecular azopolymers with a highly directional and constrained azobenzene–chain interaction involving the aromatic ring of the photoactive molecule, by exploiting the 2-aminopyrimidine/carboxylic acid supramolecular synthon as the tool for molecular recognition. We have shown that this approach is advantageous for producing affordable and versatile photopatternable azomaterials by complexation with polyacrylic acid (PAA). Molecular model complexes were successfully prepared and characterized by X-ray diffraction analysis and FTIR spectroscopy to reveal the multiple, non-ionic interaction occurring between the azobenzene units and the polymer chains. Surface photopatterning of thin films, driven by the typical mass migration phenomenon occurring in azopolymers, resulted strongly enhanced with increasing azobenzene content until equimolar composition. Results show that polymers with synthon-based azobenzenes markedly outperform single H-bonded systems bearing azomolecules with similar structure and electronic properties. We finally demonstrated that the azobenzene units can be easily extracted from a photopatterned film by a simple solvent rinse and without any chemical pre-treatment, leaving the periodicity of the inscribed surface relief gratings unaltered. This result was enabled by the orthogonal solubility of the components in the supramolecular system.

Received 17th May 2021,
Accepted 15th July 2021

DOI: 10.1039/d1tc02266k

rsc.li/materials-c

Introduction

Materials functionalized with azobenzene or its derivatives have been the object of extended research for decades because of their ability to respond to light.[1] The absorption of radiation with proper wavelength gives rise to photoisomerization of the azomolecules between *trans* and *cis* isomers showing a strong conformational difference. The possibility of sustaining the continuous *trans–cis–trans* cycle through irradiation is at the origin of the reorientation of the azomolecules under illumination with a linearly polarized laser beam. The resulting induced anisotropy and birefringence can be advantageously exploited to drive the orientation of mesophases in liquid crystals based materials[2–5] or in optical devices for reversible holographic data storage.[6–9] Macroscopic mass migration occurring on the surface of azopolymers thin films is recognized as another important phenomenon resulting from *trans–cis* photoisomerization in azomolecules.[10] Irradiation of the surface with an interference light pattern of polarized laser beams can induce highly directional polarization dependent mass transport, with formation of topographic modulations known as surface relief gratings (SRG), which replicate the illuminating intensity pattern[11] and can be erased by irradiation with circularly polarized light or by heating.[12] The result is a single-step all-optical reversible process to control surface topography which can be exploited in numerous technological applications, from photonics and optoelectronics such as DFB lasers[13,14] and organic solar cells[15] to complex textured surfaces,[16,17] templates for lithography[18] or tuning of wettability.[19] In a polymeric material, mass migration and SRG formation efficiently occur when azochromophores are linked to the polymer chain, thus mainly covalently bonded side-chain and main-chain polymer systems were initially investigated. However, in the last decades the supramolecular approach has emerged as a

[a] Department of Chemical Sciences, University of Napoli Federico II, Complesso Universitario di Monte Sant'Angelo, Via Cintia, Naples 80126, Italy. E-mail: fabio.borbone@unina.it
[b] CNST@POLIMI – Fondazione Istituto Italiano di Tecnologia, Via Pascoli 70, Milan 20133, Italy. E-mail: antonio.ambrosio@iit.it
[c] Department of Physics E. Pancini, University of Napoli Federico II, Complesso Universitario di Monte Sant'Angelo, Via Cintia, Naples 80126, Italy

† Electronic supplementary information (ESI) available. CCDC 2073781–2073786. For ESI and crystallographic data in CIF or other electronic format see DOI: 10.1039/d1tc02266k

powerful tool in the design of azomaterials, because of the high flexibility offered by simple synthetic procedures, mainly based on mixing components in solution, the possibility to investigate a wide range of noncovalent interactions of variable strength and the effortless optimization of composition. Indeed, different types of supramolecular chromophore–chain interactions have been successfully exploited to produce efficient SRG formation, from non-directional and strong ionic bonds to hydrogen and halogen bonding.[20–27] Supramolecular polymers based on halogen-bonded azochromophores grafted onto poly-4-vinylpyridine have revealed interesting performances in terms of SRG inscription efficiency and in some cases outperformed hydrogen-bonded systems based on the same photopassive polymer, although they suffered from phase separation at high azochromophore content.[28] The reason of the higher efficiency has been ascribed to the high directionality of the halogen bond, in which the σ-hole on the aromatic halogen involved in the electrostatic interaction is confined on the elongation of the R–X covalent bond axis, resulting in a more rigid chromophore–chain connection, improved "dragging" of the chains by the photoactive azomolecules during isomerizations and hence better overall mass migration compared to conventional H bonded systems. Moreover, given the same directionality, efficiency increased with halogen bond strength.[29] Herein we propose a model of a supramolecular azopolymer in which the degrees of freedom in the relative motion of azobenzene unit and polymer chain are further reduced through the direct involvement of the azobenzene aromatic ring in an additional weak bond. We investigated the role of hydrogen bonding in increasing strength and directionality of the chromophore–chain interaction and the effect on the efficiency of SRG formation, by exploiting the action of cooperative multiple hydrogen bonds. In this regard, we used the concept of the supramolecular synthon as a design element to provide a strong molecular recognition system for a stable and directional grafting. The double hydrogen bond occurring between a carboxylic acid group and a 2-aminopyridine type moiety is recognized as a robust supramolecular heterosynthon in crystal engineering and proved as a useful tool to produce stable amorphous solid dispersions.[30,31] In this work, we designed new supramolecular azopolymers by grafting 2-aminopyrimidine functionalized azochromophores onto polyacrylic acid (PAA) and investigated the efficiency of SRG formation.[32] A comparative study of SRG inscription performances with a single H bonded system revealed a very strong influence of the supramolecular synthon on the efficiency of mass migration.

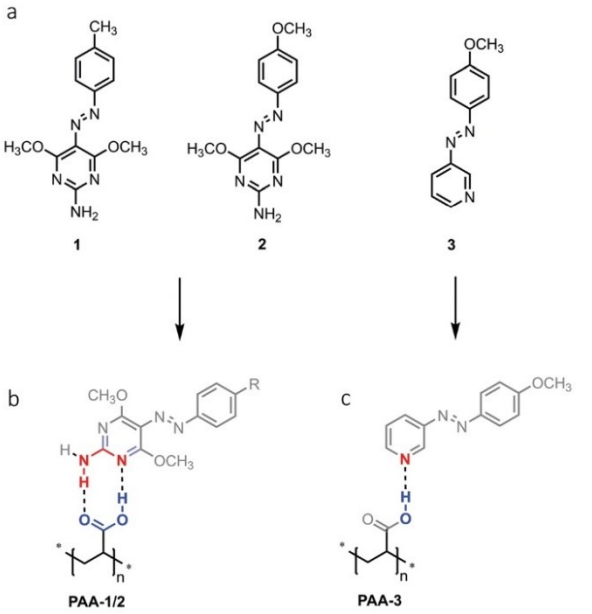

Fig. 1 Chemical structure of azochromophores (a) and grafted polymers (b and c).

Results and discussion

Synthesis and structural characterization

The azochromophores **1** and **2** reported in Fig. 1 were synthesized in high yields and purity through a simplified single step procedure (see Schemes S1 and S2, ESI†). In brief, diazonium salts (isolated as tetrafluoroborates) were directly coupled onto 2-amino-4,6-dimethoxypyrimidine in dichloroethane, to give the corresponding Azo·HBF_4 product, then deprotonated and crystallized by treatment with triethylamine in ethanol/water. These compounds were suitable for grafting onto polyacrylic acid (PAA) through complexation based on the supramolecular heterosynthon showed in Fig. 1b. It has been recently demonstrated that this polymer is able to produce very stable amorphous solid dispersions of drugs containing a 2-aminopyridine based pharmacophore. A second type of PAA based polymer was also prepared by using compound **3**, with the aim to compare the mass migration performances of synthon-based polymers with those of a similar system characterized by a single chromophore–chain hydrogen bond (Fig. 1c). To investigate at a molecular level the guest–host interactions occurring in the **PAA-1/2** azopolymers we first studied the crystal structure of the azopyrimidine derivatives and that of model compounds of the azopyrimidine–polymer system by single crystal X-ray diffraction. Compound **1** was crystallized in two polymorphs, named **1-I** and **1-II**, while **2** as one phase. The crystal packing of both the polymorphs of **1** and of compound **2** is driven by the common motif of double hydrogen bonds between the NH_2 donor and two OCH_3 acceptors, with no involvement of the aromatic nitrogen of the pyrimidine ring as possible acceptor (Fig. S1–S3, ESI†). This pattern of interactions changes when carboxylic monomers were used to induce molecular recognition. Compound **1** was successfully co-crystallized with methacrylic acid (**MA-1**) to obtain a monomeric model compound of the **PAA-1** polymer. A dimeric model compound of the polymer was also obtained by co-crystallization with bifunctional adipic acid (**AA-1**). Single crystals were grown by evaporation from chloroform/heptane in both cases with high yields. X-Ray diffraction analysis revealed a 1 : 1 ratio for the complex

MA-1. The azomolecule is in almost planar conformation, and there is no disorder in the azo group. A very stable $R_2^2(8)$ cyclic structure with eight atoms and two hydrogen bonds is formed. This structure, in principle, can be realized in three ways: between two carboxylic acid groups (AA homosynthon), between two aminopyrimidine groups (PP homosynthon) and between an acid and an aminopyrimidine group (AP heterosynthon).

The azomolecule in **MA-1** is involved in two double hydrogen bonding patterns (Fig. 2), an AP heterosynthon and a PP homosynthon, and two $R_2^2(8)$ ring patterns are formed. In the PP homosynthon, the N–H···N hydrogen bond shows N···N and H···N distances of 3.172(2) Å and 2.32(2) Å respectively, while the bond angle is 168(2)°. In the AP heterosynthon, for the N–H···O bond, N···O and H···O distances are 2.836(2) Å and 1.91(2) Å respectively, while the angle is 175(2)°; for the OH···N bond, O···N and H···N distances are 3.051(2) Å and 2.19(2) Å respectively, with an angle of 175(2)°. The resulting $(\mathbf{MA\text{-}1})_2$ dimers are laterally packed to form infinite layers. These layers are parallel to the lattice planes of Miller indices $\bar{1}21$ and stacked with a spacing of 3.28 Å. Crystals of the **AA-1** complex revealed a melting peak at 138 °C in the DSC diagram, which is lower than those of the two components (152 °C for both adipic acid and **1**). The complex **AA-1** crystallized in a 1 : 2 ratio, with each adipic acid molecule involved in two AP heterosynthons with two azomolecules (Fig. 3). Each of these two azomolecules are linked through a PP homosynthon to the azomolecule of another **AA-1** complex, giving rise to a 1-D polymeric chain through alternated PP and AP synthons. These chains are packed to form layers as in **MA-1**, which are stacked with a spacing of 3.38 Å. In the PP homosynthon, the N–H···N hydrogen bond shows N···N and H···N distances of 3.207(2) Å and 2.41(2) Å respectively, while the bond angle is 167(2)°. In

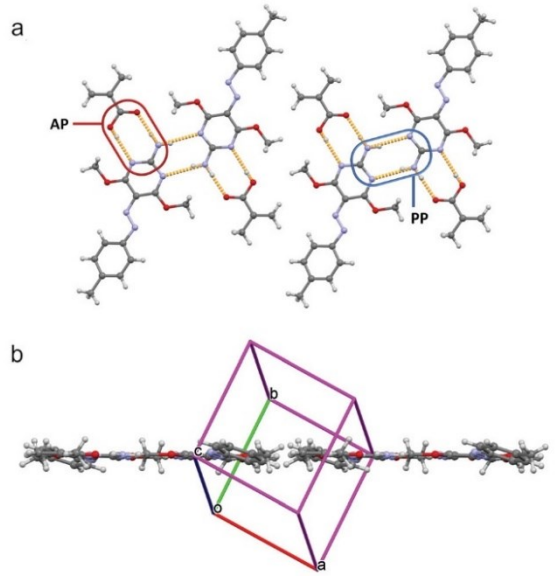

Fig. 2 Partial packing of **MA-1**. (a) Face view with H bond pattern in orange; (b) edge view.

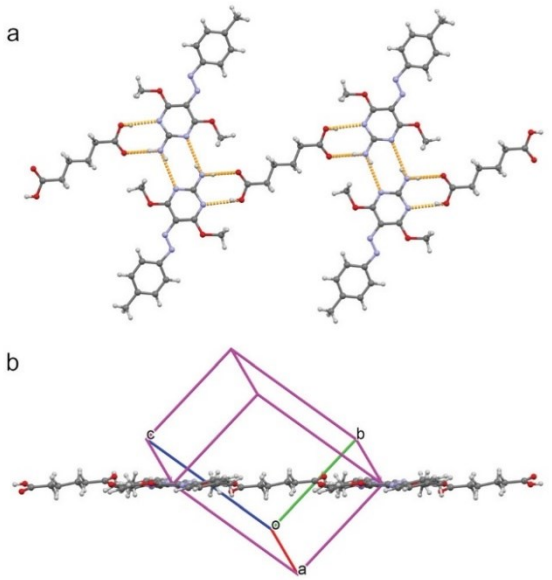

Fig. 3 Partial packing of **AA-1**. (a) Face view with H bond pattern in orange; (b) edge view.

the AP heterosynthon, for the N–H···O bond, N···O and H···O distances are 2.895(2) Å and 2.04(3) Å respectively, while the angle is 174(2)°; for the OH···N bond, O···N and H···N distances are 2.974(2) Å and 2.18(2) Å respectively, with an angle of 170(2)°.

The corresponding bond distances in the two complexes are similar and show that the hydrogen bonds in the heterosynthons are shorter, as expected due to the higher acid–base character of this interaction. However, the lengths of C=O and C–O bonds in the carboxylic group (1.198 Å and 1.334 Å respectively for **AA-1**, 1.209 Å and 1.333 Å respectively for **MA-1**) are in the normal range for fully double and single bond respectively and suggest that no proton transfer occurs from hydroxyl to the nitrogen of pyrimidine ring. To support this observation, we performed a statistical analysis of all the compounds containing the same 2-aminopyrimidine/carboxylic acid heterosynthon reported in the CSD database. The mean values of C=O and C–O bond lengths of the 143 hits reported are 1.2127 Å (σ = 0.0172) and 1.3084 Å (σ = 0.0136) respectively and confirm that formation of carboxylate ion is not expected in this type of heterosynthon. The X-ray analysis confirmed the robustness and non-ionic character of the supramolecular synthon and supported the assignment and comparison of FT-IR signals (*vide infra*).

Spectroscopic characterization

The azochromophores **1** and **2** were used to prepare the PAA based supramolecular polymers $\mathbf{PAA\text{-}1}_x$ and $\mathbf{PAA\text{-}2}_x$ with x = 0.5, 0.75 and 1.0 dye/polymer molar ratio, by dissolving the proper amount of azochromophore and PAA (M_w 1800) in dimethylformamide (DMF), in order to have a 1 : 3 azopolymer/solvent weight ratio. The solutions were spin-coated on glass slides or

KBr pellets for characterization. All the solutions gave rise to perfectly transparent and amorphous films, without any evidence of phase separation or dye aggregation, even for the highest chromophore content, corresponding to 79.1 wt% and 80.1 wt% respectively for **PAA-1$_{1.0}$** and **PAA-2$_{1.0}$**. The UV-vis absorption spectra of polymers in DMF solution and thin films show maxima at 359 nm and 364 nm for respectively **PAA-1$_x$** and **PAA-2$_x$**, corresponding to the $\pi \rightarrow \pi^*$ transition, with a shoulder at longer wavelengths corresponding to the $n \rightarrow \pi^*$ transition (Fig. S4, S5 and Table S3, ESI†). The spectra of thin films are similar to those in solution and exhibit an expected slight broadening, indicating that no aggregation occurs in the films even at the highest concentration. The relative slight increase of the visible band with decreasing azobenzene concentration observed in both polymer series can be attributed to the absorption by the hydrazone tautomer produced after the partial protonation of the azo groups by the increasing free carboxylic acid groups.[33,34] The same effect was observed in the UV-vis spectra of **1** and **2** in ethyl acetate added with acetic acid (Fig. S6 and S7, ESI†), while in acetic acid the chromophores resulted completely protonated. The refractive index dispersion of polymers was evaluated by ellipsometry (Fig. S8, ESI†). Values of n at the relevant wavelength of 633 nm ranged from 1.638 of **PAA-3$_{1.0}$** to 1.706 of **PAA-2$_{1.0}$** (Table S3, ESI†). In order to investigate the supramolecular interaction in the synthesized azopolymers, a comparative FT-IR analysis was performed on azochromophores, model compounds and polymers. In the IR spectrum of pure PAA (Fig. S9, ESI†), absorption at 1706 cm^{-1} is attributed to the carbonyl stretching of carboxylic acid dimer in the polymer matrix.[31] This signal is shifted to 1725 cm^{-1} in the grafted azomaterials (Fig. 4 and Fig. S9, S10, ESI†), indicating that the carboxylic acid dimer group is no longer present. The same band is observed at 1727 cm^{-1} in the spectrum of the **AA-1** complex (Fig. 4). Therefore, this band has to be assigned to the carbonyl of the carboxylic group involved in the AP heterosynthon observed in the crystal structure. Evidence of the second hydrogen bond involving the amino group can be gathered from the analysis of the characteristic NH stretching and bending frequencies. In the spectra of pure **1**, the band at 1622 cm^{-1} corresponds to the typical scissoring of the NH_2 group, as known for amines and reported for 2-amino-4,6-dimethoxypyrimidine.[35] This bending mode is dependent on the hydrogen bonding and occurs at higher vibrational energy with increasing strength and number of hydrogen bonds.[36] In **AA-1**, this band is considerably shifted to higher frequency (1667 cm^{-1}) because the amino group of the azochromophore is involved in two hydrogen bonds of the PP and AP type synthons, as shown by the X-ray analysis. In the spectra of all **PAA-1$_x$** and **PAA-2$_x$** polymers (Fig. S9 and S10, ESI†) this signal is split at 1665 cm^{-1} and 1640 cm^{-1}, suggesting that part of the amino groups in the polymer matrix can participate in second hydrogen bond with surrounding acceptors. The second evidence of hydrogen bonding is given by the analysis of vibrational frequencies of the NH stretching. In the spectrum of **1**, asymmetric and symmetric stretching are visible at 3461 cm^{-1} and 3354 cm^{-1} respectively, while the weak band at 3222 cm^{-1} typically results from the Fermi resonance coupling between an overtone of the NH_2 bending/scissoring at 1600 cm^{-1} and the symmetric N–H stretching mode. When the amino group is involved in hydrogen bonds, the NH stretching shifts to lower frequencies and its oscillator strength increases significantly. This effect and the reduced energy gap with the overtone transition leads to a strong enhancement of the Fermi resonance coupling and to a dramatic increase of the 3200 cm^{-1} band intensity, dependent on the strength of the hydrogen bonds.[37,38] This coupling is clearly visible in the spectrum of **AA-1**, where the intensity of the band at 3226 cm^{-1} exceeds that of the double band at 3385 cm^{-1}. A very similar coupling and band pattern is observed for polymers (Fig. 4 and Fig. S9, S10, ESI†) and confirms that the double hydrogen bond of the AP heterosynthon effectively takes place within the grafted polymers. The formation of the hydrogen bond between PAA and **3** in **PAA-3$_{1.0}$** was verified by following the shift of the stretching of carbonyl from 1706 cm^{-1} to 1716 cm^{-1} and that of the free pyridyl ring (1020 cm^{-1}) to higher frequency, with the appearing of a second band at 1040 cm^{-1} (Fig. S11, ESI†).[39]

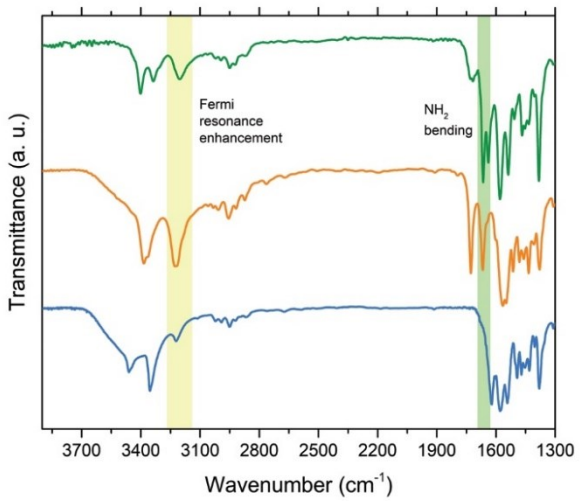

Fig. 4 FT-IR spectra of **PAA-1$_{1.0}$** (green line), **AA-1** (orange line) and **1** (blue line).

Efficiency of SRG formation

The efficiency of mass migration was investigated by performing SRG inscription experiments on thin films of the prepared polymers. Structuring was carried out by irradiating the samples with an interference pattern obtained with p-polarized beams, producing regular and high quality SRGs for all polymers. A laser wavelength of 457 nm was used to work in a range of relatively low chromophore absorption, with the aim to compare the performances of synthon-based systems with those of the conventional hydrogen bonded **PAA-3$_{1.0}$** in a regime not affected by thermal effects. Fig. 5a shows the growth of the 1st order diffraction efficiency (DE) produced by the forming grating as a function of time. The efficiency of mass

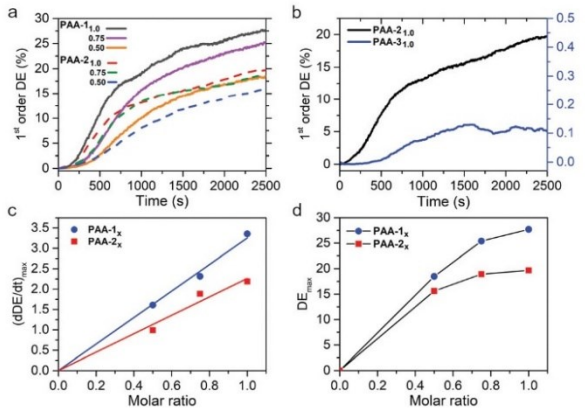

Fig. 5 (a) Diffraction efficiency of **PAA-1**$_x$ and **PAA-2**$_x$ (x = 0.5, 0.75, 1.0; film thickness: 880–950 nm; irradiance: 175 mW cm^{-2}); (b) diffraction efficiency of **PAA-2**$_{1.0}$ and **PAA-3**$_{1.0}$; (c) SRG inscription rate and (d) maximum of diffraction efficiency for **PAA-1**$_x$ and **PAA-2**$_x$ as a function of composition.

migration can be related to the rate of SRG formation, calculated as the slope of the straight line obtained by fitting the data in the range of linear growth, corresponding approximately to the section of curves between 10% and 30% of the DE maximum value attained at the end of the experiment. These data are reported in Fig. 5c and d for all the polymers as a function of the azobenzene content. The results show that the SRG inscription rate linearly increases with the concentration of the azochromophore in the polymer and a regular growth trend is also observed for the maximum DE value, for both **PAA-1** and **PAA-2**. Interestingly, for each composition **PAA-1** noticeably outperforms **PAA-2** (by 41%, 34% and 18% for x = 1.0, 0.75 and 0.50 respectively) although the only structural difference between azochromophores **1** and **2** is the oxygen on the terminal methoxy group of **2**. This electron donor can act as an additional hydrogen bond acceptor within the polymer matrix and contribute to reduce the effectiveness of *cis–trans* isomerizations on molecular and chain motions, thus affecting overall mass migration. This different performance is also evident by comparing the AFM cross-sectional profiles of SRGs inscribed on **PAA-1** and **PAA-2** in the same time lapse (Fig. 6, see also Fig. S12 and S13, ESI† for x = 0.75 and x = 0.50). The modulation depth increased with the azo content for both

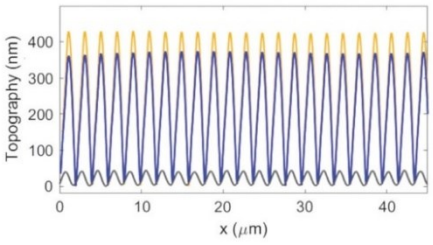

Fig. 6 AFM cross-sectional profiles of SRGs inscribed on **PAA-1**$_{1.0}$ (orange line), **PAA-2**$_{1.0}$ (blue line) and **PAA-3**$_{1.0}$ (black line) in the same time lapse.

series, reaching maximum average values of 420 and 355 nm for **PAA-1**$_{1.0}$ and **PAA-2**$_{1.0}$ respectively. Table S3 (ESI†) reports the corresponding values of DE.

We further compared the SRG formation performances of **PAA-2**$_{1.0}$ and **PAA-3**$_{1.0}$ at 457 nm. Compounds **2** and **3** show a similar structure and bear the same methoxy group on the unbound ring of the azobenzene structure. Moreover, the same position of the hydrogen bond accepting nitrogen on the pyridyl and pyrimidyl rings is expected to produce the same positioning of the azo unit respect to the polymer chain. The comparison shows that **PAA-2**$_{1.0}$ is considerably more efficient than **PAA-3**$_{1.0}$ (maximum modulation depth of 40 nm, Fig. 6), although their absorption spectra do not differ significantly (λ_{max} of 364 nm and 343 nm for **PAA-2**$_{1.0}$ and **PAA-3**$_{1.0}$ respectively, Fig. S14, ESI†). Therefore, we evaluated the lifetime of the *cis* isomer for all the **PAA-i**$_{1.0}$ polymers according to a literature procedure (Fig. S15, ESI†).[40] The *cis–trans* thermal isomerization rate of **PAA-3**$_{1.0}$ (1.40 ± 0.03 s^{-1}) resulted more than three times higher than that of **PAA-1**$_{1.0}$ and **PAA-2**$_{1.0}$ (0.42 ± 0.03 s^{-1} and 0.38 ± 0.03 s^{-1} respectively), indicating that thermal isomerization of the *cis* isomer is not a limiting factor for the performance of **PAA-3**$_{1.0}$. Conversely, the dramatic efficiency difference suggests that the presence of a second hydrogen bond involving a further position on the aromatic ring of the azobenzene entails, for the same polymer, a considerable increase in the ability of the photoactive units to drag the polymer chains during the structuring of the material. This effect can be reasonably attributed to the nature of the used supramolecular heterosynthon, which is at the same time a weak and reversible but highly directional and constrained interaction, resulting in an improved conversion of energy into effective mass transport.

Selective removal of azobenzene

We also investigated the possibility to extract the azobenzene units from the polymer after SRG inscription. This operation is highly desirable in azomaterials for technological purposes, as the removal of the azo units expands the possibility of use in optical devices to the whole range of wavelengths where absorption by chromophores would occur. Seki and coworkers[41] proposed an H bonding based supramolecular system in which the selective extraction of azobenzene units was successfully performed on a patterned sample after crosslinking of the polymer matrix by exposure to reactive vapors and subsequent rinsing with solvent. Here we demonstrate that this operation could be successfully performed on polymers with x = 0.50 without any chemical reaction. Fig. 7 shows AFM topography and UV-vis spectra of a patterned film of **PAA-1**$_{0.50}$ before and after rinsing the sample in dichloromethane for 1 min (see Fig. S16 for **PAA-2**$_{0.50}$, ESI†). The film appeared transparent after treatment and the absorption band of the azochromophore disappears in the spectrum (Fig. 7d). However, the profile of inscribed SRG is preserved, although with some loss of quality, accompanied by an expected volume shrinkage, with a visible reduction of the feature heights from about 110 nm to 60 nm (Fig. 7c). This possibility is enabled by the quite different solubility properties of PAA and **1**. While **1** is

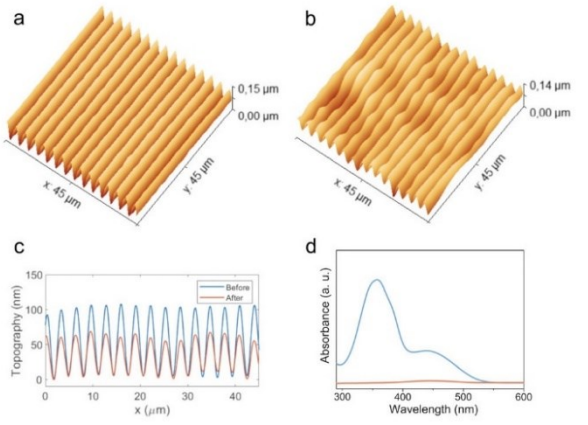

Fig. 7 Selective extraction of **1** from SRG of **PAA-1$_{0.50}$**. Topographical AFM image of SRG before (a) and after (b) rinse with solvent; cross-sectional profiles (c) and UV-vis spectra of film (d) before (blue line) and after (orange line) rinse with solvent.

highly soluble in all common organic solvents, PAA is only soluble in water, alcohols and formamides. Selective extraction of azobenzene units with dichloromethane produces a rapid replacement of the AP type chain–chromophore interactions with the crosslinking AA type dimerization of the freed carboxylic groups, which contribute to the preservation of the SRG dimensional stability. The same procedure applied to samples with higher azo content leads to unsatisfactory results, with severe loss of pattern quality and regularity due to the excessive volume fraction of the material occupied by the azobenzene.

Experimental

All the reagents were commercially available and used without further purification: *p*-toluidine, 2-amino-4,6-dimethoxypyrimidine, tetrafluoroboric acid 48% aq. sol. (Alfa Aesar), *p*-anisidine, polyacrylic acid average M_w 1800 (Merck). Optical observations were performed by using a Zeiss Axioscop polarizing microscope equipped with a FP90 Mettler heating stage. ^{1}H and ^{13}C NMR spectra were recorded on Varian Inova 500 (500 MHz) and Bruker Avance III TM HD (400 MHz) spectrometers. UV-Visible spectra were recorded with a JASCO V-750 spectrometer. The FT-IR measurements were performed on a Thermo Nicolet 5700 FT-IR spectrometer. Solid samples were dispersed in KBr tablets, polymeric materials were cast from solutions. Thin films of azopolymers were prepared by spin coating DMF solutions of the polymers on glass substrates, using a Laurell WS-650Mz-23NPP spin coater.

X-Ray diffraction analysis

Single crystals of **1-I** and **1-II** suitable for X-ray diffraction analysis were obtained by slow cooling of a heptane solution (or evaporation from acetone) and by recrystallization from ethanol/water, respectively. Single crystals of **2** were obtained by slow evaporation from acetone, while those of the complexes **1-MA** and **1-AA** were grown by evaporation from chloroform/heptane. One selected crystal of each compound was mounted in flowing N_2 at 173 K on a Bruker-Nonius Kappa CCD diffractometer equipped with Oxford Cryostream apparatus (graphite monochromated MoKα radiation, λ = 0.71073 Å, CCD rotation images, thick slices, φ and ω scans to fill asymmetric unit). Reduction of data and semiempirical absorption correction were done using SADABS program. The structures were solved by direct methods (SIR97 program)[42] and refined by the full-matrix least-squares method on F^2 using SHELXL-2016 program[43] with the aid of the program Olex2.[44] H atoms bonded to C were generated stereochemically and refined by the riding model, those bonded to O and N were found in difference Fourier maps and their coordinates were refined. For all H atoms, U_{iso}(H) equal to 1.2 U_{eq} or 1.5 U_{eq} (C_{methyl}) of the carrier atom was used.

Crystal data and structure refinement details are reported in Tables S1 and S2 (ESI†). The figures were generated using Mercury CSD 3.3.[45] All crystal data were deposited at Cambridge Crystallographic Data Centre with assigned number CCDC 2073781 (**1-I**), 2073782 (**1-II**), 2073784 (**1-AA**), 2073785 (**1-AA-RT**), 2073786 (**1-MA**), 2073783 (**2**).†

Synthesis of 1 and 2

The tetrafluoroborate diazonium salts of *p*-toluidine (**td**) and *p*-anisidine (**ad**) were synthesized and isolated according to a reported procedure.[46]

1. 2-Amino-4,6-dimethoxypyrimidine (1.55 g, 10 mmol) was dissolved in 1,2-dichloroethane (70 ml). **td** (2.93 g, 1.0 equiv.) was added in small portions and reaction stirred overnight at room temperature. The hydrotetrafluoroborate product was deprotonated and purified by recrystallization in ethanol/water in the presence of excess triethylamine, giving large plate-like crystals. Yield: 77%. ^{1}H NMR (DMSO-d_6) δ 7.52 (d, 2H); 7.32 (s, 2H); 7.27 (d, 2H); 3.91 (s, 6H); 2.35 (s, 3H). ^{13}C NMR (DMSO-d_6) δ 164.3, 161.2, 151.9, 138.7, 129.5, 121.3, 112.9, 53.9, 20.8.

2. The same procedure for the synthesis of **1** was applied using an equimolar amount of **ad** to give **2** in 71% yield. ^{1}H NMR (DMSO-d_6) δ 7.61 (d, 2H); 7.25 (s, 2H); 7.02 (d, 2H); 3.91 (s, 6H); 3.81 (s, 3H). ^{13}C NMR (DMSO-d_6) δ 164.2, 161.0, 160.2, 148.0, 122.9, 114.2, 112.8, 55.4, 53.8.

Synthesis of 3-(4′-hydroxyphenylazo)pyridine

To a solution of 3-aminopyridine (2.51 g, 26.7 mmol) in H_2O (11 ml), aqueous HBF_4 50 wt% was added (9.1 ml) and the mixture was stirred at 5 °C. A solution of sodium nitrite (1.84 g, 26.7 mmol) in 5 ml water was slowly added, the mixture was stirred at 5 °C for 45 min and then added to a solution of phenol (2.51 g, 26.7 mmol) and NaOH (3.74 g, 93.5 mmol) in 150 ml H_2O. After 30 min stirring, the pH was lowered to 7 with HCl. The orange precipitate was filtered and washed with water. Yield: 66%. ^{1}H NMR (DMSO-d_6) δ 10.49 (s, 1H); 9.02 (s, 1H); 8.66 (d, 1H); 8.08 (d, 1H); 7.84 (d, 2H); 7.55 (m, 1H); 6.96 (d, 2H). ^{13}C NMR (DMSO-d_6) δ 161.6, 151.1, 147.5, 145.9, 145.4, 126.6, 125.2, 124.4, 116.1.

Synthesis of 3

3-(4′-Hydroxyphenylazo)pyridine (1.20 g, 6.00 mmol) and K_2CO_3 (1.66 g, 12.0 mmol) were added to 30 ml DMF. Dimethyl sulfate (0.757 g, 6.00 mmol) were slowly added and the mixture was stirred at room temperature for 48 h. After addition of water (50 ml) the mixture was extracted with ethyl acetate. The organic phase was washed three times with water, anhydrified with Na_2SO_4 and the solvent removed *in vacuo*. Ethanol (10 ml) was added to the liquid residue and a solid precipitated by addition of a solution of sodium acetate (1 g) in 30 ml H_2O. The brown solid was treated with 600 ml boiling heptane. After cooling, the residue was filtered and the volume was reduced to 20 ml. By cooling the solution, the product was crystallized as an orange solid. Yield: 62%. ^{1}H NMR (DMSO-d_6) δ 9.07 (m, 1H); 8.71 (m, 1H); 8.16–8.13 (m, 1H); 7.94 (d, 2H); 7.62–7.59 (m, 1H); 7.17 (d, 2H); 3.89 (s, 3H). ^{13}C NMR (DMSO-d_6) δ 162.5, 151.4, 147.4, 146.2, 146.0, 126.7, 124.9, 124.9, 124.51, 114.7, 55.7.

SRG inscription

Thin films for SRG inscription experiments were prepared by spin coating filtered 25 wt% DMF solutions of the polymers on glass slides (film thickness 880–950 nm). The samples were kept under vacuum at room temperature for 24 h to remove solvent traces. The interference pattern was set up with two *p* polarized laser beams of 5.5 mW power and 2 mm section each (irradiance 175 mW cm^{-2}, wavelength 457 nm, from Samba source of Cobolt 05-01 Series by HÜBNER PHOTONICS) hitting the sample at an incidence angle of 13°40′. The first order diffraction efficiency was monitored with a He–Ne laser beam impinging normally on the growing grating and the diffracted light power was monitored by means of biased photodetectors (DET36A2 model from Thorlabs, based on fast PIN Si photodiodes) placed at the angular directions of the zero and the two first diffraction orders for the 633 nm radiation. The DE was calculated as the power ratio of the He–Ne diffracted beam and the transmitted beam prior to exposure to the 457 nm intensity pattern, by averaging the signal of both −1 and +1 first orders.

Conclusions

Here we demonstrated the possibility to exploit polyacrylic acid as an affordable polymer matrix to produce supramolecular azopolymers with high performances and versatility, through a molecular recognition approach based on a hydrogen bond supramolecular synthon. These materials can be prepared with the desired chromophore content without undergoing phase separation or chromophore aggregation until equimolar ratio. The proposed system exploits for the first time a double weak interaction acting on two positions of the aromatic ring of the azobenzene unit. This approach promotes a highly directional chromophore–chain interaction, while also preventing any degree of freedom with respect to rotation around the molecular long axis of azobenzene units. This stronger and more rigid constraint resulted in a huge improvement in mass migration and SRG inscription efficiency compared to a single H-bonded system based on the same polymer matrix and positioning of the azomolecule relative to the chain. Rapid and straightforward removal of the light absorbing chromophores from a photopatterned sample was enabled by the orthogonal solubility properties of the polyacrylic acid and the dye component and demonstrated through simple rinsing of the thin film samples with dichloromethane.

Conflicts of interest

There are no conflicts to declare.

Acknowledgements

This work has been financially supported by the European Research Council (ERC) under the European Union's Horizon 2020 research and innovation programme "METAmorphoses", grant agreement no. 817794. This work has been supported by Fondazione Cariplo, grant no 2019-3923.

Notes and references

1 A. Natansohn and P. Rochon, *Chem. Rev.*, 2002, **102**, 4139–4176.
2 M. O'Neill and S. M. Kelly, *J. Phys. D: Appl. Phys.*, 2000, **33**, R67–R84.
3 L. Corvazier and Y. Zhao, *Macromolecules*, 1999, **32**, 3195–3200.
4 T. H. Ware, M. E. McConney, J. J. Wie, V. P. Tondiglia and T. J. White, *Science*, 2015, **347**, 982–984.
5 H. Zeng, O. M. Wani, P. Wasylczyk, R. Kaczmarek and A. Priimagi, *Adv. Mater.*, 2017, **29**, 1701814.
6 X. Meng, A. Natansohn and P. Rochon, *Supramol. Sci.*, 1996, **3**, 207–213.
7 M. Eich, J. Wendorff, B. Reck and H. Ringsdorf, *Makromol. Chem., Rapid Commun.*, 1987, **8**, 59–63.
8 A. Shishido, *Polym. J.*, 2010, **42**, 525–533.
9 S. Hvilsted, C. Sánchez and R. Alcalá, *J. Mater. Chem.*, 2009, **19**, 6641–6648.
10 P. Rochon, E. Batalla and A. Natansohn, *Appl. Phys. Lett.*, 1995, **66**, 136–138.
11 S. L. Oscurato, M. Salvatore, P. Maddalena and A. Ambrosio, *Nanophotonics*, 2018, **7**, 1387–1422.
12 N. K. Viswanathan, D. Y. Kim, S. Bian, J. Williams, W. Liu, L. Li, L. Samuelson, J. Kumar and S. K. Tripathy, *J. Mater. Chem.*, 1999, **9**, 1941–1955.
13 L. M. Goldenberg, V. Lisinetskii, Y. Gritsai, J. Stumpe and S. Schrader, *Adv. Mater.*, 2012, **24**, 3339–3343.
14 L. M. Goldenberg, V. Lisinetskii, Y. Gritsai, J. Stumpe and S. Schrader, *Opt. Mater. Express*, 2012, **2**, 11.
15 S.-I. Na, S.-S. Kim, J. Jo, S.-H. Oh, J. Kim and D.-Y. Kim, *Adv. Funct. Mater.*, 2008, **18**, 3956–3963.
16 S. L. Oscurato, M. Salvatore, F. Borbone, P. Maddalena and A. Ambrosio, *Sci. Rep.*, 2019, **9**, 6775.

17 M. Salvatore, F. Borbone and S. L. Oscurato, *Adv. Mater. Interfaces*, 2020, **7**, 1902118.
18 S. Lee, H. S. Kang and J.-K. Park, *Adv. Mater.*, 2012, **24**, 2069–2103.
19 S. L. Oscurato, F. Borbone, P. Maddalena and A. Ambrosio, *ACS Appl. Mater. Interfaces*, 2017, **9**, 30133–30142.
20 Q. Zhang, X. Wang, C. J. Barrett and C. G. Bazuin, *Chem. Mater.*, 2009, **21**, 3216–3227.
21 J. Gao, Y. He, F. Liu, X. Zhang, Z. Wang and X. Wang, *Chem. Mater.*, 2007, **19**, 3877–3881.
22 O. Kulikovska, L. M. Goldenberg and J. Stumpe, *Chem. Mater.*, 2007, **19**, 3343–3348.
23 A. Priimagi, G. Cavallo, A. Forni, M. Gorynsztejn-Leben, M. Kaivola, P. Metrangolo, R. Milani, A. Shishido, T. Pilati, G. Resnati and G. Terraneo, *Adv. Funct. Mater.*, 2012, **22**, 2572–2579.
24 A. Priimagi, K. Lindfors, M. Kaivola and P. Rochon, *ACS Appl. Mater. Interfaces*, 2009, **1**, 1183–1189.
25 J. Vapaavuori, V. Valtavirta, T. Alasaarela, J.-I. Mamiya, A. Priimagi, A. Shishido and M. Kaivola, *J. Mater. Chem.*, 2011, **21**, 15437.
26 J. Gao, Y. He, H. Xu, B. Song, X. Zhang, Z. Wang and X. Wang, *Chem. Mater.*, 2007, **19**, 14–17.
27 A. Priimagi, S. Cattaneo, R. H. A. Ras, S. Valkama, O. Ikkala and M. Kauranen, *Chem. Mater.*, 2005, **17**, 5798–5802.
28 J. E. Stumpel, M. Saccone, V. DIchiarante, O. Lehtonen, M. Virkki, P. Metrangolo and A. Priimagi, *Molecules*, 2017, **22**, 1844.
29 M. Saccone, V. Dichiarante, A. Forni, A. Goulet-Hanssens, G. Cavallo, J. Vapaavuori, G. Terraneo, C. J. Barrett, G. Resnati, P. Metrangolo and A. Priimagi, *J. Mater. Chem. C*, 2015, **3**, 759–768.
30 G. R. Desiraju, *Angew. Chem., Int. Ed. Engl.*, 1995, **34**, 2311–2327.
31 N. K. Duggirala, J. Li, N. S. Krishna Kumar, T. Gopinath and R. Suryanarayanan, *Chem. Commun.*, 2019, **55**, 5551–5554.
32 L. Čechová, J. Kind, M. Dračínský, J. Filo, Z. Janeba, C. M. Thiele, M. Cigáň and E. Procházková, *J. Org. Chem.*, 2018, **83**, 5986–5998.
33 D. R. C. Matazo, R. A. Ando, A. C. Borin and P. S. Santos, *J. Phys. Chem. A*, 2008, **112**, 4437–4443.
34 N. J. Dunn, W. H. Humphries, A. R. Offenbacher, T. L. King and J. A. Gray, *J. Phys. Chem. A*, 2009, **113**, 13144–13151.
35 N. Sundaraganesan, K. Sathesh Kumar, C. Meganathan and B. Dominic Joshua, *Spectrochim. Acta, Part A*, 2006, **65**, 1186–1196.
36 Q. Huo, L. Dziri, B. Desbat, K. C. Russell and R. M. Leblanc, *J. Phys. Chem. B*, 1999, **103**, 2929–2934.
37 S. Mishra, J. L. Kuo and G. N. Patwari, *Phys. Chem. Chem. Phys.*, 2018, **20**, 21557–21566.
38 C. Greve, E. T. J. Nibbering and H. Fidder, *J. Phys. Chem. B*, 2013, **117**, 15843–15855.
39 E. R. Berg, S. A. Freeman, D. D. Green and D. J. Ulness, *J. Phys. Chem. A*, 2006, **110**, 13434–13446.
40 C. Barrett, A. Natansohn and P. Rochon, *Chem. Mater.*, 1995, **7**, 899–903.
41 N. Zettsu, T. Ogasawara, N. Mizoshita, S. Nagano and T. Seki, *Adv. Mater.*, 2008, **20**, 516–521.
42 A. Altomare, M. C. Burla, M. Camalli, G. L. Cascarano, C. Giacovazzo, A. Guagliardi, A. G. G. Moliterni, G. Polidori and R. Spagna, *J. Appl. Crystallogr.*, 1999, **32**, 115–119.
43 G. M. Sheldrick, *Acta Crystallogr., Sect. C: Struct. Chem.*, 2015, **71**, 3–8.
44 O. V. Dolomanov, L. J. Bourhis, R. J. Gildea, J. A. K. Howard and H. Puschmann, *J. Appl. Crystallogr.*, 2009, **42**, 339–341.
45 C. F. Macrae, I. J. Bruno, J. A. Chisholm, P. R. Edgington, P. McCabe, E. Pidcock, L. Rodriguez-Monge, R. Taylor, J. van de Streek and P. A. Wood, *J. Appl. Crystallogr.*, 2008, **41**, 466–470.
46 W. Erb, A. Hellal, M. Albini, J. Rouden and J. Blanchet, *Chem. – Eur. J.*, 2014, **20**, 6608–6612.

Publication III

S. L. Oscurato, F. Reda, M. Salvatore, F. Borbone, P. Maddalena, and A. Ambrosio

Large-scale multiplexed azopolymer gratings with engineered diffraction behavior

Reprinted from

Advanced Materials Interfaces 2101375, 1–9 (2021)

ADVANCED MATERIALS INTERFACES
www.advmatinterfaces.de

Large-Scale Multiplexed Azopolymer Gratings with Engineered Diffraction Behavior

Stefano L. Oscurato, Francesco Reda, Marcella Salvatore, Fabio Borbone, Pasqualino Maddalena, and Antonio Ambrosio**

The diffraction of polychromatic light from periodic superficial structures is often responsible for the structural colors observed in Nature. Similarly, engineered microtextures fabricated on metallic or dielectric surfaces can be used to design diffracted optical patterns with desired shapes and colors. To this aim, advanced diffraction gratings with exceptional design and functionality are continuously proposed, and new fabrication methods follow to stay abreast with the improving design capabilities. Multiplexed surface reliefs, acting as complex gratings with tunable diffraction behavior, can be readily produced on films of azobenzene containing materials by exposing the surface to controlled sequences of holographic interference patterns. This work fully investigates, both theoretically and experimentally, the use of light-induced surface relief on azopolymers for the realization of large-scale multiplexed gratings with optimized diffraction performances. The reconfigurable diffraction gratings able to diffract polychromatic light in the same direction with controllable relative color intensities by tuning exposure parameters in a switchable two-beam interference setup are designed and fabricated. The results can be generalized to more complex diffractive devices, usable in emerging display application areas.

1. Introduction

The morphology at micro and nanoscales strongly influences surface functionality. Optimized surface textures with advanced effects on wettability, friction, adhesion, and visual appearance have been developed by evolution in natural world to ensure survival.[1,2] In particular, the bright and shiny colors of many animals and plants often originate from the diffraction of light from sophisticated periodic structures present on their surface.[3] Understanding and controlling surface geometry for structural colors is the subject of many research efforts in material science, chemistry, and physics, that aim to fabricate artificial light modulating devices with advanced optical and chromatic functionalities[4–8] by improving the design and the fabrication of diffraction gratings.[9,10]

Diffraction gratings are optical components made of grooves periodically arranged on the surface of metallic or dielectric substrates.[11] A diffraction grating splits incoming monochromatic light in multiple emerging waves, referred to as diffraction orders.[12] The diffraction angle for each order depends on the wavelength of incoming light and on grating periodicity, while the shape and the depth of surface profile (e.g., sinusoidal), together with the optical properties of the grating material (refractive index, metallic coating, etc.), influences the amount of light diffracted in each specific order.[10]

Diffraction gratings of different geometries including periodicity, orientation, groove depth and surface profile can be overlayed to realize a single combined and complex grating (referred to as multiplexed grating).[13] A similar grating produces a complex diffraction pattern, simultaneously dependent on the combined geometry and chromatic behavior of each composing grating. Engineering the geometrical parameters of the superposition gives control on the emerging light distribution.[14–16] For example, a multiplexed grating can be designed to diffract light of different wavelengths into a same diffraction order, eventually partially re-balancing the angular spreading of polychromatic light that single gratings would produce alone due to chromatic dispersion.[16–20] When the superimposed gratings have sinusoidal profiles, the multiplexed structure is often referred to as an Optical Fourier surface.[17]

S. L. Oscurato, F. Reda, M. Salvatore, P. Maddalena
Department of Physics "E. Pancini"
University of Naples "Federico II"
Complesso Universitario di Monte Sant'Angelo, Via Cintia 21
Naples 80126, Italy
E-mail: stefanoluigi.oscurato@unina.it

S. L. Oscurato, F. Borbone, P. Maddalena, A. Ambrosio
CNST@POLIMI—Fondazione Istituto Italiano di Tecnologia
Via Pascoli 70, Milan 20133, Italy
E-mail: antonio.ambrosio@iit.it

S. L. Oscurato, M. Salvatore, P. Maddalena
Centro Servizi Metrologici e tecnologici Avanzati (CeSMA)
University of Naples "Federico II"
Complesso Universitario di Monte Sant'Angelo, Via Cintia 21
Naples 80126, Italy

F. Borbone
Department of Chemical Sciences
University of Naples "Federico II"
Complesso Universitario di Monte Sant'Angelo, Via Cintia 21
Naples 80126, Italy

The ORCID identification number(s) for the author(s) of this article can be found under https://doi.org/10.1002/admi.202101375.

DOI: 10.1002/admi.202101375

The fabrication of this class of advanced diffraction gratings requires highly accurate surface structuration techniques. Standard fabrication methods for diffraction gratings include direct machining technology, in which a ruling engine[9] or an ion beam[21] makes grooves on a grating plate, and holographic photolithography, in which the periodic structure of sinusoidal diffraction gratings is produced by interference lithography on a photoresist,[22] that is successively developed and transferred on a dielectric or metallic support via chemical etching or vapor deposition. However, grating multiplexing with these standard methods is either impossible or it requires multiple complex lithographic steps.[10]

Recently, holographic inscription of sinusoidal gratings, directly achieved as surface reliefs on azobenzene-containing polymers (azopolymers), has been demonstrated to be a powerful approach for the realization of multiplexed gratings with engineered directional[23–25] and chromatic[19] diffraction behavior. The azopolymer structuration process is sensitive to intensity and polarization distributions of the irradiated field,[26,27] so that both intensity and polarization interference pattern can be used to produce the sinusoidal surface relief gratings (SRGs).[28–30] The dimension of the structured area depends only on the diameter of the interference beams, and SRGs on areas as large as several cm^2 can be realized in single lithographic steps. The use of azopolymers as materials for diffraction components[26,31] is further incentivized by the possibility to make the grating reconfigurable and then usable for multistep structuration processes. The surface structuration of azopolymers is a nondestructive process that, conversely to the chemical etching of standard photolithography, involves a light-driven directional[32–35] polymer mass transport,[36,37] that generates surface relief with the same geometry of the illumination pattern (e.g. sinusoidal for the two-beam interferogram).[38,39] The polymer can be transported back to restore the original state both optically or thermally, erasing then the surface pattern, or moved again by a new lithographic illumination step which combines the preexisting texture with a new one.[29,40,41] We recently explored the light-induced dynamical and reversible behavior of azopolymer surfaces by directly structuring small areas of a polymer film through structured digital holography illumination and optical erasing, achieving advanced state-of-the art reconfigurable diffractive gratings and lenses, which we applied in operating devices as motionless monochromators and reconfigurable imaging systems.[16]

Here we extend the use of dynamical surface reliefs on the azopolymer to design and characterize large-scale multiplexed gratings realized via sequential two-beam interference lithography. To this aim, we first analyze the theoretical aspects of the diffraction from a general multiplexed grating made of superposition of sinusoidal reliefs, providing a solid and practical framework for the design of these devices. Then we specify our analysis, by means of theory, simulations, and experiments, to a large-scale three-component 1D multiplexed grating that diffracts red (R), green (G), and blue (B) light, in a fixed common diffraction order (RGB grating). A similar grating design has been demonstrated suitable for the realization of pixelated azopolymer surfaces with apparent structured colors.[19] We experimentally realize the designed SRGs with high structural control and optimized inscription performances by using a switchable interference setup able to inscribe, monitor in real time, and eventually erase gratings of different periodicity on the azopolymer surface. The results shown here further enlarge the panorama of applications for reconfigurable SRGs, paving the way toward the design and realization of large-scale, flat, and lightweight optical components with engineered diffraction capability,[42] usable in the emerging fields of displays technologies for augmented[43] and virtual reality,[8] as well as wearable optical devices.

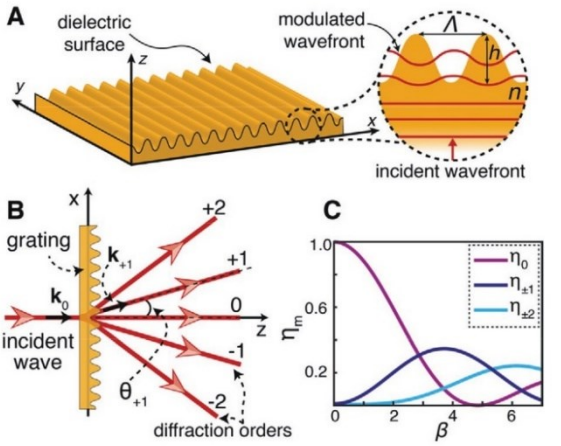

Figure 1. Diffraction from a dielectric sinusoidal surface. A) Schematic illustration of the wavefront modulation produced by a sinusoidal surface relief grating placed in the plane $z = 0$ of the reference system, inscribed in a material of refractive index n, with periodicity Λ and topographic amplitude h. B) Schematic representation of Bragg's diffraction law for plane wave incident normally on the dielectric sinusoidal grating. The propagation direction of the first diffraction order, taken as an example, is equivalently defined as the angle θ_{+1} or as the x-component of the wavevector $\mathbf{k}_{+1}$. C) Diffraction efficiency (DE) η_m as function of the dimensionless parameter β for the first five diffraction orders of a sinusoidal grating.

2. Theory and Simulations

2.1. Diffraction from Sinusoidal Multiplexed Gratings

A typical multiplexed grating, realized as a surface relief on an azopolymer film, can be described as a general structured dielectric surface that modulates the wavefront of an incoming light field. In the scalar theory of light diffraction,[11] the morphological surface profile, e.g., sinusoidal as the one shown in **Figure 1**A, entirely determines the shape of the emerging wavefront. The resulting modulation is a consequence of differences in the optical path lengths for light travelling in the surface medium of a local thickness $h(x,y)$ and refractive index n, in respect to same travel length in the medium surrounding the surface (typically air, whose refractive index is $n_0 = 1$). For a monochromatic plane wave of wavevector $k_0 = 2\pi/\lambda_0$, propagating along the z axis and incident perpendicularly on the dielectric grating, the phase delay resulting from the modulation reads as:

$$\varphi(x,y) = k_0 (n-1) h(x,y) \tag{1}$$

Equation (1) is at the basis of the design general diffractive optical components and constitutes the operative relation between the geometry $h(x,y)$ of the dielectric surface and the optical functionality for any generic diffractive optical element (DOE),[10] including single or multiplexed sinusoidal surfaces. The case of a DOE made of a 1D single sinusoidal surface relief is of particular interest for the present analysis, also because some of the relevant properties in the diffraction behavior of generic DOEs are easily generalized from this simple case.

Figure 1A shows the schematic representation of a dielectric sinusoidal grating of period Λ and amplitude modulation depth h, described by the one-dimensional surface relief function $h(x)=h\left(1+sin\frac{2\pi x}{\Lambda}\right)/2$. This grating diffracts the incoming light field into a finite number of propagating diffraction orders (plus an infinite set of evanescent orders), identified by an integer number $m = 0, \pm1, \pm2, \ldots$, emerging from the surface at the angles θ_m determined by light wavelength λ_0 and grating periodicity Λ (Figure 1B) via Bragg's relation (see also Supporting Information):

$$k_0 sin\,\theta_m = m\frac{2\pi}{\Lambda} \tag{2}$$

For this grating, the diffraction efficiency (DE) η_m, which is a measure of the amount of the incident light power converted in the m^{th} propagating order, is related to the maximum phase modulation depth $\beta = k_0\,(n-1)h$ induced by the sinusoidal surface relief according to the relation (Figure 1C):

$$\eta_m = \left|J_m\left(\frac{\beta}{2}\right)\right|^2 \tag{3}$$

Here J_m are the Bessel functions of first kind of order m. For a given material and light wavelength, the parameter β is directly proportional to the grating amplitude h, which is then the actual structural parameter to be eventually tuned to achieve specific distribution of light power among the diffraction orders in the pattern generated by a sinusoidal grating (Figure 1B). For example, the behavior of $\eta_{\pm1}$ is approximately linear in respect to h for relatively small modulation depths (Figure 1C).

Bragg's relation in Equation (2) can be alternatively interpreted in terms of the direction of the wavevector $\mathbf{k}_m = (k_{x,m}, k_{z,m})$ for the m^{th} diffraction order emerging from the dielectric grating (Figure 1B). Diffraction theory (see also Supporting Information) requires indeed that a propagating order m must have an in-plane wavevector component $k_{x,m} = k_0\ sin\theta_m$ that is an integer multiple of the grating vector $\mathbf{g} = (g_x, g_z) = (2\pi/\Lambda, 0)$ of the diffraction grating or, equivalently, borrowing well-known concepts of solid state physics, that $k_{x,m}$ must be a vector of the reciprocal lattice of the surface.[25] As the reciprocal lattice only depends on the in-plane surface morphology (for a 1D sinusoidal grating, the reciprocal lattice is entirely known by specifying only the grating periodicity Λ), the geometry of the entire diffraction pattern is completely defined by the grating vector $\mathbf{g}$ (which is a base in the reciprocal space). Such considerations, apparently more complicated than Bragg's law for a single sinusoidal grating, are particularly useful in the analysis of the diffraction patterns produced by more complex gratings, like the diffraction gratings obtained as superposition of N sinusoidal gratings (multiplexed grating)

$$h(x)=\sum_{l=1}^{N} h_l\left(1+sin\frac{2\pi x}{\Lambda_l}\right)/2 \tag{4}$$

each having periodicity Λ_l (grating vector $\mathbf{g_l} = (2\pi/\Lambda_l, 0)$) and surface modulation amplitude h_l. While the results for the scalar diffraction theory could be extended to diffractive surfaces described by Equation (4) (see also Supporting Information), the relevant features of their diffraction patterns can be understood by generalizing the concepts developed for the single sinusoidal grating in the interpretation of Equations (2) and (3).

Diffraction orders produced by a multiplexed grating propagate, following a generalized Bragg's law, at directions $\theta_{\boldsymbol{\alpha}}$ (where $\boldsymbol{\alpha} = (\alpha_1, \alpha_2, \ldots, \alpha_N)$ is an array of integer numbers) which make the in-plane component of the diffracted wavevector $k_{x,\boldsymbol{\alpha}}$ a vector of the reciprocal lattice of the total surface:

$$k_0 sin\ \theta_{\boldsymbol{\alpha}} = \sum_{l=1}^{N}\alpha_l\frac{2\pi}{\Lambda_l} = \sum_{l=1}^{N}\alpha_l g_l \tag{5}$$

Properly tuning the periodicities Λ_l, which, analogously to the case of the single sinusoid, completely defines the spatial distribution of the spots in the diffraction pattern, and the modulation amplitudes h_l, that control the relative intensity of those spots, complex diffraction functionalities (and eventually engineered chromatic behaviors) can be directly encoded in the geometry of a multiplexed grating designed as the superposition of Equation (4).

These concepts are here used for the design of the RGB multiplexed grating, which generates different perceived light color in a specific direction as weighted superposition of three diffraction orders of a three-components multiplexed grating simultaneously illuminated with light at red, green, and blue wavelengths.

2.2. Design of a RGB Multiplexed Grating

Figure 2 describes the design of a RGB multiplexed grating that diffracts light of wavelengths λ_1 = 633 nm (red), λ_2 = 532 nm (green), and λ_3 = 488 nm (blue) at the common angle, arbitrary chosen as θ_{target} = 18.5° (see also Figure S2, Supporting Information). The periodicities Λ_1 = 2.00 µm, Λ_2 = 1.68 µm, and Λ_3 = 1.54 µm of the three sinusoidal diffraction gratings composing the multiplexed grating are calculated by solving the equation $sin\theta_{target} = \lambda_l/\Lambda_l$, obtained from Equation (2) with $m = 1$, and graphically represented in Figure 2A.

The effect of multiplexing for these sinusoidal gratings is simulated in Figure 2B, in which the morphology of the single components G_l^s is rendered by grayscale topographic images, that overlay in a linear even superposition ($h_1 = h_2 = h_3 = h/3$) to compose the multiplexed surface of the RGB grating according to Equation (4). For clearer visualization, the simulated surface profiles are also presented in Figure 2C.

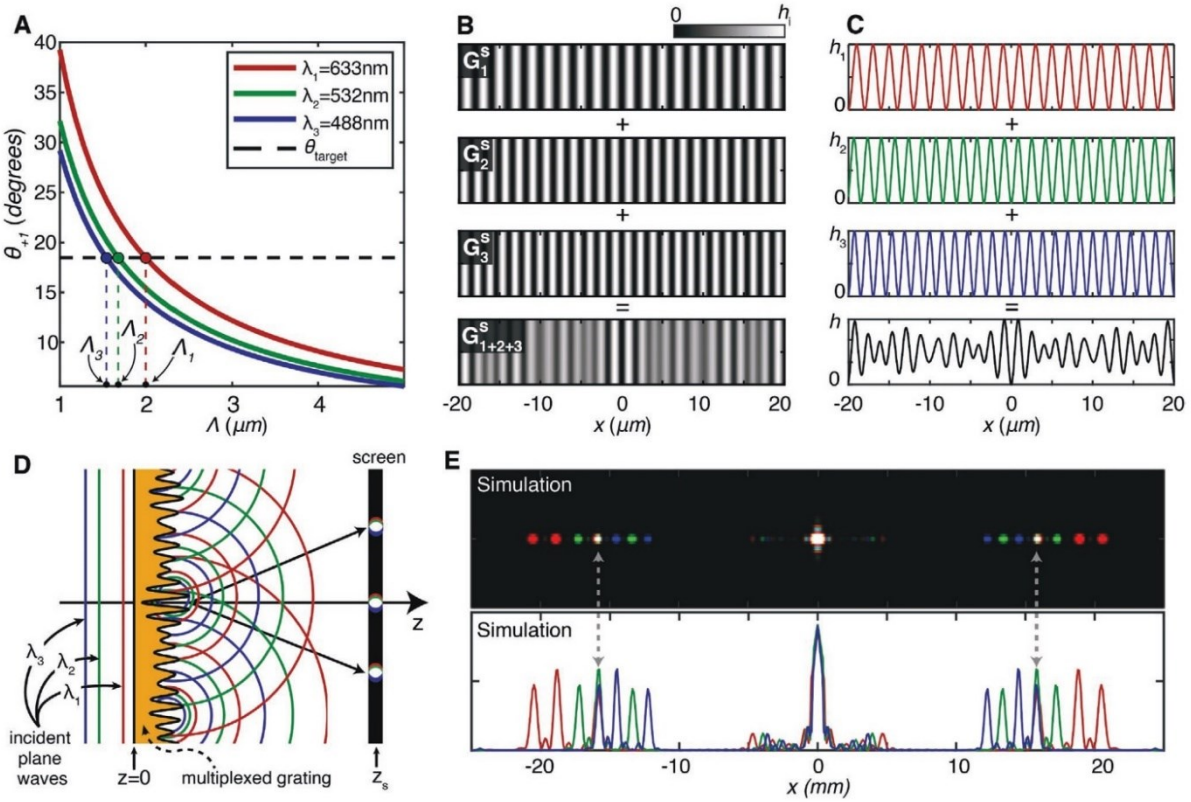

Figure 2. Design and operation of a multiplexed RGB diffraction grating. A) Plot of angle θ_{+1} of the first diffraction order in Bragg's law as function of grating periodicity Λ for the three considered wavelengths. The periodicities Λ_l of the sinusoidal components are defined by requiring that the three gratings diffract light at λ_l under the same angle θ_{target}. B) Simulated surface morphology and C) normalized surface profiles for the three sinusoidal components and for their multiplexed combination (with $h_1 = h_2 = h_3 = h/3$) producing the target RGB grating. D) Schematization of the geometry for the calculation, as Fresnel superposition of secondary spherical waves generated at the interface, of the diffraction pattern that the multiplexed RGB dielectric grating produces for simultaneous incidence of plane waves at design wavelengths λ_l, shown in (E) with a screen at $z = 50$ mm from the surface. The gray arrows highlight the RGB diffraction spot at the angles $\pm\,\theta_{target}$, where the three wavelengths are spatially superimposed. For the simulation in (E) the approximately equal diffraction efficiency (DE) in the target diffraction order at the three operating wavelengths is obtained by choosing the grating amplitudes h_l to maintain the parameter $\beta = k_l\,(n_l - 1)h_l$ fixed.

According to Equation (5), the diffraction pattern produced by the multiplexed grating is characterized, even under illumination with monochromatic light, by several diffraction spots spatially distributed in the directions of the reciprocal lattice. For a total grating amplitude $h = \sum_l^3 h_l$ comparable to the incident light wavelength (e.g. $h = 500$ nm) and refractive index $n = 1.7$, most of the diffracted light is contained in three first orders (defined as the orders for which $|\alpha| = 1$ in Equation (5)), one of which is the target RGB order of our design (see Figure S2, Supporting Information). To better visualize the spatial distribution of light in the diffraction pattern produced by the multiplexed RGB grating under simultaneous illumination of the three design wavelengths, Figure 2E shows the simulated diffraction pattern that the dielectric surface produces, on a screen placed at large distance ($z_s = 50.0$ mm), in the configuration schematized in Figure 2D. Details about the simulation are given in Experimental Section. The simulated diffraction pattern clearly shows the presence of a white diffraction spot, in which the three colors are spatially superimposed, confirming the design principle of the RGB grating and, more in general, of the multiplexing approach to engineer a complex diffraction pattern via the tailored superposition of sinusoidal surfaces. The simulation is also able to calculate the effects of having eventual different amplitude weights for h_l. Additionally, it should be noted the presence in the pattern also of the other diffraction orders predicted by the reciprocal lattice. In principle, these orders could be spatially filtered out because they propagate at different angles in respect to the design RGB direction. However, their presence should not be neglected in the definition of the operation performances of real devices based on the multiplexed design, because, even not compromising the overall device functionality, they necessarily reduce the DE of the grating in the target diffraction order.

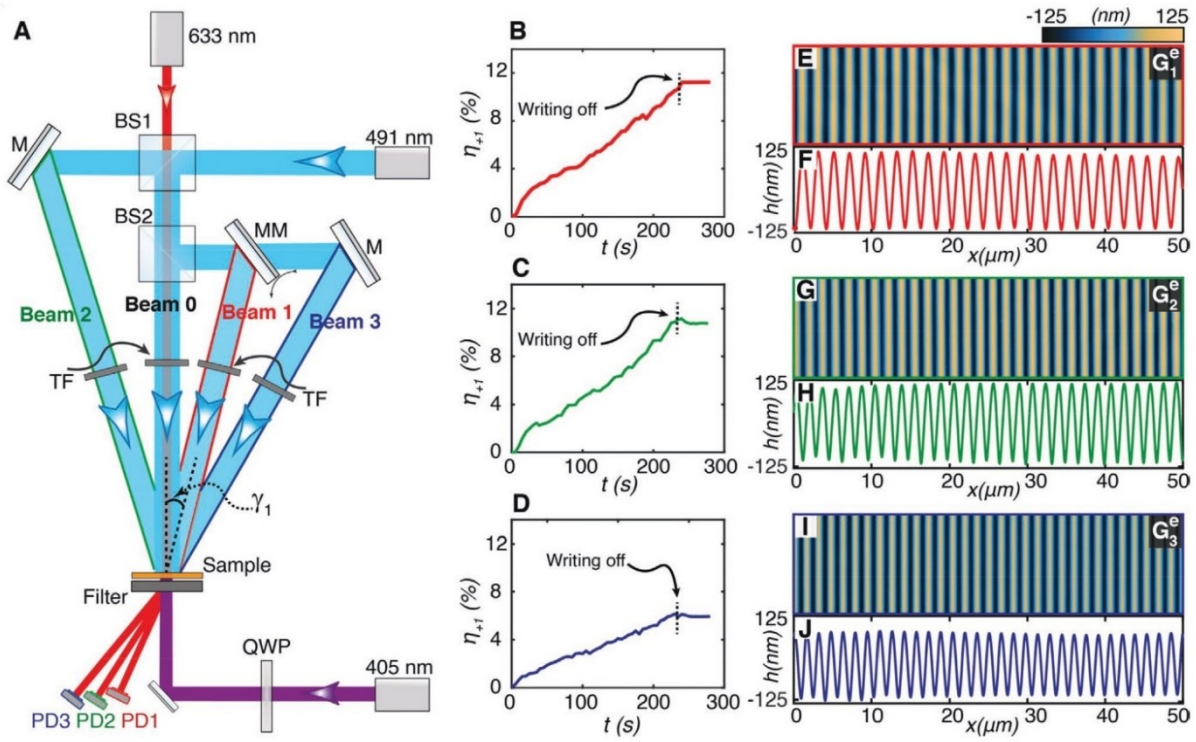

Figure 3. Switchable interference setup for SRGs of engineered periodicity. A) Schematic representation of the setup. In each exposure step, only one couple of the illustrated beams (Beam 0 + Beam i, with $i = 1, 2, 3$) is irradiated on the sample. B–D) First order time-dependent diffraction efficiency for the probe beam at $\lambda = 633$ nm recorded by PD1, PD2, and PD3 during a typical inscription experiment (exposure time 240 s) of the gratings G1, G2, and G3, respectively. E–J) Atomic force microscope (AFM) micrograph and relative topographic profile of the azopolymer surface resulting from the three illumination configurations.

3. Results and Discussion

3.1. Large-Scale Dynamical and Multiplexed Azopolymer Gratings

To experimentally implement the designed multiplexed RGB grating over large scales, we realized a switchable two-beam interference setup able to sequentially irradiate an azopolymer film with p-polarized sinusoidal intensity interferograms having accurately controlled periodicities. This illumination configuration, largely used for efficient surface relief inscription in azopolymers,[26,31,44–47] has been demonstrated to provide very accurate structural control and high inscription efficiency for our azopolymer.[25]

The principle of the design of our setup is to have a stable interference system, in which the desired interferogram periodicity can be chosen by alternatively selecting one couple of interfering beams between three possible configurations with minimum mechanical movement, while simultaneously monitoring the dynamical diffraction behavior of the developing surface grating by means of a diffracting probe beam. The schematic representation of the setup is presented in **Figure 3**A.

A horizontally polarized beam from a solid-state laser (Cobolt Calypso) at 491 nm was divided a first time by 70:30 (R:T) beamsplitter (BS1 in Figure 3A). The direction of beam reflected by BS1 (Beam 0) defines the optical axis of the system. Before impinging orthogonally over an area of ≈2 mm in diameter on the azopolymer surface placed in the sample plane, Beam 0 was divided a second time by a 50:50 beamplitter (BS2). To produce the three interferograms of different periodicity in the sample plane, Beam 0 was alternatively recombined with one of the three other beams (namely, Beam 1; Beam 2; Beam 3) represented in Figure 3A. The angle γ_i between Beam 0 and each of the three beams was accurately controlled by means of micrometric rotating mirrors. A movable mirror (MM in Figure 3A) was used to switch between the configurations with Beam 1 and Beam 3. Tunable neutral density filters were finally used to equilibrate the incident intensity for each beam and improve the visibility of the p-polarized interference pattern in the sample plane. A constant total average intensity of 0.14 W cm^{-2} in the interferogram was used in the experiments.

To monitor in real-time the diffraction produced by the developing surface relief gratings during the inscription process, a horizontally polarized He-Ne laser beam at wavelength of 633 nm was irradiated at normal incidence (transmitted through BS1 and BS2) in the structuring sample area. Three photodiodes (PD1; PD2; PD3), properly placed along directions predicted by Bragg's law, were used to record the time

evolution of probe light diffracted in the +1 order for each of the three periodicities. DE was calculated by dividing the time-depended photodiode signal produced by the evolving grating by the signal transmitted through the flat sample surface before starting the writing process. A notch filter, placed right after the sample, discards light of the writing beam from the detection space. An additional circularly polarized collimated beam from a diode laser at the wavelength of 405 nm (referred to as assisting beam), and intensity ≈0.4 W cm^{-2} incident on the sample from the substrate side, was also included in the structuration process. This beam, highly absorbed by our azopolymer,[34,38] improves the grating inscription rate by redistributing the orientation of azobenzene molecules, which otherwise tend to be realigned perpendicular to the polarization of the writing beams, with a resulting gradual reduction of absorption probability and overall relief inscription efficiency.[26,48–50] We extensively studied the influence of this beam on the writing dynamics of our azopolymer in our recent work.[16]

Figure 3B–D shows the diffraction curves recorded in 240 s inscription experiments of the gratings G1, G2, and G3, realized to have the periodicities Λ_l ($l = 1, 2, 3$) calculated above. The approximate linear behavior observed in the rising of the first diffraction order efficiency can be used to eventually control the height of the surface relief gratings, by properly tuning the exposure time.[16,46] Additionally, the stable signal recorded also when the writing interferogram is switched off (Figure 3B–D) demonstrates a diffraction behavior dominated by the stable surface relief grating, with only small contributions from the eventual birefringence grating typically observed in the interference-based photostructuration of azopolymers due to the photoalignment of the chromophores.[19,26,31]

Figure 3E–J reports the atomic force microscope (AFM) images and the relative topographic profiles of the three azopolymer surfaces at the end of the grating inscription process. The periodicities of the sinusoidal gratings measured by the AFM were in perfect agreement with the design (see also Figure S3, Supporting Information), confirming the highly accurate control over grating periodicities achievable in our switchable interference configuration.

In the experimental configuration of Figure 3A, both reconfigurable and multiplexed large-scale surface relief gratings can be easily realized and eventually tuned in real-time by using the monitored diffraction of the probe beam as indirect measure of the surface relief amplitude. **Figure 4** presents the results of a dynamical experiment in which the grating G2 was inscribed, erased, and re-inscribed on the surface before a multiplexed grating was realized by adding to it the grating G1 in a successive exposure step. The dynamical evolution of the surface was characterized by simultaneously monitoring the signal of the two photodiodes PD2 and PD1, detecting the +1 diffraction order of G2 and G1, respectively. The diffraction curves are reported in Figure 4A, together with the AFM micrographs (in the insets) of the azopolymer surface after the first writing of G2 (i), after its erasing (ii) and after its rewriting (iii), which clearly show the connection between the surface topography and its dynamical diffraction behavior. The erasure of the surface from (i) to (ii) was realized by means of the 405 nm laser beams in the configuration of Figure 3A, but with higher intensity (≈0.9 W cm^{-2}), as characterized in detail in our previous work.[16] At the instant (iii), the interference pattern was switched to the configuration for G2, so that a multiplexed grating with the geometry G2 + G1 started to develop on the azopolymer surface.

The exposure time in the final step was chosen to make the diffraction efficiencies for G2 and G1 approximately the same (difference less than 1%), which, according to the diffraction analysis in this surface modulation regime, would correspond also to approximated similar weight h_1 and h_2 for the sinusoidal components of the multiplexed grating in the Equation (4). This is confirmed by the AFM analysis presented in Figure 4B, where a very good agreement between the experimental topographic profile and the theoretical profile, obtained by overlaying the two sinusoidal functions with experimental periodicity and equal amplitudes, is observed.

The possibility of empirically selecting the appropriate exposure time to realize a target balance in diffraction efficiencies (in our case, approximately equal DE) is a clear advantage of direct dynamic efficiency monitoring during grating inscription, which avoids a priori calibration of surface relief heights in respect to the exposure time. This calibration has been demonstrated to be a difficult task for 1D topographies realized as sequences of exposures on azopolymer films[19,51] because

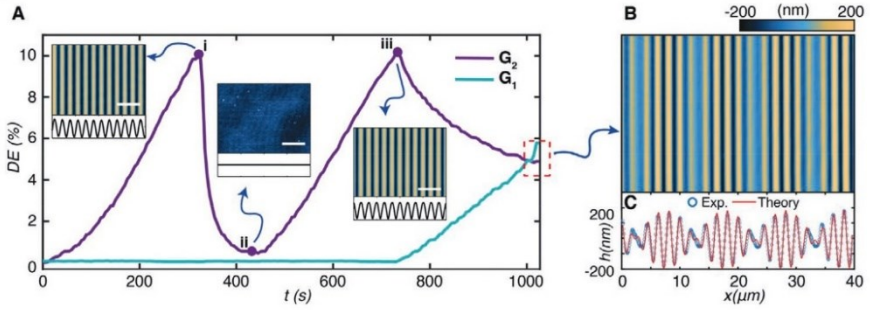

Figure 4. Reconfigurable and multiplexed azopolymer surface relief gratings (SRGs). A) Dynamical diffraction curves recorded, by the photodiodes PD1 and PD2, during a surface reconfiguration experiment in which the grating G2 is first inscribed, erased, and re-inscribed (steps i to iii) and then combined with the grating G1 to realize a multiplexed G2 + G1 grating. Insets in (A) show the AFM micrographs and profiles of the surface at the relative reconfiguration step (scale bars 5 μm). B) AFM micrograph of the multiplexed G2 + G1 grating. Exposure times for G2 and G1 were 300 and 270 s, respectively. C) Comparison between AFM and theoretical profiles of the multiplexed grating.

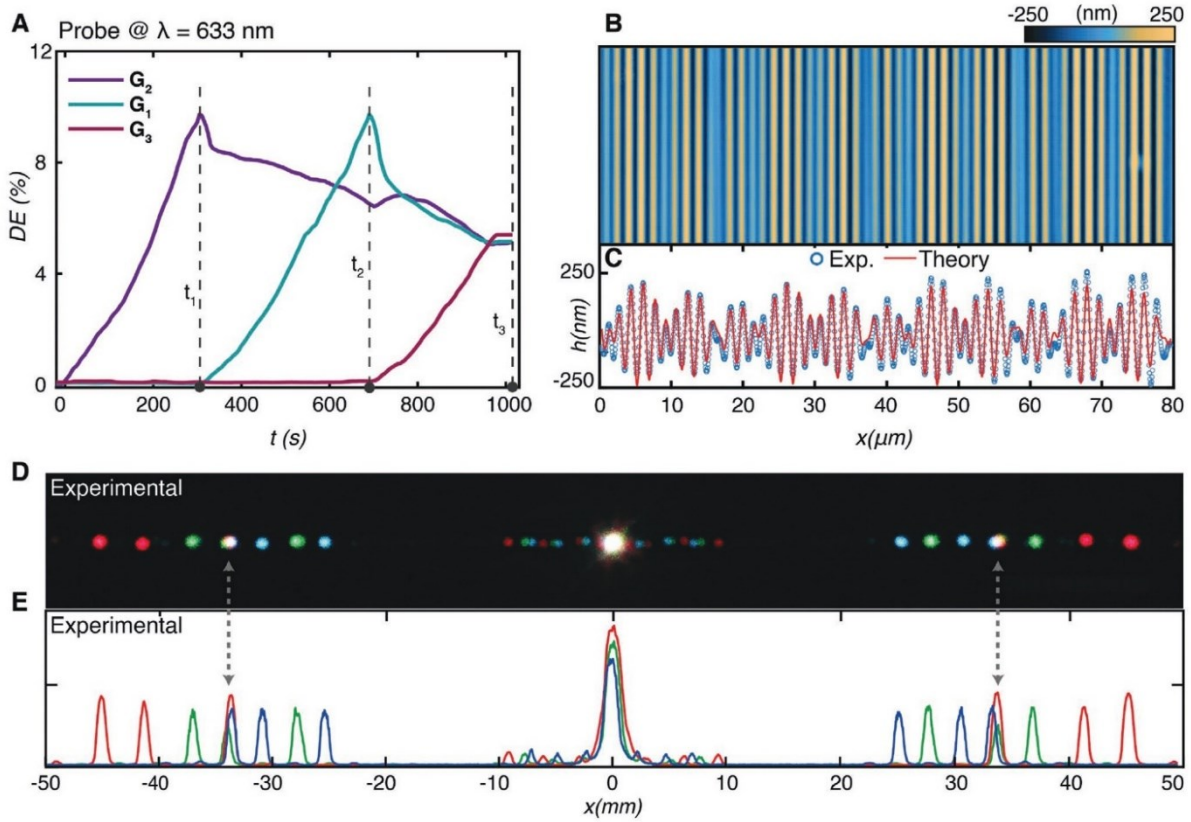

Figure 5. Optimized RGB multiplexed grating. A) Dynamical first-order diffraction curves recorded in the multistep inscription of G2, G1, and G3. Exposure times: $t_1 = 300$ s, $t_2 = 380$ s, $t_3 = 270$ s. B) AFM micrograph of the multiplexed polymer surface. C) Comparison between measured and theoretical surface profile. D) Experimental RGB diffraction pattern acquired by a CCD irradiating the surface of the polymer with three collinear laser beams at the three wavelengths λ_i. E) Intensity profiles of the three channels (R, G, and B) extracted by the image in (D).

pre-existing grooves on the surface can affect the inscription efficiencies for gratings in the following steps of the multiplexing sequence. Additionally, we also observed a possible influence of inscription efficiency in subsequent exposures on the specific order of the sequence (see also Figure S5, Supporting Information), which further weakens the feasibility of an approach based on a priori grating depth calibration for the realization of reliable and repeatable multiplexed gratings.

3.2. RGB Grating on Azopolymer Film

For the realization of the designed multiplexed RGB grating, three sequential exposures of the polymer film were used. In our experiment, we aimed not only at achieving the correct superposition of sinusoidal reliefs that produces the common (white) diffraction spot for the design wavelengths simulated in Figure 2E, but also at realizing multiplexed structures with controllable relative weight of the superimposed components. For the latter goal, real-time monitoring of the probe beam DE for the three gratings and empirical tuning of the exposure time for each component were used. **Figure 5**A shows the time evolving diffraction curves recorded during the inscription of a RGB grating, designed to have approximately equal final DE in the first orders of the superposed sinusoidal reliefs at $\lambda = 633$ nm, which again directly correlates with having approximately equal amplitude weights in the multiplexed structure.

In the inscription process described in Figure 5A, after the first structuration step (grating G2) lasting until the instant t_1, the interference configuration was switched in the second one (grating G1) and the irradiation of the sample continued until the empirically selected instant t_2, when the DE for the second grating reached approximately the same maximum level of the first exposure step. At that instant, the last grating component (grating G3) was superimposed in the third illumination step, which continued until all the three first-order diffraction efficiencies were similar at the time t_3. The AFM micrograph of the final azopolymer surface is show in Figure 5B, while the comparison of its experimental profile with the theoretical profile (calculated as equal-weight superposition of the sinusoidal components) is presented in Figure 5C. Similar to the analysis of two-component multiplexed grating of Figure 4B,C, the empirical tuning of exposure times in the multiplexed superposition by real-time diffraction monitoring, produced also for the

three component RGB grating an experimental profile in very good agreement with the target one. It should be noted that a similar exposure sequence, with a-priori definition of exposure times[19] (for example equal exposure times for all Gi), provided a worst structural result in terms of final component balance (see Figure S5, Supporting Information).

Finally, the diffraction pattern produced by the azopolymer multiplexed RGB grating under simultaneous irradiation of three collinear laser beams at design wavelengths (see Experimental Section), is shown in Figure 5D. The spatial distribution of the diffraction orders quantitatively matches the simulated pattern calculated for the ideal multiplexed surface in Figure 2 (see also Supporting Information), with the presence of a white diffraction spot in which the three diffraction orders at the three colors (Figure 5E) are angularly superimposed. This confirms the validity of diffraction analysis, design principle, and experimental implementation we used for the realization of the RGB azopolymer grating, which could be eventually extended to other multiplexed large-scale diffraction devices, realized as superposition of sinusoidal surface reliefs with controlled periodicity and relative amplitude weights.

4. Conclusions

In this work, we used sequential inscription of sinusoidal surface relief gratings on the surface of an azopolymer film to realize diffraction gratings with overlayed morphology, having engineered structural and chromatic behavior. A multiplexed grating that diffracts polychromatic light in the same direction has been designed from the accurate analysis of the results that scalar diffraction theory provides for light modulation from dielectric surfaces. The periodicity of the superimposed gratings plays the crucial role in the definition of the diffraction pattern produced by the multiplexed grating: excellent agreement between theory and experiments has been obtained by taking advantage from a stable switchable interference setup realized to inscribe SRGs with accurate periodicity control. Real-time diffraction monitoring has been used to optimize the superposition of the single sinusoidal components in the experiment, providing an empirical but powerful approach for the tuning of relative sinusoidal weights of the superposition. Our results could be used to engineer perceived color saturation in RGB diffractive devices designed as multiplexed diffraction gratings, offering new paths for future flat and light-weight optical components.

5. Experimental Section

Azopolymer Synthesis, Characterization, and Film Preparation: The material used in this work for the realization of dielectric surface relief gratings is an azobenzene-containing polymer (azopolymer) in amorphous state. The details about the synthesis and structural, thermal, and optical characterizations have been extensively reported in the previous works.[25,34,38]

The solution for film fabrication was prepared by dissolving 70 mg of the polymer in 0.50 mL of 1,1,2,2-tetrachloroethane and filtered on 0.2 µm PTFE membrane filters. Amorphous thin films were prepared by spin coating the solution on 24 × 60 mm cover slides at 300 rpm for 4 min, obtaining typical film thickness of 1.0 ± 0.1 µm. Before photostructuration experiments, the samples were kept under vacuum at room temperature for 24 h to remove solvent traces. Refractive index of the fabricated film was measured via ellipsometry. Measured values at the device operating wavelengths (633, 532, 488 nm) are: $n_{633} = 1.70$; $n_{532} = 1.74$; $n_{488} = 1.78$. After synthesis and holographic structuring, the azopolymer samples are stored at room temperature. The topological analysis and optical analysis were repeated also after several months from fabrication, showing no degradation effects for both the material and the surface structure over time.

Morphological Surface Characterization: The topographic analysis of the structured surfaces was performed by AFM (WITEC Alpha RS300) operating in tapping mode with a cantilever of 75 kHz resonance frequency. Analysis and elaboration of AFM data was accomplished by means of the open-source software "Gwyddion."

Simulations of Diffraction Patterns: To simulate the diffracted field from the structured azopolymer surfaces, incident plane waves of unitary amplitudes were considered. In the calculations the incident field is assumed to be phase modulated in the plane at $z = 0$, in which the structured dielectric surface is placed. The field transmitted just behind the phase mask is equal to $U_{out}(x,y) = e^{i\phi(x,y)}$. The diffracted field $U(x, y, z)$ in each transverse plane, orthogonal to the optical axis z, behind the surface is evaluated by solving the Helmholtz scalar equation (see also Supporting Information), considering the Rayleigh–Sommerfeld diffraction integral in Fresnel approximation:[10,52]

$$U(x,y,z) = \frac{e^{ikz}}{i\lambda z}\iint U_{out}(x',y')\exp\left\{i\frac{k}{2z}\left[(x-x')^2+(y-y')^2\right]\right\}dx_1dy_1 \quad (6)$$

A discretized form of this integral was implemented coding a MATLAB script. In the case of RGB diffraction, the Fresnel integral was calculated for each wavelength and then the results were summed according to optical field superposition principle.

Experimental Imaging of RGB Diffraction Patterns: The experimental diffraction patterns produced by the azopolymer single (see Figure S4, Supporting Information) and multiplexed RGB gratings were obtained by illuminating the structured sample with three collimated and collinear laser beams, incident normally from the substrate side. The beams had the same wavelengths of the theoretical analysis ($\lambda_1 = 633$ $\lambda_2 = 532$, and $\lambda_3 = 488$ nm) and were produced by three different laser sources (He-Ne, Nd:YVO4 frequency-doubled laser, and a Cobolt Obis diode laser, respectively) which were made propagating along a common optical axis by a proper combination of mirrors and beam splitters. The three beams were tuned to have the approximately same intensity before the sample (9.5×10^{-3} Wcm^{-2}). Low intensity ensures that the green and blue light (which are absorbed by the azopolymer) do not significantly affect the surface pattern. The transmitted diffraction pattern was collected on an opaque screen placed at 205 mm from the sample and recorded by a color reflex CCD camera.

Supporting Information

Supporting Information is available from the Wiley Online Library or from the author.

Acknowledgements

This work has been financially supported by the European Research Council (ERC) under the European Union's Horizon 2020 research and innovation programme "METAmorphoses", grant agreement no. 817794. This work has been supported by Fondazione Cariplo, grant no. 2019–3923.

Open Access Funding provided by Universita degli Studi di Napoli Federico II within the CRUI-CARE Agreement.

Conflict of Interest

The authors declare no conflict of interest.

Data Availability Statement

The data that support the findings of this study are available from the corresponding author upon reasonable request.

Keywords

azopolymers, diffraction gratings, interference lithography, mass migration, polychromatic diffraction, reconfigurable diffractive optical elements, RGB gratings

Received: July 30, 2021
Revised: September 2, 2021
Published online: October 11, 2021

[1] M. J. Hancock, K. Sekeroglu, M. C. Demirel, *Adv. Funct. Mater.* **2012**, *22*, 2223.
[2] F. A. Müller, C. Kunz, S. Gräf, *Materials* **2016**, *9*, 476.
[3] A. G. Dumanli, T. Savin, *Chem. Soc. Rev.* **2016**, *45*, 6698.
[4] K. Huang, F. Qin, H. Liu, H. Ye, C.-W. Qiu, M. Hong, B. Luk'yanchuk, J. Teng, *Adv. Mater.* **2018**, *30*, 1704556.
[5] S. Banerji, M. Meem, A. Majumder, F. G. Vasquez, B. Sensale-Rodriguez, R. Menon, *Optica* **2019**, *6*, 805.
[6] W. T. Chen, A. Y. Zhu, F. Capasso, *Nat. Rev. Mater.* **2020**, *5*, 604.
[7] Z. Yang, T. Albrow-Owen, W. Cai, T. Hasan, *Science* **2021**, *371*, eabe0722.
[8] Z. Li, P. Lin, Y.-W. Huang, J.-S. Park, W. T. Chen, Z. Shi, C.-W. Qiu, J.-X. Cheng, F. Capasso, *Sci. Adv.* **2021**, *7*, eabe4458.
[9] C. Palmer, *Diffraction Grating Handbook*, 8th ed., MKS Instruments Inc. Rochester, New York, USA **2020**.
[10] D. C. O'shea, T. J. Suleski, A. D. Kathman, D. W. Prather, *Diffractive Optics*, SPIE, Bellingham, WA, USA **2003**.
[11] J. W. Goodman, *Introduction to Fourier Optics*, W. H. Freeman, Stuttgart, Germany **2017**.
[12] M. Born, E. Wolf, *Principles of Optics: Electromagnetic Theory of Propagation, Interference and Diffraction of Light*, Cambridge University Press, Cambridge **1999**.
[13] S. M. Kamali, E. Arbabi, A. Arbabi, Y. Horie, M. Faraji-Dana, A. Faraon, *Phys. Rev. X* **2017**, *7*, 041056.
[14] E. Arbabi, A. Arbabi, S. M. Kamali, Y. Horie, A. Faraon, *Sci. Rep.* **2016**, *6*, 32803.
[15] S. Chen, W. Liu, Z. Li, H. Cheng, J. Tian, *Adv. Mater.* **2020**, *32*, 1805912.
[16] S. L. Oscurato, F. Reda, M. Salvatore, F. Borbone, P. Maddalena, A. Ambrosio, (Preprint) *arXiv:2107.12786*, v1, July **2021**.
[17] N. Lassaline, R. Brechbühler, S. J. W. Vonk, K. Ridderbeek, M. Spieser, S. Bisig, B. le Feber, F. T. Rabouw, D. J. Norris, *Nature* **2020**, *582*, 506.
[18] F. Aieta, M. A. Kats, P. Genevet, F. Capasso, *Science* **2015**, *347*, 1342.
[19] H. Rekola, A. Berdin, C. Fedele, M. Virkki, A. Priimagi, *Sci. Rep.* **2020**, *10*, 19642.
[20] H. S. Kang, J. C. Jolly, H. Cho, A. Kalpattu, X. A. Zhang, S. Yang, *Adv. Mater.* **2021**, *33*, 2170001.
[21] F. Yong-Qi, N. K. A. Bryan, O. N. Shing, *Opt. Express* **2000**, *7*, 141.
[22] M. Campbell, D. N. Sharp, M. T. Harrison, R. G. Denning, A. J. Turberfield, *Nature* **2000**, *404*, 53.
[23] S. Lee, Y.-C. Jeong, J.-K. Park, *Opt. Express* **2007**, *15*, 14550.
[24] M. Guo, Z. Xu, X. Wang, *Langmuir* **2008**, *24*, 2740.
[25] M. Salvatore, F. Borbone, S. L. Oscurato, *Adv. Mater. Interfaces* **2020**, *7*, 1902118.
[26] S. L. Oscurato, M. Salvatore, P. Maddalena, A. Ambrosio, *Nanophotonics* **2018**, *7*, 1387.
[27] S. L. Oscurato, M. Salvatore, F. Borbone, P. Maddalena, A. Ambrosio, *Sci. Rep.* **2019**, *9*, 6775.
[28] N. Sekhar Yadavalli, S. Loebner, T. Papke, E. Sava, N. Hurduc, S. Santer, *Soft Matter* **2016**, *12*, 2593.
[29] J. Jelken, S. Santer, *RSC Adv.* **2019**, *9*, 20295.
[30] M. Salvatore, S. L. Oscurato, M. D'Albore, V. Guarino, S. Zeppetelli, P. Maddalena, A. Ambrosio, L. Ambrosio, *J. Funct. Biomater.* **2020**, *11*, 8.
[31] A. Priimagi, A. Shevchenko, *J. Polym. Sci., Part B: Polym. Phys.* **2014**, *52*, 163.
[32] S. Lee, H. S. Kang, A. Ambrosio, J.-K. Park, L. Marrucci, *ACS Appl. Mater. Interfaces* **2015**, *7*, 8209.
[33] J. Choi, W. Cho, Y. S. Jung, H. S. Kang, H.-T. Kim, *ACS Nano* **2017**, *11*, 1320.
[34] S. L. Oscurato, F. Borbone, P. Maddalena, A. Ambrosio, *ACS Appl. Mater. Interfaces* **2017**, *9*, 30133.
[35] M. Salvatore, F. Borbone, F. Reda, P. Maddalena, S. L. Oscurato, *J. Phys. Photonics* **2021**, *3*, 034013.
[36] M. Saphiannikova, V. Toshchevikov, *J. Soc. Inf. Disp.* **2015**, *23*, 146.
[37] S. Loebner, N. Lomadze, A. Kopyshev, M. Koch, O. Guskova, M. Saphiannikova, S. Santer, *J. Phys. Chem. B* **2018**, *122*, 2001.
[38] A. Ambrosio, L. Marrucci, F. Borbone, A. Roviello, P. Maddalena, *Nat. Commun.* **2012**, *3*, 989.
[39] A. Ambrosio, P. Maddalena, L. Marrucci, *Phys. Rev. Lett.* **2013**, *110*, 146102.
[40] X. L. Jiang, L. Li, J. Kumar, D. Y. Kim, S. K. Tripathy, *Appl. Phys. Lett.* **1998**, *72*, 2502.
[41] J. Vapaavuori, R. H. A. Ras, M. Kaivola, C. G. Bazuin, A. Priimagi, *J. Mater. Chem. C* **2015**, *3*, 11011.
[42] W. T. Chen, F. Capasso, *Appl. Phys. Lett.* **2021**, *118*, 100503.
[43] J.-Y. Hong, C.-K. Lee, S. Lee, B. Lee, D. Yoo, C. Jang, J. Kim, J. Jeong, B. Lee, *Sci. Rep.* **2017**, *7*, 2753.
[44] P. Rochon, E. Batalla, A. Natansohn, *Appl. Phys. Lett.* **1995**, *66*, 136.
[45] D. Y. Kim, S. K. Tripathy, L. Li, J. Kumar, *Appl. Phys. Lett.* **1995**, *66*, 1166.
[46] N. S. Yadavalli, S. Santer, *J. Appl. Phys.* **2013**, *113*, 224304.
[47] F. Borbone, S. L. Oscurato, S. D. Sorbo, F. Pota, M. Salvatore, F. Reda, P. Maddalena, R. Centore, A. Ambrosio, *J. Mater. Chem. C* **2021**, *113*, 11368.
[48] K. Yang, S. Yang, X. Wang, J. Kumar, *Appl. Phys. Lett.* **2004**, *84*, 4517.
[49] N. C. R. Holme, L. Nikolova, P. S. Ramanujam, S. Hvilsted, *Appl. Phys. Lett.* **1997**, *70*, 1518.
[50] F. Lagugné Labarthet, T. Buffeteau, C. Sourisseau, *J. Phys. Chem. B* **1998**, *102*, 2654.
[51] Y. Lim, B. Kang, S. Lee, *Adv. Funct. Mater.* **2021**, *31*, 2100839.
[52] J. W. Goodman, *Introduction to Fourier Optics*, Roberts and Company Publishers, Englewood **2005**.

ADVANCED MATERIALS INTERFACES

Supporting Information

for *Adv. Mater. Interfaces,* DOI: 10.1002/admi.202101375

Large-Scale Multiplexed Azopolymer Gratings with Engineered Diffraction Behavior

Stefano L. Oscurato, Francesco Reda, Marcella Salvatore, Fabio Borbone, Pasqualino Maddalena, and Antonio Ambrosio**

Supporting Information

Large-scale multiplexed azopolymer gratings with engineered diffraction behavior

Stefano L. Oscurato, Francesco Reda, Marcella Salvatore, Fabio Borbone, Pasqualino Maddalena and Antonio Ambrosio**

1. Diffraction of light from phase-only modulating surface reliefs

Maxwell's equations imply that the propagation of the spatial-dependent term of a monochromatic electromagnetic field of frequency ω in a homogeneous, isotropic and linear medium is governed by Helmholtz equation, which for the (scalar) electric field $E(\boldsymbol{r},t) \equiv U(\boldsymbol{r},t) = U(\boldsymbol{r})e^{i\omega t}$ is written as:

$$(\nabla^2 + k^2)U(\boldsymbol{r}) = 0, \tag{S1}$$

where $k = (\omega/c)n$ and $n = \sqrt{\epsilon\mu}$ is the refractive index of the material. Equation (S1) can be solved evaluating the fields in planes transverse to an arbitrary z axis and considering the two-dimensional Fourier transforms of the fields in those planes:

$$\widehat{U}(k_x,k_y) = \frac{1}{4\pi^2}\iint_{-\infty}^{+\infty} U(x,y)\, e^{-i[k_x x + k_y y]}dxdy, \tag{S2}$$

$$U(x,y) = \iint_{-\infty}^{+\infty} \widehat{U}(k_x,k_y)\, e^{i[k_x x + k_y y]}dk_x dk_y. \tag{S3}$$

With the introduction of the Fourier spectrum of the fields (S2), Helmholtz equation is solved for the spectrum of the field in any plane at axial position z as

$$\widehat{U}(k_x,k_y,z) = \widehat{U}(k_x,k_y,0)e^{ik_z z}, \tag{S4}$$

where $k_z = \sqrt{k^2 - k_x^2 - k_y^2}$ and $\widehat{U}(k_x,k_y,0)$ is the known spectrum of the field in a plane (source plane) which can be arbitrarily chosen to coincide with the plane $z = 0$. Writing equation (S4) in real space gives [1,2].

$$\begin{aligned} &U(x,y,z) \\ &= \frac{1}{4\pi^2}\iint_{-\infty}^{+\infty} U(x',y',0)\iint_{-\infty}^{+\infty} e^{i[k_x(x-x')+k_y(y-y')+k_z z]}\,dx'dy'dk_x dk_y \\ &= U(x,y,0) * H(x,y,z). \end{aligned} \tag{S5}$$

Where $H(x,y,z)$ is the propagator in the direct space. Equations (S4) and (S5) pose the basis of the Fourier optics. The optical field in any plane of the space is determined from the Fourier spectrum of the field in the source plane. Using the convolution theorem, equation (S5) is equivalently rewritten as

$$U(x,y,z) = FT^{-1}\{FT\{U(x,y,0)\} \times FT\{H(x,y,z)\}\}. \quad \text{(S6)}$$

From this relation it is clearly understood that once the spectrum of the source field is known, the spatial distribution of the propagated field depends only on the transfer function $H(x,y,z)$, which is determined by the geometry of the source and observation planes, but it is independent on the source field. The different levels of approximation of the transfer function for propagation in *far-field* ($z \gg \lambda$, where the evanescent terms in the propagator do not contribute to the field) bring to the Rayleigh-Sommerfeld, Fresnel and Fraunhofer theories, largely used for the solution of the diffraction problems. [2,3]

Equations (S5)and (S6) are at the basis of the design of a diffracted field by engineering the spectral content of the field in the source plane by tailoring the geometry of a diffracting surface. In this case, the structured surface in the object plane is an amplitude and/or phase mask, described by the functions $A(x,y)$ and $\varphi(x,y)$, which modulates an incident beam U_{inc} through a complex space-dependent transmission function $t(x,y)$:

$$U(x,y,0) = U_{inc}(x,y,0) \times t(x,y) = U_{inc}(x,y,0) \times A(x,y)e^{i\varphi(x,y)}. \quad \text{(S7)}$$

If the incident field is a plane wave propagating along the z axis, from $z < 0$ half plane, $U_{inc}(x,y,z) = U_0 e^{ik_0 z}$, then equations (S6) and (S7) specify the diffracted field as only dependent on the transfer function of the system and the Fourier transform of the transmission function $t(x,y)$. Here we consider surfaces which only modulate the phase $\varphi(x,y)$, while having no amplitude modulation:

$$t(x,y) = A(x,y)e^{i\varphi(x,y)} = 1 \times e^{i\varphi(x,y)} = e^{i\varphi(x,y)}. \quad \text{(S8)}$$

The phase modulation is the result of the differences in the optical path that the incident plane wave accumulates in respect to the surrounding medium (refractive index n_s) as the wave propagates in a medium whose refractive index n and/or geometrical shape is spatially structured:

$$\varphi(x,y) = (n(x,y) - n_s) \times k_0 \times h(x,y). \quad \text{(S9)}$$

Sinusoidal surface reliefs

As first example, let's consider a periodic sinusoidal phase modulating surface constituted of a surface relief $h(x,y)$ in a medium of index n immersed in air ($n_s = n_0 = 1$). For such diffracting surface, equation (S5) can be solved analytically, allowing to highlight the connection between the Fourier spectrum of the surface texture and the diffracted field in far-field. The results of this simple situation will permit us to classify the diffracting surfaces in different types of Fourier surfaces, which differentiate for the number and the complexity of

spectral components necessary to accurately reconstruct their spatial structure in a finite region of the source plane. Furthermore, the dependence of the diffraction efficiency, which is a measure of the light intensity propagating or confined in a defined region of the space, is clearly related to the phase modulation depth (S9) imposed on the incident wavefront by the surface relief. The result of the analysis is a common properties of every diffractive relief surface, in which the in-plane geometry of the relief defines the diffraction pattern, while the out-of-plane geometry (the amplitude of the relief) determines the efficiency for light propagating in specific directions.

Let us consider a plane wave incident on the surface in the source plane at $z = 0$ with an angle θ_i, $U_{inc}(x, y, 0) = U_0 e^{ik_0(x\,sin\theta_i)}$. Due to the symmetry, we can simplify the analysis by considering the unidimensional problem (Figure S1). The phase transmission function of the sinusoidal surface (assumed to be thin in respect to the propagation distance) is written in terms of Bessel functions of first kind J_m of m^{th} order as (Jacobi–Anger identity [3]):

$$t(x,y) \equiv t(x) = e^{ik_0(n-1)h(x)} = e^{ik_0(n-1)\frac{\left(1+sin\frac{2\pi x}{\Lambda}\right)}{2}h} = t_0 \sum_{m=-\infty}^{m=+\infty} J_m\left(\frac{k_0(n-1)h}{2}\right) e^{i\left(m\frac{2\pi x}{\Lambda}\right)}. \tag{S10}$$

The field in source plane is then

$$U(x,y,0) = U_{inc}(x,y,0)t(x) = U_0 e^{ik_0[x\,sin\theta_i + (n-1)h(x)]}. \tag{S11}$$

Substituting equation (S11)in equation (S5), we obtain the diffracted field as:

$$\begin{aligned} U(x,z) &= \frac{U_0}{2\pi}\int_{-\infty}^{+\infty} dk_x \int_{-\infty}^{+\infty} e^{ik_0[x'\,sin\theta_i + (n-1)h(x')]}\, e^{i[k_x(x-x')+k_z z]}\, dx' \\ &= \frac{U_0\, t_o}{2\pi}\int_{-\infty}^{+\infty} dk_x \int_{-\infty}^{+\infty} e^{ik_0 x'\,sin\theta_i}\left(\sum_{m=-\infty}^{m=+\infty} J_m\left(\frac{k_0(n-1)h}{2}\right) e^{i\left(m\frac{2\pi x'}{\Lambda}\right)}\right) e^{i[k_x(x-x')+k_z z]}\, dx' \\ &= \frac{U_0\, t_o}{2\pi}\int_{-\infty}^{+\infty} dk_x \sum_{m=-\infty}^{m=+\infty} J_m\left(\frac{k_0(n-1)h}{2}\right) e^{i[k_x x + k_z z]} \int_{-\infty}^{+\infty} e^{i\left(m\frac{2\pi}{\Lambda} + k_0\,sin\theta_i - k_x\right)x'}\, dx'. \end{aligned} \tag{S12}$$

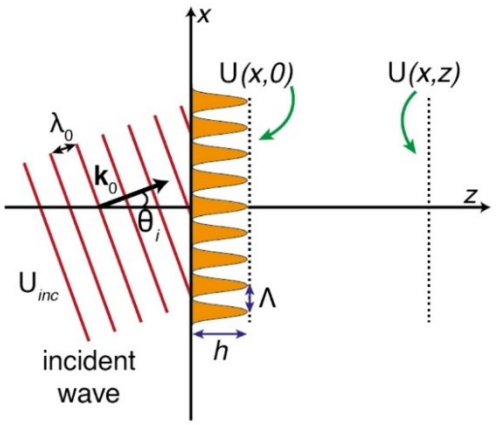

Figure S1. Diffraction from a sinusoidal phase-modulating surface.

Solving the last integral in (S12) using the relation $\int dt\, e^{i(\omega-\omega')t} = 2\pi\delta(\omega - \omega')$, we obtain:

$$U(x,z) = U_0\, t_o \sum_{m=-\infty}^{m=+\infty} J_m\left(\frac{k_0(n-1)h}{2}\right) e^{i\left(k_0 sin\theta_i + m\frac{2\pi}{\Lambda}\right)x}\, e^{iz\sqrt{k_0^2-\left(k_0 sin\theta_i + m\frac{2\pi}{\Lambda}\right)^2}} \quad \text{(S13)}$$

The diffracted field is a superposition of waves characterized by the wavevector components

$$k_x \equiv k_0 sin\theta_m = k_0 sin\theta_i + m\frac{2\pi}{\Lambda} \quad \text{(S14)}$$

$$k_z = \sqrt{k_0^2 - \left(k_0 sin\theta_i + m\frac{2\pi}{\Lambda}\right)^2}, \quad \text{(S15)}$$

which include a finite number of propagating orders and evanescent non-propagating terms. Equation (S14) is the familiar Bragg's relation, which defines the diffraction angle of the propagating orders produced by the sinusoidal diffracting surface in terms of diffraction order m and surface periodicity Λ.

The intensity carried by each of the terms of the field expansion is:

$$I_m = |U_0|^2 \left| J_m\left(\frac{k_0(n-1)h}{2}\right)\right|^2, \quad \text{(S16)}$$

directly related to the phase modulation depth of the surface through the values of refractive index and surface modulation depth h. As the coefficients of the expansion (S10) are normalized to unity, the diffraction efficiency for the order m, defined as the ratio of the intensity in the order and the total intensity of the field, is given as:

$$\eta_m = \frac{I_m}{\sum_m I_m} = \left| J_m\left(\frac{k_0(n-1)h}{2}\right)\right|^2. \quad \text{(S17)}$$

Maximum efficiency for each order happens for different values of h and hence the amplitude of the relief is the structural parameter to be tuned to control the relative distribution of light intensity in the diffracted pattern. The results in equations (S13)-(S16) can be generalized to diffractive surfaces built as sum or multiple sinusoids. As first example, let us consider the sum of two sinusoidal functions $s_1(x)$ and $s_2(x)$ of periodicity Λ_1 and Λ_2 respectively:

$$h(x) = h_1 s_1(x) + h_2 s_2(x). \quad \text{(S18)}$$

According to equation (S10) the phase transmission function of such surface can be decomposed using Jacobi–Anger identity:

$$t(x) = t_{01}t_{02}\left(\sum_{\alpha_1=-\infty}^{\alpha_1=+\infty} J_{\alpha_1}\left(\frac{k_0(n-1)h_1}{2}\right) e^{i\left(\alpha_1\frac{2\pi x}{\Lambda_1}\right)}\right)\left(\sum_{\alpha_2=-\infty}^{\alpha_2=+\infty} J_{\alpha_2}\left(\frac{k_0(n-1)h_2}{2}\right) e^{i\left(\alpha_2\frac{2\pi x}{\Lambda_1}\right)}\right). \quad \text{(S19)}$$

The diffracted field can be easily calculated as showed in equation (S12), obtaining:

$$U(x,z) = U_0 t_{01} t_{02} \sum_{\alpha_1=-\infty}^{\alpha_1=+\infty}\sum_{\alpha_2=-\infty}^{\alpha_2=+\infty} J_{\alpha_1}\left(\frac{k_0(n-1)h_1}{2}\right) J_{\alpha_2}\left(\frac{k_0(n-1)h_2}{2}\right) \times$$
$$\times\, e^{i\left(k_0 \sin\vartheta_i + \alpha_1\frac{2\pi}{\Lambda_1} + \alpha_2\frac{2\pi}{\Lambda_2}\right)x}\, e^{iz\sqrt{k_0^2-\left(k_0\sin\vartheta_i + \alpha_1\frac{2\pi}{\Lambda_1} + \alpha_2\frac{2\pi}{\Lambda_2}\right)^2}}. \quad \text{(S20)}$$

Again, the diffracted field is a superposition of plane and evanescent waves with wavectors:

$$k_x = k_0 \sin\vartheta_i + \alpha_1 \frac{2\pi}{\Lambda_1} + \alpha_2 \frac{2\pi}{\Lambda_2} \tag{S21}$$

$$k_z = \sqrt{k_0^2 - \left(k_0 \sin\vartheta_i + \alpha_1 \frac{2\pi}{\Lambda_1} + \alpha_2 \frac{2\pi}{\Lambda_2}\right)^2}, \tag{S22}$$

each carrying an amount of intensity equal to:

$$I_{(\alpha_1,\alpha_2)} = |U_0|^2 \left| J_{\alpha_1}\left(\frac{k_0(n-1)h_1}{2}\right)\right|^2 \left| J_{\alpha_2}\left(\frac{k_0(n-1)h_2}{2}\right)\right|^2. \tag{S23}$$

Equation (S18) can be further generalized to the sum of N sinusoidal functions $s_l(x)$ each of periodicity Λ_l:

$$h(x) = \sum_{l=1}^{N} h_l s_l(x)\,. \tag{S24}$$

The transmission function, as showed in the simpler case of two sinusoidal surface relief, is the product of N terms, each representing the Jacobi–Anger expansion of the $s_l(x)$ function:

$$t(x) = \prod_{l=1}^{N} t_{0l}\left(\sum_{\alpha_l=-\infty}^{\alpha_l=+\infty} J_{\alpha_l}\left(\frac{k_0(n-1)h_l}{2}\right) e^{i\left(\alpha_l \frac{2\pi x}{\Lambda_l}\right)}\right) \tag{S25}$$

According to equation (S20), the optical field diffracted by this surface is:

$$U(x,z) = \\ = U_0\left[\prod_{l=1}^{N} t_{0l}\left(\sum_{\alpha_l=-\infty}^{\alpha_l=+\infty} J_{\alpha_l}\left(\frac{k_0(n-1)h_l}{2}\right)\right)\right] e^{i\left(k_0 \sin\vartheta_i + \sum_l \alpha_l \frac{2\pi}{\Lambda_l}\right)x} e^{iz\sqrt{k_0^2 - \left(k_0 \sin\vartheta_i + \sum_l \alpha_l \frac{2\pi}{\Lambda_l}\right)^2}} \tag{S26}$$

The optical field, diffracted by surface $h(x)$ is a superposition of a finite number of propagating and evanescent waves characterized by the wavevector components:

$$k_x = k_0 sin\theta_i + \sum_l \alpha_l \frac{2\pi}{\Lambda_l}$$
$$k_z = \sqrt{k_0^2 - \left(k_0 sin\theta_i + \sum_l \alpha_l \frac{2\pi}{\Lambda_l}\right)^2} \tag{S27}$$

which represent a generalized Bragg's relation.

The diffracted orders carry an amount of intensity equal to:

$$I_{(\alpha_1,\alpha_2,\ldots,\alpha_N)} = |U_0|^2 \prod_{l=1}^{N} \left| J_{\alpha_l}\left(\frac{k_0(n-1)h_l}{2}\right)\right|^2 \tag{S28}$$

2. Supplementary Figures

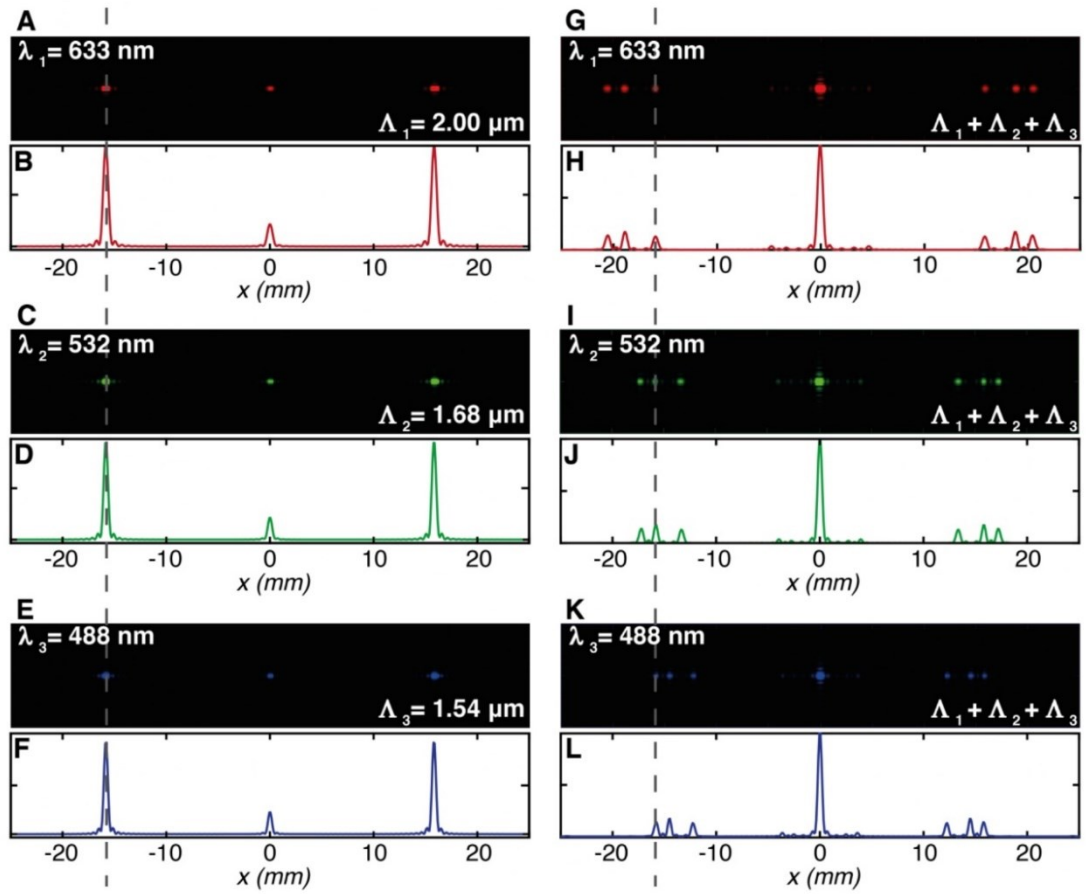

Figure S2. Simulation of the diffraction patterns produced by designed single and multiplexed gratings for incident monochromatic light. (A) Simulated diffraction pattern and (B) intensity profile produced by the grating with periodicity $\Lambda_1 = 2.00\ \mu m$ and incident wavelength $\lambda_1 = 633\ nm$ on a screen placed at distance z=50 mm from the surface. (C)-(E) Simulated diffraction patterns and (D)-(F) relative intensity profiles produced by the gratings with periodicity $\Lambda_2 = 1.68\ \mu m$ and $\Lambda_3 = 1.54\ \mu m$ for incident wavelength $\lambda_2 = 532\ nm$ and $\lambda_3 = 488\ nm$, respectively. The ±1 diffraction orders for the three gratings and the three wavelengths propagate in the same direction, as highlighted by the vertical dashed line superimposed in the simulations, which indicates same x position on the screen. (G to L) simulated diffraction patterns and intensity profiles for the multiplexed grating G1+G2+G3, illuminated with the single wavelengths of the RGB design. Dashed gray line in figure represent the common angular position of the first diffraction order for each grating composing the multiplexed RGB grating. This is the position of the white diffraction spot indicated in Figure 2E.

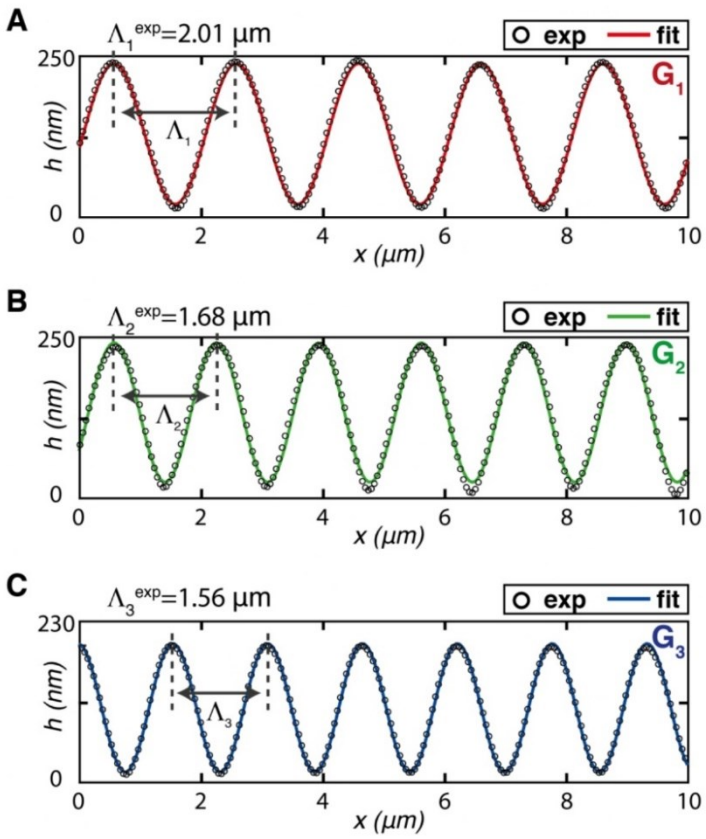

Figure S3. Measure of the azopolymer SRG periodicity produced by the three illumination configurations. (A) Plot of a zoomed view of the experimental AFM profile for the azopolymer grating G1. The experimental periodicity is calculated from the sinusoidal fit of the surface profile data, resulting in a value $\Lambda_1^{exp} = 2.01\ \mu m$, in excellent agreement with the designed periodicity $\Lambda_1 = 2.00\ \mu m$. (B) and (C) same analysis for the gratings G2 and G3, showing experimental periodicities $\Lambda_2^{exp} = 1.68\ \mu m$ and $\Lambda_3^{exp} = 1.56\ \mu m$, that accordingly match with the designed ones $\Lambda_2 = 1.68\ \mu m$ and $\Lambda_3 = 1.54\ \mu m$.

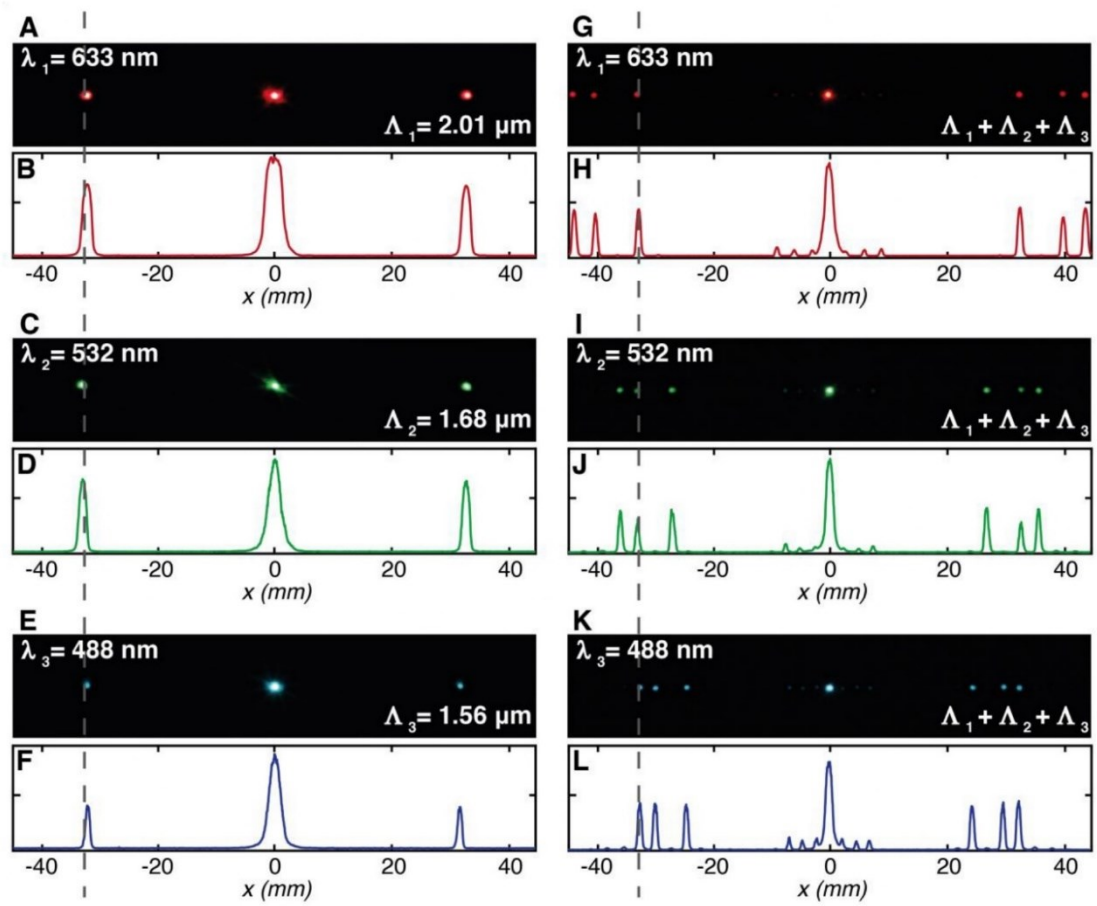

Figure S4. Experimental diffraction patterns produced by single and multiplexed gratings on the azopolymer film for incident monochromatic light. The figure reproduces the experimental version of the simulations reported in Figure S2, using the SRG reported in Figure 3 for the images of diffraction from single gratings (A to F), and the multiplexed RGB grating of Figure 5 for the multiplexed diffraction patterns (G to L). The experimental diffraction patterns quantitatively match the geometry of the simulations, showing the presence of a common diffraction order (indicated by the gray dashed line in the panels), propagating in the same direction for all the three illumination wavelengths.

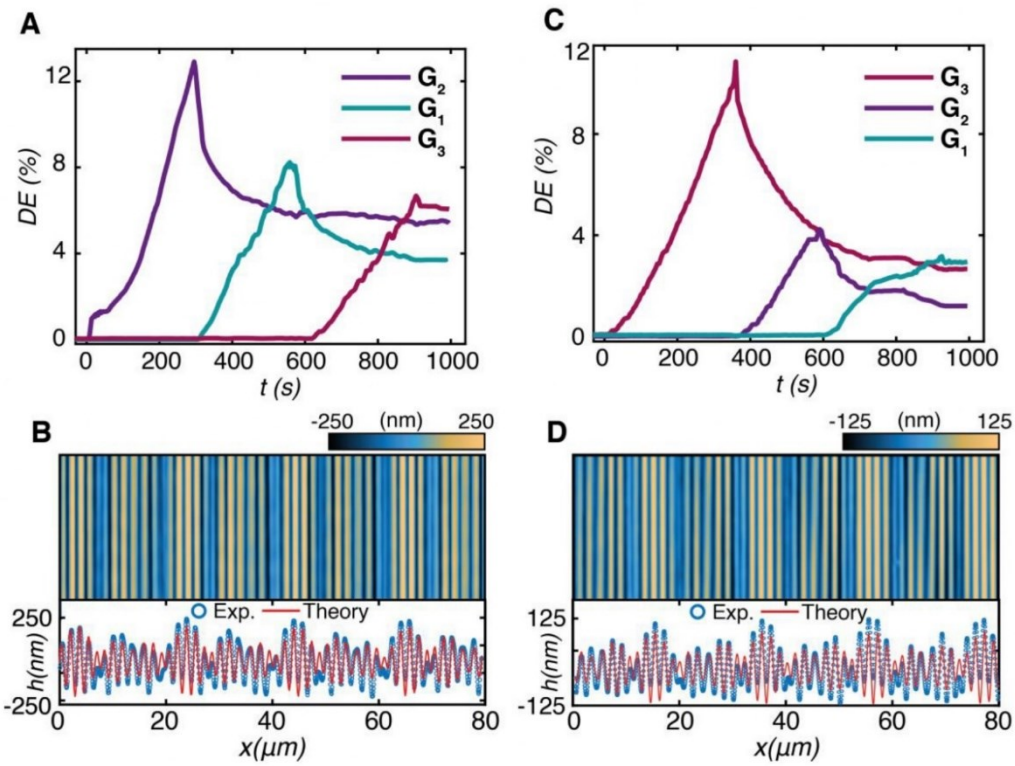

Figure S5. Multiplexed azopolymer RGB grating obtained with fixed exposure time and different illumination sequences. (A) and (C) Dynamical diffraction curves recorded, by the photodiodes PD1, PD2 and PD3, during surface structuration step with grating sequence G2+G1+G3 and G3+G2+G1, respectively. During each illumination step, the azopolymer surface is irradiated with the relative interference pattern for a fixed time of 300s. (B) and (D) AFM micrographs and topographic experimental and theoretical profiles of the multiplexed polymer surface after irradiation. Comparison between measured and theoretical (calculated by assuming equal amplitude weight for the three sinusoidal surface reliefs composing the total structure) profiles highlights bigger structural discrepancies for these configurations in respect to the exposure time-optimized one shown in Figure 5 of the main text.

Supplementary References

[1] J. W. Goodman, *Introduction to Fourier Optics*, W. H. Freeman, Stuttgart, Germany, **2017**.
[2] L. Novotny, B. Hecht, *Principles of Nano-Optics*, Cambridge University Press, Cambridge, **2006**.
[3] J. W. Goodman, *Introduction to Fourier Optics*, Roberts And Company Publishers, **2005**.

Publication IV

F. Reda, M. Salvatore, F. Borbone, P. Maddalena, and S. L. Oscurato

Accurate morphology-related diffraction behavior of light-induced surface relief gratings on azopolymers

Reprinted from

ACS Materials Letters 4(5), 953–959 (2022)

ACS MATERIALS LETTERS

www.acsmaterialsletters.org

LETTER

Accurate Morphology-Related Diffraction Behavior of Light-Induced Surface Relief Gratings on Azopolymers

Francesco Reda, Marcella Salvatore, Fabio Borbone, Pasqualino Maddalena, and Stefano L. Oscurato*

Cite This: ACS Materials Lett. 2022, 4, 953–959

Read Online

ACCESS | Metrics & More | Article Recommendations

ABSTRACT: Holographic relief gratings can be fabricated directly on the surface of azobenzene-containing materials (or simply *azomaterials*) without additional development steps. Despite often being described to have ideal sinusoidal profiles, the developing surface morphology in large amplitude gratings can affect the light distribution of the writing interferogram, causing profile deformations and deviations in the expected diffraction behavior. In this work, we characterize the temporal evolution of the surface relief grating (SRG) morphology fabricated by means of interference lithography on azopolymer films, quantitatively relating the results of a Fourier analysis of their surface profiles to the accurate measurement of efficiencies in the transmitted diffraction orders. A reliable surface structuration dynamics is empirically extracted from the analysis and used to formulate a simple but detailed diffraction model that, within the scalar diffraction theory, exhaustively describes the diffraction behavior of real SRGs without the need of complex rigorous electromagnetic theories. Our results add a deeper insight in the quantitative description of the morphology and the diffraction behavior of SRGs, which can contribute to their adoption for operating high-performance, reconfigurable, compact, and lightweight diffractive optical devices.

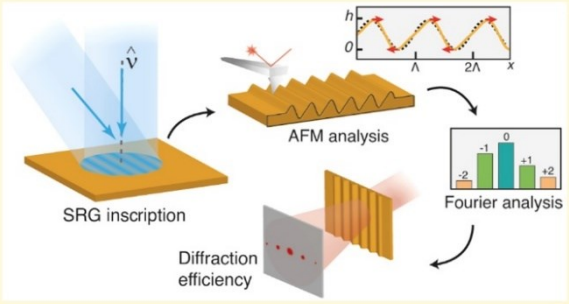

Diffraction gratings are among the most relevant experimental devices in many fields of science, finding applications amid optics, astronomy, and chemistry, to name a few.[1] The diffracted optical field emerging from a grating realized as phase-modulating structured surface in air is entirely determined by the refractive index of the material and by the morphology of the surface, specified through the periodicity, the shape, and the modulation depth of the groove profile.[2] Phase-modulating sinusoidal SRGs can be easily produced through interference lithography, where a photoresist is exposed to the stationary sinusoidal fringe pattern of two interfering light beams to inscribe a grating with the same periodicity of the interferogram.[3] Differently from standard photoresists, which require chemical development after light exposure to transfer the grating in a substrate, thin films of azomaterials can be used to fabricate diffraction gratings directly as surface reliefs on an operating device.[4,5] The light-induced structuration is the result of a reversible material transport originated by the photoisomerizing azobenzene units.[6−8] The surface pattern is dependent on both the intensity and the polarization of the irradiated light.[9−13] Reconfigurable vectorial photolithography[14−16] is then achievable with these material systems, finding increasing applications in photonics,[17−23] surface engineering,[24−29] and biology.[30−32]

The SRGs on azomaterials are typically described as perfect sinusoidal surfaces replicating the sinusoidal interference fringes in the modulation of the surface, with an amplitude determined by the exposure dose. This description is often sufficiently accurate when the surface modulation is moderate[13,33,34] and can be effectively retained in comparative studies, where the diffraction efficiency in one of the diffraction orders of the developing SRG is monitored to provide a direct measure of the surface structuration performances, in relation to the material design[35−39] or the illumination configura-

Received: February 21, 2022
Accepted: April 11, 2022
Published: April 13, 2022

https://doi.org/10.1021/acsmaterialslett.2c00171
ACS Materials Lett. 2022, 4, 953–959

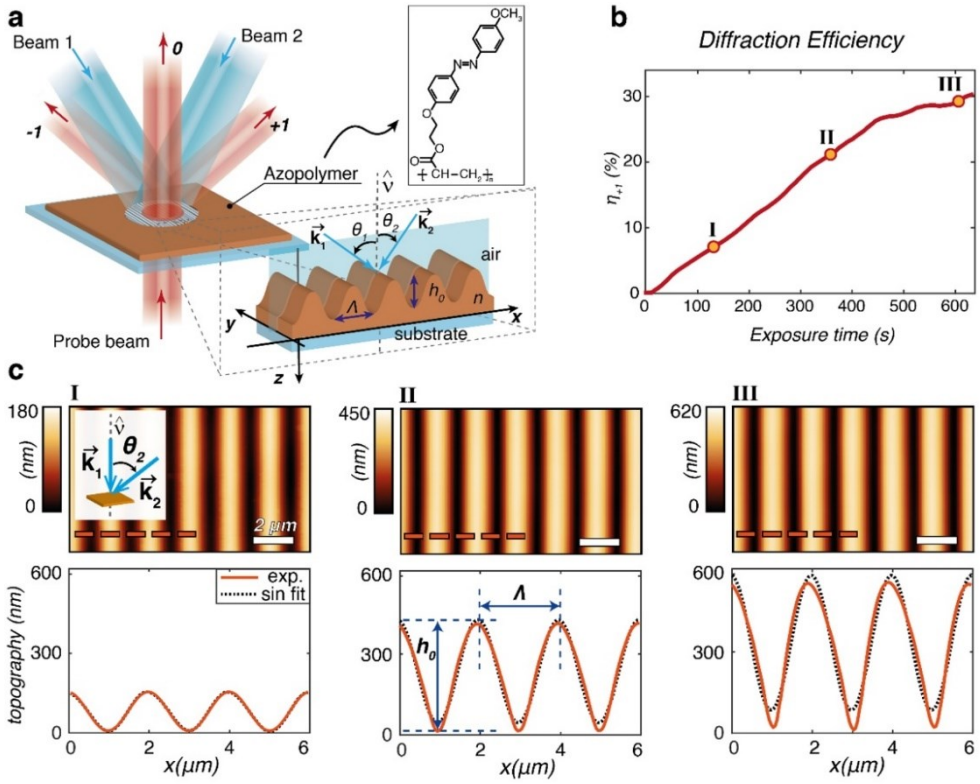

Figure 1. (a) Optical configuration for SRGs inscription and diffraction measurement. The inset shows the azopolymer chemical structure; (b) first-order time-evolving diffraction efficiency. Relief estimated amplitude at the instants I, II, III: h^{I}_{est} = 149 nm, h^{II}_{est} = 305 nm, and h^{III}_{est} = 396 nm; (c) AFM characterization of the SRGs and experimental profiles compared with a sinusoidal fit. Relief measured amplitude h^{I}_{mea} = 142 nm, h^{II}_{mea} = 413 nm and h^{III}_{mea} = 522 nm.

tion.[40−42] However, considerable deviation from ideal sinusoidal profiles is observed in large amplitude SRGs,[43,44] which are designed, for example, to work with the highest diffraction efficiency allowed for sinusoidal gratings by scalar diffraction theory (e.g., 33.86% in the first diffraction order).[19,20,45]

Recently, Lee et al. investigated, in a theoretical analysis, the geometry of the optical field of the interferogram during the inscription of SRGs on azomaterials.[46] The corrugation of the surface at later stages of the direct grating inscription process, and eventual asymmetries in the illumination configuration (e.g nonsymmetric incidence of the interfering beams) can affect the spatial distribution of light absorbed by the azomaterial, resulting in a deformation of the ideally sinusoidal profile that increases with the exposure dose. A direct consequence of this deformation is that the diffraction behavior of large deformation SRGs requires a more careful analysis, especially when quantitative diffraction performances are targeted.[19,20,22,23]

Here, we comprehensively study the accurate relationship between the surface profile and the diffraction behavior observed in SRGs achieved from the direct optical patterning of an azopolymer film through sinusoidal intensity interferograms. The morphology of the surface grating is analyzed at different stages of the light-induced surface structuration process by means of a decomposition of the surface profile in a Fourier series. The temporal evolution of the amplitude and the phase of the Fourier components has been used to phenomenologically model the entire SRG formation dynamics, describing the modulation depth, the deformation magnitude, and the directionality observed in the reliefs produced by different interference illumination configurations. The resulting analytic expression for the surface profile has been used to calculate the evolution of the diffraction efficiency of the SRGs by means of the simple scalar diffraction theory. Despite lacking the total quantitative prediction capabilities offered by rigorous vectorial theories of diffraction,[47−49] the simple scalar model captures all the main aspects of the diffraction pattern produced by real SRGs, including the diffraction efficiency unbalance in symmetric orders determined by the actual shape of the SRG profile. Our results provide a simple and practical framework to design high-performance diffraction gratings to be used in operating optical systems based on azopolymer diffractive optical components. Herein, light-induced SRGs are inscribed on the surface of an azopolymer thin film using two interfering *p*-polarized laser beams at λ_w = 491 nm (Figure 1a), having an incident average intensity of ∼330 mW/cm^2 over a spot diameter of ∼2.0 mm.[19] The azopolymer used in the experiments (M_w = 27 000; phase sequence: glass, 67 °C; Nematic, 113 °C; isotropic; maximum absorbance at λ_{max} = 350 nm) was prepared as previously reported[14,27] by synthesis and radical polymerization of (*E*)-2-(4-((4-methoxyphenyl) diazenyl)phenoxy)-ethyl acrylate. The chemical structure of the material is shown in the inset of Figure 1a. The films were prepared by spin coating a filtered (0.2 μm PTFE) solution of polymer in 1,1,2,2-tetrachloroethane on 24 mm × 60 mm cover slides at

https://doi.org/10.1021/acsmaterialslett.2c00171
ACS Materials Lett. 2022, 4, 953−959

300 rpm for 4 min, resulting in a typical thickness of 1.0 μm. The samples were kept under vacuum at room temperature for 24 h to remove solvent traces before being used for SRG inscription.

Assuming the film surface to be parallel to the xy-plane of the coordinate system, the total angle $\theta = \theta_1 + \theta_2$ and the difference angle $\Delta\theta = (\theta_1 - \theta_2)$ between the beam wavevectors $\vec{\mathbf{k}}_1$ and $\vec{\mathbf{k}}_2$ (Figure 1a) determine the periodicity Λ (in the x-direction) of the interferogram, according to the relation $\Lambda = \lambda_w/[2\sin(\theta/2)\cos(\Delta\theta/2)]$. This expression also holds for asymmetric beam incidence, with respect to the surface normal, and reduces to the standard relation[18,19] for symmetric incidence ($\Delta\theta = 0$). In our setup, the angles θ_1 and θ_2 can be independently controlled, as extensively detailed elsewhere.[19] During the SRG inscription, an additional incoherent circularly polarized beam at $\lambda_a = 405$ nm illuminates the area of the developing SRG (not shown in Figure 1, for simplicity). This beam enhances the relief formation dynamics by restoring the isotropic orientational distribution of the azomolecules across the film,[19,20,50,51] which otherwise have a tendency to be photoaligned by the linearly polarized light of the interferogram, resulting in an additional birefringence grating in the film volume and in a partial saturation of the surface structuration process.

To evidence the effects that the accurate description of the SRG surface profile has on their diffraction behavior, we show, in Figure 1b, the time-evolving diffraction efficiency η_{+1} in the +1 diffraction order of a probe beam at $\lambda_p = 633$ nm (TM polarization), recorded in real time during one of our typical SRG inscription experiments. In this case, an asymmetric incidence configuration for the interfering beams was used ($\theta_1 = 0°$ and $\theta_2 \approx 14.1°$, inset Figure 1c). Here, the diffraction efficiency η_m is defined as the ratio of the power of the probe beam diffracted in the mth order to the power transmitted through the initial flat azopolymer sample.

The rising trend of the curve in Figure 1b is directly associated with the growing modulation amplitude h_0 (Figure 1a) of the azopolymer surface grating with the increasing exposure time. For an ideal sinusoidal surface grating, having refractive index n at λ_p (immersed in air), the scalar diffraction theory analytically relates h_0 at each instant of the surface structuration process to the diffraction efficiency measured in the order m, according to the following expression:[2]

$$\eta_m = \left| J_m\left[\frac{\pi(n-1)h_0}{\lambda_p}\right]\right|^2 \tag{1}$$

Here, J_m is the Bessel function of the first kind of order m. The estimations of eq 1, assuming $n = 1.70$, for the grating amplitude $h_{est}^{(i)}$ resulting from the measure of $\eta_{+1}^{(i)}$ of at three increasing exposure times indicated by the orange dots in Figure 1b, are in agreement with the direct measures of $h_{mea}^{(i)}$ from atomic force microscopy (AFM) micrographs only for shallow SRGs, while an increasing discrepancy is observed for larger surface modulations (Figure 1c). In addition, the comparison of the AFM profiles (solid lines) with the profiles of the ideal sinusoidal functions (dashed lines) fitting the same data in Figure 1c, also highlights increasing deviations of the SRG topographic profiles from ideal sinusoids. To exclude possible AFM artifacts as a source of these deformations, we repeated the surface characterizations for different scan directions and tip geometries, obtaining consistent results. The deformed profiles make the simple scalar diffraction model in eq 1 not suitable for quantitative description of large modulated SRGs. To extend its applicability to real SRGs, we quantitatively analyzed the time-evolving morphology of SRGs by describing the measured surface profiles and their deformations from ideal sinusoids as high-order terms in the expansion of a truncated Fourier series of K+1 terms:

$$h(x) = \frac{A_0}{2} + \sum_{k=1}^{K} A_k \cos\left(\frac{2\pi}{\Lambda}kx - \varphi_k\right) \tag{2}$$

With this formalism, the SRG profiles obtained from different exposure times can be fitted with eq 2 to extract the amplitudes $A_k > 0$ and the phases φ_k of the kth term of the series that completely describe the geometry of the surface. In particular, the coefficients A_0 and (A_1,φ_1) describe an ideal sinusoidal profile with periodicity Λ, while the higher-order coefficients (A_k,φ_k) with $k \geq 2$ are associated with eventual profile deformations. As the deformations are small compared to ideal sinusoids, we limited our analysis at the first three terms of the series ($K = 3$). In addition, from the characterization in Figure 1c, the amplitudes in the series are expected to be dependent on the exposure time τ ($A_k = A_k(\tau)$), while the phases can be reasonably assumed constants, as further detailed below. The total relief amplitude $h_0(\tau)$, for a certain exposure time, is then given as

$$h_0(\tau) = 2\sqrt{\sum_{k=1}^{K} |A_k(\tau)|^2} \tag{3}$$

Figure 2a shows the histogram of the coefficients $A_k(\tau)$ (with $k = 1, 2, 3$), interpretable as the magnitude of surface

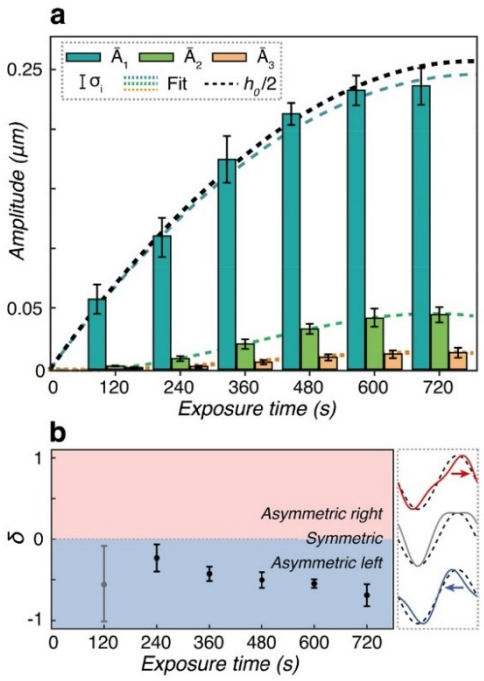

Figure 2. (a) Time evolution of first three Fourier amplitudes of the surface decomposition; (b) temporal evolution of the surface deformation asymmetry described by the parameter δ.

https://doi.org/10.1021/acsmaterialslett.2c00171
ACS Materials Lett. 2022, 4, 953−959

deformation, extracted from the fit of the SRG profile with eq 2 at increasing exposure times.

To improve data reliability, the results in plot are the average of nine independent AFM characterizations at each exposure time, measured on different azopolymer films structured with constant illumination parameters. As expected, the contributions of A_2 and A_3 to the total relief geometry at the very early stages of the surface structuration dynamics (up to $\tau \approx 240$s) are negligible, and the profile can be well-approximated as a pure sinusoid with modulation depth $h_0(\tau) = 2|A_1(\tau)|$. At longer exposure times, the higher-order terms of the series become non-negligible, monotonically increasing with time until a partial saturation of surface deformation occurs ($\tau > 600$ s). We empirically found that the temporal evolution of the measured Fourier amplitudes $A_k(\tau)$ is well-fitted by third-order polynomials ($A_k(\tau) = \sum_{i=1}^{3} a_{ik}\tau^i$, dashed lines in Figure 2a). According to eq 3, also the total surface relief modulation depth $h_0(\tau)$ follows the same temporal evolution.

The complete description of the surface profile requires the analysis of the phases φ_k of the Fourier components too. In particular, the phases strongly affect the symmetry of the Fourier superposition of eq 2, having a relevant role in the quantitative analysis of the SRG diffraction pattern.[20,22,46] We used the information contained in the fitted values of φ_k to quantitatively evaluate the symmetry (or the tilt) of the measured SRG surface profile for each exposure time. To reach this goal, we approximate the surface profile with the first two Fourier components, as A_3 is relatively small and can be neglected for this analysis. We defined the symmetry parameter Δ in the eventually deformed sinusoidal profile by evaluating the unbalance in area underlying $h(x)$ in a half and in a quarter of the grating periodicity as

$$\begin{aligned}\Delta &= I_2 - 2I_1 \\ &= \int_{\alpha}^{\Lambda/2+\alpha} h(x)\,\mathrm{d}x - 2\int_{\alpha}^{\Lambda/4+\alpha} h(x)\,\mathrm{d}x \\ &= A_2\frac{\Lambda}{2\pi}\sin(\varphi_2 - 2\varphi_1)\end{aligned} \tag{4}$$

In eq 4, $\alpha = \varphi_1\Lambda/2\pi$. The coefficient A_2 specifies the maximum deformation achievable in the profile, whose strength and directionality are dependent, instead, on the relative phases φ_1 and φ_2 through the parameter $\delta = \sin(\varphi_2 - 2\varphi_1)$. Figure 2b shows schematically the relationship between δ and the surface deformation for any given value A_2. The case $\delta = 0$ corresponds to a symmetric deformed surface shape, while $\delta > 0$ and $\delta < 0$ are associated with tilted topographic profiles. We refer to *right* deformations when $\delta > 0$ and the topographic maxima in the profile (red solid line in Figure 2b) are shifted toward the right, with respect to the maxima of the ideal sinusoid with the same period (dashed black line in Figure 2b). The opposite holds for *left* asymmetric profiles (blue solid line in Figure 2b).

Figure 2b reports the average parameter δ, as estimated from the Fourier analysis. Neglecting the shortest exposure time ($\tau = 120$ s), denoted by the gray dot in Figure 2b, in which δ is not appropriately defined, because of negligible deformation ($A_2 \approx 0$), all the deformed profiles are characterized by consistent values of δ, including its sign (<0) and magnitude. This corresponds to a specific and reproducible asymmetry of the surface profiles, ultimately determined by the geometry of the tilted interferogram used to inscribe the SRGs on the azopolymer film with nonsymmetric incidence beams.[46] For the specific case under consideration ($\theta_1 = 0$ and $\theta_2 > 0$), the SRGs are characterized by left asymmetry, which corresponds to a slanted surface profile, tilted toward the direction of the incident angled interfering beam (beam 2 in Figure 1).

A direct consequence of the consistent deformation symmetry and its interpretation, in terms of (static) geometry of the interferogram, is that the phases φ_k of the Fourier decomposition in eq 2 can be considered reasonably independent of the exposure time τ. With this consideration, the analytic time-dependent evolution of the SRG morphology $h(x,\tau)$ can be entirely described by the time-dependent amplitudes $A_k(\tau)$ and by a single set of (constant) φ_k that define the deformation parameter δ in the specific illumination geometry.

The knowledge of an analytic expression for $h(x,\tau)$, as given by eq 2, allows a more accurate description of the dynamical diffraction efficiency within the scalar diffraction theory. For a SRGs having periodicity Λ and refractive index n, $\eta_m(\tau)$ is given by

$$\eta_m(\tau) = \left|\frac{1}{\Lambda}\int_{-\Lambda/2}^{\Lambda/2} e^{i2\pi/\lambda_p(n-1)h(x,\tau)} e^{-im2\pi/\Lambda x}\,\mathrm{d}x\right|^2 \tag{5}$$

The plot of eq 5 for the first five diffraction orders ($m = 0$, ±1, ±2), numerically calculated for the surface profile $h(x,\tau)$ resulting from the analysis in Figure 2, are shown as dashed lines in Figure 3a. The total relief depth $h_0(\tau)$ of the Fourier grating (eq 3) is used as the abscissa of the plot to facilitate a direct comparison of the results of eq 5 with the scalar model of ideal sinusoidal gratings (eq 1),[19,20] reported in the graph only for $\eta_{\pm1}$. As expected, the deformed and tilted SRG profile causes the separation of symmetric diffraction orders (e.g., $m = \pm1$), with an effect similar to that produced by blazed diffraction gratings. As a result, the diffraction efficiency in one of the first orders is, in principle, no longer limited to the theoretical maximum of 33.86% of the ideal sinusoidal gratings.

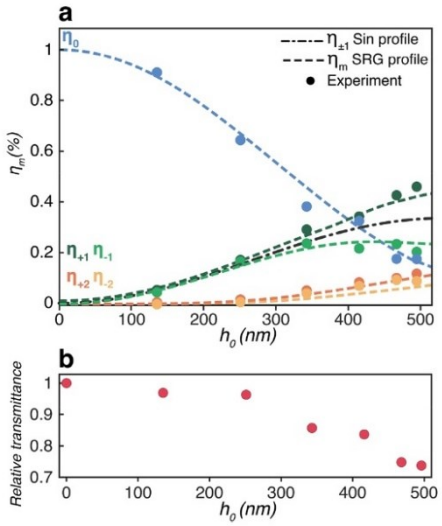

Figure 3. (a) Theoretical and experimental diffraction efficiency for the first five diffraction orders of the gratings; (b) total transmittance measured for increasing surface modulation depth.

https://doi.org/10.1021/acsmaterialslett.2c00171
ACS Materials Lett. 2022, 4, 953−959

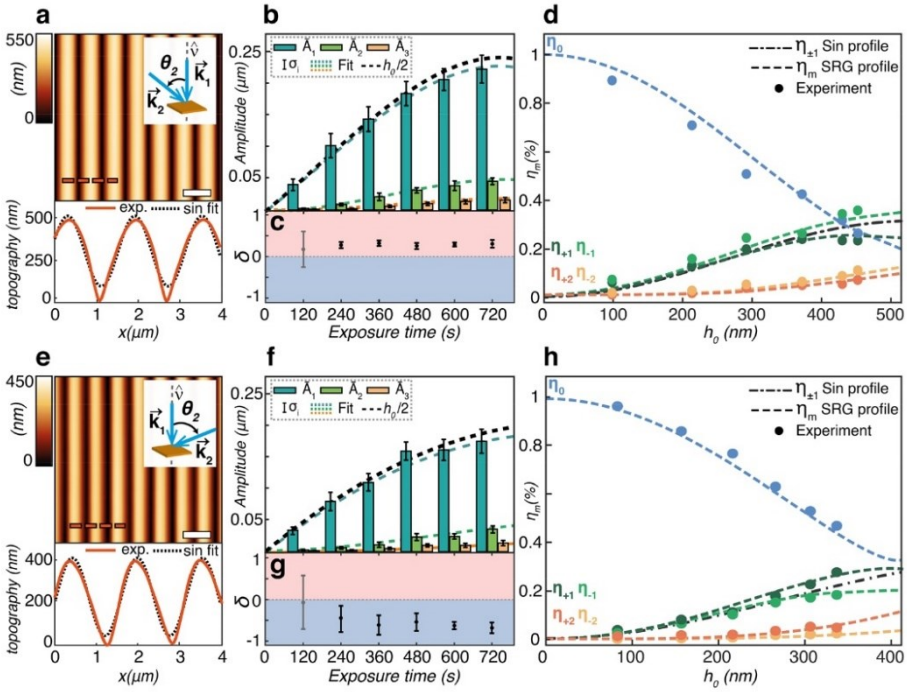

Figure 4. (a–d) Time-evolving AFM, Fourier, and diffraction efficiency characterization for SRGs inscribed with the right asymmetric interferogram; (e–h) same characterization for higher left asymmetric SRGs.

To test the accuracy of both the structural analysis and the scalar diffraction model for the description of real SRGs on azopolymers, we measured the diffraction efficiency at λ_p for the first five diffraction orders of the gratings characterized in Figure 2b. The results, reported as dots in Figure 3a, are the average of at least three independent measurements on different SRGs fabricated with the same interference illumination parameters. In the definition of the experimental diffraction efficiency, one should note that we observed a systematic reduction of the total transmittance of the grating as the surface modulation depth increased (Figure 3b). To describe this effect, a full-vectorial diffraction theory should be used, that is behind the scope of this work. However, following the prescriptions of nonparaxial treatments aiming at extending the validity of scalar theory,[52,53] by defining the measured diffraction efficiency as the intensity in the order m, with respect to the total transmitted intensity in the propagating orders ($I_{tot} = \sum_{m=-3}^{+3} I_m$), the experimental diffraction efficiency will closely follow the theoretically behavior described by eq 5. In particular, the predicted asymmetry in the diffraction efficiency between +1 and −1 diffraction orders is quantitatively obtained in the experiment.

To additionally test the model, we repeated the Fourier analysis for SRGs having different periodicity and morphological asymmetries. As a first step, we evaluated the effect of having an opposite asymmetry in the interferogram, with respect to the previous case.[46] This is achieved by an interference configuration with incidence angles $\theta_1 = 0°$ and $\theta_2 = -16.8°$ (see inset in Figure 4a). An exemplary AFM micrograph of a realized deformed SRG is shown in Figure 4a. The deviation of the measured topographic profile from the ideal sinusoid are evident in this case too, also showing the expected opposite tilt direction of the grooves (asymmetric right), with respect to the previous case, that follow the symmetry of the writing interferogram.[46] The deformation of the grating profiles at different exposure times are quantitatively characterized from the Fourier analysis reported in Figures 4b and 4c. Their time evolution is again well-described by third-order polynomials for $A_k(\tau)$ (dashed lines in Figure 4b), while an approximately constant right profile asymmetry is again obtained from the parameter δ in eq 4. Also, in this case, the resulting phenomenological function $h(x,\tau)$ accurately describes the measurement of diffraction efficiency in the propagating transmitted diffraction orders as predicted by eq 5. In particular, the roles of the orders +1 and −1 is reversed in Figure 4d, with respect to the previous case (Figure 3a), resulting in the expected opposed blazing effect arising from the inverse profile tilt direction.

As the last step of our study, we report in Figures 4e–h the Fourier morphological analysis and the diffraction characterization for SRGs realized in a higher left asymmetric configuration for the interfering beams ($\theta_1 = 0°$; $\theta_2 = 18.3°$, as shown in the inset of Figure 4e). Besides further sustaining the general validity of our approach for the accurate description of the evolution of the geometry of the SRGs on azopolymers and their diffraction behavior, this analysis also highlights a reduced surface structuration efficiency for SRGs having smaller periodicity. This result agrees with the recent analysis of Lee et al.[46] regarding periodicity-dependent formation efficiency of SRGs, ascribable to the lower fraction of incident light absorbed (because of increased reflectance) by the azopolymer film irradiated at larger incidence angles.

In conclusion, we have presented a comprehensive characterization of SRGs inscribed on an azopolymer film by means of interfering light beams, relating the precise description of the surface grating morphology as a time-

https://doi.org/10.1021/acsmaterialslett.2c00171
ACS Materials Lett. 2022, 4, 953–959

dependent Fourier series to the accurate analysis of the efficiency measured in their diffraction pattern. AFM characterization of the SRGs, realized with increasing exposure doses to writing interferograms characterized by different asymmetries, have been used to phenomenologically model the evolution of the grating morphology and its deviations from the ideal sinusoidal profiles, that are typically used to describe the relief geometry in the experiments. Maintaining the theory for the grating diffraction at the simplest level, the diffraction behavior of the SRGs has been completely described by means of scalar diffraction model that include the time-evolving analytic expression obtained for the developing grating morphology.

AUTHOR INFORMATION

Corresponding Author

Stefano L. Oscurato − *Physics Department "E. Pancini, University of Naples "Federico II", Complesso Universitario di Monte Sant'Angelo, 80126 Naples, Italy; Centro Servizi Metrologici e tecnologici Avanzati (CeSMA), University of Naples "Federico II", Complesso Universitario di Monte Sant'Angelo, 80126 Naples, Italy;* orcid.org/0000-0002-1814-8033; Email: stefanoluigi.oscurato@unina.it

Authors

Francesco Reda − *Physics Department "E. Pancini, University of Naples "Federico II", Complesso Universitario di Monte Sant'Angelo, 80126 Naples, Italy*

Marcella Salvatore − *Physics Department "E. Pancini, University of Naples "Federico II", Complesso Universitario di Monte Sant'Angelo, 80126 Naples, Italy; Centro Servizi Metrologici e tecnologici Avanzati (CeSMA), University of Naples "Federico II", Complesso Universitario di Monte Sant'Angelo, 80126 Naples, Italy*

Fabio Borbone − *Department of Chemical Sciences, University of Naples "Federico II", Complesso Universitario di Monte Sant'Angelo, 80126 Naples, Italy;* orcid.org/0000-0001-7433-9267

Pasqualino Maddalena − *Physics Department "E. Pancini, University of Naples "Federico II", Complesso Universitario di Monte Sant'Angelo, 80126 Naples, Italy; Centro Servizi Metrologici e tecnologici Avanzati (CeSMA), University of Naples "Federico II", Complesso Universitario di Monte Sant'Angelo, 80126 Naples, Italy*

Complete contact information is available at: https://pubs.acs.org/10.1021/acsmaterialslett.2c00171

Author Contributions

S.L.O. conceived the project; S.L.O. and P.M. developed and designed the methodology; F.B. synthesized the polymer and prepared the films; S.L.O., F.R., M.S., and F.B. conducted the investigation process and performed the experiments and data analysis; S.L.O. wrote the manuscript with input from all authors; S.L.O. supervised the project. All authors have given approval to the final version of the manuscript.

Notes

The authors declare no competing financial interest.

ACKNOWLEDGMENTS

This work has been financially supported by the project ACTRIS-Aerosol, Clouds and Trace Gases Research Infrastructure, funded by Italian MIUR Programma Nazionale Infrastrutture di Ricerca (PNIR) (Grant No. CIR01_00015).

REFERENCES

(1) Palmer, C. *Diffraction Grating Handbook*, 8th Edition; MKS Instruments, Inc.: Rochester, NY, USA, 2020.

(2) Goodman, J. W. *Introduction to Fourier Optics*; W. H. Freeman: Stuttgart, Germany, 2017.

(3) O'Shea, D. C.; Suleski, T. J.; Kathman, A. D.; Prather, D. W. *Diffractive Optics*; SPIE: Bellingham, WA, USA, 2003.

(4) Rochon, P.; Batalla, E.; Natansohn, A. Optically Induced Surface Gratings on Azoaromatic Polymer Films. *Appl. Phys. Lett.* **1995**, *66*, 136−138.

(5) Kim, D. Y.; Tripathy, S. K.; Li, L.; Kumar, J. Laser-induced Holographic Surface Relief Gratings on Nonlinear Optical Polymer Films. *Appl. Phys. Lett.* **1995**, *66*, 1166−1168.

(6) Bandara, H. M. D.; Burdette, S. C. Photoisomerization in Different Classes of Azobenzene. *Chem. Soc. Rev.* **2012**, *41*, 1809−1825.

(7) Toshchevikov, V.; Ilnytskyi, J.; Saphiannikova, M. Photoisomerization Kinetics and Mechanical Stress in Azobenzene-Containing Materials. *J. Phys. Chem. Lett.* **2017**, *8*, 1094−1098.

(8) Yadav, B.; Domurath, J.; Kim, K.; Lee, S.; Saphiannikova, M. Orientation Approach to Directional Photodeformations in Glassy Side-Chain Azopolymers. *J. Phys. Chem. B* **2019**, *123*, 3337−3347.

(9) Natansohn, A.; Rochon, P. Photoinduced Motions in Azo-Containing Polymers. *Chem. Rev.* **2002**, *102*, 4139−4176.

(10) Yager, K. G.; Barrett, C. J. Novel Photo-Switching Using Azobenzene Functional Materials. *J. Photochem. Photobiol., A* **2006**, *182*, 250−261.

(11) Lee, S.; Kang, H. S.; Park, J.-K. Directional Photofluidization Lithography: Micro/Nanostructural Evolution by Photofluidic Motions of Azobenzene Materials. *Adv. Mater.* **2012**, *24*, 2069−2103.

(12) Priimagi, A.; Shevchenko, A. Azopolymer-Based Micro- and Nanopatterning for Photonic Applications. *J. Polym. Sci., Part B: Polym. Phys.* **2014**, *52*, 163−182.

(13) Oscurato, S. L.; Salvatore, M.; Maddalena, P.; Ambrosio, A. From Nanoscopic to Macroscopic Photo-Driven Motion in Azobenzene-Containing Materials. *Nanophotonics* **2018**, *7*, 1387−1422.

(14) Ambrosio, A.; Marrucci, L.; Borbone, F.; Roviello, A.; Maddalena, P. Light-Induced Spiral Mass Transport in Azo-Polymer Films under Vortex-Beam Illumination. *Nat. Commun.* **2012**, *3*, 989.

(15) Ambrosio, A.; Maddalena, P.; Marrucci, L. Molecular Model for Light-Driven Spiral Mass Transport in Azopolymer Films. *Phys. Rev. Lett.* **2013**, *110*, 146102.

(16) Oscurato, S. L.; Salvatore, M.; Borbone, F.; Maddalena, P.; Ambrosio, A. Computer-Generated Holograms for Complex Surface Reliefs on Azopolymer Films. *Sci. Rep.* **2019**, *9*, 6775.

(17) Lim, Y.; Kang, B.; Lee, S. Photo-Transformable Gratings for Augmented Reality. *Adv. Funct. Mater.* **2021**, *31*, 2100839.

(18) Salvatore, M.; Borbone, F.; Oscurato, S. L. Deterministic Realization of Quasicrystal Surface Relief Gratings on Thin Azopolymer Films. *Advanced Materials Interfaces* **2020**, *7*, 1902118.

(19) Oscurato, S. L.; Reda, F.; Salvatore, M.; Borbone, F.; Maddalena, P.; Ambrosio, A. Large-Scale Multiplexed Azopolymer Gratings with Engineered Diffraction Behavior. *Advanced Materials Interfaces* **2021**, *8*, 2101375.

(20) Oscurato, S. L.; Reda, F.; Salvatore, M.; Borbone, F.; Maddalena, P.; Ambrosio, A. Shapeshifting Diffractive Optical Devices. *Laser Photonics Rev.* **2022**, *16*, 2100514.

(21) Kim, K.; Park, H.; Park, K. J.; Park, S. H.; Kim, H. H.; Lee, S. Light-Directed Soft Mass Migration for Micro/Nanophotonics. *Adv. Opt. Mater.* **2019**, *7*, 1900074.

(22) Rekola, H.; Berdin, A.; Fedele, C.; Virkki, M.; Priimagi, A. Digital Holographic Microscopy for Real-Time Observation of Surface-Relief Grating Formation on Azobenzene-Containing Films. *Sci. Rep.* **2020**, *10*, 19642.

(23) Reda, F.; Salvatore, M.; Borbone, F.; Maddalena, P.; Ambrosio, A.; Oscurato, S. L. Varifocal Diffractive Lenses for Multi-Depth Microscope Imaging. *Opt. Express, OE* **2022**, *30*, 12695−12711.

(24) Park, K. J.; Park, J. H.; Huh, J.-H.; Kim, C. H.; Ho, D. H.; Choi, G. H.; Yoo, P. J.; Cho, S. M.; Cho, J. H.; Lee, S. Petal-Inspired Diffractive Grating on a Wavy Surface: Deterministic Fabrications and Applications to Colorizations and LED Devices. *ACS Appl. Mater. Interfaces* **2017**, *9*, 9935−9944.
(25) Choi, J.; Cho, W.; Jung, Y. S.; Kang, H. S.; Kim, H.-T. Direct Fabrication of Micro/Nano-Patterned Surfaces by Vertical-Directional Photofluidization of Azobenzene Materials. *ACS Nano* **2017**, *11*, 1320−1327.
(26) Choi, J.; Cho, W.; Jung, Y. S.; Kang, H. S.; Kim, H.-T. Direct Fabrication of Micro/Nano-Patterned Surfaces by Vertical-Directional Photofluidization of Azobenzene Materials. *ACS Nano* **2017**, *11*, 1320−1327.
(27) Oscurato, S. L.; Borbone, F.; Maddalena, P.; Ambrosio, A. Light-Driven Wettability Tailoring of Azopolymer Surfaces with Reconfigured Three-Dimensional Posts. *ACS Appl. Mater. Interfaces* **2017**, *9*, 30133.
(28) Pirani, F.; Angelini, A.; Ricciardi, S.; Frascella, F.; Descrovi, E. Laser-Induced Anisotropic Wettability on Azopolymeric Micro-Structures. *Appl. Phys. Lett.* **2017**, *110*, 101603.
(29) Salvatore, M.; Borbone, F.; Reda, F.; Maddalena, P.; Oscurato, S. L. Programmable Surface Anisotropy from Polarization-Driven Azopolymer Reconfiguration. *J. Phys. Photonics* **2021**, *3*, 034013.
(30) Fedele, C.; Netti, P.; Cavalli, S. Azobenzene-Based Polymers: Emerging Applications as Cell Culture Platforms. *Biomater. Sci.* **2018**, *6*, 990.
(31) Chang, V. Y.; Fedele, C.; Priimagi, A.; Shishido, A.; Barrett, C. J. Photoreversible Soft Azo Dye Materials: Toward Optical Control of Bio-Interfaces. *Adv. Opt. Mater.* **2019**, *7*, 1900091.
(32) Salvatore, M.; Oscurato, S. L.; D'Albore, M.; Guarino, V.; Zeppetelli, S.; Maddalena, P.; Ambrosio, A.; Ambrosio, L. Quantitative Study of Morphological Features of Stem Cells onto Photopatterned Azopolymer Films. *J. Functional Biomater.* **2020**, *11*, 8.
(33) Lagugné Labarthet, F.; Buffeteau, T.; Sourisseau, C. Analyses of the Diffraction Efficiencies, Birefringence, and Surface Relief Gratings on Azobenzene-Containing Polymer Films. *J. Phys. Chem. B* **1998**, *102*, 2654−2662.
(34) Kulikovska, O.; Gharagozloo-Hubmann, K.; Stumpe, J.; Huey, B. D.; Bliznyuk, V. N. Formation of Surface Relief Grating in Polymers with Pendant Azobenzene Chromophores as Studied by AFM/UFM. *Nanotechnology* **2012**, *23*, 485309.
(35) Nakano, H.; Takahashi, T.; Kadota, T.; Shirota, Y. Formation of a Surface Relief Grating Using a Novel Azobenzene-Based Photochromic Amorphous Molecular Material. *Adv. Mater.* **2002**, *14*, 1157−1160.
(36) Priimagi, A.; Lindfors, K.; Kaivola, M.; Rochon, P. Efficient Surface-Relief Gratings in Hydrogen-Bonded Polymer-Azobenzene Complexes. *ACS Appl. Mater. Interfaces* **2009**, *1*, 1183−1189.
(37) Yadavalli, N. S.; Loebner, S.; Papke, T.; Sava, E.; Hurduc, N.; Santer, S. A Comparative Study of Photoinduced Deformation in Azobenzene Containing Polymer Films. *Soft Matter* **2016**, *12*, 2593−2603.
(38) Borbone, F.; Oscurato, S. L.; Del Sorbo, S.; Pota, F.; Salvatore, M.; Reda, F.; Maddalena, P.; Centore, R.; Ambrosio, A. Enhanced Photoinduced Mass Migration in Supramolecular Azopolymers by H-Bond Driven Positional Constraint. *J. Mater. Chem. C* **2021**, *9*, 11368−11375.
(39) Li, X.; Huang, H.; Wu, B.; Liao, C.; Wang, X. Comparative Study of Photoinduced Surface-Relief-Gratings on Azo Polymer and Azo Molecular Glass Films. *RSC Adv.* **2021**, *11*, 34766−34778.
(40) Audorff, H.; Walker, R.; Kador, L.; Schmidt, H.-W. Polarization Dependence of the Formation of Surface Relief Gratings in Azobenzene-Containing Molecular Glasses. *J. Phys. Chem. B* **2009**, *113*, 3379−3384.
(41) Yadavalli, N. S.; Santer, S. In-Situ Atomic Force Microscopy Study of the Mechanism of Surface Relief Grating Formation in Photosensitive Polymer Films. *J. Appl. Phys.* **2013**, *113*, 224304.
(42) Yadavalli, N. S.; Saphiannikova, M.; Santer, S. Photosensitive Response of Azobenzene Containing Films towards Pure Intensity or Polarization Interference Patterns. *Appl. Phys. Lett.* **2014**, *105*, 051601.
(43) Priimagi, A.; Saccone, M.; Cavallo, G.; Shishido, A.; Pilati, T.; Metrangolo, P.; Resnati, G. Photoalignment and Surface-Relief-Grating Formation Are Efficiently Combined in Low-Molecular-Weight Halogen-Bonded Complexes. *Adv. Mater.* **2012**, *24*, OP345−OP352.
(44) Kulikovska, O.; Goldenberg, L. M.; Stumpe, J. Supramolecular Azobenzene-Based Materials for Optical Generation of Microstructures. *Chem. Mater.* **2007**, *19*, 3343−3348.
(45) Goldenberg, L. M.; Kulikovsky, L.; Kulikovska, O.; Stumpe, J. Extremely High Patterning Efficiency in Easily Made Azobenzene-Containing Polymer Films. *J. Mater. Chem.* **2009**, *19*, 6103−6105.
(46) Lim, Y.; Kang, B.; Hong, S. J.; Son, H.; Im, E.; Bang, J.; Lee, S. A Field Guide to Azopolymeric Optical Fourier Surfaces and Augmented Reality. *Adv. Funct. Mater.* **2021**, *31*, 2104105.
(47) Moharam, M. G.; Gaylord, T. K. Rigorous Coupled-Wave Analysis of Planar-Grating Diffraction. *J. Opt. Soc. Am., JOSA* **1981**, *71*, 811−818.
(48) Maystre, D. Rigorous Vector Theories of Diffraction Gratings. In *Progress in Optics*; Wolf, E., Ed.; Elsevier, 1984; Vol. *21*, Chapter I, pp 1−67.
(49) Moharam, M. G.; Pommet, D. A.; Grann, E. B.; Gaylord, T. K. Stable Implementation of the Rigorous Coupled-Wave Analysis for Surface-Relief Gratings: Enhanced Transmittance Matrix Approach. *J. Opt. Soc. Am. A, JOSAA* **1995**, *12*, 1077−1086.
(50) Yang, K.; Yang, S.; Wang, X.; Kumar, J. Enhancing the Inscription Rate of Surface Relief Gratings with an Incoherent Assisting Light Beam. *Appl. Phys. Lett.* **2004**, *84*, 4517−4519.
(51) Rahmouni, A.; Bougdid, Y.; Moujdi, S.; Nesterenko, D. V.; Sekkat, Z. Photoassisted Holography in Azo Dye Doped Polymer Films. *J. Phys. Chem. B* **2016**, *120*, 11317−11322.
(52) Harvey, J. E.; Krywonos, A.; Bogunovic, D. Nonparaxial Scalar Treatment of Sinusoidal Phase Gratings. *J. Opt. Soc. Am. A, JOSAA* **2006**, *23*, 858−865.
(53) Harvey, J. E.; Pfisterer, R. N. Understanding Diffraction Grating Behavior: Including Conical Diffraction and Rayleigh Anomalies from Transmission Gratings. *Opt. Eng.* **2019**, *58*, 087105.

https://doi.org/10.1021/acsmaterialslett.2c00171
ACS Materials Lett. 2022, 4, 953−959

Publication V

S. L. Oscurato, F. Reda, M. Salvatore, F. Borbone, P. Maddalena, and A. Ambrosio

Shapeshifting diffractive optical devices

Reprinted from

Laser & Photonics Reviews 16(4), 2100514 (2022)

Shapeshifting Diffractive Optical Devices

Stefano L. Oscurato, Francesco Reda, Marcella Salvatore, Fabio Borbone, Pasqualino Maddalena, and Antonio Ambrosio**

In optical devices like diffraction gratings and Fresnel lenses, light wavefront is engineered through the structuring of device surface morphology, within thicknesses comparable to the light wavelength. Fabrication of such diffractive optical elements involves highly accurate multistep lithographic processes that in fact set into stone both the surface morphology and optical functionality, resulting in intrinsically static devices. In this work, this fundamental limitation is overcome by introducing shapeshifting diffractive optical elements directly written on an erasable photoresponsive material, whose morphology can be changed in real time to provide different on-demand optical functionalities. First a lithographic configuration that allows writing/erasing cycles of aligned optical elements directly in the light path is developed. Then, the realization of complex diffractive gratings with arbitrary combinations of grating vectors is shown. Finally, a shapeshifting diffractive lens that is reconfigured in the light-path in order to change the imaging parameters of an optical system is demonstrated. The approach leapfrogs the state-of-the-art realization of optical Fourier surfaces by adding on-demand reconfiguration to the potential use in emerging areas in photonics, like transformation and planar optics.

1. Introduction

Diffraction gratings[1] are among the first optical devices ever realized. Light structuring through gratings results from the periodic phase modulation accumulated across the grating profile.[2,3] A diffraction grating made of periodically spaced grooves produces, far from the grating, a line of light dots (diffraction orders) along a direction perpendicular to the grating grooves (grating vector). Although simple, diffraction gratings represent the first example of structuring light by means of an engineered phase modulation.[4] This concept is at the core of holography and Fourier optics (when the field structuring can be considered as only due to the propagation of component plane waves).[3] Moreover, phase masks can be multiplexed, so gratings with different Fourier components can be combined together to achieve more complex bi-dimensional light structuring.[5,6]

Diffraction gratings represent also the first example of planar optics.[7,8] For a grating with sinusoidal profile made of a 1.7 refractive index transparent material, the maximum diffraction efficiency is achieved with a morphology modulation of 0.84 times the illuminating light wavelength (i.e., only 531 nm thickness for an illuminating light of 633 nm).[4]

Other diffractive optical elements (DOEs) of common use are Fresnel lenses, in practice, cylindrically symmetric gratings optimized to focus collimated light at a design distance.[9] Such lenses, used for instance in lighthouses, become handy to reduce space and weight constraints related to standard refractive lenses.[10–12]

Once the optical parameters of the material are fixed, the optical functionality of a DOE is controlled through the device morphology, in case of a grating: spacing, height and profile of the grooves. Such design principle has been continuously developed for DOE manufacturing, resulting in optimized

S. L. Oscurato, F. Reda, M. Salvatore, P. Maddalena
Department of Physics "E. Pancini"
University of Naples "Federico II"
Complesso Universitario di Monte Sant'Angelo
Via Cintia, Naples 80126, Italy
E-mail: stefanoluigi.oscurato@unina.it; francesco.reda@unina.it; marcella.salvatore@unina.it; pasqualino.maddalena@unina.it

The ORCID identification number(s) for the author(s) of this article can be found under https://doi.org/10.1002/lpor.202100514

DOI: 10.1002/lpor.202100514

S. L. Oscurato, M. Salvatore, P. Maddalena
Centro Servizi Metrologici e tecnologici Avanzati (CeSMA)
University of Naples "Federico II"
Complesso Universitario di Monte Sant'Angelo
Via Cintia 21, Naples 80126, Italy

F. Borbone
Department of Chemical Sciences
University of Naples "Federico II"
Complesso Universitario di Monte Sant'Angelo
Via Cintia, Naples 80126, Italy
E-mail: fabio.borbone@unina.it

S. L. Oscurato, F. Borbone, P. Maddalena, A. Ambrosio
CNST@POLIMI—Fondazione Istituto Italiano di Tecnologia
Via Pascoli 70, Milan 20133, Italy
E-mail: antonio.ambrosio@iit.it

elements for specific applications. An interesting discussion about advanced diffraction elements for spectroscopy is provided in a recent review.[13] However, most of the standard DOE manufacturing techniques consist of at least two steps, typically a molding process, that involves the patterning of a lithographic material with the target surface geometry, followed by a development stage requiring a selective etching of a substrate, along with an eventual additional surface coating step in case of reflective DOEs.[4] Direct machining technologies, instead, allow direct DOE fabrication by selectively grooving a metallic or dielectric plate through ruling engines or ion beam etching, but they provide coarser surface profile control.[14] Only recently, a direct grayscale lithographic method based on thermal scanning probe lithography has been successfully employed to realize accurate complex diffractive surfaces on a polymer film.[6] All the mentioned fabrication approaches, however, result in static DOEs, with surface geometry and optical functionality defined once for all during device manufacture. Here we report, instead, the direct realization of planar diffractive optical elements whose surface morphology can be changed in real time to provide different on-demand optical functionalities.

Phase and amplitude masks for diffractive optics can be also realized with different approaches. On one hand, there are fast but pixeled modulators, spanning from commercially available liquid-crystal-based spatial light modulators (SLMs) or digital mirror devices,[15,16] to recent 2D materials devices.[17] On the other hand, in the last ten years, research on optical metasurfaces exploded, providing new devices with unprecedented modulation possibilities and resolution[8,18,19] but, in fact, much limited in terms of optical tunability.[20–22]

In this work, we develop a grayscale holographic photolithography scheme employing a reconfigurable polymer to realize diffractive optical elements that can be reshaped directly in the light-path to provide a specific optical functionality; in fact, shapeshifting diffractive optical elements that do not need any additional lithographic process (e.g., resist development, substrate etching, surface coating, etc.) for tunable and reprogrammable practical operation. Complex gratings are showed together with a reconfigurable monochromator. Finally, variable focal lengths diffractive lenses are demonstrated that allow magnification tuning of a complex optical system.

2. Results

The central equation to design within the realm of the scalar Fourier optics a phase mask $\varphi(x, y)$ for the operation of a transmissive DOE is[3,4]

$$\varphi\ (x, y) = k_0\ \left(n - n_0\right) h\,(x, y) \tag{1}$$

Once the refractive indices of the grating material (n) and the surrounding material (n_0) are fixed, together with the illuminating light wavelength λ_0 (wavevector $k_0 = 2\pi/\lambda_0$), the phase mask, and hence the output diffracted field from the DOE, is entirely defined by the surface morphology $h(x,y)$. For an operating DOE, the surface profile needs to be faithfully transferred on a dielectric substrate using accurate lithographic processes. To this aim, we use here a polymer containing azobenzene molecules[23–25] (or simply *azopolymer*) that requires only a single photostructuration step to directly realize the working phase mask (details about the polymer can be found in the Experimental Section). When illuminated by a specific light pattern, the surface of an azopolymer film is directly deformed by a reversible light-induced material transport, resulting in a morphology that follows the illuminating light distribution.[26–31] For example, illuminating such polymer with a 2D light pattern with sinusoidal profile, results in a surface relief with similar profile, i.e., a diffraction grating (see also Figure S4, Supporting Information). In this case, the periodic light distribution can be as simple as that produced by two interfering light beams.[32–35] The same configuration has been demonstrated to be suitable also for the direct realization of more complex multiplexed gratings.[36–43] In our experiment we used, instead, a holographic setup[44] that projects arbitrary grayscale light patterns on the polymer surface to realize the profile of complex DOEs. With our system, the surface morphology is analytically calculated and converted in a grayscale bitmap image that defines the holographic light pattern irradiated on the polymer surface for any designed DOE. Such light patterns can also be changed in time by simply updating the bitmap image with a new and completely independent one, making the system ready for dynamical surface structuration of a photo-transformable material as the azopolymer we use. The details of our experimental setup can be found in the Experimental Section.

Figure 1 shows the principle of dynamical holographic surface structuration process by realizing, as a first simple DOE, a transformable (by light) sinusoidal diffraction grating (see Figure S2, Supporting Information). The writing beam is a holographically patterned laser beam with a wavelength of 491 nm (circularly polarized). The generated light pattern is projected onto the polymer film surface by means of a 50X long working distance objective (Figure 1A). The formation of the diffraction grating on the surface can be monitored in real time by detecting the light power in the first diffraction order of a probe laser beam at wavelength of 633 nm, collimated through the same objective. Figure 1E shows the rising diffraction efficiency during the writing process (see also Movie S1, Supporting Information). In our configuration, another circularly polarized laser beam with wavelength of 405 nm also illuminates the grating area, from the substrate side. The function of the 405 nm beam is twofold (see also the Experimental Section): at low power density (≈0.5 W cm^{-2}) it keeps *active* the photosensitive molecules in the polymer, avoiding partial saturation, assisting and speeding-up the writing process;[45–47] at high power density (≈1.0 W cm^{-2}), the violet beam erases the polymer surface[48–51] (see also Figure S5, Supporting Information), that is then ready to write the next DOE. It is important to note that, once the writing process is concluded, the realized DOEs are still stable for years at room temperature and ambient illumination conditions, due to structural stability of the patterned surfaces and the absence of preferential orientation of the photoisomerizable molecules during the writing (see also Figure S6, Supporting Information). Figure 1F,H shows the atomic force microscope (AFM) micrograph of the polymer film surface after writing and after erasing, respectively. Figure 1E also shows the decreasing of the diffraction efficiency over the erasing process: both the morphology (see also Figure S7, Supporting Information) and diffraction residuals are negligible, demonstrating fast (≈10 s) and complete surface erasure. At this point, a new DOE can be realized on the film surface; for instance, a new grat-

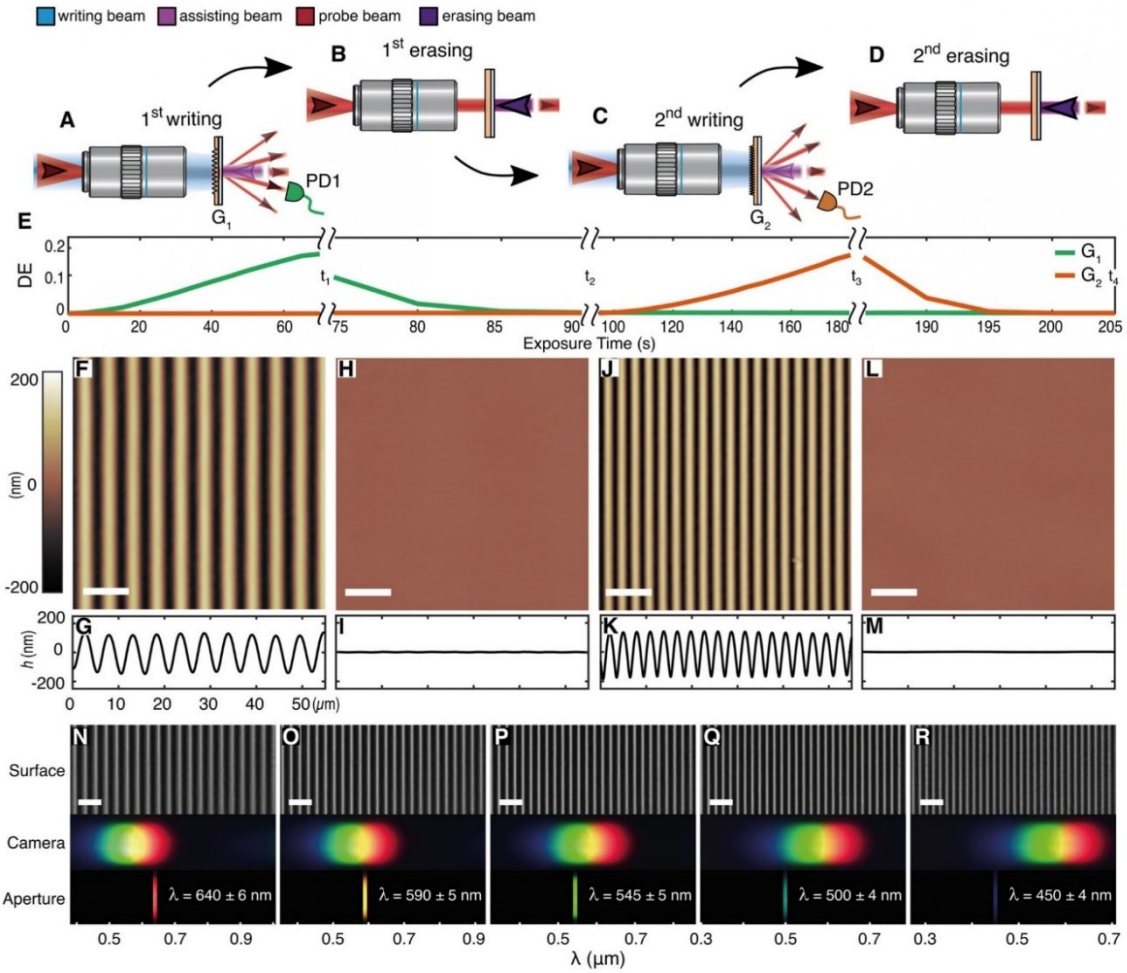

Figure 1. Direct all-optical realization of reconfigurable diffraction gratings. A–D) Schematic illustrations of optical configurations used for the writing, erasing, and the real-time monitoring of dynamically reconfigurable diffraction gratings. In the writing steps A,C), the writing beam (light blue color) illuminates a photoresist area (≈200 μm in diameter) with holographically-controlled sinusoidal intensity patterns through a 50X (NA = 0.55) microscope objective. A collimated beam (λ = 405 nm) is used at low intensity to enhance the surface structuration dynamics (light violet beam) and at higher intensity (dark violet beam) in the erasing steps B,D) when the writing beam is switched off. E) Time-evolving first-order diffraction efficiency curves recorded by two photodiodes (PD1 and PD2 shown in panels A and C) for a He–Ne probe beam (red beam) during the reconfiguration of two gratings of different periodicity (green curve for G_1 and orange curve for G_2). F–M) AFM micrographs and relative horizontal topographic profiles of the surface at the instants (t_i) of the time sequence in E). Scale bars in AFM images are 10 μm. N–R) Dynamical tuning of diffraction dispersion obtained through multiple grating periodicity reconfigurations. Top panels show optical micrographs of the surface (scale bar 10 μm). The colored diffraction patterns produced by the surface from a white LED source are imaged by a CCD camera in the surface Fourier conjugate plane. A fixed aperture on the CCD camera intercepts color bands of shifting central wavelength.

ing with different periodicity (Figure 1J), to be later eventually erased again (Figure 1L) and morphed into any other DOE (see Movie S3, Supporting Information). In our experimental conditions, we noticed no significant degradation of the surface for at least 15 writing-erasing cycles (see also Figure S8, Supporting Information).

As next step, we tested the possibility of having reconfigurable DOEs in the light-path of an operating optical device. To this aim, we realized the proof-of-concept of a reconfigurable monochromator (see also Movie S2, Supporting Information). In this case, the light diffracted by the grating is detected by means of a CCD camera. The probe beam is a white light beam provided by a LED. Figure 1N–R shows the effect of reshaping the grating periodicity. As expected, the smaller the grating pitch, the higher the diffractive power and the separation between the light spectral components. In this case, changing the DOE directly in the light-path allows real time tuning of the spectrometer resolution through the grating dispersion. In the same configuration, fixing an aperture on the camera (same as using a physical aperture and a point detector) allows to observe how the wavelength diffracted

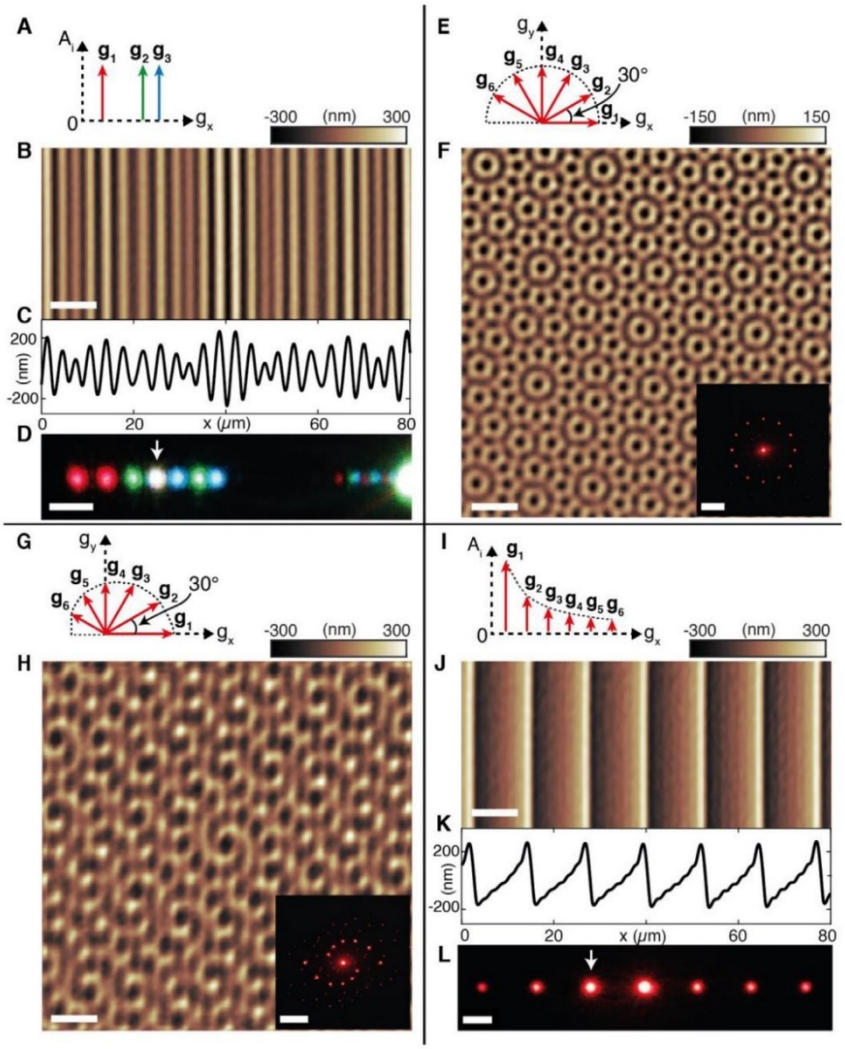

Figure 2. Diffraction gratings with arbitrary combination of grating vectors. A–D) Three-component RGB diffraction grating. A) The surface is designed as superposition of three sinusoids of periodicity $\Lambda_{x,i}$ (grating vectors $g_{x,i} = 2\pi/\Lambda_{x,i}$) and equal amplitude A_i. Measured AFM micrograph B) and topographic profile C) of the surface. D) Photograph of the far-field diffraction pattern produced by the surface upon simultaneous illumination with three collinear laser beams at design wavelengths. The white arrow indicates the RGB diffraction order. E–H) 2D diffraction gratings obtained as superposition of six sinusoidal functions. F,H) AFM micrographs of quasicrystal surfaces designed with grating vector distributions schematized in E,G), respectively. Photographs of far-field diffraction patterns, produced (on a screen at distance $d = 8.5$ cm) when the diffractive elements are illuminated with a He–Ne laser beam, are shown as inset (scalebar 1.0 cm). I–L) Blazed grating realized as superposition of six grating vectors of length $g_{x,i} = i*g_1$ and amplitudes $A_i \approx A_1/i$ I). J) AFM and K) topography of the surface. The grating is designed to direct most of the diffracted light in one of the first diffraction orders (highlighted by an arrow in the diffraction photograph in L)). The power in the design diffraction order is more than 6 times higher than in the other first order. Scale bars in AFM micrographs are 10 μm; scale bars in D and L are 0.2 cm.

in the detection area changes as a function of the realized grating. This last configuration works in fact as a tunable monochromator, without any moving part, that can be used together with a broadband source to select an illuminating wavelength band while preserving the original alignment of the entire system.

Another unique characteristic of our lithographic approach stands in the noise reduction of the holographic light pattern and the resulting enhanced quality of the morphology produced on the azopolymer surface. Usually, light structuring through digital holography suffers of a random speckles distribution that degrades the contrast and limits the achievable gray levels in the projected light pattern, also compromising the definition of small features. To minimize such effects, we continuously refresh the light pattern at a refresh rate of 20 Hz. Each new light pattern has a random speckle distribution that averages down during the writing time, improving in fact the quality of the structured polymer morphology.[44] For instance, in order to realize a grating with a single vector (like that of Figure 1F–J), we expose the

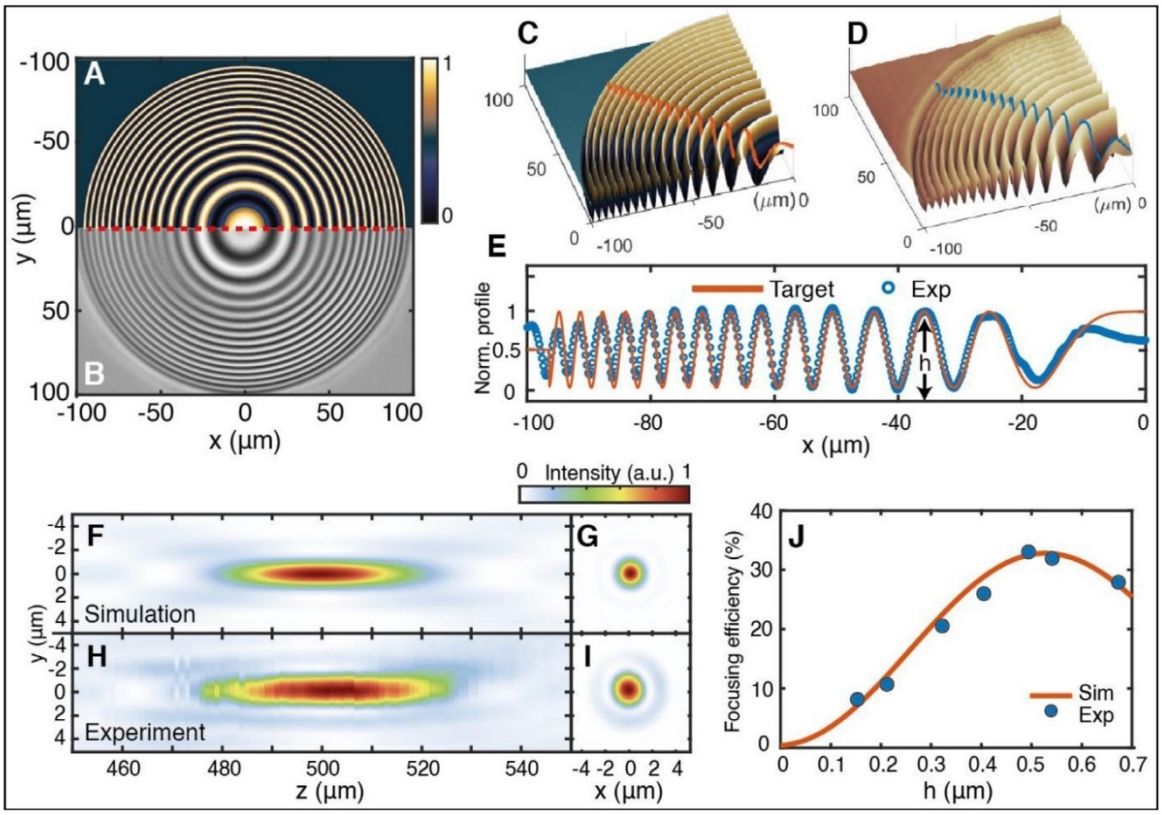

Figure 3. Diffractive lens. A) Target surface (normalized) of a Gabor phase zone plate, designed to focus light of wavelength $\lambda = 633$ nm at distance $f_0 = 500$ μm from the surface. B) Scanning electron micrographs (SEM) of the holographically structured photoresist surface. C,D) 3D views for a section of the target C) and AFM measured D) surface. E) Target and experimental profiles traced along the radial directions shown in C) and D), respectively. F–I) Comparison of the normalized axial F) and transverse G) Point-Spread Functions (PSFs), simulated for the target lens profile in A) through Fresnel diffraction integral, and experimental axial H) and lateral I) PSFs produced by the experimental surface in B) under illumination with a collimated beam at design wavelength. J) Comparison of simulated and experimental focusing diffraction efficiency as function of average surface modulation amplitude h (defined in E)).

polymer to the required light pattern with random speckle distribution changing every 50 ms over the writing time. The writing beam power can be set to values that make the polymer structuring dynamics slow enough to respond in fact to an averaged light pattern, allowing the possibility of inscribing on the film surface, in a single exposure step, the morphology of complex grayscale holograms.

This approach can be used for example to realize, with an identical experimental configuration as the previous one, DOEs with any distribution of grating vectors, directly encoded in the analytical design of grayscale digital holograms (see also Figure S9, Supporting Information). **Figure 2** shows some examples. First a RGB grating,[40,42] designed as even superposition of three grating vectors (Figure 2A), is realized (Figure 2B) to diffract three different wavelengths ($\lambda_1 = 633$ nm, $\lambda_2 = 532$ nm, and $\lambda_3 = 488$ nm) into the same diffraction order. The surface profile (Figure 2C), realized on the polymer film in the single grayscale holographic exposure step, faithfully match the targeted DOE profile (see also Figure S9, Supporting Information), that correctly produce the designed white diffraction spot (Figure 2D).

Then, the same design can be extended even to more complex Optical Fourier Surfaces.[6] Figure 2F shows a 2D quasicrystal structure[52] characterized by 6 grating vectors g_i, differently oriented in the transverse plane (Figure 2E). Figure 2H shows the effect of having same vectors orientation as Figure 2F but different vectors lengths (different periodicity) in the designed superposition of sinusoidal functions. This results into a spiral quasicrystal DOE, whose fabrication would be very demanding in standard sequential interference lithography.[39,43]

Additionally, Figure 2I-L shows the realization of a blazed grating that can diffract a probe beam into a preferential diffraction order. In this case, the blazed structure results from combining 6 gratings vectors with same direction but different lengths and weighted amplitudes. Besides being reconfigurable, DOE structures like those showed in Figure 2 are comparable with the state of the art of the most recent multiplexed structures obtained by static and serial lithography techniques.[6]

Related to the quality of the obtained structures, it is to be considered that the polymer that we used is fully compatible with a further lithographical step, where the obtained morphology

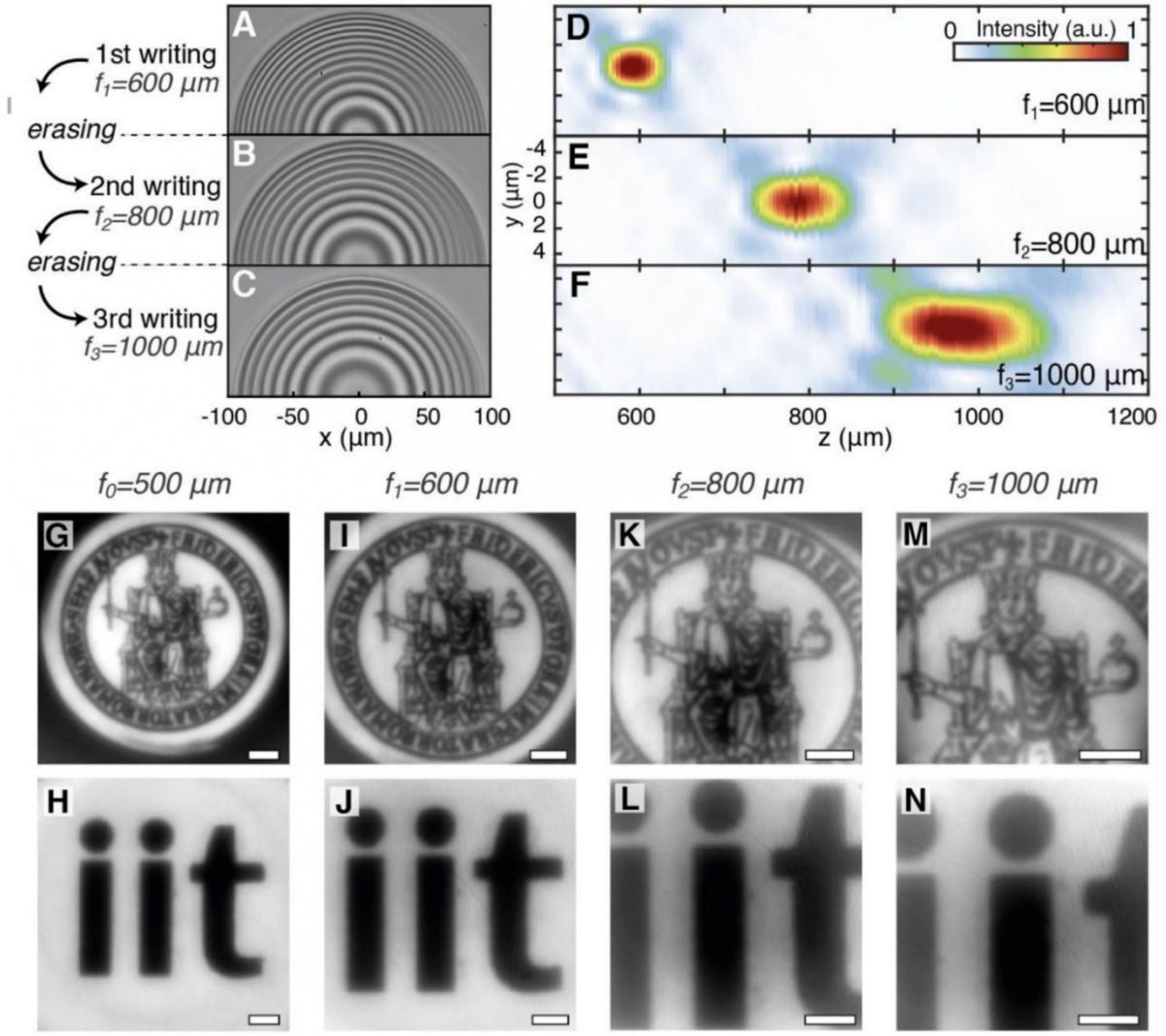

Figure 4. Reconfigurable diffractive lenses in the light-path of dynamical imaging systems. A–C) SEM micrographs of a fixed photoresist surface area, holographically restructured as a diffractive lens of three different focal lengths f_i. D–F) axial PSFs measured at each reconfiguration step for lenses in A–C). The focal position axially translates according to the reconfigured surface geometry. G–N) Optical images of transparencies depicting our Institution logos produced at increasing magnifications (1.0X,1.2X,1.67X, and 2.0X), upon the in-place reconfiguration of the diffractive lens focal length. Scale bars are 2.0 and 5.0 mm in top and bottom panels, respectively.

can be transferred to a PDMS stamp for high quality replicas (see also Figure S9, Supporting Information) that provides our process with technological significance as new photolithography technique to be applied to optical systems as well as functionalized surfaces and microfluidics.[28]

To further highlight the potential of our approach, in **Figures 3** and **4** we show the realization of reconfigurable diffraction lenses working in real imaging systems. DOEs with such profiles are known as Gabor phase zone plates[53] (details about such design can be found in the Experimental Section) and have been out of reach of previous experiments on azopolymers.[54,55] Figure 3A shows the computed profile for a lens with 500 μm focal length and numerical aperture NA = 0.19. The light distribution in the yz plane around the focal position can be calculated through the Fresnel diffraction integral[3] (see also the Experimental Section) The calculated diffraction limited spot of this lens has FWHM of ≈1.7 μm when illuminated by a beam with 633 nm wavelength (Figure 3F). The simulated features are well reproduced in the measured intensity distribution (Figure 3H,I), obtained from the experimental diffractive lens shown in Figure 3B. Figure 3J also compares the predicted and realized efficiency for this DOE as a function of average grooves height, achieved in different ex-

posure times. For this planar lens, the predicted maximum efficiency of ≈34% is achieved in 50s exposure (see also Figures S10 and S11, Supporting Information).

Figure 4 demonstrates the possibility of re-shaping our diffractive lens in real-time in the aligned optical system. Figure 4A–C shows three lenses of different focal length realized one after the other in the same polymer area. The respective experimental focal field distributions are reported in Figure 4D–F: as the focal length increases according to the design, the numerical aperture decreases and the focused light spot increases according to the fixed diameter of our lenses (see also the Experimental Section). Notably, the focal length reconfiguration resulting from the surface transformation demonstrated in Figure 4D–F, achieves about 70% shift of the focal position, without involving any mechanical movement in the system. This large deformation range is comparable to electrically tunable LC-based DOE lenses,[16,56] characterized by a faster switching speed, which comes at the expenses of complex electrode configurations, reduced spatial resolution and significantly larger thicknesses with respect to our flat diffractive devices.

The tunable shapeshifting lenses demonstrated by means of our approach can be used to realize an imaging system able to dynamically provide different magnifications of extended scenes. Standard zooming systems require the axial movement of at least two lenses to produce a magnified image in the camera plane. In our system instead one of the mechanical motions can be replaced by the lens reconfiguration into the needed new optical element (see also Figure S12, Supporting Information). This is evident in the magnified images of our Institutions logos presented in Figure 4G–N. In this case, one lens of the optical system is physically shifted to regain the focal position while changing on-demand the focal length of the reconfigurable diffractive lens. The observed magnification factors reproduce the expected values from focal lengths ratios: $f_1/f_0 = 1.2$ in Figure 4I,J; $f_2/f_0 = 1.6$ for Figure 4K,L; $f_3/f_0 = 2$ for Figure 4M,N.

An important aspect to highlight is that our devices are just made of a structured surface, thinner than the illuminating light wavelength, on a polymer film spin coated on a glass coverslip. The photolithography process to obtain such lightweight and planar devices is fully scalable and compatible with raster scanning method for increased throughput and with curved substrates, opening new possibilities in functionalizing surfaces of objects as diverse as wearable items and vehicle parts.

3. Conclusions

In conclusion, we have proved that diffraction optical elements with efficiency equal to the theoretical efficiency can be fabricated by direct structuring of the surface of a photosensitive polymer, avoiding any further lithographic step. The realized gratings and lenses can be reshaped completely while aligned in the optical setup. Grating periodicity can be changed; lenses focal length can be tuned; one optical element can be morphed into another optical element with completely different optical functionality, without affecting the alignment of the specific optical setup. More than 100 years after Michelson was reporting about optical effects from imperfect gratings, we show that it is possible to realize optical elements with theory-matching efficiency and practical use, reconfigurable on demand right where and when needed.

4. Experimental Section

Azopolymer Synthesis and Characterization: The photoresponsive material used in this work is an azobenzene-containing polymer (azopolymer) in amorphous state. All reagents were purchased from Merck and used without further purification. The azopolymer was synthesized, purified, and characterized as previously reported ($M_w = 27\,000$; phase sequence: Glass 67 °C Nematic 113 °C Isotropic; $\lambda_{max} = 350$ nm).[26,28] The solution for film deposition was prepared by dissolving (70 mg) the polymer in (0.50 mL) of 1,1,2,2-tetrachloroethane and filtered on 0.2 µm PTFE membrane filters. The desired film thickness (typically 1.0 ± 0.1 µm) was obtained by spin coating the solution on 24 × 60 mm cover slides at 300 rpm for 4 min. In the final stage, the samples were kept under vacuum at room temperature for 24 h to remove solvent traces.

Refractive index of the fabricated film was measured via ellipsometry. Measured values at some relevant wavelengths (633, 532, 488 nm) are: $n_{633} = 1.70$; $n_{532} = 1.74$; $n_{488} = 1.78$.

Holographic Illumination Setup: The experimental configuration for the azopolymer surface photopatterning is based on a phase-only Computer-Generated Holograms (CGHs) system. Its schematic representation is shown in Figure S1 (Supporting Information). A laser diode source (Cobolt Calypso) emits a TEM_{00} beam at wavelength $\lambda = 491$ nm and, after a beam expander, is phase-modulated by a computer-controlled reflective phase-only Spatial Light Modulator (SLM, Holoeye Pluto). The modulated beam is propagated through a 4f lenses system with the input plane located in the SLM plane. The output plane coincides with the back focal plane of an infinity-corrected long-working distance 50X objective (Mitutoyo), with numerical aperture NA = 0.55. This configuration allows the reconstruction of a structured intensity pattern in the focal plane of the objective (where the azopolymer is placed).

Arbitrary intensity patterns can be generated imposing the proper phase profile (kinoform) for the beam in the SLM plane. The phase hologram is calculated according to the Fourier transform relations[3] existing between 4f system conjugate planes. The focal lengths of the lenses L_3 and L_4 (Figure S1, Supporting Information) are chosen in order to maximize the spatial resolution in the hologram reconstruction planes.[44] This choice also defines the diameter (≈200 µm) of the accessible circular area in the objective front focal plane, which can be used to structure the photoresist surface in a single illumination step. The position of the sample near the objective focal region is accurately controlled by means of a x-y-z translation stage. Average intensity in the range 12.7–14.0 W cm^{-2} and circular polarization are used for the structuration of the azopolymer surface. For visual inspection, and proper focusing of the holographic pattern on the photoresist surface, a beam splitter placed in the light-path redirects the light retroreflected by the surface and re-collimated through the objective toward a tube lens. This lens forms an image of the holographic pattern in the second focal plane, where a CCD camera is positioned to observe the surface plane in real-time (Figure S1, Supporting Information).

When needed, an additional diode laser beam at 405 nm illuminates the photoresist film from the substrate (glass microscope coverslip) side. The beam has circular polarization and set on different intensity levels depending on its intended functionality. When the intensity is in the range 0.4–0.8 W cm^{-2}, the beam favors the surface structuring process, acting as a writing assisting beam. At intensity higher than 0.9 W cm^{-2}, its absorption causes the erasure of previously inscribed surface structures, acting as an erasing beam (see also Figure S5, Supporting Information).

For the DOEs with optimized diffraction efficiency demonstrated in Figure 3 (and Figure S4, Supporting Information) a total exposure time of 50 s is used over an area of 3.14×10^3 µm^2. This provides an estimation of processing throughput of our structuration method of ≈630 µm^2 s^{-1}.

Algorithm for Calculation of Phase-Only Holograms: The Iterative Fourier transform algorithm (IFTA) used for the calculation of the phase profile of the writing beam in the SLM plane is the mixed region amplitude freedom (MRAF) algorithm,[57] based on an extension of the standard Gerchberg–Saxton (GS) algorithm.[58] The IFTA has been implemented in MATLAB, using Fast Fourier Transform (FFT). In the first step of the calculation, a target 8-bit grayscale image (see also Figure S2, Supporting Information), representing the desired intensity pattern (e.g., sinusoidal)

to be reconstructed in the polymer plane, is analytically defined. Next, with an iterative calculation loop, based on direct and inverse FFTs, the algorithm returns a grayscale (8-bit, 256 phase levels) image (1080 × 1920 px) for the phase profile (the *kinoform*) to be imposed on the writing beam in the SLM plane. In the MRAF algorithm, the reconstruction plane is divided in two regions: one that is considered important, called signal region, that corresponds to the area of sample effectively illuminated; the region outside that domain (the noise region) is used to spatially redirect some of the calculation noise intrinsically related to IFTA methods (speckle, ghost hologram, etc.) in the periphery of the system field of view. A single parameter (the mixing parameter) in MRAF[57] controls the relative fraction of light power directed in each of the two domains of the reconstruction plane. An optimum value for the mixing parameter was selected to maximize intensity contrast in the target patterns. An iris placed in the intermediated hologram reconstruction plane (Figure S1, Supporting Information) is used to filter out the noise region.

Optical Real-Time Characterization of Structured Surfaces: For real-time observation of the polymer surfaces during the structuration process, the holographic setup was integrated with a collimated white LED source for a bright-field transmission microscopy system (see also Figure S3(A) (Supporting Information)). Scattered light from the sample surface is collected by the objective. Real time image of the sample surface is obtained with the same configuration for holographic pattern acquisition. The retroreflected holographic pattern, propagating along the same light path, can be eventually discarded in the imaging using a low pass filter before the camera.

For the collection of real-time diffraction patterns shown in Figure 1 and in Movie S2 (Supporting Information), a second beam splitter redirects part of the white light emerging from the tube lens through a positive lens realizing a 2f configuration with the tube lens. A second CCD camera, positioned in the second focal plane of the lens, provides a Fourier transform image of the structured surface, corresponding to the far-field diffraction pattern.

A second configuration, shown in Figure S3(B) (Supporting Information), allows to produce real-time diffraction patterns from photoresist structured surface using a He–Ne as probe beam, whose wavelength (λ = 633 nm) lies outside the absorption band of the azopolymer,[26,28] not interfering then with the writing process. The probe beam is focused in the back focal plane of the objective using the beam splitter and the tube lens. The collimated beam, emerging from the objective, illuminates the same photoresist area simultaneously structured by the holographic writing beam. For the time-dependent analysis of diffraction efficiencies produced by 1D diffraction gratings (Figure 1E), photodiodes are used to measure the light power of the probe beam diffracted in far-field in the first diffraction order.

Morphological Characterization of Structured Surfaces: Topographic characterization of polymer surfaces is performed using AFM and SEM.

For AFM measurements, a WITec Alpha RS300 microscope is used. The AFM is operated in tapping mode using a cantilever with 75 kHz resonance frequency and nominal force constant of 2.8 N m^{-1}. AFM tips (Arrow FM type from Nano World), with nominal radius of curvature of ≈10 nm, are used in all the experiments. The maximum scanned area has a size of 100 × 100 μm^2.

Scanning electron microscopy images are acquired with a field-emission gun (FEG–SEM) FEI/ThermoFisher Nova NanoSEM 450 microscope. Samples are sputtered with a layer of Au/Pd using a Denton Vacuum Desk V TSC coating system prior to observation.

Design and Diffraction Properties of Complex Diffraction Gratings: The scalar wavefront modulation provided by thin transmissive DOEs can be described by a phase-only space-dependent complex transmission function $t(x,y)$, able to modulate an incident light field. For an incident monochromatic plane wave (at wavelength λ), propagating through the structured DOE layer, the modulation function is

$$t(x,y) = e^{i\varphi(x,y)} = e^{ik_0(n-n_0)s(x,y)h} \tag{2}$$

The phase modulation $\varphi(x,y)$ is the result of the differences in the optical path that the incident monochromatic plane wave accumulates with respect to the surrounding medium (air in the case $n_s = n_0 = 1$) as the wave propagates in DOE medium of refractive index n. In Equation (1), $k_0 = 2\pi/\lambda = \omega/c$ is the wavevector of the incident plane and the surface relief geometry is described using a normalized structural function $s(x,y)$ (with $s(x,y)\in[0,1]$), defining the DOE pattern, and the total relief amplitude h, which defines the maximum phase modulation depth provided by the DOE.

For the complex diffraction gratings reported in Figure 2, the structural function $s(x,y)$ is designed as sum on of N sinusoidal patterns

$$s(x,y) = \frac{1}{2A}\sum_{i=1}^{N} A_i\left(1+\sin\left(\frac{2\pi x}{\Lambda_{xi}}+\frac{2\pi y}{\Lambda_{yi}}+\varphi_i\right)\right) \tag{3}$$

Here, $\Lambda_i = (\Lambda_{xi}{}^2+\Lambda_{yi}{}^2)^{1/2}$ is the spatial periodicity of the i-th sinusoidal pattern, characterized by a grating vector oriented at the angle $\gamma_i = \mathrm{atan}(\Lambda_{yi}/\Lambda_{xi})$ with respect to the x direction, A_i is the amplitude weight for each sinusoid in the superposition, $A = \sum_{i=1}^{N} A_i$ and φ_i are relative phases between sinusoids. The field diffracted by a phase mask described by Equations (1) and (2) can be obtained by expanding the transmission function $t(x,y)$ in Fourier series

$$t(x,y) = e^{ik_0(n-1)s(x,y)h} = \sum_{m,q=-\infty}^{m,q=+\infty} f_{mq}\, e^{i\left(m\frac{2\pi x}{\Lambda_m}+q\frac{2\pi y}{\Lambda_q}\right)} \tag{4}$$

where f_{mq} are the complex Fourier coefficients and $g_m = 1/\Lambda_m$ and $g_q = 1/\Lambda_q$ are the coordinates in the Fourier space. The solution of the scalar Helmholtz equation for a plane wave of amplitude U_0, incident on DOE surface with and angle θ_i, is[59]

$$U(x,y,z) = U_0 \sum_{m,q=-\infty}^{m,q=+\infty} f_{mq}\, e^{i\left(k_0\sin\theta_i+m\frac{2\pi x}{\Lambda_m}+q\frac{2\pi y}{\Lambda_q}\right)} \times e^{iz\sqrt{k_0^2-\left(k_0\sin\theta_i+m\frac{2\pi}{\Lambda_m}+q\frac{2\pi}{\Lambda_q}\right)^2}} \tag{5}$$

Only a finite number of diffraction orders, (defined by the indices (m,q)) which make the quantity $k_0^2-(k_0\sin\theta_i+m\frac{2\pi}{\Lambda_m}+q\frac{2\pi}{\Lambda_q})^2 > 0$ (depending also on the periodicities of the superimposed sinusoids in $s(x,y)$), propagates in far-field from the surfaces as plane waves. All the other possible (infinite) orders give rise to evanescent waves localized at the DOE surface. Each term of the expansion (4) carries a power $P_{mq} = U_0{}^2\,|f_{mq}|^2$, which also define the diffraction efficiency $\eta_{mq} = |f_{mq}|^2$ for propagating orders.

For the realization of the complex diffraction gratings reported in Figure 2, relation (2) was used to analytically design the surface pattern $s(x,y)$. This pattern is encoded in a grayscale 8-bit digital image (1080 × 1920 px and 256 discrete intensity levels in the interval [0 255]), used as target image in the MRAF algorithm for hologram calculation. The parameters Λ_i, φ_i and γ_i used for the design of the surfaces reported in Figure 2 are summarized in Table S1 (Supporting Information)

Design of Gabor Phase Zone Plates: A Gabor phase zone plate[53] is a diffractive phase mask, designed to focus light at a specific distance. The radial profile $h(r)$ of a surface relief acting as a Gabor phase lens is

$$h(r) = \left(\frac{1+\cos\alpha r^2}{2}\right)h \tag{6}$$

where h is the relief amplitude and α is a structural parameter that sets the lateral size of the relief, defining the focal distance f on the optical axis. The relation between the size parameter α and the focal length f of the lens can be found considering the total phase delay accumulated by a plane wave of wavelength λ in the propagation through the surface relief. Each point of the surface introduces a space-dependent phase delay on

a portion of the incident plane wavefront determined by the propagation distance $h(r)$ (according to Equation (1)) in the material and the optical path accumulated due to propagation in air from the plane $z = h$ to the target axial focal point at $z = h+f$. Imposing that the diffracted light from each of the topographic maxima (located at $r = \sqrt{((2\pi M)/\alpha)}$, M integer number) constructively interferes at the focal plane (having a phase delay of 2πM), the following relation is obtained

$$\alpha = \frac{2\pi}{\lambda^2 - 2\lambda f} \tag{7}$$

In addition to the focus at the distance f, the phase mask (5) produces also secondary foci of decreasing intensity at the distances $f_m = f/m$ (with $m = \pm 1, \pm 2...$).[53]

The smallest focal distance f realizable with the system is determined by the discrete nature of the SLM pixels, which limits the spatial resolution in the holographic light distribution and induces large speckle noise affecting the contrast in the holographic intensity patterns. A lower limit of $f = 300$ µm for lenses maintaining good structural quality was found. This parameter, together to the lens diameter of ≈2µm defined by the field of view of the holographic system, set also the maximum numerical aperture NA ≈ 0.32 achievable with the specific experimental configuration. Using an improved holographic system, involving a higher resolution SLM and a larger NA microscope objective, the maximum achievable NA for the diffractive lenses can be enhanced even further. The lower NA limit, for the same lens diameter, is instead mainly determined by the photostructuration properties of the azopolymer, which limit the focal length at approximately the value $f = 1200$ µm and minimum NA ≈ 0.08.

It should also be noted that, from Equation (6), the focal distance of a Gabor phase zone plate does not depend on the total relief amplitude h. This degree of freedom can be used in the design to impose constructive interference for other points of the topography, allowing the improvement of the total diffraction efficiency of the device. The optimum value for h can be obtained by simulating the diffracted field in the lens focal region.

Fourier Integral for Focusing Efficiency Simulations: For the simulations at $\lambda = 633$ a refractive index $n = 1.70$ for the azopolymer as provided by ellipsometry measurements was used.

A unitary amplitude for the incident plane wave in the structured surface relief area was assumed, such as the input field can be written as $U_{in}(x,y) = A_{in}(x,y)\, e^{ikz}$. Here, $A_{in}(x,y) = \mathrm{circ}(R)$, is a mask circular function, whose value is 1 within the circle of radius R, where the DOE is present, and 0 outside. The minima of the surface are located at $z = 0$ plane and the phase modulation provided by the relief gives the output modulated field in the plane $z = h$ as: $U_{out}(x,y) = e^{(i\varphi(x,y))}$. The field $U(x,y,z)$, propagated in any plane at the axial position z is obtained solving Helmholtz equation, considering the Rayleigh–Sommerfeld diffraction integral in Fresnel approximation[4,11]

$$U(x,y,z) = \frac{e^{ikz}}{i\lambda z} \iint U_{out}(x',y') \exp\left\{ i\frac{k}{2z}\left[(x-x')^2 + (y-y')^2\right]\right\} dx_1 dy_1 \tag{8}$$

For the simulation, Equation (2) is numerically implemented through a MATLAB script using the convolution theorem with the transfer function of the Fresnel propagator

$$U(x,y,z) = FT^{-1}\left\{FT\left\{U_{out}(x',y')\right\} \times H(f_x, f_y)\right\} \tag{9}$$

Equation (3) is also used to simulate the focusing diffraction efficiency for the diffractive lens as function of relief amplitude h, reported in Figure 3J. Efficiency in the simulation is defined as the ratio of the light power integrated over an area of size (3 x FWHM)^2 in the focal plane (where FWHM is the Full Width at Half Maximum of the simulated focus) and the power of the unitary incident plane wave in the circular area of the structured surface (of radius $R = 100$ µm). Maximum efficiency (≈34%) in the focal plane (at $f = 500$ µm) is obtained for a value $h \approx 530$ nm. For this relief amplitude, the lens produces secondary foci at $f/2$ (with efficiency ≈10.6%) and at $f/3$ (≈1.8%) and virtual foci at distances $z = -f/m$ (with m = 1,2,...). Experimentally, the maximum diffraction efficiency from the lens can be achieved by tuning the exposure time of the polymer film surface to the relative holographic writing pattern, as demonstrated in Figure 3J; and Figure S10 (Supporting Information).

Focusing Efficiency and Axial Point Spread Function Measurements: The measurement of focusing efficiency reported in Figure 3J of the main text was performed using a He–Ne laser beam, incident on the diffractive lens from the substrate side. Light focused by the lens is collected through the same microscope imaging system used for brightfield surface observation. An iris and a power meter are used to intercept and measure only the light power transmitted through an aperture of the same diameter as the image of the structured area. Additional details about the experimental configuration can be found in Figure S11 (Supporting Information). Focusing efficiency is calculated as the ratio of the light power measured when the lens is written on the surface with respect to the same measurement with no structures in the photoresist area.

For the measurement of the axial point spread function of the reconfigured diffractive lenses, the iris is removed and the images of the transmitted He–Ne laser beam obtained axially translating the diffractive lens with 1 µm (Figure 3) or 5 µm (Figure 4) steps are collected with the CCD in the focal plane of the tube lens (Figure S11, Supporting Information).

Supporting Information

Supporting Information is available from the Wiley Online Library or from the author.

Acknowledgements

This work has been financially supported by the European Research Council (ERC) under the European Union's Horizon 2020 research and innovation programme "METAmorphoses", Grant Agreement No. 817794. This work has been supported by Fondazione Cariplo, Grant No. 2019-3923; and by the project ACTRIS-Aerosol, Clouds and Trace Gases Research Infrastructure funded by Italian MIUR Programma Nazionale Infrastrutture di Ricerca (PNIR), Grant No. CIR01_00015.

Open Access Funding provided by Istituto Italiano di Tecnologia within the CRUI-CARE Agreement.

Conflict of Interest

The authors declare no conflict of interest.

Data Availability Statement

The data that support the findings of this study are available from the corresponding author upon reasonable request.

Keywords

azopolymers, computer-generated holography, mass migration, optical fourier surfaces, reconfigurable diffractive optical elements, tunable diffractive lenses

Received: September 10, 2021
Revised: December 6, 2021
Published online: January 24, 2022

[1] E. G. Loewen, E. Popov, *Diffraction Gratings and Applications*, CRC Press, Boca Raton, FL **2018**.

[2] M. Born, E. Wolf, *Principles of Optics: Electromagnetic Theory of Propagation, Interference and Diffraction of Light*, Cambridge University Press, London **1997**.
[3] J. W. Goodman, *Introduction to Fourier Optics*, Roberts and Company Publishers, Greenwood Village, CO **2005**.
[4] D. C. O'Shea, T. J. Suleski, A. D. Kathman, D. W. Prather, *Diffractive Optics*, SPIE, Bellingham, WA **2003**).
[5] S. M. Kamali, E. Arbabi, A. Arbabi, Y. Horie, M. Faraji-Dana, A. Faraon, *Phys. Rev. X* **2017**, *7*, 041056.
[6] N. Lassaline, R. Brechbühler, S. J. W. Vonk, K. Ridderbeek, M. Spieser, S. Bisig, B. le Feber, F. T. Rabouw, D. J. Norris, *Nature* **2020**, *582*, 506.
[7] P. Lalanne, P. Chavel, *Laser Photonics Rev.* **2017**, *11*, 1600295.
[8] N. Yu, F. Capasso, *Nat. Mater.* **2014**, *13*, 139.
[9] D. Gabor, *Nature* **1948**, *161*, 777.
[10] S. Banerji, M. Meem, A. Majumder, F. G. Vasquez, B. Sensale-Rodriguez, R. Menon, *Optica* **2019**, *6*, 805.
[11] K. Huang, F. Qin, H. Liu, H. Ye, C.-W. Qiu, M. Hong, B. Luk'yanchuk, J. Teng, *Adv. Mater.* **2018**, *30*, 1704556.
[12] W. T. Chen, F. Capasso, *Appl. Phys. Lett.* **2021**, *118*, 100503.
[13] Z. Yang, T. Albrow-Owen, W. Cai, T. Hasan, *Science* **2021**, *371*.
[14] C. Palmer, *Diffraction Grating Handbook*, 8th ed., MKS Instruments Inc., Rochester, NY **2020**.
[15] H. Rubinsztein-Dunlop, A. Forbes, M. V. Berry, M. R. Dennis, D. L. Andrews, M. Mansuripur, C. Denz, C. Alpmann, P. Banzer, T. Bauer, E. Karimi, L. Marrucci, M. Padgett, M. Ritsch-Marte, N. M. Litchinitser, N. P. Bigelow, C. Rosales-Guzmán, A. Belmonte, J. P. Torres, T. W. Neely, M. Baker, R. Gordon, A. B. Stilgoe, J. Romero, A. G. White, R. Fickler, A. E. Willner, G. Xie, B. McMorran, A. M. Weiner, *J. Opt.* **2016**, *19*, 013001.
[16] J. Kobashi, H. Yoshida, M. Ozaki, *Nat. Photon.* **2016**, *10*, 389.
[17] F. Qin, B. Liu, L. Zhu, J. Lei, W. Fang, D. Hu, Y. Zhu, W. Ma, B. Wang, T. Shi, Y. Cao, B. Guan, C. Qiu, Y. Lu, X. Li, *Nat. Commun.* **2021**, *12*, 32.
[18] M. Khorasaninejad, A. Ambrosio, P. Kanhaiya, F. Capasso, *Sci. Adv.* **2016**, *2*, e1501258.
[19] R. C. Devlin, A. Ambrosio, N. A. Rubin, J. P. B. Mueller, F. Capasso, *Science* **2017**, *358*, 896.
[20] A. M. Shaltout, V. M. Shalaev, M. L. Brongersma, *Science* **2019**, *364*.
[21] C. U. Hail, A.-K. U. Michel, D. Poulikakos, H. Eghlidi, *Adv. Opt. Mater.* **2019**, *7*, 1801786.
[22] M. Y. Shalaginov, S. An, Y. Zhang, F. Yang, P. Su, V. Liberman, J. B. Chou, C. M. Roberts, M. Kang, C. Rios, Q. Du, C. Fowler, A. Agarwal, K. A. Richardson, C. Rivero-Baleine, H. Zhang, J. Hu, T. Gu, *Nat. Commun.* **2021**, *12*, 1225.
[23] A. Natansohn, P. Rochon, *Chem. Rev.* **2002**, *102*, 4139.
[24] K. G. Yager, C. J. Barrett, *J. Photochem. Photobiol.A* **2006**, *182*, 250.
[25] H. M. D. Bandara, S. C. Burdette, *Chem. Soc. Rev.* **2012**, *41*, 1809.
[26] A. Ambrosio, L. Marrucci, F. Borbone, A. Roviello, P. Maddalena, *Nat. Commun.* **2012**, *3*, 989.
[27] A. Ambrosio, P. Maddalena, L. Marrucci, *Phys. Rev. Lett.* **2013**, *110*, 146102.
[28] S. L. Oscurato, F. Borbone, P. Maddalena, A. Ambrosio, *ACS Appl. Mater. Interfaces* **2017**, *9*, 30133.
[29] S. L. Oscurato, M. Salvatore, P. Maddalena, A. Ambrosio, *Nanophotonics* **2018**, *7*, 1387.
[30] S. Lee, H. S. Kang, J.-K. Park, *Adv. Mater.* **2012**, *24*, 2069.
[31] A. Priimagi, A. Shevchenko, *J. Polym. Sci., Part B: Polym. Phys.* **2014**, *52*, 163.
[32] P. Rochon, E. Batalla, A. Natansohn, *Appl. Phys. Lett.* **1995**, *66*, 136.
[33] D. Y. Kim, S. K. Tripathy, L. Li, J. Kumar, *Appl. Phys. Lett.* **1995**, *66*, 1166.
[34] J. Jelken, S. Santer, *RSC Adv.* **2019**, *9*, 20295.
[35] F. Borbone, S. L. Oscurato, S. D. Sorbo, F. Pota, M. Salvatore, F. Reda, P. Maddalena, R. Centore, A. Ambrosio, *J. Mater. Chem. C* **2021**, *9*, 11368.
[36] S. Lee, Y.-C. Jeong, J.-K. Park, *Opt. Express* **2007**, *15*, 14550.
[37] S. J. Yeo, K. J. Park, K. Guo, P. J. Yoo, S. Lee, *Adv. Mater.* **2016**, *28*, 5268.
[38] K. J. Park, J. H. Park, J.-H. Huh, C. H. Kim, D. H. Ho, G. H. Choi, P. J. Yoo, S. M. Cho, J. H. Cho, S. Lee, *ACS Appl. Mater. Interfaces* **2017**, *9*, 9935.
[39] M. Salvatore, F. Borbone, S. L. Oscurato, *Adv. Mater. Interfaces* **2020**, *7*, 1902118.
[40] H. Rekola, A. Berdin, C. Fedele, M. Virkki, A. Priimagi, *Sci. Rep.* **2020**, *10*, 19642.
[41] Y. Lim, B. Kang, S. Lee, *Adv. Funct. Mater.* **2021**, *31*, 2100839.
[42] S. L. Oscurato, F. Reda, M. Salvatore, F. Borbone, P. Maddalena, A. Ambrosio, *Adv. Mater. Interfaces* **2021**, *8*, 2101375.
[43] Y. Lim, B. Kang, S. J. Hong, H. Son, E. Im, J. Bang, S. Lee, *Adv. Funct. Mater.* **2021**, *31*, 2104105.
[44] S. L. Oscurato, M. Salvatore, F. Borbone, P. Maddalena, A. Ambrosio, *Sci. Rep.* **2019**, *9*, 6775.
[45] K. Yang, S. Yang, X. Wang, J. Kumar, *Appl. Phys. Lett.* **2004**, *84*, 4517.
[46] F. Fabbri, Y. Lassailly, K. Lahlil, J. P. Boilot, J. Peretti, *Appl. Phys. Lett.* **2010**, *96*, 081908.
[47] A. Rahmouni, Y. Bougdid, S. Moujdi, D. V. Nesterenko, Z. Sekkat, *J. Phys. Chem. B* **2016**, *120*, 11317.
[48] X. L. Jiang, L. Li, J. Kumar, D. Y. Kim, S. K. Tripathy, *Appl. Phys. Lett.* **1998**, *72*, 2502.
[49] H. S. Kang, S. Lee, S.-A. Lee, J.-K. Park, *Adv. Mater.* **2013**, *25*, 5490.
[50] J. Vapaavuori, R. H. A. Ras, M. Kaivola, C. G. Bazuin, A. Priimagi, *J. Mater. Chem. C* **2015**, *3*, 11011.
[51] A. Tofini, L. Levesque, O. Lebel, R. G. Sabat, *J. Mater. Chem. C* **2018**, *6*, 1083.
[52] Z. V. Vardeny, A. Nahata, A. Agrawal, *Nat. Photonics* **2013**, *7*, 177.
[53] O. Hignette, J. Santamaria, J. Bescos, *J. Opt.* **1979**, *10*, 231.
[54] R. G. Sabat, *Opt. Express* **2013**, *21*, 8711.
[55] J. Leibold, R. G. Sabat, *Photon. Res.* **2015**, *3*, 158.
[56] Y.-H. Lin, Y.-J. Wang, V. Reshetnyak, *Liq. Cryst. Rev.* **2017**, *5*, 111.
[57] M. Pasienski, B. DeMarco, *Opt. Express* **2008**, *16*, 2176.
[58] R. W. Gerchberg, W. O. Saxton, *Optik* **1972**, *35*, 237.
[59] I. Andries, T. Galstian, A. Chirita, *J. Optoelectron. Adv. Mater.* **2016**, *18*, 56.

LASER
& PHOTONICS
REVIEWS

Supporting Information

for *Laser Photonics Rev.*, DOI 10.1002/lpor.202100514

Shapeshifting Diffractive Optical Devices

Stefano L. Oscurato, Francesco Reda, Marcella Salvatore, Fabio Borbone, Pasqualino Maddalena and Antonio Ambrosio**

Supporting Information

Shapeshifting diffractive optical devices

Stefano L. Oscurato, Francesco Reda, Marcella Salvatore, Fabio Borbone, Pasqualino Maddalena and Antonio Ambrosio**

Azopolymer photo-structuration for sinusoidal illumination patterns

To describe the phenomenology of the light-induced direct surface structuration of our photoresist, we refer to the simplest case of one-dimensional gratings produced by the irradiation of holographically generated sinusoidal intensity patterns, whose parameters (e.g periodicity, orientation, phase) can be entirely digitally controlled in our system (see also Figure S2).

Our photoresist is an azobenzene-containing polymer. The photo-induced surface structuration of the photoresist film arises from a light-driven microscopic motion involving cyclic isomerizations of the azobenzene molecules[25] which drive a macroscopic transport of the entire polymeric matrix under illumination.[29] The geometry of the resulting surface reliefs depends on both the intensity $I(x,y)$ and the polarization distribution of the irradiated light across the surface.[26-28] In the case of circularly polarized light in low focalization regimes[26] (valid in our experimental configuration), the polarization dependence is averaged out and the relief pattern $h(x,y)$ is proportional to the Laplacian of the intensity distribution:[26, 29]

$$h(x,y,\tau) = c(\tau)\,\nabla^2 I(x,y). \qquad \text{S1}$$

Here, τ is the exposure time and $c(\tau)$ is a phenomenological material parameter determining the relief inscription efficiency. In low intensity regimes ($< 100\ W/cm^2$), the material parameter can be considered independent on the exposure time and amplitude of the surface relief is approximately linearly increasing with the exposure time $c(\tau) = c * \tau$, [26-39] (see also Figure S4).

For sinusoidal surface intensity patterns, equation S1 simply predicts a surface relief geometry proportional to the inverse of the intensity pattern:

$$h(x,y,\tau) = -c\,I(x,y)\tau. \qquad \text{S2}$$

According to equation S2, topographic maxima occur at intensity minima (p phase shift) (Figure S4), while the periodicity of the relief is the same as illumination. Equation S2 can be applied to all the DOEs reported in this work, being designed as superposition of sinusoids (complex gratings) or as cosinusoidal functions (Gabor phase lenses).

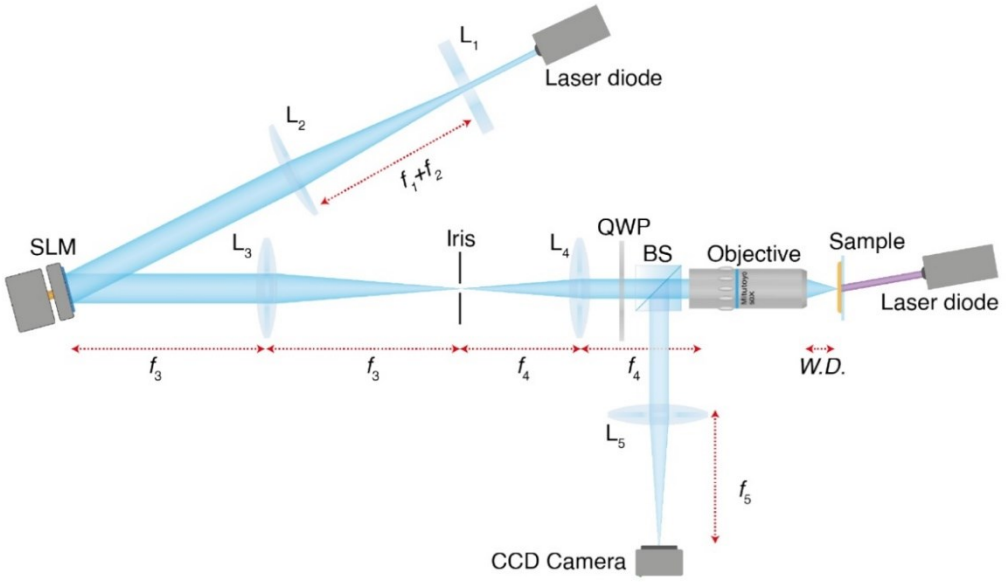

Figure S1

Setup for holographic structuration of photoresist surface.

The writing laser beam at wavelength λ=491 nm is modulated, after a beam expander (lenses L_1 and L_2), by a reflective phase-only Spatial Light Modulator (SLM). The SLM is placed in the first focal plane of a bi-convex lens (L_3), with a focal length of f_3=300 mm, realizing a 2f configuration with the plane of an iris placed in the second focal plane. The iris allows the spatial filtering of the beam, blocking all the undesired lower-intensity diffraction orders and the un-modulated light emerging from the SLM. The laser beam is re-collimated using a bi-convex lens L_4 (with focal length f_4=175 mm), which projects a rescaled version of the optical field of the SLM plane in its second focal plane. That plane coincides with the back focal plane of an infinity corrected "50X Mitutoyo" objective (OBJ). The structured holographic intensity distribution is then reconstructed and focused on the objective focal plane (objective working distance WD 13mm) over a circular area of ~200 μm in diameter, where the photoresist film is placed. Writing beam is circular polarized using a quarter wave plate (QWP). A 70/30 beam splitter (BS), placed between objective and L_4 lens, allows the collection of part of retroreflected writing light which is collected and recollimated by the objective. Finally, the tube lens (L_5) (f_5=200 mm) focuses the image of the objective focal plane on a “DCC3240M Thorlabs” camera (CCD). The assisting (or erasing) beam at λ=405 nm is circularly polarized before being redirected in the writing\erasing area at near-normal incidence.

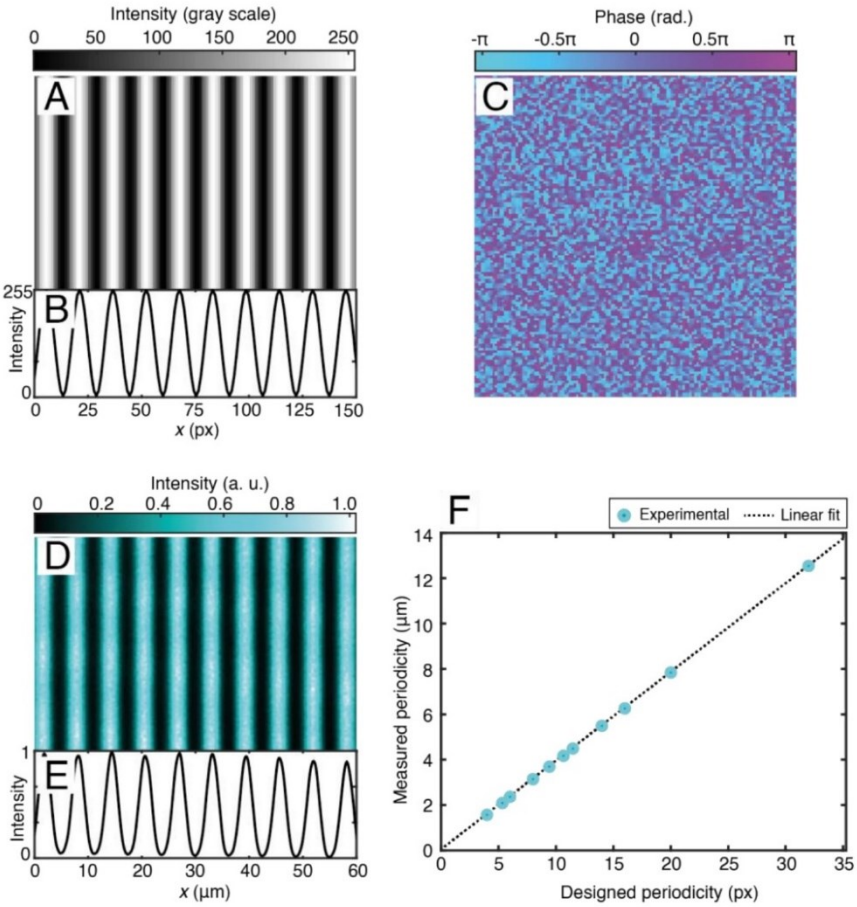

Figure S2

Design of holographic sinusoidal intensity patterns

The fundamental aspects of the holographic design and calibration for sinusoidal patterns in our system are described. **(A)** Typical grayscale 8-bit target image used for the calculation of a one-dimensional holographic sinusoidal intensity patterns. **(B)** Target sinusoidal profile. The *Mixed Region Amplitude Freedom* (MRAF) algorithm calculates the phase profile (the kinoform) for the writing laser beam in the Spatial-Light Modulator plane necessary to reconstruct the desired intensity distribution in photoresist plane. **(C)** Kinoforms are in the range [-π,π] interval and are encoded in 8-bit grayscale images, directly transferred to the modulator. **(D)** Reconstructed intensity pattern in the photoresist plane: image is acquired using tube lens-CCD camera system, collecting retroreflected light from the photoresist plane with a CCD. The image is the result of averaging the holographic speckle noise over 1000 independent images of the pattern. CCD counts are renormalized in [0,1] interval. **(E)** Reconstructed intensity pattern profile. **(F)** Measured periodicity of different reconstructed sinusoidal intensity patterns as function of the designed pitch in the target image. The slope of the line trend defines the calibration of physical dimensions of patterns in the polymer plane with respect to the analytically designed target images.

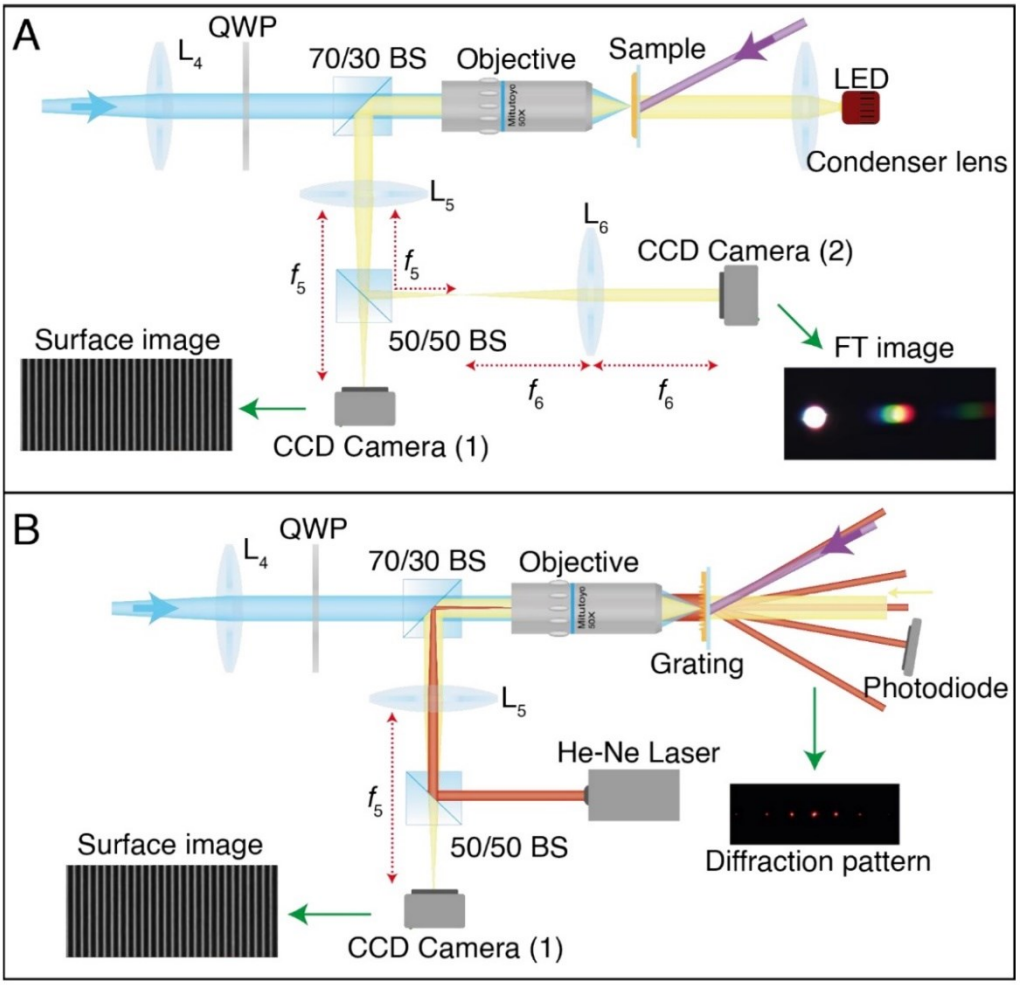

Figure S3

Optical setup for real-time surface grating characterization

(A) Brightfield imaging setup: white light from a LED is collimated using a condenser lens and used as sample back-illumination source. Scattered light from the surface is collected and recollimated by the objective. The 70/30 beam splitter (BS), placed between objective and L_4 lens, allows the collection of part of this light without interfering with the writing process. The image of the surface is projected on the CCD Camera (1) by the tube lens (L_5, f_5=200 mm). For surface observation, a long-pass filter is used to discard writing back-reflected light. A second beam splitter (50/50 BS) allows to perform surface image Fourier transform using another lens L_6 (f_6=350 mm), realizing a 2f configuration with the tube lens. Fourier transform image is captured with second camera (CCD Camera (2)). **(B)** Diffraction efficiency measurement configuration. A He-Ne laser beam is focused in the back focal plane of the objective using the tube-lens (L_5). The probe beam is collimated by the objective in the writing area. Transmitted diffraction patterns can be observed in far-field. A photodiode collecting the light diffracted in the first order can be used to monitor the dynamical evolution of grating diffraction efficiency.

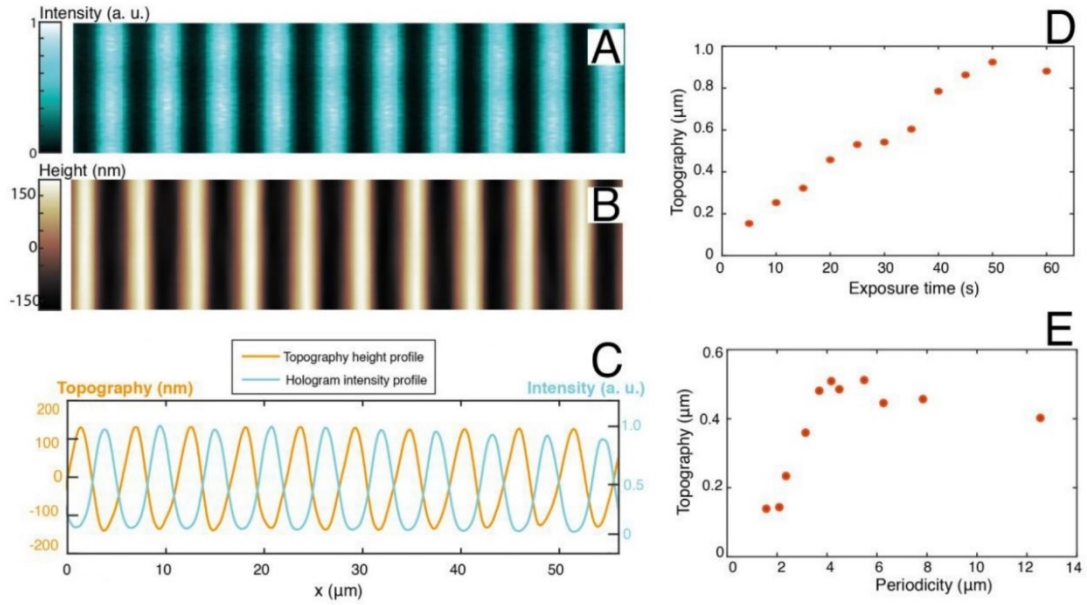

Figure S4

Sinusoidal illumination patterns and azopolymer photo-structuration

(A) Sinusoidal intensity pattern, of periodicity 5.49 μm, used as example of illumination pattern for the direct inscription of sinusoidal gratings on the photoresist surface. **(B)** AFM micrograph of the structured photoresist surface after 10s of holographic exposure. **(C)** Comparison between measured AFM profile and the holographic intensity pattern profile. **(D)** Measured relief amplitude obtained for different exposure times at fixed illumination intensity. The linear trend shows a direct proportionality between relief height and exposure time. **(E)** Dependence of the relief amplitude with respect to the periodicity of the holographic sinusoidal illumination pattern. We observe a reduction of modulation efficiency for grating periodicities smaller than $3\mu m$, due to deterioration in the holographic pattern determined by SLM pixel size and holographic speckle noise. A lower limit of ~ 2μm can be established for the periodicity of reconfigurable gratings in our configuration. Larger grating periodicities ($> 4\mu m$) have decreasing amplitude modulation according to the prediction of equation S1, due to the reduction of the local intensity gradient strength, which is driving the surface structuration in our configuration. This effect is opposed to the situation described in Ref. 40 for sinusoidal surface gratings realized by interference lithography. In that case, smaller periodicities require larger incidence angles for the interfering beams, which result also in an increase of surface reflectance and lower absorbed light from the polymer. Provided that the illumination is of sufficiently good quality, the theoretical expected behavior for azopolymer structuration efficiency is instead observed in our case, taking advantage from our versatile holographic illumination, which allows the isolation of the influence of different grating periodicity on the relief amplitude while maintaining fixed and reproducible irradiation parameters (intensity, exposure time, polymer absorbed light power).

It should be noted, however, that, if needed, the differences observed in (E) could be eventually compensated by tuning the exposure time for each sinusoidal periodicity.

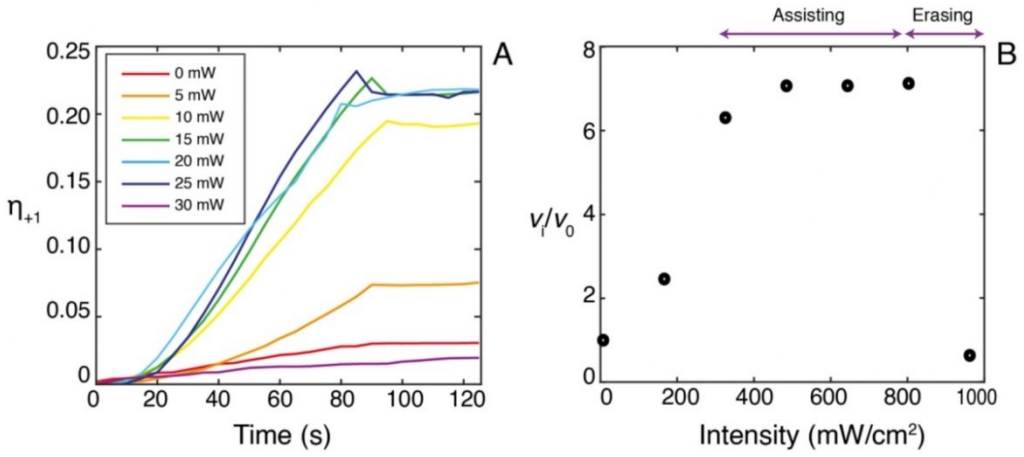

Figure S5

Influence of assisting/erasing beam on relief inscription dynamics

Influence of the assisting beam on the sinusoidal structuration process, studied in real time by exposing the azopolymer film to a holographic sinusoidal intensity pattern. The structuration dynamics is monitored through real-time diffraction efficiency measurement (configuration in Figure S3(B)). **(A)** Real-time diffraction curves of the +1 diffraction order, recorded for different power of the assisting beam (at 405 nm) incident (collimated, diameter ~2.0 mm) on the azopolymer area during the holographical writing process. The exposure time is fixed at 90 s. According to the diffraction efficiency dynamics (A) and its velocity **(B)** (extracted from the slope of the linear portion of the trends in A), surface relief inscription efficiency increases under the influence of low intensity (in the range 400-800 mW/cm^2) assisting beam. At higher intensity (>900 mW/ cm^2), surface structuration process is slowed down by the 405 nm beam, until reaching the situation where the high intensity completely avoids the formation of surface structures or erase eventual previously inscribed ones (*erasing* configuration).

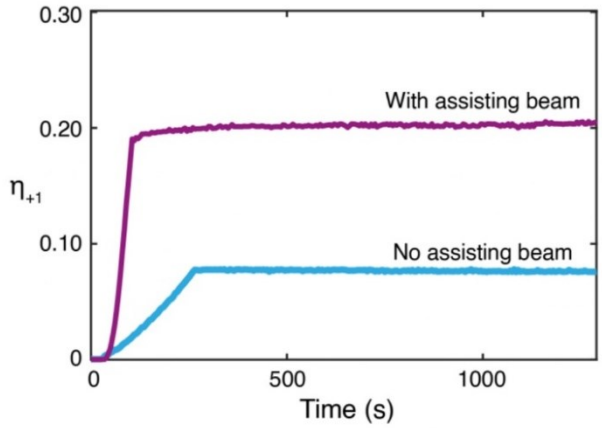

Figure S6
Surface relief stability over time
The time stability of DOEs realized on the azopolymer surface are analyzed through the measurement of real-time first order diffraction efficiency of a sinusoidal diffraction grating (configuration in Figure S3(B)). In the experiment, after the initial efficiency rising from the forming diffraction grating under holographic illumination, the writing beam (and the assisting beam) is switched off, while the monitoring of diffraction of the probe beam is continued for 30 minutes. Both the structures inscribed with and without the assisting beam result stable over time, indicating a diffraction behavior entirely determined by the surface relief pattern for DOEs produced by our photo-structuration method. This behavior is different from the typical diffraction gratings fabricated on azobenzene-containing materials via interference lithography, in which the linearly polarized electric field of the interferogram (for both intensity and polarization interference patterns) inside the material causes a significant realignment of the azomolecules, which results in a birefringence grating in addition to the morphological relief grating. Because the chromophore orientation can be perturbed much easier than the surface shape, the birefringence grating is typically a source of long-term instability for the diffraction efficiency of azomaterial gratings. In our case, however, the formation of efficient light-induced birefringence gratings inside the holographic illuminated film is inefficient because the circularly polarized light of the writing beam does not promote the formation of well-ordered patterns of molecular alignment. Furthermore, in our operating configuration, which uses an additional circularly polarized assisting beam during the writing process, the molecular orientational distribution is further averaged, lowering even more the probability of patterned molecular order in the film.
It is reasonable then to assume that the optical functionality of our DOEs can be the same of the surface morphology, that is preserved for years by maintaining the polymer at normal room conditions.

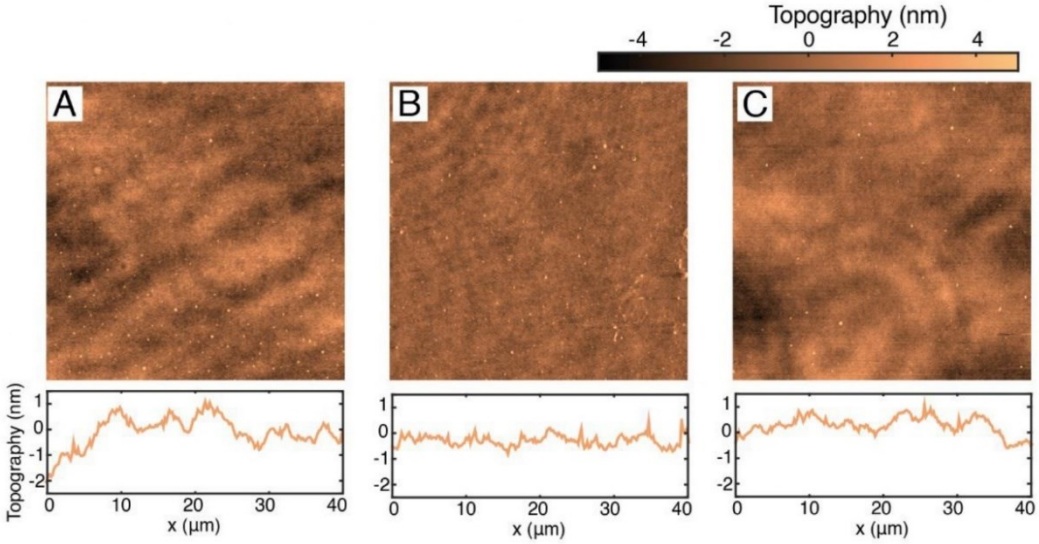

Figure S7

AFM analysis of the erased azopolymer surface

(A) AFM image of the typical pristine azopolymer surface before being exposed to any holographic pattern. **(B)** Zoomed version of the AFM micrograph of Figure 1H of the main text reporting the surface after the erasure process. **(C)** Zoomed version of the AFM micrograph of Figure 1L of the main text reporting the surface after the erasure process. Both scans show a complete erasure of the inscribed structures, with a residual roughness comparable to that of the pristine surface.

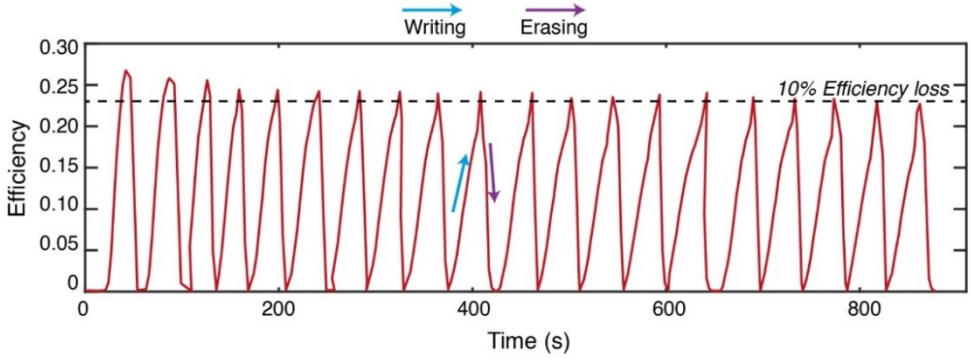

Figure S8

Analysis of multiple surface writing and erasing cycles

To characterize the repeatability of the surface remodulation process, the same area of an azopolymer surface is cyclically structured and erased with a sinusoidal intensity pattern, having periodicity of Λ=5.5 μm. The intensities of the writing (~14.0 W/cm^2), the assisting (~500 mW/cm^2) and the erasing (~1.0 W/cm^2) beams are kept fixed during every surface inscription and the erasing step. The writing+assisting exposure time is set at ~30s (in which the sinusoidal relief amplitude reaches approximately 550 nm), while the exposure to the erasing beam is slightly varied in each cycle until complete erasure is achieved.

Real-time, quantitative characterization of the surface structuration/erasing behaviour are obtained by measuring the dynamical time-dependent efficiency of a probe beam (He-Ne, configuration of Figure S3(B)) diffracted by the evolving surface grating in +1 order with a photodiode. At least 15 writing and erasing cycles were obtained without significant efficiency reduction. Only a loss of 10% in the maximum diffraction efficiency was measured between the first and last writing step, while the time necessary for complete surface erasure remained less than 15s in every step, with only a slightly slower erasing dynamics observed in the final cycle in respect to the initial one. The morphology of the completely erased surfaces, as measured from AFM analysis (not shown here), is compatible with a completely flat film (as characterized in Figure S7), even after the 15th cycle.

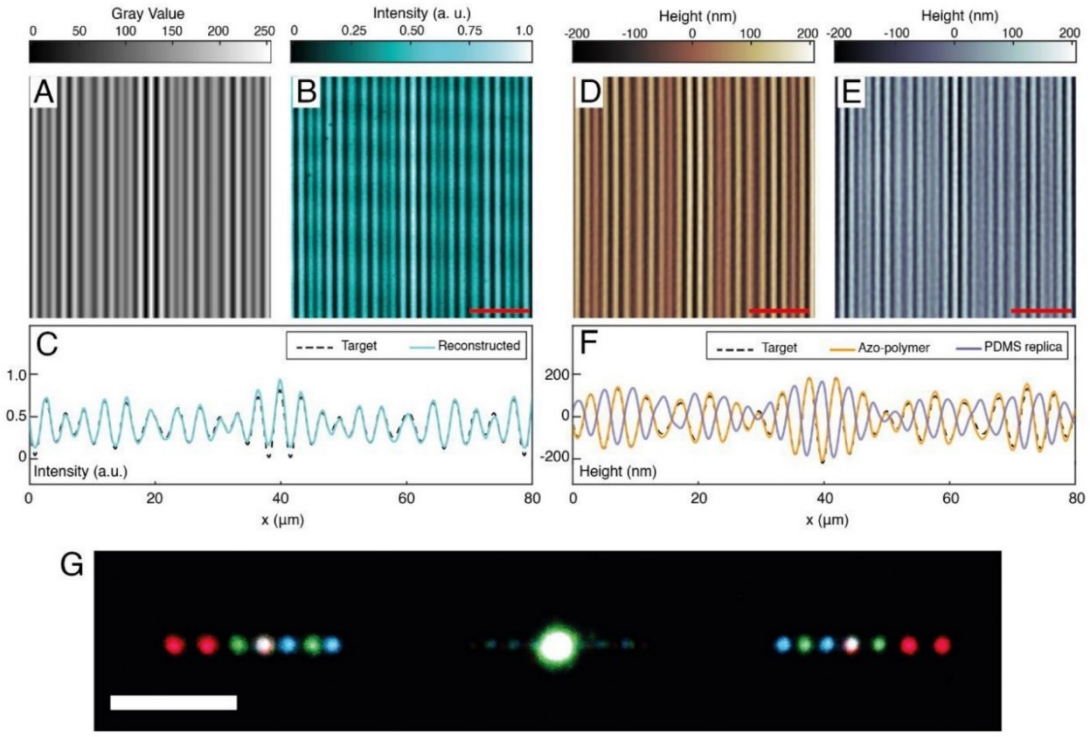

Figure S9

Design and realization of the RGB grating

RGB grating design, encoding in the holographic pattern and lithographic process on the azopolymer surface with subsequent pattern transfer on a Polydimethylsiloxane (PDMS) mold. **(A)** Target image encoded in a grayscale 8-bit bitmap image, calculated as superposition of three sinusoidal patterns having equal amplitudes A_i and different spatial periodicities Λ_1=3.13 μm, Λ_2=3.42 μm, Λ_3=4.05 μm satisfying the Bragg relation $\theta_1=\text{asin}(\lambda_i/\Lambda_i)$ at the common first order diffraction angle θ_1 for the three different light wavelengths λ_1=633 nm, λ_2=532 nm and λ_3=488 nm). The relative phases φ_i and rotation angles γ_i were both been set to zero for all the three sinusoids in the superposition of (A). **(B)** Reconstructed intensity pattern in the focal plane of the objective produced by our Computer-Generated Hologram systems, using the grayscale image in (A) as input data of the kinoform calculation process of the MRAF algorithm. The image in (B) is the result of averaging the holographic speckle noise over 1000 independent images of the pattern collected by the CCD (CCD counts are mapped in [0,1] interval). **(C)** Comparison between the lateral profiles of the target image (normalized in [0,1] interval) and the experimental holographic intensity pattern. **(D)** AFM scan of the azopolymer surface (from Figure 2B in the main text) after being exposed to the averaged (by refreshing the kinoform on the SLM at 20 Hz) holographic intensity pattern. **(E)** AFM micrograph of the PDMS replica obtained with standard molding process, using the azopolymer surface in (D) as master. The PDMS (Sylgard 184, Dow Corning) mixture was prepared by mixing the precursor and the curing agent in a 10:1 weight ratio. After degassing in a vacuum chamber, the PDMS mixture was gently poured onto the azopolymer film without further surface treatment and cured at 30 °C for 6 hours before being carefully released from the film. **(F)** Comparison between topographic profiles of the azopolymer surface and PDMS mold (inverse replica) with respect

to the target designed pattern: the graph shows an optimum agreement between the surface topography of the photoresist and the target. The total height amplitude is preserved in the pattern transfer (with a measured loss of less than 8%). The fabricated PDMS is fully compatible with standard lithographic replica molding processes for the transfer of the surface pattern on other materials. Scale bars in A-B-D-E are 20 μm. **(G)** Full view of the RGB diffraction pattern of Figure 2D of the main text, produced by the surface in (**D**) from simultaneous illumination of the DOE with three collinear laser beams at design wavelengths (λ_1=633 nm; λ_2=532 nm; λ_3=488 nm). Scale bar in (G) is 0.5 cm.

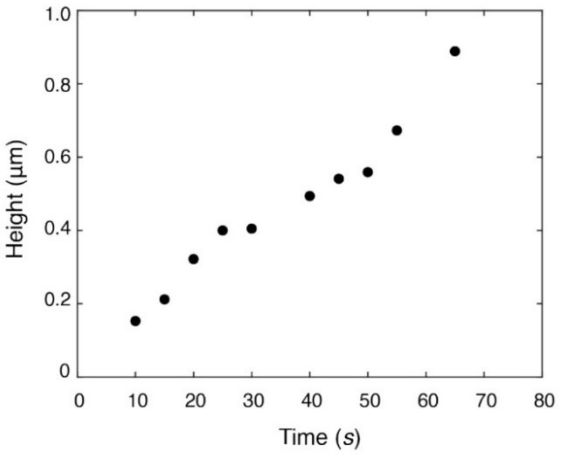

Figure S10

Tuning of Gabor phase zone plate relief amplitude

Graph shows the measured average relief amplitude h in the radial surface profile of the experimental Gabor phase zone plate lens reported in Figure 3 of the main text measured for different exposure times. A linear amplitude increase is obtained for increasing exposure time. The target amplitude h ≈ 530 nm (producing the theoretical maximum focusing efficiency) is realized in 50s of exposure at the holographic pattern in the presence of the assisting beam.

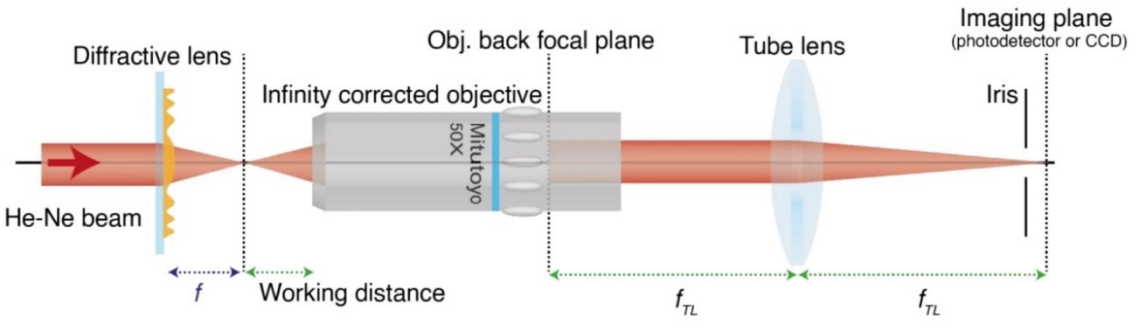

Figure S11

Diffractive lens efficiency measurement

Optical configuration used to measure of the Point Spread Function (PSF) and the diffraction efficiency of the azopolymer Gabor zone plate lenses . A collimated He-Ne laser beam, incident on the structured surface from the substrate side is focused by the diffractive lens. For the focusing efficiency measurement, the lens is properly translated along the optical axis so that its focal plane (placed at a distance *f* from the structured surface) coincides with the objective focal plane. Objective and tube lens provide an image of the focused spot. An iris and a power meter are used to intercept and measure light power in focal spot. This measured value is compared with the total transmitted power measured before diffractive lens structuration, setting the iris aperture size of the same diameter as the image of the structured area in order to measure only the fraction of light power that is diffracted by the modulated area of the surface. For PSF measurements, the diffractive lenses are axially translated at discrete steps with a micrometer positioner (with accuracy of 1μm) with respect to the objective focal plane. Images of the focal spot for each position of the lens are collected with the CCD placed in the tube lens focal plane and stacked together to extract the axial yz sections reported in Figure 3 and Figure 4 of the main text.

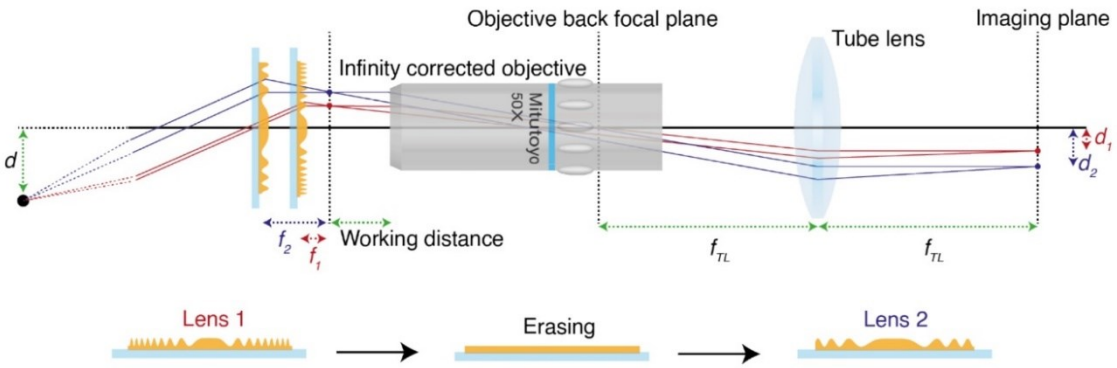

Figure S12

Optical zooming system with reconfigurable focal length diffractive lenses

Optical configuration used to realize the zooming imaging system based on the reconfigurable azopolymer lenses reported in Figure 4 of the main text. A transparency printed with logos of our institutions is placed at a long distance (considered infinite) from the photoresist surface of the diffractive lens. The azopolymer lens is a positive lens, forming an image of the object (with transverse dimensions d) at a distance from the surface equal to the focal length f_i. For the formation of the image in the CCD plane (focal plane of the tube lens) the diffractive lens is axially translated in order to make its focal plane to coincide with the focal plane of the infinity corrected objective. Transverse dimensions d_i of the acquired images are directly related to focal length f_i of the system. Shifting the surface geometry of the lens and translating the sample axially to regain focused images in the CCD plane, images with different magnification are produced by the system. The ratio between the lateral dimensions of two images obtained with two different diffractive lenses is equal to the focal ratio: $d_1/d_2 = f_1/f_2$.

RGB grating $N = 3$	Sinusoidal pitch Λ_i (μm)	$(3.1 - 3.4 - 4.1)$
	Relative amplitude A_i	1
	Relative phase φ_i (rad)	$(0 - 0 - 0)$
	In plane orientation γ_i (deg)	$(0 - 0 - 0)$
	T (s)	60

Quasi-crystal $N = 6$	Sinusoidal pitch Λ_i (μm)	$(3.1 - 3.1 - 3.1 - 3.1 - 3.1 - 3.1)$
	Relative amplitude A_i	1
	Relative phase φ_i (rad)	$(0 - 0 - 0 - 0 - 0 - 0)$
	In plane orientation γ_i (deg)	$(0 - 30 - 60 - 90 - 120 - 150)$
	T (s)	120

Spiral quasi-crystal $N = 6$	Sinusoidal pitch Λ_i (μm)	$(3.1 - 3.9 - 4.7 - 5.5 - 6.3 - 7.1)$
	Relative amplitude A_i	1
	Relative phase φ_i (rad)	$(0 - 0 - 0 - 0 - 0 - 0)$
	In plane orientation γ_i (deg)	$(0 - 30 - 60 - 90 - 120 - 150)$
	T (s)	120

Blazed grating $N = 6$	Sinusoidal pitch Λ_i (μm)	$(12.5 - 6.3 - 4.2 - 3.1 - 2.5 - 2.1)$
	Relative amplitude A_i	$1/i$
	Relative phase φ_i (rad)	$(0 - \pi - 0 - \pi - 0 - \pi)$
	In plane orientation γ_i (deg)	$(0 - 0 - 0 - 0 - 0 - 0)$
	T (s)	120

Table S1.

Design parameters for the realization of the complex diffraction gratings

Table of design parameters for the realization of the diffractive surfaces shown in Figure 2(B-F-H-J) of the main text, named in the first column of each sub-table. For every surface pattern, the number N of combined sinusoidal functions included in the structure design is reported. The remaining rows refer to the periodicity Λ_i of the sinusoids, their relative amplitude A_i, their relative phase φ_i, the in-plane orientation γ_i of each of the N components of the designed geometry. Total exposure time T is related to the total relief amplitude h.

Movie S1.
Dynamical grating inscription with multiplexing. Real-time evolution of the azopolymer surface and its diffraction efficiency, monitored during the grating reconfiguration experiment reported in Figure 1 of the main text. An additional writing step, involving the inscription of the complex diffraction grating calculated as the combination (G1+G2), which produces the simultaneous rise of the diffraction efficiency detected by the two photodiodes, is also included as final surface reconfiguration step in the movie.

Movie S2.
Dynamical tuning of grating diffraction dispersion. Evolution of the azopolymer diffraction gratings (experiment reported in Figure 1N-R of the main text), sequentially reshaped with ten different periodicities, recorded in real-time with the bright-field microscope in the configuration of Figure S3(A). The time-evolving diffraction pattern produced by the structured photoresist surface under illumination of a white LED source is shown together with a fixed Region of Interest (ROI) on the CCD. This configuration mimics the effect of having a physical slit in the diffraction plane in order to dynamically select the center of a spectral band via surface periodicity reconfiguration, similarly to a monochromator.

Movie S3.
Shapeshifting DOEs. Azopolymer surface, repeatedly reconfigured as different DOEs, observed by the real-time bright-field microscope during the shapeshifting experiments. The surface is structured first as a diffraction grating (Grating 1). After erasing, the surface is transformed in a Gabor phase zone plate (Lens), before becoming a new diffraction grating (Grating 2) in the successive reconfiguration step. Finally, a quasicrystal surface is inscribed in the same area as example of arbitrary DOE, demonstrating versatile and completely independent sequence of on-demand optical functionalities achievable with our approach.

Publication VI

F. Reda, M. Salvatore, F. Borbone, P. Maddalena, A. Ambrosio, and S. L. Oscurato

Varifocal diffractive lenses for multi-depth microscope imaging

Reprinted from

Optics Express, 30(8), 12695–12711 (2022)

with the permission of Optica Publishing Group

Research Article | Vol. 30, No. 8 / 11 Apr 2022 / Optics Express 12695
Optics EXPRESS

Varifocal diffractive lenses for multi-depth microscope imaging

FRANCESCO REDA,[1] MARCELLA SALVATORE,[1,2] FABIO BORBONE,[3,4] PASQUALINO MADDALENA,[1,2,4] ANTONIO AMBROSIO,[4,*] AND STEFANO LUIGI OSCURATO[1,2,4]

[1]*Department of Physics "E. Pancini", University of Naples "Federico II", Complesso Universitario di Monte Sant'Angelo, Via Cintia, 80126 Naples, Italy*
[2]*Centro Servizi Metrologici e tecnologici Avanzati (CeSMA), University of Naples "Federico II", Complesso Universitario di Monte Sant'Angelo, Via Cintia 21, 80126 Naples, Italy*
[3]*Department of Chemical Sciences, University of Naples "Federico II", Complesso Universitario di Monte Sant'Angelo, Via Cintia, 80126 Naples, Italy*
[4]*CNST@POLIMI—Fondazione Istituto Italiano di Tecnologia, Via Pascoli 70, 20133 Milan, Italy*
[*]*antonio.ambrosio@iit.it*

Abstract: Flat optical elements enable the realization of ultra-thin devices able to either reproduce or overcome the functionalities of standard bulky components. The fabrication of these elements involves the structuration of material surfaces on the light wavelength scale, whose geometry has to be carefully designed to achieve the desired optical functionality. In addition to the limits imposed by lithographic design-performance compromises, their optical behavior cannot be accurately tuned afterward, making them difficult to integrate in dynamic optical systems. Here we show the realization of fully reconfigurable flat varifocal diffractive lens, which can be in-place realized, erased and reshaped directly on the surface of an azopolymer film by an all-optical holographic process. Integrating the lens in the same optical system used as standard refractive microscope, results in a hybrid microscope capable of multi-depth object imaging. Our approach demonstrates that reshapable flat optics can be a valid choice to integrate, or even substitute, modern optical systems for advanced functionalities.

1. Introduction

Conventional lenses allow light focusing and imaging formation by exploiting light refraction at spherical surfaces of a bulky component made of a dielectric material (e.g. glass) [1,2]. The optical properties of the medium and the surface macroscopic geometrical parameters, as the radius of curvature and the diameter, determine its functionality by defining the focal length and the numerical aperture. The miniaturization trend demanded by emerging technologies for smartphones, wearables, automotive and virtual reality, is not fully compatible with size and weight requirements of bulky lenses, strongly pushing, instead, the research toward flat and lightweight optical devices able to perform as their conventional counterpart [3].

Flat optical components realize the modulation of the incident light wavefront with thicknesses comparable or even smaller than the light wavelength [4–6]. The optical functionality of these devices is designed by accurately engineering the geometries of light modulating surfaces at micro and nanoscales [7]. Flat optical components acting as beam deflectors, diffraction gratings, lenses and holograms, have been demonstrated over years [8]. Using the laws of light diffraction, flat lenses are traditionally designed as circular apertures in opaque screens or as topographic reliefs with radial symmetry on a dielectric material. Light modulation from these diffractive elements is the result of the coherent superposition of infinite wavelets, emerging from each infinitesimal element constituting the structured surface [7–10]. In addition to diffractive devices, recent developments in the new metasurfaces technology led to the explosion of metalenses, in

#455520 https://doi.org/10.1364/OE.455520
Journal © 2022 Received 3 Feb 2022; revised 11 Mar 2022; accepted 14 Mar 2022; published 31 Mar 2022

Optics EXPRESS

which incident light is modulated, in a subwavelength regime, according to the geometry and the orientation of accurately designed resonant subwavelength scatterers [11].

In both cases, flat lenses bring many advantages in terms of weight saving and reduced dimensions in respect to the standard bulky lenses, constituting valid alternatives to refractive optics in demanding situations, e.g. space exploration [12,13] or depth sensing [14,15]. As further benefits, flat lenses can integrate more functionalities than their refractive counterparts [8] when used alone or when combined with other refractive optics to realize hybrid systems [16–19]. For example, diffractive lenses able to focus light beyond the diffraction limit by exploiting light super-oscillations [20,21], capable of broadband achromatic imaging [22,23], or designed for X-rays focusing or imaging [24,25] have been demonstrated, while new metalenses-based devices with even more advanced functionalities and performances are continuously reported [26–29].

Surface design of these compact devices was widely investigated over years [30,31] in order to optimize their functionality taking also into account the limits imposed by manufacturing techniques. The fabrication process is indeed demanding for devices with high performances and is typically accomplished through complex multistep and multilevel lithographic techniques, whose accuracy strongly affects the ultimate operation performances of the device [32–34]. Furthermore, metalenses require also challenging design and optimization processes that, together with expensive fabrication techniques needed, make their large-scale production more burdensome in respect to diffractive devices [35]. However, several conventional lens applications, as light focusing and imaging, do not often require the highest performances offered by metalenses, and even diffractive lenses, when properly designed and fabricated, can provide remarkable optical quality, while maintaining the advantage of a simpler and cheaper design and manufacture [36,37].

After the fabrication process of standard lithography, the crucial parameters for lens operation, like the focal length and the focusing efficiency, are essentially frozen. This limits the possibility to use them as dynamically tunable devices only in sophisticated systems [38–45] and with limited tunability ranges [41,46,47], becoming not suitable where dynamic optical devices are required [48,49]. Tunable diffractive lenses can be, for example, realized using liquid crystals (LC) devices with many limitations in terms of layer thickness and tunability range and also additional challenges related to their strong polarization dependence [50].

We recently moved forward in this direction by developing a reversible lithographic technique for creating diffractive surfaces on azopolymer thin films [51,52]. We demonstrated the realization of fully reconfigurable phase-modulating diffractive surfaces with engineered diffraction behavior such as reconfigurable flat lenses, extending the design proposed by Gabor for the realization of amplitude zone plates [53–55]. Similar to a familiar diffraction grating, these lenses produce multiple diffraction orders, each focused at different positions of the optical axis. By acting as intrinsic multifocal lenses, both positive and negative, then, these devices could be useful in several applications, as the realization of a compact radial shearing interferometer [56].

In this work we further investigated focusing and imaging properties of lenses realized as cosinusoidal phase zone plates, showing that the multifocal behavior can be also applied in the design of advanced hybrid imaging systems, based on both refractive and diffractive optics. In particular, we show here the realization of a hybrid microscope with controllable magnification, field of view and working distance, obtained using a diffractive reconfigurable lens acting as a Barlow lens. This lens is directly realized on the surface of a photo-responsive azobenzene-containing polymer, which can be completely re-morphed in-place to achieve different parameters, as focal length and numerical aperture, by an all-optical reversible lithographic process. Our approach proves the benefits of well-engineered flat optics that in the future can integrate or even replace standard optics, leading to compact, lightweight, low cost and high performances optical systems.

Optics EXPRESS

2. Phase-only cosinusoidal zone plate lenses

The cosinusoidal Phase Zone Plate (c-PZP) is the counterpart to the amplitude Gabor zone plate [53,55], in which the alternating absorbing and transmitting circular zones are replaced with transparent phase modulating zones, each imposing a position dependent phase delay on the incoming wavefront. In the same way that a diffraction grating separates an incoming plane wave into a sum of emerging plane waves with different wavevectors, a c-PZP acts as a phase grating with circular symmetry and radially variable groove spacing, splitting an incident wave into a sum of spherical emerging waves, each converging at distances f_m from the lens, where the integer number m defines the focal diffraction order.

For an incoming monochromatic plane wave at wavelength λ, travelling in positive z direction, the transversal (in x-y plane) phase modulation produced by the cosinusoidal zone plate is [30]:

$$\varphi(x,y) = \varphi(r) = \frac{\beta}{2}(1 + \cos(\alpha r^2)). \tag{1}$$

Here, the parameter β is the maximum phase modulation depth imposed on the incident wavefront, the parameter α is related to lens geometry and determines the first order focal distance $f=f_{+1}$, and $r=(x^2+y^2)^{1/2}$ is the radial coordinate in c-PZP plane.

This phase profile can be realized through a structured dielectric surface with periodicity-varying grooves, which encodes the required phase modulation pattern in local optical path differences for the incident wave, travelling in surface medium with refractive index $n=n(\lambda)$ and local thickness $h(x,y)$. If the medium surrounding the structured dielectric is air, as schematized in Fig. 1(a), the maximum phase modulation depth β is proportional to the relief height h, according to:

$$\beta = \frac{2\pi}{\lambda}(n-1)h. \tag{2}$$

The explicit relation between the parameter α and the first order focal distance f of the c-PZP is obtained by requiring constructive interference at $z=f$ of the wavelets emerging from the topographic maxima (or minima) of the surface:

$$\alpha = \frac{2\pi}{\lambda^2 - 2\lambda f}. \tag{3}$$

Diffraction properties of a c-PZP are strongly related both to the relief height and to their lateral geometry. This becomes clear if the phase zone plate is represented through a radial complex transmittance function $t(r)$ modulating, in the scalar approximation of wave optics, the wavefront of an incident optical field U_{in} propagating through the device. In this situation, the optical field U_{out} immediately after the phase mask is given simply by $U_{\text{in}} \cdot t(r)$. In the case of a c-PZP, $t(r)$ can be written as:

$$t(r) = \exp[i\varphi(r)] = \exp\left[i\frac{\beta}{2}(1 + \cos(\alpha r^2))\right]. \tag{4}$$

This complex transmittance function can be expanded in the base of radial harmonics using the Jacobi expansion [57], resulting in [30]:

$$t(r) = t_0 \sum_{m=-\infty}^{+\infty} i^m J_m\left(\frac{\beta}{2}\right)\exp(im\alpha r^2), \tag{5}$$

where t_0 is a constant phase term, i^2=-1, J_m is a first kind Bessel function of the m^{th} order, and β and α are the surface structural parameters given in Eq. (2) and (3), respectively. Assuming that the light wavelength is negligible compared to the focal length ($\lambda \ll f$), λ^2 can be neglected in

Optics EXPRESS

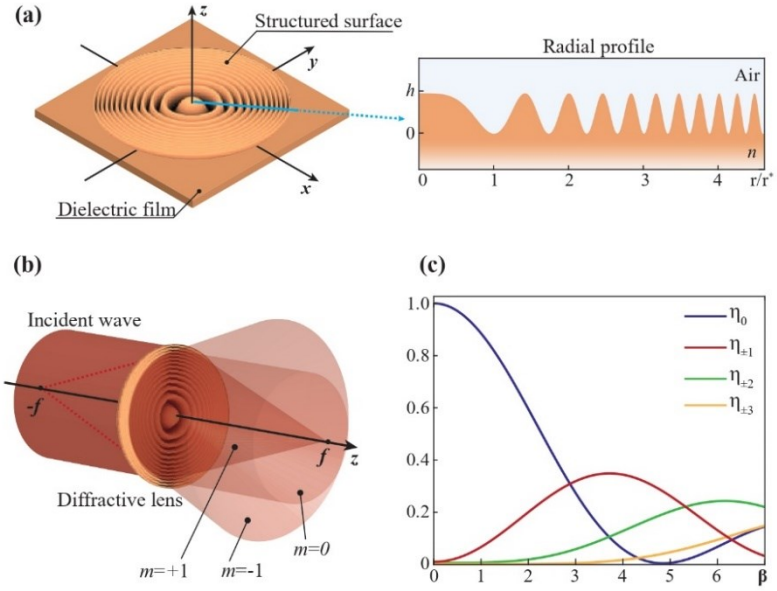

Fig. 1. Design and functionality of a phase-only cosinusoidal zone plate (c-PZP) lens: (a) Schematic of a Gabor zone plate realized on the surface of a dielectric film. Inset shows the radial profile of the cosinusoidal Gabor zone plate, obtained by renormalizing the radial coordinate with respect to the distance of the first minima in the phase mask: $r^* = (\pi/\alpha)^{1/2}$. (b) Schematic of the multiple diffraction foci produced by a c-PZP lens. (c) Diffraction efficiency of first seven diffraction orders plotted with respect the maximum phase mask modulation depth β, directly related to the surface relief amplitude h for a given material of refractive index n.

Eq. (3), so that the expansion in Eq. (5) demonstrates that a c-PZP has a transmission function of a multifocal lens. A plane wave incident on the device emerges as a sum of spherical waves with focals that are fractions of the first order focal length $f_m = f/m$. As schematized in Fig. 1(b), each of the emerging waves represents a specific diffraction order: spherical divergent ($m < 0$), spherical convergent ($m > 0$) and a plane wave ($m = 0$), that corresponds to the unmodulated component. An ideal c-PZP introduces no energy loss, and $|t(r)|^2 = 1$. In this case, the square modulus of each term of the sum in Eq. (5) represents the fraction of energy carried by each emerging spherical wave, allowing the definition of the focusing efficiency for a given order m as:

$$\eta_m = \left| J_m\left(\frac{\beta}{2}\right)\right|^2. \tag{6}$$

This parameter, defined as the intensity of light in each focus f_m, normalized with respect to the incident light intensity, is directly related to the modulation depth β, which then determines, through the relief amplitude h, the redistribution of the incident light power in the emerging diffraction orders. In Fig. 1(c), the efficiency $\eta_m(\beta)$ for the first seven diffraction orders produced by a c-PZP is plotted. Maximum focusing efficiency of ≈ 34% is obtained in the first order (m=±1) for the value $\beta^* \approx 3.68$. For a dielectric surface with $n = 1.7$ (like the one used in this work) this condition is achieved, for monochromatic light at λ=633 nm, at $h \approx 530$ nm. A diffractive c-PZP lens of optimized efficiency can be then realized with thickness smaller than

Optics EXPRESS

the incident light wavelength. It is worth noting that the diffraction efficiency as defined by Eq. (6) does not depend on the sign of m so, if the efficiency of one of the real focal diffraction orders ($m > 0$) is suitably optimized, the same amount of incident light is diffracted also in the corresponding virtual focal order ($m < 0$).

A c-PZP can be also used for imaging [51]. In geometric optics the imaging process of a lens is a form of information transfer between the object plane and an imaging plane. The axial position where the image is formed (imaging plane) is determined by both the axial object position (object plane) and by the focal length of the lens, according to the conjugate planes law [1]. These relations remain valid also for the description of the image formation from a multifocal c-PZP, which simply requires a generalization of the Newton equation for thin lenses [7], in order to take into account for the simultaneous presence of multiple focal lengths, each for every diffraction order m:

$$\left(p - \frac{f}{m}\right)\left(q - \frac{f}{m}\right) = \left(\frac{f}{m}\right)^2. \tag{7}$$

As usual, in Eq. (7), p is the distance between the object and the lens, q is the position of the image plane relative to the plane of the lens, and f is the designed focal distance for the first diffraction order. This relation can be useful to design versatile optical imaging systems working as multifocal diverging or converging lenses. For example, a c-PZP can be used with the same efficiency simultaneously in microscope and telescope configurations. In the first case, the diffractive lens must act as a diverging lens, like the standard objective lens of a compound microscope, while the second configuration is realized with a simple converging lens, able to image objects placed at large distances [51]. Considering a fixed focal length $|f_m|$, in a c-PZP, the two operating regimes correspond to two sets of foci with the same value of m (for example, m=−1 and m=+1, for the microscope and the telescope configuration, respectively), and same diffraction efficiency.

Moreover, if the geometry of the c-PZP can be modified in real time to affect its efficiency, or its focal length f, as happens for diffractive surfaces realized as light-induced surface reliefs on azopolymer films [51], even more functionalities can be realized form Eq. (7), as tunable telescope zoom imaging systems [51] or a multi-depth microscope able to focus at objects placed at different positions.

3. Realization of azopolymer c-PZPs

For the realization of reconfigurable c-PZP, we have used an amorphous azobenzene-containing polymer film (azopolymer), whose surface can be structured through a direct single-step optical lithographic process. The light-induced structuration of these materials originates from a macroscopic material displacement, triggered by cyclic light-fuelled photo-isomerization of the azobenzene units included in the material via different chemical interactions [58–63]. The resulting surface reliefs on the azopolymer free surface are strongly dependent on both the intensity distribution and polarization of the incident light. In the case of circularly polarized light in low intensity regimes [51,64], the relief geometry is proportional to the Laplacian of the intensity pattern [65] and the average surface relief height increases linearly with the total exposure time [51,52].

Light structuration on the film surface can be easily achieved using interference [52,66–69] but in this work we used a Computer-Generated Hologram (CGH) setup based on a Spatial Light Modulator (SLM), which allows to project an arbitrary grayscale spatially structured intensity distribution of light on the surface of the azopolymer film, directly transferring the desired relief geometry on the material surface [64]. We realized the optical setup with a microscope configuration allowing the in-place fabrication [51], characterization and operation of the azopolymer diffractive lenses.

Optics EXPRESS

The scheme of the optical system is presented in Fig. 2(a). An expanded TEM_{00} laser beam (Cobolt Calypso, at wavelength 491 nm) is phase modulated by a computer-controlled reflective phase-only Spatial Light Modulator (Holoeye, Pluto). The modulated beam is propagated through a 4*f* lenses system with the input plane located in the SLM plane. An iris allows spatial filtering of the unwanted components emerging from the SLM. The output plane coincides with the back focal plane of an infinity-corrected long-working distance 50X objective (Mitutoyo), with numerical aperture NA = 0.55 and 13 mm working distance. The writing beam is circular polarized by means of a quarter wave plate (QWP) and its measured intensity, in the sample plane, is approximately 14.0 W/cm^2. This configuration allows the reconstruction of arbitrary structured intensity patterns in the focal plane of the objective, where the azopolymer film is placed. The phase profile (*kinoform*) to be imposed in the SLM plane to reconstruct the desired holographic distribution is defined by an iterative Fourier transform algorithm (Mixed Region Amplitude Freedom (MRAF) algorithm [70]), implemented in MATLAB. The calculation process is initialized providing a target 8-bit grayscale image, shown in Fig. 2(b), representing the desired intensity pattern to be finally reconstructed in the azopolymer plane. Additional details about holographic system and the MRAF algorithm used here can be found in our previous work [51].

The optical image of the intensity hologram, reconstructed in the sample plane, to realize a c-PZP with focal length of $f = 0.6$ mm at λ=633 nm, is shown in Fig. 2(c). This image is acquired through a tube lens (TL) and a CCD camera, that collect the light retroreflected by the sample surface by means of a 70:30 (T:R) beam splitter, Fig. 2(a). The holographic image is the result of an averaging process: many independent calculated kinoforms are buffered to the SLM with a repetition rate of 20 Hz, in order to reduce speckle noise and improve contrast and resolution in the average holographic intensity pattern [64,71].

In the azopolymer structuration processes, an additional diode laser beam at 405 nm illuminates the sample film from the substrate (a standard glass microscope coverslip) side. This beam has circular polarization and different intensity levels depending on its intended role. For low intensity regimes (0.5 W/cm^2) the beam enhances the surface structuring process acting as a writing *assisting* beam. At higher intensity (0.9 W/cm^2), its absorption causes the erasure of previously inscribed surface structures, acting as an *erasing* beam [51,72].

The optical system in Fig. 2(a) can also be used as a brightfield microscope, integrating the holographic setup with a collimated white LED source that simultaneously illuminates the sample, to reconstruct an image of the surface in the camera plane during the lithographic exposure process. The image is reconstructed with a magnification of 50X, according to tube lens and objective focal lengths. Figure 2(d) shows the optical image of the azopolymer surface after 45s of irradiation with the holographic pattern sequence. This exposure time, according to our previous calibration [51], optimize the average relief height ($\approx$ 530 nm), ensuring maximum diffraction efficiency of the lens in the first diffraction order for our material, whose refractive index is equal to 1.7 at the selected working wavelength (λ=633 nm). A detailed morphological characterization of the polymer surface after irradiation by means of Atomic Force Microscopy (AFM) is provided in our previous work [51].

Optics EXPRESS

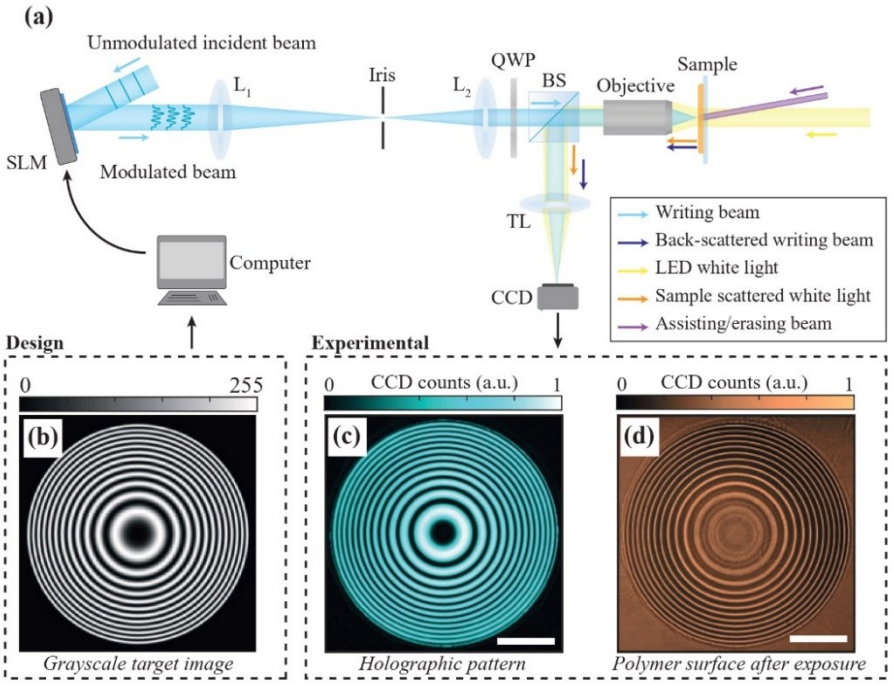

Fig. 2. Experimental realization of a cosinusoidal Gabor lens using holographic inscription on azopolymer film: (a) Representation of the holographic lithography setup: the SLM realizes a 4*f* configuration with a biconvex lens (L_1) with focal length equal to 300 mm, a biconvex lens (L_2) with focal length equal to 175 mm and the objective. A beam splitter (BS) allows the collection of retroreflected light. Light is focused with a tube lens (TL), with 200 mm focal length, on a "DCC3240M Thorlabs" camera (CCD Camera). Colored arrows indicate the direction of the writing beam, the LED beam, and the scattered components from the surface. (b) Gray scale image representing the target image used for generating the holographic pattern through the iterative algorithm. (c) Reconstructed hologram in the sample plane for the realization of a cosinusoidal Gabor zone plate. (d) Optical image of the azopolymer free surface, after 45 seconds of irradiation with both the holographic and the assisting beam, obtained with the brightfield microscopy. Scale bar in panels (c-d) correspond to a physical dimension of 50 µm. CCD counts were remapped in the interval [0 1].

4. Focusing properties of azopolymer c-PZPs

In order to characterize the focusing properties of the realized c-PZP, the emerging light diffraction pattern has been first simulated for an incident plane wave with wavelength λ=633 nm, modulated by the diffractive lens according to the transmission function shown in Eq. (4). In the simulation, material refractive index $n = 1.70$ and relief amplitude $h = 530$ nm, have been considered [51]. In the simulation, the diffractive surface is described as a circular structured area with radius R = 96.4 µm, which corresponds to the radius of the field of view of our holographic writing system. Assuming the modulated surface at $z = 0$, the optical field propagated in any plane at the axial position z is evaluated by solving Helmholtz equation, using the Rayleigh-Sommerfeld diffraction integral in Fresnel approximation [73]. For the simulation, Fresnel integral has been

Optics EXPRESS

numerically implemented in MATLAB using the convolution theorem with the transfer function of the Fresnel propagator [74]. Simulation results are provided in Fig. 3(a) where the axial Point Spread Function (PSF) for a c-PZP with $f = 0.6$ mm is plotted.

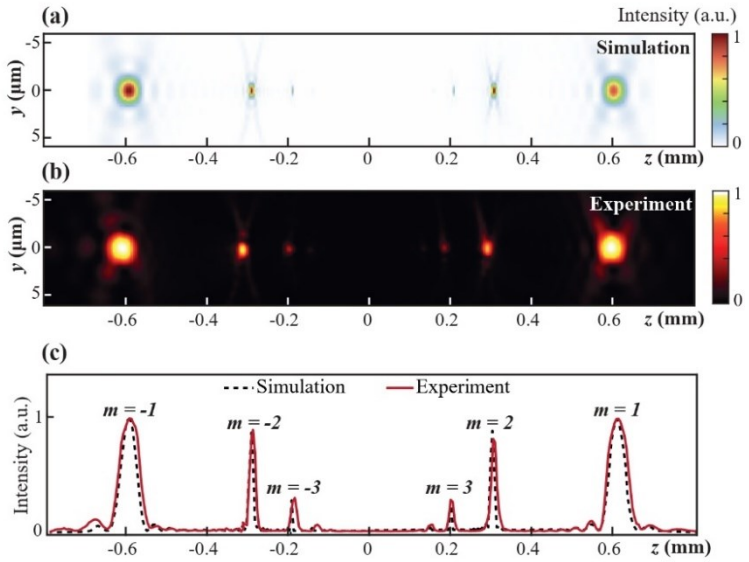

Fig. 3. Focusing properties of realized c-PZP: (a) Simulation of the y-z point spread function obtained evaluating intensity distribution of the optical field. Simulation is performed in the z range (−0.80 mm to 0.80 mm) and in y range (−6.0 μm to 6.0 μm). (b) Experimental PSF reconstructed by collecting the diffracted field from a He-Ne laser beam. CCD counts were remapped in the interval [0 1]. (c) Normalized experimental axial intensity profile of the PSF compared with the axial profile provided by the simulation.

Experimental measurement of the PSF has been performed using a collimated circularly polarized He-Ne laser beam (λ=633 nm), orthogonally incident on the diffractive lens from the substrate side. Light diffracted by the lens is collected though the same microscope imaging system used for brightfield surface observation. The images of the transmitted He-Ne intensity pattern, at different positions, have been obtained by axially translating the c-PZP with a manual micro-positioner. For each sample position, determined with steps of 0.005 mm, an image of the field intensity profile is acquired using the CCD in the focal plane of the tube lens. The images are then stacked together to reconstruct the experimental PSF (Fig. 3(b)). The experimental axial intensity profile, shown in Fig. 3(c) together with the analogous simulated profile, confirms the predictions of the scalar diffraction theory for a c-PZP. The c-PZP acts as a multifocal lens with first diffraction order focal spots at $z = f_{\pm 1} = \pm 0.6$ mm. Both real and virtual foci have the same relative axial intensity, as predicted by Eq. (6).

Focal spot characterization has been performed acquiring the focal intensity distribution for real and virtual foci (m=±1) and their relative transversal profiles, shown in Fig. 4(a-c), respectively. In order to quantitatively describe quality of the focus, we have used the Strehl ratio as figure of merit. The Strehl ratio (SR) is defined as the ratio of the peak intensity $I_{measured}(0)$ in the focal plane with respect to the intensity of an ideal Airy disk (AD), normalized in order to have the

Optics EXPRESS

same area under the curve with respect to the experimental profile [75]:

$$SR = \frac{I_{measured}(0)}{I_{ideal}(0)} = I_{measured}(0)\frac{\lambda^2 f^2}{P_0 \pi R^2}, \tag{8}$$

where P_0 is the normalization factor for the ideal peak intensity $I_{ideal}(0)$ at the center of the diffraction pattern produced at distance $z = f$ by a circular aperture with radius R [76]. For an ideal lens with a diffraction limited behavior and focal intensity distribution of an Airy disk, the Strehl ratio is 1. In real cases, even small aberrations affecting lens functionality cause a significant drop of SR toward smaller values. A SR greater than 0.8 typically denotes a diffraction limited performance for a real lens [75]. In our case a SR = 0.79 has been obtained for both real and virtual focal spots, comparable with values reported for high quality metalenses [26,77].

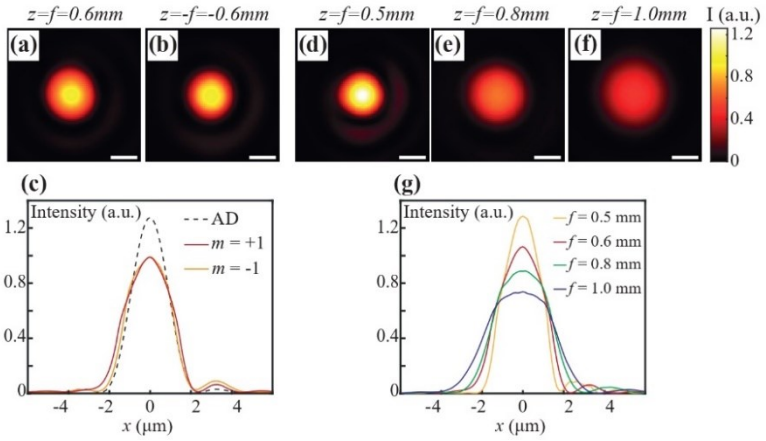

Fig. 4. Characterization of the focal spot quality: (a,b) Light intensity distribution of the first order focal spot of a c-PZP with nominal focal length $f = 0.6$ mm. Images are acquired at $z = f$ and $z = -f$, respectively. (c) Plot of the x-profiles of both real (m=+1) and virtual (m=−1) first order focal spot of the lens with $f = 0.6$ mm and simulated profile of an ideal Airy Disk (AD) used for the evaluation of the Strehl ratio. (d,e,f) Light intensity distribution of the real first order focal spot of c-PZPs with nominal focal length equal to 0.5, 0.8 and 1.0 mm. Images were acquired with the same exposure time fixed for the lens with 0.6 mm focal length. Scale bar in panels (a,b,d,e,f) correspond to a physical dimension of 2 μm. (g) Plot of the experimental focal spot x-profiles obtained at different focal lengths.

The same analysis has been repeated also for c-PZP designed with different focal lengths, obtained by properly reshaping the diffractive lens through azopolymer erasure and rewriting processes. Figure 4(d-f) shows the first order focal intensity distribution for three diffractive lenses with f equal to 0.5 mm, 0.8 mm and 1.0 mm respectively. These lenses are obtained by exposing the same free azopolymer surface area to a proper holographic pattern (after erasure step) with fixed holographic irradiation parameters (intensity and irradiation time). Strehl ratio of 0.78, 0.83 and 0.81 have been respectively obtained for experimental intensity profiles, reported in Fig. 4(g). Since the diameter of the c-PZP are fixed by the field of view of the optical setup, the Numerical Aperture (NA) of the lenses is inversely proportional to the focal length. Accordingly, the Full Width at Half Maximum (FWHM) of the focal spots increases with the focal length. The total optical power in the focal spot, measured by integrating the intensity distribution shown in Fig. 4(a,d,e,f) over a circular area with diameter three times of the FWHM, is conserved within 91% by changing the focal length. This ensures that the erasing and rewriting process of a new

c-PZP with the same writing parameters will preserve the overall quality of the lens focal spot in terms of both efficiency and aberrations. In order to characterize the noise contribution produced by the defocused diffraction orders in the focal plane, we measured the Signal to Noise Ratio (SNR) from the acquired focal spot profiles reported in Fig. 4(g) defined as the ratio between the intensity profile maxima (I_{max}) and minima (I_{min}). The analysis provided a minimum SNR of ~22 dB, that correspond also to a minimum spot visibility, defined as $(I_{max} - I_{min})/(I_{max} + I_{min})$, of 0.99, confirming small contribution in the focal plane from other out of focus diffraction orders.

It is worth mentioning that our current setup allows the realization of c-PZPs with focal lengths in the range from 0.3 to 1.2 mm, with limits dictated only by the resolution of the holographic system and by objective field of view. Using different combinations of optics and SLM for the holographic projection, we could easily expand this range. However, in the operating focal length range, our c-PZPs can be fully in-place reshaped with no quality loss, allowing the realization of dynamical light focusing systems.

5. Hybrid Barlow lens configuration for multi-depth microscope imaging

An ideal imaging optical system, such as an optical microscope, reconstructs in a specific plane of the optical axis, the image, eventually inverted and magnified, of objects lying in a range of planes determined by the depth of field of the system. Typically, microscope objectives, as the one composing our setup in Fig. 2(a), are designed with very short depth of field in order to increase their lateral and axial resolution. For such systems, sharp imaging is limited only to objects placed at a fixed distance from the front lens of the objective, that is defined as the working distance.

The field of view of a microscope can be enlarged properly translating, replacing or integrating the optical elements composing the system. An example is represented by Barlow lenses. A Barlow lens is a diverging lens that increase the focal length of an imaging system. As a result, also its field of view is accordingly increased [78]. When used in microscopy, the working distance of a system equipped with a Barlow lens is increased and the magnification power of the microscope is reduced.

The working principle of a standard refractive Barlow is schematized in Fig. 5(a): this lens, with focal length f, is placed after the front lens of a converging lens (e.g. an objective). The lens forms a virtual image of an object placed at distance z_O from the plane identified by the working distance (WD), assumed to be at $z = 0$ in our coordinate system. If the position z_L of the Barlow lens is properly chosen according to its focal length, the virtual image from this lens is reconstructed in the imaging plane (at $z = 0$) of the objective and transformed then into a real image by the subsequent optical elements in the microscope.

Due to the presence of virtual foci, diffractive c-PZPs can be directly used as Barlow lenses in refractive/diffractive hybrid imaging systems. When realized on azopolymers, the c-PZPs can even enlarge the range of applications behind the field of extender of classical Barlow lenses, due to the possibility of dynamically changing their focal length. In this work, we implement the c-PZP Barlow imaging configuration directly combining the holographic system and the lithographically produced c-PZPs on azopolymer films, as schematized in Fig. 5(b). As a results, we obtain a hybrid microscope composed of a part of fixed refractive optics and a reconfigurable cosinusoidal zone plate, whose focal length can be tuned on demand through an in-place all-optical reshaping process of the azopolymer surface. This system can provide images of extended objects placed at arbitrary positions of the optical axis by proper tuning both the position and the focal length of the c-PZP.

The object used for our experiments is a microscope calibration target (from Thorlabs) composed by a grid of orthogonal lines, with spacing of 50 μm, printed on a glass substrate. The object is mounted on a manual micro-positioner that allows its translation along the optical axis. A reference image of the object, obtained by placing the grid in the objective focal plane ($z_O = 0$)

Optics EXPRESS

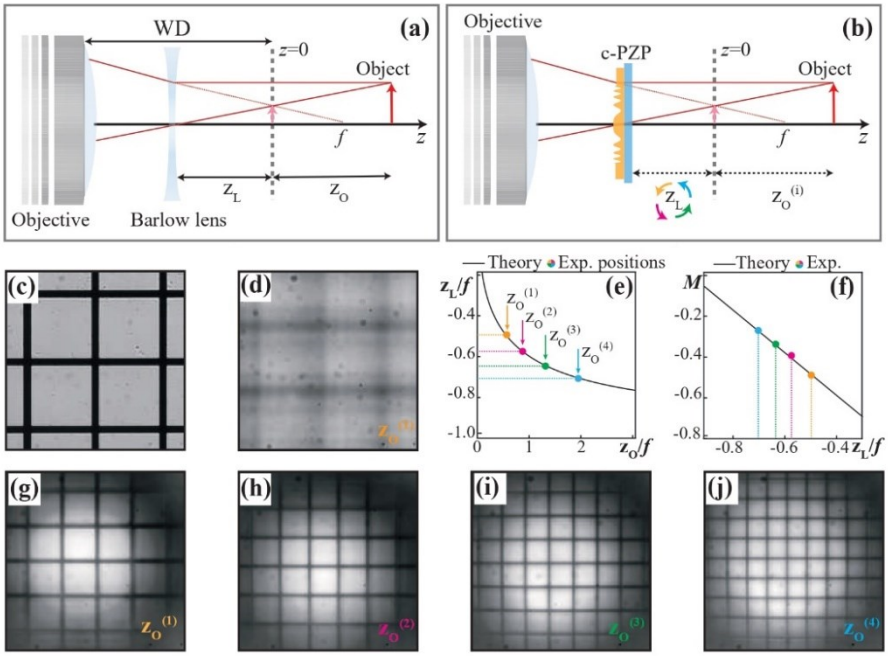

Fig. 5. Barlow lens configuration for multi-depth imaging microscope. (a) Representation of the working principle of a Barlow lens coupled with a microscope objective. (b) Barlow lens can be easily replaced with a c-PZP obtaining the same effect. (c) Optical image of the calibration grid with grid spacing equal to 50 µm. Image is obtained fixing the grid position at $z_O = 0$ before the azopolymer structuration. (d) Optical image of the grid at $z_O = 0.300$ mm. (e) Theoretical and experimental values for the ratio z_L/f of the diffractive lens with respect to the object position z_O/f. (f) Theoretical and experimental values for the magnification with respect z_L/f . (g) Optical image of the grid obtained for $z_O^{(1)} = 0.300$ mm and $z_L^{(1)} = -0.300$ mm. (h) Optical image of the grid obtained for $z_O^{(2)} = 0.500$ mm and $z_L^{(2)} = -0.350$ mm. (i) Optical image of the grid obtained for $z_O^{(3)} = 0.800$ mm and $z_L^{(3)} = -0.400$ mm. (j) Optical image of the grid obtained for $z_O^{(4)} = 1.100$ mm and $z_L^{(4)} = -0.430$ mm. Images in panels (e,f,g-j) were obtained fixing the CCD region of interest in order to highlight magnification effects.

before that the c-PZP is inscribed on the azopolymer film, is shown in Fig. 5(c). This image, is reconstructed collecting scattered light from the object, transmitted through the flat azopolymer film which was already aligned in the microscope light-path.

When the object is moved in a new position (e.g. $z_O^{(1)} = 0.300$ mm) using the micro-positioner (with sensitivity equal to 0.005 mm), the resulting out-of-focus image acquired by the CCD camera appears blurred, Fig. 5(d). To bring back the image in focus, a diffractive lens with $f = 0.6$ mm is holographically inscribed on the azopolymer film, by first translating the azopolymer film in the lithographic plane at $z = 0$ and then re-translating the structured film with the c-PZP in the working position z_L, found from Newton equation (Eq. (7)) imposing that the diffractive lens

Optics EXPRESS

of focal f forms an image of the object at $z = 0$:

$$\frac{z_L}{f} = \frac{1}{2}\left(\frac{z_O}{f} - \sqrt{\frac{z_O^2}{f^2} - \frac{4z_O}{mf}}\right). \tag{9}$$

Only the class of solutions such that z_L is in a finite range is considered, in order to realize a more compact optical system. Despite classical Barlow configuration requires a negative focal length ($m < 0$) placed between the microscope lens and the object ($z_L < 0$), in writing Eq. (9), we explicitly maintained the diffractive lens focal order m still unspecified in order to highlight some of the advantages of building a hybrid imaging configuration based on a c-PZP. From Eq. (9), indeed, for every position of the object z_O, at least two distinct positions z_L of the diffractive lens can realize the imaging condition, each corresponding to an explicit choice of $|m|$ and $sign(m)$. Limiting the discussion to the first order foci ($|m|=1$) of c-PZPs, that have the maximum diffraction efficiency, if $m=+1$ (converging lens), image formation is possible only if the c-PZP is placed in the same half space of the object ($z_L > 0$), and only if the object lies at distances larger than four times the focal length f of the lens ($z_O > 4f$). This configuration works as a microscope with extended depth of field, able even to image large objects placed very far (at $z_O \gg 0$) from the original imaging plane (telescope configuration), as we demonstrated recently by our azopolymer-based c-PZPs [51]. Conversely, the same c-PZP operates simultaneously as a classical Barlow lens through its negative focal order ($m=-1$), resulting in a compact ($z_L < 0$) imaging system with extended depth of field.

The solid line plot in Fig. 5(e) shows the correct positions (in units of f) for the azopolymer c-PZP Barlow lens calculated by solving Eq. (9) for different normalized positions z_O/f of the object translating along the optical axis. From the plot, is evident that any position of the object is correctly imaged by the system by tuning the ratio z_L/f of the azo c-PZP in a finite domain.

Newton equation allows also to define the magnification power M of the system by extending the standard equation of linear magnification [1] valid for a thin glass lens to a diffractive multifocal c-PZP:

$$M = m\frac{z_L}{f} - 1, \tag{10}$$

whose solutions, obtained for $m=-1$, are plotted in Fig. 5(f).

According to the solution of Eq. (9), by positioning in the experiment the azopolymer c-PZP with $f = 0.6$ mm at $z_L = -0.300$ mm, the previously blurred object placed at $z_O^{(1)} = 0.300$ mm appears again in focus in the area of the image identified by the aperture of the diffractive lens, Fig. 5(g). As the hybrid configuration grants a high axial selectivity for image formation, no contributions from other diffraction orders are visible, allowing for the reconstruction of an hight contrast image as result of the achieved efficiency-optimized condition for the azopolymer c-PZP.

Also, the measured magnification is in accordance with theoretical predictions of Eq. (10). To further prove the correct image reconstruction of the hybrid microscope, we sequentially moved the position of the object along the optical axis, before re-gaining an in-focus image by adapting the position of the diffractive c-PZP lens. The tested position pairs ($z_O^{(i)}$, $z_L^{(i)}$) are shown as experimental points in Fig. 5(e), while Fig. 5(f) shows the experimental magnification measurements obtained from the focused images of the grid, Fig. 5(g-j), compared to theoretical prediction.

Regarding the quality of the image produced by the hybrid Barlow system in Fig. 5(g-j), one should consider that, similar to standard diffractive lens, the c-PZP is designed here to focus only beams with normal incidence with respect to the structured surface. This condition is no longer true if the object is placed very close to the lens. As a result, a loss of contrast is observed at the periphery of the images, where the angle of the incidence increases. This aberration effect, known as vignetting, is typically observed in diffractive imaging systems [79], and could be

Optics EXPRESS

eventually reduced by properly designing an optimized radial surface profile for the diffractive lens [80].

The results in Fig. 5(g-j) demonstrate a successful realization of a hybrid microscope that requires only the motion of a thin and lightweight diffractive component to provide in focus images of objects placed at different axial positions. However, together with the physical motion of the diffractive lens, the in-place all-optical reconfiguration of the azopolymer can be used to realize varifocal c-PZP Barlow lenses with advanced functionalities.

An example is the possibility to realize an operating Barlow configuration with a fixed position z_L of the varifocal diffractive lens. According to Eq. (9), the operation of the in focus image of a translating object along the axis can be recovered by substituting the translation of the c-PZP lens (as schematized in Fig. 5(b)) with a shift of the focal length f to tune the ratio z_L/f (Fig. 6(a)). Figure 6(b-d) show the in-focus images of the object placed at different positions $z_O^{(i)}$ obtained by reconfiguring the focal length of a Barlow c-PZP lens at proper values $f^{(i)}$, satisfying Eq. (9) for a fixed position of the lens z_L=−0.300 mm. It should be noted that a similar approach for multi-depth imaging requires a high precision lens fabrication to match the analytically calculated values of the focal length. With our holographic system, this requirement is instead accomplished effortlessly, as the desired lens design is directly included in the holographic calculation process with arbitrary degree of precision.

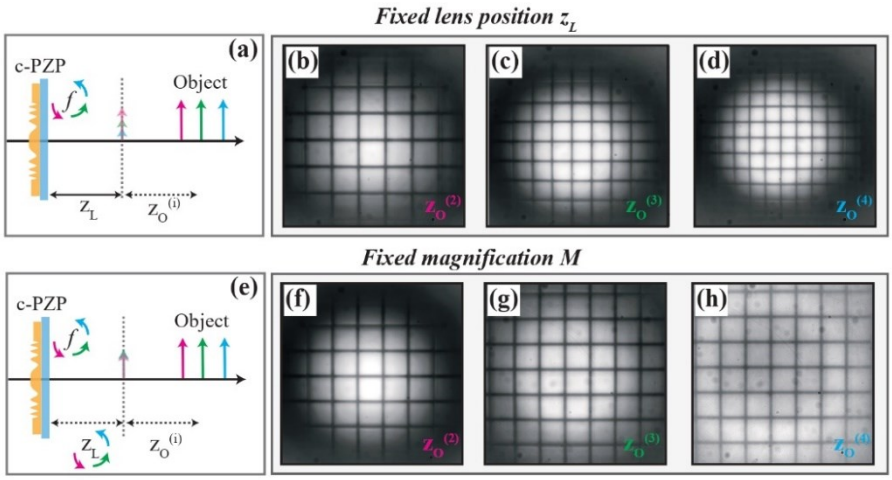

Fig. 6. Barlow lens configuration with fixed diffractive lens position and fixed magnification. (a) Representation of the working principle of a c-PZP Barlow lens with fixed position allowing object imaging through its focal length remodulation. (b-d) Optical images of the grid obtained for $z_O^{(i)}$ and $z_L^{(i)}$=−0.300 mm with c-PZP with focal length equal to $f^{(1)}$ = 0.4800 mm, $f^{(2)}$ = 0.4125 mm and $f^{(3)}$ = 0.3818 mm respectively. (e) Representation of the working principle of a c-PZP Barlow lens with tunable position and reshapable focal length allowing object imaging with controlled magnification. (f-h) Optical images of the grid obtained for $z_O^{(i)}$ with c-PZP with focal length equal to $f^{(1)}$ = 0.4142 mm, $f^{(2)}$ = 0.6627 mm and $f^{(3)}$ = 0.9112 mm placed at $z_L^{(1)}$=−0.270 mm, $z_L^{(2)}$=−0.430 mm and $z_L^{(3)}$=−0.590 mm respectively.

The c-PZP reconfiguration is achieved by erasing and reinscribing the azopolymer surface with a properly designed new surface relief geometry for the lens by irradiating the same area of the film with a new properly designed holographic pattern. It is worth mentioning that the reconfiguration of the azopolymer surface in our experimental configuration still requires the

movement of the azopolymer film in the lithographic plane ($z = 0$), where the writing holographic pattern is projected. Additionally, as the object to be imaged is placed close to the azopolymer surface, the erasure, in each reconfiguration step, is accomplished by irradiating the azopolymer film through the object itself, that has to be transparent. Both these limits could be in principle overcome by using a three-dimensional control over the holographic light pattern for structuring the surface in planes different from $z = 0$ [81] and by collimating the erasing beam through the same writing objective. With these clarifications, the results of Fig. 6(a-d) can be intended as a proof of concept of motionless multi-depth imaging system based on a varifocal diffractive lens.

As additional advanced configuration for the operation of the varifocal azopolymer c-PZP, we demonstrate in Fig. 6(e-h) a Barlow configuration able to maintain a fixed magnification in imaging objects at different positions of the optical axis. This requires the variation of both the position z_L and the focal length f of the Barlow lens (Fig. 6(e)) to simultaneously satisfy Eq. (9) and Eq. (10) for a fixed value M of the magnification. In the experiment of Fig. 6(f-h), a magnification $M = -0.35$ was fixed and the corresponding ratio z_L/f was calculated from Eq. (10). Then, the solutions $(z_L{}^{(i)}, f^{(i)})$ from Eq. (9) for different $z_O{}^{(i)}$ and fixed z_L/f have been used to define both the position and the focal length of the azopolymer c-PZP Barlow lens. As usual, the c-PZP focal length variation is achieved as holographically repeated erasing and rewriting steps of the azopolymer film surface. The direct measure of the magnification in the re-gained in-focus images of the object reported in Fig. 6(f-h), provided a value of M equal to -0.35 ± 0.02, -0.37 ± 0.02 and -0.36 ± 0.02, respectively, with the uncertainty dictated only by the positioning error of both the c-PZP and the object, and in perfect agreement with a constant magnification of the design.

In addition, as evidenced in the images Fig. 6(f-h), one should note that the imaging configuration with simultaneous translating/varifocal c-PZP results also in an effective reduction of the vignetting effect in a fixed region of interest of the image. This effect arises from the fact that the overall distance between the object and the diffractive lens increases passing from Fig. 6(f) to Fig. 6(h), with a larger number of light rays from the object that satisfy the condition of paraxial incidence. These results clearly demonstrate the advanced applications achievable with a hybrid microscope imaging system based on tunable varifocal diffractive lenses.

6. Conclusions

In this work we showed the realization of reshapable cosinusoidal phase zone plates through surface structuring of an azopolymer thin film. These phase-modulating diffractive lenses can be accurately designed using scalar diffraction theory and directly realized, in a single lithographic step, by exposing the surface of the azopolymer film to a computer-generated holographic intensity pattern. Precise focal length design and controlled diffraction efficiency are easily achievable through our lithographic method. The multifocal nature of the realized lenses, predicted by diffraction theory and characterized in our experiment, has been used to design an hybrid microscope imaging systems, capable to provide images of objects placed at any position of the optical axis. In addition, the all-optical reconfiguration of azopolymer films have been used here to realize varifocal diffractive lenses, that further extend the functionality of the hybrid microscope system. Tuning the focal length and the position of the diffractive lens provides simultaneous and independent control over the magnification, the field of view and the working distance of the hybrid imaging system, surpassing some of the limits of standard configurations based on Barlow lenses

As azopolymers can be optically erased, we demonstrated an in-place surface reshaping resulting in varifocal flat diffractive lenses. We also investigated focusing properties of these devices using a probe beam integrated in the holographic setup, demonstrating that the reshaping process preserves their efficiency and their overall quality: image formation from a phase diffractive lens obeys to a generalized conjugate planes equation, verified through experimental

Optics EXPRESS

results, allowing an easy design of optical systems based both on refractive and diffractive optics, also adding further useful degrees of freedom. As proof we have shown the possibility of using flat reshapable cosinusoidal phase zone plates to obtain a hybrid microscope capable of reconstructing in-focus images of small objects placed at different positions of the optical axis.

Our approach proves the advantages of flat shapeshifting optics as the basis of next-generation optical systems.

Funding. H2020 European Research Council (817794, research and innovation program "METAmorphoses"); Ministero dell'Istruzione, dell'Università e della Ricerca (CIR01_00015); Fondazione Cariplo (2019-3923).

Disclosures. The authors declare no conflicts of interest.

Data availability. Data underlying the results presented in this paper are not publicly available at this time but may be obtained from the authors upon reasonable request.

References

1. M. Born and E. Wolf, *Principles of Optics: Electromagnetic Theory of Propagation, Interference and Diffraction of Light*, 7th ed. (Cambridge University Press, 1999).
2. B. Saleh and M. Teich, *Fundamentals of Photonics*, 2nd Edition (Wiley-Interscience, 2007).
3. W. T. Chen and F. Capasso, "Will flat optics appear in everyday life anytime soon?" Appl. Phys. Lett. **118**(10), 100503 (2021).
4. P. Genevet, F. Capasso, F. Aieta, M. Khorasaninejad, and R. Devlin, "Recent advances in planar optics: from plasmonic to dielectric metasurfaces," Optica **4**(1), 139–152 (2017).
5. F. Capasso, "The future and promise of flat optics: a personal perspective," Nanophotonics **7**(6), 953–957 (2018).
6. W. Liu, H. Cheng, J. Tian, and S. Chen, "Diffractive metalens: from fundamentals, practical applications to current trends," Advances in Physics: X **5**(1), 1742584 (2020).
7. D. C. O'Shea, T. J. Suleski, A. D. Kathman, and D. W. Prather, *Diffractive Optics: Design, Fabrication, and Test* (SPIE Press, 2004).
8. B. C. Kress and P. Meyrueis, *Applied Digital Optics: From Micro-Optics to Nanophotonics* (Wiley, 2009).
9. A. Vijayakumar and S. Bhattacharya, *Design and Fabrication of Diffractive Optical Elements with MATLAB* (SPIE, 2017).
10. S. Sinzinger and M. Testorf, "Transition between diffractive and refractive micro-optical components," Appl. Opt. **34**(26), 5970–5976 (1995).
11. F. Aieta, M. A. Kats, P. Genevet, and F. Capasso, "Multiwavelength achromatic metasurfaces by dispersive phase compensation," Science **347**(6228), 1342–1345 (2015).
12. G. Andersen and D. Tullson, "Broadband antihole photon sieve telescope," Appl. Opt. **46**(18), 3706–3708 (2007).
13. X. Luo, "Subwavelength Artificial Structures: Opening a New Era for Engineering Optics," Adv. Mater. **31**(4), 1804680 (2019).
14. Q. Guo, Z. Shi, Y.-W. Huang, E. Alexander, C.-W. Qiu, F. Capasso, and T. Zickler, "Compact single-shot metalens depth sensors inspired by eyes of jumping spiders," Proc. Natl. Acad. Sci. **116**(46), 22959–22965 (2019).
15. S. Colburn and A. Majumdar, "Metasurface Generation of Paired Accelerating and Rotating Optical Beams for Passive Ranging and Scene Reconstruction," ACS Photonics **7**(6), 1529–1536 (2020).
16. A. Flores, M. R. Wang, and J. J. Yang, ""Achromatic hybrid refractive-diffractive lens with extended depth of focus," Appl. Opt. **43**(30), 5618–5630 (2004).
17. O. Cakmakci and J. Rolland, "Head-Worn Displays: A Review," J. Display Technol. **2**(3), 199–216 (2006).
18. G. Zhou, H. M. Leung, H. Yu, A. S. Kumar, and F. S. Chau, "Liquid tunable diffractive/refractive hybrid lens," Opt. Lett. **34**(18), 2793–2795 (2009).
19. G. Fluder, "Design of a hybrid refractive-diffractive telescope for observations in UV," Exp Astron **50**(2-3), 159–168 (2020).
20. E. T. F. Rogers, J. Lindberg, T. Roy, S. Savo, J. E. Chad, M. R. Dennis, and N. I. Zheludev, "A super-oscillatory lens optical microscope for subwavelength imaging," Nat. Mater. **11**(5), 432–435 (2012).
21. A. Yu, G. Chen, Z. Zhang, Z. Wen, L. Dai, K. Zhang, S. Jiang, Z. Wu, Y. Li, C. Wang, and X. Luo, "Creation of Sub-diffraction Longitudinally Polarized Spot by Focusing Radially Polarized Light with Binary Phase Lens," Sci Rep **6**(1), 38859 (2016).
22. O. Avayu, E. Almeida, Y. Prior, and T. Ellenbogen, "Composite functional metasurfaces for multispectral achromatic optics," Nat. Commun. **8**(1), 14992 (2017).
23. N. Mohammad, M. Meem, B. Shen, P. Wang, and R. Menon, "Broadband imaging with one planar diffractive lens," Sci Rep **8**(1), 2799 (2018).
24. M. M. Greve, A. M. Vial, J. J. Stamnes, and B. Holst, ""The Beynon Gabor zone plate: a new tool for de Broglie matter waves and hard X-rays? An off axis and focus intensity investigation," Opt. Express **21**(23), 28483–28495 (2013).
25. I. Mohacsi, I. Vartiainen, B. Rösner, M. Guizar-Sicairos, V. A. Guzenko, I. McNulty, R. Winarski, M. V. Holt, and C. David, "Interlaced zone plate optics for hard X-ray imaging in the 10 nm range," Sci Rep **7**(1), 43624 (2017).

26. M. Khorasaninejad, W. T. Chen, R. C. Devlin, J. Oh, A. Y. Zhu, and F. Capasso, "Metalenses at visible wavelengths: Diffraction-limited focusing and subwavelength resolution imaging," Science **352**(6290), 1190–1194 (2016).
27. H. Liang, Q. Lin, X. Xie, Q. Sun, Y. Wang, L. Zhou, L. Liu, X. Yu, J. Zhou, T. F. Krauss, and J. Li, "Ultrahigh Numerical Aperture Metalens at Visible Wavelengths," Nano Lett. **18**(7), 4460–4466 (2018).
28. W. T. Chen, A. Y. Zhu, J. Sisler, Z. Bharwani, and F. Capasso, "A broadband achromatic polarization-insensitive metalens consisting of anisotropic nanostructures," Nat. Commun. **10**(1), 355 (2019).
29. N. A. Rubin, G. D'Aversa, P. Chevalier, Z. Shi, W. T. Chen, and F. Capasso, "Matrix Fourier optics enables a compact full-Stokes polarization camera," Science **365**(6448), eaax1839 (2019).
30. V. Moreno, J. F. Román, and J. R. Salgueiro, "High efficiency diffractive lenses: Deduction of kinoform profile," Am. J. Phys. **65**(6), 556–562 (1997).
31. M. B. Fleming and M. C. Hutley, ""Blazed diffractive optics," Appl. Opt. **36**(20), 4635–4643 (1997).
32. K. Huang, F. Qin, H. Liu, H. Ye, C.-W. Qiu, M. Hong, B. Luk'yanchuk, and J. Teng, "Planar Diffractive Lenses: Fundamentals, Functionalities, and Applications," Adv. Mater. **30**(26), 1704556 (2018).
33. N. Lassaline, R. Brechbühler, S. J. W. Vonk, K. Ridderbeek, M. Spieser, S. Bisig, B. le Feber, F. T. Rabouw, and D. J. Norris, "Optical Fourier surfaces," Nature **582**(7813), 506–510 (2020).
34. M. Meem, A. Majumder, S. Banerji, J. C. Garcia, O. B. Kigner, P. W. C. Hon, B. Sensale-Rodriguez, R. Menon, and R. Menon, ""Imaging from the visible to the longwave infrared wavelengths via an inverse-designed flat lens," Opt. Express **29**(13), 20715–20723 (2021).
35. M. Meem, S. Banerji, C. Pies, T. Oberbiermann, A. Majumder, B. Sensale-Rodriguez, and R. Menon, ""Large-area, high-numerical-aperture multi-level diffractive lens via inverse design," Optica," Optica **7**(3), 252–253 (2020).
36. S. Banerji, M. Meem, A. Majumder, F. G. Vasquez, B. Sensale-Rodriguez, and R. Menon, ""Imaging with flat optics: metalenses or diffractive lenses?," Optica," Optica **6**(6), 805–810 (2019).
37. J. Engelberg and U. Levy, "The advantages of metalenses over diffractive lenses," Nat. Commun. **11**(1), 1991 (2020).
38. S. Nagelberg, L. D. Zarzar, N. Nicolas, K. Subramanian, J. A. Kalow, V. Sresht, D. Blankschtein, G. Barbastathis, M. Kreysing, T. M. Swager, and M. Kolle, "Reconfigurable and responsive droplet-based compound micro-lenses," Nat. Commun. **8**(1), 14673 (2017).
39. A. She, S. Zhang, S. Shian, D. R. Clarke, and F. Capasso, "Adaptive metalenses with simultaneous electrical control of focal length, astigmatism, and shift," Sci. Adv. **4**(2), 9957 (2018).
40. E. Arbabi, A. Arbabi, S. M. Kamali, Y. Horie, M. Faraji-Dana, and A. Faraon, "MEMS-tunable dielectric metasurface lens," Nat. Commun. **9**(1), 812 (2018).
41. A. M. Shaltout, V. M. Shalaev, and M. L. Brongersma, "Spatiotemporal light control with active metasurfaces," Science **364**(6441), eaat3100 (2019).
42. Y. Guo, M. Pu, X. Ma, X. Li, R. Shi, and X. Luo, "Experimental demonstration of a continuous varifocal metalens with large zoom range and high imaging resolution," Appl. Phys. Lett. **115**(16), 163103 (2019).
43. S. Colburn, A. Zhan, and A. Majumdar, ""Varifocal zoom imaging with large area focal length adjustable metalenses," Optica **5**(7), 825–831 (2018).
44. S. Colburn and A. Majumdar, "Simultaneous Achromatic and Varifocal Imaging with Quartic Metasurfaces in the Visible," ACS Photonics **7**(1), 120–127 (2020).
45. S. Wei, G. Cao, H. Lin, X. Yuan, M. Somekh, and B. Jia, "A Varifocal Graphene Metalens for Broadband Zoom Imaging Covering the Entire Visible Region," ACS Nano **15**(3), 4769–4776 (2021).
46. M. Y. Shalaginov, S. An, Y. Zhang, F. Yang, P. Su, V. Liberman, J. B. Chou, C. M. Roberts, M. Kang, C. Rios, Q. Du, C. Fowler, A. Agarwal, K. A. Richardson, C. Rivero-Baleine, H. Zhang, J. Hu, and T. Gu, "Reconfigurable all-dielectric metalens with diffraction-limited performance," Nat. Commun. **12**(1), 1225 (2021).
47. H.-S. Ee and R. Agarwal, "Tunable Metasurface and Flat Optical Zoom Lens on a Stretchable Substrate," Nano Lett. **16**(4), 2818–2823 (2016).
48. T. Zhan, K. Yin, J. Xiong, Z. He, and S.-T. Wu, "Augmented Reality and Virtual Reality Displays: Perspectives and Challenges," iScience **23**(8), 101397 (2020).
49. Z. Li, P. Lin, Y.-W. Huang, J.-S. Park, W. T. Chen, Z. Shi, C.-W. Qiu, J.-X. Cheng, and F. Capasso, "Meta-optics achieves RGB-achromatic focusing for virtual reality," Sci. Adv. **7**(5), eabe4458 (2021).
50. Y.-H. Lin, Y.-J. Wang, and V. Reshetnyak, "Liquid crystal lenses with tunable focal length," Liq. Cryst. Rev. **5**(2), 111–143 (2017).
51. S. L. Oscurato, F. Reda, M. Salvatore, F. Borbone, P. Maddalena, and A. Ambrosio, "Shapeshifting Diffractive Optical Devices," *Laser Photonics Rev.*, 2100514 (2022), early access.
52. S. L. Oscurato, F. Reda, M. Salvatore, F. Borbone, P. Maddalena, and A. Ambrosio, "Large-Scale Multiplexed Azopolymer Gratings with Engineered Diffraction Behavior," Adv. Mater. Interfaces **2101375**, 1–9 (2021).
53. D. Gabor, "A New Microscopic Principle," Nature **161**(4098), 777–778 (1948).
54. M. H. Horman and H. H. M. Chau, ""Zone Plate Theory Based on Holography," Appl. Opt. **6**(2), 317–322 (1967).
55. G. L. Rogers, "Gabor Diffraction Microscopy: the Hologram as a Generalized Zone-Plate," Nature **166**(4214), 237 (1950).
56. Z. Wang, S. Wang, P. Yang, and B. Xu, "Radial Shearing Interferometer Based on a Cosinusoidal Zone Plate," IEEE Photonics Technol. Lett. **31**, 1116–1119 (2019).
57. G. N. Watson, *A Treatise on the Theory of Bessel Functions*, 2nd ed. (Cambridge U.P., 1966).

Optics EXPRESS

58. S. L. Oscurato, M. Salvatore, P. Maddalena, and A. Ambrosio, "From nanoscopic to macroscopic photo-driven motion in azobenzene-containing materials," Nanophotonics **7**(8), 1387–1422 (2018).
59. F. Borbone, S. Luigi Oscurato, S. D. Sorbo, F. Pota, M. Salvatore, F. Reda, P. Maddalena, R. Centore, and A. Ambrosio, "Enhanced photoinduced mass migration in supramolecular azopolymers by H-bond driven positional constraint," J. Mater. Chem. C **9**(34), 11368–11375 (2021).
60. J. M. Ilnytskyi, V. Toshchevikov, and M. Saphiannikova, "Modeling of the photo-induced stress in azobenzene polymers by combining theory and computer simulations," Soft Matter **15**(48), 9894–9908 (2019).
61. K. Kim, H. Park, K. J. Park, S. H. Park, H. H. Kim, and S. Lee, "Light-Directed Soft Mass Migration for Micro/Nanophotonics," Adv. Opt. Mater. **7**(16), 1900074 (2019).
62. B. Yadav, J. Domurath, K. Kim, S. Lee, and M. Saphiannikova, "Orientation Approach to Directional Photodeformations in Glassy Side-Chain Azopolymers," J. Phys. Chem. B **123**(15), 3337–3347 (2019).
63. A. Priimagi and A. Shevchenko, "Azopolymer-based micro- and nanopatterning for photonic applications," Journal of Polymer Science Part B: Polymer Physics **52**(3), 163–182 (2014).
64. S. L. Oscurato, M. Salvatore, F. Borbone, P. Maddalena, and A. Ambrosio, "Computer-generated holograms for complex surface reliefs on azopolymer films," Sci. Rep. **9**(1), 6775 (2019).
65. A. Ambrosio, L. Marrucci, F. Borbone, A. Roviello, and P. Maddalena, "Light-induced spiral mass transport in azo-polymer films under vortex-beam illumination," Nat. Commun. **3**(1), 1–9 (2012).
66. H. Rekola, A. Berdin, C. Fedele, M. Virkki, and A. Priimagi, "Digital holographic microscopy for real-time observation of surface-relief grating formation on azobenzene-containing films," Sci Rep **10**(1), 19642 (2020).
67. J. Jelken and S. Santer, "Light induced reversible structuring of photosensitive polymer films," RSC Adv. **9**(35), 20295–20305 (2019).
68. M. Salvatore, F. Borbone, and S. L. Oscurato, "Deterministic Realization of Quasicrystal Surface Relief Gratings on Thin Azopolymer Films," Adv. Mater. Interfaces **7**(11), 1902118 (2020).
69. Y. Lim, B. Kang, S. J. Hong, H. Son, E. Im, J. Bang, and S. Lee, "A Field Guide to Azopolymeric Optical Fourier Surfaces and Augmented Reality," Adv. Funct. Mater. **31**(39), 2104105 (2021).
70. M. Pasienski and B. DeMarco, ""A high-accuracy algorithm for designing arbitrary holographic atom traps," Opt. Express **16**(3), 2176–2190 (2008).
71. J. W. Goodman, ""Some fundamental properties of speckle," J. Opt. Soc. Am. **66**(11), 1145–1150 (1976).
72. J. Vapaavuori, R. H. A. Ras, M. Kaivola, C. G. Bazuin, and A. Priimagi, "From partial to complete optical erasure of azobenzene–polymer gratings: effect of molecular weight," J. Mater. Chem. C **3**(42), 11011–11016 (2015).
73. J. W. Goodman, *Introduction to Fourier Optics* (Roberts and Company Publishers, 2005).
74. D. Voelz, *Computational Fourier Optics: A MATLAB Tutorial* (Society of Photo Optical, 2011).
75. B. D. Guenther and D. Steel eds., *Encyclopedia of Modern Optics*, 2nd edition (Academic Press, 2018).
76. E. Hecht, *Optics*, 4th edition (Addison-Wesley, 2001).
77. M. Khorasaninejad, W. T. Chen, A. Y. Zhu, J. Oh, R. C. Devlin, C. Roques-Carmes, I. Mishra, and F. Capasso, "Visible Wavelength Planar Metalenses Based on Titanium Dioxide," IEEE J. Sel. Top. Quantum Electron. **23**(3), 43–58 (2017).
78. S. J. Anderson, "The Barlow lens," J. Brit. Astro. Assoc. **92**(3), 135–136 (1982).
79. S. Banerji, M. Meem, A. Majumder, B. Sensale-Rodriguez, and R. Menon, "Imaging over an unlimited bandwidth with a single diffractive surface," arXiv:1907.06251 [physics] (2019).
80. S. Banerji, M. Meem, A. Majumder, J. C. Garcia, P. Hon, C. Pies, T. Oberbiermann, B. S. Rodriguez, R. Menon, and R. Menon, "Inverse Designed Flat Optics with Diffractive Lenses," in *Imaging and Applied Optics Congress (2020), Paper ITh5E.3* (Optical Society of America, 2020), p. ITh5E.3.
81. J. Leach, K. Wulff, G. Sinclair, P. Jordan, J. Courtial, L. Thomson, G. Gibson, K. Karunwi, J. Cooper, Z. J. Laczik, and M. Padgett, ""Interactive approach to optical tweezers control," Appl. Opt. **45**(5), 897–903 (2006).

Publication VII

S. Fusco, S. L. Oscurato, M. Salvatore, F. Reda, S. Moujdi, M. De Oliveira, A. Ambrosio, R. Centore, and F. Borbone

Efficient high-refractive-index azobenzene dendrimers based on a hierarchical supramolecular approach

Reprinted from

Chemistry of Materials 35(9), 3722–3730 (2023)

CHEMISTRY OF MATERIALS

pubs.acs.org/cm

Article

Efficient High-Refractive-Index Azobenzene Dendrimers Based on a Hierarchical Supramolecular Approach

Sandra Fusco,[⊥] Stefano Luigi Oscurato,[⊥] Marcella Salvatore, Francesco Reda, Sara Moujdi, Michael De Oliveira, Antonio Ambrosio, Roberto Centore, and Fabio Borbone*

Cite This: *Chem. Mater.* 2023, 35, 3722−3730

Read Online

ACCESS | Metrics & More | Article Recommendations | Supporting Information

ABSTRACT: Real-time manipulation of light in a diffractive optical element made with an azomaterial, through the light-induced reconfiguration of its surface based on mass transport, is an ambitious goal that may enable new applications and technologies. The speed and the control over photopatterning/reconfiguration of such devices are critically dependent on the photoresponsiveness of the material to the structuring light pattern and on the required extent of mass transport. In this regard, the higher the refractive index (RI) of the optical medium, the lower the total thickness and inscription time can be. In this work, we explore a flexible design of photopatternable azomaterials based on hierarchically ordered supramolecular interactions, used to construct dendrimer-like structures by mixing specially designed sulfur-rich, high-refractive-index photoactive and photopassive components in solution. We demonstrate that thioglycolic-type carboxylic acid groups can be selectively used as part of a supramolecular synthon based on hydrogen bonding or readily converted to carboxylate and participate in a Zn(II)−carboxylate interaction to modify the structure of the material and fine-tune the quality and efficiency of photoinduced mass transport. Compared with a conventional azopolymer, we demonstrate that it is possible to fabricate high-quality, thinner flat diffractive optical elements to reach the desired diffraction efficiency by increasing the RI of the material, achieved by maximizing the content of high molar refraction groups in the chemical structure of the monomers.

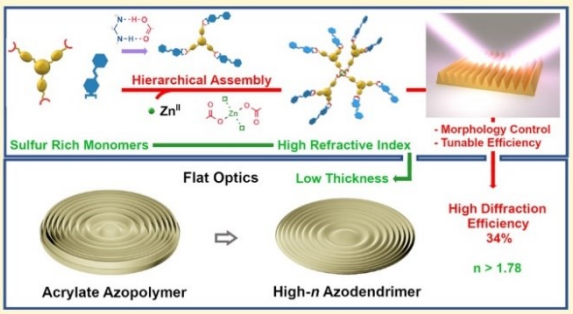

INTRODUCTION

Photoisomerization of azobenzene and its derivatives is a unique and powerful feature as it involves a significant conformational change of this kind of molecules due to the *trans-cis* isomerization, which is accompanied by considerable molecular motion. Functionalization of a material with azobenzenes ("azomaterial") is the practical way to amplify this light-induced nanoscopic movement to produce macroscopic structural modifications of the material bulk, through collective reorientation of azomolecules sustained by light irradiation.[1] When an azomaterial film is irradiated with an interference pattern of light, the macroscopic reconfiguration can translate into mass transport occurring on the surface, with the formation of periodic topographic modulations known as surface relief gratings (SRG).[2] This simple and reversible all-optical process is a unique and intriguing phenomenon and has been object of extended research because of potential applications in numerous fields. While the texturing or reconfiguration of a surface may be exploited to anisotropically control the wettability,[3,4] to influence the growth of living cells,[5−7] or in soft lithographic techniques,[8−10] the spatial modulation of the refractive index, reflecting the modulation of the optical path of an incident light beam in a structured film of a homogeneous azomaterial, is at the core of applicability of SRGs in photonics. Mono- and bidimensional diffractive optical elements (DOE) can be easily fabricated on a large area and with the desired structural complexity to provide different optical functionalities, for applications in spectral filters,[11−13] light couplers,[14−16] light-harvesting layers in solar cells,[17,18] optical outcouplers to improve OLED efficiency,[19,20] and DFB lasers.[21,22] Recently, we have demonstrated that a planar DOE can be generated and reshaped in real time into a different one on the same area of an azopolymer film by tuning the surface morphology directly in the light path,[23,24] a possibility not offered by conventional photolithographic techniques. This approach may enable applications based on the real-time light manipulation through continuous reconfiguration of a DOE. To this aim, highly efficient photoresponsive azomaterials are required to provide rapid rewriting of a surface

Received: March 10, 2023
Revised: April 12, 2023
Published: April 20, 2023

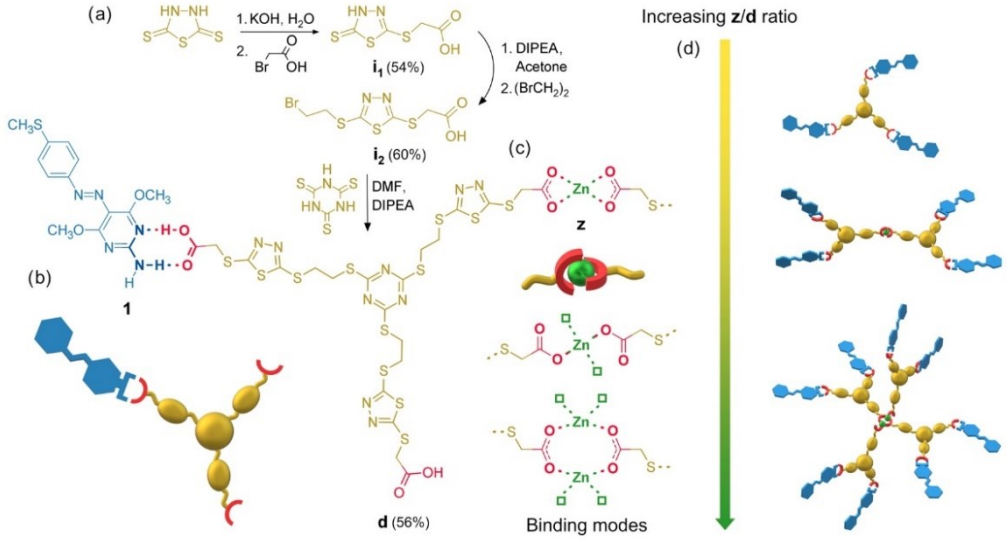

Figure 1. Synthesis scheme of **d** (a); supramolecular synthon between **1** and **d** (b); possible Zn(II)-carboxylate binding modes (c); and scheme of increasing aggregation due to bridging Zn(II)−carboxylate interactions with increasing **z**/**d** ratio (d).

texture. Additionally, increasing the bulk refractive index of the material could produce the desired diffraction efficiency with a lower SRG amplitude, eventually reducing the exposure time and total thickness of the device. Increasing the refractive index is a sought-after feature to improve properties such as light confinement, propagation efficiency, and acceptance angle for the development of waveguides and components such as sensors or waveguide combiners, the latter being key components of Augmented Reality or Mixed Reality devices.[25,26] In this work, we address these problems by designing an efficient high-refractive-index azomaterial. One of the best strategies to increase the refractive index of organic materials while maintaining high optical transparency is the introduction of atoms/groups possessing high molar refraction,[27] as −C−S(II)−C− (7.80) and heteroaromatic units containing −C═N−N− (3.46) and −C═N−C− (4.10) bonds.[28,29] Polymers with a high content of these groups are reported to show the highest refractive indexes known in the literature (n > 1.7),[27] thus convenient and easily accessible sulfur-functionalized triazines and thiadiazoles are good candidates to maximize the density of these high molar refraction groups and enhance the n values of a material. On the other hand, to avoid dilution by low molar refraction alkyl chains, the resulting rigid, heterocycle-rich material structure would not meet the requirements of solubility and responsiveness for a fast SRG inscription process. In this regard, supramolecular chemistry is a powerful, versatile, and well-established tool for overcoming these problems and in general for the design of efficient azomaterials. Particularly, supramolecular azodendrimers, in which azobenzene molecules are linked to the peripheral groups of a dendrimeric oligomer through weak interactions, have proven to be very efficient in terms of SRG formation and to outperform dendrons and dendronized polymers, probably due to their isolated architecture.[30−32] In this work, we designed a practical and flexible multifunctional dendrimeric supramolecular assembly approach to increase the density of high molar refraction heterocycles in the dendrimer core, without adversely affecting solubility and simultaneously maximizing the efficiency of photoresponsiveness in the resulting material. We have recently demonstrated that the high directional double hydrogen bonding in the 2-aminopyrimidine/carboxylic acid supramolecular synthon is an effective strategy to graft an aminopyrimidine-containing azomolecule to a carboxyl group of a polymer chain to produce stable amorphous azopolymers with enhanced mass transport properties.[33] On the other hand, metal coordination has been widely demonstrated as a simple and efficient strategy to grow dendritic structures by self-assembly, without the need for purification.[34] The cooperative action of Zn(II)-carboxylate coordination interactions has been proposed as a straightforward way to tune the properties of a material by simply varying the metal-to-ligand molar ratio.[35] Thus, our supramolecular design has been inspired by this double functionality of the carboxyl group, which may act as one-half of a hydrogen-bonding-based supramolecular synthon and as a carboxylate in a coordination bond to a metal, giving rise to two types of orthogonal and hierarchically ordered weak interactions, which can be selectively used to change the material structure by effortless tuning of the building blocks composition in solution. Through this approach, high-refractive-index azomaterials were easily prepared and their photoresponsive behavior proved to be readily tunable to optimize the efficiency and quality of the SRG inscription process and to fabricate planar holographic lenses with reduced thickness and optimized diffraction efficiency.

■ RESULTS AND DISCUSSION

Material Design and Synthesis. The model of the azomaterial is based on a first-generation three-arm dendrimer with thioglycolic-type carboxyl peripheral groups (**d**, Figure 1). Heterocycles containing high-molar-refraction atoms/bonds were selected among sulfur-functionalized triazines and thiadiazoles to build the dendritic core. The optimal synthetic pathway to dendrimer **d** was found by the convergent approach shown in Figure 1. Straightforward sequential functionalization of thiol groups of 1,3,4-thiadiazole-2,5-dithiol with bromoacetic acid and 1,2-dibromoethane led to the

https://doi.org/10.1021/acs.chemmater.3c00550
Chem. Mater. 2023, 35, 3722−3730

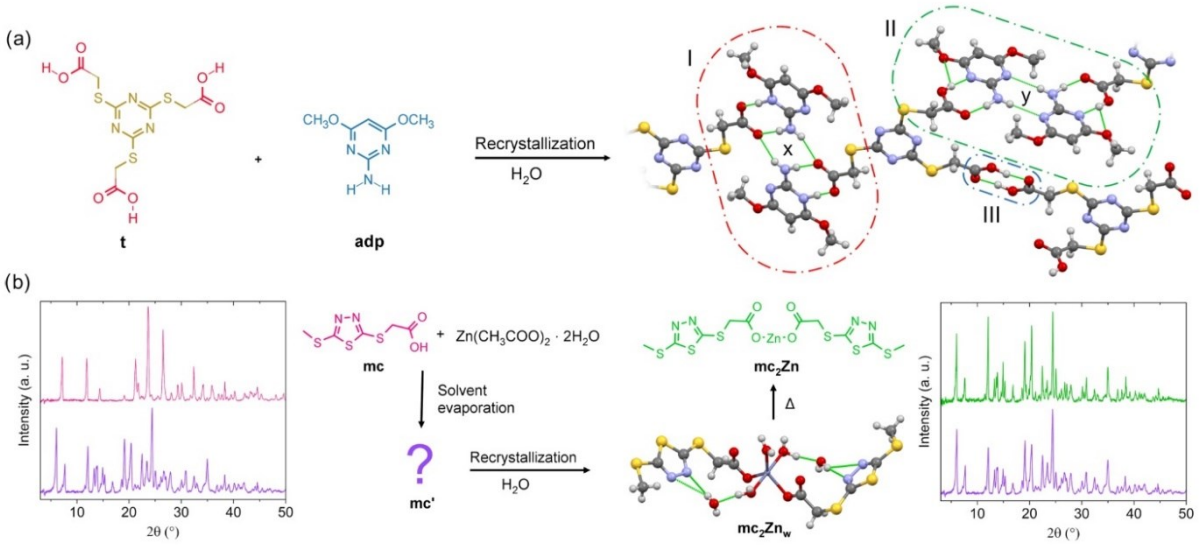

Figure 2. Crystallization scheme of $\mathbf{t(adp)_2}$ complex and SCXRD structure (a). PXRD spectra of **mc** (red line) **mc′** (purple line), $\mathbf{mc_2Zn}$ (dehydrated $\mathbf{mc_2Zn_w}$, green line), and SCXRD structure of $\mathbf{mc_2Zn_w}$ (b).

intermediate $\mathbf{i_2}$ in good yields, then reacted with trithiocyanuric acid to give the final product. The azobenzene structure (**1**, Figure 1) was functionalized with a methylthio group and a 2-aminopyrimidine heterocycle and synthesized according to our recently reported simplified procedure.[33] Direct alkylation of trithiocyanuric acid with bromoacetic acid afforded the product **t** (Figure 2a) used as a model compound for X-ray study.

Complexation with azomolecules can be realized through the supramolecular heterosynthon based on two hydrogen bonds between the acid and aminopyrimidine groups (AP heterosynthon) shown in Figure 1b, giving rise to an $R_2^2(8)$ ring pattern. By this strong molecular recognition interaction, the photoresponsive molecules are grafted as termini of the dendritic core. Alternatively, one or more carboxylic functions can be converted to carboxylate and used as focal points of dendrons to build dendrimers with higher molecular weight through Zn(II)−carboxylate coordination interactions (Figure 1c,d). According to the different possible Zn(II)−carboxylate coordination binding modes and to the crystal structures of zinc(II)-carboxylate complexes,[36,37] increasing contribution by bridging tetra-coordination modes is expected to occur by increasing the ratio between Zn^{2+} and **d**. Therefore, evolution of the material structure toward 1D/2D dendronized coordination polymers or crosslinked systems is expected for high zinc content. However, the SRG inscription efficiency on azomaterials thin films was used as feedback for choosing the appropriate range of compositions to be investigated.

Model Compounds. The structure of azomolecule **1** was solved by single-crystal X-ray diffraction analysis (SCXRD) and is shown in Figure S1 (crystal data are reported in Table S1). We also investigated by SCXRD the interaction in the supramolecular synthon of thioglycolic peripheral groups with the aminopyrimidine moiety of the azomolecule, after successful cocrystallization of compound **t** with 2-amino-4,6-dimethoxypyrimidine (**adp**) in hot water, which afforded single crystals of the $\mathbf{t(adp)_2}$ complex (Figure 2a). In the structure of the complex, each molecule of **t** is coordinated to two **adp** molecules through an AP-type supramolecular heterosynthon, while the third carboxyl is involved in an acid/acid type (AA) homosynthon (Figure $2a_{III}$). In the AP synthon of Figure $2a_{II}$, the bond distances and angles of the N−H···O, OH···N, C−O, and C═O bonds are in agreement with typical values (Table S2)[33] while a more ionic character of the interaction was observed in the case of Figure $2a_I$, where a stronger donation in the OH···N bond occurs, as evidenced by the closer values of C−O and C═O bond distances (1.262 and 1.238 Å, respectively). In case I, the carbonyl and amino groups of two different AP synthons are bridged to form a further ring pattern of hydrogen bonds of the $R_4^2(8)$ type (x), while in case II, a further $R_2^2(8)$-type ring due to the PP homosynthon between two **adp** molecules is established (y). These situations illustrate two possible ways of supramolecular interactions between different dendrimers in the azomaterials.

Due to the stronger acidity of thioglycolic-type carboxylic group (pK_a of thioglycolic acid = 3.55[38,39]) compared to acetic acid (pK_a = 4.76), easy conversion of dendrimer peripheral groups to Zn(II)-carboxylate can be directly accomplished in situ, during the formulation of the azomaterial in solution, by acid−base reaction with zinc acetate dihydrate. This mechanism, which may lead to an increase of the dendrimer generation, was demonstrated by preparing the zinc salt of the model compound **mc** (Figure 2b). By simple dissolution of **mc** and zinc acetate dihydrate with a 2:1 molar ratio in ethanol and subsequent removal of solvent in vacuo, a white crystalline powder was obtained, **mc′**, showing a different PXRD spectrum than **mc**. This product was recrystallized by slow evaporation of a hot water solution to give large block-shaped single crystals. SCXRD analysis showed the new product to be the hydrated form of the $\mathbf{mc_2Zn}$ salt, $\mathbf{mc_2Zn_w}$. The complex shows three water molecules coordinated to the metal center and two water molecules as crystallization solvent, which give rise to a bidimensional network of hydrogen bonds (Figure S2). The weight loss in the thermogravimetric diagram is consistent with this structure, showing two steps due to the sequential loss of crystallization and coordinated water

https://doi.org/10.1021/acs.chemmater.3c00550
Chem. Mater. 2023, 35, 3722−3730

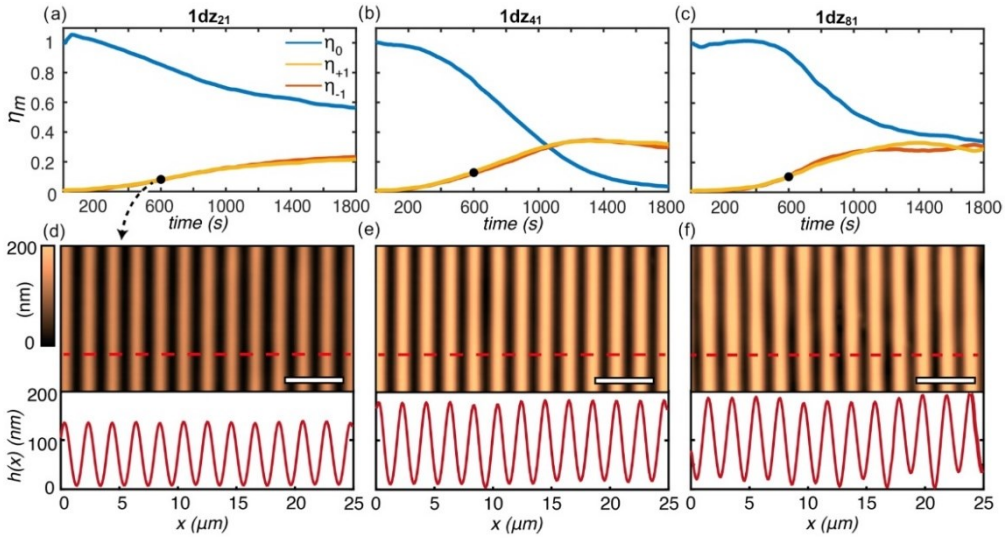

Figure 3. Comparative mass transport dynamics in an SRG inscription experiment. Evolution of the relative diffraction efficiency in the first three diffraction orders of the developing SRG gratings for the $\mathbf{1dz_{21}}$, $\mathbf{1dz_{41}}$, and $\mathbf{1dz_{81}}$ materials (a–c, respectively). Fixed intensity and exposure time of 1800 s have been used. AFM micrographs and topographic cross sections of the SRGs measured for SRGs obtained by 600 s of exposure time (d–f). Both the diffraction efficiency and the topographic analyses highlight increasing mass transport efficiency and increasing profile inhomogeneities from $\mathbf{1dz_{21}}$ to $\mathbf{1dz_{81}}$.

molecules (Figure S3). Treatment of $\mathbf{mc_2Zn_w}$ crystals at 150 °C aimed at removing all of the water content and isolating the $\mathbf{mc_2Zn}$ salt produced a white powder showing the same PXRD pattern as **mc′**, thus proving that the process of mixing **mc** and zinc acetate dihydrate in solution followed by solvent evaporation quantitatively yields the Zn(II)-thioglycolate salt, $\mathbf{mc_2Zn}$. This mechanism allows the structure and properties of the azomaterial to be easily and hierarchically tuned by simply adjusting the ratio of complementary functions to COOH groups, directly in situ.

Azomaterials. The azodendrimers $\mathbf{1dz_{ij}}$ were prepared by mixing **1**, **d**, and zinc acetate dihydrate in dimethylformamide (DMF) to have an overall 1:3 azodendrimer/solvent weight ratio. To investigate the effect of the metal concentration on the photoresponsive behavior of the materials, the composition of the building blocks was chosen by setting different i/j molar ratios between **d** and Zn^{2+} ($\mathbf{dz_{ij}}$) and adjusting the azochromophore content to saturate the remaining free COOH groups. Since a highest **dz** ratio than $\mathbf{dz_{21}}$ resulted in unstable solutions and liquid-phase separation, we investigated four compositions below this value, namely, **1d**, $\mathbf{1dz_{81}}$, $\mathbf{1dz_{41}}$, and $\mathbf{1dz_{21}}$. Stable transparent thin films were obtained over the entire range of compositions by spin coating or drop-casting the solutions, followed by treatment under vacuum. The FT-IR analysis shows the shift of the absorption band associated with the carbonyl stretching of the carboxylic group from 1713 cm^{-1} of **d** to 1735 cm^{-1} of **1d**, indicating a change of the interaction pattern from the dimer of the AA homosynthon to that of the AP heterosynthon (Figure S4).[33] Moreover, the NH_2 scissoring band of **1** at 1631 cm^{-1} is shifted to a higher frequency (1678 cm^{-1}) in **1d**.[40] This shift increases with the strength and number of hydrogen bonds, and its value is compatible with the double hydrogen-bond patterns described in Figure $2a_{I\text{-}II}$.[33,41] Formation of zinc carboxylates species could not be observed in the spectra of azodendrimers $\mathbf{1dz_{ij}}$, showing the same spectrum as **1d**, because of signal overlapping in the diagnostic range 1400–1600 cm^{-1}. Thus, we recorded the spectrum of $\mathbf{dz_{21}}$ without the azochromophore, showing the expected increase of the band of COO^- stretching at 1625 cm^{-1} due to Zn(II)-carboxylate species compared to the spectrum of **d** (Figure S4), while the stretching band of zinc acetate at 1570 cm^{-1} is not visible. The UV–visible absorption spectrum of **1** in DMF shows an intense band at 376 nm due to the $\pi \rightarrow \pi^*$ transition of the azobenzene system and a second band at about 450 nm corresponding to the $n \rightarrow \pi^*$ transition (Figure S5). The spectrum of **d** is shifted toward lower wavelengths and shows a local maximum at 286 nm, so there is no absorption overlap between the photopassive and photoactive components at the wavelengths used for SRG inscription. This separation is also evident in the spectra of $\mathbf{1dz_{ij}}$ as thin films (Figure S6), characterized by the expected broadening and an increasing ratio of the bands at 264 and 382 nm along the **1d** -$\mathbf{1dz_{21}}$ series, reflecting the trend of relative concentration. The refractive index n of $\mathbf{1dz_{ij}}$ azomaterials and the acrylic azopolymer **azp** used as comparison model, whose structure is reported in Figure S7,[4,42] were evaluated by ellipsometry and the values of n at the standard wavelength of 633 nm obtained from the dispersion curves reported in Figure S8. The results for **1d** (1.773), $\mathbf{1dz_{81}}$ (1.785), $\mathbf{1dz_{41}}$ (1.783), and $\mathbf{1dz_{21}}$ (1.748) confirm that the optimized design with highly polarizable atoms and groups in the structure of both the azomolecule and the photopassive dendrimer core can produce azomaterials with distinctly high absolute values of the refractive index, even if compared with azopolymers containing higher concentrations of standard fully aromatic azobenzene units (**azp**, 1.691) or even similar aminopyrimidine-based azomolecules (1.638–1.706).[33]

Differential scanning calorimetry (DSC) diagrams of the samples revealed an increase of the glass-transition temperature from 10.0 °C of **1d** to 14.9 °C of $\mathbf{1dz_{21}}$, which can be attributed to the effect of increasing aggregation of first-

https://doi.org/10.1021/acs.chemmater.3c00550
Chem. Mater. 2023, 35, 3722–3730

generation dendrimers induced by Zn(II)−carboxylate interactions (Figure S9). Although the increase of T_g is limited to only 5 °C, the actual change in material structure occurring in the range of compositions investigated was found to be suitable to define the best compromise between inscription efficiency and stability of induced SRGs, as discussed below.

SRG and Diffractive Lenses. To investigate the relative efficiency and the stability of the mass transport in the $\mathbf{1dz_{ij}}$ azodendrimers, we performed comparative SRG inscription experiments by exposing the films to the sinusoidal intensity pattern of two p-polarized laser beams at λ = 491 nm. According to the scalar diffraction theory, the relative diffraction efficiency η_m of the mth propagating diffraction order of an ideal sinusoidal surface relief grating at the probe wavelength λ is given by

$$\eta_m = \frac{I_m}{I_0} = \left| J_m\left(\frac{\pi}{2\lambda}(n_\lambda - 1)h\right)\right|^2 \quad (1)$$

where I_0 is the total transmitted intensity; I_m is the intensity of the mth diffracted wave; J_m is the Bessel function of first kind of order m; and h is the modulation depth of the sinusoidal grating (Figure S10). When applied to the quasi-sinusoidal SRG growing on an azomaterial film during the interferogram irradiation, eq 1 allows a direct connection between the temporal evolution of the recorded diffraction efficiency $\eta_m(t)$ in a specific order and the amplitude $h(t)$ of the relief grating. The same principle can be applied to directly compare the SRG inscription efficiency of different azomaterials, provided they have a comparable n_λ. In addition, as extensively discussed elsewhere,[43] eventual discrepancies of the diffraction efficiency of the developing SRG from the predictions of eq 1 can be used to characterize eventual structural deformations of the gratings, providing more elements to evaluate the inscription performances of different azomaterials. In the comparative experiment, we measured the temporal evolution of the diffraction efficiency in the first three orders (m = 0, ± 1) for SRGs inscribed on the three $\mathbf{1dz_{ij}}$ azodendrimers, using a He−Ne laser at the wavelength λ_p = 633 nm as a probe. The writing intensity and the exposure time has been maintained fixed in the three experiments. The measured diffraction curves are shown in Figure 3a−c. During the SRG inscription experiment, the area of the developing SRGs was additionally irradiated from the substrate side with a collimated circularly polarized laser beam at the λ_a = 405 nm. This beam enhances the mass transport and reduces the typical formation of the birefringence grating due to the photoalignment of azomolecules, making the diffraction efficiency dynamics closer to the ideal surface relief grating case of eq 1. Due to the small variations of the refractive index n_λ for the three materials at the probe wavelength, the diffraction curves in Figure 3 can be directly used to assess the mass transport quality and efficiency. According to eq 1, the initial part of the formation dynamics of a stable quasi-sinusoidal surface relief grating is characterized by monotonic identical increase in the efficiency of ±1 orders, accompanied by a simultaneous decrease in the 0 order. This condition is verified for $\mathbf{1dz_{21}}$ and $\mathbf{1dz_{41}}$, with a clearly slower dynamic in the case of the first azodendrimer. The lower inscription efficiency for $\mathbf{1dz_{21}}$ is further validated by the reduced relief amplitude resulting from AFM analysis of the surfaces at the intermediate exposure time (Figure 3d−f). According to our material design, the azodendrimer $\mathbf{1dz_{81}}$ was expected to show even higher efficiency. However, both the diffraction and the topographic characterizations show that the slight increase in the structuration speed with respect to $\mathbf{1dz_{41}}$ is associated with a reduced stability of the inscription process, with increased structural inhomogeneity in the grating profiles (Figure 3f) and nonideal diffraction behavior (Figure 3c). This instability was even more pronounced in the case of **1d** and was accompanied by a rapid decrease in inscribed SRGs amplitude after the inscription process, which prevented a complete characterization of this material, while the amount of Zn(II)−carboxylate interactions in $\mathbf{1dz_{81}}$ was enough to grant a shelf stability of at least 6 months to the relief amplitude. This trend clearly highlights the flexibility of such materials, where the stability of the inscribed gratings and the photoresponsive behavior can be easily and finely tuned by appropriate balancing of the two hierarchical supramolecular interactions through small changes of the composition of the three molecular building blocks in solution.

Another direct consequence of eq 1 is that the diffraction efficiency of a surface diffraction grating, and more in general of a diffractive optical component build as a surface relief pattern, can be increased by a higher refractive index n_λ for a given relief amplitude h. Then, a higher-refractive-index material requires a lower modulation amplitude for the maximum diffraction efficiency, allowing the realization of thinner optical diffractive elements. To further highlight the strength of our material design with respect to this aspect, we fabricate and characterize flat diffractive lenses, selected as a prototype of a general diffractive optical element, on the surface of a $\mathbf{1dz_{41}}$ azodendrimer film, compared with same lenses inscribed in the acrylate azopolymer (**azp**). We choose the $\mathbf{1dz_{41}}$ dendrimer according to good compromise between inscription speed and structural stability in the relief formation performances shown in the previous comparative SRGs analysis. For the fabrication of the diffractive lenses, we used a holo-lithographic method based on the projection of a computer-generated structured light intensity pattern on the surface of the azomaterials, which accordingly develop the surface relief with the same geometry. The description of the lens design can be found in refs 23, 24, while additional details about the optical configuration for the experimental inscription and characterization of the lenses are given in the Experimental Section and in the Supporting Information. In the comparative experiment between $\mathbf{1dz_{41}}$ and **azp**, we measured the diffraction efficiency for λ_p = 633 nm in the first focal spot produced by the lenses. Lenses with different relief amplitudes are obtained by varying the exposure time at the writing holographic pattern in different regions of the films. AFM analysis has been used to measure the relief amplitude h in each of the inscribed lenses as the average of three radial topographic profiles. Figure 4a shows the comparison of the diffraction efficiency measured as a function of the lens amplitude for the two materials. According to scalar diffraction theory, we included in the plot also the expected diffraction efficiency behavior calculated using the refractive indices obtained by ellipsometry for the two materials at the probe wavelength. The two sets of experimental data closely follow the theoretical curves. If, on the one hand, this additionally sustains the accuracy of the measured refractive index by ellipsometry, on the other hand, it allows us to use the theoretical curves to characterize the effect of the refractive index on the performance of the diffractive components. According to Figure 4a, the maximum diffraction efficiency of $\eta \approx 0.34$ is obtained for a relief amplitude of h_d = 475 nm for

https://doi.org/10.1021/acs.chemmater.3c00550
Chem. Mater. 2023, 35, 3722−3730

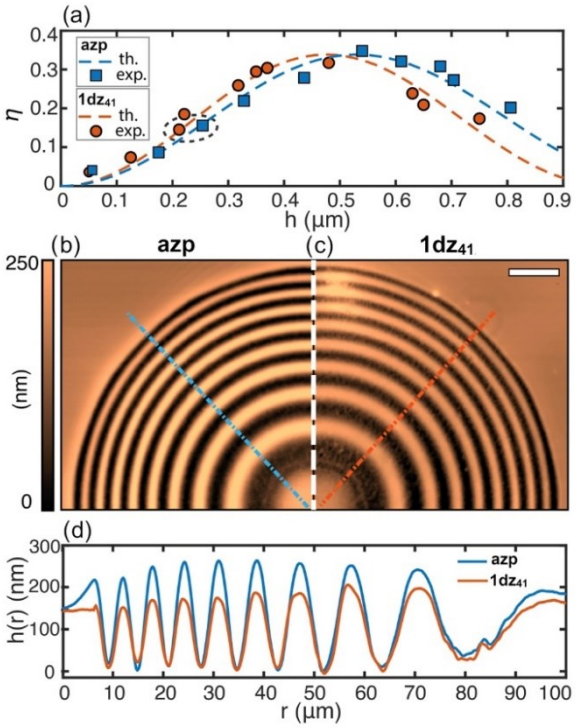

Figure 4. Effect of increased refractive index of the azodendrimers in the fabrication of thin diffractive optical elements. Comparison between the focusing efficiency in the first focal order for a diffractive lens inscribed in the $\mathbf{1dz_{41}}$ azodendrimer (orange circles) and in the acrylic azopolymer (**azp**, blue squares), measured for different average relief amplitude h (a). Dashed lines are the prediction of the scalar diffraction theory calculated for $n_d = 1.783$ and $n_p = 1.691$ at $\lambda = 633$ nm. AFM micrographs (b, c) and exemplary radial topographic profiles of the lenses (d) highlighted by the dashed ellipse in (a). The measured average amplitudes, where $h_d = 210 \pm 5$ nm for $\mathbf{1dz_{14}}$ and $h_p = 255 \pm 5$ nm for **azp** resulting in a $(h_p - h_d)//h_p \sim 18\%$ amplitude reduction.

the dendrimeric material and for $h_p = 529$ nm for the polymer, requiring then 10% thinner amplitude for a $\mathbf{1dz_{41}}$ relief with optimized efficiency. Figure 4b compares the AFM micrographs of the lenses of the two materials having an experimental comparable diffraction efficiency of $\eta \sim 0.15 \pm 0.05$ (highlighted by the dashed circle in Figure 4a). As visible from the radial topographic profiles shown in Figure 4c, the lens on $\mathbf{1dz_{41}}$ is characterized by an ~18% reduction in the average modulation amplitude arising from the increase in the refractive index.

■ CONCLUSIONS

Here, we present efficient azomaterials with a high refractive index obtained through a flexible design based on hierarchical hydrogen bonding and Zn(II)−carboxylate supramolecular interactions. High refractive index values were achieved by maximizing the density of high molar refraction groups as −C−S(II)−C−, −C═N−N−, and −C═N−C− in the structure of both the photoactive azomolecule and the dendrimer-shaped photopassive component, with almost 0.1 increase compared to conventional acrylate azopolymer and supramolecular polymers with similar azobenzene units. Aggregation and growth of hydrogen-bonded azodendrimers through Zn(II)−carboxylate interactions can be readily induced by the addition of zinc acetate to the formulation and consequent complete anion exchange with thioglycolate-type dendrimer termini. By changing the zinc content, it was possible to finely modulate and balance the efficiency and quality of mass transport during the SRG inscription process, until a theory-matching response of the material. We demonstrated that a thinner holographic lens with the same diffraction efficiency can be fabricated on a thin film of the most performing $\mathbf{1dz_{41}}$ material compared to the standard acrylate polymer **azp**, as a result of the increased refractive index. The combination of high refractive index and high inscription efficiency and quality, enabled by flexible supramolecular chemistry and design, is a key factor in the development of real-time reconfigurable planar photonic devices.

■ EXPERIMENTAL SECTION

All of the reagents were commercially available and used without further purification. ^{1}H and ^{13}C NMR spectra were recorded on Varian Inova 500 (500 MHz) and Bruker Ascend 400 (400 MHz) spectrometers. DSC diagrams were recorded on a METTLER TOLEDO DSC3+ calorimeter. UV−visible spectra were recorded with a JASCO V-750 spectrometer. The FT-IR measurements were performed on a Thermo Nicolet 5700 FT-IR spectrometer. Solid samples were dispersed in KBr tablets, azomaterials were cast from solution. Ellipsometry data were collected using a commercially available M-2000 Spectroscopic Ellipsometer (J. A. Woollam). Data analysis was performed using Complete EASE software (version 6.57). Topographic analysis of the structured surfaces was performed by an AFM (WITEC α RS300) operating in tapping mode with a cantilever of 75 kHz resonance frequency and spring constant of 3 N/m. Analysis and elaboration of AFM data were accomplished by means of the open-source software Gwyddion. Thin films of azomaterials were prepared by spin-coating DMF solutions on glass substrates, using a Laurell WS-650Mz-23NPP spin coater.

X-ray Diffraction Analysis. PXRD spectra were recorded on a Panalytical Empyrean multipurpose X-ray diffractometer. Selected crystals of **1**, $\mathbf{mc_2Zn_w}$, and $\mathbf{t(adp)_2}$ were mounted on a Bruker-Nonius KappaCCD diffractometer equipped with Oxford Cryostream apparatus (graphite monochromated Mo Kα radiation, $\lambda = 0.71073$ Å, CCD rotation images, thick slices, φ and ω scans to fill asymmetric unit). Reduction of data and semiempirical absorption correction were done using SADABS program. The structures were solved by direct methods (SIR97 program)[44] and refined by the full-matrix least-squares method on F^2 using SHELXL-2016 program[45] with the aid of the program Olex2.[46] H atoms bonded to C were generated stereochemically and refined by the riding model, those bonded to O and N were found in difference Fourier maps and their coordinates were refined. For all H atoms, U_{iso}(H) equal to 1.2 U_{eq} or 1.5 U_{eq} (C_{methyl}) of the carrier atom was used. Crystal data and structure refinement details are reported in Table S1. The figures were generated using Mercury CSD 3.3.[47] All crystal data were deposited at Cambridge Crystallographic Data Centre with assigned numbers CCDC 2234125 (**1**), 2234126 ($\mathbf{t(adp)_2}$), and 2234127 ($\mathbf{mc_2Zn_w}$). These data can be obtained free of charge from www.ccdc.cam.ac.uk/data_request/cif.

Synthesis. *Synthesis of Diazonium Salt of 4-(Methylthio)aniline (**md**).* 4-(Methylthio)aniline (4,00 g, 28.7 mmol) and 10.5 g of tetrafluoroboric acid solution 48% in H_2O were added to 25 mL of water. Sodium nitrite (1.98 g, 28.7 mmol) was slowly added to the mixture at 0−5 °C under stirring. After 30 min, the tetrafluoroborate salt was filtered, washed with cold water and ethyl ether, and dried. Yield: 5.77 g, 84.4%.

*Synthesis of **1**.* 2-Amino-4,6-dimethoxypyrimidine (3.76 g, 24.2 mmol) was dissolved in 1,2-dichloroethane (70 mL). **md** (5.77 g, 24.2 mmol) was slowly added under stirring at room temperature. After 24

https://doi.org/10.1021/acs.chemmater.3c00550
Chem. Mater. 2023, 35, 3722−3730

h, the solvent was evaporated in vacuo and the solid was recrystallized in ethanol/water in the presence of triethylamine. The filtered and dried product was purified by Soxhlet extraction in heptane, giving reddish plate crystals of **1**. Yield: 42%. ^{1}H NMR (DMSO-d_6) δ 2.52 (s, 3H), 3.92 (s, 6H), 7.33 (m, 4H), 7.58 (d, 2H). ^{13}C NMR (DMSO-d_6) δ 14.57, 53.91, 112.96, 121.90, 125.94, 139.52, 151.14, 161.24, 164.35. Single crystals of **1** were grown by slow evaporation of acetone solution and used for SCXRD analysis.

Synthesis of i_1. Bromoacetic acid (1.85 g, 13.3 mmol) was added to a solution of 1,3,4-thiadiazole-2,5-dithiol (2.00 g, 13.3 mmol) and KOH 85% (1.76 g, 26.6 mmol) in water (20 mL) under stirring. After 2 h, a white solid was filtered and dissolved in water (25 mL) with gentle warming. The pH was adjusted to 6 with KOH, and the solution was poured into concentrated HCl (50 mL) under stirring. After a few minutes, a pale yellow solid crystallized. After cooling, the product was filtered under vacuum. Yield: 1.50 g, 54%. ^{1}H NMR (DMSO-d_6) δ 4.04 (s, 2H). ^{13}C NMR (DMSO-d_6) δ 35.10,157.42, 169.10, 188.20.

Synthesis of i_2. 1,2-Dibromoethane (6.83 g, 36.4 mmol) was added to a solution of i_1 (1,50 g, 7.20 mmol) and DIPEA (0.931 g, 7.20 mmol) in 15 mL of acetone. After 24 h, the solvent was removed under vacuum and the residue was dissolved in 100 mL of chloroform. The organic phase was washed with water containing HCl. After anhydrification and evaporation of the solvent, the solid was recrystallized in acetone/hexane to give pale yellow crystals of the product (1.35 g yield 60%). ^{1}H NMR (Acetone-d_6) δ 3.80 (m, 4H), 4.21 (s, 2H). ^{13}C NMR (DMSO-d_6) δ 30.95, 35.34, 35.79, 164.12, 164.89, 169.10.

Synthesis of **d**. i_2 (3.42 g, 10.8 mmol) and trithiocyanuric acid (0.641 g, 3.60 mmol) were dissolved in 6 mL of DMF under stirring. DIPEA (1.46 g, 11.3 mmol) was added, and the reaction was stirred for 48 h. The product was precipitated into a mixture of 10 mL of water and 15 mL of concentrated HCl as a sticky solid on the bottom of the beaker. After removal of the supernatant, the solid was dissolved in 30 mL of acetone and slowly precipitated into a mixture of 70 mL of water and 30 mL of concentrated HCl to remove residual DMF. The isolated solid was dried, treated with chloroform under stirring, and filtered in vacuo. Finally, the product was dissolved in the minimum amount of acetone, filtered, and isolated by solvent evaporation as a yellowish powder (yield 56%). ^{1}H NMR (DMSO-d_6) δ 3.53 (m, 12H), 4.06 (s, 6H). ^{13}C NMR (DMSO-d_6) δ 29.42, 33.37, 35.76, 164.45, 164.75, 169.10, 178.50.

Synthesis of **mc**. Bromoacetic acid (2,80 g, 20.2 mmol) was added to a solution of 5-methylthio-1,3,4-thiadiazole-2-thiol (3.31 g, 20.2 mmol) and NaOH (1.62 g, 40.4 mmol) in 40 mL of ethanol under stirring. After 1 h, water (2 mL) was added to the white suspension and the mixture was stirred for 24 h at room temperature. The solvent was evaporated in vacuo, the residue was dissolved in water (20 mL) and precipitated in 20 mL of concentrated HCl. The product was washed with water and recrystallized from ethanol (yield 77%). ^{1}H NMR (DMSO-d_6) δ 2.73 (s, 3H), 4.13 (s, 2H). ^{13}C NMR (DMSO-d_6) δ 16.55, 35.83, 163.69, 167.10, 169.14.

Synthesis of $\mathbf{mc_2Zn_w}$. A mixture of **mc** (0.222 g, 1.00 mmol) and zinc acetate dihydrate (0.110 g, 0.500 mmol) was dissolved in 30 mL of ethanol. After 10 min, the solvent was removed in vacuo to give a white crystalline solid. The solid was dissolved in 10 mL of boiling water, then the solution was left at room temperature. After solvent evaporation, large plate crystals formed, suitable for SCXRD analysis.

Synthesis of $\mathbf{t(adp)_2}$. Compound **t** was prepared according to a literature procedure.[48] A mixture of **t** (35.0 mg, 0.100 mmol) and 2-amino-4,6-dimethoxypyrimidine (46.5 mg, 0.300 mmol) was dissolved in 2 mL of boiling water, and the solution was kept at 80 °C for 24 h, after which needle-like crystals of $\mathbf{t(adp)_2}$ were obtained, suitable for SCXRD analysis.

SRG Inscription and Monitoring. The experimental configuration used for the inscription of SRGs on the azomaterial films consisted of two coplanar p-polarized laser beams (Cobolt Calypso, at wavelength λ_w = 491 nm), interfering with the sample surface (Figure S11). The sinusoidal intensity fringes had a periodicity of $\Lambda \approx 2.0$ μm, obtained by tuning, symmetrically with respect to the surface normal, the incidence angle of the two beams according to Bragg's law. The exposure time and the irradiation intensity were kept fixed at 30 min and 230 mW/cm^2, respectively, for all tested materials. The power and the diameter of each interfering beam were P∼17.0 mW and D∼4.5 mm, respectively. A homogeneous collimated assisting laser beam (at λ_a = 405 nm) was included in the inscription process, impinging on the sample from the substrate side. Circular polarization and intensity ≈70 mW/cm^2 were used for this beam in all of the SRG inscription experiments. The dynamics of surface structuration for the different materials were investigated by recording the time-evolving relative diffraction efficiencies in the 0 and ±1 diffraction orders of a He−Ne probe beam at λ_p = 633 nm (TE polarized), incident on the growing SRGs.

Diffractive Lens Inscription and Characterization. To inscribe the surface profile of the cosinusoidal Phase Zone Plates (c-PZPs), acting as multifocal diffractive lenses,[24] the writing laser beam at λ_w was phase-modulated by a reflective Spatial Light Modulator (SLM), (Holoeye, Pluto) in a Computer-Generated Hologram (CGH) configuration to generate the corresponding structured intensity pattern in the sample plane (Figure S12). To this aim, the modulated beam is first propagated through a 4f lens system, with the input plane located in the SLM plane. The 4f output plane coincided with the back focal plane of an infinity-corrected long-working-distance 50× objective (Mitutoyo), having numerical aperture NA = 0.55 and WD = 13 mm working distance, focusing the holographic intensity pattern on the surface of the tested materials. The writing beam was circularly polarized by means of a quarter wave plate placed before the objective, while its intensity at the sample plane was ≈14.0 W/cm^2. The assisting beam at λ_a, with intensity ≈0.5 W/cm^2, was used also in this configuration to enhance the surface structuring process. The exposure time interval was chosen based on previous experiments on the azopolymer structuration in similar conditions.[23] To fully explore the expected focusing efficiency dynamics, an interval of 5−60 s was used to inscribe c-PZPs with focal length f = 0.8 mm at λ_p = 633 nm, reaching modulation amplitudes in the range 100−800 nm for the tested materials. The relative diffraction efficiency in the first focus of the c-PZPS was measured using the probe beam at λ_p orthogonally incident on the diffractive lens from the substrate side, following the procedure extensively described in previous works.[24]

■ ASSOCIATED CONTENT

Supporting Information

The Supporting Information is available free of charge at https://pubs.acs.org/doi/10.1021/acs.chemmater.3c00550.

Crystal packing views of **1** and $\mathbf{mc_2Zn_w}$; crystal, collection, and refinement data; relevant bond lengths and angles; thermogravimetric curves; FT-IR and UV−visible spectra of molecules and azomaterials; chemical structure of **azp**; refractive index dispersion curves and DSC diagrams of azomaterials; plot of theoretical diffraction efficiency for an ideal SRG; experimental setup scheme for SRG inscription and holographic structuration; and ^{1}H and ^{13}C NMR spectra of compounds (PDF)

Accession Codes

CCDC 2234125 (**1**), 2234126 ($\mathbf{t(adp)_2}$), and 2234127 ($\mathbf{mc_2Zn_w}$) contain the supplementary crystallographic data for this paper. These data can be obtained free of charge via www.ccdc.cam.ac.uk/data_request/cif, by emailing data_request@ccdc.cam.ac.uk, or by contacting The Cambridge Crystallographic Data Centre, 12 Union Road, Cambridge CB2 1EZ, UK; fax: +44 1223 336033.

https://doi.org/10.1021/acs.chemmater.3c00550
Chem. Mater. 2023, 35, 3722−3730

AUTHOR INFORMATION

Corresponding Author

Fabio Borbone − *Department of Chemical Sciences, University of Napoli Federico II, Complesso Universitario di Monte Sant'Angelo, 80126 Napoli, Italy; CNST@POLIMI - Fondazione Istituto Italiano di Tecnologia, 20133 Milano, Italy;* orcid.org/0000-0001-7433-9267; Email: fabio.borbone@unina.it

Authors

Sandra Fusco − *Department of Chemical Sciences, University of Napoli Federico II, Complesso Universitario di Monte Sant'Angelo, 80126 Napoli, Italy*

Stefano Luigi Oscurato − *Department of Physics E. Pancini, University of Napoli Federico II, Complesso Universitario di Monte Sant'Angelo, 80126 Napoli, Italy;* orcid.org/0000-0002-1814-8033

Marcella Salvatore − *Centro Servizi Metrologici e tecnologici Avanzati (CeSMA), University of Napoli Federico II, Complesso Universitario di Monte Sant'Angelo, 80126 Napoli, Italy*

Francesco Reda − *Department of Physics E. Pancini, University of Napoli Federico II, Complesso Universitario di Monte Sant'Angelo, 80126 Napoli, Italy*

Sara Moujdi − *CNST@POLIMI - Fondazione Istituto Italiano di Tecnologia, 20133 Milano, Italy*

Michael De Oliveira − *CNST@POLIMI - Fondazione Istituto Italiano di Tecnologia, 20133 Milano, Italy;* orcid.org/0000-0001-5007-1577

Antonio Ambrosio − *CNST@POLIMI - Fondazione Istituto Italiano di Tecnologia, 20133 Milano, Italy;* orcid.org/0000-0002-8519-3862

Roberto Centore − *Department of Chemical Sciences, University of Napoli Federico II, Complesso Universitario di Monte Sant'Angelo, 80126 Napoli, Italy;* orcid.org/0000-0002-2797-0117

Complete contact information is available at: https://pubs.acs.org/10.1021/acs.chemmater.3c00550

Author Contributions

[⊥]S.F. and S.L.O. contributed equally to this work. F.B. designed the concept; F.B., S.F., and R.C. synthesized and characterized the materials; S.L.O., M.S., and F.R. designed and performed the SRG experiments; S.M., M.D.O., and A.A. performed the ellipsometry measurements; F.B. wrote the manuscript with contribution from all authors. All authors have given approval to the final version of the manuscript.

Notes

The authors declare no competing financial interest.

ACKNOWLEDGMENTS

This work was financially supported by the European Research Council (ERC) under the European Union's Horizon 2020 research and innovation programme "METAmorphoses", grant agreement no. 817794. This work was also supported by Fondazione Cariplo, grant no. 2019-3923.

REFERENCES

(1) Natansohn, A.; Rochon, P. Photoinduced Motions in Azo-Containing Polymers. *Chem. Rev.* **2002**, *102*, 4139−4176.

(2) Rochon, P.; Batalla, E.; Natansohn, A. Optically Induced Surface Gratings on Azoaromatic Polymer Films. *Appl. Phys. Lett.* **1995**, *66*, 136−138.

(3) Zhao, Y.; Lu, Q.; Li, M.; Li, X. Anisotropic Wetting Characteristics on Submicrometer-Scale Periodic Grooved Surface. *Langmuir* **2007**, *23*, 6212−6217.

(4) Oscurato, S. L.; Borbone, F.; Maddalena, P.; Ambrosio, A. Light-Driven Wettability Tailoring of Azopolymer Surfaces with Reconfigured Three-Dimensional Posts. *ACS Appl. Mater. Interfaces* **2017**, *9*, 30133−30142.

(5) Baac, H.; Lee, J.-H.; Seo, J.-M.; Park, T. H.; Chung, H.; Lee, S.-D.; Kim, S. J. Submicron-Scale Topographical Control of Cell Growth Using Holographic Surface Relief Grating. *Mater. Sci. Eng. C* **2004**, *24*, 209−212.

(6) Rianna, C.; Calabuig, A.; Ventre, M.; Cavalli, S.; Pagliarulo, V.; Grilli, S.; Ferraro, P.; Netti, P. A. Reversible Holographic Patterns on Azopolymers for Guiding Cell Adhesion and Orientation. *ACS Appl. Mater. Interfaces* **2015**, *7*, 16984−16991.

(7) Barillé, R.; Janik, R.; Kucharski, S.; Eyer, J.; Letournel, F. Photo-Responsive Polymer with Erasable and Reconfigurable Micro- and Nano-Patterns: An in Vitro Study for Neuron Guidance. *Colloids Surf. B* **2011**, *88*, 63−71.

(8) Qin, D.; Xia, Y.; Whitesides, G. M. Soft Lithography for Micro- and Nanoscale Patterning. *Nat. Protoc.* **2010**, *5*, 491−502.

(9) Guo, L. J. Nanoimprint Lithography: Methods and Material Requirements. *Adv. Mater.* **2007**, *19*, 495−513.

(10) Xia, Y.; Whitesides, G. M. Soft Lithography. *Angew. Chem., Int. Ed.* **1998**, *37*, 550−575.

(11) Lausten, R.; Rochon, P.; Ivanov, M.; Cheben, P.; Janz, S.; Desjardins, P.; Ripmeester, J.; Siebert, T.; Stolow, A. Optically Reconfigurable Azobenzene Polymer-Based Fiber Bragg Filter. *Appl. Opt.* **2005**, *44*, 7039−7042.

(12) Kang, J.-W.; Kim, M.-J.; Kim, J.-P.; Yoo, S.-J.; Lee, J.-S.; Kim, D. Y.; Kim, J.-J. Polymeric Wavelength Filters Fabricated Using Holographic Surface Relief Gratings on Azobenzene-Containing Polymer Films. *Appl. Phys. Lett.* **2003**, *82*, 3823−3825.

(13) Stockermans, R. J.; Rochon, P. L. Narrow-Band Resonant Grating Waveguide Filters Constructed with Azobenzene Polymers. *Appl. Opt.* **1999**, *38*, 3714−3719.

(14) Golghasemi Sorkhabi, Sh.; Ahmadi-Kandjani, S.; Cousseau, F.; Loumaigne, M.; Zielinska, S.; Ortyl, E.; Barille, R. Surface Quasi Periodic and Random Structures Based on Nanomotor Lithography for Light Trapping. *J. Appl. Phys.* **2017**, *122*, No. 015303.

(15) Perschke, A.; Fuhrmann, T. Molecular Azo Glasses as Grating Couplers and Resonators for Optical Devices. *Adv. Mater.* **2002**, *14*, 841−843.

(16) Paterson, J.; Natansohn, A.; Rochon, P.; Callender, C. L.; Robitaille, L. Optically Inscribed Surface Relief Diffraction Gratings on Azobenzene-containing Polymers for Coupling Light into Slab Waveguides. *Appl. Phys. Lett.* **1996**, *69*, 3318−3320.

(17) Tadeson, G.; Sabat, R. G. Enhancement of the Power Conversion Efficiency of Organic Solar Cells by Surface Patterning of Azobenzene Thin Films. *ACS Omega* **2019**, *4*, 21862−21872.

(18) Na, S.-I.; Kim, S.-S.; Jo, J.; Oh, S.-H.; Kim, J.; Kim, D.-Y. Efficient Polymer Solar Cells with Surface Relief Gratings Fabricated by Simple Soft Lithography. *Adv. Funct. Mater.* **2008**, *18*, 3956−3963.

(19) Lim, T.-B.; Cho, K. H.; Kim, Y.-H.; Jeong, Y.-C. Enhanced Light Extraction Efficiency of OLEDs with Quasiperiodic Diffraction Grating Layer. *Opt. Express* **2016**, *24*, 17950−17959.

(20) Park, K. J.; Park, J. H.; Huh, J.-H.; Kim, C. H.; Ho, D. H.; Choi, G. H.; Yoo, P. J.; Cho, S. M.; Cho, J. H.; Lee, S. Petal-Inspired Diffractive Grating on a Wavy Surface: Deterministic Fabrications and Applications to Colorizations and LED Devices. *ACS Appl. Mater. Interfaces* **2017**, *9*, 9935−9944.

(21) Ubukata, T.; Isoshima, T.; Hara, M. Wavelength-Programmable Organic Distributed-Feedback Laser Based on a Photoassisted Polymer-Migration System. *Adv. Mater.* **2005**, *17*, 1630−1633.

(22) Goldenberg, L. M.; Lisinetskii, V.; Gritsai, Y.; Stumpe, J.; Schrader, S. Single Step Optical Fabrication of a DFB Laser Device in Fluorescent Azobenzene-Containing Materials. *Adv. Mater.* **2012**, *24*, 3339−3343.

(23) Oscurato, S. L.; Reda, F.; Salvatore, M.; Borbone, F.; Maddalena, P.; Ambrosio, A. Shapeshifting Diffractive Optical Devices. *Laser Photonics Rev.* **2022**, *16*, No. 2100514.
(24) Reda, F.; Salvatore, M.; Borbone, F.; Maddalena, P.; Ambrosio, A.; Oscurato, S. L. Varifocal Diffractive Lenses for Multi-Depth Microscope Imaging. *Opt. Express* **2022**, *30*, 12695−12711.
(25) Kress, B. C.; Chatterjee, I. Waveguide Combiners for Mixed Reality Headsets: A Nanophotonics Design Perspective. *Nanophotonics* **2020**, *10*, 41−74.
(26) Yang, Z.; Albrow-Owen, T.; Cai, W.; Hasan, T. Miniaturization of Optical Spectrometers. *Science* **2021**, *371*, No. eabe0722.
(27) Higashihara, T.; Ueda, M. Recent Progress in High Refractive Index Polymers. *Macromolecules* **2015**, *48*, 1915−1929.
(28) Zhang, G.; Bai, D.; Li, D.; Long, S.; Wang, X.; Yang, J. Synthesis and Properties of Polyamides Derived from 4,6-Bis(4-Chloroformylphenylthio)Pyrimidine and 3,6-Bis(4-Chloroformylphenylthio)Pyridazine. *Polym. Int.* **2013**, *62*, 1358−1367.
(29) Javadi, A.; Shockravi, A.; Rafieimanesh, A.; Malek, A.; Ando, S. Synthesis and Structure-Property Relationships of Novel Thiazole-Containing Poly(Amide Imide)s with High Refractive Indices and Low Birefringences. *Polym. Int.* **2015**, *64*, 486−495.
(30) Vapaavuori, J.; Bazuin, C. G.; Priimagi, A. Supramolecular Design Principles for Efficient Photoresponsive Polymer−Azobenzene Complexes. *J. Mater. Chem. C* **2018**, *6*, 2168−2188.
(31) Koskela, J. E.; Liljeström, V.; Lim, J.; Simanek, E. E.; Ras, R. H. A.; Priimagi, A.; Kostiainen, M. A. Light-Fuelled Transport of Large Dendrimers and Proteins. *J. Am. Chem. Soc.* **2014**, *136*, 6850−6853.
(32) Vapaavuori, J.; Priimagi, A.; Soininen, A. J.; Canilho, N.; Kasëmi, E.; Ruokolainen, J.; Kaivola, M.; Ikkala, O. Photoinduced Surface Patterning of Azobenzene-Containing Supramolecular Dendrons, Dendrimers and Dendronized Polymers. *Opt. Mater. Express* **2013**, *3*, 711−722.
(33) Borbone, F.; Oscurato, S. L.; Del Sorbo, S.; Pota, F.; Salvatore, M.; Reda, F.; Maddalena, P.; Centore, R.; Ambrosio, A. Enhanced Photoinduced Mass Migration in Supramolecular Azopolymers by H-Bond Driven Positional Constraint. *J. Mater. Chem. C* **2021**, *9*, 11368−11375.
(34) Xu, L.; Chen, L.-J.; Yang, H.-B. Recent Progress in the Construction of Cavity-Cored Supramolecular Metallodendrimers via Coordination-Driven Self-Assembly. *Chem. Commun.* **2014**, *50*, 5156−5170.
(35) Lai, J.-C.; Li, L.; Wang, D.-P.; Zhang, M.-H.; Mo, S.-R.; Wang, X.; Zeng, K.-Y.; Li, C.-H.; Jiang, Q.; You, X.-Z.; Zuo, J.-L. A Rigid and Healable Polymer Cross-Linked by Weak but Abundant Zn(II)-Carboxylate Interactions. *Nat. Commun.* **2018**, *9*, No. 2725.
(36) Goldschmied, E.; Rae, A. D.; Stephenson, N. C. The Crystal Structure of Zn ^{II} Propionate $(C_6H_{10}O_4Zn)_n$. *Acta Crystallogr., Sect. B: Struct. Crystallogr. Cryst. Chem.* **1977**, *33*, 2117−2120.
(37) Clegg, W.; Little, I. R.; Straughan, B. P. Orthorhombic Anhydrous Zinc(II) Propionate. *Acta Crystallogr., Sect. C: Cryst. Struct. Commun.* **1987**, *43*, 456−457.
(38) Kortüm, G.; Vogel, W.; Andrussow, K. Dissociation Constants of Organic Acids in Aqueous Solution. *Pure Appl. Chem.* **1960**, *1*, 187−536.
(39) Kellogg, B. A.; Neverov, A. A.; Aman, A. M.; Brown, R. S. Catalysis of Acyl Transfer from Amides to Thiolate Nucleophiles: The Reaction of a Distorted Anilide with Thioglycolic Acid and Ethyl 2-Mercaptoacetate. *J. Am. Chem. Soc.* **1996**, *118*, 10829−10837.
(40) Sundaraganesan, N.; Sathesh Kumar, K.; Meganathan, C.; Dominic Joshua, B. Vibrational Spectroscopy Investigation Using Ab Initio and Density Functional Theory Analysis on the Structure of 2-Amino-4,6-Dimethoxypyrimidine. *Spectrochim. Acta, Part A* **2006**, *65*, 1186−1196.
(41) Huo, Q.; Dziri, L.; Desbat, B.; Russell, K. C.; Leblanc, R. M. Polarization-Modulated Infrared Reflection Absorption Spectroscopic Studies of a Hydrogen-Bonding Network at the Air-Water Interface. *J. Phys. Chem. B* **1999**, *103*, 2929−2934.
(42) Ambrosio, A.; Marrucci, L.; Borbone, F.; Roviello, A.; Maddalena, P. Light-Induced Spiral Mass Transport in Azo-Polymer Films under Vortex-Beam Illumination. *Nat. Commun.* **2012**, *3*, No. 989.
(43) Reda, F.; Salvatore, M.; Borbone, F.; Maddalena, P.; Oscurato, S. L. Accurate Morphology-Related Diffraction Behavior of Light-Induced Surface Relief Gratings on Azopolymers. *ACS Mater. Lett.* **2022**, *4*, 953−959.
(44) Altomare, A.; Burla, M. C.; Camalli, M.; Cascarano, G. L.; Giacovazzo, C.; Guagliardi, A.; Moliterni, A. G. G.; Polidori, G.; Spagna, R. SIR 97: A New Tool for Crystal Structure Determination and Refinement. *J. Appl. Crystallogr.* **1999**, *32*, 115−119.
(45) Sheldrick, G. M. Crystal Structure Refinement with SHELXL. *Acta Crystallogr., Sect. C: Struct. Chem.* **2015**, *71*, 3−8.
(46) Dolomanov, O. V.; Bourhis, L. J.; Gildea, R. J.; Howard, J. A. K.; Puschmann, H. OLEX2: A Complete Structure Solution, Refinement and Analysis Program. *J. Appl. Crystallogr.* **2009**, *42*, 339−341.
(47) Macrae, C. F.; Bruno, I. J.; Chisholm, J. A.; Edgington, P. R.; McCabe, P.; Pidcock, E.; Rodriguez-Monge, L.; Taylor, R.; van de Streek, J.; Wood, P. A. Mercury CSD 2.0 − New Features for the Visualization and Investigation of Crystal Structures. *J. Appl. Crystallogr.* **2008**, *41*, 466−470.
(48) Wang, S.-N.; Sun, R.; Wang, X.-S.; Li, Y.-Z.; Pan, Y.; Bai, J.; Scheer, M.; You, X.-Z. Versatile Lanthanide Coordination Assemblies Due to the Synergistic Effect of Lanthanide Contraction and Flexibility of a Flexible Tricarboxylate Ligand. *CrystEngComm* **2007**, *9*, 1051−1061.

https://doi.org/10.1021/acs.chemmater.3c00550
Chem. Mater. 2023, 35, 3722−3730

Supporting Information

Efficient High-Refractive-Index Azobenzene Dendrimers Based on a Hierarchical Supramolecular Approach

Sandra Fusco, [a] *Stefano Luigi Oscurato,* [b] *Marcella Salvatore,* [c] *Francesco Reda,* [b] *Sara Moujdi,* [d] *Michael De Oliveira,* [d] *Antonio Ambrosio,* [d] *Roberto Centore*[a] *and Fabio Borbone**[a,d]

[a] Department of Chemical Sciences, University of Napoli Federico II, Complesso Universitario di Monte Sant'Angelo, Via Cintia, 80126 Napoli, Italy

[b] Department of Physics E. Pancini, University of Napoli Federico II, Complesso Universitario di Monte Sant'Angelo, Via Cintia, 80126 Napoli, Italy

[c] Centro Servizi Metrologici e tecnologici Avanzati (CeSMA), University of Napoli Federico II, Complesso Universitario di Monte Sant'Angelo, Via Cintia, 80126, Napoli, Italy.

[d] CNST@POLIMI - Fondazione Istituto Italiano di Tecnologia, Via Pascoli 70, 20133, Milano, Italy

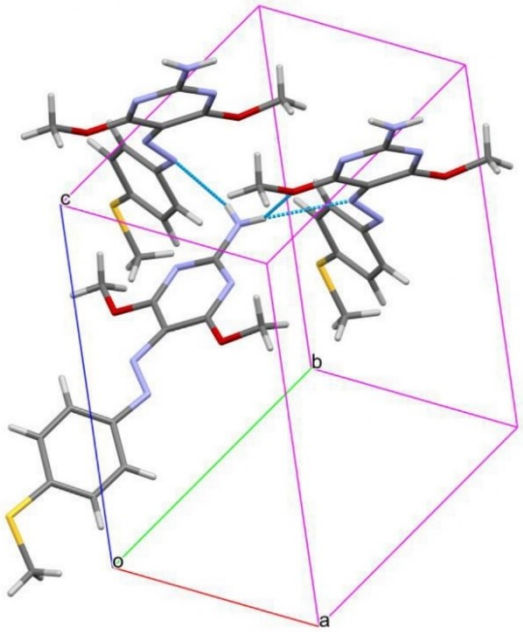

Figure S1 – Partial crystal packing of **1** with highlighted hydrogen bonds.

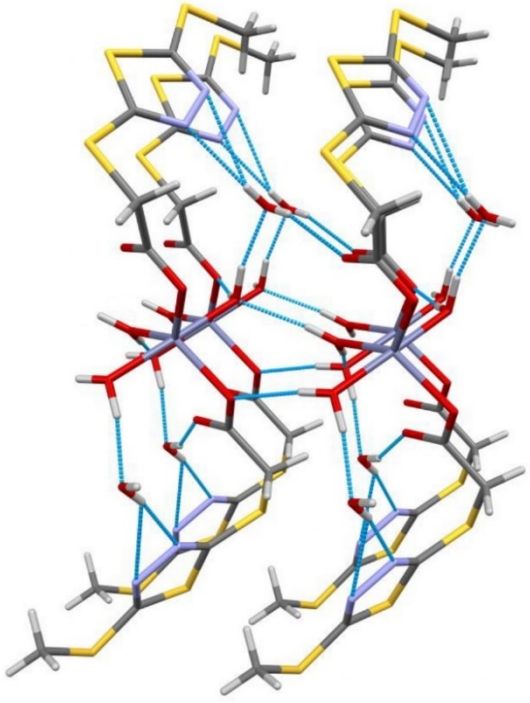

Figure S2 – Partial crystal packing of $\mathbf{mc_2Zn_w}$ showing the portion of a layer with bidimensional network of hydrogen bonds.

Table S1 Crystal data and structure refinement details for **1**, **t(adp)$_2$** and **mc$_2$Zn$_w$**.

	1	**t(adp)$_2$**	**mc$_2$Zn$_w$**
CCDC number	2234125	2234126	2234127
Empirical formula	$C_{13}H_{15}N_5O_2S$	$C_{21}H_{27}N_9O_{10}S_3$	$C_{10}H_{20}N_4O_9S_6Zn$
Formula weight	305.36	661.69	598.03
T (K)	293(2)	293(2)	173(2)
λ (Å)	0.71073	0.71073	0.71073
Crystal system	Monoclinic	Triclinic	Tetragonal
Space group	*P2$_1$/c*	*P-1*	*P4$_1$2$_1$2*
a (Å)	6.524(2)	4.9860(3)	5.423(4)
b (Å)	21.701(5)	10.8500(16)	5.423(8)
c (Å)	11.253(4)	27.126(2)	74.528(14)
α (°)	90	97.117(9)	90
β (°)	109.93(2)	92.981(8)	90
γ (°)	90	96.637(13)	90
V (Å^3)	1497.8(8)	1443.1(3)	2192(3)
Z	4	2	4
D_{calc} (Mg/m^3)	1.354	1.523	1.812
μ (mm^{-1})	0.228	0.326	1.743
F(000)	640.0	688.0	1224.0
θrange (°)	2.69 – 27.50	2.77 - 27.50	3.28 – 27.45
Reflections collected / unique [R(int)]	8923/3290 [0.0272]	11949/6302 [0.0325]	8639/2364 [0.0364]
Data/restraints/parameters	3290/20/232	6302/2/413	2364/1/155
Goodness-of-fit on F^2	1.044	1.029	1.196
Final*R1*, *wR2* indices [I>2σ(I)]	0.0408, 0.0944	0.0469, 0.0976	0.0355, 0.0761
Final *R1*, *wR2* indices (all data)	0.0701, 0.1089	0.0918, 0.1141	0.0431, 0.0780
Largest diff. peak / hole (eA^{-3})	0.20/-0.21	0.26/-0.25	0.42/-0.37

Table S2 Bond length distances (Å) and angles (°).

Type I heterosynthon		
N_{1B}-H_{1BA}···O_{3A}	O_{4A}···$H_{3B}N_{3B}$	C_{7A}-O_{4A}
2.811	2.617	1.262
N_{1B}-**H_{1BA}**···O_{3A}	O_{4A}···$H_{3B}N_{3B}$	C_{7A}-O_{3A}
1.894	1.711	1.238
N_{1B}-H_{1BA}···O_{3A} angle	O_{4A}···$H_{3B}N_{3B}$ angle	
178.17	178.26	
Type II heterosynthon		
N_{1C}-H_{1CA}···O_{1A}	$O_{2A}H_{2A}$···N_{3C}	C_{5A}-O_{2A}
2.851	2.612	1.293
N_{1C}-**H_{1CA}**···O_{1A}	$O_{2A}H_{2A}$···N_{3C}	C_{5A}-O_{1A}
1.967	1.621	1.214
N_{1C}-H_{1CA}···O_{1A} angle	$O_{2A}H_{2A}$···N_{3C} angle	
172.44	178.79	

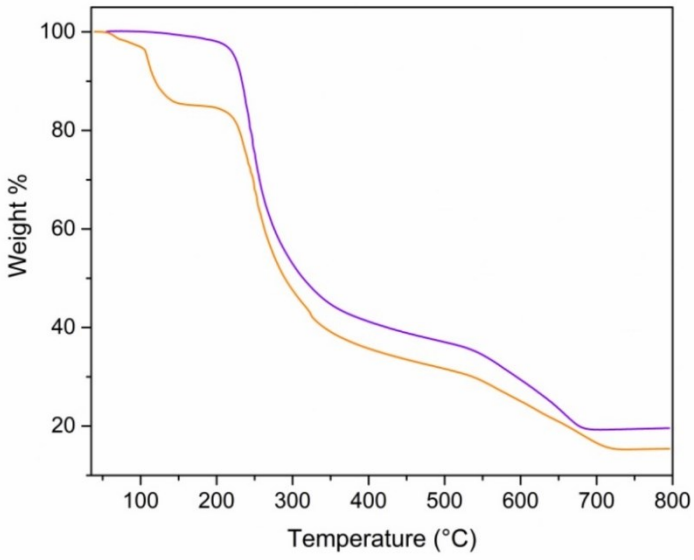

Figure S3 – Thermogravimetric curves of **mc′** (purple line) and **mc$_2$Zn$_w$** (orange line).

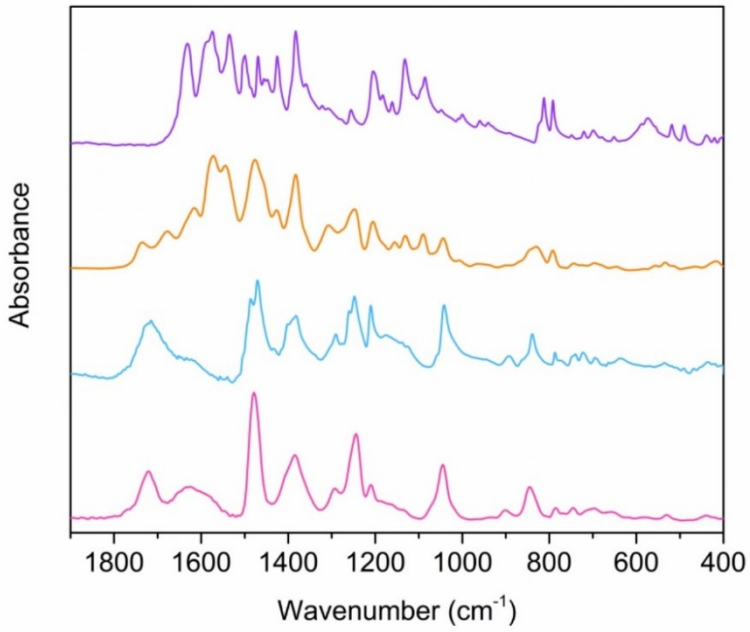

Figure S4 – FT-IR spectra of **1** (purple line), **1d** (orange line), **d** (blue line) and **dz$_{21}$** (magenta line).

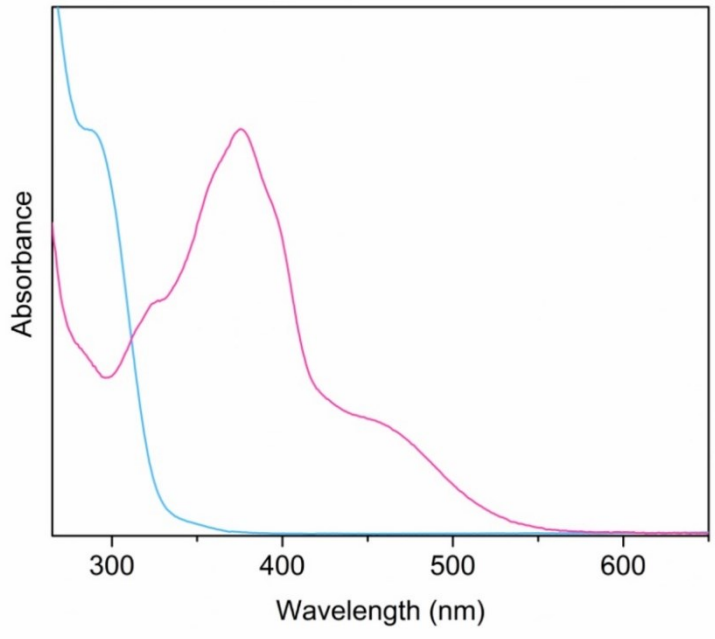

Figure S5 – UV-Visible spectra of **1** (red line) and **d** (blue line) in DMF.

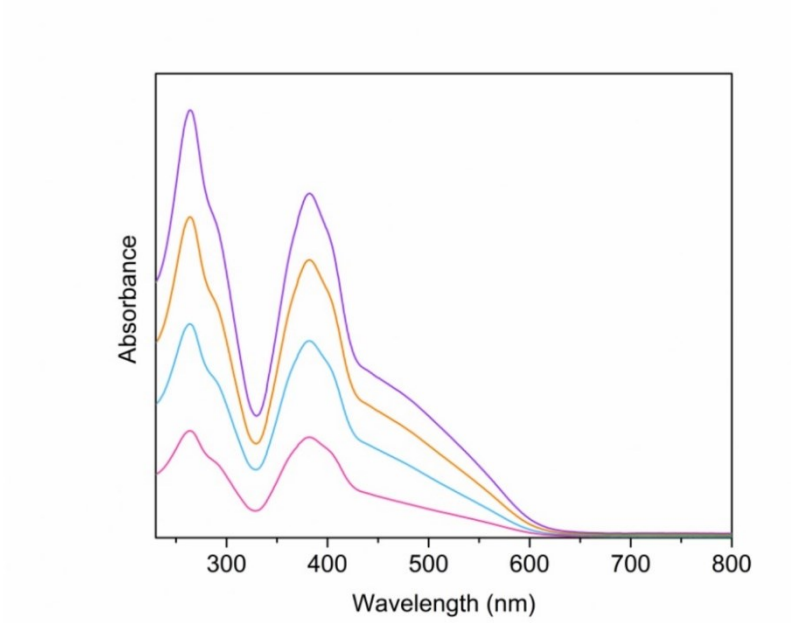

Figure S6 – UV-Visible spectra of **1d** (red line), **1dz$_{81}$** (blue line), **1dz$_{41}$** (orange line) and **1dz$_{21}$** (purple line) as thin films.

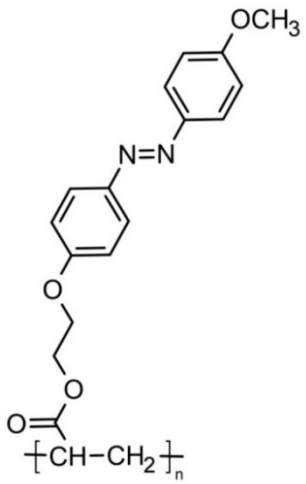

Figure S7 – Chemical structure of polymer **azp**.

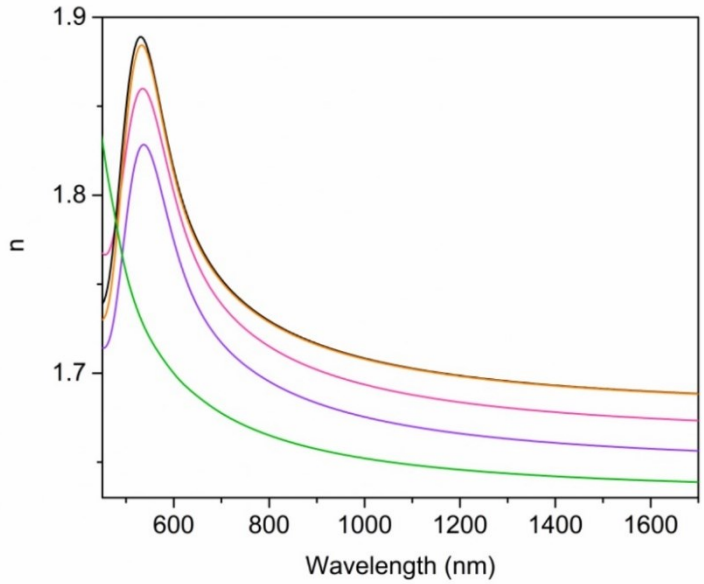

Figure S8 – Refractive index dispersion of **1dz$_{81}$** (blue line), **1dz$_{41}$** (orange line), **1d** (red line), **1dz$_{21}$** (purple line) and **azp** (green line).

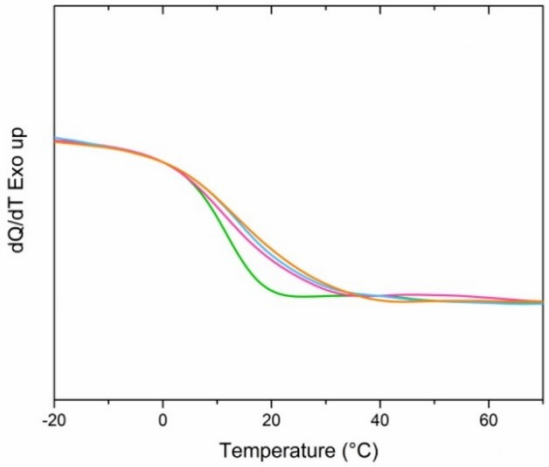

Figure S9 – DSC curves of **1d** (green line), **1dz$_{81}$** (red line), **1dz$_{41}$** (blue line) and **1dz$_{21}$** (orange line).

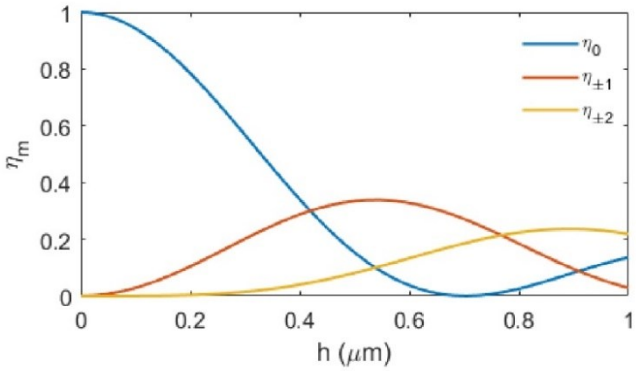

Figure S10 – Diffraction efficiency of the first five diffraction orders plotted with respect to the amplitude modulation h of an ideal sinusoidal surface relief grating. Refractive index n=1.69 and probe wavelength λ=633 nm are assumed for the plot.

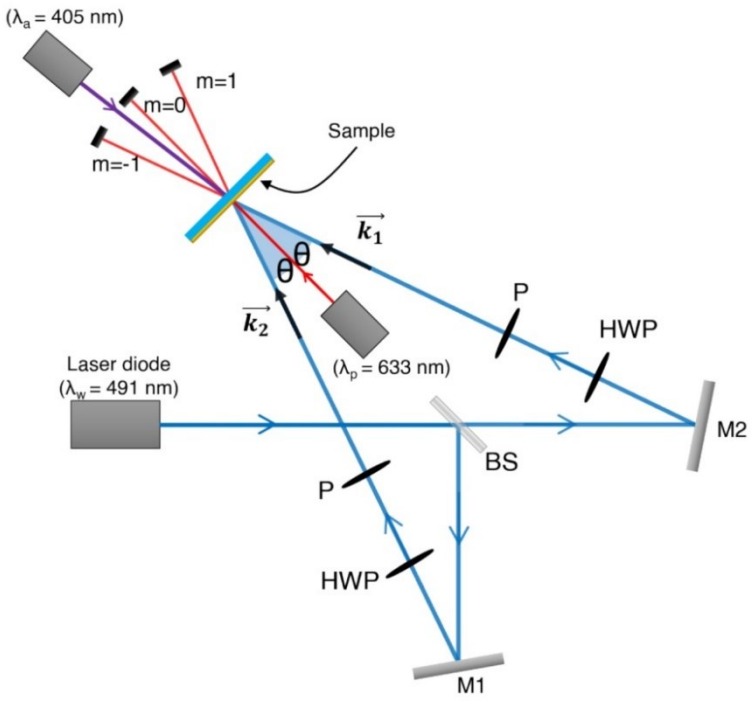

Figure S11 – Experimental setup for the inscription of SRGs. A λ_w=491 nm laser beam is splitted by means of a 50:50 Beam Splitter (BS). Two mirrors (M_1 and M_2) allow to control the angle between the two interfering beams over the material surface. The optical power of each beam is independently tuned by a Half Wave Plate (HWP) and a linear Polarizer (P) in order to maximize fringes visibility in the interferogram. A He-Ne laser beam (λ_p=633 nm) is used for diffraction efficiency measurements. The assisting beam at λ_a=405 nm is circularly polarized before being redirected in the writing area at near-normal incidence.

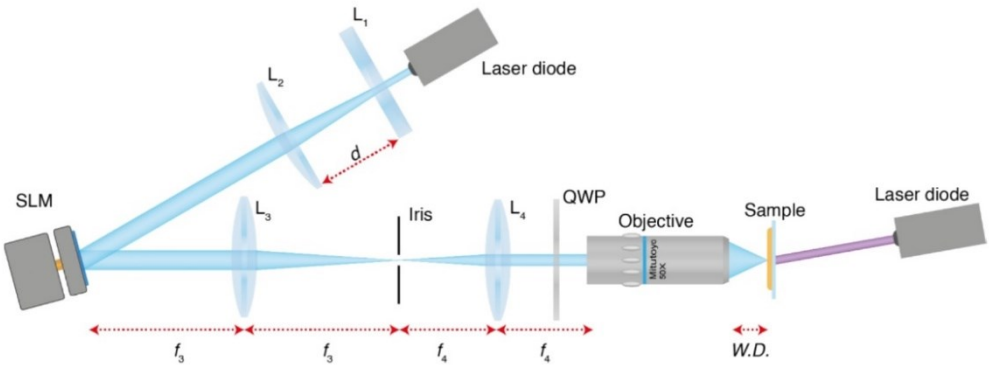

Figure S12 – Experimental setup for holographic structuration of the materials surface. The writing laser beam, at wavelength λ_w=491 nm, after a beam expander (lenses L_1 and L_2), is phase-modulated by a reflective phase-only Holoeye Pluto Spatial Light Modulator (SLM). The SLM realizes a 4*f* configuration with a convex lens (L_3), with a focal length of f_3=300 mm and a convex lens L_4, with focal length f_4=175 mm. An iris is used to filter out all the undesired orders from the SLM. The laser beam is then projected in the back focal plane of an infinity corrected "50X Mitutoyo" objective (OBJ) after imposing circular polarization by means of a quarter wave plate (QWP). The structured holographic intensity distribution is then reconstructed and focused on the objective focal plane (objective working distance WD 13mm) where the azopolymer film is placed. The assisting beam at λ_a=405 nm is circularly polarized before being redirected in the writing area at near-normal incidence.

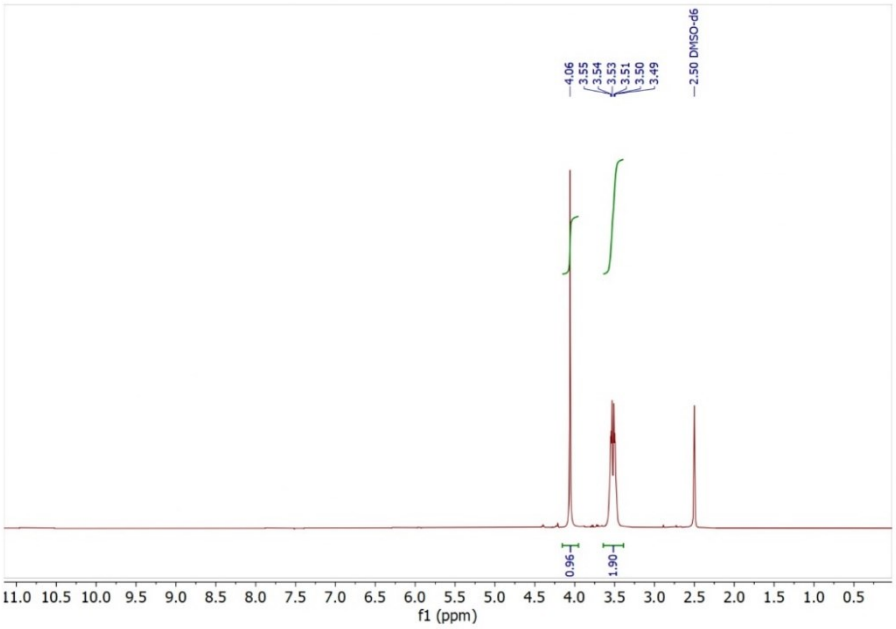

Figure S13 – ^{1}H NMR spectrum of **d**.

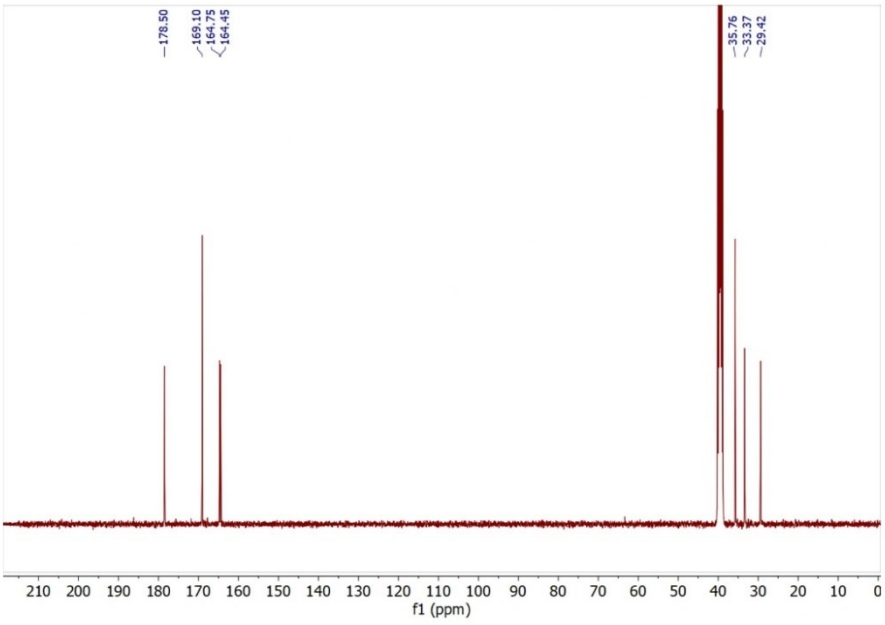

Figure S14 – ^{13}C NMR spectrum of **d**.

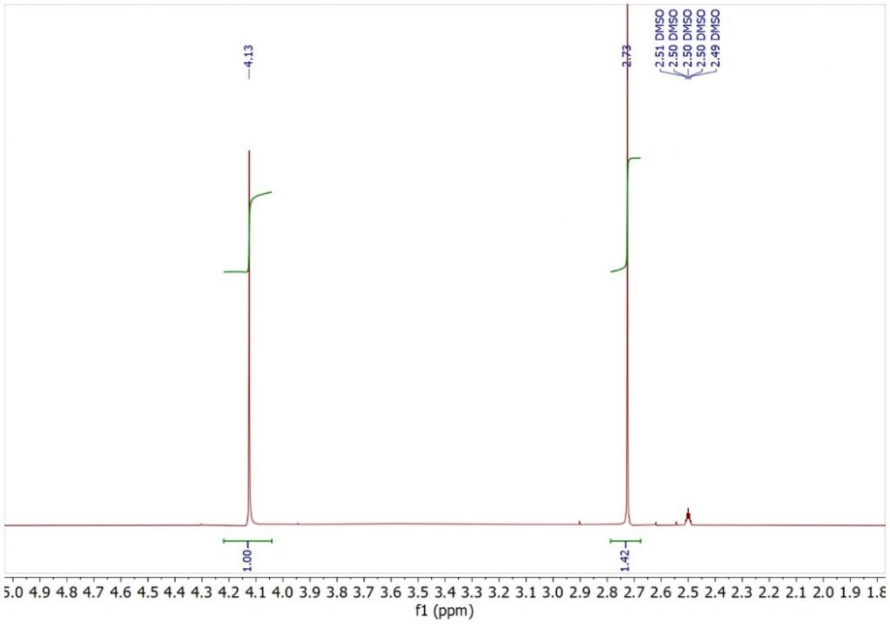

Figure S15 – ^{1}H NMR spectrum of **mc**.

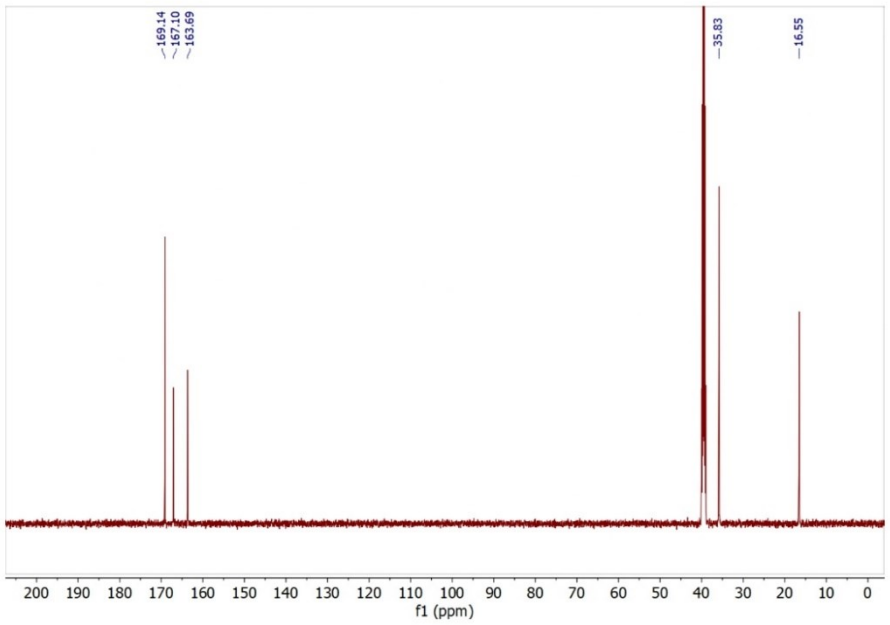

Figure S16 – ^{13}C NMR spectrum of **mc**.

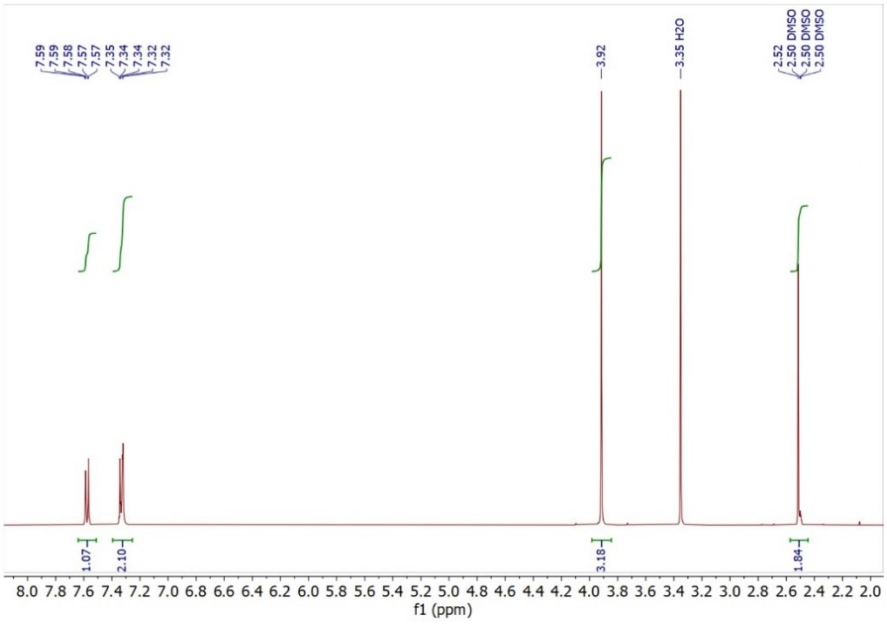

Figure S17 – ^{1}H NMR spectrum of **1**.

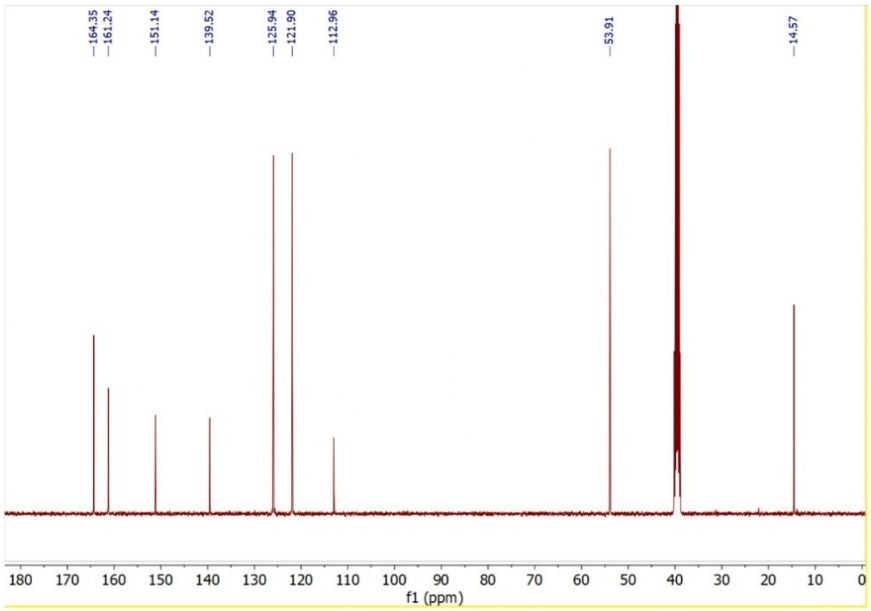

Figure S18 – ^{13}C NMR spectrum of **1**.

Publication VIII

M. Salvatore, F. Reda, F. Borbone, I. K. Januariyasa, P. Maddalena, and S. L. Oscurato

Diffractive refractometer based on scalar theory

Reprinted from

Polymers 15(7), 1605 (2023)

with the permission of MDPI

polymers

IMPACT FACTOR 4.967

Indexed in: PubMed

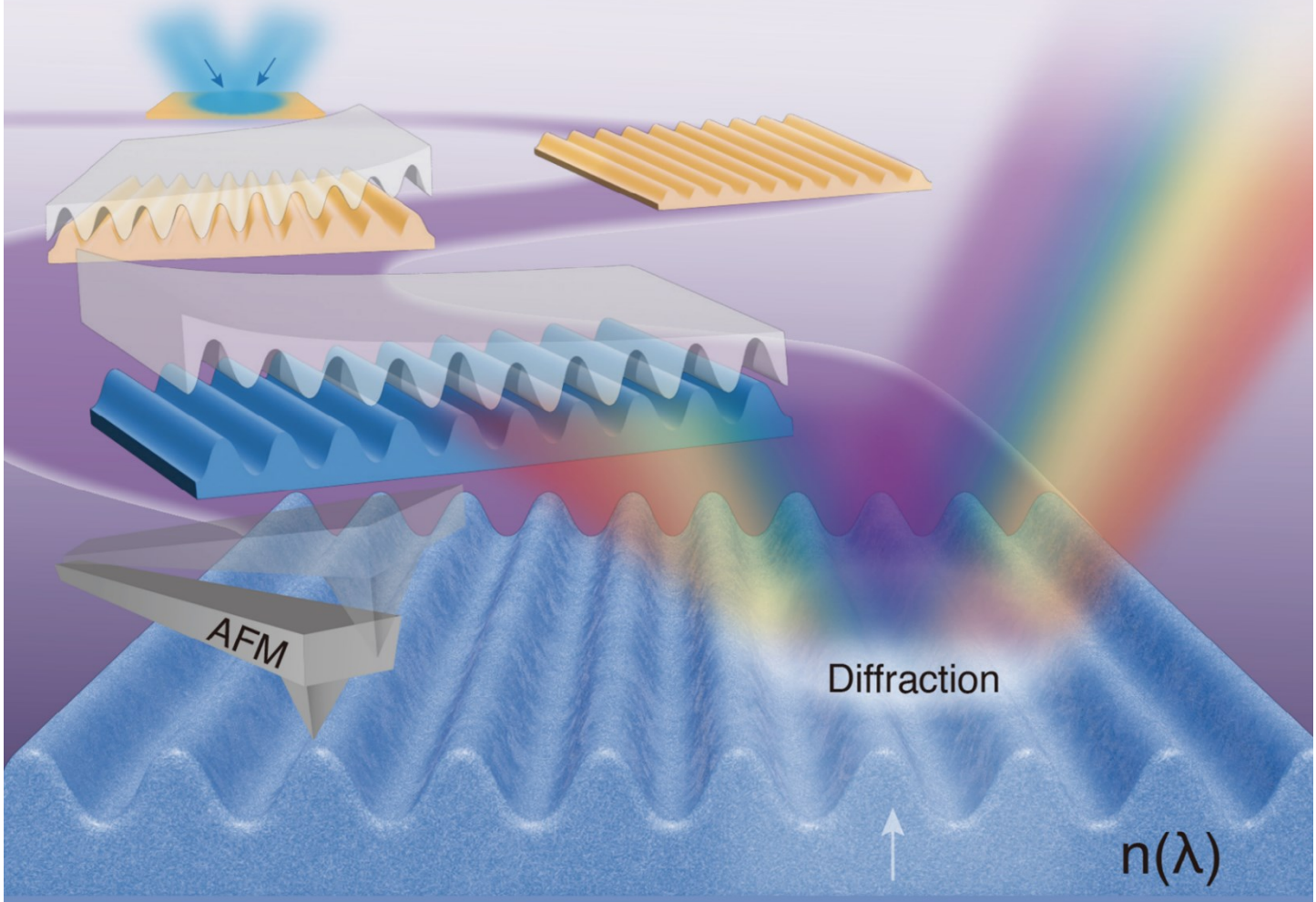

Diffractive Refractometer Based on Scalar Theory

Volume 15 · Issue 7 | April (I) 2023

MDPI

mdpi.com/journal/polymers
ISSN 2073-4360

polymers

MDPI

Article

Diffractive Refractometer Based on Scalar Theory

Marcella Salvatore [1,2], Francesco Reda [2], Fabio Borbone [3], I Komang Januariyasa [2], Pasqualino Maddalena [2] and Stefano Luigi Oscurato [2,*]

[1] Centro Servizi Metrologici e Tecnologici Avanzati (CeSMA), University of Naples "Federico II", Complesso Universitario di Monte Sant'Angelo, Via Cintia 21, 80126 Naples, Italy
[2] Physics Department "E. Pancini", University of Naples "Federico II", Complesso Universitario di Monte Sant'Angelo, Via Cinthia 21, 80126 Naples, Italy
[3] Department of Chemical Sciences, University of Naples "Federico II", Complesso Universitario di Monte Sant'Angelo, Via Cinthia 21, 80126 Naples, Italy
* Correspondence: stefanoluigi.oscurato@unina.it

Abstract: The measurement of the refractive index typically requires the use of optical ellipsometry which, although potentially very accurate, is extremely sensitive to the structural properties of the sample and its theoretical modeling, and typically requires specialized expertise to obtain reliable output data. Here, we propose a simple diffractive method for the measurement of the refractive index of homogenous solid thin films, which requires only the structuring of the surface of the material to be measured with the profile of a diffraction grating. The refractive index of an exemplary soft-moldable material is successfully estimated over a wide wavelength range by simply incorporating the measured topography and diffraction efficiency of the grating into a convenient scalar theory-based diffraction model. Without the need for specialized expertise and equipment, the method can serve as a simple and widely accessible optical characterization of materials useful in material science and photonics applications.

Keywords: refractive index; diffraction gratings; scalar diffraction theory; azopolymers; soft lithography

Citation: Salvatore, M.; Reda, F.; Borbone, F.; Januariyasa, I.K.; Maddalena, P.; Oscurato, S.L. Diffractive Refractometer Based on Scalar Theory. *Polymers* **2023**, *15*, 1605. https://doi.org/10.3390/polym15071605

Academic Editor: Bożena Jarząbek

Received: 22 February 2023
Revised: 20 March 2023
Accepted: 21 March 2023
Published: 23 March 2023

1. Introduction

The refractive index N is a complex number that describes the optical properties of materials [1]. Microscopically, the refractive index characterizes the response of the polarizing atoms and molecules composing the material to the electromagnetic field of incident radiation. Macroscopically, the refractive index ultimately describes the effect of a material on an interacting light field. From ray optics to the electromagnetic treatment of light, the real part n and the imaginary part κ of the refractive index determine the ability of material interfaces to bend light rays, the velocity of the light in the bulk medium, the attenuation of propagating light due to material absorption, and the reflection and transmission characteristics of interfaces between different media, to name a few factors they determine [1,2]. In wave optics, the spatial modulation of the complex refractive index of a material on the scale of the wavelength of light can also be seen as the ultimate origin of the phenomenon of light diffraction, causing spatially selective absorption and wavefront retardation [1]. The measurement of the refractive index $N = n + i\,\kappa$ and its wavelength dependence, called dispersion, in solid or liquid materials is of fundamental relevance for applications in many fields, including bulk [1] and emerging flat and metasurface optics [3–5], biological and biomedical research [6], and the chemical analysis of solutes in liquids [7].

The state-of-the-art measurement technique for solid material samples, especially in the form of thin films, is optical ellipsometry [8], which determines the optical constants (i.e., the refractive index n and the extinction coefficient κ) in a broad wavelength range based on the attenuation and change in polarization of light that occurs

when light is reflected at the surface of a material sample. To be effective, ellipsometry requires the construction of an optical model for the sample structure from the measured optical data, the suitability of which is critical to avoid artifacts or large errors in the final results, especially when high accuracy is desired. One of the drawbacks of ellipsometry is its high sensitivity to the sample geometry, including the surface roughness and volume homogeneity, which requires advanced modeling techniques and ultimately independent sample characterization to maintain high data reliability, with a critical role also played by the experienced user [9]. In addition to ellipsometry, other optical techniques can measure the optical constants of solid and liquid materials. Standard absorption spectroscopy using dedicated spectrophotometers can provide measurements of the extinction coefficient κ in a wide spectral range with high accuracy, while the refractive index n can finally be measured via geometrical [10], interferometric [6,11], or reflectance methods [12,13], which are particularly suitable for the analysis of liquid [14,15] and scattering samples.

Diffractive refractometers based on diffraction gratings or photonic crystal fibers have been proposed to measure liquid materials surrounding the diffractive optical element [16–18], but light diffraction has rarely been used to build refractometers for characterizing solid materials. Despite the clear dependence of the efficiency of a diffractive device on its refractive index n, the parametric form for this dependence made explicit in simple theoretical models is rarely achievable under experimental conditions. In the general case, the model that quantitatively describes the diffraction efficiency can instead be very complex and computationally demanding, with additional complications imposed by device fabrication defects that can make the analysis for refractometry untenable. Scalar diffraction theory, although approximate in some aspects when compared to the full electromagnetic theory of diffraction, can provide a simple parametric model to determine the refractive index n of the solid dielectric material used to fabricate a diffractive element from the measure of its diffraction efficiency and the characterization of its surface profile.

Here, we present a general framework for broadband refractive index measurement based on the analysis of the diffraction performance at different wavelengths of light of a transmissive sinusoidal diffraction grating, taken as an example of a possible device with structural properties falling within the scope of scalar diffraction theory. The method is potentially applicable to any unknown homogeneous dielectric material compatible with a simple replica molding process capable of replicating the surface pattern of a lithographically fabricated diffraction grating. A sinusoidal surface relief Grating (SRG) fabricated on the surface of an azopolymer thin film by two-beam interference lithography is used here as a controllable and cost-effective master for grating fabrication.

2. Materials and Methods

2.1. Grating Fabrication

Light-induced SRGs, used as master for the fabrication of PMMA gratings, were inscribed on the surface of an azopolymer thin film using two interfering p-polarized laser beams at λ = 491 nm with an average incident intensity of about 185 mW/cm^2 over a spot diameter of ~4.0 mm. The PMMA (Merck KGaA, Darmstadt, Germany, Mw 10000, 4% wt. solution in 1,1,2,2-tetrachloroethane) grating was fabricated using a two-step replica molding technique [19–21] in which a PDMS (Sylgard 184—Dow Corning, Midland, Michigan, USA precursor: curing agent = 10:1 w/w) mold reproducing the complementary surface texture of the master was first fabricated and then used for PMMA patterning in the second step. The amplitude of the replicated grating was controlled by adjusting the exposure time of the azopolymer master during the SRG inscription.

2.2. Diffraction Efficiency Measurement

The relative diffraction efficiencies of the grating were calculated by measuring the laser power in the propagating diffraction orders using a NOVA II power meter (OPHIR

photonics, Darmstadt, Germany) equipped with a PD300-3W photodiode sensor (sensitivity spectral range 350–1100 nm). To demonstrate the working principle of the method with a monochromatic light source, a TE-polarized He-Ne laser at λ = 633 nm was used to irradiate the grating from the substrate side at normal incidence. The broadband measurements were instead collected at several discrete wavelengths (450–900 nm) using a supercontinuum TE-polarized laser source (SuperK COMPACT—NKT Photonics, Birkeroed, Denmark) in the same incidence configuration. A set of FKB—Thorlabs bandpass filters (FWHM 10 nm) was used to select the narrow wavelength band centered on the nominal wavelength of interest. The spot size was maintained at ~2 mm in diameter by means of an adjustable telescope collimating the beam at different wavelengths and a fixed iris placed in front of the sample.

2.3. AFM Characterization

The surface topography was characterized using an Atomic Force Microscope (Alpha RS 300, WITec, Ulm, Germany) operated in tapping mode. High-aspect-ratio probes (ISC-225C3_0-R, Team Nanotec, Villingen-Schwenningen, Germany) mounted on a cantilever with a resonance frequency of 75 kHz and a spring constant of 3 N/m were used to reduce errors in the quantitative topographic characterization. Typical AFM scans for grating profile measurements were taken over a sample area of 40 × 0.8 μm^2 with a resolution of 2000 × 40 px^2.

3. Results

3.1. Refractive Index in the Scalar Diffraction Theory of Phase Gratings

To illustrate the working principle of the proposed diffractive refractometers, we first review some general aspects of the diffraction behavior of standard surface diffraction gratings, which are built as periodic reliefs on the surface of an isotropic dielectric material, as schematized in Figure 1 for the case of a sinusoidal grating.

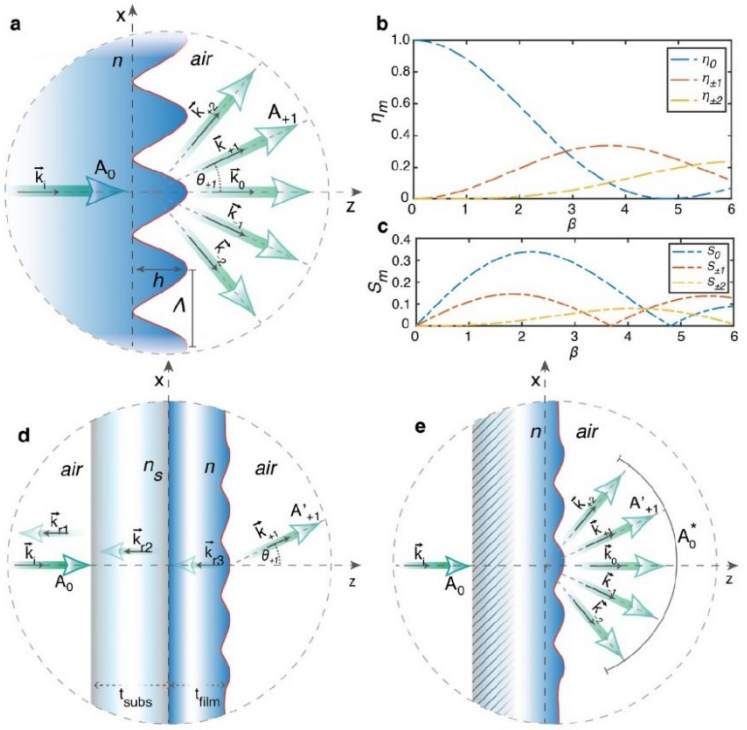

Figure 1. Diffraction behavior of an ideal sinusoidal surface relief grating within the scalar diffraction theory. (**a**) Scheme of the sinusoidal grating boundary at the interface of the infinite semi-spaces

made of the dielectric material and air. (**b**) Scalar diffraction efficiency in the first five diffraction orders as a function of the maximum phase modulation parameter β. (**c**) Sensitivity of the diffraction efficiency variation in the first five orders as a function of β. (**d**) Simplified schematization of a real diffractive grating with finite thickness and multiple reflections (for simplicity, only the first backward reflected waves, with wavevectors k_{ri} are shown). Although the additional contribution to the transmitted diffracted field has low power (proportional to the product of the reflectance of the material-air and material-substrate interfaces), its inclusion prevents the analytical inversion of Equation (1). (**e**) Definition of the relative diffraction efficiency in the scalar diffraction model for a real grating configuration.

A surface diffraction grating splits the incident radiation into different beams (diffraction orders) whose propagation direction and relative intensity depend on the incident light wavelength λ, the refractive indices of the grating n and the surrounding material n_s, and the details of the grating geometry, including the actual surface profile $s(x)$, the periodicity Λ, and the modulation amplitude h of the periodic grating grooves (Figure 1a). The grating equation [1] defines the angle θ_m of the propagating diffraction orders for an incident plane wave with wavevector $k_i = ksin\ \theta_i$ as $k_m = k_i + mG$, where $k = 2\pi/\lambda$; $G = 2\pi/\Lambda$ and $m = 0, \pm1, \pm2, \cdots$. For normal incidence ($\theta_i = 0$), the condition $|m| < \Lambda/\lambda$ defines the maximum number M of propagating orders allowed. According to this relation, the diffraction angles $\theta_m = \mathrm{asin}(mG/k)$ for normal incidence depend on the groove periodicity Λ, while they are independent of the details of the grating structure, including the refractive index n of the grating material, the surface profiles, and other structural parameters (e.g., the modulation amplitude, the thickness of the unmodulated material layer, the possible presence of a substrate, etc.). Instead, the structural and chemical properties affect the diffraction efficiency of the grating η_m, which is a measure of the fraction of the incident light power that is converted into a specific propagating diffraction order.

A comprehensive quantitative understanding of the diffraction efficiency in the general case, involving absorbing, inhomogeneous and anisotropic materials, arbitrary periodic surface profiles, and periodicity-related and polarization-dependent effects, requires a full electromagnetic treatment of the light-matter interaction in the grating [22]. However, in many cases the diffraction behavior of a surface relief grating made of a homogeneous dielectric material can be successfully described within the framework of the scalar diffraction theory [23,24]. In addition to requiring a significant reduction in modeling and computational resources, the scalar diffraction theory preserves a simple parametric dependence of the diffraction efficiency on the grating characteristics, including the surface profile and the refractive index of the grating material. This theory potentially allows the retrieval of information regarding the morphology and the refractive index of the grating to be extracted from the quantitative measure of its diffraction efficiency. However, there are several theoretical and experimental aspects to be considered for the direct application of the scalar model for a refractometer. These include the operation of the grating within the range of the validity of the scalar model and the possibility of incorporating the details of the actual grating profile, as they result from the characteristics of the lithographic process used for fabrication and possible fabrication defects. The scalar theory is generally accepted to provide a sufficiently accurate diffraction efficiency, compared to fully vectorial electromagnetic theories, only for relatively simple surface profiles (e.g., sinusoidal, rectangular, triangular), at quasi-normal incidence, and for low λ/Λ and low h/Λ ratios [25]. Among the simple geometries falling within such limits, sinusoidal surface grating profiles are of particular practical interest. First, the analytic diffraction behavior of these gratings is completely described by the smallest number of geometrical parameters, requiring only the specification of the periodicity Λ and the amplitude h of the sinusoidal surface profile $h(x) = 0.5(1 + \sin(2\pi x/\Lambda))h$. Second, other periodic surface profiles can be described as a superposition of sinusoids via Fourier decomposition, allowing a simple extension of the analytical results of ideal sinusoidal gratings to more complex surface geometries, possibly including deformations or manufacturing defects [26]. In addition, (quasi-ideal) sinusoidal

surface profiles in the range of applicability of the scalar diffraction theory can be readily fabricated using interference lithography, making them easily and cheaply available for applications [27].

Figure 1a shows the schematic of the diffraction behavior of an ideal sinusoidal surface grating. In the simplest geometry suitable for scalar diffraction theory, the sinusoidal grating is assumed to be a boundary surface between two semi-infinite half-spaces, consisting of a dielectric material with refractive index n and a surrounding material with refractive index n_s (air is considered here, so $n_s = 1$). For a plane wave of amplitude A_0 normally incident on the grating (Figure 1a), the diffraction efficiency $\eta_m = |A_m|^2/|A_0|^2$ of the mth diffraction order is expressed analytically in terms of Bessel functions of first kind of order m, as:

$$\eta_m = |J_m(\beta/2)|^2 \tag{1}$$

According to Equation (1), the parameter

$$\beta = \pi(n-1)h/\lambda \tag{2}$$

completely defines the diffraction efficiency of each order. This can be interpreted as the maximum phase delay accumulated in the surrounding medium by the incident plane wavefront as it propagates through the grating structure. Figure 1b shows the behavior of Equation (1) as a function of β for the first five diffraction orders.

From Equations (1) and (2), it is easy to see that, for a given grating amplitude h and incident wavelength λ, the diffraction efficiency in any order m depends only on the refractive index n of the grating material. This simple consideration then gives a potential strategy to directly measure the real part of the refractive index n of the grating material by (numerically) reversing Equation (1) through an accurate measurement of the grating depth h and the diffraction efficiency in one of the propagating orders. To achieve higher accuracy in the estimation of n at the specific light wavelength λ, the grating depth could eventually be optimized to operate in a range of maximum sensitivity $S_m = |\partial\eta_m/\partial\beta|$ for efficiency variations in the considered order with respect to the parameter β (Figure 1c). Maximum sensitivity is expected in the 0th for β = 2.16. However, the typical experimental conditions, as schematized in Figure 1d, prevent the direct use of Equations (1) and (2) in this simple form for a reliable estimation of n. First sources of discrepancy are the portions of light power reflected at each interface of a real device, which are not accounted for in the simple scalar picture of Figure 1a. In addition to the simple effect on the absolute value of the diffraction efficiency, the reflectance of the devices depends on the refractive index of the grating material itself, which, although it typically gives a negligible practical contribution due to the small power carried by the reflected fields, makes the unambiguous inversion of Equation (1) impossible. In addition, a physical grating has a finite thickness, possibly non-zero absorption at the probe wavelength, and requires the presence of a supporting substrate, the presence of which further alters the transmitted and reflected light power. The inclusion of all these effects makes the use of ellipsometry a typical necessity for the characterization of the optical constants of solid material layers in the general case. In addition, the surface profile of a real diffraction grating is never perfectly sinusoidal due to unavoidable fabrication errors common to any lithographic method used for its fabrication, which further deviate the absolute diffraction efficiencies $\eta'_m = |A'_m|^2/|A_0|^2$ in experiments from the predictions of Equation (1).

Fortunately, the scalar diffraction theory, which differs from fully vectorial methods, offers simple ways to overcome these limitations, making a direct refractive index measurement from diffraction analysis effectively feasible. First, the real surface profile $h(x)$ of the grating, as measured for example by using an Atomic Force Microscope (AFM), can be retained in the calculation of the diffraction efficiency [26,28]. Second, the effect of the finite grating thickness and the reflections at each interface in the light path can be averaged out by simply defining the (relative) transmitted diffraction efficiency as the ratio of the intensity in propagating in the diffraction order m and the intensity A_0^*, mea-

sured in all the propagating diffraction orders as $\eta_m^* = |A_m|^2 / \sum_m^M |A_m|^2 = |A_m|^2 / |A_0^*|^2$, as schematized in Figure 1e. This alternative definition of the diffraction efficiency also removes the sensitivity of the method to the absorbance of the material (and hence to the extinction coefficient κ) at the operating wavelength, and it is compatible with the conservation of the irradiance in the interaction of the incident light wave with the diffractive surface within the scalar diffraction theory, which is also valid in the non-paraxial approximation [22,25,29,30].

We have recently shown that this simple generalization of the scalar theory can be successfully applied to the quantitative description of the diffraction behavior of real (quasi-sinusoidal) Surface Relief Gratings (SRGs), inscribed directly on the surface azobenzene-containing materials [31–33] by interference lithography [28,34–40] and Digital Holography [41–43]. However, the results of this scalar model are, however, applicable to any diffraction grating made of a dielectric material, provided that the scalar approximation remains valid. Within such a model, the relative diffraction efficiency for the mth propagating diffraction order is explicitly related to the actual surface profile $h(x)$ of the grating by a simple relation [22,26,28]:

$$\eta_m^* = \left| \frac{1}{\Lambda} \int_{-\Lambda/2}^{\Lambda/2} e^{i\frac{2\pi}{\lambda}(n-1)h(x)} e^{-im\frac{2\pi}{\Lambda}x} dx \right|^2 \quad (3)$$

Similar to the case of ideal sinusoidal gratings, η_m^* in Equation (3) retains the explicit parametric dependence on the refractive index n of the grating, even though $h(x)$ may eventually differ from a sinusoid. A fitting technique can then be used to extract the best estimate for the unknown parameter n from the accurate measure of the relative diffraction efficiency produced by the grating and the results of the scalar model in Equation (3).

3.2. Workflow of the Method

The workflow of the proposed diffraction-based information retrieval method for the measurement of n at the wavelength λ is shown in Figure 2. In the first step, the surface of the material to be measured is structured with a 1D (quasi-sinusoidal) diffraction grating, having a geometry compatible with the scalar diffraction approximation. Then, the grating is characterized by the measure of the relative transmitted diffraction efficiency in one of the propagating orders and by the topographic analysis of the surface profile, both of which enter into the fitting process of n using the scalar diffraction model of Equation (3). In principle, a single high-resolution surface profile measured on a large homogeneous grating and a single measure of the relative diffraction order may be sufficient to achieve a good fit convergence. In this case, the accuracy of the refractive index estimation is mainly determined by the grating depth h, with a sensitivity behavior similar to that of the ideal sinusoidal grating described in Figure 1c. However, possible inhomogeneities in the profile depth and/or shape of the grating, e.g., introduced during fabrication, may impose a trade-off between the optimal sensitivity to the diffraction efficiency variations and the number of independent estimates of the method necessary to average the inhomogeneities. As discussed below, grating inhomogeneities are the ultimate source of uncertainty for the refractive index measurement using this method.

3.3. Measurement of the Refractive Index of PMMA

To demonstrate the validity of the proposed method, we measure the refractive index of a poly(methyl methacrylate) (PMMA) grating at different discrete wavelengths in the range 450–900 nm, using the 0th diffraction order for maximum accuracy (Figure 1c) in the scalar model fit. We selected this material for a reliable comparison of our results with a large literature of refractive index data measured via ellipsometry [44,45]. In addition, PMMA is also considered as a prototype of dielectric moldable material to which the proposed method can be applied, being fully and directly compatible with soft lithographic replication of the quasi-sinusoidal SRGs fabricated on azopolymer thin films via interference

lithography, used here as a master for grating molding [31]. The description of the light-induced fabrication of the azopolymer SRG for the master quasi-sinusoidal grating and its transfer onto the PMMA layer is given in Experimental Methods, while additional details on the polymer for the surface structuring process and its applications can be found in our previous works [41,46–49].

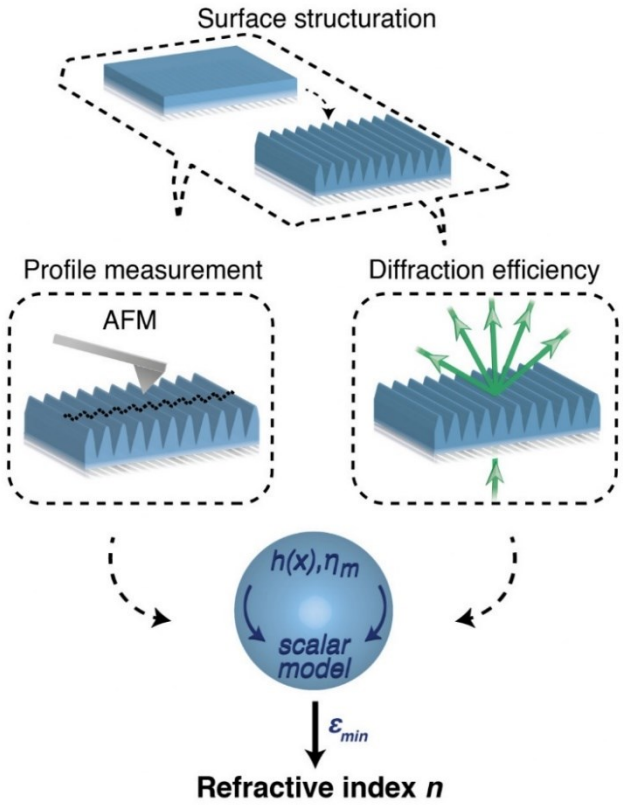

Figure 2. Workflow of the method. The diffractive refractometer based on the scalar theory involves structuring the material with a surface grating profile whose geometry satisfies the scalar approximation. The actual surface profile of the grating and the relative diffraction efficiency are measured and compared with the scalar diffraction model to estimate the best fit of n.

Figure 3a shows the AFM micrograph of the quasi-sinusoidal PMMA grating resulting from the replica molding process. The quasi-sinusoidal surface profile has a periodicity $\Lambda \approx 2.04$ μm and a modulation depth of approximately 480 nm. Such a grating amplitude results in a good compromise between an optimized sensitivity of the diffraction efficiency to the refractive index variations in the whole wavelength range (β~1.7–0.84) and the necessity to be in a monotonically decreasing range for the zeroth order diffraction order (Figure 1b). The latter allows the accurate identification of the region of the grating for both optical and topographic analysis, which has an inhomogeneous gaussian depth due to gaussian beam profiles of the interfering light beams used to fabricate the azopolymer SRG master. The target grating region for the analysis is then uniquely identified via the simultaneous minimum zeroth order light diffraction efficiency and the maximum surface modulation depth in the grating topography. However, to fully characterize the consistency of the method, J = nine different AFM profiles $h_j(x)$ around the region of the topographic maximum over an area approximately 2 mm in diameter (comparable to the size of the probing diffraction beam) were collected and used for the independent diffraction efficiency calculation in the model of Equation (3). To further reduce errors due to the discretization of the measured AFM

profile, a third-order Fourier series fit of the quasi-sinusoidal grating profiles is used in the effective diffraction calculation, as described in detail elsewhere [28].

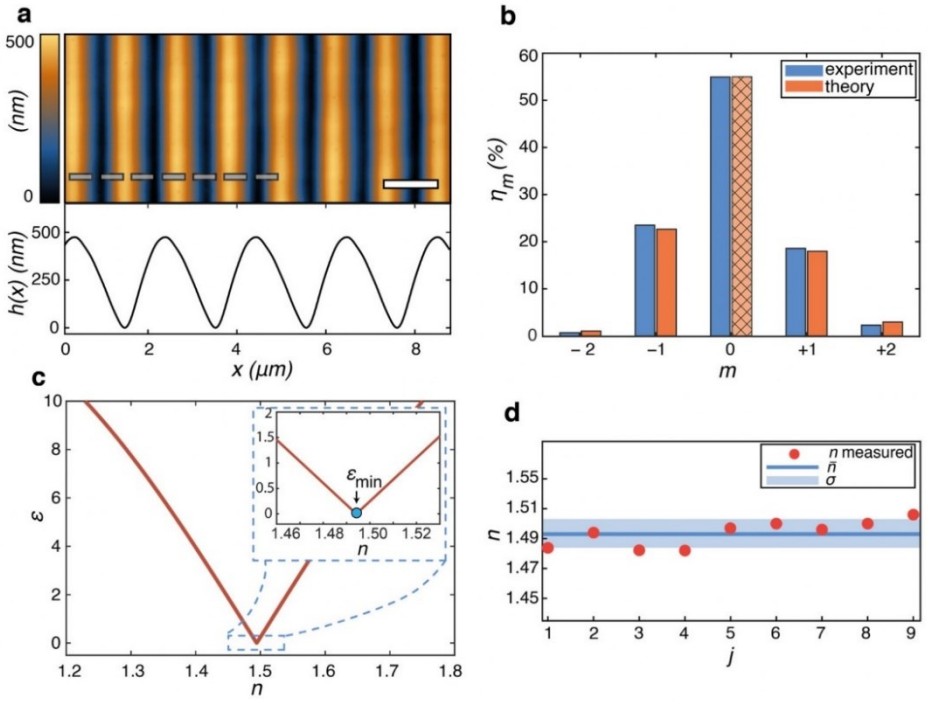

Figure 3. Measurement of the refractive index of a PMMA grating using the diffractive refractometer. (**a**) Typical AFM micrograph and surface profile $h(x)$ in the measured grating region. (**b**) Measured (blue) and theoretical (orange) relative diffraction efficiencies in the first five orders. The theoretical efficiencies for $m \neq 0$ are calculated using the refractive index estimate obtained from the fit of the zeroth order to the experiment, which requires minimization of the error parameter ε. (**c**) Typical behavior of the error ε parameter as a function of the n in the scalar model. The inset shows an enlarged view of the minimum region. (**d**) Average and standard deviation of the different n estimates resulting from the different measured grating profiles $h_j(x)$.

To illustrate the working principle of our method, we first measure the diffraction efficiency of the grating for a He-Ne laser of a wavelength of 633 nm (Figure 3). To increase consistency, five independent measurements of the relative diffraction efficiencies η_m^{exp} in the first seven orders were individually averaged by repositioning the grating in the target area each time. The relative diffraction efficiency measured in the first five diffraction orders is shown in Figure 3b, while the power in the $m = \pm 3$ orders was below the detection sensitivity of the optical power meter and was neglected in the analysis. As expected from the quasi-sinusoidal surface profile, asymmetric diffraction efficiency is observed in the homologous ($m = \pm 1$ and $m = \pm 2$) diffraction orders [28], which further strengthens the necessity to use the extended scalar model in Equation (3) for the accurate analysis of the diffraction of the considered grating.

According to the workflow in Figure 2, we used an error minimization procedure to estimate the refractive index of the grating material at the He-Ne laser wavelength, in which the numerical results of Equation (3) for $\eta_0^*(n)$, calculated for a measured AFM profile $h_j(x)$ and different discrete guesses of n, are compared with the average measured data η_0^{exp}. As a figure of merit, we used the adimensional parameter $\varepsilon(n)$, defined as:

$$\varepsilon(n) = \left| \left(\frac{\eta_0^*(n) - \eta_0^{exp}}{\sigma_{\eta 0}} \right) \right| \quad (4)$$

where $\sigma_{\eta 0}$ is the standard deviation of the five independent measurements of η_0. The best estimate for the refractive index is simply obtained as the value n^* that minimizes Equation (4), as shown graphically in Figure 3c. Finally, the best estimate $\overline{n}$ for the refractive index at the considered wavelength is the average of the J independent estimates of n_j resulting from the different measured grating profiles $h_j(x)$. The standard deviation $\sigma_n = \sqrt{\sum_j \left(\overline{n} - n_j^*\right)^2/(J-1)}$, determined by the systematic profile variation due to grating inhomogeneities and defects, is used as the accuracy limit of the method (Figure 3d) and then as the (conservative) error limit for our refractive index estimates. At λ = 633 nm, we obtain with the proposed diffractive refractometer $\overline{n}_{633} = 1.49 \pm 0.01$, which is in full agreement with the accurate ellipsometry measurements of PMMA films $n_{633}^{ell} = 1.491 \pm 0.001$ [44]. It should be noted that a more homogeneous grating could have provided a higher accuracy for the estimation, allowing the use of an optimized grating depth to maximize sensitivity in the model and reduce systematic data scattering, so that the standard deviation of the mean $\sigma_{\overline{n}} = \sigma_n/\sqrt{J}$ of the J independent estimates could have been used as an error limit.

The accuracy of our estimate for $\overline{n}_{633}$ is additionally validated in Figure 3b by the close agreement of the measured diffraction efficiencies in the $m \neq 0$ diffraction orders (blue bars) with the prediction of the scalar model Equation (3) (orange bars), calculated by using the best estimate $\overline{n}_{633}$ for the refractive index and an arbitrary measured surface profile $h_j(x)$ of the dataset.

To further maintain the strength and the versatility of the proposed diffractive refractometer, we used the same grating to measure the refractive index of PMMA at several discrete wavelengths λ_p ranging from the visible to the NIR. For this purpose, we used a supercontinuum laser as a broadband light source and a set of different bandpass filters to sequentially select the narrow wavelength band (see Experimental Methods) for measuring the zero-order diffraction efficiency of the grating. In this configuration, schematized in Figure 4a, we repeated the fitting process using the same set of measured grating profiles $h_j(x)$ as in the previous analysis. Figure 4b shows the estimated refractive index $n(\lambda)$ as compared with the ellipsometry data from the literature [44]. Again, the error in the estimate is dominated by the grating inhomogeneities rather than by the deviations introduced by the finite width of the spectral window in the model, showing a potential use of broadband lamps as light sources for the refractometer. Figure 4b shows the agreement with ellipsometry as highly evident in the entire spectral range, with a better match in the visible light due to the increased sensitivity of the method in this wavelength range for the actual grating used.

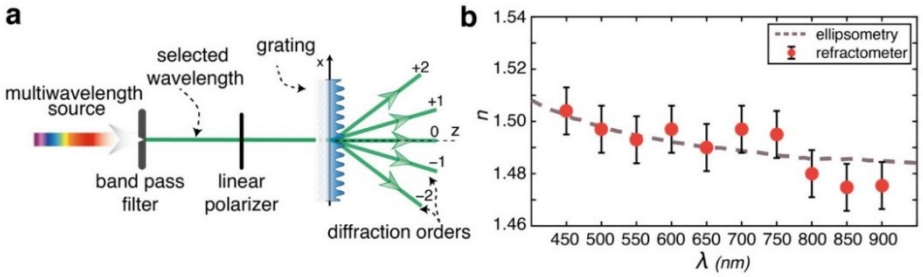

Figure 4. Measurement of the PMMA refractive index dispersion at discrete wavelengths using the diffractive refractometer. (**a**) Schematic of the optical setup. (**b**) Comparison of the measured refractive index $n(\lambda_p)$ and ellipsometry data from ref. [44].

For a deeper insight into this aspect of the method performance, Figure 5 shows the combined parametric dependence of the sensitivity of the zero-order diffraction efficiency on the variations of the grating amplitude h ($S_{0,h}(\lambda, h) = |\partial\eta_0(\lambda, h)/\partial h|$) and light wavelength λ ($S_{0,\lambda}(\lambda, h) = |\partial\eta_0(\lambda, h)/\partial\lambda|$) in the scalar diffraction theory of a sinusoidal

grating. To make such a dependence explicit from the dependence on β (Equation (2)) of the sensitivity $S_0 = |\partial\eta_0(\beta)/\partial\beta|$ shown in Figure 1c, a model for the refractive index dispersion of the material is needed. According to the literature, [44] for the analysis in Figure 5, a Sellmeier model [9] for the refractive index $n = n(\lambda)$ was used to describe the dispersion of the PMMA in the VIS-NIR spectral region, where it is transparent. Further details on this model, and the study of the effects of a more dispersive material (e.g., a TiO_2 layer [50]) on the performance of the method also for higher diffraction orders, can be found in the Supplementary Materials. The sensitivity dependence $S_{0,h}(\lambda, h)$, shown in Figure 5a, allows the definition of the optimized grating amplitude h for maximized sensitivity at any target wavelength (as further illustrated by horizontal cross-sections at example wavelengths). Longer wavelengths of light generally require deeper surface relief gratings to operate at maximum efficiency. However, the method shows potentially better absolute accuracy in the visible compared to the NIR, even with grating amplitudes optimized for this regime. The wavelength sensitivity $S_{0,\lambda}(\lambda, h)$, shown in Figure 5b, describes the effect of measuring the diffraction efficiency at different wavelengths with a single diffraction grating of fixed depth h. Its analysis is useful for characterizing the refractive index dispersion reconstructed with the diffractive refractometer using a single grating, as in the case of the experiment reported in Figure 4. From the analysis in Figure 5b, a general decreasing trend in sensitivity is observed from visible to near-infrared wavelengths is observed for PMMA grating modulation amplitudes below 0.6 µm, providing another basis to explain the NIR discrepancy in our experiment. If, on the one hand, the grating amplitude could be increased to work in this range with improved performance (e.g., as indicated by the brown horizontal cross section), on the other hand, wavelengths at zero sensitivity appear for higher grating modulations, preventing the broadband operation of the method.

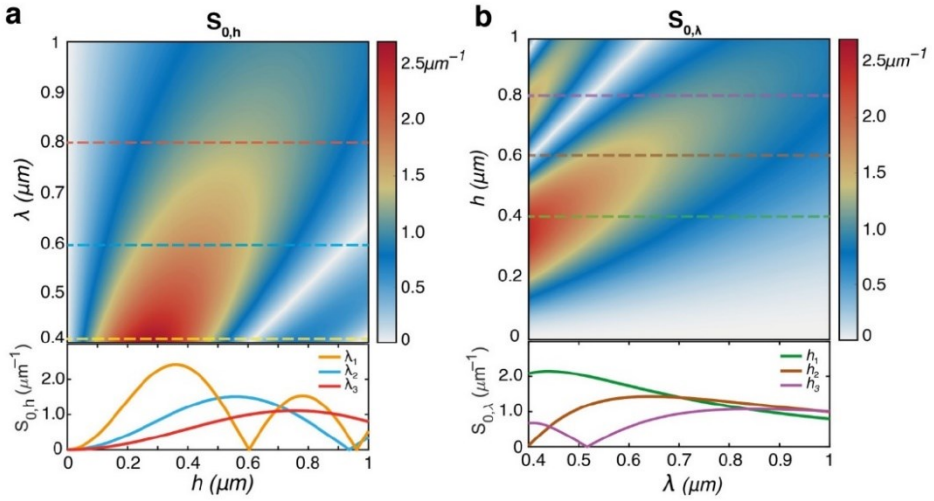

Figure 5. Simulated parametric diffraction sensitivity for PMMA in the 0-order of a sinusoidal surface relief grating. (**a**) Sensitivity $S_{0,h}(h, \lambda)$ of the efficiency variations to the parameter h. The plot shows the horizontal cross-sectional profiles (dashed lines) of the sensitivity $S_{0,h}(h)$ at λ_1 = 0.4 µm (yellow), λ_2 = 0.6 µm (blue), and λ_3 = 0.8 µm (red). (**b**) Sensitivity $S_{0,\lambda}$ to the parameter λ. The cross-sectional profiles for $S_{0,\lambda}(\lambda)$ are calculated for h_1 = 0.4 µm (green), h_2 = 0.6 µm (brown), and h_3 = 0.8 µm (violet).

In addition, the use of longer wavelengths with a single grating also leads to an increase in the λ/Λ ratio, which reduces the validity of the scalar approximation on which the proposed method is based, and further contributes to the reduced accuracy of the NIR data in the experiment of Figure 4.

These considerations suggest that the use of two or more diffraction gratings, with optimized grating amplitude and periodicity, could achieve better performance in retrieving the refractive index dispersion over a wider wavelength range with the proposed method. These two structural grating parameters are easily tunable in our direct writing configuration for master fabrication on azopolymer films, where the periodicity and the modulation depth of the grating are controlled via the irradiation dose of a tunable writing interferogram.

It is worth nothing, however, that even with the non-optimized broad-band performance of a single grating, the additional information about the refractive index dispersion of the material requires only trivial optical power measurements in our analysis.

4. Discussion

When evaluating the performance of the proposed diffractive method for the refractive index measurements of moldable solid thin films, one should consider the simplicity of the entire process, which involves very simple optical and topographical measurements without the need for multistep measurements (e.g., of the substrate alone) or modeling and dedicated expertise, as required for highly accurate measurements via ellipsometry.

Although the proposed diffractive spectrometer could not be the primary choice for the characterization of materials in general situations (anisotropic materials, multi-layers, non-transmissive materials, etc.), where ellipsometry still maintains a clear advantage, by dealing with the simultaneous and continuous characterization of both the refractive index and extinction coefficient of the material over a broader spectrum, the method has both theoretical and practical relevance. First, it is an elegant practical application of the simple scalar diffraction theory, here properly adapted here to describe the general complex light diffraction in a surface grating. Second, the method is effective for dielectrically isotropic and partially transmissive materials, which are often of practical interest in applications, such as in the fabrication of flat diffractive optical components. However, the method is also potentially applicable to monitor possible real-time variations of the grating material properties, provided that its topography is not altered. This capability arises from the use of the relative diffraction efficiency in relation to the refractive index extraction theory. Indeed, the dynamic evolution of the material index could be characterized by using an array detector (e.g., a CCD) to simultaneously record the power in all the propagating diffraction orders, and then by using their time-evolving relative diffraction efficiency. By correlating this information with the topography of the grating (e.g., previously measured), variations in the refractive index can be revealed. Furthermore, the use of an AFM is not mandatory for the method. Since the bottleneck for the accuracy of the method is mainly the homogeneity of the structural grating, recent holographic microscopes and optical profilometers [37], which are able to optically measure the topography of the surface with an accuracy of a few nanometers, could be used in spite of an AFM, achieving results similar to those presented in the manuscript.

5. Conclusions

In this work, we have proposed a theoretical and experimental framework for an operational diffraction-based method capable of measuring the refractive index of structured material layers from a simple optical and topographic characterization of a sinusoidal diffraction grating.

In addition to being applicable to structured surfaces where ellipsometry and other methods are ineffective, the proposed method has the advantage of being agnostic to several of the parameters relevant to conventional refractive index measurement of solid samples, including the film thickness, the substrate nature, and the surface roughness.

Since our approach is based on simple optical and topographical characterizations, it does not require dedicated equipment or specialized personnel and could be easily

accessible to a broad audience working in optics, chemistry, and materials science, with reduced cost and high versatility.

Supplementary Materials: https://www.mdpi.com/article/10.3390/polym15071605/s1, Figure S1: Sellmeier model for the refractive index dispersion n = n(λ); Figure S2: Parametric dependence of the diffraction efficiency in the first five orders produced by a sinusoidal surface relief grating in scalar diffraction theory on the light wavelength λ and grating amplitude h; Figure S3: Sensitivity for PMMA in the first five diffraction orders of the scalar diffraction theory for a sinusoidal surface relief grating; Figure S4: Sensitivity for TiO2 in the first five diffraction orders of the scalar diffraction theory for a sinusoidal surface relief grating.

Author Contributions: Conceptualization: S.L.O. and M.S.; methodology: S.L.O., M.S., I.K.J. and F.R.; software: S.L.O. and F.R.; validation, S.L.O., F.B. and M.S.; investigation: S.L.O., F.R., F.B., I.K.J. and M.S.; data curation: S.L.O. and M.S.; writing—original draft preparation: S.L.O.; writing—review and editing: all authors; visualization: S.L.O., F.R. and M.S.; supervision, S.L.O. and P.M. All authors have read and agreed to the published version of the manuscript.

Funding: This research received no external funding.

Institutional Review Board Statement: Not applicable.

Informed Consent Statement: Not applicable.

Data Availability Statement: The data presented in this study are available upon request from the corresponding author.

Conflicts of Interest: The authors declare no conflict of interest.

References

1. Eugene Hecht. *Optics*, 4th ed.; Addison-Wesley: San Francisco, CA, USA, 2002; ISBN 0-321-18878-0.
2. Saleh, B.E.A.; Teich, M.C. *Fundamentals of Photonics*; Wiley Series in Pure and Applied Optics; John Wiley & Sons, Inc.: New York, NY, USA, 1991; ISBN 978-0-471-83965-1.
3. Lalanne, P.; Chavel, P. Metalenses at Visible Wavelengths: Past, Present, Perspectives. *Laser Photonics Rev.* **2017**, *11*, 1600295. [CrossRef]
4. Banerji, S.; Meem, M.; Majumder, A.; Vasquez, F.G.; Sensale-Rodriguez, B.; Menon, R. Imaging with Flat Optics: Metalenses or Diffractive Lenses? *Optica* **2019**, *6*, 805. [CrossRef]
5. Chen, W.T.; Capasso, F. Will Flat Optics Appear in Everyday Life Anytime Soon? *Appl. Phys. Lett.* **2021**, *118*, 100503. [CrossRef]
6. Tearney, G.J.; Brezinski, M.E.; Southern, J.F.; Bouma, B.E.; Hee, M.R.; Fujimoto, J.G. Determination of the Refractive Index of Highly Scattering Human Tissue by Optical Coherence Tomography. *Opt. Lett. OL* **1995**, *20*, 2258–2260. [CrossRef] [PubMed]
7. Chang, K.-A.; Lim, H.-J.; Su, C.B. A Fibre Optic Fresnel Ratio Meter for Measurements of Solute Concentration and Refractive Index Change in Fluids. *Meas. Sci. Technol.* **2002**, *13*, 1962. [CrossRef]
8. Tompkins, H.G.; Irene, E.A. *Handbook of Ellipsometry*; William Andrew Publishing: Norwich, UK, 2005; ISBN 978-0-8155-1499-2.
9. Fujiwara, H.; Collins, R.W. (Eds.) *Spectroscopic Ellipsometry for Photovoltaics: Volume 1: Fundamental Principles and Solar Cell Characterization*; Springer Series in Optical Sciences; Springer International Publishing: Cham, Switzerland, 2018; Volume 212, ISBN 978-3-319-75375-1.
10. Rheims, J.; Köser, J.; Wriedt, T. Refractive-Index Measurements in the near-IR Using an Abbe Refractometer. *Meas. Sci. Technol.* **1997**, *8*, 601. [CrossRef]
11. Kachiraju, S.R.; Gregory, D.A. Determining the Refractive Index of Liquids Using a Modified Michelson Interferometer. *Opt. Laser Technol.* **2012**, *44*, 2361–2365. [CrossRef]
12. Kim, C.-B.; Su, C.B. Measurement of the Refractive Index of Liquids at 1.3 and 1.5 Micron Using a Fibre Optic Fresnel Ratio Meter. *Meas. Sci. Technol.* **2004**, *15*, 1683. [CrossRef]
13. Zhang, X.U.; Faber, D.J.; Post, A.L.; van Leeuwen, T.G.; Sterenborg, H.J.C.M. Refractive Index Measurement Using Single Fiber Reflectance Spectroscopy. *J. Biophotonics* **2019**, *12*, e201900019. [CrossRef]
14. An, N.; Zhuang, B.; Li, M.; Lu, Y.; Wang, Z.-G. Combined Theoretical and Experimental Study of Refractive Indices of Water–Acetonitrile–Salt Systems. *J. Phys. Chem. B* **2015**, *119*, 10701–10709. [CrossRef]
15. Li, M.; Zhuang, B.; Lu, Y.; Wang, Z.-G.; An, L. Accurate Determination of Ion Polarizabilities in Aqueous Solutions. *J. Phys. Chem. B* **2017**, *121*, 6416–6424. [CrossRef]
16. Barbosa, E.A.; Dib, L.F.G. Diffractive Refractometer for Liquid Characterization and Transient Processes Monitoring. *Rev. Sci. Instrum.* **2017**, *88*, 073103. [CrossRef]

17. Calixto, S.; Piazza, V.; Gonzalez-Suarez, A.M.; Garcia-Cordero, J.L.; Bruce, N.C.; Rosete-Aguilar, M.; Garnica, G. Liquid Refractive Index Measured through a Refractometer Based on Diffraction Gratings. *Opt. Express OE* **2019**, *27*, 34705–34720. [CrossRef] [PubMed]
18. Martelli, C.; Canning, J.; Kristensen, M.; Groothoff, N. Refractive Index Measurement within a Photonic Crystal Fibre Based on Short Wavelength Diffraction. *Sensors* **2007**, *7*, 2492–2498. [CrossRef]
19. Xia, Y.; Whitesides, G.M. Soft Lithography. *Angew. Chem. Int. Ed.* **1998**, *37*, 550–575. [CrossRef]
20. Liu, B.; Wang, M.; He, Y.; Wang, X. Duplication of Photoinduced Azo Polymer Surface-Relief Gratings through a Soft Lithographic Approach. *Langmuir* **2006**, *22*, 7405–7410. [CrossRef] [PubMed]
21. Na, S.-I.; Kim, S.-S.; Jo, J.; Oh, S.-H.; Kim, J.; Kim, D.-Y. Efficient Polymer Solar Cells with Surface Relief Gratings Fabricated by Simple Soft Lithography. *Adv. Funct. Mater.* **2008**, *18*, 3956–3963. [CrossRef]
22. Loewen, E.G.; Popov, E. *Diffraction Gratings and Applications*; CRC Press: Boca Raton, FL, USA, 2017; ISBN 978-1-315-21484-9.
23. Popov, E.K.; Tsonev, L.V.; Loewen, E.G. Scalar Theory of Transmission Relief Gratings. *Opt. Commun.* **1991**, *80*, 307–311. [CrossRef]
24. Goodman, J.W. *Introduction to Fourier Optics*; Roberts and Company Publishers: Greenwood Village, CO, USA, 2005; ISBN 978-0-9747077-2-3.
25. Harvey, J.E.; Krywonos, A.; Bogunovic, D. Nonparaxial Scalar Treatment of Sinusoidal Phase Gratings. *J. Opt. Soc. Am. A JOSAA* **2006**, *23*, 858–865. [CrossRef]
26. Andries, I.; Galstian, T.; Chirita, A. Approximate Analysis of the Diffraction Efficiency of Transmission Phase Holographic Gratings with Smooth Non-Sinusoidal Relief. *J. Optoelectron. Adv. Mater.* **2016**, *18*, 56–64.
27. O'Shea, D.C.; Suleski, T.J.; Kathman, A.D.; Prather, D.W. *Diffractive Optics*; SPIE: Bellingham, WA, USA, 2003; ISBN 978-0-8194-5171-2.
28. Reda, F.; Salvatore, M.; Borbone, F.; Maddalena, P.; Oscurato, S.L. Accurate Morphology-Related Diffraction Behavior of Light-Induced Surface Relief Gratings on Azopolymers. *ACS Mater. Lett.* **2022**, *4*, 953–959. [CrossRef]
29. Harvey, J.E.; Pfisterer, R.N. Understanding Diffraction Grating Behavior: Including Conical Diffraction and Rayleigh Anomalies from Transmission Gratings. *OE* **2019**, *58*, 087105. [CrossRef]
30. Harvey, J.E.; Pfisterer, R.N. Understanding Diffraction Grating Behavior, Part II: Parametric Diffraction Efficiency of Sinusoidal Reflection (Holographic) Gratings. *OE* **2020**, *59*, 017103. [CrossRef]
31. Oscurato, S.L.; Salvatore, M.; Maddalena, P.; Ambrosio, A. From Nanoscopic to Macroscopic Photo-Driven Motion in Azobenzene-Containing Materials. *Nanophotonics* **2018**, *7*, 1387–1422. [CrossRef]
32. Priimagi, A.; Shevchenko, A. Azopolymer-Based Micro- and Nanopatterning for Photonic Applications. *J. Polym. Sci. Part B Polym. Phys.* **2014**, *52*, 163–182. [CrossRef]
33. Natansohn, A.; Rochon, P. Photoinduced Motions in Azo-Containing Polymers. *Chem. Rev.* **2002**, *102*, 4139–4176. [CrossRef]
34. Jelken, J.; Santer, S. Light Induced Reversible Structuring of Photosensitive Polymer Films. *RSC Adv.* **2019**, *9*, 20295–20305. [CrossRef] [PubMed]
35. Loebner, S.; Yadav, B.; Lomadze, N.; Tverdokhleb, N.; Donner, H.; Saphiannikova, M.; Santer, S. Local Direction of Optomechanical Stress in Azobenzene Containing Polymers During Surface Relief Grating Formation. *Macromol. Mater. Eng.* **2022**, *307*, 2100990. [CrossRef]
36. Lim, Y.; Kang, B.; Lee, S. Photo-Transformable Gratings for Augmented Reality. *Adv. Funct. Mater.* **2021**, *31*, 2100839. [CrossRef]
37. Rekola, H.; Berdin, A.; Fedele, C.; Virkki, M.; Priimagi, A. Digital Holographic Microscopy for Real-Time Observation of Surface-Relief Grating Formation on Azobenzene-Containing Films. *Sci. Rep.* **2020**, *10*, 19642. [CrossRef]
38. Lim, Y.; Kang, B.; Hong, S.J.; Son, H.; Im, E.; Bang, J.; Lee, S. A Field Guide to Azopolymeric Optical Fourier Surfaces and Augmented Reality. *Adv. Funct. Mater.* **2021**, *31*, 2104105. [CrossRef]
39. Audia, B.; Pagliusi, P.; Mazzulla, A.; Cipparrone, G. Multi-Wavelength Optical Patterning for Multiscale Materials Design. *Photonics* **2021**, *8*, 481. [CrossRef]
40. Pagliusi, P.; Audia, B.; Provenzano, C.; Piñol, M.; Oriol, L.; Cipparrone, G. Tunable Surface Patterning of Azopolymer by Vectorial Holography: The Role of Photoanisotropies in the Driving Force. *ACS Appl. Mater. Interfaces* **2019**, *11*, 34471–34477. [CrossRef] [PubMed]
41. Oscurato, S.L.; Reda, F.; Salvatore, M.; Borbone, F.; Maddalena, P.; Ambrosio, A. Shapeshifting Diffractive Optical Devices. *Laser Photonics Rev.* **2022**, 2100514. [CrossRef]
42. Strobelt, J.; Stolz, D.; Leven, M.; Soelen, M.V.; Kurlandski, L.; Abourahma, H.; McGee, D.J. Optical Microstructure Fabrication Using Structured Polarized Illumination. *Opt. Express OE* **2022**, *30*, 7308–7318. [CrossRef]
43. Strobelt, J.; Van Soelen, M.; Abourahma, H.; McGee, D.J. Supramolecular Azopolymers for Dynamic Surface Microstructures Using Digital Polarization Optics. *Adv. Opt. Mater.* **2023**, 2202245. [CrossRef]
44. Sultanova, N.; Kasarova, S.; Nikolov, I. Dispersion Properties of Optical Polymers. *Acta Phys. Pol. A* **2009**, *116*, 585–587. [CrossRef]
45. Beadie, G.; Brindza, M.; Flynn, R.A.; Rosenberg, A.; Shirk, J.S. Refractive Index Measurements of Poly(Methyl Methacrylate) (PMMA) from 0.4–1.6 Mm. *Appl. Opt. AO* **2015**, *54*, F139–F143. [CrossRef]
46. Oscurato, S.L.; Borbone, F.; Maddalena, P.; Ambrosio, A. Light-Driven Wettability Tailoring of Azopolymer Surfaces with Reconfigured Three-Dimensional Posts. *ACS Appl. Mater. Interfaces* **2017**, *9*, 30133–30142. [CrossRef]
47. Salvatore, M.; Borbone, F.; Oscurato, S.L. Deterministic Realization of Quasicrystal Surface Relief Gratings on Thin Azopolymer Films. *Adv. Mater. Interfaces* **2020**, *7*, 1902118. [CrossRef]

48. Oscurato, S.L.; Reda, F.; Salvatore, M.; Borbone, F.; Maddalena, P.; Ambrosio, A. Large-Scale Multiplexed Azopolymer Gratings with Engineered Diffraction Behavior. *Adv. Mater. Interfaces* **2021**, *8*, 2101375. [CrossRef]
49. Reda, F.; Salvatore, M.; Borbone, F.; Maddalena, P.; Ambrosio, A.; Oscurato, S.L. Varifocal Diffractive Lenses for Multi-Depth Microscope Imaging. *Opt. Express OE* **2022**, *30*, 12695–12711. [CrossRef] [PubMed]
50. DeVore, J.R. Refractive Indices of Rutile and Sphalerite. *J. Opt. Soc. Am. JOSA* **1951**, *41*, 416–419. [CrossRef]

Supporting Information for

Diffractive refractometer based on scalar theory

Marcella Salvatore[†,‡], *Francesco Reda*[‡], *Fabio Borbone*[§], *Pasqualino Maddalena*[‡,†] *and Stefano L. Oscurato*[‡,†,*]

[†]Centro Servizi Metrologici e tecnologici Avanzati (CeSMA), University of Naples "Federico II", Complesso Universitario di Monte Sant'Angelo, Via Cintia 21, 80126, Naples, Italy.

[‡]Physics Department "E. Pancini", University of Naples "Federico II", Complesso Universitario di Monte Sant'Angelo, via Cinthia 21, 80126, Naples, Italy.

[§]Department of Chemical Sciences, University of Naples "Federico II", Complesso Universitario di Monte Sant'Angelo, Via Cintia, 80126 Naples, Italy

***Corresponding author**

Email: stefanoluigi.oscurato@unina.it

Parametric dependence of diffraction efficiency and sensitivity for surface relief sinusoidal diffraction gratings in scalar diffraction theory

Model for refractive index dispersion in transparent materials

Sellmeier equation successfully describe the refractive index dependence on light wavelength for transparent materials exhibiting normal dispersion.[1,2] This model is a simplified version of the Lorentz model of oscillating dipoles for the dielectric function of materials, where dissipation terms are neglected (no absorption). The general form of the Sellmeier dispersion equation is: $n^2(\lambda) - 1 = A\lambda^2/(\lambda^2 - \lambda_0^2)$,where A and λ_0 are the amplitude and the resonance wavelength of the oscillating dipoles, respectively. The validity of this model is restricted to wavelength regions far from the resonance wavelength (located typically in the UV).

To evaluate the parametric dependence of the diffraction efficiency of a sinusoidal grating on the grating amplitude *h* and light wavelength λ within scalar diffraction theory, we consider PMMA and TiO2 as exemplary low and high dispersion transparent materials in the VIS-NIR wavelength range.

According to Ref.[3] (PMMA) and Ref. [4] (TiO_2), Sellmeier models for the two materials in this range, shown in Figure S1, are:

$$n(\lambda)_{PMMA}{}^2 - 1 = \frac{1.1819\lambda^2}{\lambda^2 - 0.11313} \qquad \textit{eq. (S1)}$$

$$n(\lambda)_{TiO2}{}^2 - 5.913 = \frac{0.2441\lambda^2}{\lambda^2 - 0.00803} \qquad \textit{eq. (S2)}$$

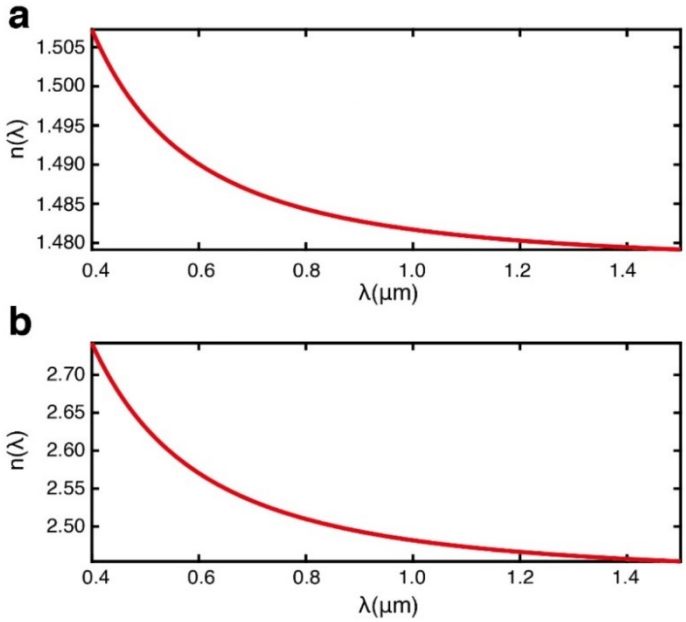

Figure S1. Sellmeier model for the refractive index dispersion n=n(λ) of PMMA(a) and TiO2(b) in region λ=0.4-1.5 μm.

Dependence of diffraction efficiency on wavelength and grating amplitude

According to scalar diffraction theory, the diffraction efficiency in the m^{th} order produced by a sinusoidal surface relief grating, in the ideal case depicted in Figure 1a on the main text, is described in terms of Bessel functions of first kind and order m as:

$$\eta_m(\lambda, h, n) = \left| J_m\left[\pi(n-1)\frac{h}{\lambda}\right]\right|^2 \qquad \textit{eq. (S3)}$$

By using a model for the refractive index dispersion $n=n(\lambda)$, the diffraction efficiency η_m in this model parametrically depends only on the wavelength and the grating amplitude $\eta_m = \eta_m(\lambda,h)$. This consideration allows a deeper analysis of the combined influence of the grating structural parameter h and light wavelength on the diffraction behavior of the grating. Figure S2a and Figure S2a show this relation in the fist five diffraction orders ($m=0, \pm1, \pm2$) sinusoidal gratings made of PMMA and TiO_2, respectively in parametric range ($h = 0 \div 1.0\ \mu m$; $\lambda = 0.4 - 1.0\ \mu m$) compatible with the experimental conditions of the experiment in the main text. Sellmeier relations in eq. (S1) and eq. (S2) have been used in the simulation of the dispersion for the two materials.

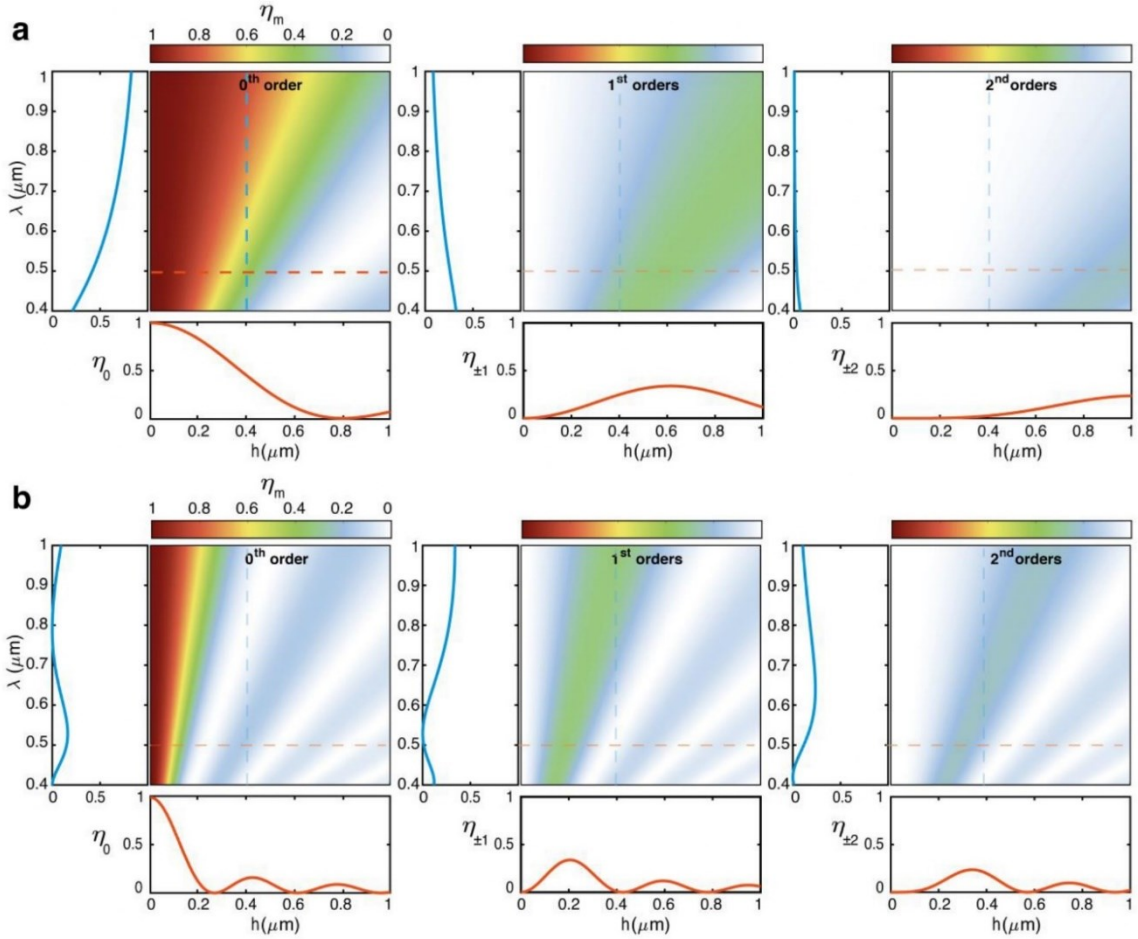

Figure S2. Parametric dependence of the diffraction efficiency in the first five orders produced by a sinusoidal surface relief grating in scalar diffraction theory on the light wavelength λ and grating amplitude h. Sellmeier models for the refractive index dispersion of PMMA (a) and TiO2 (b) have been used. For deeper insight, each panel shows also single parameter dependence for fixed wavelength (λ=0.5 μm, red curves) and fixed grating amplitude (h=0.4 μm, blue curves)

Dependence of efficiency sensitivity on wavelength and grating amplitude

The derivatives of eq. (S3) with respect to the parameters λ and h can be used to define *sensitivity* functions for the variations of the diffraction efficiency with the wavelength and grating amplitude:

$$S_{m,h}(\lambda, h) = \left|\frac{\partial \eta_m(\lambda, h)}{\partial h}\right| \qquad \textit{eq. (S4)}$$

$$S_{m,\lambda}(\lambda, h) = \left|\frac{\partial \eta_m(\lambda, h)}{\partial \lambda}\right| \qquad \textit{eq. (S5)}$$

Figure S3 and Figure S4 show the plot of the grating amplitude sensitivity (panels a) and the wavelength sensitivity (panels b) for PMMA and TiO_2 gratings, respectively. While the amplitude grating sensitivity can be used to design the best grating amplitude optimizing the sensitivity to diffraction efficiency variations in the desired wavelength range for the diffractive refractometer, the wavelength sensitivity gives more details on the expected effectiveness of the method when a single grating with fixed amplitude is used to investigate a large wavelength range, as in the case of the experiment in Figure 4 of the main text. It is worth noting that higher dispersive materials (TiO_2 here) show less sensitivity of diffraction efficiency variations with the wavelength, when compared to lower dispersive materials (e.g. PMMA).

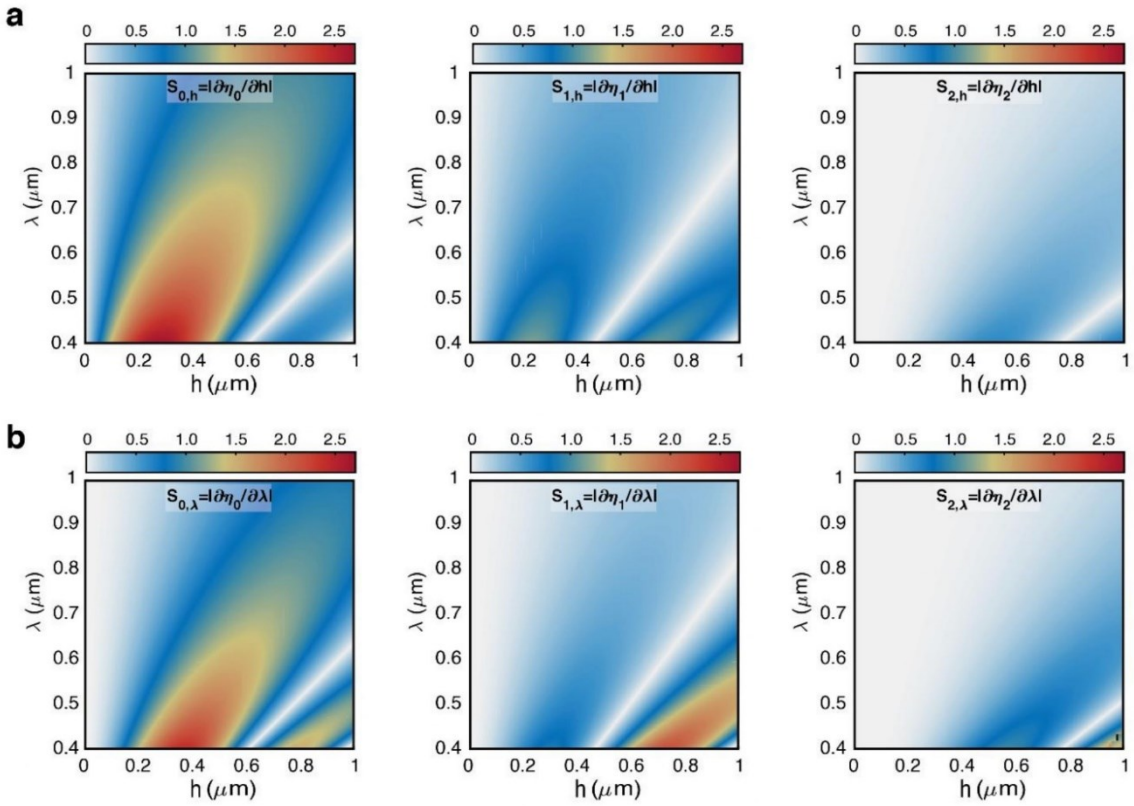

Figure S3. Sensitivity for PMMA in the first five diffraction orders of the scalar diffraction theory for a sinusoidal surface relief grating. (a) Sensitivity $S_{m,h}$ to the parameter h and (b) sensitivity $S_{m,\lambda}$ to the parameter λ. Sellmeier model (eq. (S1)) for refractive index dispersion has been used for n(λ) in these calculations.

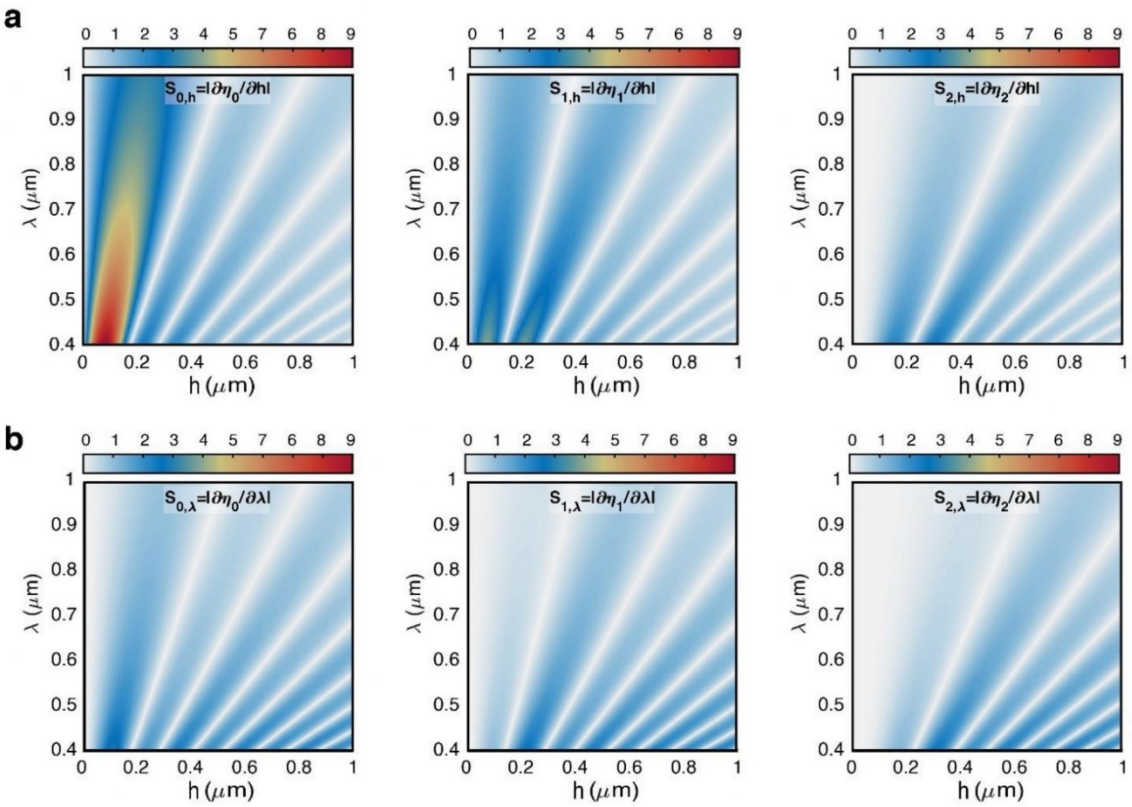

Figure S4. Sensitivity for TiO_2 in the first five diffraction orders of the scalar diffraction theory for a sinusoidal surface relief grating. (a) Sensitivity $S_{m,h}$ to the parameter h and (b) sensitivity $S_{m,\lambda}$ to the parameter λ. Sellmeier model (eq. (S2)) for refractive index dispersion has been used for n(λ) in these calculations. The higher refractive index and dispersion of TiO_2 with respect to PMMA results in several narrow bands of high sensitivity in the considered parameter space.

References

(1) *Spectroscopic Ellipsometry for Photovoltaics: Volume 1: Fundamental Principles and Solar Cell Characterization*; Fujiwara, H., Collins, R. W., Eds.; Springer Series in Optical Sciences; Springer International Publishing: Cham, 2018; Vol. 212. https://doi.org/10.1007/978-3-319-75377-5.

(2) Harland G. Tompkins; Eugene A. Irene. *Handbook of Ellipsometry*; William Andrew Publishing: Norwich, 2005.

(3) Sultanova, N.; Kasarova, S.; Nikolov, I. Dispersion Properties of Optical Polymers. *ACTA PHYSICA POLONICA A* **2009**, *116*, 585–587. https://doi.org/10.12693/APhysPolA.116.585.

(4) DeVore, J. R. Refractive Indices of Rutile and Sphalerite. *J. Opt. Soc. Am., JOSA* **1951**, *41* (6), 416–419. https://doi.org/10.1364/JOSA.41.000416.

Publication IX

F. Reda, M. Salvatore, M. Astarita, F. Borbone, and S. L. Oscurato

Reprogrammable holograms from maskless surface photomorphing

Reprinted from

Advanced Optical Materials 11(21), 2300823 (2023)

with the permission of Wiley

ADVANCED OPTICAL MATERIALS
www.advopticalmat.de

Reprogrammable Holograms from Maskless Surface Photomorphing

*Francesco Reda, Marcella Salvatore, Marco Astarita, Fabio Borbone, and Stefano L. Oscurato**

Holographic technologies have been envisioned as potentially impacting many areas of everyday life, including science, entertainment, and healthcare, but their adoption is still at an early stage. Recent achievements in flat optics research gave an unprecedented strength to this field, proposing holographic devices as light-modulating structured surfaces at micro and nanoscale. However, these components are typically static, requiring demanding, burdensome, and irreversible lithographic processes. Here a maskless lithographic framework is reported which only uses light irradiation to fabricate reprogrammable diffractive holographic projectors directly on the surface of a dielectric photomorphable polymer film. Lithographic and characterization optical schemes are combined to optimize in real-time the light-modulating performances of the surface, producing holograms with enhanced efficiency. Reprogrammable holograms are then demonstrated to change shape and position according to dynamical optical remorphing of the surface, realizing a proof-of-concept of a pixel-less morphological projector. The approach opens new routes for holographic image displaying and dynamic optical data encoding and sharing.

1. Introduction

Flat optics can empower emerging photonic technologies[1,2] with enhanced optical performances in ultracompact devices. Potential applications include optical wireless communication,[3] green energy harvesting,[4] and optical information storing, encryption, and sharing.[5,6] In addition, the next-generation of displays and holographic projectors[7,8] can take advantage of the miniaturized and light-weight systems made possible by flat optics, with increasing inclusion in wearables and components for extended reality.[9,10] Planar holographic components, capable of arbitrarily shaping of an incident light wavefront, can be implanted both as diffractive optical elements (DOEs)[11–13] and as metasurfaces.[14–16]

The advanced performances of such planar components come at the expense of complex surface geometries to be fabricated at the light (sub-)wavelength scale. Optical lithography (OL) and electron beam lithography (EBL) are among the most widely used manufacturing techniques[17–19] for planar optics. The typical fabrication workflow starts with the irradiation of a resist with UV patterned light from a photomask (OL) or using e-beam raster scanning (EBL). In both cases, additional postexposure chemical, physical, and mechanical processes are required to transfer the final pattern to a suitable light-modulating substrate. OL techniques, which typically require fewer resources than EBL, guarantee higher throughput and lower production costs, although with additional resolution limitations. Further progress toward increased sustainability and throughput has been made with emerging UV-Nanoimprint lithography[20] or using digital-based projection of spatially structured intensity patterns in a maskless OL workflow.[21–23] However, if a multilevel surface morphology is required, several iterations of the OL scheme[11] or scanning probe techniques[24]

F. Reda, M. Salvatore, S. L. Oscurato
Department of Physics "E. Pancini"
University of Naples "Federico II"
Complesso Universitario di Monte Sant'Angelo
Via Cintia, Naples 80126, Italy
E-mail: stefanoluigi.oscurato@unina.it

The ORCID identification number(s) for the author(s) of this article can be found under https://doi.org/10.1002/adom.202300823

DOI: 10.1002/adom.202300823

M. Salvatore, S. L. Oscurato
Centro Servizi Metrologici e tecnologici Avanzati (CeSMA)
University of Naples "Federico II"
Complesso Universitario di Monte Sant'Angelo
Via Cintia, Naples 80126, Italy

M. Astarita
Department of Physics
Politecnico di Milano
Piazza Leonardo da Vinci
Milan 20133, Italy

F. Borbone
Department of Chemical Sciences
University of Naples "Federico II"
Complesso Universitario di Monte Sant'Angelo
Via Cintia, Naples 80126, Italy

are involved, which further affects the fabrication cost and its scalability.[18,19] In any case, all the standard lithographic processes produce intrinsically static surface geometries. Today, liquid crystal technology[25–27] is the only alternative when a fully reprogrammable optical device is required, with well-known limitations related to electronics and miniaturization problems.

To overcome these limitations, the active research field of dynamical metasurfaces[28,29] is exploring reusable templates,[30] deformable substrates,[31,32] or active electrical tuning.[33] However, large-area scalability, limited tunability, and low efficiency in the visible range are still challenges to be, respectively, solved. On the other hand, reprogrammable planar DOEs would require a complete remorphing of the surface device, which is not feasible with any existing material or method. As a result, fully reprogrammable planar devices operating in the visible range, fabricated with scalable and sustainable solutions, are still lacking.

Here, we demonstrate the direct all-optical maskless fabrication of fully reconfigurable diffractive holograms, implemented as structured transmissive phase retarders in a dielectric material. A digital maskless optical scheme is used to generate and project a grayscale spatially structured intensity distribution of light onto an azobenzene-containing polymer film, whose surface is locally deformed according to the irradiated spatial light distribution. This photomechanical process allows the direct fabrication of the desired device without any additional lithographic step and opens the possibility of optically reprogramming the fabricated surface geometry at will. Our innovative approach fully exploits the possibility of arbitrary spatio-temporal modulation of the writing beam in a maskless lithographic system, seamlessly integrated with a real-time optical characterization setup. This combination allows surface geometry to be analyzed and optimized during the fabrication, resulting in unprecedented control over the final diffractive devices. Reprogrammable grayscale holograms with enhanced visibility, tunable axial position, and optical encryption capabilities are then demonstrated. This framework can support the development of the next generation of photonics devices, from prototyping, testing, and assembly to their large-scale distribution.

2. Experimental Results

2.1. Direct Azo-Resist Surface Structuration

The core of our technique is the use of an azobenzene-containing polymer film (hereafter referred to as azo-resist) as a lithographic photosensitive material. Due to their unconventional sensitivity to both the intensity and the polarization of the irradiated light, azopolymers have been exploited as promising materials for surface photopatterning under several illumination configurations. Interference-based patterning,[34–36] achieved from two or more interfering beams across the azopolymer surface, is the most common configuration. However, the achievable surface geometries are limited to sinusoidal or periodic profiles. Recently, the use of spatial light modulators to locally modulate the inscribing light,[37–39] has allowed to overcome this limitation, but surface geometries with simultaneous control of complex lateral patterns and high modulation depths were still lacking.

The direct all-optical maskless surface patterning scheme used in this work is shown in **Figure 1**. We used a computer-generated

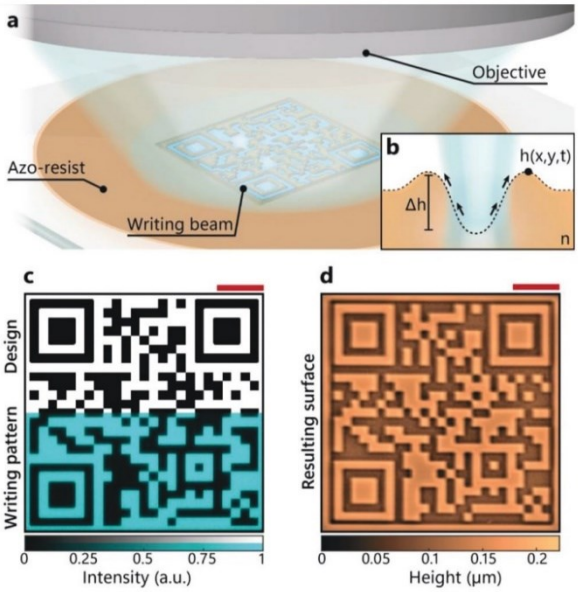

Figure 1. Holographic structuration of the azo-resist surface. a) Graphical representation of the holographic inscription scheme. Writing beam, with arbitrary shaped intensity profile, is directly projected over the azo-resist surface by an objective. b) Schematization of the light induced mass migration occurring at surface of amorphous azopolymer films under structured illumination absorption. c) Design and reconstruction of a writing pattern with the geometry of a QR code. The experimental intensity pattern is the result of a holographic sequence time averaging. d) AFM micrograph of the structured surface collected right after the light exposure. Red scale bars, in panels (c,d), corresponds to a physical size of 20 μm on the sample.

hologram (CGH) system, based on a phase-only spatial light modulator (SLM), to generate and project circularly polarized grayscale intensity patterns over the azo-resist surface. More details about the lithographic setup can be found in Figures S1–S3 (Supporting Information). As shown schematically in Figure 1b, under UV–vis irradiation, the azo-resist flows from the high-intensity region to the dark areas and directly forms a surface relief pattern $h(x, y, t)$ that replicates the lateral geometry of the illumination intensity.[40] Under our illumination conditions, the relief depth Δh is approximately proportional to the exposure time.[41]

We propose a two-level QR code as target binary surface geometry (Figure 1c) to demonstrate the direct azo-resist surface photopatterning capability in a single exposure step. In the experiment shown in Figure 1, the spatially structured intensity pattern was irradiated at the typical average light intensity of 14.0 W cm^{-2} for $t = 20$ s on the azo-resist. Figure 1d shows the atomic force microscope (AFM) micrograph of the azo-resist surface taken immediately after the exposure. The AFM data, rendered as a 2D image with a linear colormap, confirms the correct pattern transfer on the surface, which faithfully reproduces the (complementary) target geometry. To extend the visual comparison to a quantitative morphological analysis, we characterized possible local mismatch errors (Figure S4, Supporting Information) by comparing the target and the experimental surface height distributions. We

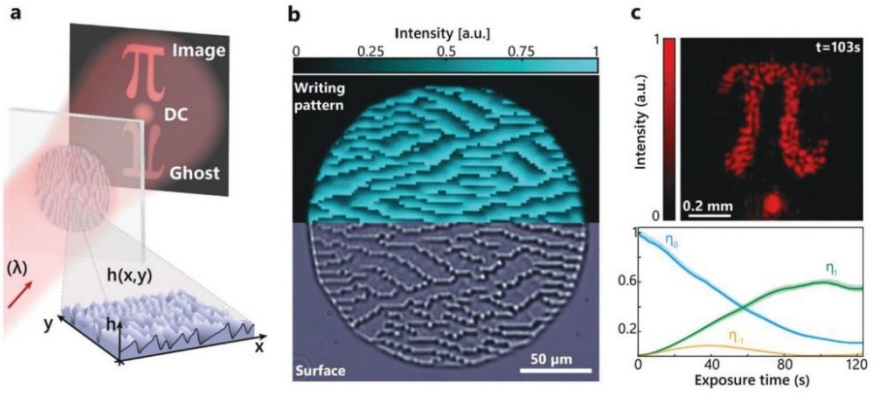

Figure 2. Design, fabrication, and optimization of azopolymer holographic projectors implemented as kinoforms. a) Design of a dielectric phase retarder (kinoform), producing an arbitrary far-field diffraction pattern. Wavefront modulation for monochromatic wave depends on the local surface thickness $h(x, y)$. b) Grayscale light pattern reproducing the kinoform design and the resulting SEM image of the structured surface after the exposure. c) Diffraction pattern acquired at the optimal exposure time which maximizes the diffracted light power in the target holographic image. The experimental trends of the diffraction efficiency, reconstructed in each holographic term, are measured during the inscription process. Trends are the results of five independent exposures: the average value for the experimental diffraction efficiency at each exposure time is represented by a solid line. The shadow represents the punctual standard deviation.

report a root mean square error (RMSE) of 22 nm. This mismatch, equal to 10% of the measured Δh, is the result of relief smoothing that occurs where sharp contrast jumps are present in the illumination pattern, according to the azo-resist response to structured incident light (see also the Experimental Section). However, as further detailed below, the all-optical scheme used here for the fabrication and the simultaneous characterization of diffractive optical components allows to minimize these effects on their optical performances while maintaining a much simpler design scheme. The results in Figure 1 fully summarize the potential of our direct maskless holographic technique for the microscale surfaces patterning. This task is crucial for the fabrication of a diffractive phase-modulating mask acting as a holographic projector.

2.2. Holographic Projectors: Design, Optimization, and Fabrication

According to the scalar diffraction theory,[26] a planar diffractive holographic projector can be designed as a surface relief pattern $h(x, y)$ in a dielectric material. The wavefront shaping results from differences in the optical path traveled by the incoming wave in the locally varying material thickness. The resulting far-field from this phase-modulating planar device, usually referred to as a kinoform,[42] is the 2D spatial Fourier transform of the modulation function. For any given far-field target holographic image (corresponding to the diffracted far-field intensity distribution), the surface pattern of the kinoform can generally be retrieved by iterative Fourier transform algorithms (IFTAs).[8]

Figure 2 shows the design and fabrication process for the case of a holographic projector reconstructing the image of the Greek letter "π." In this case, the conventional Gerchberg–Saxton algorithm[43] (GSA) was used to retrieve the kinoform (see also Figure S5, Supporting Information). It should be noted that once the kinoform has been calculated, all the challenges associated with high quality hologram reconstruction are shifted to the manufacturing level. Any defect arising in the lithographic process will degrade the quality of the hologram, leading to a decrease in the diffraction efficiency and the appearance of spurious contributions (DC and ghosts) in the image.[44] They may even overlap in the reconstruction plane, requiring an off-axis design for the hologram (Figure 2a), which reduces the available target domain by half.[45] Even in the case of a defect-free lateral pattern transfer in the modulating surface, a deviation from a full 2π phase modulation depth still causes the appearance of the spurious holographic terms and the decrease in efficiency. To avoid this effect, an optimal relief depth of $\Delta h = \lambda/(n(\lambda) - 1)$ should be realized for an ideal surface kinoform made of a material of refractive index $n(\lambda)$ at the operating wavelength λ, immersed in air.

In our direct lithographic scheme, the lateral surface relief pattern and the relief depth can be controlled independently by the digital illumination design and by exposure time, respectively. As a first step, we generalized the inscription scheme to project grayscale light patterns, encoding multiple discrete intensity levels of light in a single illumination step (see also Figure S6, Supporting Information). We then directly inscribed the azo-resist surface with the grayscale surface profile corresponding to the required kinoform (Figure 2b). To analyze the lateral pattern and determine the total height excursion, we performed SEM and AFM analysis of the patterned azo-resist surface after the exposure process. The SEM analysis confirms a correct lateral geometry transfer. To quantitatively evaluate the quality of the fabricated surface kinoform, we retrieved the height profile $h(x, y)$ from the AFM analysis. From the height distributions obtained with fixed illumination parameters at different exposure times, we determined the total modulation depth $\Delta h(t)$. Under our experimental conditions, a total exposure time of $t = 86\ s$ is sufficient to obtain the optimal 2π modulation depth in the kinoform for the probe light at $\lambda_p = 632.8$ nm, with $n(\lambda_p) = 1.70$.[37] Faster relief formation dynamics could be achieved at higher irradiation intensities.

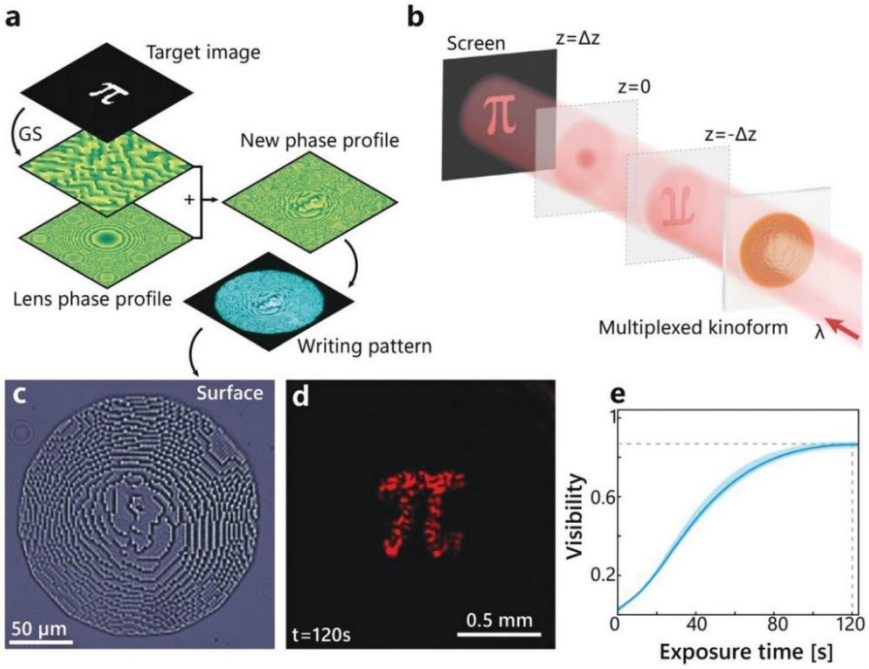

Figure 3. Design, fabrication, and optimization of multiplexed kinoforms. a) Process of kinoform multiplexing and the subsequent encoding into the writing pattern. b) Representation of the diffractive behavior of a multiplexed kinoform. When illuminated with monochromatic coherent light, different diffractive orders are reconstructed on axially shifted planes. c) SEM image of the azo-resist surface after the exposure to the writing beam for the optimized exposure time. d) Diffraction pattern acquired at $z = \Delta z$. e) Experimental trend of the pattern visibility reconstructed during the inscription process as result of five independent exposures. The average value for the pattern visibility at each exposure time is represented by a solid line. The shadow represents the punctual standard deviation.

Further details of the AFM analysis are shown in Figures S7–S9 (Supporting Information).

However, this off-line structural characterization roadmap would be required for each different relief geometry and illumination parameters, resulting in a time-consuming optimization workflow that would eventually have to be repeated for each new hologram. Although various techniques based on mechanical[46] and optical[35] real-time topographic investigation of the developing azo-resist have been successfully proposed, the direct evaluation of the optimal writing parameters can also be performed directly by observing the generated diffraction pattern.[37,47] For this purpose, simultaneously with the optical lithographic process that produces the surface kinoform, the azo-resist film is illuminated with an additional laser beam at the probe wavelength λ_p. The developing diffraction pattern is continuously recorded with a CCD, providing the relative diffraction efficiencies η_i in the target holographic image and in the spurious terms in real time (Figure 2c; and Figure S10, Supporting Information). The optimal exposure time ($t_0 = 103 \pm 1$ s) was chosen to maximize the light power diffracted in the target holographic image. Under this condition, an experimental efficiency of $\eta_{+1} = 0.60 \pm 0.02$ was obtained. We also observed a relative transmittance $|t(x, y)|^2 = 0.96$ for the diffraction hologram generated by the surface with optimized exposure time (see also Figure S11, Supporting Information), also demonstrating a minimal influence of possible light scattering sources generated by the lithographic process.

Furthermore, for the final operating kinoform, we determined an addressable field of view for far-field image projection up to $\approx 40°$ (see also Figure S12, Supporting Information), directly related to the minimum lateral size of surface features (Figure S7, Supporting Information).

An additional advantage of phase-only modulating masks is the ability to encode multiple optical functionalities in the same device. Multiplexed kinoforms can be designed by combining the initial phase profile with additional phase functions. A relevant example is the superposition of the kinoform with the phase profile of a thin lens of focal length f. The multiplexed effect is an axial shift of the target holographic image with respect to the ghost and DC orders[26] generated by the original kinoform. With this design, the target image can therefore be isolated in a specific (and possibly tunable) plane (**Figure 3**a,b). High image visibility can be achieved in the entire target domain, without the need for a physical filtering aperture to remove the spurious terms (required by the off-axis design). Figure 3c shows a SEM image of the surface relief pattern inscribed on the azo-resist surface using the lens multiplexed kinoform design. The corresponding diffraction pattern recorded in the target reconstruction plane is shown in Figure 3d. In this plane, only the target image is clearly visible, while the blurred DC and ghost terms contribute with negligible background. We used the image visibility $\mathcal{V}$ (see also Figure S13, Supporting Information) as a quality estimator for the holographic image (Figure 3e). The real-time analysis of this

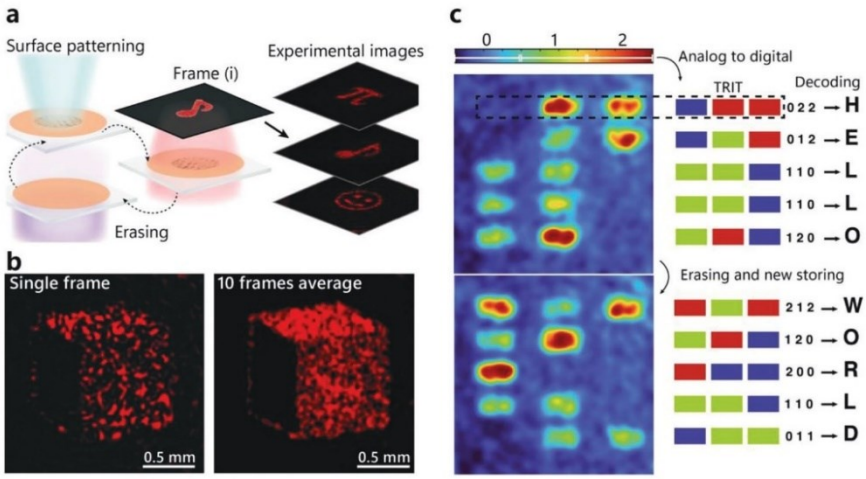

Figure 4. Fully reprogrammable kinoform for image quality improvement and data storing and sharing. a) Demonstration of a reprogrammable holographic projector. After surface pattering and holographic image acquisition, azo-resist morphology can be completely restored to the pristine flat state, enabling a new patterning step. Quality enhancement in experimental images is the result of time average of sequentially generated holographic patterns. b) Grayscale enhanced image quality arising from time averaging of speckle noise. The three intensity levels of the holographic image are clearly visible in ten frames average. c) Experimental results of the holographic data storing and sharing with reprogrammable kinoforms. Holographic patterns are plotted with a rainbow colormap, highlighting the three possible intensity levels associated with three digital logic states, encoded by the alphabet.

parameter allowed the direct optimization of the exposure time $t_0 = 120 \pm 1$ s and the multiplexed phase design to obtain a maximum visibility of $= 0.83 \pm 0.03$.

2.3. Reprogrammable Holograms

A requirement for versatile photonics applications is that the morphology of the light-modulating planar device should be fully reversible and repeatedly reprogrammable on demand. The azo-resist photopatterning inherently provides this unique feature. When illuminated with unstructured light in the absorption band, the pristine flat surface of the azo-resist film can be restored at will, allowing multiple and reversible patterning cycles.[37] **Figure 4**a schematically shows our all-optical reprogrammable surface patterning process for creating dynamically evolving holographic images. As an additional application of the reprogrammable surface photomorphing, we repeatedly inscribed kinoforms to produce a time-averaged holographic diffracted image with a reduced speckle noise (see also Figure S14, Supporting Information). Such noise is intrinsic to any IFTA kinoform design[26] and is not caused by eventual defects in the surface pattern. In the experiment, the image of the optimized (in terms of visibility $\mathcal{V}$) hologram obtained from a first azo-resist inscription process was collected and stored as a single frame of a holographic projection movie. Then, the surface was completely (optically) erased, and the same area of the azo-resist was exposed to a new writing pattern with the same global geometry but producing a different random distribution of speckle grains. After $N = 10$ writing/erasing steps, the time-averaged holographic image was calculated from the frames taken at the end of each writing step. As expected, the averaged image is characterized by a speckle severity[39] reduced by a factor of $1/\sqrt{N}$ (see also Figure S15, Supporting Information). The artificial image improvement obtained by such a time-averaging process is the same as that performed by an ideal slow "eye" or detector, with a time response slower than the typical surface reconfiguration time ($\approx 120\ s$). Extending this scheme, we show speckle noise filtering for a three-level target holographic image, as a simple example of grayscale holographic images. Figure 4b shows the diffraction pattern and the corresponding time-averaged holographic pattern representing the image of a cube, where each of the three displayed faces encodes a different diffracted intensity level. The grayscale nature of the hologram became visually clearer after speckle averaging (Figure S16, Supporting Information), significantly improving the single holographic image.

Further exploiting our ability to precisely structure surfaces, we designed a morphological reprogrammable device capable of encoding and storing encrypted information in the form of dynamic grayscale holographic images. To this end, we used nonbinary bits of light intensity levels to increase the information storage capacity. For a simple proof-of-principle, kinoforms inscribed in the azo-resist encode information in the form of a reprogrammable complex surface topography. For the experiment, a simple secreted message, "HELLO-WORLD," was converted into a ternary intensity level alphabet. Each letter was codified as a series of three trits (ternary digits) arranged in a row. The entire message was assembled into two grayscale images, which were then used as the target for kinoform calculation via IFTA. Further details of this encryption process are discussed in Figure S17 (Supporting Information). Figure 4c shows the two grayscale holographic images, sequentially reconstructed by reprogramming the kinoform inscribed on the azo-resist surface. The hidden message was correctly retrieved by measuring the light intensity in each trit and by using the cryptographic key (the ternary alphabet lookup table in Figure S17, Supporting Information). In

this example, the time-splitting of the information in two dynamically remorphing surfaces provided enhanced encryption capabilities and security of information sharing. Fourier-transform coding also offers the advantage that if part of the surface were to be damaged or destroyed, it would theoretically still be possible to read the hidden holographic information from the remaining parts of the surface. We also estimated a simultaneous encoding of 3125 bytes of information in each kinoform for our simple design.

3. Conclusions

In this work, we first demonstrated the accurate all-optical transfer of complex 2D geometries with a binary relief depth on the surface of azobenzene-containing polymer films. Although it does not represent the highest degree of complexity achievable with the proposed maskless holo-lithographic scheme, such a simple design can already be interpreted as a form of storage of digital information encoded in microstructured surfaces, using the induced azo-resist morphology can as a memory support. This possibility suggests promising alternative strategies for the use of azomaterials in optical data storage.

As an additional milestone, we have extended the holo-lithographic technique to the realization of diffractive kinoforms, where complex lateral geometries and grayscale modulation depth are required simultaneously. The characterization of the diffractive properties during the fabrication process allows a cost-effective design and prototyping of planar optical components. This leads to a fully functional and tested device immediately after the fabrication, without requiring further time-consuming surface analysis or preliminary calibration procedures. This approach enabled the fabrication of fully operational pixel-free morphological holographic projectors with turnaround times of a few minutes, resulting in highly efficient ultracompact devices with performance levels comparable to the state-of-the-art in planar optics.[5,6]

Since the azopolymer surface can be optically restored to the flat pristine state in situ, multiple write/erase cycles can be performed. This possibility allowed to improve the quality in the holographic images by time averaging, paving the way for the fabrication of morphological reshapable devices capable of encoding optical information with both morphological and temporal encryption.

Although being still far from the refresh rates achievable with other dynamical light modulators, such as commercial liquid crystal (LC) SLMs, our results demonstrate real dynamical modulation capabilities in an operational and fully reprogrammable holographic system based on a diffractive planar optical device. When compared to current LC panels, which have intrinsic limitations related to pixel size miniaturization, manufacturing complexity, voltage requirements, and crosstalk and light leakage effects, the morphological holographic projectors shown here have higher spatial resolution, higher pixel density, reduced thickness, and higher modulation efficiency. Future strategies to improve reconfiguration times may include the optimization of the azo-resist molecular design to enable faster photomechanical response and increased number of write/erase cycles.

The proposed hololithographic approach is also suitable to address different challenges in the realm of surface microstructuring, exploiting the versatility of the grayscale maskless direct patterning and the absence of additional development steps. For example, high resolution features can be obtained on the azo-resist surface by equipping the holographic writing setup with high resolution modulators and optical elements with higher numerical apertures. Larger areas can be accessed by parallel laser writing, high field of view optics and/or raster scans. In addition, our technique is fully compatible with prototyping and development of templates for imprint lithography,[36,48] opening the doors to cheaper and faster fabrication of functionalized surfaces.

In conclusion, in this work we have demonstrated that azobenzene materials, when illuminated with digitally reconstructed intensity patterns of light, can be used as a platform for the fabricating reprogrammable planar photonic devices with multiple applications. Although still at a preliminary level, our technique offers a promising route to the fabrication of flat optics with potential applications in emerging technologies such as VR\AR displays, wearable devices, and reversible high-density memory substrates.

4. Experimental Section

Experimental Setup: The experimental configuration for the azopolymer surface relief inscription is represented in Figure S1 (Supporting Information). A laser diode source (Cobolt Calypso) produces a TEM_{00} beam at wavelength $\lambda = 491$ nm which, after a beam expander, is phase-modulated by a computer-controlled reflective phase-only SLM (Holoeye Pluto). The modulated beam is propagated through a 4*f* lenses system with the input plane located in the SLM plane. The output plane coincides with the back focal plane of an infinity-corrected long-working distance 50X objective (Mitutoyo), with numerical aperture $NA = 0.55$. The focal lengths of the lenses are chosen to maximize the spatial resolution in the hologram reconstruction plane. This choice also defines the addressable area of ≈ 200 µm in diameter in the objective front focal plane, which can be used to structure the azopolymer surface in a single illumination step. The position of the sample near the objective focal region is accurately controlled by means of a x-y-z translation stage. Average intensity in the range $12.7 - 14.0$ W cm^{-2} and circular polarization are used for the structuration of the azopolymer surface. To reduce the speckle noise contrast effects, the holographic illumination over the azopolymer surface is the result of the time average of 1000 holographic patterns generated from different kinoforms, with independent design.[39] The mixed region amplitude freedom (MRAF) algorithm was used,[49] implemented in MATLAB, using the fast Fourier transform (FFT) algorithm. The SLM refresh time is set to 30 Hz, faster than the azopolymer time response. For visual inspection, and proper focusing of the holographic pattern on the photoresponsive surface, a 70/30 beam splitter, placed in the light-path, redirects the light retroreflected by the surface and recollimated through the objective toward a tube lens. This lens forms an image of the holographic pattern in its second focal plane, where a "DCC3240M Thorlabs" CCD camera is positioned. During the exposure, an additional diode laser beam at 405 nm illuminates the photoresist film from the substrate side. The beam has circular polarization and different intensity levels depending on its intended function. When the intensity is 0.6 W cm^{-2}, the beam favors the surface structuring process, acting as a writing assisting beam. At intensity higher than 0.9 W cm^{-2}, its absorption causes the erasure of previously inscribed surface structures, acting as an erasing beam. Azo-resist reconfiguration can be performed with no significant material degradation for 20 times.[37] Further characterizations about assisting/erasing beam are described in a previous work.[37] An additional He—Ne laser beam, at 632.8 nm, is used as sample back-illumination source to test diffraction behavior of the modulated surface during the structuration process. The beam splitter also allows the collection of part of this light without interfering with the writing

process. The image of the surface is projected on the back focal plane of the tube lens and coupled by means of a mirror (mounted on a flip mount) to an additional 2*f* system. Fourier transform image is captured with an additional CCD camera at a repetition rate of 5 Hz.

Azo-Resist Synthesis and Film Preparation: The azo-resist used in this work is an azobenzene-containing polymer (azopolymer) in amorphous state. All reagents were purchased from Merck and used without further purification. The azopolymer was synthesized, purified, and characterized as previously reported (M_w = 27 000; phase sequence: Glass 67 °C Nematic 113 °C Isotropic; λmax = 350 nm).[41] The solution for film deposition was prepared by dissolving 70 mg of the polymer in 0.50 mL of 1,1,2,2-tetrachloroethane and filtered on 0.2 µm PTFE membrane filters. The desired film thickness (1.8 ± 0.1 µm) was obtained by spin coating the solution on 24*x*60 mm cover slides at 300 rpm for 4 min. In the final stage, the samples were kept under vacuum at room temperature for 24 h to remove solvent traces. Molecular structural formula and the absorbance in the UV–visible are provided in Figure S3 (Supporting Information).

Azo-resist response to intensity structured light: When irradiated with a circularly polarized light patten I_W (x,y) in a low-focusing regime, the spatiotemporal evolution of the azo-resist surface morphology $h(x, y, t)$ can be phenomenologically described as[41]

$$h(x, y, t) = \nabla^2 [I_W(x, y)] \cdot \Delta h(t) \quad (1)$$

where ∇^2 denotes the Laplacian of the light intensity pattern at the azo-resist surface. For sufficiently low intensity ($\leq$ 100 W cm^{-2}), the relief depth increases approximately linearly with the exposure time, $\Delta h(t) = c \cdot t$. Here $c > 0$ is a phenomenological parameter. The nonlinear response of the azo-resist is the origin of structural mismatches observed in the experiments, causing the relief smoothing occurring at the positions where sharp contrast jumps are present in the illumination pattern. Although this issue might be circumvented by limiting quantitative pattern designs to sequences of smooth sinusoidal surfaces,[36,37,50] sharp features could in principle still be encoded if a suitable optimized holographic pattern is designed by reversing the above equation rather than approximate the process as a simple linear pattern transfer as done for the patterns presented in the work.

Morphological Characterization of Structured Surfaces: Topographic characterization of inscribed azopolymer surface reliefs was performed using AFM and SEM. For AFM measurements, a WITec Alpha RS300 microscope was used. The AFM was operated in tapping mode using a cantilever with 75 kHz resonance frequency and nominal force constant of 2.8 N m^{-1}. AFM tips (Arrow FM type from Nano World), with nominal radius of curvature of ≈ 10 nm, were used. The maximum scanned area has a size of 100 × 100 µm^2. For each AFM the minimum of the topography was set to zero to extract the height distribution P_j, representing the probability to find a pixel in the image with a height value between h_j and h_{j+1}. Here j ranges from zero to $N - 1$ where N is the number of occupied bins in each image, while bin width is set to 10 nm. Each height distribution is normalized to match the condition $\sum_N P_j = 1$. To retrieve an estimation of the modulation depth Δh the full dispersion range of each distribution was considered. SEM images are acquired with a field emission gun (FEG–SEM) FEI/ThermoFisher Nova NanoSEM 450 microscope. Samples are sputtered with a layer of Au/Pd using a Denton Vacuum Desk V TSC coating system prior to observation.

Supporting Information

Supporting Information is available from the Wiley Online Library or from the author.

Conflict of Interest

The authors declare no conflict of interest.

Data Availability Statement

The data that support the findings of this study are available from the corresponding author upon reasonable request.

Keywords

azobenzene photopatterning, computer-generated holography, maskless lithography, planar photonics, reprogrammable holograms

Received: April 5, 2023
Revised: June 16, 2023
Published online: July 19, 2023

[1] W. T. Chen, F. Capasso, *Appl. Phys. Lett.* **2021**, *118*, 100503.
[2] A. Karabchevsky, A. Katiyi, A. S. Ang, A. Hazan, *Nanophotonics* **2020**, *9*, 3733.
[3] L. Xu, M. Rahmani, *Light: Sci. Appl.* **2022**, *11*, 196.
[4] A. Peter Amalathas, M. Alkaisi, *Micromachines* **2019**, *10*, 619.
[5] P. Georgi, Q. Wei, B. Sain, C. Schlickriede, Y. Wang, L. Huang, T. Zentgraf, *Sci. Adv.* **2021**, *7*, eabf9718.
[6] G. Qu, W. Yang, Q. Song, Y. Liu, C.-W. Qiu, J. Han, D.-P. Tsai, S. Xiao, *Nat. Commun.* **2020**, *11*, 5484.
[7] Z. He, X. Sui, G. Jin, L. Cao, *Appl. Opt.* **2019**, *58*, A74.
[8] K. Matsushima, *Introduction to Computer Holography: Creating Computer-Generated Holograms as the Ultimate 3D Image*, Springer, Cham, Switzerland **2020**.
[9] C. Chang, K. Bang, G. Wetzstein, B. Lee, L. Gao, *Optica* **2020**, *7*, 1563.
[10] B. C. Kress, I. Chatterjee, *Nanophotonics* **2021**, *10*, 41.
[11] D. C. O'Shea, T. J. Suleski, A. D. Kathman, D. W. Prather, *Diffractive Optics: Design, Fabrication, and Test*, SPIE Press, Washington, DC **2004**.
[12] B. C. Kress, P. Meyrueis, *Applied Digital Optics: From Micro-Optics to Nanophotonics*, Wiley, Chichester **2009**.
[13] H. Wang, Y. Liu, Q. Ruan, H. Liu, R. J. H. Ng, Y. S. Tan, H. Wang, Y. Li, C. Qiu, J. K. W. Yang, *Adv. Opt. Mater.* **2019**, *7*, 1900068.
[14] Q. Jiang, G. Jin, L. Cao, *Adv. Opt. Photon.* **2019**, *11*, 518.
[15] G. Lee, J. Sung, B. Lee, *ETRI J.* **2019**, *41*, 10.
[16] Y. Hu, X. Luo, Y. Chen, Q. Liu, X. Li, Y. Wang, N. Liu, H. Duan, *Light: Sci. Appl.* **2019**, *8*, 86.
[17] P. van Assenbergh, E. Meinders, J. Geraedts, D. Dodou, *Small* **2018**, *14*, 1703401.
[18] J. A. Liddle, G. M. Gallatin, *Nanoscale* **2011**, *3*, 2679.
[19] E. Sharma, R. Rathi, J. Misharwal, B. Sinhmar, S. Kumari, J. Dalal, A. Kumar, *Nanomaterials* **2022**, *12*, 2754.
[20] D. K. Oh, T. Lee, B. Ko, T. Badloe, J. G. Ok, J. Rho, *Front. Optoelectron.* **2021**, *14*, 229.
[21] K. Jain, T. J. Dunn, J. M. Hoffman, *US Patent 6,312,134*, **2001**.
[22] H.-L. Chien, Y.-H. Chiu, Y.-C. Lee, *Opt. LasersEng.* **2021**, *136*, 106313.
[23] M. S. Khan, R. lachmayer, B. Roth, *OSA Continuum.* **2020**, *3*, 2808.
[24] N. Lassaline, R. Brechbühler, S. J. W. Vonk, K. Ridderbeek, M. Spieser, S. Bisig, B. le Feber, F. T. Rabouw, D. J. Norris, *Nature* **2020**, *582*, 506.
[25] C. Slinger, C. Cameron, M. Stanley, *Computer* **2005**, *38*, 46.
[26] J. W. Goodman, *Introduction to Fourier Optics*, Roberts And Company Publishers, Englewood, CO **2005**.
[27] D. Pi, J. Liu, Y. Wang, *Light: Sci. Appl.* **2022**, *11*, 231.
[28] J. Yang, S. Gurung, S. Bej, P. Ni, H. W. Howard Lee, *Rep. Prog. Phys.* **2022**, *85*, 036101.
[29] K. Du, H. Barkaoui, X. Zhang, L. Jin, Q. Song, S. Xiao, *Nanophotonics* **2022**, *11*, 1761.

[30] J. Li, P. Yu, S. Zhang, N. Liu, *Nano Lett.* **2020**, *20*, 6845.
[31] E. Arbabi, A. Arbabi, S. M. Kamali, Y. Horie, M. Faraji-Dana, A. Faraon, *Nat. Commun.* **2018**, *9*, 812.
[32] S. C. Malek, H.-S. Ee, R. Agarwal, *Nano Lett.* **2017**, *17*, 3641.
[33] P. Thureja, R. Sokhoyan, C. U. Hail, J. Sisler, M. Foley, M. Y. Grajower, H. A. Atwater, *Nanophotonics* **2022**, *11*, 3745.
[34] Y. Lim, B. Kang, S. Lee, *Adv. Funct. Mater.* **2021**, *31*, 2100839.
[35] H. Rekola, A. Berdin, C. Fedele, M. Virkki, A. Priimagi, *Sci. Rep.* **2020**, *10*, 19642.
[36] S. L. Oscurato, F. Reda, M. Salvatore, F. Borbone, P. Maddalena, A. Ambrosio, *Adv. Mater. Interfaces* **2021**, *8*, 2101375.
[37] S. L. Oscurato, F. Reda, M. Salvatore, F. Borbone, P. Maddalena, A. Ambrosio, *Laser Photonics Rev.* **2022**, *16*, 2100514.
[38] J. Strobelt, M. Van Soelen, H. Abourahma, D. J. McGee, *Adv. Opt. Mater.* **2023**, *11*, 2202245.
[39] S. L. Oscurato, M. Salvatore, F. Borbone, P. Maddalena, A. Ambrosio, *Sci. Rep.* **2019**, *9*, 6775.
[40] S. L. Oscurato, M. Salvatore, P. Maddalena, A. Ambrosio, *Nanophotonics* **2018**, *7*, 1387.
[41] A. Ambrosio, L. Marrucci, F. Borbone, A. Roviello, P. Maddalena, *Nat. Commun.* **2012**, *3*, 989.
[42] L. B. Lesem, P. M. Hirsch, J. A. Jordan, *IBM J. Res. Dev.* **1969**, *13*, 150.
[43] R. W. Gerchberg, *Optik* **1972**, *35*, 237.
[44] I. Moreno, J. Campos, C. Gorecki, M. J. Y. M. J. Yzuel, *Jpn. J. Appl. Phys.* **1995**, *34*, 6423.
[45] T.-C. Poon, *Digital Holography and Three-Dimensional Display: Principles and Applications*, Springer, New York **2006**.
[46] J. Jelken, C. Henkel, S. Santer, *Appl. Phys. B* **2019**, *125*, 218.
[47] F. Reda, M. Salvatore, F. Borbone, P. Maddalena, S. L. Oscurato, *ACS Mater. Lett.* **2022**, *4*, 953.
[48] B. Yang, M. Yu, H. Yu, *ChemPlusChem* **2020**, *85*, 2166.
[49] M. Pasienski, B. DeMarco, *Opt. Express* **2008**, *16*, 2176.
[50] F. Reda, M. Salvatore, F. Borbone, P. Maddalena, A. Ambrosio, S. L. Oscurato, *Opt. Express* **2022**, *30*, 12695.

ADVANCED OPTICAL MATERIALS

Supporting Information

for *Adv. Optical Mater.*, DOI 10.1002/adom.202300823

Reprogrammable Holograms from Maskless Surface Photomorphing

*Francesco Reda, Marcella Salvatore, Marco Astarita, Fabio Borbone and Stefano L. Oscurato**

Supporting Information

Reprogrammable holograms from maskless surface photo-morphing

*Francesco Reda, Marcella Salvatore, Marco Astarita, Fabio Borbone and Stefano L. Oscurato**

Supplementary materials include:

- Supplementary Text
- Figure S1 to S17
- Captions for movies S1 to S3
- Movies S1 to S3

Supplementary Text

Diffraction properties of holographic morphological projectors.

Phase-only holographic plates, named kinoforms, are typically represented by a complex transmission function $t(x,y)$ describing in the scalar approximation of wave optics, the wavefront phase modulation of an incident monochromatic optical field, at wavelength λ passing through the device. Isotropic dielectric phase retarders implement phase modulation as result of local variations in thickness $h(x,y)$ and refractive index $n(x,y,\lambda)$ of the device, whereby the planar modulation function can be written as:

$$t(x,y) = \exp[i\varphi(x,y)] = \exp\left[i\frac{2\pi}{\lambda}(n(x,y,\lambda) - n_s)h(x,y)\right]$$

representing the local phase delay $\varphi(x,y)$ accumulated by the light due to optical path variation imposed by the plate immersed in a surrounding material whose refractive index is n_s. When a kinoform, supposed to be at $z = 0$, is illuminated by the coherent monochromatic light field $U_{in}(x,y,0)$, the resulting complex field $U_{out}(x,y,z)$ formed due to Fraunhofer ($z \gg 0$) diffraction is the two-dimensional spatial Fourier transform of the modulated beam at the kinoform plane. The reconstructed image $I_{out}(x,y,z)$ is determined by the relation[26]:

$$I_{out}(x,y,z) = |FT[U_{in}(x,y,0) \cdot t(x,y,0)]|^2$$

Where *FT* denotes the Fourier Transform operator. The phase encoding process, from the phase design to its implementation by lithography, leads to a device whose real transmittance is a function of the designed phase $t^{real}(x,y) = e^{ig[\varphi(x,y)]}$. To consider any possible deviation from this ideal case, the complex transmittance of the real kinoform can be decomposed into a linear superposition of functions, clearly describing the effects of phase mismatches. Assuming that the deformation is space invariant, the spatial coordinates can be

omitted and the function $t^{real}(x,y)$ can be expanded in terms of its argument, according to the generalized harmonic analysis[45]:

$$t^{real} = \sum_{\alpha=-\infty}^{+\infty} G_\alpha e^{i\alpha\varphi}$$

where $G_\alpha = \int_0^{2\pi} t^{real} e^{i\alpha\varphi}\, d\varphi$ with α an integer index. The $\alpha = +1$ term is the only one whose Fourier transform results in an optical field with intensity $I_{out}(x,y,z)$. The amount of optical power shaped in the reconstructed intensity profile with respect to the total transmitted power, is equal to $\eta_1 = |G_1|^2$ and it is one only in the ideal case $g(\varphi) = \varphi$. The other terms of the series, apart from the term $\alpha = 0$ which determines an unmodulated optical component named DC term, contribute with shifted and scaled replicas of the desired intensity pattern, known as ghosts or false images. The total reconstructed pattern is a weighted sum of the desired image, the DC term, and false images, typically also spatially overlapped in the reconstruction plane and with a relative efficiency $\eta_\alpha = |G_\alpha|^2$. At best, once the geometry $h(x,y)$ is fixed, g is linear with the total surface reliefs amplitude Δh, which must be tuned to reach a fully 2π modulation depth. This condition is achieved for $\Delta h = \lambda/(n(\lambda) - n_S)$. For our material at the operating probe wavelength $\lambda = 0.6328\ \mu m$, $n(\lambda) = 1.696$ and $n_S = 1$ (air immersed kinoforms), the condition is satisfied for $\Delta h_0 = 0.9092\ \mu m$. The diffraction efficiency η_α in this case, introducing the parameter $m = \Delta h/\Delta h_0$ denoting a quantitative estimation of the real/ideal mismatch, can be written as[44]:

$$\eta_\alpha = sinc^2(m - \alpha)$$

The requirement $m = 1$ guarantees the maximum diffraction efficiency ($\eta_{+1} = 1$), ensuring that all the incident optical power is effectively shaped in the reconstructed holographic pattern, Figure S5. During the encoding process, more complex distortion effects can determine a non-linear form for g. These certainly include quantization and pixelation effects and non-linear responses of the material to the structuring process that results in additional phase mismatches, causing efficiency losses ($\eta_{+1} < 1$) even if target modulation depth is reached.

In this case a multiplexed design of the kinoform can guarantee high quality for the holographic image enabling the axial filtering of ghost holograms. The target kinoform $\varphi(x,y)$ is simply obtained by adding the phase profile of a thin lens:

$$\varphi_L\,(x,y) = \left(\frac{\pi}{\lambda_p\, f}\right) \cdot (x^2 + y^2)$$

to the original kinoform, renormalizing then the result to modulo 2π. As described by the generalized Fourier analysis for the light propagation after the multiplexed modulating device, each diffraction order is shifted along the optical axis and reconstructed in a different plane located at $z = i \cdot \Delta z$, where $z = 0$ denotes the reconstruction plane of the original kinoform alone. As the distance Δz between the reconstruction planes of each term is function of the focal length f of the multiplexed lens, the holographic image quality is also affected by this parameter. The optimization results, to simultaneously maximize orders separation and holographic image contrast, are presented in Figure S14.

Supplementary figures

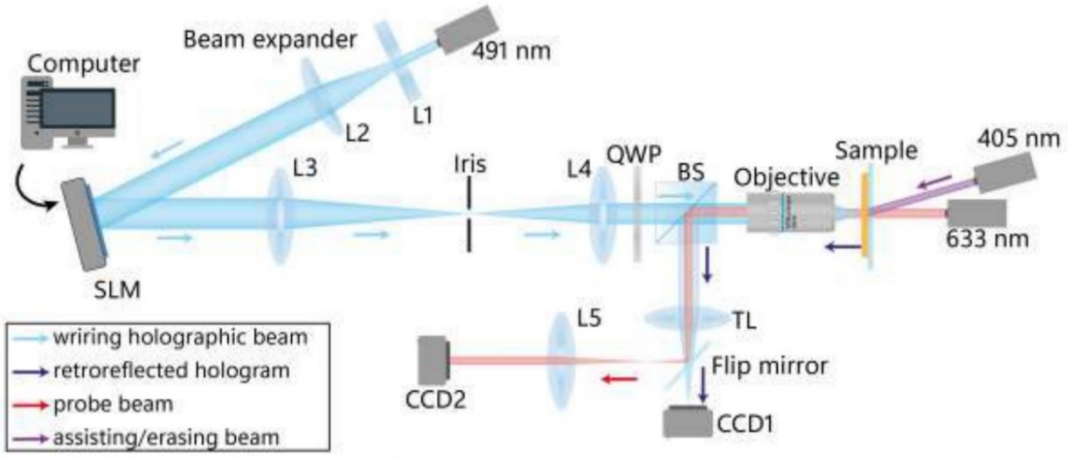

Figure S1: Schematic of the experimental setup:
Beam expander - lenses *L*1 (f1=-50 mm) and *L*2 (f2=250 mm).
SLM - Holoeye Pluto, LCOS spatial light modulator, phase only (reflective).
4f configuration - lenses *L*3, (f3=300 mm) and *L*4 (f2=175 mm).
QWP - quarter wave plate.
BS - 70/30 beam splitter.
Objective - 50X Mitutoyo Plan Apo Infinity Corrected Long WD Objective.
TL - tube lens (fTL=200 mm).
Fourier transforming lens - lens *L*5, (f5=300 mm).
CCD1/2 - "DCC3240M Thorlabs" camera.

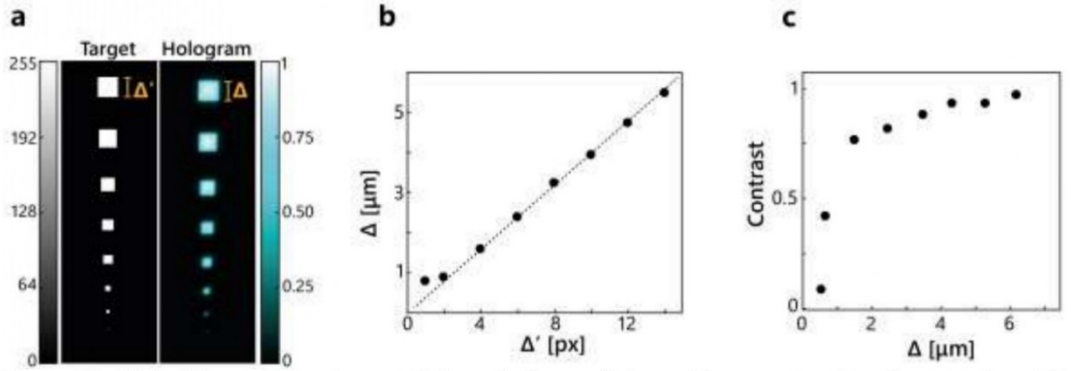

Figure S2: Holo-lithographic setup spatial resolution: a Holographic reconstruction of square shaped light patterns with lateral size Δ. **b** Square size Δ as function of designed size Δ'. The slope $b = 0.376 \pm 0.002\ \mu m$ of the fitted line trend $\Delta = b\Delta'$ defines the calibration of physical dimensions with respect to the analytically designed target images. **c** Contrast of the holographic reconstructed square as function of lateral size Δ. Contrast is defined as $C = (I_W + I_B)/(I_W - I_B)$ with I_W and I_B representing the average experimental intensity levels corresponding to white and black areas of the target image, respectively. Resolution limit is reasonably set to $\Delta_0 = 5b = 1.88\ \mu m$.

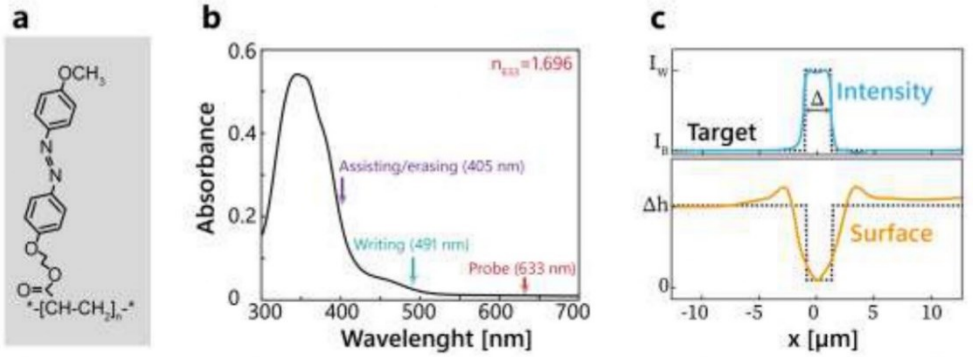

Figure S3: Azopolymer optical characterization. a Azopolymer structural formula. **b** Absorbance in the UV-visible range. Refractive index at probe wavelength $\lambda_p = 633\ nm$ was measured via ellipsometry. **c** Azopolymer response to an intensity structured field with designed lateral size $\Delta = 1.88\ \mu m$.

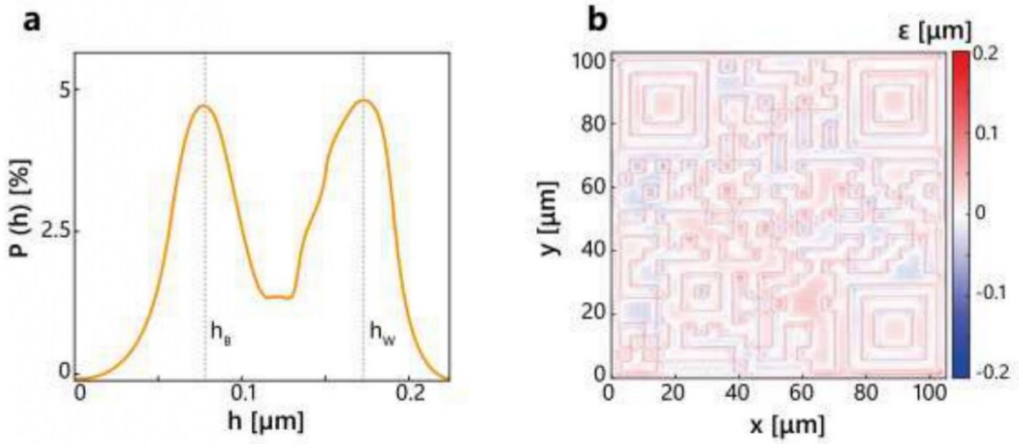

Figure S4: Mismatch error characterization for QR code structure: a Height distribution probability: each point of the line plot represents the probability $P(h)$ of having a fixed height value h in the AFM image. **b** Error map $\epsilon(x,y) = h^{target}(x,y) - h^{exp.}(x,y)$. Target heigh profile is obtained from the heigh distribution, binarizing the experimental AFM map and using h_0 and h_1 as target height levels. For a quantitative mismatch error estimation, the root mean square error has used, defined as: $RMSE = \left[\sum_{x,y} \frac{\epsilon(x,y)^2}{N^2}\right]^{\frac{1}{2}}$, where N is the size of the image.

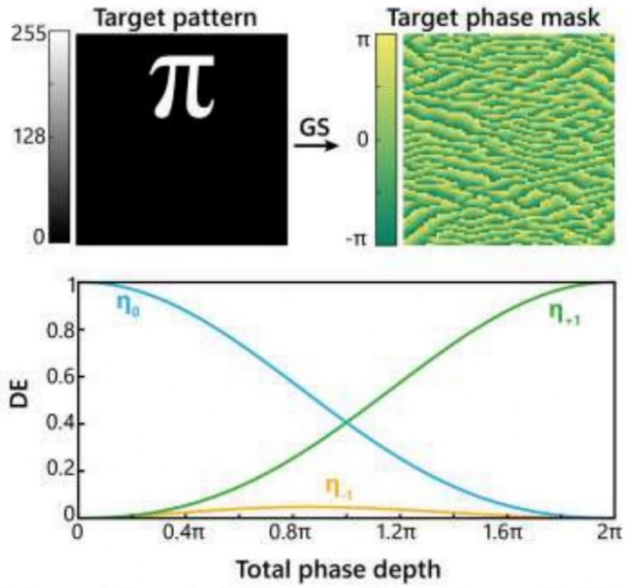

Figure S5: Kinoform design and theoretical diffraction efficiency from an ideal kinoform as function of the phase mismatch error.

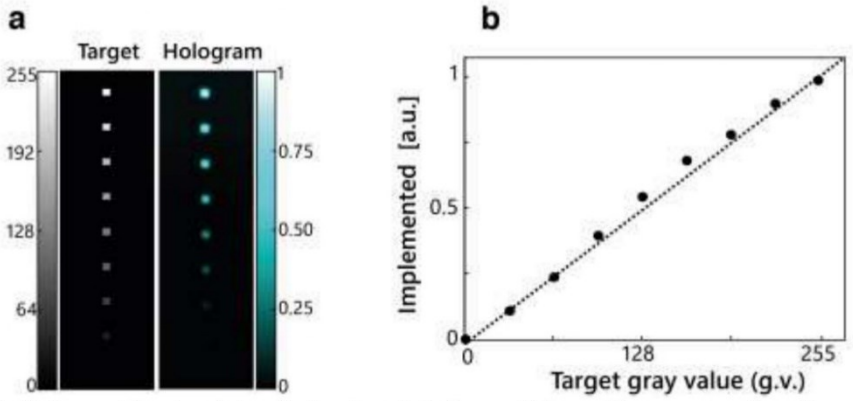

Figure S6: Holographic setup intensity level modulation: a Holographic reconstruction of square shaped light pattern with lateral size $\Delta = 1.88\ \mu m$ and linearly spaced gray levels. **b** Implemented intensity levels as function of the addressed gray value in the target image. The line trend has a slope equal to $0.077\ (a.u.)$.

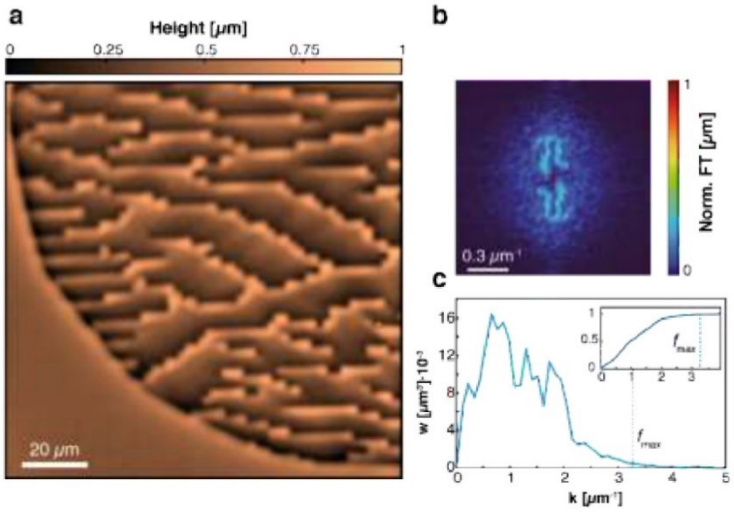

Figure S7: Morphological characterization of the surface kinoform: a AFM scan of a quarter portion of the structured surface ($100\ X\ 100\ \mu m$) collected right after the exposure process. **b** Fourier transform of the surface topography, representing the spatial frequency distribution of the inscribed surface pattern. **c** Plot of the Power Spectral Density (PSD) ($w(k)$) of the Fourier transform image. The maximum frequency f_{max} was determined satisfying the (arbitrary) condition $I\big(w(f_{max})\big) = 0.990$, where I is the cumulative integral function of the PSD, plotted in the inset of the panel c. We obtained $f_{max} = (3.22 \pm 0.03)\ \mu m^{-1}$, corresponding to a pixel size of $\Delta_{\mathrm{surf}} = 2\pi/f_{max} = (1.95 \pm 0.02)\ \mu m$. This value is in full agreement with the optical minimum feature size Δ we designed in the grayscale pattern, defined in Figure S2.

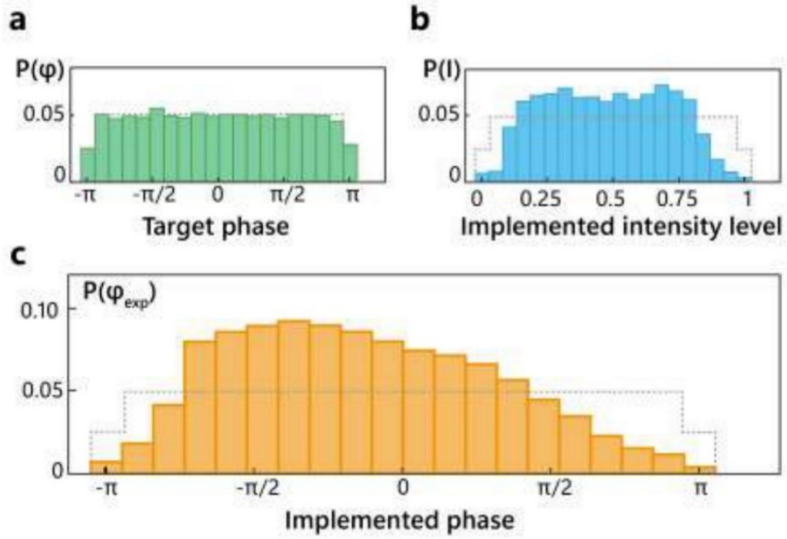

Figure S8: Phase distribution transferring accuracy: a Phase distribution probability in the target phase map resulting from GS algorithm. **b** **I**ntensity distribution probability in the holographic pattern. **c** Implemented phase distribution retrieved from the AFM image. For visual clarity, data are binned in $N = 20$ bins.

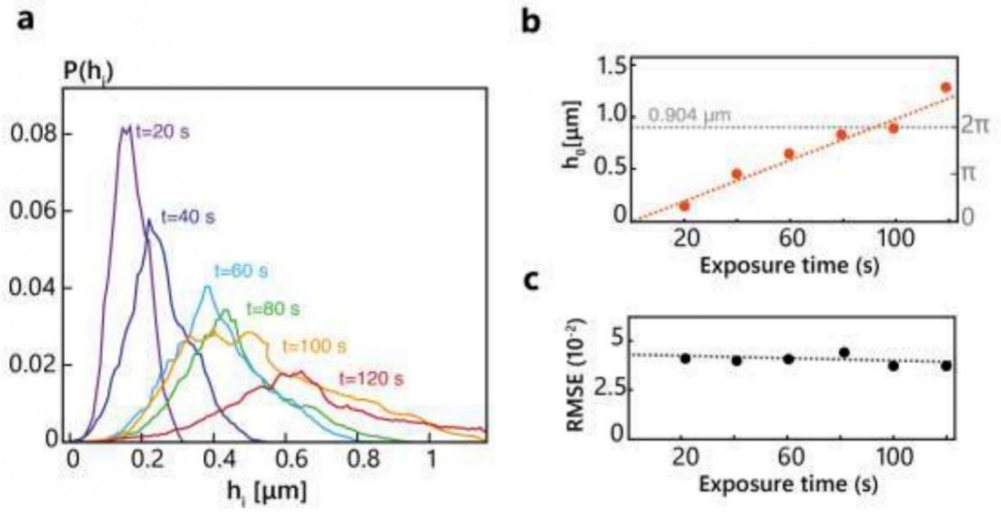

Figure S9: Temporal characterization of structured surfaces: a Height distribution for six different exposure times. **b** Modulation depth Δh as function of the total exposure time. Experimental data are fitted with the model trend $h_0 = c \cdot t$, allowing for the experimental determination of the surface inscription efficiency $c = 10.5 \pm 0.5\ nm/s$. Right gray axis shows the implemented phase depth for a probe wavelength λ_P. **c** Root Mean Square Error defined as RMSE $= \sqrt{\sum_N (P_i - \bar{P})^2}$ as function of the total exposure time. $\bar{P}$ represents the target uniform distribution expected at different exposure times.

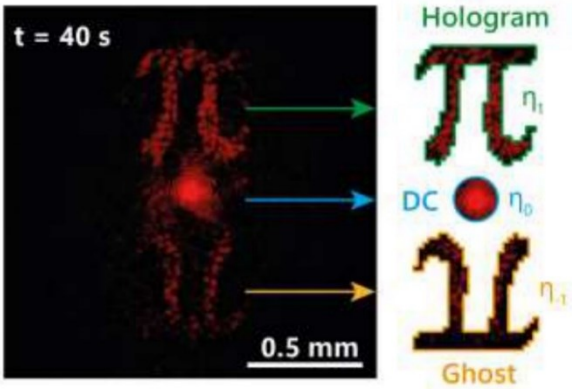

Figure S10: Experimental determination of diffraction efficiency η_i determined by integrating the CCD signal over the regions of interest delimited by the colored trace in the image. Green area corresponds to the holographic image efficiency while light blue and orange area correspond to the DC order and ghost image, respectively.

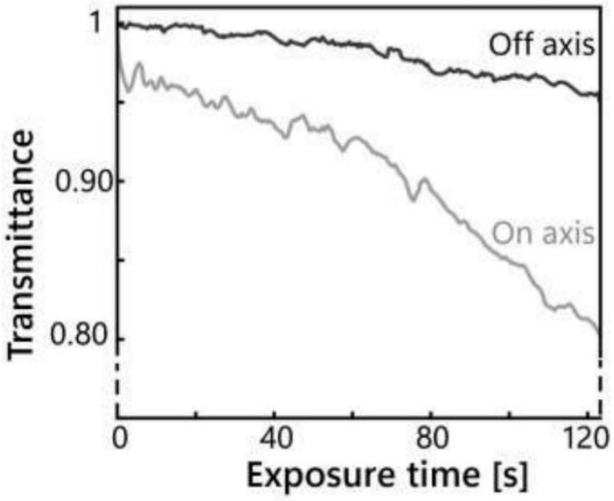

Figure S11: Kinoform transmittance over exposure time determined by integrating the CCD signal over the full sensor size.

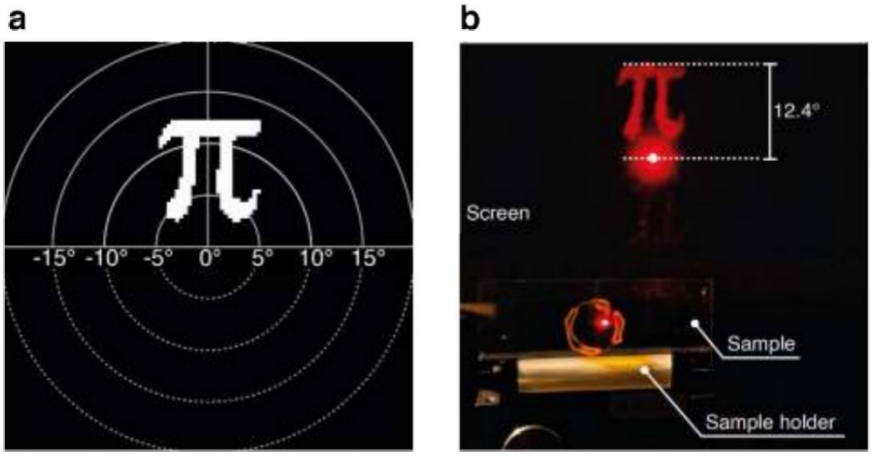

Figure S12: Holographic field-of-view and far-field image projection: **a** Target image used for the kinoform design, plotted with respect to the addressable diffraction angles by our surface at $\lambda_p = 0.633\,\mu m$. The maximum diffraction angle ϑ addressable by the surface can be derived from the Bragg's law: $\vartheta = \sin^{-1}(\lambda_p/\Delta)$, where $\Delta = 1.88\,\mu m$ is the pixel size imposed during the surface geometry design. For our system, the hologram field-of-view is $FoV = 2\vartheta = 39.4°$ at λ_p. **b** Photograph of the structured azo-resist film acting as a holographic projector. The image was taken by illuminating the structured area with a collimated laser beam at λ_p, collecting the resulting diffraction pattern on an opaque screen at a distance of 20 cm from the sample. The photo was taken with a smartphone camera with F1.8, 1/25s, ISO 640. The size of the holographic image measured on the screen provided the angle 12.4° for the outermost feature of the "π" image, which agrees with the expected theoretical value given in panel a.

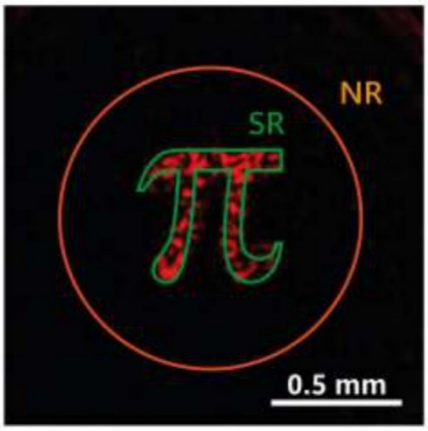

Figure S13: Experimental determination of pattern visibility: visibility is defined as $\mathcal{V} = (I_{SR} + I_{NR})/(I_{SR} - I_{NR})$ where I_{SR} is the average intensity inside the signal region (green area) and I_{NR} is the average noise level outside the holographic image. The orange area has a diameter equal to two times the size of the holographic image.

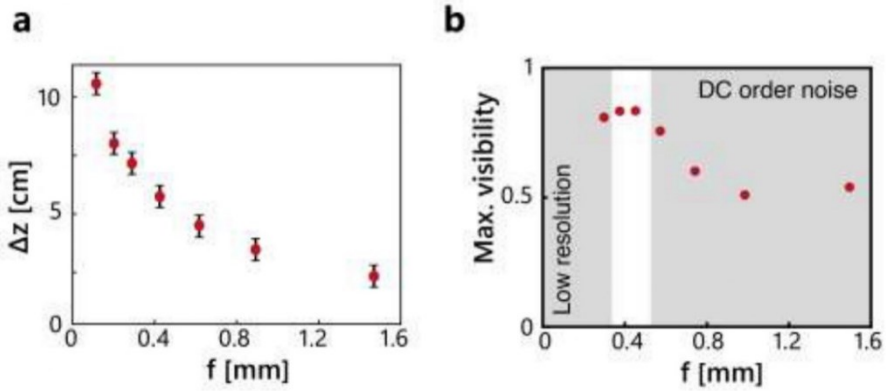

Figure S14: Optimization of multiplexed spherical profile: a Axial shifting Δz of the holographic image as function of the spherical phase profile parameter f. **b** Maximum visibility achieved with different spherical phase profile parameter f. Best value for multiplexed focal length is $f = 0.450\ mm$, allowing for high visibility and reasonable orders separation.

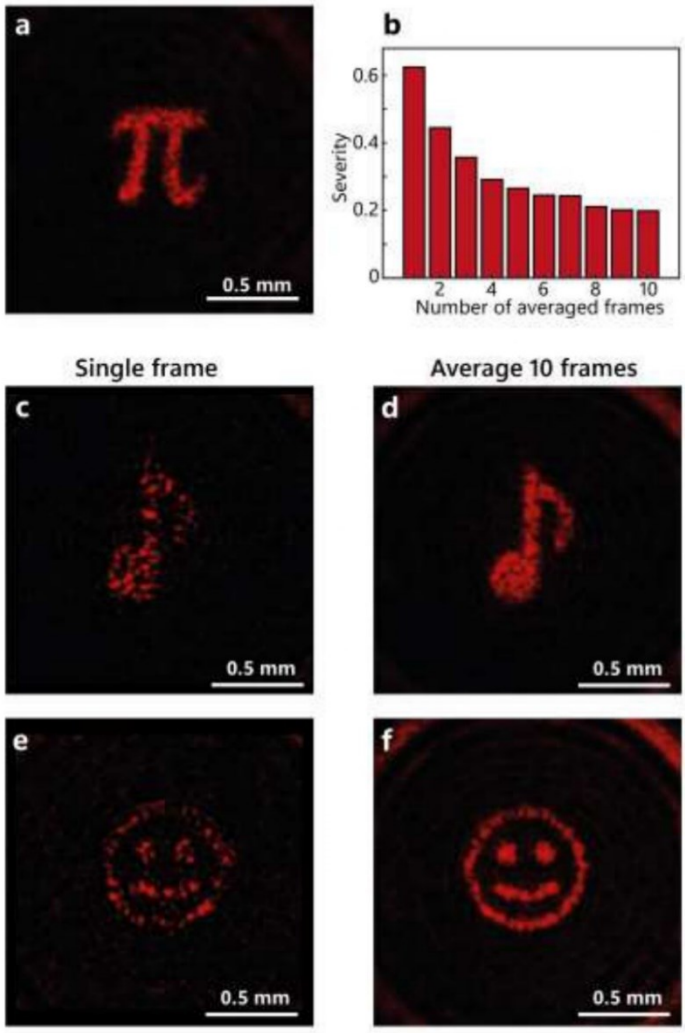

Figure S15: Speckle contrast reduction process by holograms time averaging: a Average holographic pattern acquired after 10 writing/erasing cycles representing the on-axis image of the Greek letter "π". **b** Speckle noise severity as function of the number of averaged frames. Severity is defined as $S = \sigma/\langle I \rangle$ where $\langle I \rangle$ is the mean intensity and σ is its standard deviation measured in the image domain. **c-d** Single frame and average holographic pattern acquired after 10 writing/erasing cycles representing the on-axis image of a music note and **e-f** a smile face.

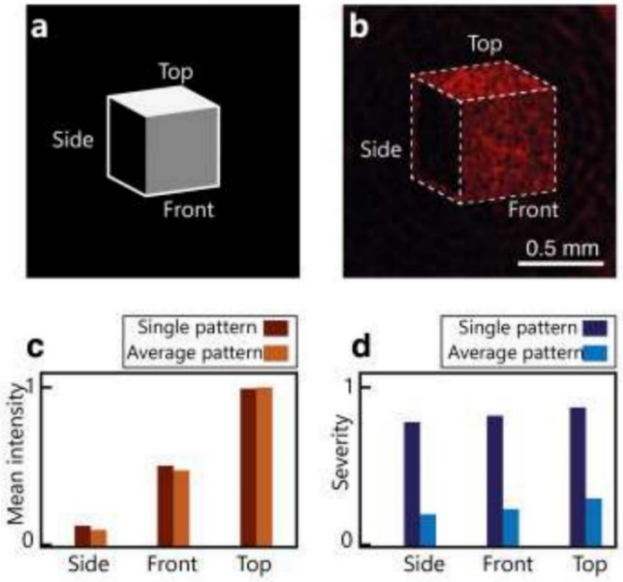

Figure S16: Speckle analysis of a time-averaged grayscale pattern: a Target image. **b** Resulting average holographic pattern acquired after 10 writing/erasing cycles. **c** Comparison between the mean intensity level of three cube faces for the single frame and the time average. **d** Comparison between the speckle severity of three cube faces for the single frame and the time average.

Char	Decimal	Trit		
space	0	0	0	0
A	1	0	0	1
B	2	0	0	2
C	3	0	1	0
D	4	0	1	1
E	5	0	1	2
F	6	0	2	0
G	7	0	2	1
H	8	0	2	2
I	9	1	0	0
J	10	1	0	1
K	11	1	0	2
L	12	1	1	0
M	13	1	1	1
N	14	1	1	2
O	15	1	2	0
P	16	1	2	1
Q	17	1	2	2
R	18	2	0	0
S	19	2	0	1
T	20	2	0	2
U	21	2	1	0
V	22	2	1	1
W	23	2	1	2
X	24	2	2	0
Y	25	2	2	1
Z	26	2	2	2

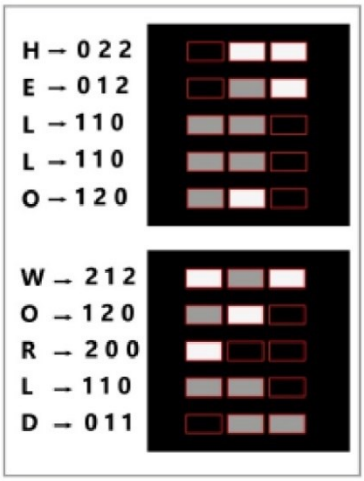

Figure S17: Lookup table for encryption and decryption of optical messages encoded as trits. Images on the right were used as input for IFTA in order to retrieve the target kinoform design to be implemented on the azo-resist surface.